FRIEDRICH-SCHILLER-
UNIVERSITÄT
JENA

The enhanced delivery of biologically active substances by tailor-made polymers

Dissertation

(kumulativ)

zur Erlangung des akademischen Grades

doctor rerum naturalium (Dr. rer. nat.)

vorgelegt dem Rat der Chemisch-Geowissenschaftlichen Fakultät

der Friedrich-Schiller-Universität Jena

von M.Sc. Tanja Buś

geboren am 01.09.1989 in Hildburghausen

Gutachter:

1. Prof. Dr. Ulrich S. Schubert, Friedrich-Schiller-Universität Jena
2. Prof. Dr. Thomas Heinze, Friedrich-Schiller-Universität Jena

Tag der öffentlichen Verteidigung: 29.03.2019

Table of contents

Documentation of authorship

This section contains a list of individual authors' contributions to the publications reprinted in this thesis. ‡ Equal contribution to both authors.

Pub1	T. Bus,[1] A. Traeger,[2] U. S. Schubert,[3] The great escape: How cationic polyplexes overcome the endosomal barrier, *J. Mater. Chem. B* **2018**, 6, 6904-6918.		
Author	**1**	**2**	**3**
Conceptual development	×		
Preparation of the manuscript	×		
Correction of the manuscript		×	×
Supervision of T. Bus		×	×
Proposed publication equivalent	0.5		

Pub2	A.-K. Trützschler,[1, ‡] T. Bus,[2, ‡] M. Reifarth,[3] J. C. Brendel,[4] S. Hoeppener,[5] A. Traeger,[6] U. S. Schubert,[7] Beyond gene transfection with methacrylate-based polyplexes – the influence of the amino substitution pattern, *Bioconjugate Chem.* **2018**, *29*, 2181-2194.						
Author	**1**	**2**	**3**	**4**	**5**	**6**	**7**
Conceptual development	×	×				×	
Polymer synthesis	×						
Polymer characterization	×						
Polyplex formation & characterization		×					
Biological investigations *in vitro*		×					
STEM images			×				
Preparation of the manuscript	×	×					
Correction of the manuscript			×	×	×	×	×
Supervision of A.-K. Trützschler						×	×
Supervision of T. Bus						×	×
Proposed publication equivalent		1.0					

Pub3	A.-K. Trützschler,[1] T. Bus,[2] M. Sahn,[3] A. Traeger,[4] C. Weber,[5] U. S. Schubert,[6] The power of shielding: Low toxicity and high transfection performance of cationic graft copolymers containing poly(2-oxazoline) side chains, *Biomacromolecules* **2018**, *19*, 2759-2771.						
Author	**1**	**2**	**3**	**4**	**5**	**6**
Conceptual development	×				×	
Polymer synthesis	×					
Polymer characterization	×					
POx macromonomer preparation			×			
Biological investigations *in vitro*		×				
Preparation of the manuscript	×					
Correction of the manuscript		×		×	×	×
Supervision of A.-K. Trützschler				×	×	×
Supervision of T. Bus				×		×
Proposed publication equivalent		0.5				

Pub4	T. Bus,[1, ‡] C. Englert,[2, ‡] M. Reifarth,[3] P. Borchers,[4] M. Hartlieb,[5] A. Vollrath,[6] S. Hoeppener,[7] A. Traeger,[8] U. S. Schubert,[9] 3rd Generation poly(ethylene imine)s for gene delivery, *J. Mater. Chem. B* **2017**, *5*, 1258-1274.								
Author	**1**	**2**	**3**	**4**	**5**	**6**	**7**	**8**	**9**
Conceptual development	×	×			×	×		×	
Polymer and material synthesis		×		×					
Polymer and material characterization		×		×					
Biological investigations *in vitro*	×								
Microscopy studies	×		×						
Preparation of the manuscript	×	×							
Correction of the manuscript			×		×		×	×	×
Supervision of C. Englert									×
Supervision of T. Bus								×	×
Proposed publication equivalent	1.0								

Pub5	C. Englert,[1, ‡] A.-K. Trützschler,[2, ‡] M. Raasch,[3] T. Bus,[4] P. Borchers,[5] A. S. Mosig,[6] A. Traeger,[7] U. S. Schubert,[8] Crossing the blood-brain barrier: Glutathione-conjugated poly(ethylene imine) for gene delivery, *J. Control. Release* **2016**, *241*, 1-14.								
Author		**1**	**2**	**3**	**4**	**5**	**6**	**7**	**8**
Conceptual development		×	×	×	×		×	×	
Polymer synthesis and characterization		×	×			×			
Biological investigations *in vitro*					×				
Microchip investigations				×					
Preparation of the manuscript		×	×						
Correction of the manuscript				×	×		×	×	×
Supervision of C. Englert									×
Supervision of A.-K. Trützschler								×	×
Supervision of T. Bus								×	×
Proposed publication equivalent					0.5				

Pub6	I. Yildirim,[1] T. Bus,[2] M. Sahn,[3] T. Yildirim,[4] D. Kalden,[5] S. Hoeppener,[6] A. Traeger,[7] M. Westerhausen,[8] C. Weber,[9] U. S. Schubert,[10] Fluorescent amphiphilic heterografted comb polymers comprising biocompatible PLA and PEtOx side chains, *Polym. Chem.* **2016**, *7*, 6064-6074.										
Author		**1**	**2**	**3**	**4**	**5**	**6**	**7**	**8**	**9**	**10**
Conceptual development		×								×	
Polymer synthesis and characterization		×									
Biological investigations *in vitro*			×								
POx macromonomer preparation				×							
DLS measurements					×						
Catalyst/Co-initiator synthesis						×					
Cryo-TEM measurement							×				
Preparation of the manuscript		×									
Correction of the manuscript			×	×	×	×	×	×	×	×	×
Supervision of I. Yildirim										×	×
Supervision of T. Bus								×			×
Proposed publication equivalent			0.5								

Pub7	M. Hartlieb,[1, ‡] T. Bus,[2, ‡] J. Kübel,[3] D. Pretzel,[4] S. Hoeppener,[5] M. N. Leiske,[6] K. Kempe,[7] B. Dietzek,[8] U. S. Schubert,[9] Tailoring cellular uptake and fluorescence of poly(2-oxazoline)-based nanogels, *Bioconjugate Chem.* **2017**, *28*, 1229-1235.								
Author	**1**	**2**	**3**	**4**	**5**	**6**	**7**	**8**	**9**
Conceptual development	×								
Polymer synthesis	×								
Polymer characterization	×		×		×				
Biological investigations *in vitro*		×		×					
Preparation of the manuscript	×								
Correction of the manuscript		×	×	×	×	×	×	×	×
Supervision of M. Hartlieb							×		×
Supervision of T. Bus									×
Proposed publication equivalent		0.75							

Pub8	D. Hoelzer,[1, ‡] M. N. Leiske,[2, ‡] M. Hartlieb,[3] T. Bus,[4] D. Pretzel,[5] S. Hoeppener,[6] K. Kempe,[7] R. Thierbach,[8] U. S. Schubert,[9] Tumor targeting with pH-responsive poly(2-oxazoline)-based nanogels for metronomic doxorubicin treatment, *Oncotarget* **2018**, *9*, 22316-22331.								
Author	**1**	**2**	**3**	**4**	**5**	**6**	**7**	**8**	**9**
Conceptual development	×		×		×		×	×	
Polymer and material synthesis		×	×						
Polymer and material characterization		×				×			
Biological investigations *in vitro*				×					
Biological investigations *in vivo*	×	×							
Preparation of the manuscript	×	×	×						
Correction of the manuscript				×	×	×	×	×	×
Supervision of D. Hoelzer								×	
Supervision of M. N. Leiske			×						×
Supervision of T. Bus									×
Proposed publication equivalent				0.5					

Erklärung zu den Eigenanteilen der Promovendin sowie der weiteren Doktoranden/Doktorandinnen als Koautoren an den Publikationen und Zweitpublikationsrechten bei einer kumulativen Dissertation

Für alle in dieser kumulativen Dissertation verwendeten Manuskripte liegen die notwendigen Genehmigungen der Verlage („Reprint permissions“) für die Zweitpublikation vor.

Die Co-Autoren der in dieser kumulativen Dissertation verwendeten Manuskripte sind sowohl über die Nutzung, als auch über die oben angegebenen Eigenanteile der weiteren Doktoranden/Doktorandinnen als Co-Autoren an den Publikationen und Zweitpublikationsrechten bei einer kumulativen Dissertation informiert und stimmen dem zu.

Die Anteile der Promovendin sowie der weiteren Doktoranden/Doktorandinnen als Co-Autoren an den Publikationen und Zweitpublikationsrechten bei einer kumulativen Dissertation sind in den vorausgehenden Tabellen aufgeführt.

Tanja Buś _____ Jena, _____

Ich bin mit der Abfassung der Dissertation als publikationsbasiert, d.h. kumulativ, einverstanden und bestätige die vorstehenden Angaben. Eine entsprechend begründete Befürwortung mit Angabe des wissenschaftlichen Anteils des Doktoranden/der Doktorandin an den verwendeten Publikationen werde ich parallel an den Rat der Fakultät der Chemisch-Geowissenschaftlichen Fakultät richten.

Prof. Dr. Ulrich S. Schubert _____ Jena, _____

1. Introduction

Nanotechnology, a key technology of the 21th century, encompasses cross-cutting research in classical sciences including physics, chemistry, biology as well as modern engineering to generate smart molecules at the nanoscale. Nowadays, nanomedicine is one of the most demanded and promising sub-disciplines within the broad field of nanotechnology. The classical way of administering pharmaceuticals as pure substances often shows limited clinical efficacy characterized by low bioavailability, limited circulating half-lives or unspecific toxicity profiles. Nanomedicines are capable to improve the delivery of therapeutically relevant molecules including imaging agents, drugs, nucleic acids, proteins or theranostics to effectively diagnose, treat or prevent diseases as well as injuries.[1] The delivery of these biologically active substances is accomplished by vectors or so-called nanocarriers, which are predominantly based on polymers, liposomes, nanocrystals or inorganic materials.[2-3] Since the first approval of the nanodrug Doxil® in the USA in 1995, more than 50 novel nanomedicines have been approved by the U. S. Food and Drug Administration (FDA) as well as the European Medicines Agency (EMA) to date. However, even more potent products are in the pipelines of pre-clinical research or under investigation in clinical trials, but high obstacles through regulatory guidelines limit a fast approval.[3-4]

Due to the broad diversity of chemical compositions with tunable functionalities and, consequently, varying physicochemical characteristics including size, shape and surface properties, polymers represent a manifold platform for tailor-made delivery systems. These features facilitate (i) the bioavailability of (critical) substances to be delivered, (ii) the protection of the cargo from enzymatic degradation, acid hydrolysis or tissue/organ-specific clearance, (iii) the extrinsic or intrinsic targeting specificity, and (iv) the controlled release of the active substances. Dependent on the biomedical approach, the delivery strategy of polymeric nanocarriers is commonly distinguished into gene delivery, *i.e.*, the transport of nucleic acids (pDNA, siRNA, mRNA, *etc.*) or into drug delivery, *i.e.*, the transport of hydrophilic and hydrophobic pharmaceuticals. Despite their benefits and promises, multiple barriers have to be overcome by the polymeric nanocarriers during the delivery process. These obstacles are defined by their chemical composition with corresponding characteristics but also by various biological barriers. Challenges that have to be met are (i) the successful and efficient encapsulation

of the cargo into stable nanocarriers, (ii) the interaction of the nanocarrier with cellular membranes followed by an internalization and (iii) the transport of the carrier to its intracellular site of action with successful release of the cargo (Figure 1.1).[5-6] Although gene and drug nanocarriers share similar biological barriers at the cellular level, they differ in their delivery performances due to their physicochemical characteristics. These differences are evident not only in the formulation of the loaded nanocarriers but also in the energy-dependent uptake mechanism (active *vs*. passive) as well as the kind and site of cargo release by corresponding stimuli (Figure 1.1).

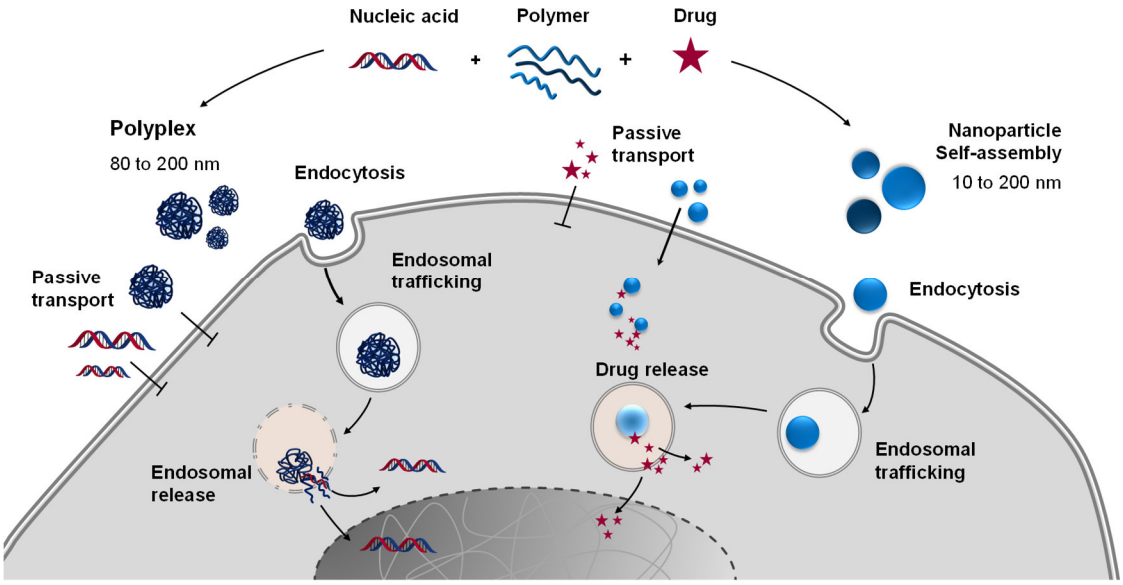

Figure 1.1. Schematic overview of polymer-mediated gene and drug delivery including nanocarrier formulation, cellular internalization and intracellular trafficking.

The principal aim of gene therapy is the delivery of therapeutic nucleic acids to treat hereditary diseases, such as heamophilia, but also acquired diseases including infections or cancer.[1, 7] Besides viral- or lipid-based systems, polymers represent promising alternatives for the delivery of therapeutic nucleic acids, since they provide a variety of architectures with tailored functionalities, show low immunogenicity and can be produced cost-efficiently on a large scale in combination with the need of comparatively simple storage conditions. A straightforward strategy to deliver nucleic acids is the formation of polyelectrolyte complexes or so-called polyplexes due to electrostatic interactions (Figure 1.1).[8] In particular, long and circular DNA (*e.g.*, pDNA) is efficiently encapsulated by condensation into small and compact structures, whereas the

complexation of DNA or RNA molecules comprising only a few base pairs (*e.g.*, siRNA) is more challenging due to their intrinsic rigid structure and low spatial charge density.[9] Polyplexes typically exhibit sizes between 80 to 200 nm and, therefore, are too large for a passive uptake mechanism. They predominantly enter cells by various energy-dependent endocytic pathways.[10-11] Once internalized, gene delivery vectors have to escape from the membrane-bound endocytic vesicles for the successful delivery to their specific site of action, *i.e.*, cell nucleus or cytoplasm (Figure 1.1).[12]

A detailed explanation of the biological barriers during the polyplex-mediated gene delivery process with emphasis on the characteristics and pitfalls of endocytic pathways including the cellular internalization, the endosomal release and the transport of the nucleic acid to its site of action will be given in *Chapter 2*.

The development in the polymer design for gene therapy approaches increased in the last decades.[13-14] More than 20 years ago, the polycations poly(L-lysine) (PLL), poly(amidoamine) (PAMAM) dendrimers, poly(ethylene imine) (PEI) or poly(2-dimethylamino)ethyl methacrylate (PDMAEMA) became established and well-characterized polymers for the delivery of nucleic acids *in vitro* (Figure 1.2 A).[15]

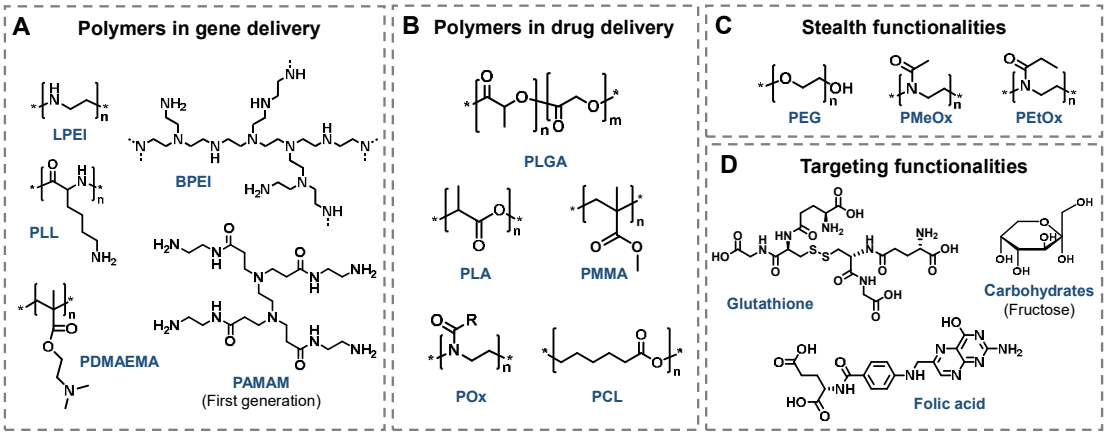

Figure 1.2. Schematic representation of an overview of polymers used in gene and drug delivery with stealth and targeting moieties for enhanced delivery performances. Selected polymers or polymer classes are described in the following chapters.

In particular PEI, which exists as a linear (LPEI) and branched (BPEI) form, reveals outstanding transfection efficiencies and, thus, is considered as the "gold standard" for transfection.[16-17] The good transfection efficiency is attributed to the high cationic

charge density based on the polyelectrolyte structure bearing (different) amino groups. This feature was shown to be beneficial in terms of polyplex formation, the affinity to cellular membranes followed by endocytosis as well as the endosomal escape. In general, the binding ability of polymers to nucleic acids was attributed to primary as well as secondary amino groups (PLL, PEI, PAMAM), while tertiary amino groups (PDMAEMA, PAMAM) are thought to be beneficial for buffering capacity and, thus for an efficient endosomal escape. However, the high charge density of these polymers leads to severe cytotoxic effects, which harm the membrane integrity or the metabolic activity of cells.[18-20] A concept to circumvent such undesired side effects is the introduction of biocompatible stealth polymers into the polymer structure (Figure 1.2 C). The most prominent representative with a stealth effect is the non-ionic polymer poly(ethylene glycol) (PEG). PEG facilitates the water solubility as well as the reduction of cytotoxicity, aggregation affinity and unspecific interactions with cellular or non-cellular components due to the decrease in the surface charge and steric hinderance to the access to functional groups.[21-22] Despite its widespread utilization, it was recently revealed that PEG is able to increase immunogenicity and antigenicity.[23-24] A highly suitable alternative to PEG are the non-ionic, water soluble poly(2-oxazoline)s (POx): Poly(2-ethyl-2-oxazoline) (PEtOx) and poly(2-methyl-2-oxazoline) (PMeOx). Their stealth effect is considered to be responsible for the reduction of unspecific interactions with non-cellular and cellular components, elongated blood circulation times, low immunogenicity and reduced clearance *in vivo*.[25-26] Despite their beneficial impact, the functionalization of polymers with PEG or POx bears the risk of diminished transfection efficiencies due to weak nucleic acid complexation and decreased cell interactions by the cell- and protein-repellent properties.[27-28] This phenomenon is known as the "PEG dilemma" and should be take into account for the design of polymers. Another common strategy to improve the specificity of the nanocarriers is the introduction of targeting ligands within the polymer structure (Figure 1.2 D).[10, 29] A large variety of natural receptor substrates are used for the targeting of specific cells, tissues or organs. Cancer cells, for instance, can be targeted by carbohydrates (breast cancer)[30] or folic acid (ovarian, colorectal cancer).[10, 29] A great challenge in gene delivery is the passage of the blood-brain barrier to target the brain. This can be realized, for instance, by the use of glutathione ligands.[31-32] Nevertheless, in contrast to viral vectors, a commercial breakthrough as nanomedicines is still missing. A deeper understanding of the chemical composition and the structure-property-relationship of polyplexes on the molecular as

well as on the cellular level is required in order to exploit the full potential of this promising technology.

Chapter 3 provides new insights into the influence of different amino functionalities as well as PEtOx stealth moieties on the overall gene delivery process utilizing well-defined homo- and copolymers based on poly(methacrylate)s and linear poly(ethylene imine)s (LPEI). Detailed information about the ideal amino substitution pattern for the most efficient transfection *via* poly(methacrylate)s is provided in *Chapter 3.1*. Furthermore, the potential of PEI-based copolymers for targeted gene delivery by the introduction of a therapeutic relevant ligand is highlighted in *Chapter 3.2*.

In contrast to the delivery of genetic material, polymeric vectors for drug delivery must meet different requirements to provide improved biocompatibility, pharmacokinetics, target specificity as well as a controlled release behavior. The loading of hydrophilic or hydrophobic drugs can be accomplished by the conjugation to the polymer molecule, encapsulation, covalent attachment or adsorption into as well as onto nanoparticles.[33-34] Drug carriers are mostly internalized into cells by endocytosis similar to polyplexes. However, some carriers are able to enter cells by the passive penetration of the cell membrane if their sizes are below 20 nm in diameter.[35] Polymeric drug vectors exhibit stimuli-responsive degradation properties that enable the controlled release of the drug. The (bio)degradation can be of chemical or enzymatic origin and can be triggered by pH value, temperature, ionic strength or enzymatic substrate stimuli.[34, 36] Synthetic polymers utilized for the formulation of nanocarriers are for example poly(lactic acid) (PLA), poly(lactic-*co*-glycolic acid) (PLGA), poly(*ε*-caprolactone) (PCL) or poly((meth)acrylate)s (*e.g.*, PMMA) (Figure 1.2 B).[36] The most extensively studied polymers for drug delivery are PLA and PLGA. They show high biocompatibility and have been approved by the FDA and EMA in drug formulations and medical devices.[37-38] The presence of hydrolytically labile ester bonds in the polymer backbone provides degradation abilities, which are beneficial for a controlled release kinetics of the active substance. Furthermore, drug delivery systems are often modified with biocompatible but non-degradable PEG or POx (Figure 1.2 C). The majority of polymer-based drug nanocarriers exploit non-specific accumulation within diseased tissue by passive targeting strategies. In particular, the popularity of anticancer nanomedicines is based on the enhanced permeability and retention (EPR) effect.[39] It is thought that nano-

scaled carriers with sizes between 30 to 200 nm preferably accumulate within the leaky vascular structure of tumor tissue leading to improved therapeutic effects.[40-41]

Chapter 4 is dedicated to the utilization of biodegradable and biocompatible polymers based on PLA and POx for the delivery of a range of molecules including fluorescent probes and a cytostatic agent.

The scope of this thesis is the evaluation of polymers and polymer derivatives as versatile vectors for the enhanced delivery of therapeutic relevant nucleic acids and drugs *in vitro* and *in vivo*. In addition to the structure-property relationship, the convenience of stealth polymers on the overall delivery process with focus on the cytocompatibility, the cellular internalization and trafficking as well as delivery efficiency is discussed in more detail.

2. Exploring the biological barriers for targeted gene delivery

Parts of this chapter have been published in **Pub1**: T. Bus, A. Traeger, U. S. Schubert, The great escape: How cationic polyplexes overcome the endosomal barrier, *J. Mater. Chem. B* **2018**, *6*, 6904-6918.

Along with the discoveries and developments in the field of polymer-based non-viral gene delivery within the last 50 years, powerful technology platforms were established with the aim to accelerate gene therapy concepts and to accomplish the vision of precision nanomedicine.[13] Several extra- as well as intracellular bottlenecks were identified within the entire polymer-mediated gene delivery process that, consequently, may impede the transfection efficiency. The most crucial (biological) barriers are illustrated in Figure 2.1 comprising (I) the nucleic acid packaging and the nanocarrier stability to protect the cargo against (enzymatic) degradation, (II) the internalization mechanism and the intracellular pathway, (III) the endo-lysosomal escape into the cytoplasm and, finally, (IV) the transport of the cargo to its site of action.[5, 42]

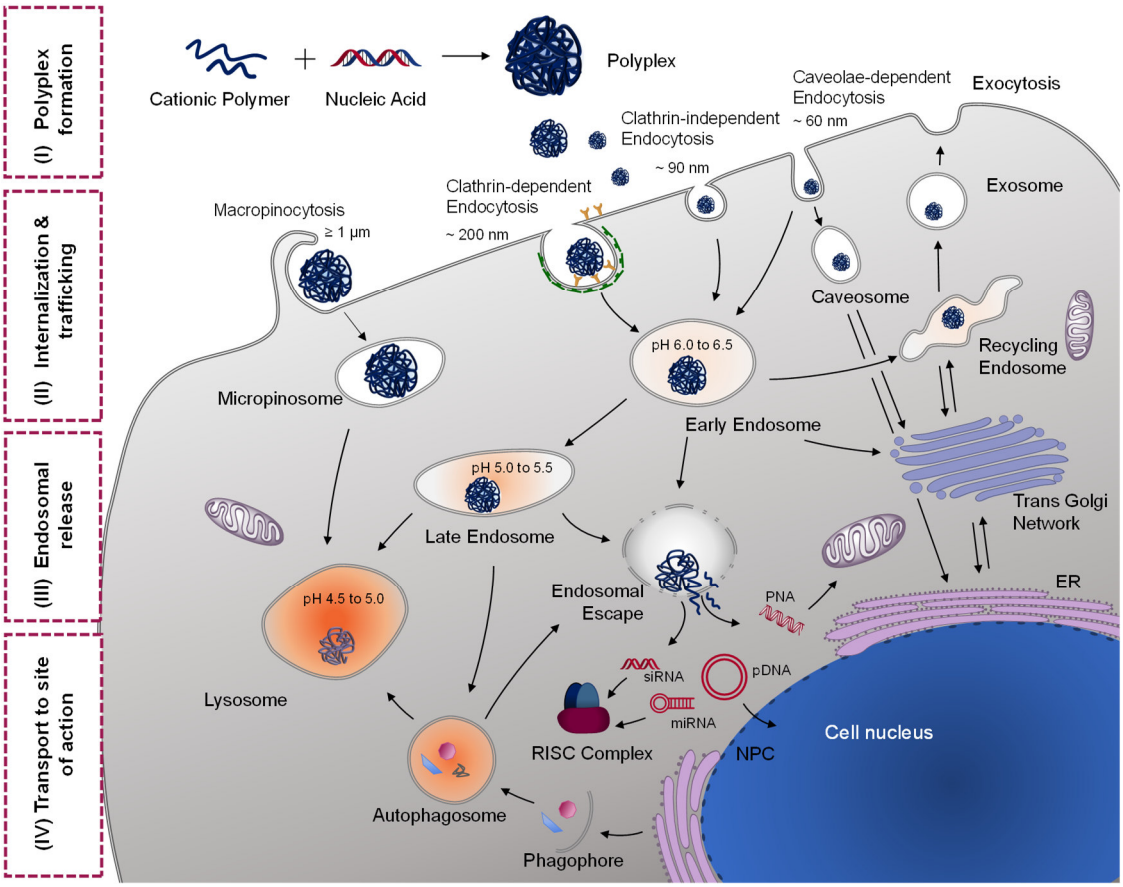

Figure 2.1. The general gene delivery process of cationic polymers at a glance. The barriers along this process are defined as (I) the nucleic acid packaging and nanocarrier formulation, (II) the cellular internalization by endocytosis and intracellular trafficking, (III) the endosomal escape from endo-lysosomal compartments and (IV) the transport of the cargo to its site of action. Dependent on the nature of the delivered nucleic acids, the site of action is either located within the cytoplasm (*e.g.*, siRNA, miRNA) or in the nucleus. NPC: nuclear pore complex; ER: endoplasmic reticulum.

Dependent on the nature and the characteristics of nucleic acids, different polymer-based strategies can be utilized to achieve a stable and protective packaging of the cargo as well as the safe and efficient delivery to its site of action.[43] The first two mentioned prerequisites can be accomplished by either (i) the electrostatically binding *via* complex formation, (ii) the encapsulation by means of particle formation, (iii) the covalent binding to the polymer structure, or (iv) the adsorption onto micro or nanospheres.[42, 44] Furthermore, the efficient and targeted delivery of nucleic acids *in vitro* and *in vivo* can be achieved by the introduction of functional moieties within the polymer structure or by the binding onto the carrier system including targeting ligands (carbohydrates,

peptides, vitamins, antibodies, *etc.*), labels or dyes, shielding domains (*e.g.*, stealth moieties) or endosomolytic units.[43, 45-46]

The most popular method for the delivery of nucleic acids by cationic polymers is the formation of polyelectrolyte complexes. Cationic polymers bear protonatable nitrogen atoms, responsible for the positive charge at physiological pH conditions. Hence, these protonated amino groups will electrostatically interact with the phosphate groups of the genetic material, which provokes the spontaneous self-organization of the so-called polyplexes (Figure 2.1, (I) polyplex formation). The N/P ratio, which represents the ionic balance within the polyplex, is defined as the number of nitrogen (N) of the polymer in relation to the number of phosphate groups of the nucleic acid (P). An excess of polymer, indicated by a high N/P ratio, has an essential impact on the surface charge, size as well as the stability of polyplexes and are recommended for successful gene delivery. Therefore, polyplexes mostly feature a positive net charge, which is beneficial for the affinity to the cell membrane. Interestingly, the phospholipid bilayer of the mammalian plasma membrane is predominantly composed of neutral lipids like glycerophospholipids, sphingolipids and sterols (*e.g.*, cholesterol).[47] The affinity of cationic polyplexes to the cell membrane is facilitated by the presence of anionic sulfated proteoglycans or receptors (e.*g.,* transferrin, epidermal growth factor).[48] After the attachment of the polyplex to the plasma membrane, the invagination of the plasma membrane leads to the entrapment of the polyplex into membrane-bound vesicles. This process is generally known as endocytosis and this broad term encompasses complex internalization mechanisms including clathrin-dependent, clathrin-independent, caveolae-mediated endocytosis as well as micropinocytosis (Figure 2.1, (II) internalization & trafficking).[45] It is known that the exact endocytosis mechanism of the nanocarrier is strongly dependent on its size and shape, as well as the type of polymer and type of cells.[11, 49-50] Both, clathrin-dependent as well as clathrin-independent endocytosis will result in the localization of polyplexes within early endosomes. Within these compartments the pH value quickly drops from neutral to lower pH values (6.5 to 6.0) due to the activity of membrane-bound vacuolar-type ATPases (V-ATPase, proton pump). The early endosomes are directed towards sorting endosomes destined either for recycling pathways back to the extracellular milieu (exocytosis) or to the lysosomal pathway resulting in an enzymatic digestion (Figure 2.1, (II) internalization & trafficking). In the latter case, the early endosomes will

maturate to late endosomes that are characterized by a pH environment of 5.5 to 5.0. Late endosomes are furthermore able to fuse with lysosomal compartments, which exhibit the most acidic milieu with pH values from 5.0 to 4.5. These conditions are optimal for the activity of lysosomal hydrolases and the degradation of the entrapped cargo. Besides this "classical" pathway, polyplexes can be furthermore internalized by the caveolae-mediated endocytosis, thus being located within caveosomes. In contrast to early and late endosomes, caveosomes exhibit a less hostile interior with a neutral pH environment (Figure 2.1, (II) internalization & trafficking). The motion of caveosomes was reported towards the Golgi apparatus and the endoplasmic reticulum (ER) *via* microtubules.[49] However, it was also reported that caveosomes are able to interact with early endosomes, thus getting involved in the acidification processes.[51] As the fate of the polyplexes and the related transfection efficiency is strongly dependent on the trafficking route, it is assumed that polyplexes should escape endocytic vesicles at an early stage of endocytosis, *i.e.*, previous to cellular expulsion or to the enzymatic degradation (Figure 2.1, (III) endosomal release). Several strategies were provided to overcome the endosomal entrapment. These includes the modification of the vector or the chemical composition by the introduction of various functional groups, fusogenic ligands, peptides, pH-sensitive polymer properties or photosensitive agents.[12, 46, 52] In the past decades, various studies were performed to explore the release mechanism of cationic polyplexes. The most popular endosomal escape mechanism of cationic polyplexes is the "proton sponge" hypothesis (Figure 2.2 A).[17, 53] It was the first effort to explain the outstanding transfection efficiencies of PEI in various cell lines, independent of the topology (branched, linear) and without the need of membrane-disruptive agents. The key characteristics of this hypothesis are (i) the build-up of an osmotic gradient within the endo-lysosomal lumen, (ii) the inhibition of the activity of degradative enzymes and (iii) the rupture of the vesicle membrane. In brief, once a polyplex is entrapped within an endo-lysosomal compartment the remaining non-protonated amino groups undergo further protonation, resulting in the buffering of the endosomal pH value and a slowed acidification. While, the V-ATPases try to maintain the proton gradient across the membrane and the acidification of the vesicle, an increased influx of chloride counter-ions leads to an osmotic imbalance.[54] This evolving imbalance is compensated by the continuous entrance of water, which causes the swelling of the endosome. This effect as well as the expansion of the polymer itself due to stronger repulsion effects results in a critical membrane tension and finally, in the

bursting of the endo-lysosomal compartment followed by the release of its cargo into the cytoplasm. This release mechanism was attributed to various cationic polymers containing protonatable amino groups, in particular secondary and tertiary amino functionalities, and a broad pH value buffering capacity ranging from pH values of 5.0 to 8.0. Hence, it was assumed that amino functionalized poly(methacrylate)s (*e.g.*, PDMAEMA)[55] and poly(amidoamine)s (*e.g.* PAMAM dendrimers)[56] act in a similar way as PEI. Although this hypothesis is still popular and frequently used in literature, it needs to be revised due to the lack of vital experimental data and several counter evidences.[57-59] In particular, the endosomal membrane rupture or membrane lysis was found to be highly implausible and was more or less disproved so far.[59] Certainly, all amino-containing polymers will act as a "proton sponge" by capturing a high amount of protons. Undoubtedly, pK_a values and high buffering capacities in the range of physiological and lysosomal pH values are necessary,[60-61] but do not seem to be the predominant factors for the efficient endosomal escape of polyplexes. Based on numerous experimental studies *in vitro* and *in silico*, further release strategies were discussed. Another hypothesis describes the endosomal escape by the direct charge-driven interaction of polyplexes with the exoplasmic membrane (Figure 2.2 B).[62-63] This interaction is thought to mediate local membrane destabilization and membrane permeability, which leads to the formation of nano-scaled holes.[6, 62] Hence, the polyplex or the nucleic acid is able to escape through these holes into the cytoplasm. In contrast to the "proton sponge" hypothesis, the endo-lysosomal compartment remains intact during and after the escape. Later on, a related version was proposed, explaining the endosomal escape of cationic polymeric vectors by the intercalation of free cationic polymer chains into the endosomal membrane (Figure 2.2 C).[64-65] It is hypothesized that a continuous dynamic equilibrium between polyplex dissociation and rebinding is an essential mechanism behind this hypothesis.[66-68] Free polymer chains, that dissociated from the polyplex, might intercalate into the cell plasma membrane prior to endocytosis. Hence, the polymer chains keep circulating in the membrane during the entire endocytosis and endosomal maturation process. The free polymer chains interact with the membrane in a so-called "carpet structure" or polymer-supported holes, thus, causing defects in the lipid membrane, which results in a leakage of molecules or nano-sized particles.[69-71] Additionally, this model may also explain cytotoxic effects of cationic polymers, in particular of PEI, found to harm the plasma membrane but also to permeabilize lipid membranes of mitochondria or the endoplasmic reticulum.[19, 72]

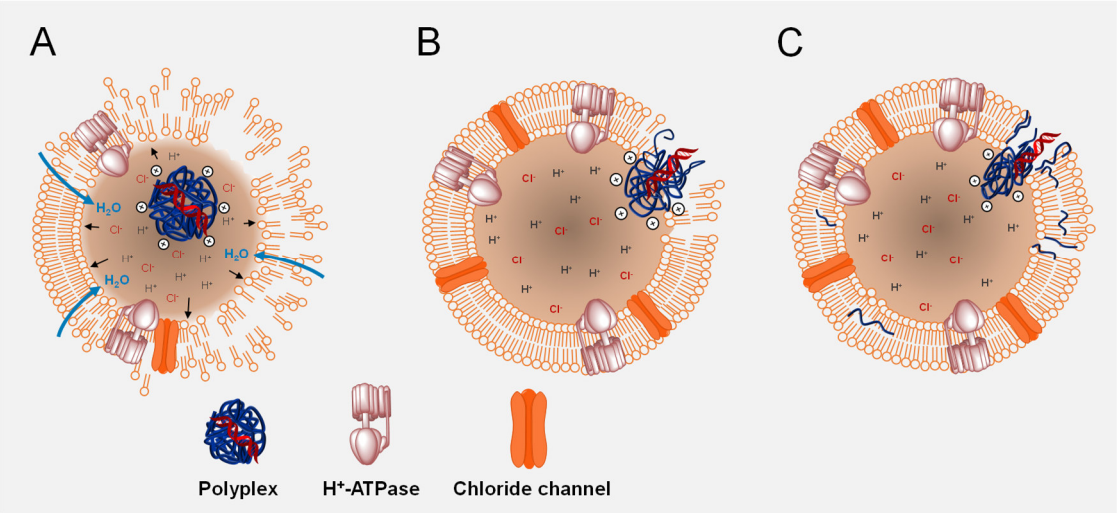

Figure 2.2. Graphical illustration of the different escape mechanism of polyplexes from endo-lysosomal compartments. **(A)** "Proton Sponge"-mediated escape: The protonated polyplex is located within the endo-lysosomal compartment and will cause a concentration gradient due to the influx of chloride ions, which is counteracted by the entrance of water resulting in the swelling of the endo-lysosomal compartment and, finally, to the endosomal burst and release of carrier and cargo into the cytoplasm. **(B)** Polyplex-mediated escape: The time-dependent protonation of amino groups in the acidic endo-lysosomal compartment leads to a charge-driven interaction of the polyplex with the exoplasmic membrane. Thus, causing membrane disintegration, permeability and local hole formation. The endo-lysosomal compartment remains intact. **(C)** Free polymer-mediated escape: Free cationic polymers intercalate into cell and vesicle membrane, thus causing membrane disintegration and permeability or polymer-supported hole formation. Endo-lysosomal compartment remains intact.

After efficient endosomal escape, the cargo needs to be released from its vector and transported to its site of action (Figure 2.1, (IV) transport to site of action). Up to now, it is still unclear if the cargo is completely released from its vector during the escape process or if the release occurs in the cytoplasm by anionic molecules, *e.g.*, cytoplasmic RNA or heparin-like glycosaminoglycans, or even within the nucleus.[73-74] In the case of different RNA types including siRNA and miRNA, the release within the cytoplasm is sufficient to create the RNA-induced silencing complex (RISC) and to exert their activity. In contrast to that, pDNA has to cover a relatively long distance through the cytoplasm to reach the nucleus. Thereby, a complete release of the nucleic acid from its vector within the periphery of the cytoplasm leads to the loss of protection and increases the risk of enzymatic degradation by nucleases. Furthermore, the motion of the naked DNA to the nuclear envelope is characterized by Brownian movement and is thought to

be highly inefficient dependent on the location of release and the size of DNA. The release of pDNA or pDNA-containing polyplexes in the perinuclear region is thought to be preferable compared to a release within the outer cellular regions of dense meshed cytoplasm.[75-76] Moreover, various studies discussed an active motion of dissociated pDNA or the intact polyplex along microtubules or motor proteins to the nucleus, as common for viruses.[75, 77-78] Besides the travelling options of pDNA to the nuclear envelope, the nuclear translocation itself represents a further critical barrier towards efficient gene expression and is highly discussed with regard to cell-division dependency and nuclear pore complex involvement.[79-81]

In summary, several extra- and intracellular barriers were identified for cationic polymer-mediated gene delivery. Therefore, a deeper understanding in the chemistry and the property-relationship of polyplexes on the molecular and cellular level has to be gained to exploit the full potential of the promising polymer-mediated gene delivery technology.[59] Once the key parameters for efficient delivery are known, the adaption of strategies for the design of more powerful delivery vectors is possible. The time-efficient endosomal release of nanocarrier was identified to be a crucial bottleneck. Various aspects have an essential impact on the overall endosomal escape of polymer-based vectors and, consequently, on the overall transfection efficiency. These include (i) the polymer composition with type and content of amino functionalities, (ii) the cell type-specific internalization pathway and (iii) the polymer-specific interaction with lipid bilayers.

3. The delivery of nucleic acids by cationic polymers

3.1 Poly(methacrylate)-based polymers

Parts of this chapter have been published in **Pub2** A.-K. Trützschler, T. Bus, M. Reifarth, J. C. Brendel, S. Hoeppener, A. Traeger, U. S. Schubert, Beyond gene transfection with methacrylate-based polyplexes – the influence of the amino substitution pattern, *Bioconjugate Chem*. **2018**, *29*, 2181-2194 and in **Pub3** A.-K. Trützschler, T. Bus, M. Sahn, A. Traeger, C. Weber, U. S. Schubert, The power of shielding – Low toxicity and high transfection performance of cationic graft copolymers containing poly(2-oxazoline) side chains, *Biomacromolecules* **2018**, *19*, 2759-2771.

Poly(methacrylate)s represent a promising class of polymers for non-viral gene delivery, since they offer a large variety of polymer architectures and functionalities beneficial for the design of tailor-made vectors. Well-defined poly(methacrylate)s can be synthesized by different reversible deactivation radical polymerization techniques, *e.g.* atom transfer radical polymerization (ATRP) or reversible addition-fragmentation chain-transfer (RAFT) polymerization. These polymers show low dispersities, well-defined compositions and functionalities, as well as various macromolecular architectures.[82-84] For this reason, they can be used to investigate structure-property-relationships with regard to their biological activity. As discussed in *Chapter 2*, the efficient endosomal escape of polymer-based gene delivery vectors might be influenced by the type and content of amino functionalities. Due to the versatility of radical polymerizable methacrylate-based monomers, it is possible to introduce primary, secondary, tertiary as well as quaternary amino groups into tailored polymeric structures and to investigate their impact on the gene delivery process including the cellular uptake, the endosomal release as well as the transfection efficiency (TE).[85-86]

In the present work, a library of well-defined linear homo- and copolymers based on (2-aminoethyl)-methacrylate (AEMA), *N*-methyl-(2-aminoethyl)-methacrylate (MAEMA) and *N*,*N*-dimethyl-(2-aminoethyl)-methacrylate (DMAEMA) monomers with pendant primary, secondary and tertiary amino groups was investigated regarding their biological performances (see Figure 3.1, Table 3.1).

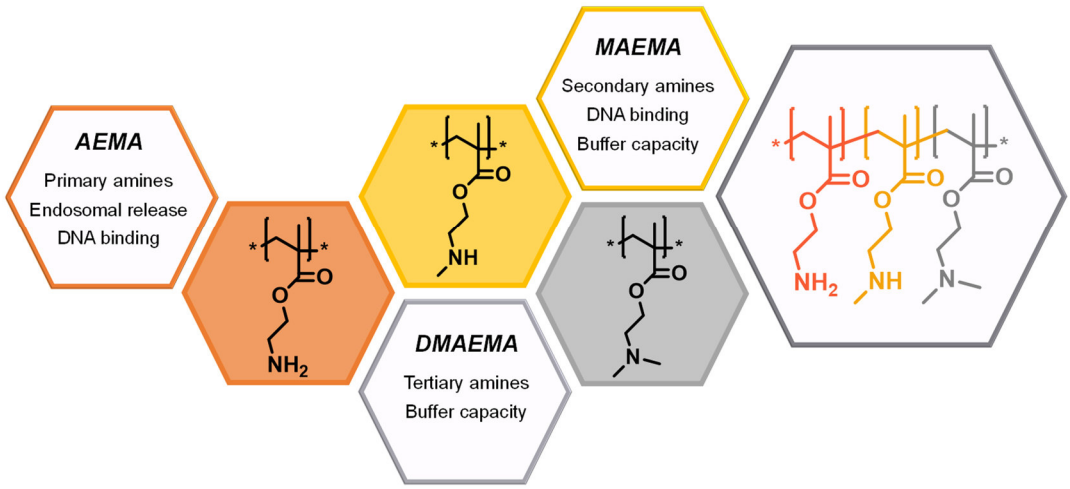

Figure 3.1. Schematic overview of the amino polymer units AEMA (primary amino groups), MAEMA (secondary amino groups) and DMAEMA (tertiary amino groups) and their potential function in gene delivery, used for the synthesis of the methacrylate library by RAFT polymerization comprising homo- and copolymers of different compositions. Asterisks indicate variable end groups.

The poly(methacrylate) library consisted of the three homopolymers **P1** (100 mol% tertiary amino groups), **P2** (100% secondary amino groups) and **P3** (100 mol% primary amino groups), the statistical copolymers **P4**, **P5**, **P6** (varying amino group compositions) and the terpolymer **P7** (comprising all three amino functionalities). All polymers revealed molar masses between 21 and 37 kDa with low dispersities. An overview of the characteristics of the examined polymers is given in Table 3.1.

Table 3.1. Poly(methacrylate) library of homo- and copolymers with selected characterization data.

Abbr.	Polymer	M_n[a] [g mol^{-1}]	Đ[a]	DP[b]
P1	P(DMAEMA$_{100\%}$)	26,200	1.09	185
P2	P(MAEMA$_{100\%}$)	24,000	1.21	167
P3	P(AEMA$_{100\%}$)	21,400	1.10	163
P4	P(DMAEMA$_{60\%}$-*stat*-MAEMA$_{40\%}$)	31,500	1.14	208
P5	P(DMAEMA$_{57\%}$-*stat*-AEMA$_{43\%}$)	37,000	1.12	249
P6	P(MAEMA$_{50\%}$-*stat*-AEMA$_{50\%}$)	46,000	1.28	348
P7	P(DMAEMA$_{33\%}$-*stat*-MAEMA$_{33\%}$-*stat*-AEMA$_{33\%}$)	36,000	1.27	250

[a] Molar masses and dispersities were determined by AF4 using a MALLS detector. [b] The degree of polymerization (DP) was calculated from AF4 results and molar ratio of monomers determined by ^{1}H-NMR.

The most prominent representative of the library, **P1**, has been intensively studied in several reports and successfully applied for the transfection *in vitro* and *in vivo* as well as in clinical studies.[44, 87] Its gene delivery efficiency is attributed to the tertiary amino groups responsible for the excellent buffering capacities (pK_a ~ 7.5) at acidic pH conditions. However, the direct comparison of the homopolymer **P1** with the other members of the methacrylate library (Figure 3.2) demonstrated a poor transfection ability of adherent HEK-293 cells with pDNA encoding the enhanced green fluorescein protein (EGFP). Herein, **P1** revealed the lowest transfection efficiency (TE < 20%) independent of increasing polymer concentrations or N/P ratios, respectively. In contrast, the highest TE was obtained by utilizing the homopolymer **P3** (TE: 66.3 ± 5.9%), the copolymer **P6** (TE: 56.1 ± 2.8%) as well as with the terpolymer **P7** (TE: 43.6 ± 9.7%). The homopolymer **P2** as well as the copolymers **P4** and **P5** revealed moderate TEs between 20% and 30%. Based on these results, the reported advantage of tertiary amino functionalities for transfection could not be confirmed for poly(methacrylate)s with an average molar mass of 20 kDa.[55, 88] Interestingly, polymers with a high primary amino content of minimum ~ 40 to 50 mol% was found to had a beneficial impact on the successful delivery of nucleic acids, whereas higher

amounts of tertiary amino groups within the polymer structure seemed to hamper the transfection process (see **P1** and **P4**).

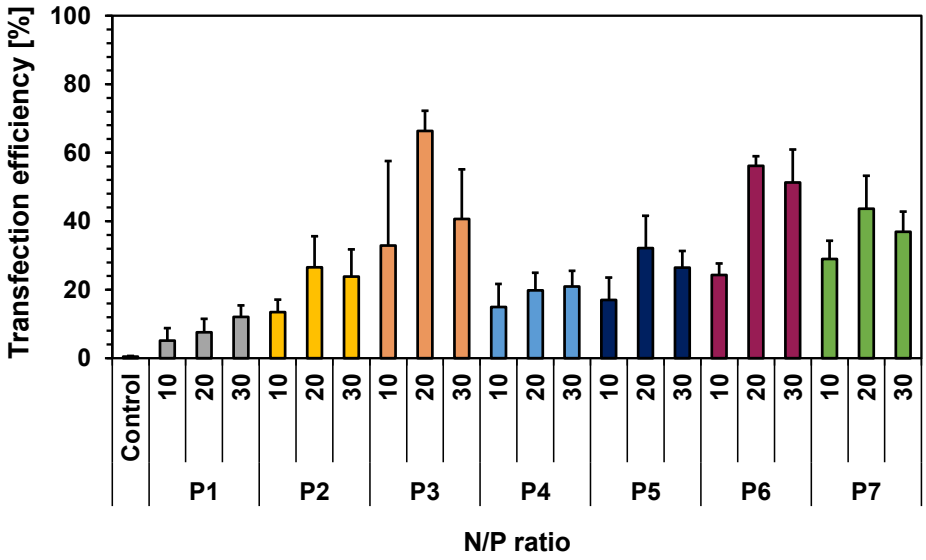

Figure 3.2. Transfection study of HEK-293 cells utilizing the methacrylate library at increasing N/P ratios for the delivery of pDNA encoding the enhanced green fluorescein protein (EGFP) in serum-reduced media (OptiMEM). Transfection efficiency was measured 24 h post-transfection *via* flow cytometry quantifying 10,000 cells. Values represent the mean ± S.D. (n = 3).

In order to find the bottleneck of poly(methacrylate)-mediated gene delivery resulting in varying transfection performances, relevant cellular barriers including the cell uptake and the endosomal release were investigated in more detail. Uptake kinetic studies at 37 °C in serum-reduced media (OptiMEM) demonstrated a time-dependent cellular internalization (Figure 3.3 A). According to the standard transfection protocol, internalized polyplexes were detected within ~ 80% of cells independent on the utilized polymers after 4 h. Surprisingly, **P1** revealed the highest amount of internalized pDNA as shown by the highest mean fluorescence intensity (MFI) of 188 ± 18.3 compared to the MFI values of the other investigated polymers (MFIs < 160). This outcome is opposed to the transfection data and implies that a fast and enhanced cellular internalization is not an exclusive prerequisite for successful gene delivery.[89-90] A high uptake rate does not necessarily result in high gene expression, since the endosomal release of entrapped polyplexes within endo-lysosomal compartments is another critical obstacle in the gene delivery machinery.[62, 91-92]

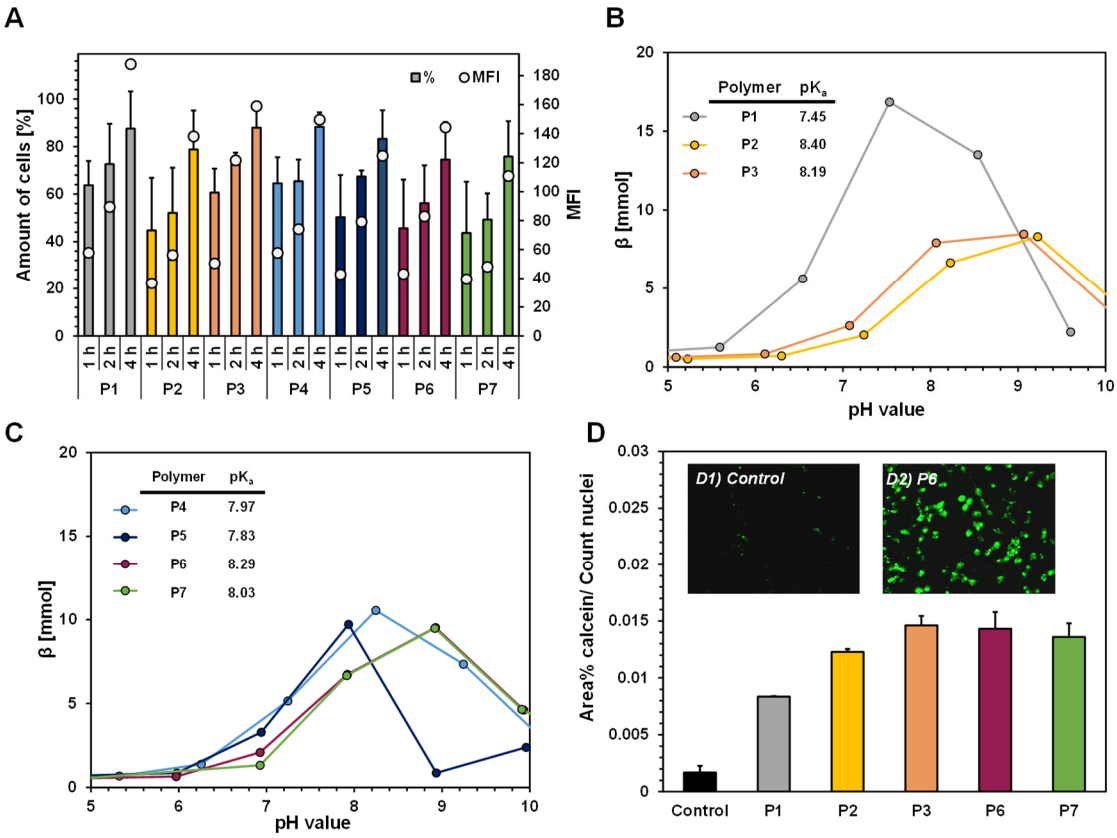

Figure 3.3. (A) Uptake kinetic of methacrylate library in HEK-293 cells using YOYO-1 labeled pDNA in serum-reduced media (OptiMEM). MFI (mean fluorescence intensity) normalized to the negative control. 10,000 cells in total were quantified by flow cytometry. Values represent the mean ± S.D. (n = 3). Buffer capacity (β) and pK_a values of the methacrylate-based homopolymers **P1** to **P3 (B)** as well as the copolymers **P4** to **P7 (C)** determined by acid-base titration and calculated by the Henderson-Hasselbalch equation.[93] **(D)** Quantification of the endosomal release of selected polyplexes by the calcein release assay. The endosomal release of polyplexes was determined after 4 h by fluorescence microscopy and imaging analysis. After successful escape from endo-lysosomes calcein diffuses into the cytoplasm leading to an increase in the fluorescent area. The ratio of the green fluorescent calcein area in % over the number of detected cell nuclei (stained with Hoechst 33324) was determined for quantification.

It is assumed that successful endosomal release is strongly connected to the ability of the polyelectrolytes to buffer acidification of the endosomes, indicated by the pK_a values as well as the buffer capacities (β) of the polymers. The pK_a values of the homo- and copolymers, determined by acid-base titration, ranges between pH values of 7.45 and 8.40, and nicely correspond to the basicity of the respective amino functionalities in aqueous solution (Figure 3.3 B and C, see tables). Furthermore, the poly(methacrylate)s revealed buffer capacities in the range of pH 6.0 to 10.0. As expected, polymers with a

high content of primary and secondary amino functionalities (**P2**, **P3**, **P6** and **P7**) showed buffer capacities at more basic conditions of pH value 8.0 and above. In contrast, polymers with an increasing content of tertiary amino groups (**P1**, **P4**, **P5**) tend to show buffer capacities from neutral to acidic conditions in agreement with the increase of the DMAEMA content. In particular, **P1** revealed an increased buffering capacity over the whole physiological pH range from pH values 6.0 to 8.0. Despite the high buffering capacities of polymers containing tertiary amino functionalities, the transfection ability of **P1**, **P4** and **P5** remains low. In order to verify the efficacy of the endosomal release of the homopolymers **P1** and **P2** against the best performers **P3**, **P6** and **P7**, the escape was quantified by the calcein release assay. In general, all tested poly(methacrylate)s were able to escape from endo-lysosomal compartments as demonstrated in Figure 3.3D. A successful endosomal release was demonstrated by the presence of numerous bright green fluorescent cell areas (Figure 3.3 D2). In contrast, non-treating control cells exhibited mostly punctuate green fluorescence (Figure 3.3 D1), which can be assigned to the entrapped calcein within the endo-lysosomes. Polyplexes based on amino functionalized poly(methacrylate)s with the highest content of primary amino groups (**P3** and **P6**) achieved the fastest and most sufficient endosomal release. **P1** revealed the lowest calcein fluorescence area per cell and, therefore, seemed to be unable to escape from the endo-lysosomes in a time-efficient manner, which might be responsible for its poor transfection efficiency. The findings clearly contradict an endosomal release of poly(methacrylate)s by the proton sponge effect, in particular for **P1**. But the findings are in agreement with former studies.[92, 94-95] In order to examine the endosomal release of these polymers by nano-hole formation due to polymer-membrane interactions, high-angle annular dark-field scanning transmission electron microscopy (HAADF-STEM) was applied (Figure 3.4). This technique provides high resolution to a few nanometer with the ability to visualize cellular ultrastructures, thus offering the possibility to track polyplexes in their intracellular pathway.[96] Due to the strong chemical affinity of their functional groups, *i.e.*, amines and phosphates, to the staining reagents (OsO_4 and uranyl acetate) polyplexes were observed as black structures within the extra- and intracellular environment. Polyplexes prepared with **P6** were found to be entrapped within endo-lysosomal compartments in close vicinity to the inner leaflet of the vesicular membrane (Figure 3.4 A and B, red arrows). In some cases, these polymer-membrane interactions lead to the alteration and deformation of the membrane (Figure 3.4 B, orange arrows). These structural changes were associated with endosomal escape events, as a disturbed

membrane integrity of polyplex-containing endo-lysosomes were observed (Figure 3.4 A, red arrow heads). Furthermore, the polyplex structure seems to penetrate through the vesicular membrane to the cytoplasm. These outcomes support the hypothesis of the endosomal escape by nano-hole formation due to local destabilization and permeabilization events of the endo-lysosomal membrane through the direct polyplex interaction as described by literature.[62, 65, 89]

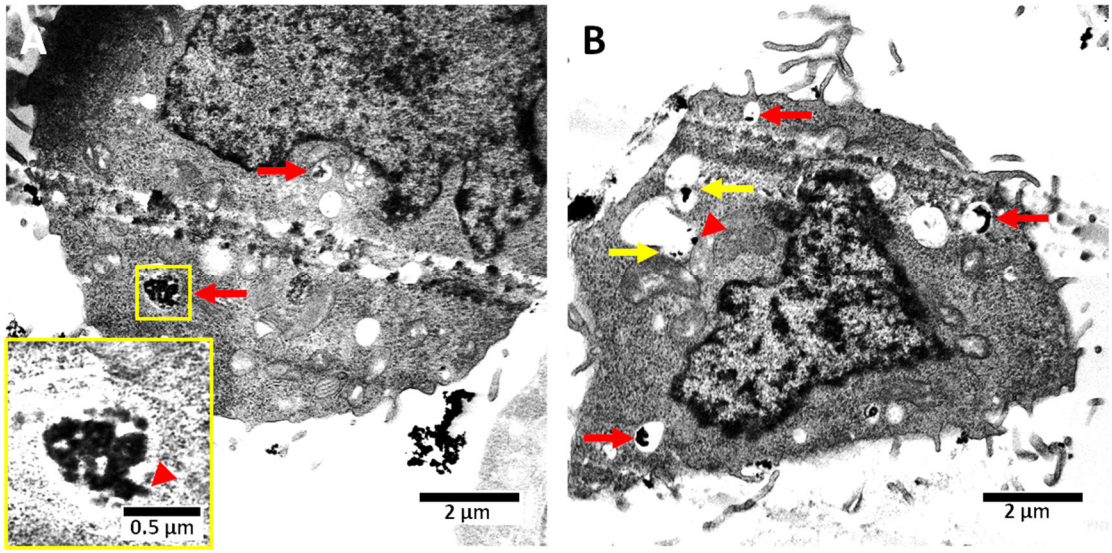

Figure 3.4. HAADF-STEM images of **P6**-polyplex treated HEK-293 cells for 4 h in serum-reduced media **(A-B)**. Polyplexes can be observed as electron dense structure (black). Red arrows indicate polyplexes entrapped within endo-lysosomal compartments in close vicinity to the exoplasmic vesicle membrane. Orange arrows indicate deformed membrane structures of endo-lysosomes caused by polyplex interactions. Red arrow heads indicate disturbed membrane integrity of polyplex-containing vesicles and potential membrane disruption or hole formation. Polyplex structures (black) seem to penetrate the membrane from the interior of endo-lysosomes to the cytoplasm.

The impact of polymer-membrane interactions was further endorsed by a protein leakage assay, *i.e.*, a hemoglobin release assay from erythrocytes (data are shown in **Pub2**). This assay revealed an increased cellular membrane damage of erythrocytes after treatment with the homo- as well as copolymers. Especially, polymethacrylates with a higher content of primary amino groups (**P3**, **P6**) demonstrated enhanced membrane activity. This outcome is in accordance to the calcein release assay and, thus, might explain the superior transfection performance of poly(methacrylate)s bearing primary amino groups. However, the high membrane disruptive activity of the

poly(methacrylate)s was associated with severe cytotoxic effects (data are shown in **Pub2**). A common strategy to accomplish the reduction of adverse side effects is the introduction of stealth polymers like poly(ethylene glycol) (PEG).[21-22] Another suitable polymer class with stealth potential is PEtOx representing a promising alternative to PEG.[25, 97] PEtOx is considered to be responsible for the reduction of unspecific interactions with non-cellular and cellular components, elongated blood circulation, low immunogenicity and reduced clearance *in vivo*.[25-26] However, such stealth polymers bear the risk of diminished transfection efficiencies presumably due to weak DNA complexation and decreased cell interactions.[98-99] In order to identify the optimal balance between the cytotoxicity and the transfection efficiency, a library of graft copolymers comprising a PAEMA or PMAEMA backbone with 2-ethyl-2-oxazoline ($EtOx_n$) side chains were examined. Since primary and also secondary amino groups demonstrated satisfying gene delivery performances, $EtOx_n$ macromonomers with a degree of polymerization (DP) of 5 and 20 were chosen in order to show whether the side chain length of the graft copolymer influences the gene delivery process. Furthermore, to examine the impact of the $EtOx_n$ density on the transfection process, a degree of grafting (DG) of 10% and 30% was aimed. Higher DG were excluded due to the fact that studies on PEG graft copolymers with longer side chains demonstrated reduced polyplex formation and transfection efficiency.[100] The members of the library featured the general structure P($MAEMA_m$-*g*-$EtOx_n$(x)), referred as **P8** to **P11**, and P($AEMA_m$-*g*-$EtOx_n$(x)), referred as **P12** to **P15** (Figure 3.5). The grafted copolymers **P8** to **P15** revealed comparable molar masses to the non-grafted homopolymers (*i.e.* **P2**, **P3**) ranging from 13.4 to 22.8 kDa with varying molar fractions of $EtOx_n$ moieties (EtOx mol%) dependent on the DP and DG.

A

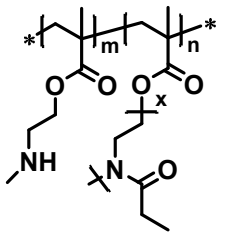

P(MAEMA$_m$-*g*-EtOx$_n$(x))

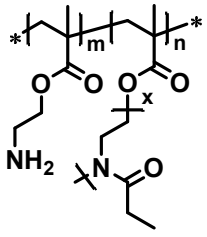

P(AEMA$_m$-*g*-EtOx$_n$(x))

B

Abbr.	Polymer	n_{EtOx}	DG_x [%][a]	M_n [g mol^{-1}] [b]	Đ[b]	Mol% EtOx[c]
P8	P(MAEMA$_{95}$-*g*-EtOx$_5$(10))	5	17	17,300	1.43	56
P9	P(MAEMA$_{95}$-*g*-EtOx$_5$(30))	5	40	20,200	1.42	77
P10	P(MAEMA$_{80}$-*g*-EtOx$_{20}$(10))	20	16	17,500	1.40	72
P11	P(MAEMA$_{80}$-*g*-EtOx$_{20}$(30))	20	31	13,400	1.30	82
P12	P(AEMA$_{95}$-*g*-EtOx$_5$(10))	5	16	16,700	1.44	53
P13	P(AEMA$_{95}$-*g*-EtOx$_5$(30))	5	41	18,400	1.49	77
P14	P(AEMA$_{80}$-*g*-EtOx$_{20}$(10))	20	10	22,800	1.48	82
P15	P(AEMA$_{80}$-*g*-EtOx$_{20}$(30))	20	41	17,300	1.59	88

Figure 3.5. Schematic representation of the chemical structures of the grafted poly(methacrylate)s **(A)** and characterization data of the eight-membered library **(B)**. [a] The degree of grafting (DG) was determined from ^{1}H-NMR spectra. [b] Molar mass (M_n) was determined by SEC (water, 0.1% trifluoroacetic acid, 0.1 M NaCl, RI detection, PVP calibration). [c] Molar ratio of EtOx (Mol% Ox) was calculated from ^{1}H-NMR spectra of the corresponding Boc-protected polymers.

Unshielded poly(methacrylate)s led to severe cytotoxicity as well as harsh but beneficial disruptive effects on the cellular membranes, as depicted in Figure 3.6. The grafting of AEMA and MAEMA bearing polymers with EtOx$_n$ shielding units significantly improved the cytocompatibility compared to the unshielded analogues (Figure 3.6 A and B). The graft copolymers **P8** and **P12** bearing EtOx$_n$ side chains with a DP of 5 and the lowest theoretical DG of 10% revealed cytotoxicity at higher polymer concentrations above 300 µg mL^{-1} or 100 µg mL^{-1}, respectively. Nevertheless, the cytotoxicity of the graft polymers could be minimized or even prevented by either the increase of the length of EOtx$_n$ side chains or the increase of DG. The shielding effect of the EtOx$_n$ did not

only improve the cytocompatibility of the AEMA and MAEMA containing homopolymers by a factor of 10 and above, it also reduced their membrane disruptive activity (Figure 3.6 C). All members of the library revealed no to low hemolytic activity at the tested conditions, endorsing the utilization of EtOx as stealth polymer.

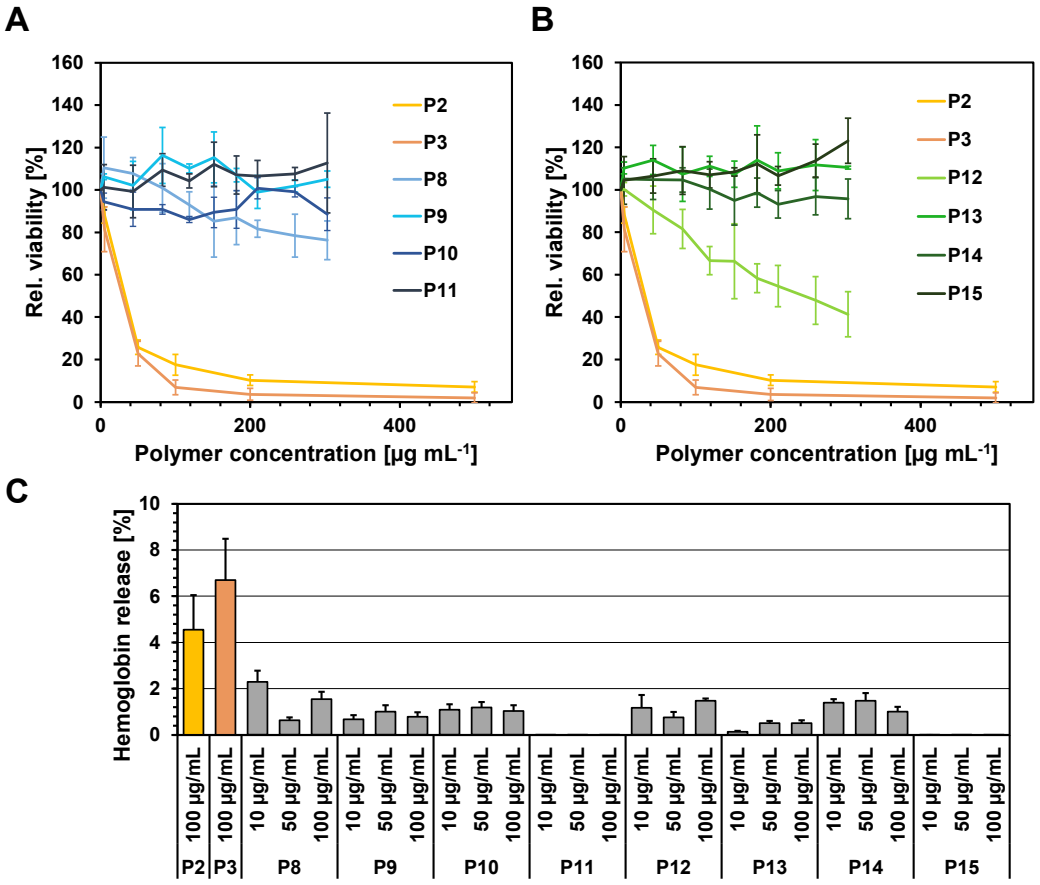

Figure 3.6. Cyto- and hemocompatibility of the grafted poly(methacrylate) library. **(A** and **B)** Evaluation of the relative viability (%) of L929 mouse fibroblast cells after polymer treatment for 24 h according to ISO10993-5. **(C)** Hemolysis assay of isolated erythrocytes from different blood samples. Erythrocytes were incubated with increasing polymer concentrations and the release of hemoglobin was determined. Complete hemolysis (100%) was achieved using Triton X-100, which served as positive control. PBS served as negative control (data not shown). A value less than 2% hemoglobin release was classified as non-hemolytic, 2 to 5% as slightly hemolytic and a value above 5% as hemolytic. Values represent the mean ± S.D. (n = 3).

Despite the positive impact of the $EtOx_n$ on the overall biocompatibility, the shielding led to adverse side effects in terms of polyplex uptake and, consequently, on the transfection efficiency. As depicted in Figure 3.7 A, polyplexes based on copolymers comprising short $EtOx_n$ side chains (DP = 5) revealed uptake efficiencies between 60 and 80% after 4 h. On the other hand, the copolymers **P10**, **P11**, **P14** and **P15** with longer $EtOx_n$ side chains (DP = 20) showed low uptake rates. Interestingly, the DG did not influence the cellular internalization in our study. It can be assumed that the longer side chains prevent the interaction of the polyplex with the cellular membrane and, consequently, a successful endocytosis. Furthermore, an influence of serum proteins on the uptake performance was observed (Figure 3.7 A, see MFI values) as the uptake level for almost all copolymers was reduced in serum-containing media. Hence, the shielding property of $EtOx_n$ did not seem to be sufficient for a complete repellent effect of proteins, as an accumulation of proteins to the polyplex can additionally impede the internalization by alteration of the polyplex physicochemical characteristics.[27, 101] Transfection studies of the grafted copolymers confirmed the influence of the $EtOx_n$ grafting on the transfection behavior (Figure 3.7 B). As assumed from the missing uptake efficiency, copolymers with long $EtOx_n$ side chains (**P10**, **P11**, **P14** and **P15**) failed in the transfection of adherent HEK-293 cells. But also, copolymers with a theoretical DG of 30% (**P9** and **P13**) revealed no transfection efficiencies despite high uptake rates, thus suggesting an inability to escape endo-lysosomal compartments. An explanation could be the decreased polymer interaction with the exoplasmic membrane of endo-lysosomal compartments as also demonstrated by the hemolysis assay and live cell imaging (data are shown in **Pub3**). In contrast to the cellular internalization, which is affected by the DP of the side chains, the transfection performance seems rather be affected by the DG. Merely the polymers with a DP of 5 and a theoretical DG of 10%, *i.e.*, **P8** and **P12**, were able to transfect HEK-293 cells with TEs of 15 ± 4.2% and 45 ± 9.5%, respectively. In particular, **P12** revealed gene delivery performances comparable to the homopolymers **P2** and **P3**. Hence, this polymer demonstrated not only high cytocompatibility but also satisfying transfection efficiencies making the pursued strategy a promising concept for the design of safe and powerful gene delivery vectors.

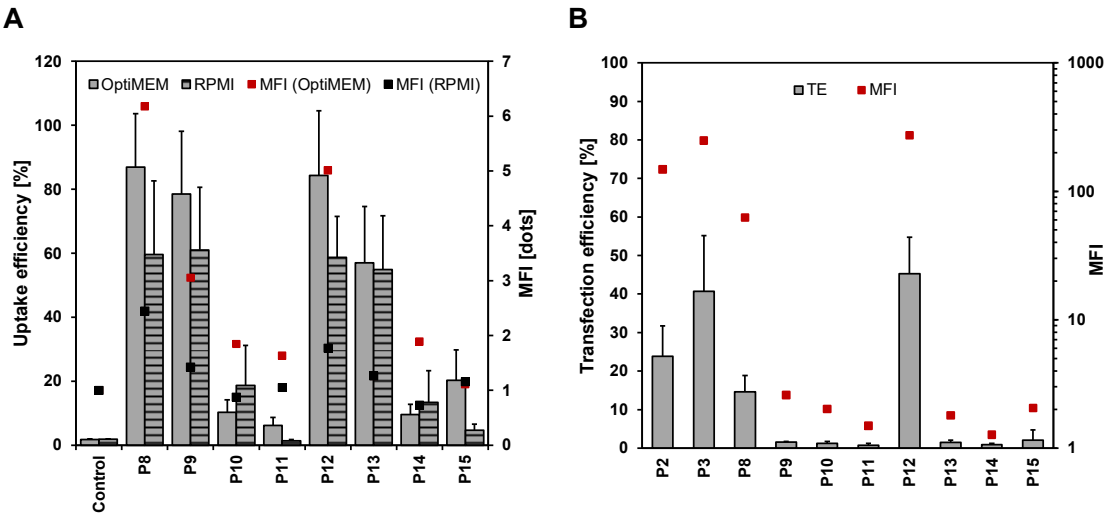

Figure 3.7. Gene delivery study of the grafted poly(methacrylate)s. **(A)** Cellular uptake study of polyplexes based on YOYO-1 labeled pDNA (N/P 30) in serum-reduced (plain columns, OptiMEM) and serum-containing (dashed columns, RPMI) media for 4 h at 37 °C. **(B)** Transfection of HEK-293 cells with pDNA encoding the enhanced green fluorescein protein (EGFP) in serum-reduced (OpiMEM) media at N/P 30 after 24 h. MFI (Mean fluorescence intensity) normalized to the negative control. 10,000 cells were quantified by flow cytometry. Values represent the mean ± S.D. (n = 3).

In summary, amino-functionalized poly(methacrylate)s represent versatile non-viral gene delivery vectors with excellent transfection efficiencies, since they offer a wide range of molar masses, well-defined architectures and various functionalities. It was found that the type and content of amino functionalities have a relevant impact on the transfection performance including (i) the cyto- and hemocompatibility, (ii) the time-efficient endosomal release and (iii) the gene expression. In accordance to literature, polymers with primary and secondary amino functionalities were beneficial for DNA binding and polyplex formation, while polymers with tertiary amino groups demonstrated the highest buffering capacities at acidic pH conditions. Nevertheless, polymers with a high content of primary amino groups revealed superior transfection performances *in vitro* at selected experimental set-ups, whereas polymers with tertiary amino functionalities showed poor transfection efficiencies. Contrary to the current opinion, a high buffering capacity do not seem to be a crucial prerequisite for the efficient poly(methacrylate)-mediated transfection of mammalian cells. The successful escape from endo-lysosomal compartments does not predominantly rely on buffering effects as proposed from the “proton sponge” hypothesis but possibly rather on the

intense interaction of the polymer or polyplex, respectively, with the vesicular membrane as described in *Chapter 2*. In particular, polymers with primary amino functionalities revealed a high membrane activity, which might lead to the formation of nano-holes within the membrane of endo-lysosomes and, thus, to a successful escape. However, this pronounced membrane affinity causes severe cytotoxic effects, which could be overcome by the introduction of shielding moieties. PEtOx represents a suitable polymer revealing the favored stealth effect and could be utilized to generate grafted poly(methacrylate)s. This strategy significantly improved the overall cell viability and was able to minimize or even eliminate cytotoxic side-effects. Nevertheless, an appropriate balance between the degree of grafting as well as the length of side chains has to be found to obtain powerful gene delivery vectors with high transfection efficiencies.

3.2 Poly(ethylene imine)-based polymers

Parts of this chapter have been published in **Pub4** T. Bus, C. Englert, M. Reifarth, P. Borchers, M. Hartlieb, A. Vollrath, S. Hoeppener, A. Traeger, U. S. Schubert, 3rd generation poly(ethylene imine)s for gene delivery, *J. Mater. Chem. B* **2017**, *5*, 1258-1274 and in **Pub5** C. Englert, A.-K. Trützschler, M. Raasch, T. Bus, P. Borchers, A. S. Mosig, A. Traeger, U. S. Schubert, Crossing the blood-brain barrier: Glutathione-conjugated poly(ethylene imine) for gene delivery, *J. Control. Release* **2016**, *241*, 1-14.

Since the first report as non-viral gene delivery agent in 1995, poly(ethylene imine) (PEI) remains the "gold standard" for gene delivery *in vitro* up to now.[16-17] Its high transfection efficiency is based on its high cationic charge density due to the polyamine structure, where every third atom is a protonatable nitrogen atom. The weak-base buffering polyelectrolyte PEI reveals a pH-dependent protonation behavior and conformational changes.[102] This structure provides optimal conditions for pDNA binding and stable polyplex formation but also reduced water solubility, molar mass-dependent cytotoxicity and non-specific interactions with cellular as well as non-cellular components.[18, 103] Various attempts have been made to improve the overall biocompatibility of PEI. In particular, the design of novel PEI derivatives comprising biodegradable linkers (e.g. disulfide bonds),[104-106] carbohydrates (*e.g*. dextran or fructose),[30, 107] hydroxyl starch[108] or stealth polymer moieties[109-110] have been in the focus of previous research. As described in *Chapter 3.1*, the presence of PEtOx functionalities within a polyamine structure represents an effective strategy to overcome undesired drawbacks. With regard to the two existing topologies of PEI, the modification and optimization of LPEI for the investigations of structure-property relationships is often preferred over the branched form, since BPEI suffers from the lack of control during synthesis and from well-defined structures.[111] The cationic ring-opening polymerization (CROP) of polyoxazolines allows the synthesis of well-defined polymers, which can be utilized for the acidic or basic hydrolysis resulting in LPEI.[112-113] Hence, the partial hydrolysis of POx results in the synthesis of premature PEIs or concretely in the copolymer P(Ox-*stat*-EI) and represents a straightforward concept to obtain polymers with improved biocompatibility. However, a high degree of stealth functionalities might impair the transfection efficiency as revealed for poly(methacrylate)s. In order to circumvent this effect, functional groups like amino groups or targeting molecules can be attached to the P(Ox-*stat*-EI) backbone by post-polymerization functionalization. An alkene functionality was installed in order to

introduce various amino groups by thiol-ene addition. To examine the biological activity and the transfection potential of such PEI-derivatives a series of different polymers based on PEtOx was synthesized (Figure 3.8 and Table 3.2) containing stealth moieties (*i.e.*, EtOx), cationic functionalities (*e.g.*, EI) and/or highly specific functional groups for DNA binding or targeting (*e.g.*, amino functionalities, ligands). As noted from *Chapter 3.1* primary amino functionalities achieved superior gene delivery performances compared to the other amino groups and were, therefore, chosen as functional moieties within the flexible side chain.

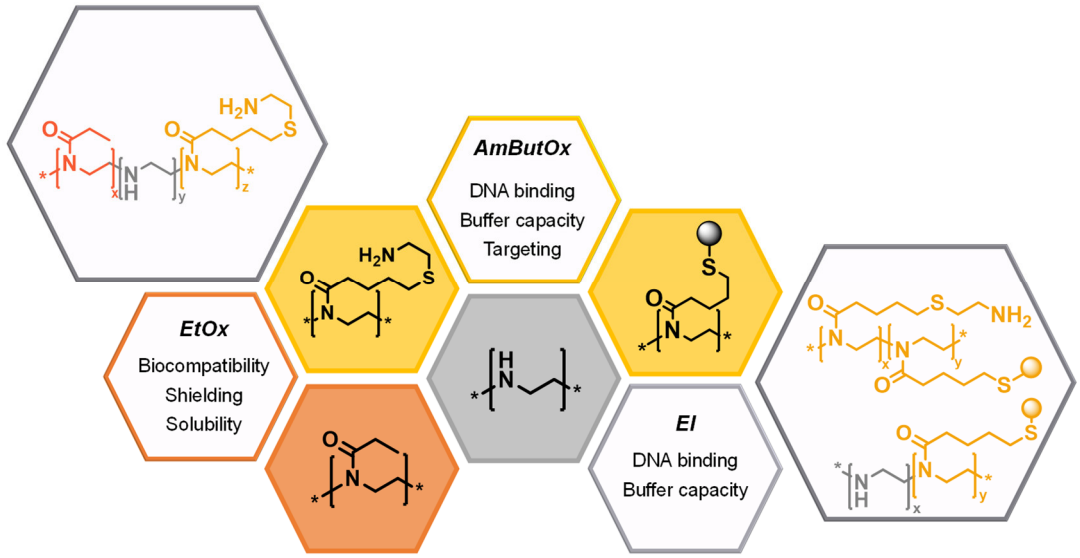

Figure 3.8. Schematic overview of the functional moieties of novel PEI derivatives providing stealth, cationic charge and targeting behavior. Spherical functionality implies a potential targeting molecule. Asterisks indicate variable end groups.

The series comprise statistical linear homo- and copolymers with narrow molar mass distributions bearing different amounts of secondary and primary amino groups. The homopolymer PEtOx (**P16**) with a DP of 575 was synthesized by CROP according to literature reports and served as starting material for the synthesis of the other library members.[97] LPEI (**P18**) was obtained by the full hydrolysis of **P16** and was used as the transfection standard. The partial hydrolysis of **P16** resulted in the copolymer P(EtOx-*stat*-EI) (**P17**) comprising an EtOx content of ~ 54%. This EtOx content was chosen in our study since P(Ox-*stat*-EI) with higher POx concentration were reported to have disadvantageous effects on the delivery performances with reduced TEs.[114-115] To

examine the effect of stealth monomers and different amino groups on the overall gene delivery process, three different statistical copolymers of the general structure P(EtOx$_{54\%}$-*stat*-EI$_n$-*stat*-AmButOx$_m$) were synthesized by post-polymerization functionalization of **P17** followed by thiol-ene photoaddition to introduce primary amino groups (AmButOx). The copolymers exhibited a constant EtOx content but varying ratios of secondary as well as primary amino groups and were named **P19**, **P20** and **P21**, respectively (Table 3.2).

Table 3.2. Selected characterization data of the PEI-based copolymers with a DP of 575.

Abbr.	Polymer	Amino ratio sec$_x$: prim$_y$	M_n[a] [g mol^{-1}]	Đ[a]
P16	P(EtOx)$_{100\%}$		57,000	1.3
P17	P(EtOx$_{54\%}$-*stat*-EI$_{46\%}$)	1:0	31,300	1.3
P18	P(EtOx$_{5\%}$-*stat*-EI$_{95\%}$)	1:0	9,900	1.4
P19	P(EtOx$_{54\%}$-*stat*-EI$_{12\%}$-*stat*-AmButOx$_{34\%}$)	1:2.8	35,300	1.6
P20	P(EtOx$_{54\%}$-*stat*-EI$_{17\%}$-*stat*-AmButOx$_{29\%}$)	1:1.7	43,700	1.6
P21	P(EtOx$_{54\%}$-*stat*-EI$_{23\%}$-*stat*-AmButOx$_{23\%}$)	1:1	30,500	1.5

[a] Molar mass and dispersity values were determined by AF4 equipped with a MALLS detector and a cellulose membrane with a molar-mass cut-off of 10 kDa.

The EtOx content of 54% within the copolymer structures clearly influenced their physicochemical properties and biological activity. As expected, the homopolymer **P16** revealed high cytocompatibility without a loss of cell viability at the tested conditions (Figure 3.9 A). In contrast, **P18** showed severe cytotoxic effects at minimal polymer concentrations indicated by the half-maximal cytotoxic concentration (CC_{50}) value of 4 µg mL^{-1}. The obtained CC_{50} data from **P18** are in accordance with previously published reports.[18, 116] However, commercially available LPEI (*e.g.* 25 kDa from Polysciences) revealed higher CC_{50} values of 25 to 30 µg mL^{-1}, which could be attributed to significant amounts of *N*-acyl residues (≥ 10%) from the manufacturing process.[115, 117-118] Interestingly, the introduction of EtOx in the ratio 1:1 was sufficient to eliminate cytotoxic effects, as **P17** showed no loss of cell viability up to the highest tested polymer concentration (1 mg mL^{-1}). Despite their high molar masses, all three copolymers bearing primary amino groups in the polymer side chain (**P19** to **P21**) also benefit from the EtOx content, as they do not harm the overall viability of cells at the

tested conditions. The positive impact of EtOx on the overall hemocompatibility of the copolymers was further demonstrated by the assessment of the hemoglobin release and agglomeration formation of erythrocytes (Figure 3.9 B and C). In contrast, **P18** revealed a strong interaction with cellular membranes of blood cells causing the aggregation of erythrocytes (Figure 3.9 B), which might cause an increase of the blood viscosity *in vivo* and could hamper the blood flow. Furthermore, higher **P18** concentrations (≥ 100 µg mL^{-1}) caused the disruption of the erythrocyte membranes indicated by the release of hemoglobin. All PEI derivatives **P19** to **P21** demonstrated neither a hemolytic activity nor the aggregation of erythrocytes in a concentration range from 10 to 100 µg mL^{-1} indicating ideal prerequisites for potential *in vivo* applications.

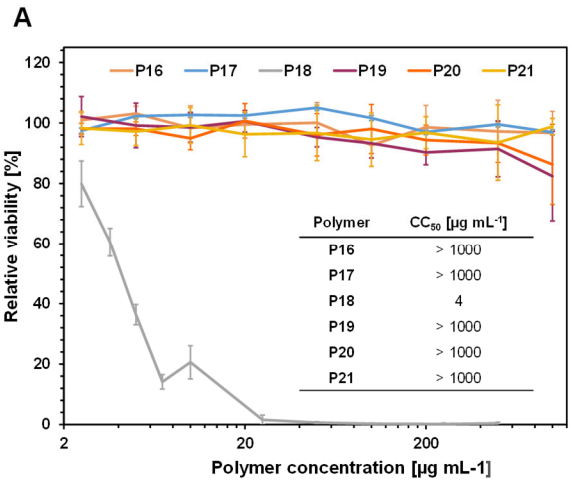

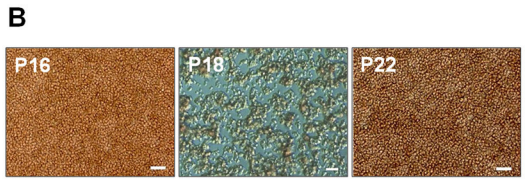

C

	Hemoglobin release [%]			Erythrocyte aggregation
	10 µg mL^{-1}	50 µg mL^{-1}	100 µg mL^{-1}	
P17	0.5 ± 0.1	0.6 ± 0.1	1.1 ± 0.1	No
P18	0.6 ± 0.1	1.1 ± 0.1	2.6 ± 0.7	Yes
P19	0.4 ± 0.1	0.6 ± 0.1	1.0 ± 0.2	No
P20	0.3 ± 0.01	0.3 ± 0.01	0.5 ± 0.1	No
P21	0.3 ± 0.01	0.4 ± 0.01	0.4 ± 0.01	No

Figure 3.9. Cytocompatibility studies PEI-based homo- and copolymers. **(A)** Evaluation of the relative viability of L929 mouse fibroblast cells and polymer's CC_{50} after 24 h polymer treatment according to ISO10993-5. **(B)** Selected microscopic images of erythrocytes after polymer treatment. A high membrane activity resulted in the clotting of erythrocytes. Scale bar represents 50 µm. **(C)** Hemolysis assay of erythrocytes after polymer incubation at indicated concentrations. Triton X-100 served as positive control (98.8% hemoglobin release) and PBS as negative control (0.2% hemoglobin release). A value less than 2% was classified as non-hemolytic, 2 to 5 as slightly hemolytic and values > 5% as hemolytic. Values represent the mean ± S.D. (n = 3).

The stealth behavior of EtOx provided biosafety beneficial for biomedical applications, but also bearing the risk for adverse effects on the nucleic acid packaging and the polyplex stability. The nucleic acid binding as well as release affinity was investigated with pDNA and siRNA, since both are used for gene therapy approaches but differ significantly in their characteristics. Most importantly, siRNA is comprised of a few

base pairs (< 30 base pairs (bp)) and, therefore, stiff and more rigid compared to the long circular pDNA (4.7 kbp). The DNA molecule is condensed and packed into a compact structure during the complexation process by interacting with the nitrogen atoms of multiple cationic polymer chains, whereas the structure of siRNA remains unaltered interacting more likely with a single polymer chain. Hence, the formation of stable polyplexes based on siRNA is more challenging. The physicochemical characterization of polyplexes based on pDNA and siRNA confirmed an influence of the EtOx on the polyplex formation. The polyplex formation of the library was evaluated by the ethidium bromide assay (Figure 3.10 A). The homopolymer **P18** as well as the copolymers **P19** to **P21** revealed a high affinity to both, pDNA and siRNA. With increasing polymer concentrations, ethidium bromide was excluded from its binding site within the nucleic acid resulting in the decrease of its fluorescence intensity. Moreover, the stable polyplex formation was indicated by a low and steady fluorescence plateau. For **P18** a low N/P ratio (10 to 20) is sufficient to achieve stable polyplexes with a z-average of 80 nm and a positive net charge of ζ = 33 mV (Figure 3.10 B). These results are in accordance to literature reports and represent ideal characteristics for cellular uptake and trafficking processes. The negative charge of the nucleic acid is masked, thus proposing a sufficient packaging and protection from degradation as well as a facilitated affinity to negatively charged cell membranes followed by endocytosis. Interestingly, **P17** failed in the formation of appropriate polyplexes as indicated by the formation of polydisperse complex fractions (Figure 3.10 A and B). Consequently, this directly affected the transfection performance, as seen in the lack of EGFP gene expression in Figure 3.10 C. But this in turn, confirm the value of stable polyplex formation for successful gene delivery. The EtOx content of 54% might weaken the electrostatic interactions or even prevent the binding of DNA to the secondary amino groups of the PEI backbone. However, the effect was compensated by the introduction of more flexible side chains containing primary amino functionalities as demonstrated for **P19**, **P20** and **P21**. Primary amino groups were shown to be essential for DNA binding and polyplex formation. Thus, the copolymers were able to form suitable polyplexes with an overall z-average below 180 nm and a positive net charge of ζ = 21 to 27 mV (Figure 3.10 B) indicating the successful masking of the nucleic acid charge. With regard to their pDNA gene delivery performance, an influence of the polymer composition was obvious. Polymers with a more equalized ratio of primary to secondary amino functionalities (**P20** and **P21**) achieved high transfection levels of ~ 60% comparable to **P18** (Figure

3.10 C). **P19** comprising a higher ratio of primary amino groups revealed lower transfection performances (TE: ~ 45%). To assess the shielding property of the copolymers, pDNA transfection was further performed in serum-containing media (Figure 3.10 C, plain columns). Adverse effects of serum proteins on the transfection efficiency were observed for all three copolymers and **P18**. However, the highest utilized N/P ratio of **P21** withstood the inhibitory influence of serum proteins and resulted in similar efficiencies as in the absence of serum. At these conditions, the polymers **P21** showed superior TE over the transfection standard **P18**.

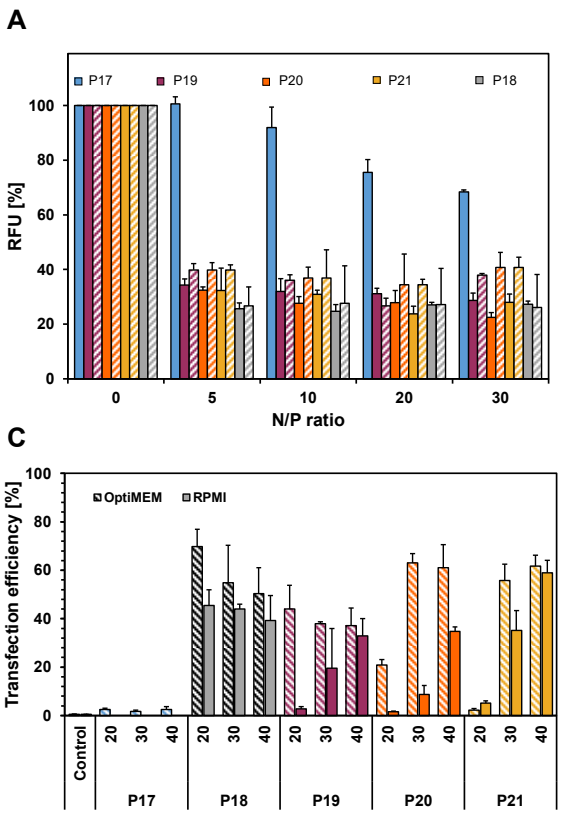

Polymer vector	Nucleic acid	z-Average [d.nm]	PDI	Zeta potential [mV]
P17	pDNA	242 ± 73.4	0.46	20 ± 0.4
P18	pDNA	80 ± 2.3	0.17	33 ± 4.2
	siRNA	83 ± 2.3	0.23	33 ± 1.6
P19	pDNA	158 ± 1.0	0.23	27 ± 0.3
	siRNA	102 ± 1.2	0.15	21 ± 1.2
P20	pDNA	143 ± 1.4	0.25	23 ± 0.1
	siRNA	124 ± 1.5	0.13	25 ± 1.0
P21	pDNA	154 ± 1.4	0.23	23 ± 0.1
	siRNA	149 ± 12.3	0.49	22 ± 0.1

Figure 3.10. (A) Complexation affinity and polyplex formation (ethidium bromide assay) of the polymer library at indicated N/P ratios with pDNA (plain columns) and siRNA (dashed columns). **(B)** Size and zeta potential (surface charge) of pDNA- and siRNA-based polyplexes at N/P 30 determined *via* dynamic light scattering and electrophoretic light scattering in a HEPES-based buffer. **(C)** Transfection efficiency of pDNA-based polyplexes for adherent HEK-293 cells in serum-reduced (OptiMEM, dashed columns) and serum-containing media (RPMI + 10% FCS, plain columns) at different N/P ratios after 24 h. **(D)** siRNA knockdown mediated by **P18**, **P19**, **P20** and **P21** and jetPRIME (positive control) at N/P 30 after 72 h. Stable EGFP-expressing CHO cells were transfected with siRNA-based polyplexes using siRNA able to knock down EGFP. Statistical analysis (t-test) against control cells, * represents $p < 0.05$ and # represents $p < 0.005$. Values represent the mean ± S.D. ($n \geq 3$).

An opposite trend was seen for the delivery of siRNA (Figure 3.10 D). Copolymers with a higher content of primary amino groups, namely **P19** and **P20**, revealed an improved silencing ability compared to **P21**. Although **P19** and **P20** demonstrated adequate knockdown levels, their design demonstrated still room for improvements as **P18** and the positive control jetPEI were more efficient in siRNA delivery. It could be suggested that the physicochemical characteristics of the nucleic acids (size, morphology) play an essential role for the interaction with the PEI copolymers (Figure 3.11). The large DNA molecule appeared to be capable to interact with both, the secondary amino groups within the PEI backbone as well as with the primary amino groups in the side chains to achieve sufficient condensation in a compact polyplex structure. In particular, the secondary amino groups seemed to be beneficial for DNA condensation and delivery. In contrast, it was assumed that the short strands of siRNA preferably interact with the primary amino groups of the flexible side chain, since they might be easier accessible than the EtOx encompassing secondary amino groups.

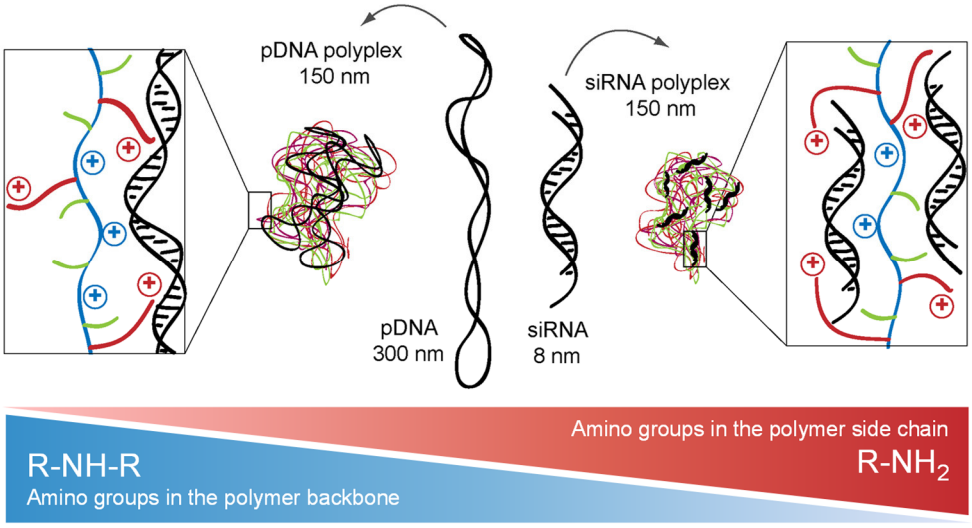

Figure 3.11. Schematic illustration of the influence of polymer composition on nucleic acid binding dependent on type and nature of nucleic acids.

Besides the sophisticated demands regarding biocompatibility and delivery efficiency of various genetic materials, the targeted delivery thereof to cells or the tissue of interest represents a further major challenge of modern gene therapy approaches. In particular, the blood-brain-barrier (BBB) is the most challenging obstacle regarding the delivery of therapeutic nucleic acids or other drugs.[119-121] The passage of macromolecules and

small molecules (98% < 400 g mol^{-1}) is strictly limited due to its defined structure: A tight cell layer of cerebral microvascular endothelial cells (CMEC) that are in close contact with astrocytes and pericytes.[122] There are several strategies to pass the BBB, on the one hand the passive diffusion by small molecules and, on the other hand, the active transport of macromolecules mainly mediated by carrier proteins or transcytosis.[120, 123-124] Thus, the introduction of targeting molecules to the polymeric vector enables the passage by receptor-initiated transport or transcytosis. The functionalization of polymers with the tripeptide L-Glutathione (GSH) was previously proven to be a promising targeting approach.[31-32, 125] Hence, the combination of the previously described PEI copolymers in the presence of primary or secondary functionalities with an additional GSH-decoration represent a powerful non-viral delivery concept to investigate the active targeting ability of the PEI derivatives through the BBB. In this context, **P18** was directly used as starting materials for the aimed copolymers. **P18** was modified by post-polymerization functionalization followed by thiol-ene photoaddition to install the GSH-targeting functionality with a simultaneous presence of either secondary or primary amino groups within the polymer backbone (Figure 3.12). The statistical copolymers P($EI_{73\%}$-*stat*-$GluBuOx_{27\%}$) stated as **P22** comprising only secondary amino groups in the polymer backbone and GSH in the sides chain as well as P($AmButOx_{82\%}$-*stat*-$ButEnOx_{10\%}$-*stat*-$GluButOx_{8\%}$) stated as **P23** containing primary amino groups and GSH in the corresponding side chains were investigated regarding their DNA delivery and targeting capabilities.

A

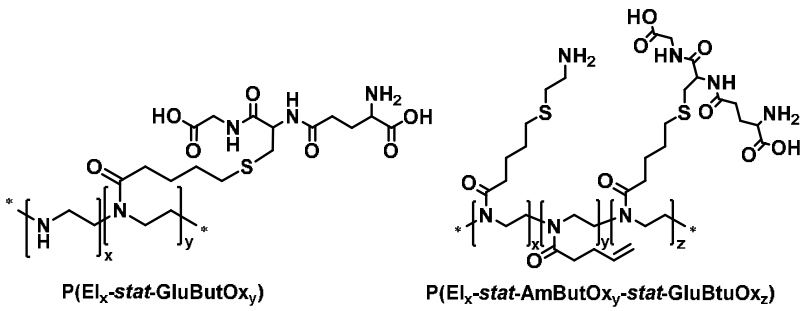

B

Abbr.	Polymer	Targeting unit	M_n[a] [g mol^{-1}]	Đ[a]
P18	P(EtOx$_{5\%}$-*stat*-EI$_{95\%}$)		9,900	1.4
P22	P(EI$_{73\%}$-*stat*-GluButOx$_{27\%}$)	GSH	21,000	2.0
P23	P(AmButOx$_{82\%}$-*stat*-ButEnOx$_{10\%}$-*stat*-GluButOx$_{8\%}$)	GSH	63,300	1.8

Figure 3.12. PEI-derivatives with GSH functionalization. **(A)** Schematic representation of the chemical structures of GSH-decorated PEI copolymers **P22** and **P23**. **(B)** Selected analysis data of the polymers. [a] Molar mass and dispersity values were determined by AF4 with a MALLS detector and a cellulose membrane with a molar-mass cut-off of 10 kDa.

Based on the polymer structure the bulky GSH moieties might cause the sterically hindrance of the accessibility to primary or secondary amino groups responsible for membrane interactions linked to toxicity as well as for DNA binding. In fact, **P22** and **P23** revealed improved cell viabilities compared to **P18** (Figure 3.13 A). This effect was more pronounced for **P22** probably due to the higher amount of GSH (27%) compared to **P23** (8%). A similar trend was observed for the pDNA binding abilities of the polymers (Figure 3.13 B). While **P18** showed a fast and stable binding to pDNA with increasing N/P ratio, both GSH-functionalized polymers, in particular **P22**, required higher polymer supplementation to achieve efficient polyplex formation. Based on its polymer composition, **P23** provides primary amino groups within the flexible side chain that in fact are easier accessible for the phosphates of the pDNA. Whereas, **P22** comprises solely secondary amino moieties for DNA binding which were presumably shielded by the presence of the GSH molecule.

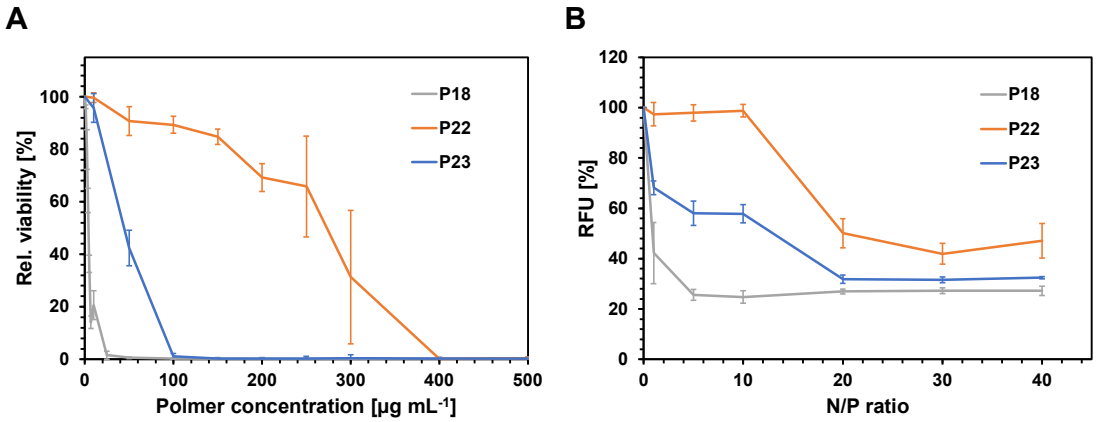

Figure 3.13. (A) Evaluation of the relative cell viability of L929 mouse fibroblast cells of GSH-decorated copolymers **P22** and **P23** as well as the non-decorated **P18** after 24 h according to ISO10993-5. **(B)** DNA binding affinity and polyplex formation by the ethidium bromide assay. Values represent the mean ± S.D. (n = 3).

A perfused microfluidic chip with an endothelial cell layer mimicking the BBB was used to investigate the capabilities of the GSH-modified polymers to cross the BBB. For this purpose, a human CMEC cell line (hCMEC/D3) resembling the cerebral endothelial cell layer of the BBB were cultured on a suspended membrane within a multi-organ-tissue-flow (MOTiF) biochip until full confluence. Labeled polyplexes (using YOYO-1 iodide labeled pDNA) based on **P18**, **P22** and **P23** were perfused under physiological conditions within the chip and the BBB passage was examined by fluorescence microscopy. The chip design allowed both, the investigation of the cellular uptake of polyplexes within the endothelial cell layer as well as the quantification of the total amount of polyplexes crossing the endothelial barrier. The highest enrichment of YOYO-1 labeled pDNA-polyplexes into the hCMEC/D3 cells was observed for **P23** as depicted in the microscopic images of Figure 3.14 A and the fluorescence intensity quantification in Figure 3.14 B. In contrast, **P22** revealed the lowest uptake into the barrier model system and **P18** exhibited moderate enrichment within the cell layer. Moreover, the determination of the trans-endothelial movement of the different polyplexes confirmed these findings. **P22**-based polyplexes revealed a time-dependent passage through the BBB as an increasing translocation was observed (Figure 3.14 C). However, **P23** was not able to cross the endothelial cell layer as the YOYO-fluorescence intensities remain low within the 60 min of perfusion. The diminished performance of

P23 could be explained by its chemical structure. The presence of primary amino functionalities as well as the unprotected double bonds lead to high cytotoxic effects and cell membrane activity, thus showing high unspecific interactions to cells. As depicted in Figure 3.14 A and B, **P23** was adhered to and internalized into the hCMEC/D3 cells probably followed by cargo release on location instead of translocation through the cell layer. The GSH content of **P23** of nearly 10% might be insufficient for translocation. The increased translocation of **P18** could be explained by its severe cytotoxicity causing defects in the endothelial layer's integrity and the disruption of tight junctions (immunofluorescence staining, data are shown in **Pub5**). Hence, the leakage of the hCMEC/D3 cell layer facilitate the translocation of **P18** but does not make it suitable for BBB gene delivery. Polyplexes based on **P22** with 27% GSH functionalities efficiently pass the BBB model barrier, thus making it a promising candidate as therapeutic nanocarrier.

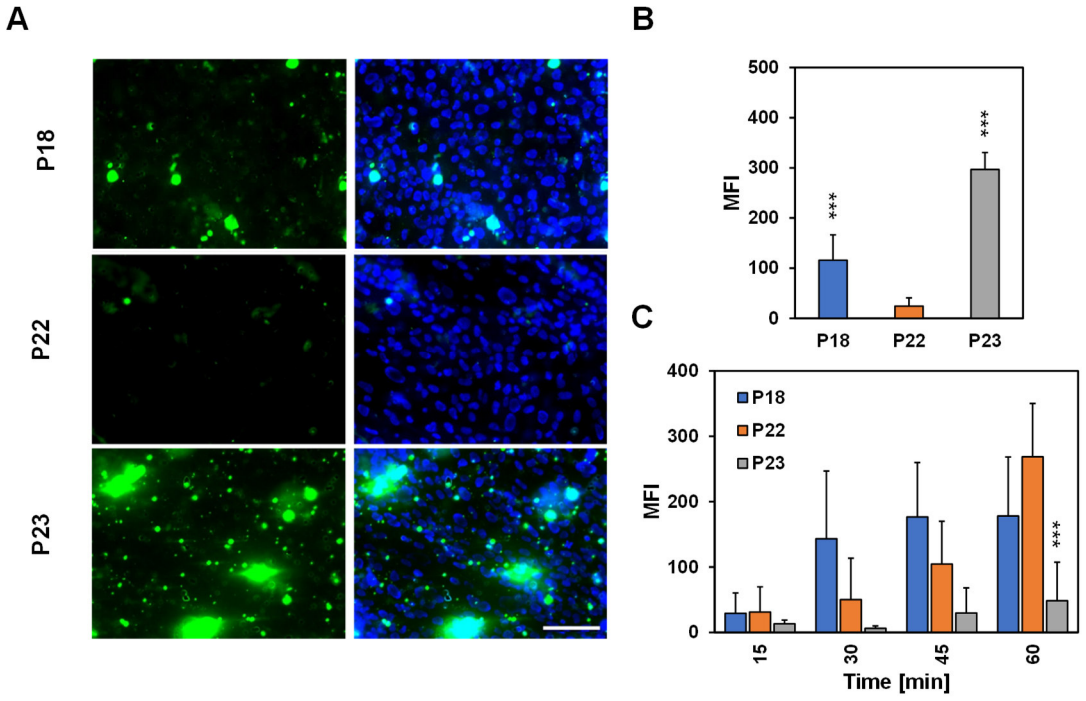

Figure 3.14. Perfusion of GSH-conjugated copolymers **P22** and **P23**, as well as **P18** in a microfluidically supported biochip assay mimicking the BBB. **(A)** Microscopic images displaying the YOYO-labeled polyplex (green) uptake within the hCMEC/D3 cells (cell nucleus stained blue by Hoechst 33342). **(B)** Quantification of polyplex internalization into hCMEC/D3 cells by image analysis. **(C)** Passage of polyplexes through the hCMEC/D3 cell layer over time. * Significances *vs.* **P22**, *** $p<0.001$, n = 3, scale bar = 100 nm.

To conclude, the presented PEI copolymers revealed several advantages over LPEI. It could be demonstrated that an EtOx content of around 50% markedly improved the overall cyto- and hemocompatibility. However, the introduction of functional moieties containing primary as well as secondary amino groups were required to ensure stable polyplex formation and sufficient internalization rates. The impact of the polymer design balancing stealth, functional and targeting moieties for efficient delivery was demonstrated. The PEI copolymers were able to outperform the gold standard LPEI in terms of (targeted) gene delivery with different types of nucleic acids at *in vivo* mimicking conditions. The introduction of L-Glutathione into the copolymer backbone resulted in successful targeting abilities. Thus, they represent promising alternatives for more complex transfection approaches including hard-to-transfect cells or tissues.

4. The delivery of drugs by poly(2-oxazoline)-based polymers

Parts of this chapter have been published in **Pub6** I. Yildirim, T. Bus, M. Sahn, T. Yildirim, D. Kalden, S. Hoeppener, A. Traeger, M. Westerhausen, C. Weber, U. S. Schubert, Fluorescent amphiphilic heterografted comb polymers comprising biocompatible PLA and PEtOx side chains, *Polym. Chem*. **2016**, *7*, 6064-6074, **Pub7** M. Hartlieb, T. Bus, J. Kübel, D. Pretzel, S. Hoeppener, M. N. Leiske, K. Kempe, B. Dietzek, U. S. Schubert, Tailoring cellular uptake and fluorescence of poly(2-oxazoline)-based nanogels, *Bioconjugate Chem.* **2017**, *28*, 1229-1235 and **Pub8** D. Hoelzer, M. N. Leiske, M. Hartlieb, T. Bus, D. Pretzel, S. Hoeppener, K. Kempe, R. Thierbach, U. S. Schubert, Tumor targeting with pH-responsive poly(2-oxazoline)-based nanogels for metronomic doxorubicin treatment, *Oncotarget* **2018**, *9*, 22316-22331.

Low solubility, diminished bioavailability and high cytotoxicity combined with strong immune responses are some of various drawbacks accompanied by the administration of pure pharmaceuticals. The utilization of polymeric nanocarriers offers the opportunity to deliver drugs to the desired site of action within the body by circumventing these drawbacks. Most drug delivery vectors are based on biocompatible and/or biodegradable polymers, which accomplish desired demands in terms of safety and controlled drug release. Pertinent polymers are polylactic acid (PLA) and poly(lactic-*co*-glycolic acid) (PLGA), which have been successfully approved for the delivery of various therapeutic agents.[37-38, 126] As both polymers are hydrophobic the most preferred drug delivery strategy is the formulation of nanoparticles by solvent evaporation using nanoprecipitation or emulsion techniques. The polymers PEG and POx are also utilized for drug delivery due to their stealth behavior, which favor high biocompatibility as well as high pharmacokinetics.[127-130] As revealed from *Chapter 3*, EtOx monomer units offer a great variation of compositions and allows the introduction of different side-chain functionalities. Therefore, PEtOx is well-suited for the formulation of drug-loaded polymeric vectors. It can be functionalized with hydrophobic moieties like PLA or others to generate amphiphilic molecules, thus facilitating the self-assembly to various structures like micelles or vesicles.[126] Due to their small sizes, which is usually below 100 nm, self-assembled structures are favored for passive targeting strategies, *i.e.* the EPR effect.[41, 131] To examine the potential of modified POx-based polymers for drug delivery, two different concepts of self-assembly were utilized and investigated (Figure 4.1): (i) Self-assembly of amphiphilic heterografted comb polymers comprising hydrophilic EtOx moieties as well as hydrophobic polylactide (LA) units and, (ii) core

cross-linked assemblies from diblock copolymers consisting of hydrophilic EtOx units as well as an amino group containing poly(4-amino-butyl-2-oxazoline) (AmOx) moieties.

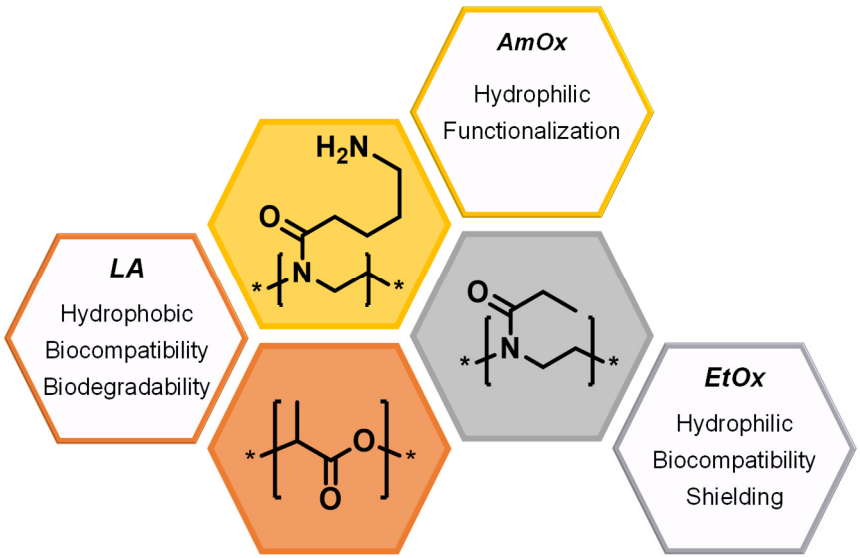

Figure 4.1. Schematic overview of the different moieties of POx-based polymers comprising stealth or biodegradation characteristics as well as amino functionalities utilized for drug delivery approaches. Asterisks indicate variable end groups.

With regard to the firstly mentioned concept, a series of heterografted comb polymers with molar masses ranging from 19.5 to 29 kDa comprising a methacrylate backbone with varying ratios of hydrophilic EtOx side chains (DP = 5) and hydrophobic LA side chains (DP = 10 or 15) were synthesized by a combination of ROP, CROP and RAFT polymerization (Figure 4.2 A and B). The obtained polymers **P24** to **P28** comprised the general structure: P($EtOx_5MA$-*stat*-$LA_{10/20}MA)_{n/m}$, and were investigated according to their increasing EtOx and decreasing LA content. Pyrene, which was covalently attached to the LA side chain, served as fluorescent drug model and additionally, was used as tracer to detect the cellular distribution. As a function of the chemical composition it was predicted that the self-assembly of the polymers in aqueous solutions led to spherical micelles or vesicles. Hence, it was assumed that the hydrophobic LA side chains with the pyrene label should be organized within the core of the self-assembled structures encompassed by the methacrylate backbone. Whereas, the hydrophilic EtOx

arms should point towards the water phase, thus shaping the outer layer of the self-assembled structures.

A

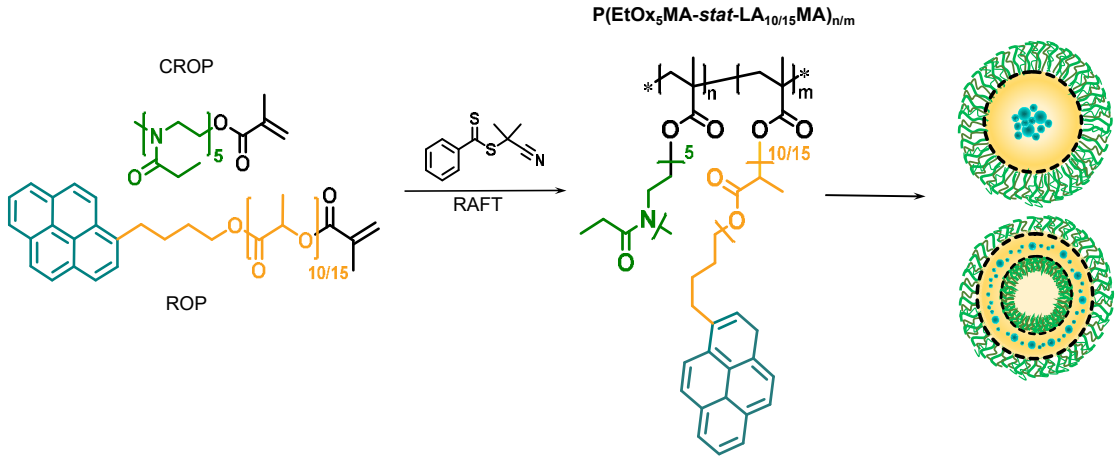

B

Abbr.	Polymer	EtOx/LA[a]	M_n[b] [g mol^{-1}]	Đ[b]
P24	P(EtOx$_5$MA-*stat*-LA$_{15}$MA)$_{45/55}$	45/55	27,500	1.2
P25	P(EtOx$_5$MA-*stat*-LA$_{10}$MA)$_{50/50}$	50/50	28,200	1.4
P26	P(EtOx$_5$MA-*stat*-LA$_{10}$MA)$_{65/35}$	65/35	29,000	1.3
P27	P(EtOx$_5$MA-*stat*-LA$_{10}$MA)$_{70/30}$	70/30	26,300	1.3
P28	P(EtOx$_5$MA-*stat*-LA$_{10}$MA)$_{80/20}$	80/20	19,500	1.2

Figure 4.2. (A) Schematic representation of the formation of the heterografted comb polymers consisting of EtOx$_n$ side chains (DP = 5), LA side chains (DP = 10 or 15) and a poly(methacrylate) backbone. The self-assembly of the amphiphilic structures was achieved by the solvent-evaporation method in water, which lead to the formation of micellular structures as well as vesicles dependent on the chemical composition. **(B)** Selected characterization data of the heterografted comb polymers. [a] Molar ratio of EtOx and LA repeating units were calculated from suitable signal integrals in the ^{1}H NMR spectra of purified polymers. [b] Molar mass and dispersity values were determined by SEC ($CHCl_3$, RI detection, PMMA calibration).

The actual morphology of the heterografted comb polymers were confirmed by dynamic light scattering (DLS) and cryogenic transmission electron microscopy (cryo-TEM) measurements revealing different self-assembled structures with varying sizes in aqueous media (Figure 4.3). The morphology correlated well with the hydrophilic character of the polymers. Polymers with a low EtOx content tend to form polydisperse mixtures of smaller spherical and worm-like micelles exhibiting sizes between 20 and

50 nm as well as large vesicles (segmented, distorted, lamellar) up to 400 nm (Figure 4.3, see cryo-TEM images of **P24** and **P25**). With increasing EtOx content more defined spherical structures with sizes around 15 to 50 nm in diameter were obtained. In particular, **P27** revealed micelles with monomodal size distributions (Figure 4.3). Due to the influence of EtOx, it is possible to tune the size and morphology of self-assemblies according to requested demands for drug delivery approaches.

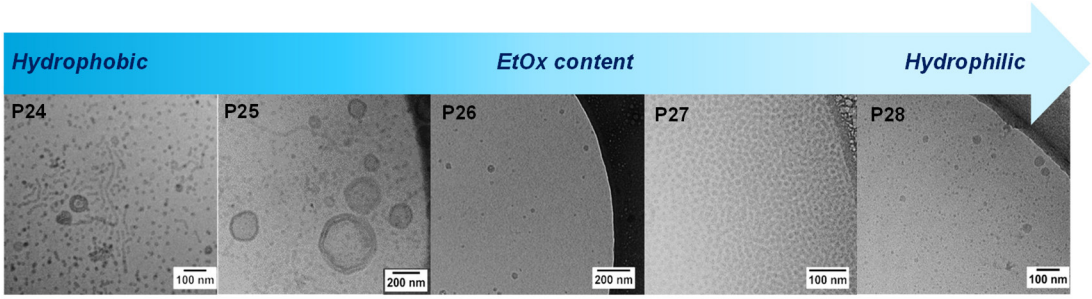

Figure 4.3. Determination of the size and morphology of heterografted comb polymer assemblies in water (5 mg mL^{-1}) by DLS and cryo-TEM measurements. Self-assembly were achieved by the dropping method (solvent to non-solvent).

No cytotoxicity for all self-assemblies was expected, as both side chains are known to be biocompatible.[37, 97] Indeed, high cell viabilities for all members of the heterografted comb polymer library were confirmed at the tested conditions, independent from the chemical compositions (Figure 4.4 A). This result furthermore endorsed the suggestion of micellar or vesicular structures including the shielding of the hydrophobic pyrene by the EtOx side chains. A gradual, but not critical, decrease in the cell viability was observed for some polymers at the highest tested concentration (200 µg mL^{-1}), which might be attributed to a slight release of pyrene from degraded LA side chains. Based on their varying size distribution, which could be prejudice passive or active internalization, the cellular entry mechanism was investigated at 37 °C and 4 °C by confocal live cell imaging (see exemplary images for **P24**, Figure 4.4 B and C)). All tested polymers revealed the cellular internalization of self-assemblies at physiological conditions, as pyrene signals (magenta) were detected in the cell cytoplasm. Interestingly, only few pyrene signals were co-localized with endo-lysosomal compartments (Figure 4.4 B, co-localization depicted as white signal), thus indicating either a rapid endosomal release after endocytosis or an alternate entry mechanism. Uptake studies at 4 °C revealed a significant reduction of intracellular pyrene signals

(Figure 4.4 C, white arrows), thus imply that a minor fraction of the self-assemblies (probably sizes below 20 nm in diameter) was able to enter cells by a passive uptake mechanism (*e.g.*, diffusion), whereas the majority was internalized by an energy-driven process (*e.g.*, endocytosis). A slow release of thereon attached hydrophobic molecules (fluorescent dye or drug) might be feasible due to the degradative nature of LA. Furthermore, as the majority of the self-assemblies was localized within the cytoplasm no advanced strategy for the endo-lysosomal barrier is required.

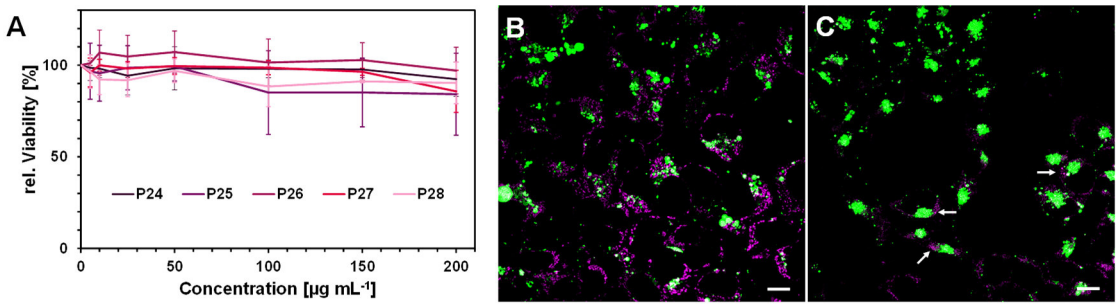

Figure 4.4. Biological evaluation of the heterografted comb polymer library. **(A)** Evaluation of the relative viability of L929 mouse fibroblasts treated with the comb polymers at indicated concentrations for 24 h, according to ISO10993-5. Values represent the mean ± S.D. (n = 3). Uptake study of **P24** (50 µg mL^{-1} in water) in HEK-293 cells at 37 °C **(B)** and 4 °C **(C)** after 4 h by confocal microscopy (overlay). Late endosomes or lysosomes were stained with LysoTracker Green (green) and pyrene is depicted in magenta. White arrows indicate the presence of pyrene within the cytoplasm. Scale bar = 10 µm.

Self-assembly is a dynamic process, which is influenced by various parameters like temperature, pH value, ionic strength or monomer/polymer composition.[132-134] Hence, the biological activity of self-assembled structures is strongly influenced by these factors and keeps the risc for failures in drug delivery. A concept to cirumvent this obstacle is the chemical cross-linking of self-assemblies to generate nanogels, revealing stable structures and controllable degradation for release purposes. POx-based diblock copolymers consisting of a hydrophilic PEtOx and an amino-containing poly(4-amino-butyl-2-oxazoline) (PAmOx) segment, which have been synthesized *via* CROP, were investigated for drug delivery (Figure 4.5 A and B). The P(EtOx-*b*-AmOx) was dissolved in chloroform to obtain micellar structures. In a next step, the amino moieties of the copolymer were further cross-linked by glutaraldehyde resulting in nanogels

comprising a hydrophilic PEtOx shell and a cross-linked core, which contained pH responsive imine bonds (Schiff base). Furthermore, fluorescein (**P29**) or doxorubicin (DOX, **P30**) have been covalently attached in a reversible manner to the cross-linked core of the nanogel to quench excessive aldehyde functions. By the variation of the degree of cross-linking, the size as well as the zeta potential could be adjusted, which consequently influenced the biological activity of the nanogels. An increase in the degree of cross-linking resulted in increased sizes (nearly two-fold), which might be explained by the swelling of the cross-linked part of the micelle. Furthermore, a decrease in the cationic zeta potential was observed with the increase in cross-linking. These effects resulted in diminished cellular internalization and demonstrated that the cell uptake of the nanogels could be fine-tuned according to respective demands for drug delivery by varying the cross-linking degree.

A

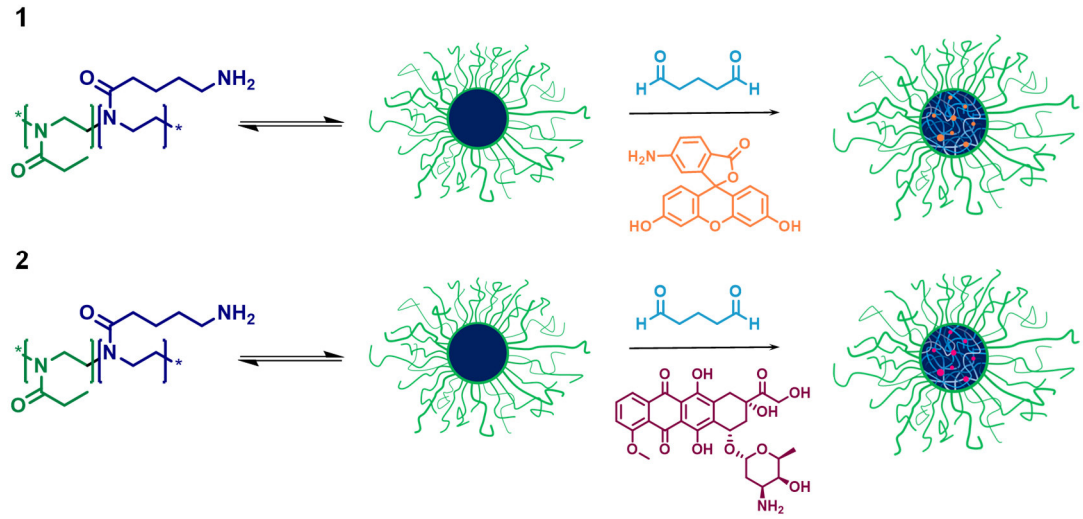

B

Abbr.	Composition	Loading	M_n[a] [g mol^{-1}]	Đ[a]
P29	P(EtOx$_{98}$-*b*-AmOx$_{32}$)	Fluorescein	13,900	1.1
P30	P(EtOx$_{98}$-*b*-AmOx$_{32}$)	Doxorubicin	13,900	1.1

Figure 4.5. (A) Schematic illustration of the formation of cross-linked PEtOx-based nanogels with covalently immobilized fluorescein **(1)** or doxorubicin **(2)**. Self-assembly was achieved in chloroform leading to micellar structures with a P(AmOx) core. Cross-linking was applied using glutaraldehyde. **(B)** Selected polymer characterization data. [a] Molar mass and dispersity values were determined by SEC (DMAc, poly(styrene) calibration).

Although the nanogels exhibited cationic charges, which are known for cytotoxic effects and low hemocompatibility, the fluorescein-loaded carrier **P29** did not affect the overall cytocompatibility (Figure 4.6 A, B and C) probably because of the EtOx shielding. To evaluate this kind of nanocarrier for therapeutic approaches in terms of drug delivery, fluorescein was replaced by DOX (**P30**). DOX is the most applied chemotherapeutic drug to combat various types of cancer, *e.g.*, hematologic malignancies, breast carcinoma or bone sarcoma.[135] Its mode of action can be divided into several mechanism including (i) the intercalation into DNA double strands, (ii) the prevention of DNA replication and transcription by the inhibition of the topoisomerase II and, (iii) the formation of free radicals causing DNA damage and apoptosis.[136-137] Despite its effectiveness in the therapeutic treatment, the administration of pure DOX causes different severe side effects.[135, 138] The loading of DOX into PEtOx-based nanogels could improve the overall biocompatibility and increase the availability at the tumor site. It was assumed that due to its small sizes (diameter < 20 nm), the nanogels are delivered to cancerous tissue by the EPR effect. The site-specific release of the drug was provoked by the pH responsive imine bonds (Schiff base). Stability studies demonstrated that the nanogels did not alter in size or polydispersity index (PDI) at physiological pH values (pH = 7.4) at 37 °C, whereas a lower pH value of 5.0 and the presence of glycine resulted in the increase of both parameters indicating the disassembling of the cross-linking connected with the potential release of the drug. Once DOX-loaded nanogels were internalized into tumor cells, the release of DOX occur within endo-lysosomal compartments exhibiting an acidic pH environment.[139] The efficient release of DOX was verified by cytotoxicity studies using a human colorectal carcinoma cell line (HT-29) (Figure 4.6 A), a well-known *in vitro* cancer model that was also used in xenograft mouse experiments. In contrast to the fluorescein-loaded nanogels **P29**, DOX-loaded nanogels (**P30**: CC_{50} = 0.752 µg mL^{-1}) revealed a concentration-dependent cytotoxicity profile comparable to free DOX (CC_{50} = 1.998 µg mL^{-1}). Besides the cytocompatibility, the hemocompatibility was evaluated as crucial prerequisite for *in vivo* applications including the absence of blood clotting for prolonged circulation times. Due to the stealth properties of the PEtOx blocks, **P30** did neither induce severe lysis of erythrocytes nor the aggregation thereof (Figure 4.6 B and C), which support the suitability of the nanogels for therapeutic administrations.

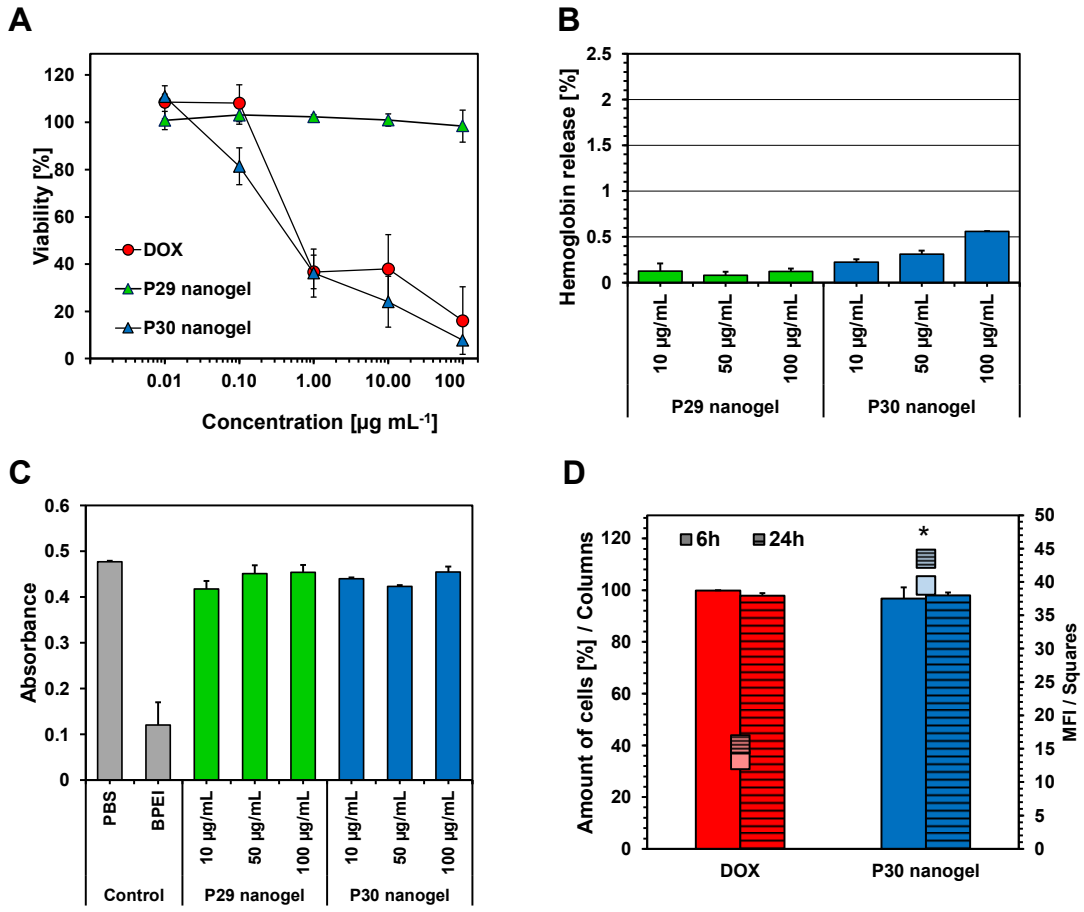

Figure 4.6. Biological investigations of free DOX, fluorescein-loaded (**P29**) as well as DOX-loaded nanogels (**P30**). **(A)** Evaluation of the relative viability of HT-29 cells after nanocarrier treatment at indicated concentrations for 72 h, according to ISO 10993-5. **(B)** Hemolysis assay at indicated concentrations on isolated erythrocytes from sheep blood samples. Triton X-100 served as positive control causing 100% hemoglobin release, while PBS served as negative control (0% hemoglobin release). A value < 2% was classified as non-hemolytic, 2 to 5% as slightly hemolytic and a value above 5% as hemolytic. **(C)** Erythrocyte aggregation of isolated erythrocytes from sheep blood samples. PBS served as negative control, while BPEI served as positive control. **(D)** Uptake study of the **P30** nanogels and DOX (0.01 mg mL^{-1}) on HT-29 cells at 37 °C. Internalization was measured by flow cytometry after 6 h (plain column) and 24 h (dashed column). Statistical analysis was performed for the MFI of DOX *vs*. **P30** nanogels after 6 h and is indicated as * $p < 0.05$ according to Student's *t*-test. Values represent the mean ± S.D. (n = 3).

To evaluate their biomedical potential, the cellular uptake of **P30** was investigated against the administration of pure DOX by flow cytometry (Figure 4.6 D) as well as CLSM measurements (Figure 4.7) using HT-29 cells. As depicted in Figure 4.6 D both

types of supplementation resulted in a rapid cellular internalization as indicated by an almost complete uptake (~100% positive cells) within the first 6 h. Nevertheless, **P30** revealed significantly increased MFI values, which increased in time, compared to the corresponding free DOX (Figure 4.6 D). These outcomes suggested an increased accumulation of the nanogels within the cells, while the reduced uptake of pure DOX might be explained by a P-glycoprotein-mediated efflux of DOX, which is a critical known phenomenon promoting the multidrug resistance of cancer cells (*e.g.*, breast cancer).[140-142] To explore the intracellular fate of the nanogels in more detail, its cellular distribution was investigated by live cell imaging. Due to the irreversible labeling of the nanogel **P30** with Alexafluor 660, the continuous tracking of the drug carrier itself as well as the detection of DOX release was possible. Within the first 6 h, **P30** were primary detected within endo-lysosomal compartments, supporting an energy-dependent uptake mechanism such as endocytosis (Figure 4.7). In contrast, free DOX showed both a diffuse localization within the cytosol but also a co-localization with the nucleus. The delayed accumulation of DOX delivered by polymer-based nanocarriers within the cell nuclei is in accordance to previous reports and is probably associated to its slow release kinetic.[143-144] After 24 h, free DOX is predominantly localized within the cell nucleus, thus suggesting either an intercalation into the DNA or a cellular efflux of cytoplasmic DOX. **P30** revealed DOX fluorescence co-localized with the nucleus counterstaining after 24 h, while the nanogel labeling (Alexafluor 660) remained within the endo-lysosomes. These findings suggested the partial degradation of the nanogel correlated with the gradual release of DOX and the entrance of the drug through the nuclear envelope. The weak DOX fluorescence signals of **P30** within the nucleus could be explained by previous reports describing that the fluorescence of DOX is highly dependent on its environment and might be decreased upon intercalation with genetic material but could be increased by the incorporation in membranes or micelles.[145-146] Nevertheless, both cytotoxicity as well as *in vitro* uptake studies of **P30** confirmed the extracellular stability and the intracellular degradation of the nanogels as well as the successful release of DOX as prerequisites for *in vivo* investigations to exploit the EPR effect.

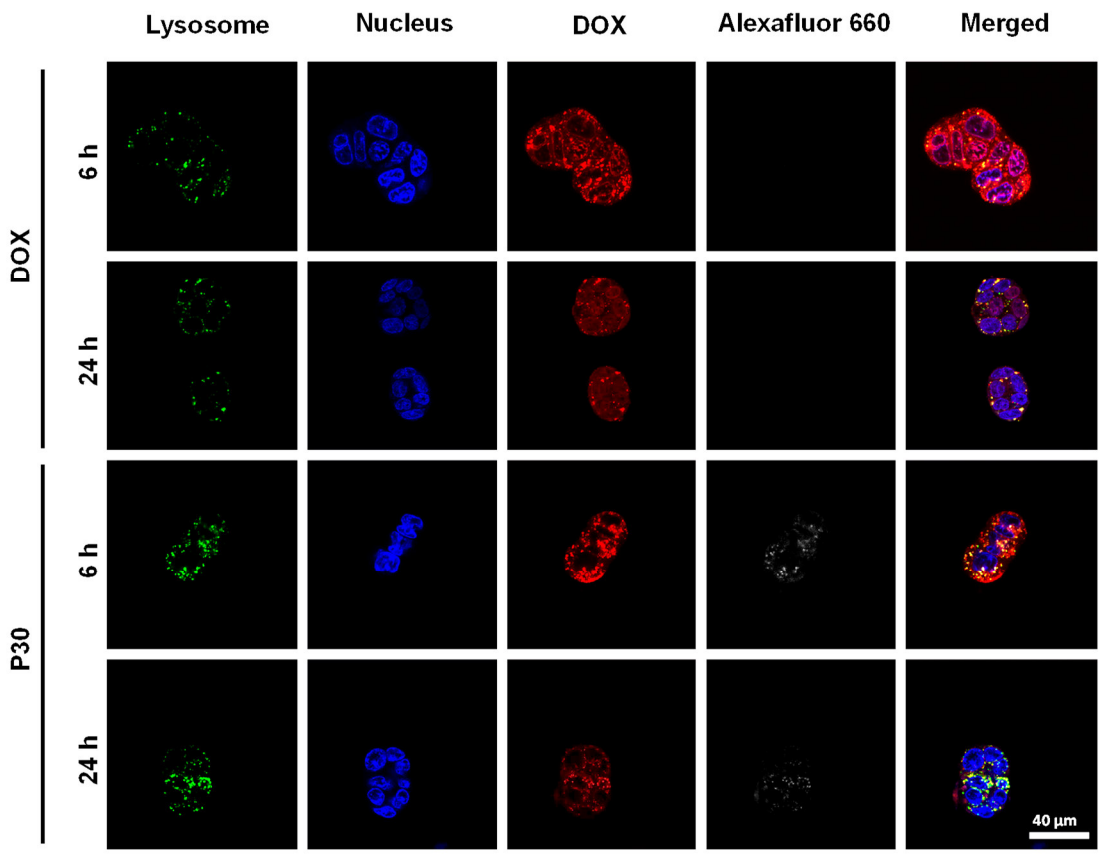

Figure 4.7. *In vitro* uptake study of pure DOX and **P30** (DOX-loaded nanogels) in HT-29 cells after 6 h and 24 h by CLSM. Endo-lysosomal compartments are depicted as green fluorescence signals, cell nuclei were counterstained by Hoechst and are depicted in blue. DOX is depicted in red and the nanogel labeling (Alexafluor 660) in white.

In vivo studies on male athymic nude mice (Crl:CD1-Foxn1^{nu}) with HT-29 originated tumors were performed to test the feasibility of passively targeted nanogels. In agreement with the concept of metronomic chemotherapy a relatively low DOX concentration (1 mg kg^{-1}) was utilized. In the first stage, the general nanogel administration (**P30**) was verified to be uncritical as no obvious signals of toxicity and no adverse effects on the body weight of mice were observed after a single dose treatment and a 2-week monitoring. The biodistribution of **P30** was investigated at different time points including 6, 48 and 72 h after a single dose injection of either **P30** (1 mg kg^{-1}) or a NaCl solution (negative control). Tumor tissue as well as selected organs (heart, liver, kidney) were excised and prepared for CLSM investigations (Figure 4.8). Histological tissue sections of the tumor demonstrated an early accumulation of

DOX indicated by an inhomogeneous red fluorescence within the first 6 h that is markedly reduced after 48 h and 72 h, respectively. A similar effect, including a high accumulation of DOX-containing nanocarriers within tumor tissue followed by a clearance within 72 h, was previously reported by Hruby and co-workers.[147] Weak traces of DOX were further observed within liver tissue, whereas the fluorescence signals increased in time. This indicated an increased accumulation and/or an excretion by this organ. Minor traces of DOX were detected in the heart and no DOX signals within the kidney, which is in accordance to other studies.[147-149] However, it could be assumed that the nanogels predominantly remain within the blood in accordance to similar studies.[147] Finally, these outcomes confirmed the concept of passive targeting of the nanogels exhibiting average diameters of around 20 nm by the EPR effect.

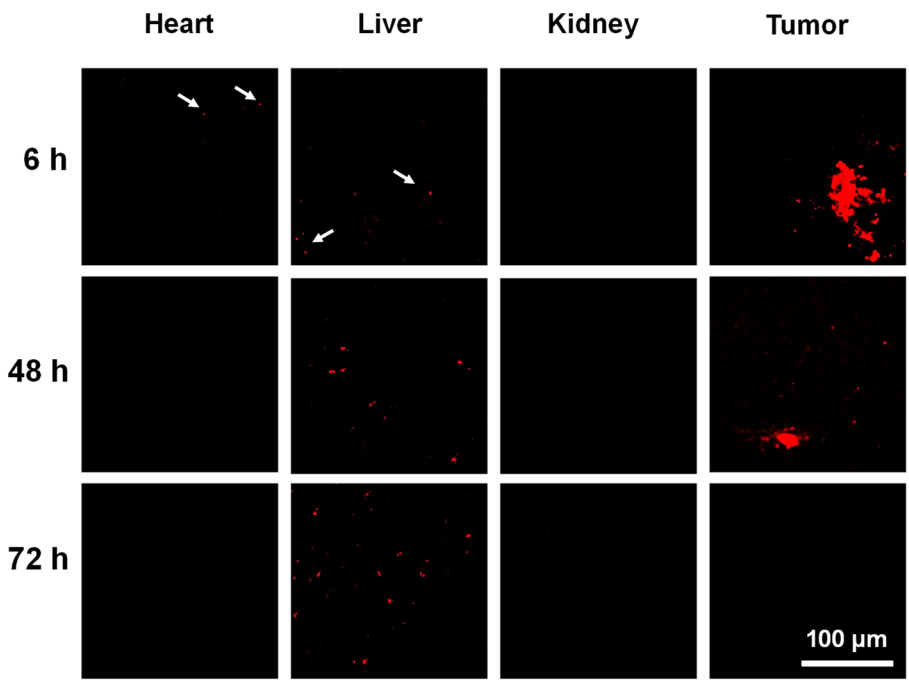

Figure 4.8. Biodistribution of DOX-loaded nanogel **P30**. Confocal fluorescence images of histological tissue sections derived from treated mice at different time points (1 mg kg^{-1} of **P30**). The fluorescence of DOX is depicted in red.

To investigate the therapeutic approach of **P30**, xenograft mouse models with HT-29 originated tumors were treated every third day with specific doses of NaCl (negative control), **P29**, **P30** and free DOX according to the metronomic schedule (six doses in total within 15 days). As depicted in Figure 4.9 A, **P30** was able to delay the tumor

growth of nude mice within the time frame of the study compared to the control groups (NaCl and **P29**). These results are supported by the Kaplan-Meier survival plot of the HT-29 xenograft models (Figure 4.9 B). The negative controls NaCl and **P29** revealed the lowest median survival time of 37 days or 24 days, respectively. The median survival time of free DOX was marginal higher indicated by 39 days. A reason for this result might be the low DOX concentration utilized in the study. However, the administration of **P30** showed highly promising results indicated by prolonged mice survival time of 73 days. This superior behavior might be explained by (i) the prolonged blood circulation time due the EtOx shielding, (ii) the passive targeting strategy by the EPR effect due to the small sizes of spherical structures (diameter < 20 nm) and (iii) the effective release within endo-lysosomal compartments leading to a highly effective toxicity profile.

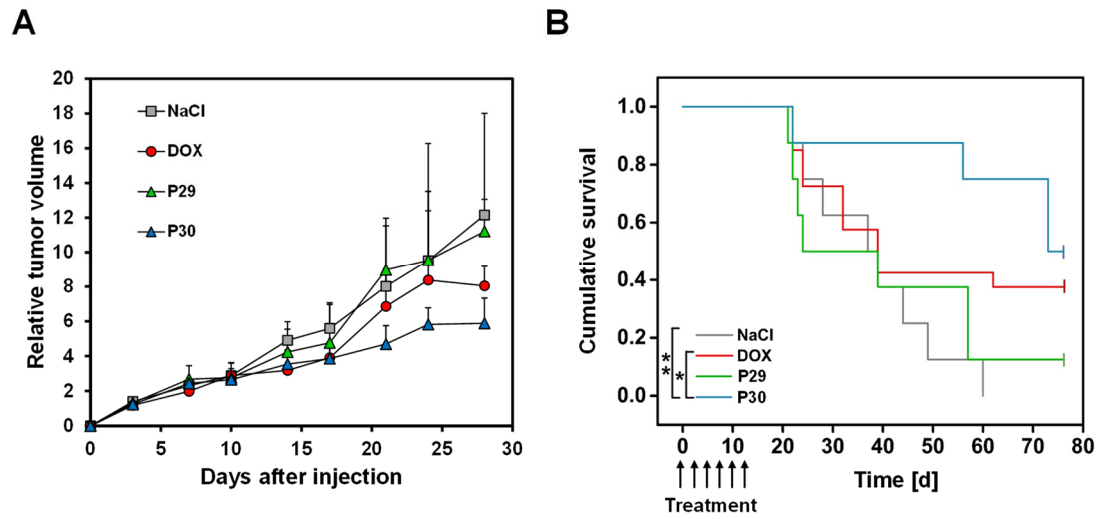

Figure 4.9. Metronomic treatment of xenograft mouse models with NaCl (negative control), DOX, **P29** (fluorescein-loaded nanogels) as well as **P30** (DOX-loaded nanogels). **(A)** The expansion of the relative tumor volume over time after administration. **(B)** Survival of mice presented as Kaplan-Meier plot. Statistical analysis is displayed as $*P < 0.05$ and $**P < 0.01$ according to the log-rank test.

In conclusion, the application of self-assembled structures based on grafted comb polymers or diblock copolymers represent a promising concept for the efficient delivery of various molecules and pharmaceuticals. Dependent on the chemical composition nano-sized micelles, vesicular structures and nanogels were obtained by nanoprecipitation and/or cross-linking. In particular, the utilization of biodegradable (*i.e.*, PLA) as well as stealth polymers (*e.g.*, PEtOx) were shown to be highly suitable

for drug delivery confirmed by the high bio- and cytocompatibility *in vitro* and *in vivo*. Different hydrophobic and hydrophilic molecules were covalently, but reversible, attached to the core of the self-assemblies, including fluorescent labels (pyrene, fluorescein) as tracer for tracking and imaging purposes as well as drug molecules (DOX) for therapeutic approaches. The controlled release of the cargo was triggered by pH stimuli within acidic endo-lysosomal compartments either due to degradation processes or pH responsiveness. Moreover, the nanocarriers were tunable in size, charge and morphology either by the content of PEtOx (micelles) or by the degree of cross-linking (nanogels), hence determining the cellular internalization.

5. Summary

Polymer-based nanocarriers represent promising tools for the modern nanomedicine as they open up new prospects in the diagnosis, prevention and treatment of various diseases and disorders. Common drawbacks of conventional medicines, such as poor bioavailability, impaired target specificity as well as toxicity and immunogenicity issues, can be overcome by the efficient and targeted delivery of therapeutically relevant substances by polymeric vectors. Due to the high flexibility in the polymer's chemical composition, the delivery strategy can be tailored individually to the specific demands of the substances to be delivered. With regard to the utilization of polymeric nanocarriers, a general distinction is made between the delivery of nucleic acids (gene delivery) and the delivery of pharmaceutical molecules (drug delivery). Since nucleic acids show different physical and chemical characteristics (size, stability, solubility *etc.*) compared to drugs, the type of polymer as well as the delivery and targeting strategy has to be customized according to the cargo and the intended purpose. This thesis deals with the utilization and evaluation of different polymer classes for the enhanced and targeted delivery of different biologically active substances (Figure 5.1).

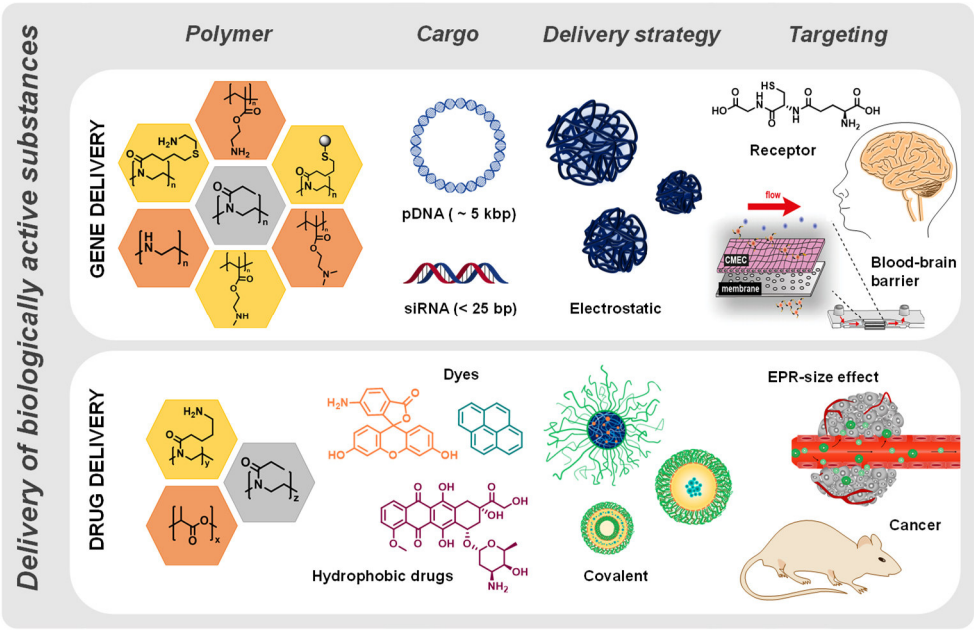

Figure 5.1. Schematic representation of an overview of the investigated polymers for the efficient and targeted gene and drug delivery.

Besides viral or lipid-based systems, cationic polymers are excellent vectors for the delivery of therapeutic nucleic acids. Cationic polymers are favored for the delivery of nucleic acids, since they can easily interact with the anionically charged genetic material through electrostatic interactions leading to the formation of nano-sized polymer-nucleic acid complexes, or so-called polyplexes. In particular, long and circular plasmid DNA (pDNA) is efficiently encapsulated by condensation into small and compact structures, whereas the complexation of small interfering RNA (siRNA), which only comprise a few base pairs, is more challenging due to the intrinsic rigid structure and the low spatial charge density. Classical cationic polymers that have successfully been applied for gene delivery for several decades are for instance poly(ethylene imine) (PEI) and poly(2-dimethylamino)ethyl methacrylate (PDMAEMA). Their good delivery performances and high transfection efficiencies are attributed to their polyelectrolyte structure comprising primary, secondary and/or tertiary amino groups. On the other hand, their high charge density is notorious to cause severe cytotoxic effects. This "efficiency-toxicity" paradox represent a crucial bottleneck and hampers the translation of the nanocarrier systems into serious clinical applications. To date, only a few studies examined the impact of amino functionalities on the final transfection performance and comparative information between such functionalities are still missing. To gain deeper knowledge on the polymer's structure-property relationship on the cellular level, the direct comparison of different amino functionalities as well as their influence on the overall transfection process was investigated. The reversible addition-fragmentation chain-transfer (RAFT) polymerization technique represents an ideal tool for this purpose, since it provides the controlled synthesis of well-defined polymers comprising primary, secondary and tertiary amino functionalities. A library of linear, well-defined homo- and copolymers based on (2-aminoethyl)-methacrylate (AEMA), *N*-methyl-(2-aminoethyl)-methacrylate (MAEMA) and *N,N*-dimethyl-(2-aminoethyl)-methacrylate (DMAEMA) monomers was investigated regarding their polyplex formation, cellular internalization, endosomal release ability and transfection efficiency. It was found that the type and content of the amino functionality clearly determined the gene delivery performance of the poly(methacrylate)s. The amino functionalized poly(methacrylate)s with a high content of primary amino groups (minimum 40 mol%) revealed superior transfection performances over secondary amino groups followed by tertiary amino groups. Contrary to the "proton sponge" hypothesis, a high buffer capacity does not seem to be the predominant factor for the efficient transfection *in vitro*. The high

efficiency of the poly(methacrylate)s could rather be explained by a strong polymer interaction with the vesicular membrane presumably leading to the formation of nano-holes and, thus, to a successful escape from endosomes. However, this enhanced membrane affinity causes severe cytotoxic effects, which could be overcome by the introduction of shielding moieties. Beside poly(ethylene glycol) (PEG), poly(2-ethyl-oxazoline) (PEtOx) reveals the favored stealth behavior and a high biocompatibility as well. Hence, PEtOx macromonomers were copolymerized with the methacrylate monomers AEMA and MAEMA to generate grafted copolymers. This strategy significantly improved the overall cell viability and was able to minimize or even eliminate cytotoxic side effects. Nevertheless, the degree of grafting as well as the length of PEtOx side chains has to be well balanced to maintain powerful gene delivery vectors, since an excessive stealth moiety functionalization bears the risk of impeding the transfection efficiency.

Since this strategy worked well for poly(methacrylate)s, it was decided to extend the scope for biocompatible but still highly efficient PEI copolymers. Although PEI remains the "gold standard" for transfection so far, major drawbacks like reduced water solubility, molar mass-dependent cytotoxicity and non-specific interactions with cellular as well as non-cellular components limit its application for biomedical approaches. Here, a straightforward strategy is provided to obtain highly functional PEI copolymers with beneficial stealth moieties. The partial hydrolysis of PEtOx combined with a post-polymerization functionalization followed by a thiol-ene photo-addition reaction enabled the introduction of functional moieties like primary amino groups or targeting ligands within a P(Ox-*stat*-EI) backbone. A series of copolymers with a constant PEtOx content but varying ratios of PEI (secondary amino groups) as well as P(AmButOx) (primary amino functionalities) was investigated for non-viral gene delivery. The results demonstrate the significance of the polymer design balancing stealth and functional moieties to assure high transfection performances. The novel PEI copolymers were able to outperform the "gold standard" PEI in terms of pDNA and siRNA delivery under *in vivo* mimicking conditions. With regard to a feasible biomedical application, the molecule L-Glutathione was introduced within the structure of PEI copolymers and examined as potential candidate for active targeting purposes. The successful passage of an artificial blood-brain-barrier (a microfluidically perfused biochip) was

demonstrated, which emphasizes the potential of the herein presented polymers for more complex transfection approaches including hard-to-transfect cells or tissues.

In contrast to gene delivery, most drug delivery vectors are composed of biocompatible and/or biodegradable polymers, which provide desired demands in terms of biosafety and controlled drug release. In particular, polylactic acid (PLA) and poly(lactic-*co*-glycolic acid) (PLGA) are the most utilized polymers with these properties. Furthermore, PEG and poly(2-oxazoline)s (POx) are utilized to improve the solubility of drugs but also to enable a prolongated blood circulation time due to the protein and cell repellent effect. Two different concepts of self-assembly were herein demonstrated to be highly suitable for the delivery of hydrophobic and hydrophilic molecules: (i) The self-assembly of amphiphilic heterografted comb polymers (micelles) comprising hydrophilic EtOx moieties and hydrophobic lactic acid (LA) units and, (ii) the core cross-linked assembly of diblock copolymers (nanogel) based on a PEtOx and a poly(2-(4-aminobutyl)-2-oxazoline) (PAmOx) segments. Contrary to gene delivery, the cargo was covalently attached to the hydrophobic part of the polymer. In a first approach, fluorescent probes including pyrene and fluorescein were successfully loaded into the self-assembled structures. The stimuli responsiveness and controlled release of the cargo was provoked at acidic pH conditions (*e.g.*, within endosomes) either by the degradation of the LA chains or by the pH-responsive imine bonds. The nanocarriers were tunable in their size, charge and morphology either by the content of PEtOx (micelles) or by the degree of cross-linking (nanogels). Moreover, their small sizes below 30 nm make them suitable for passive targeting strategies, in particular for the targeting of tumors by the enhanced permeability and retention (EPR) effect. In a proof-of-concept study, PEtOx-based nanogels were loaded with the chemotherapeutic agent doxorubicin (DOX) and evaluated *in vitro* as well as *in vivo* in xenograft mice models. The high biocompatibility of the drug carrier itself, the specific accumulation of DOX-loaded nanogels within the tumor site as well as an efficient drug release demonstrated the safety and feasibility of the nanogel for medical application. Noteworthy, the DOX-loaded nanogels outperformed the administration of pure DOX in terms of prolonged survival times.

In summary, polymer-based drug and gene delivery vectors demonstrate excellent prospects for their biomedical utilization. To exploit the full potential of this promising technology a fundamental understanding in the chemistry and the structure-property relationship of polymers on the molecular as well as cellular level are required. The presented work introduced novel multi-component polymers, which represent highly versatile systems for both, the delivery of diverse types of nucleic acids as well as relevant pharmaceuticals. New insights into polycation-mediated gene delivery were gained concerning the influence of amino functionalities and PEtOx stealth properties, which could be used to optimize the overall delivery performance. Furthermore, tailor-made PEtOx-based drug delivery vectors meet critical requirements like biosafety and efficacy, thus demonstrating their potential as therapeutic nanomedicines.

6. Zusammenfassung

Polymerbasierte Nanoträgersysteme gelten als vielversprechende Technologie der modernen Nanomedizin, da ihre Anwendung neue Perspektiven in der Diagnostik, Prävention und Behandlung verschiedenster Erkrankungen schaffen. Gegenüber konventionell verabreichten Therapeutika, welche häufig aufgrund einer schlechten Bioverfügbarkeit, fehlender Spezifität sowie einer erhöhten Toxizität oder Immunogenität nicht den gewünschten Effekt erzielen, sind Polymere in der Lage, biologisch aktive Substanzen zuverlässig und zielgerichtet an den gewünschten Wirkungsort zu transportieren. Aufgrund der hohen Flexibilität in ihrer chemischen Zusammensetzung, können Polymere individuell an die jeweilige zu vermittelnde Substanz adaptiert werden. Im Hinblick auf die Anwendung von polymeren Nanoträgersystemen wird zwischen dem Transport von Nukleinsäuren (Gentransport) und dem Transport von pharmazeutischen Wirkstoffen (Wirkstofftransport) unterschieden. Nukleinsäuren weisen im Vergleich zu pharmazeutischen Wirkstoffen andere physikalische und chemische Eigenschaften (Größe, Stabilität, Löslichkeit, etc.) auf. Daher müssen sowohl das polymerbasierte Trägersystem als auch die Transportstrategie auf die jeweilige Zielstellung zugeschnitten werden (Abbildung 6.1).

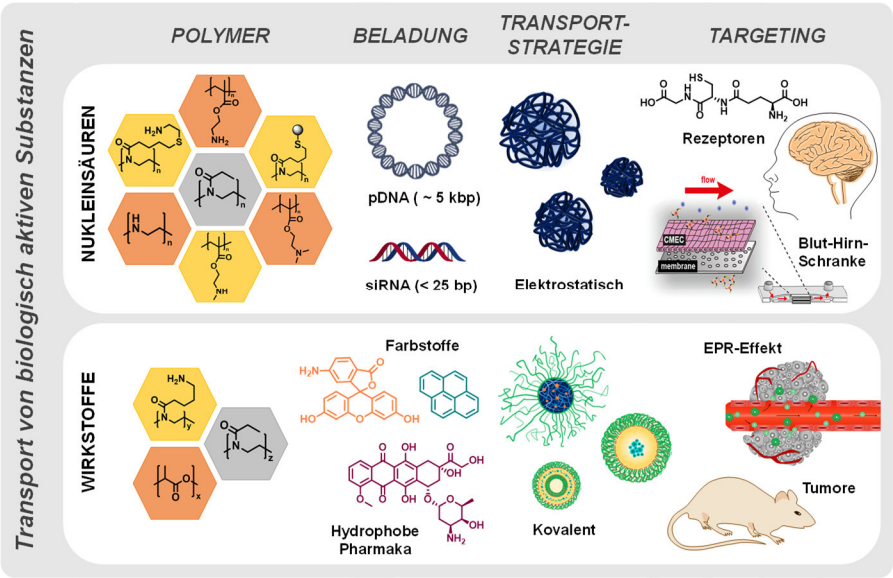

Abbildung 6.1. Schematische Darstellung einer Übersicht der hier untersuchten polymerbasierten Nanoträgersysteme für den effizienten und zielgerichteten Transport von therapeutisch relevanten Nukleinsäuren und Wirkstoffen.

Neben viralen und lipidbasierten Systemen sind kationische Polymere ausgezeichnete Trägermaterialien für die Vermittlung von therapeutischen Nukleinsäuren, da sie aufgrund von elektrostatischen Wechselwirkungen eine hohe Bindungsaffinität zu dem anionisch geladenen, genetischen Material aufweisen. Diese Wechselwirkung führt in der Regel zu einer spontanen Bildung von Polymer-Nukleinsäure-Komplexen, den sogenannten Polyplexen. Insbesondere Plasmid-DNA (pDNA) kann angesichts ihrer Größe und zirkulären Topologie sehr effizient in kleine und kompakte Strukturen verpackt werden, wohingegen die Komplexierung von „small interfering“ RNA (siRNA) infolge der starren Struktur (< 20 Basenpaare) sowie einer geringeren räumlichen Ladungsdichte eine größere Herausforderung darstellt. Poly(ethylenimin) (PEI) und Poly(2-dimethylamino)ethylmethacrylat (PDMAEMA) sind klassische Beispiele für kationische Polymere, die seit vielen Jahrzehnten erfolgreich für den Gentransport *in vitro* verwendet werden. Die hohe Transfektionseffizienz wird ihren Polyelektrolytstrukturen zugeschrieben, welche protonierbare primäre, sekundäre bzw. tertiäre Aminofunktionalitäten umfassen. Neben der Bindung und Komplexierung von genetischem Material führt die hohe Ladungsdichte zu schweren zytotoxischen Nebeneffekten. Das sogenannte „Effizienz-Toxizität“-Paradoxon erschwert die Umsetzung dieser polymeren Nanoträgersysteme in potenzielle Medizinprodukte für die klinische Anwendung. Bisher gibt es nur wenige Studien, die den Einfluss der Aminofunktionalitäten von Polymeren auf deren Transporteffizienz untersuchen oder die sich mit dem direkten Vergleich von primären, sekundären und tertiären Aminofunktionalitäten befassen. Um die Struktur-Eigenschafts-Beziehung von Polymeren auf der zellulären Ebene besser zu verstehen, wurde im Rahmen dieser Dissertation der Einfluss verschiedener Aminofunktionalitäten auf den gesamten Transfektionsprozess einschließlich Komplexierung, Aufnahme in die Zelle, endosomalen Austritt und Genexpression untersucht. Eine Bibliothek aus wohldefinierten Homo- und Copolymeren, bestehend aus (2-Aminoethyl)methacrylat (AEMA)-, *N*-Methyl-(2-aminoethyl)methacrylat (MAEMA)-und *N*,*N*-Dimethyl-(2-aminoethyl)methacrylat (DMAEMA)-Monomeren wurde hierzu *in vitro* getestet. Es konnte gezeigt werden, dass eine effiziente und hohe Transfektion entscheidend von der Art und Menge der Aminofunktionalität abhängt. Polymethacrylate mit einem hohen Anteil an primären Aminogruppen (mindestens 40 Mol-%) erzielten deutlich höhere Transfektionsraten als Polymethacrylate mit sekundären oder tertiären Aminogruppen in der Seitenkette. Entgegen der gängigen Meinung verdeutlichen diese Ergebnisse, dass

eine hohe Pufferkapazität nicht ausschlaggebend für eine hohe Transfektionseffizienz von Polymethacrylaten ist. Dies widerspricht zudem der „Protonenschwamm-Hypothese“, welche häufig als Hauptargument für die erfolgreiche Transfektion von kationischen Polymeren vorgebracht wird. Die Ergebnisse lassen die Vermutung zu, dass eine starke Wechselwirkung zwischen Polymer und endosomaler Membran für die hohe Transfektionseffizienz, insbesondere von Polymethacrylaten mit primären Aminofunktionalitäten, verantwortlich ist. Diese ausgeprägten Wechselwirkungen sind in der Lage die Membran zu permeabilisieren und den Austritt des Polyplexes aus dem Endosom über kleinste Membranöffnungen zu ermöglichen. Diese Membranaktivität führte jedoch simultan zu schweren zytotoxischen Effekten. Die Reduzierung solcher ungewollten Effekte kann über das Einbringen von biokompatiblen Monomeren mit sogenanntem „Stealth“-Effekt in die Polymerstruktur erzielt werden. Neben dem bekanntesten Vertreter Poly(ethylenglykol) (PEG) verfügt auch Poly(2-ethyl-oxazolin) (PEtOx) über derartige „Stealth“-Eigenschaften. Propfcopolymere, mit einem AEMA- bzw. MAEMA-Rückgrat und EtOx-Seitenketten, bestätigten die positive Wirkung der „Stealth“-Makromonomere auf die allgemeine Zellviabilität, da zytotoxische Effekte stark minimiert oder gänzlich eliminiert werden konnten. Dennoch muss bei Anwendung dieser Strategie auf eine angemessene Balance zwischen Kettenlänge und Propfgrad der EtOx-Makromonomere geachtet werden. Aufgrund des zell- und proteinabweisenden Effekts von „Stealth“-Polymeren kann sowohl die Bindungsaffinität zu DNA und Zellmembran als auch der endosomale Austritt beeinträchtigt werden und demzufolge zu Einbußen in der Transfektionseffizienz führen.

Die bei Polymethacrylaten erfolgreich eingesetzte Strategie wurde daher auch für PEI übertragen, um biokompatible aber dennoch höchst effiziente Copolymere zu erhalten und zu untersuchen. Obwohl PEI bis heute als „Goldstandard“ für *in vitro* Transfektionen eingesetzt wird, limitieren wesentliche Nachteile (verringerte Wasserlöslichkeit, molmassenabhängige Zytotoxizität, unspezifische Wechselwirkungen mit zellulären und nicht-zellulären Bestandteilen) die Anwendung als Nanomedizin. In unterschiedlichen Studien wurden bereits eine Reihe von Konzepten zur Steigerung der Biokompatibilität von PEI sowie die Herstellung von PEI-Derivaten vorgestellt. Die partielle Hydrolyse von PEtOx stellt einen besonders eleganten Ansatz dar, um funktionelle PEI-Copolymere mit den gewünschten „Stealth“-

Einheiten zu erhalten. Zudem erlaubt eine weiterführende Post-Polymerisationsfunktionalisierung inklusive Click-Chemie die Einführung von Aminogruppen (primäre Aminogruppen) oder Liganden für den zielgerichteten Transport. Die auf Grundlage dieser Synthesestrategie erhaltenen statistischen Copolymeren mit einem konstanten Anteil an PEtOx und variierenden Anteilen an PEI (sekundäre Amine) sowie PAmButOx (primäre Amine) wurden zellbiologisch untersucht. Diese Copolymere zeigten eine sehr gute Wirksamkeit in der Vermittlung von pDNA als auch siRNA, und waren in der Lage den „Goldstandard“ PEI unter „*in vivo*“-ähnlichen Bedingungen zu übertreffen. Im Hinblick auf eine mögliche biomedizinische Anwendung wurde das Targeting-Molekül L-Glutathion in die Struktur von PEI-Copolymeren eingefügt und erfolgreich in einem Blut-Hirn-Schranke-Modell (mikrofluidisch perfundierter Biochip) getestet. Die vielversprechenden Ergebnisse des zielgerichteten Gentransports unterstreichen das Potenzial dieser Polymere für komplexere Fragestellungen, wie beispielsweise schwer zu transfizierenden Zellen oder Gewebe.

Im Gegensatz zum Gentransport werden für den Wirkstofftransport überwiegend biokompatible und -abbaubare Polymere verwendet, da diese die gewünschten Anforderungen hinsichtlich Biosicherheit und einer kontrollierten Wirkstofffreisetzung erfüllen. Zu diesen zählen unter anderem die hydrophoben Polymere Polymilchsäure (PLA) und Poly(laktat-*co*-glykolsäure) (PLGA). Darüber hinaus spielen ebenso hydrophile Polymere mit „Stealth“-Eigenschaften, z. B. PEG und Poly(2-oxazoline) (POx), eine wichtige Rolle in der Verkapselung von Wirkstoffen. Aufgrund ihrer protein- und zellabweisenden Wirkung können u. a. die Bioverfügbarkeit und die Pharmakokinetik der Wirkstoffe deutlich verbessert werden. Neben der klassischen Verkapselung in Nanopartikeln ist die kovalente Bindung von Wirkstoffen an die Polymerstruktur eine effektive Strategie für den Wirkstofftransport. Zwei verschiedene Assemblierungskonzepte wurden in dieser Arbeit vorgestellt: (i) Die Assemblierung von amphiphilen Kammpolymeren (Mizellen) bestehend aus hydrophilen PEtOx-Einheiten und hydrophoben Milchsäureeinheiten, und (ii) die Assemblierung mit anschließender kovalenten Vernetzung (Nanogele) eines Diblock-Copolymers bestehend aus einem PEtOx- sowie einem Poly(2-(4-aminobutyl)-2-oxazoline) (PAmOx)-Segments. Im Gegensatz zu Genträgersystemen, wurde hier der Wirkstoff kovalent, aber dennoch reversibel, an das Polymer gebunden. In einem ersten Ansatz wurden

Fluoreszenzfarbstoffe (Pyren, Fluorescein) verkapselt. Die Freisetzung der Fluoreszenzfarbstoffe erfolgte entweder durch den Abbau der PLA-Ketten oder durch Abspaltung der Iminbindungen unter sauren pH-Bedingungen, beispielsweise in Endosomen. Weiterhin konnten die Größe, Ladung sowie Morphologie der Nanoträgersysteme über den PEtOx-Anteil innerhalb der Mizellen oder durch den Vernetzungsgrad der Nanogele angepasst werden. Hinsichtlich der kleinen Partikelgröße (Durchmesser kleiner als 30 nm) eignen sich diese Trägersysteme für passive Targeting-Strategien, z. B. für das Targeting von Tumoren über den erhöhten Permeabilitäts- und Retentionseffekt (EPR). In einer Machbarkeitsstudie („Proof-of-Concept“) wurden Doxorubicin-beladene (DOX) Nanogele *in vitro* und *in vivo* an Xenograft-Mausmodellen evaluiert. Die hohe Biokompatibilität des Trägermaterials, die spezifische Akkumulation der beladenen Nanogele im Tumorgewebe, die effiziente Wirkstofffreisetzung sowie die deutlich verlängerte Überlebensdauer, unterstreichen das große Potenzial dieser Systeme für die medizinische Anwendung.

Zusammenfassend konnte gezeigt werden, dass polymerbasierte Gen- sowie Wirkstoffträgersysteme eine vielversprechende Zukunft in der biomedizinischen Anwendung bieten. Um das volle Potenzial dieser Technologie auszuschöpfen, ist ein grundlegendes Verständnis hinsichtlich der chemischen Komposition und der Struktur-Eigenschafts-Beziehung des Polymers auf molekularer sowie zellulärer Ebene notwendig. In dieser Dissertation wurden neue Mehrkomponenten-Polymere vorgestellt, welche alle Voraussetzungen für den Transport von Nukleinsäuren, als auch für relevante pharmazeutische Wirkstoffe erfüllen. Es wurden neue Einblicke in den Polymer-vermittelten Gentransport hinsichtlich des Einflusses von Amino- und PEtOx-Funktionalitäten gewonnen, die zur Optimierung der Transfektionseffizienz solcher Systeme genutzt werden können. Zudem konnte gezeigt werden, dass maßgeschneiderte PEtOx-basierte Wirkstoffträgersysteme die hohen Anforderungen bezüglich Biosicherheit und Wirksamkeit erfüllen können.

7. References

[1] G. Chen, I. Roy, C. Yang, P. N. Prasad, *Chem. Rev.* **2016**, *116*, 2826-2885.
[2] D. Bobo, K. J. Robinson, J. Islam, K. J. Thurecht, S. R. Corrie, *Pharm. Res.* **2016**, *33*, 2373-2387.
[3] C. L. Ventola, *P T.* **2017**, *42*, 742-755.
[4] C. Fornaguera, M. J. García-Celma, *J. Pers. Med.* **2017**, *7*, 12, doi: 10.3390/jpm7040012.
[5] L. F. Gottfried, D. A. Dean, in *Novel Gene Therapy Approaches* (Eds.: M. Wei, D. Good), InTech, Rijeka, **2013**, p. Ch. 04.
[6] C. H. Jones, C. K. Chen, A. Ravikrishnan, S. Rane, B. A. Pfeifer, *Mol. Pharmaceutics* **2013**, *10*, 4082-4098.
[7] M. Collins, A. Thrasher, *Proc. R. Soc. Lond. B Biol. Sci.* **2015**, *282*, 20143003.
[8] V. S. Meka, M. K. G. Sing, M. R. Pichika, S. R. Nali, V. R. M. Kolapalli, P. Kesharwani, *Drug Discov. Today* **2017**, *22*, 1697-1706.
[9] S. J. Lee, S. Son, J. Y. Yhee, K. Choi, I. C. Kwon, S. H. Kim, K. Kim, *Biotechnol. Adv.* **2013**, *31*, 491-503.
[10] B. Yameen, W. I. Choi, C. Vilos, A. Swami, J. Shi, O. C. Farokhzad, *J. Control. Release* **2014**, *190*, 485-499.
[11] J. Rejman, A. Bragonzi, M. Conese, *Mol. Ther.* **2005**, *12*, 468-474.
[12] A. K. Varkouhi, M. Scholte, G. Storm, H. J. Haisma, *J. Control. Release* **2011**, *151*, 220-228.
[13] U. Lachelt, E. Wagner, *Chem. Rev.* **2015**, *115*, 11043-11078.
[14] Y. Xiang, N. N. L. Oo, J. P. Lee, Z. Li, X. J. Loh, *Drug Discov. Today* **2017**, *22*, 1318-1335.
[15] P. Zhang, E. Wagner, *Top. Curr. Chem. (Cham)* **2017**, *375*, 26, doi: 10.1007/s41061-017-0112-0.
[16] M. Neu, D. Fischer, T. Kissel, *J. Gene. Med.* **2005**, *7*, 992-1009.
[17] O. Boussif, F. Lezoualch, M. A. Zanta, M. D. Mergny, D. Scherman, B. Demeneix, J. P. Behr, *Proc. Natl. Acad. Sci. USA* **1995**, *92*, 7297-7301.
[18] D. Fischer, Y. Li, B. Ahlemeyer, J. Krieglstein, T. Kissel, *Biomaterials* **2003**, *24*, 1121-1131.
[19] G. Grandinetti, N. P. Ingle, T. M. Reineke, *Mol. Pharmaceutics* **2011**, *8*, 1709-1719.
[20] S. M. Moghimi, P. Symonds, J. C. Murray, A. C. Hunter, G. Debska, A. Szewczyk, *Mol. Ther.* **2005**, *11*, 990-995.
[21] F. M. Veronese, G. Pasut, *Drug Discov. Today* **2005**, *10*, 1451-1458.
[22] K. Knop, R. Hoogenboom, D. Fischer, U. S. Schubert, *Angew. Chem. Int. Ed.* **2010**, *49*, 6288-6308.
[23] R. P. Garay, R. El-Gewely, J. K. Armstrong, G. Garratty, P. Richette, *Expert Opin. Drug Deliv.* **2012**, *9*, 1319-1323.
[24] Q. Yang, S. K. Lai, *Wiley Interdiscip. Rev. Nanomed. Nanobiotechnol.* **2015**, *7*, 655-677.
[25] R. Luxenhofer, Y. Han, A. Schulz, J. Tong, Z. He, A. V. Kabanov, R. Jordan, *Macromol. Rapid Commun.* **2012**, *33*, 1613-1631.
[26] H. Bludau, A. E. Czapar, A. S. Pitek, S. Shukla, R. Jordan, N. F. Steinmetz, *Eur. Polym. J.* **2017**, *88*, 679-688.
[27] R. Konradi, B. Pidhatika, A. Muhlebach, M. Textort, *Langmuir* **2008**, *24*, 613-616.
[28] Y. Ikeda, Y. Nagasaki, *J. Appl. Polym. Sci.* **2014**, *131*, doi: 10.1002/app.40293.
[29] A. G. Schätzlein, *J. Biomed. Biotechnol.* **2003**, *2003*, 149-158.
[30] C. Englert, M. Prohl, J. A. Czaplewska, C. Fritzsche, E. Preussger, U. S. Schubert, A. Traeger, M. Gottschaldt, *Macromol. Biosci.* **2017**, *17*, doi: 10.1002/mabi.201600502.

[31] P. J. Gaillard, C. C. M. Appeldoorn, R. Dorland, J. van Kregten, F. Manca, D. J. Vugts, B. Windhorst, G. A. M. S. van Dongen, H. E. de Vries, D. Maussang, O. van Tellingen, *PloS One* **2014**, *9*, doi: 10.1371/journal.pone.0082331.
[32] A. Grover, A. Hirani, Y. Pathak, V. Sutariya, *Aaps PharmSciTech* **2014**, *15*, 1562-1568.
[33] H. Rainer, K. Felix, *Angew. Chem. Int. Ed.* **2006**, *45*, 1198-1215.
[34] T. Ramasamy, H. B. Ruttala, B. Gupta, B. K. Poudel, H.-G. Choi, C. S. Yong, J. O. Kim, *J. Control. Release* **2017**, *258*, 226-253.
[35] L. Shang, K. Nienhaus, G. U. Nienhaus, *J. Nanobiotechnology* **2014**, *12*, 5.
[36] O. Pillai, R. Panchagnula, *Curr. Opin. Chem. Biol.* **2001**, *5*, 447-451.
[37] B. Tyler, D. Gullotti, A. Mangraviti, T. Utsuki, H. Brem, *Adv. Drug Deliver. Rev.* **2016**, *107*, 163-175.
[38] D. N. Kapoor, A. Bhatia, R. Kaur, R. Sharma, G. Kaur, S. Dhawan, *Ther. Deliv.* **2015**, *6*, 41-58.
[39] H. Maeda, G. Y. Bharate, J. Daruwalla, *Eur. J. Pharm. Biopharm.* **2009**, *71*, 409-419.
[40] R. K. Jain, T. Stylianopoulos, *Nat. Rev. Clin. Oncol.* **2010**, *7*, 653-664.
[41] J. W. Hickey, J. L. Santos, J.-M. Williford, H.-Q. Mao, *J. Control. Release* **2015**, *219*, 536-547.
[42] S. Y. Wong, J. M. Pelet, D. Putnam, *Prog. Polym. Sci.* **2007**, *32*, 799-837.
[43] D. W. Pack, A. S. Hoffman, S. Pun, P. S. Stayton, *Nat. Rev. Drug Discov.* **2005**, *4*, 581.
[44] S. C. De Smedt, J. Demeester, W. E. Hennink, *Pharm. Res.* **2000**, *17*, 113-126.
[45] B. Yameen, W. I. Choi, C. Vilos, A. Swami, J. Shi, O. C. Farokhzad, *J. Control. Release* **2014**, *190*, 485-499.
[46] E. Wagner, *Adv. Drug Deliver. Rev.* **1999**, *38*, 279-289.
[47] G. van Meer, D. R. Voelker, G. W. Feigenson, *Nat. Rev. Mol. Cell Biol.* **2008**, *9*, 112-124.
[48] G. T. Hess, W. H. Humphries, N. C. Fay, C. K. Payne, *BBA-Mol. Cell Res.* **2007**, *1773*, 1583-1588.
[49] P. Midoux, G. Breuzard, J. P. Gomez, C. Pichon, *Curr. Gene Ther.* **2008**, *8*, 335-352.
[50] J. Rejman, V. Oberle, I. S. Zuhorn, D. Hoekstra, *Biochem. J.* **2004**, *377*, 159-169.
[51] R. G. Parton, *Dev. Cell*, *7*, 458-460.
[52] P. K. Selbo, A. Weyergang, A. Hogset, O. J. Norum, M. B. Berstad, M. Vikdal, K. Berg, *J. Control. Release* **2010**, *148*, 2-12.
[53] J. P. Behr, *Chimia* **1997**, *51*, 34-36.
[54] N. D. Sonawane, F. C. Szoka, A. S. Verkman, *J. Biol. Chem.* **2003**, *278*, 44826-44831.
[55] P. van de Wetering, E. E. Moret, N. M. Schuurmans-Nieuwenbroek, M. J. van Steenbergen, W. E. Hennink, *Bioconjugate Chem.* **1999**, *10*, 589-597.
[56] J. Haensler, F. C. Szoka, *Bioconjugate Chem.* **1993**, *4*, 372-379.
[57] R. V. Benjaminsen, M. A. Mattebjerg, J. R. Henriksen, S. M. Moghimi, T. L. Andresen, *Mol. Ther.* **2013**, *21*, 149-157.
[58] W. T. Godbey, M. A. Barry, P. Saggau, K. K. Wu, A. G. Mikos, *J. Biomed. Mater. Res.* **2000**, *51*, 321-328.
[59] Y. Y. Won, R. Sharma, S. F. Konieczny, *J. Control. Release* **2009**, *139*, 88-93.
[60] A. Kichler, C. Leborgne, E. Coeytaux, O. Danos, *J. Gene. Med.* **2001**, *3*, 135-144.
[61] A. Akinc, M. Thomas, A. M. Klibanov, R. Langer, *J. Gene. Med.* **2005**, *7*, 657-663.
[62] Z. U. Rehman, D. Hoekstra, I. S. Zuhorn, *ACS Nano* **2013**, *7*, 3767-3777.
[63] R. Rattan, S. Vaidyanathan, G. S. H. Wu, A. Shakya, B. G. Orr, M. M. B. Holl, *Mol. Pharmaceutics* **2013**, *10*, 3013-3022.
[64] S. Vaidyanathan, J. Chen, B. G. Orr, M. M. B. Holl, *Mol. Pharmaceutics* **2016**, *13*, 1967-1978.
[65] S. Vaidyanathan, B. G. Orr, M. M. B. Holl, *Accounts Chem. Res.* **2016**, *49*, 1486-1493.

[66] Y. A. Yue, F. Jin, R. Deng, J. G. Cai, Y. C. Chen, M. C. M. Lin, H. F. Kung, C. Wu, *J. Control. Release* **2011**, *155*, 67-76.
[67] A. Shakya, C. A. Dougherty, Y. Xue, H. M. Al-Hashimi, M. M. B. Holl, *Biomacromolecules* **2016**, *17*, 154-164.
[68] S. Boeckle, K. von Gersdorff, S. van der Piepen, C. Culmsee, E. Wagner, M. Ogris, *J. Gene. Med.* **2004**, *6*, 1102-1111.
[69] S. R. Clark, K. Y. Lee, H. Lee, J. Khetan, H. C. Kim, Y. H. Choi, K. Shin, Y. Y. Won, *Acta Biomater.* **2018**, *65*, 317-326.
[70] S. Vaidyanathan, K. B. Anderson, R. L. Merzel, B. Jacobovitz, M. P. Kaushik, C. N. Kelly, M. A. van Dongen, C. A. Dougherty, B. G. Orr, M. M. B. Holl, *ACS Nano* **2015**, *9*, 6097-6109.
[71] C. K. Choudhury, A. Kumar, S. Roy, *Biomacromolecules* **2013**, *14*, 3759-3768.
[72] G. Grandinetti, A. E. Smith, T. M. Reineke, *Mol. Pharmaceutics* **2012**, *9*, 523-538.
[73] I. Moret, J. Esteban Peris, V. M. Guillem, M. Benet, F. Revert, F. Dasí, A. Crespo, S. F. Aliño, *J. Control. Release* **2001**, *76*, 169-181.
[74] M. Ruponen, S. Ronkko, P. Honkakoski, J. Pelkonen, M. Tammi, A. Urtti, *J. Biol. Chem.* **2001**, *276*, 33875-33880.
[75] E. E. Vaughan, D. A. Dean, *Mol. Ther.* **2006**, *13*, 422-428.
[76] E. Dauty, A. S. Verkman, *J. Biol. Chem.* **2005**, *280*, 7823-7828.
[77] S. Grosse, Y. Aron, G. Thevenot, M. Monsigny, I. Fajac, *J. Control. Release* **2007**, *122*, 111-117.
[78] U. F. Greber, M. Way, *Cell* **2006**, *124*, 741-754.
[79] S. Grosse, G. Thevenot, M. Monsigny, I. Fajac, *J. Gene. Med.* **2006**, *8*, 845-851.
[80] R. L. Matz, B. Erickson, S. Vaidyanathan, J. F. Kukowska-Latallo, J. R. Baker, B. G. Orr, M. M. B. Holl, *Mol. Pharmaceutics* **2013**, *10*, 1306-1317.
[81] A. P. Lam, D. A. Dean, *Gene Ther.* **2010**, *17*, 439-447.
[82] K. Matyjaszewski, *Macromolecules* **2012**, *45*, 4015-4039.
[83] M. Ahmed, R. Narain, *Prog. Polym. Sci.* **2013**, *38*, 767-790.
[84] F. J. Xu, K. G. Neoh, E. T. Kang, *Prog. Polym. Sci.* **2009**, *34*, 719-761.
[85] C. H. Zhu, S. Jung, G. Y. Si, R. Cheng, F. H. Meng, X. L. Zhu, T. G. Park, Z. Y. Zhong, *J. Polym. Sci. A Polym. Chem.* **2010**, *48*, 2869-2877.
[86] D. Sprouse, T. M. Reineke, *Biomacromolecules* **2014**, *15*, 2616-2628.
[87] S. Agarwal, Y. Zhang, S. Maji, A. Greiner, *Mater. Today* **2012**, *15*, 388-393.
[88] P. vandeWetering, J. Y. Cherng, H. Talsma, W. E. Hennink, *J. Control. Release* **1997**, *49*, 59-69.
[89] T. Bieber, W. Meissner, S. Kostin, A. Niemann, H. P. Elsasser, *J. Control. Release* **2002**, *82*, 441-454.
[90] D. Hertz, M. N. Leiske, T. Wloka, A. Traeger, M. Hartlieb, M. M. Kessels, S. Schubert, B. Qualmann, U. S. Schubert, *J. Polym. Sci. A Polym. Chem.* **2018**, *56*, 1210-1224.
[91] J. M. Layman, S. M. Ramirez, M. D. Green, T. E. Long, *Biomacromolecules* **2009**, *10*, 1244-1252.
[92] R. A. Jones, M. H. Poniris, M. R. Wilson, *J. Control. Release* **2004**, *96*, 379-391.
[93] H. N. Po, N. M. Senozan, *J. Chem. Educ.* **2001**, *78*, 1499.
[94] P. Dubruel, B. Christiaens, B. Vanloo, K. Bracke, M. Rosseneu, J. Vandekerckhove, E. Schacht, *Eur. J. Pharm. Sci.* **2003**, *18*, 211-220.
[95] A. M. Funhoff, C. F. van Nostrum, G. A. Koning, N. M. Schuurmans-Nieuwenbroek, D. J. Crommelin, W. E. Hennink, *Biomacromolecules* **2004**, *5*, 32-39.
[96] M. Reifarth, S. Hoeppener, U. S. Schubert, *Adv. Mater.* **2018**, *30*, doi: 10.1002/adma.201703704.
[97] M. Bauer, C. Lautenschlaeger, K. Kempe, L. Tauhardt, U. S. Schubert, D. Fischer, *Macromol. Biosci.* **2012**, *12*, 986-998.
[98] M. Ogris, G. Walker, T. Blessing, R. Kircheis, M. Wolschek, E. Wagner, *J. Control. Release* **2003**, *91*, 173-181.

[99] S. D. Li, L. Huang, *J. Control. Release* **2010**, *145*, 178-181.
[100] S. Uzgun, O. Akdemir, G. Hasenpusch, C. Maucksch, M. M. Golas, B. Sander, H. Stark, R. Imker, J. F. Lutz, C. Rudolph, *Biomacromolecules* **2010**, *11*, 39-50.
[101] J. Hoffmann, J. Groll, J. Heuts, H. T. Rong, D. Klee, G. Ziemer, M. Moeller, H. P. Wendel, *J. Biomat. Sci. Polym. E.* **2006**, *17*, 985-996.
[102] K. A. Curtis, D. Miller, P. Millard, S. Basu, F. Horkay, P. L. Chandran, *PloS One* **2016**, *11*.
[103] P. Chollet, M. C. Favrot, A. Hurbin, J. L. Coll, *J. Gene. Med.* **2002**, *4*, 84-91.
[104] J. Liu, X. L. Jiang, L. Xu, X. M. Wang, W. E. Hennink, R. X. Zhuo, *Bioconjugate Chem.* **2010**, *21*, 1827-1835.
[105] N. Zhao, S. Roesler, T. Kissel, *Int. J. Pharm.* **2011**, *411*, 197-205.
[106] G. Y. Zhang, J. Liu, Q. Z. Yang, R. X. Zhuo, X. L. Jiang, *Bioconjugate Chem.* **2012**, *23*, 1290-1299.
[107] S. Ochrimenko, A. Vollrath, L. Tauhardt, K. Kempe, S. Schubert, U. S. Schubert, D. Fischer, *Carbohyd. Polym.* **2014**, *113*, 597-606.
[108] M. Noga, D. Edinger, E. Wagner, G. Winter, A. Besheer, *J. Biomat. Sci. Polym. E.* **2014**, *25*, 855-871.
[109] G. J. Lutz, S. R. Sirsi, J. H. Williams, *Methods Mol. Biol.* **2008**, *433*, 141-158.
[110] A. Malek, F. Czubayko, A. Aigner, *J. Drug Target.* **2008**, *16*, 124-139.
[111] C. Englert, M. Fevre, R. J. Wojtecki, W. Cheng, Q. Xu, C. Yang, X. Ke, M. Hartlieb, K. Kempe, J. M. Garcia, R. J. Ono, U. S. Schubert, Y. Y. Yang, J. L. Hedrick, *Polym. Chem.* **2016**, *7*, 5862-5872.
[112] K. M. Kem, *J. Polym. Sci. A Polym. Chem.* **1979**, *17*, 1977-1990.
[113] B. Brissault, A. Kichler, C. Guis, C. Leborgne, O. Danos, H. Cheradame, *Bioconjugate Chem.* **2003**, *14*, 581-587.
[114] A. C. Rinkenauer, L. Tauhardt, F. Wendler, K. Kempe, M. Gottschaldt, A. Traeger, U. S. Schubert, *Macromol. Biosci.* **2015**, *15*, 414-425.
[115] J. C. Fernandes, X. P. Qiu, F. M. Winnik, M. Benderdour, X. L. Zhang, K. R. Dai, Q. Shi, *Int. J. Nanomed.* **2013**, *8*, 4091-4102.
[116] A. C. Rinkenauer, A. Schallon, U. Günther, M. Wagner, E. Betthausen, U. S. Schubert, F. H. Schacher, *ACS Nano* **2013**, *7*, 9621-9631.
[117] M. Thomas, J. J. Lu, Q. Ge, C. Zhang, J. Chen, A. M. Klibanov, *Proc. Natl. Acad. Sci. USA* **2005**, *102*, 5679-5684.
[118] Z. Zhong, Y. Song, J. F. J. Engbersen, M. C. Lok, W. E. Hennink, J. Feijen, *J. Control. Release* **2005**, *109*, 317-329.
[119] P. Ehrlich, *Hirschwald, Berlin* **1885**.
[120] W. M. Pardridge, *Drug Discov. Today* **2007**, *12*, 54-61.
[121] W. M. Pardridge, *NeuroRX* **2005**, *2*, 3-14.
[122] N. J. Abbott, A. A. Patabendige, D. E. Dolman, S. R. Yusof, D. J. Begley, *Neurobiol. Dis.* **2010**, *37*, 13-25.
[123] C. C. Visser, L. H. Voorwinden, D. J. A. Crommelin, M. Danhof, A. G. de Boer, *Pharm. Res.* **2004**, *21*, 761-769.
[124] D. Ye, M. N. Raghnaill, M. Bramini, E. Mahon, C. Aberg, A. Salvati, K. A. Dawson, *Nanoscale* **2013**, *5*, 11153-11165.
[125] P. J. Gaillard, C. C. M. Appeldoorn, J. Rip, R. Dorland, S. M. A. van der Pol, G. Kooij, H. E. de Vries, A. Reijerkerk, *J. Control. Release* **2012**, *164*, 364-369.
[126] M. C. Branco, J. P. Schneider, *Acta Biomater.* **2009**, *5*, 817-831.
[127] R. Luxenhofer, G. Sahay, A. Schulz, D. Alakhova, T. K. Bronich, R. Jordan, A. V. Kabanov, *J. Control. Release* **2011**, *153*, 73-82.
[128] J. Kronek, Z. Kronekova, J. Luston, E. Paulovicova, L. Paulovicova, B. Mendrek, *J. Mater. Sci.-Mater. M* **2011**, *22*, 1725-1734.
[129] S. Zalipsky, C. B. Hansen, J. M. Oaks, T. M. Allen, *J. Pharm. Sci.* **1996**, *85*, 133-137.
[130] L. Wyffels, T. Verbrugghen, B. D. Monnery, M. Glassner, S. Stroobants, R. Hoogenboom, S. Staelens, *J. Control. Release* **2016**, *235*, 63-71.

[131] K. E. B. Doncom, L. D. Blackman, D. B. Wright, M. I. Gibson, R. K. O'Reilly, *Chem. Soc. Rev.* **2017**, *46*, 4119-4134.
[132] J. Rodríguez-Hernández, F. Chécot, Y. Gnanou, S. Lecommandoux, *Prog. Polym. Sci.* **2005**, *30*, 691-724.
[133] C. Wei, L. Junbai, D. Gero, *Adv. Mater.* **2016**, *28*, 1302-1311.
[134] N. Wiradharma, Y. Zhang, S. Venkataraman, J. L. Hedrick, Y. Y. Yang, *Nano Today* **2009**, *4*, 302-317.
[135] C. F. Thorn, C. Oshiro, S. Marsh, T. Hernandez-Boussard, H. McLeod, T. E. Klein, R. B. Altman, *Pharmacogenet. Genom.* **2011**, *21*, 440-446.
[136] D. A. Gewirtz, *Biochem. Pharmacol.* **1999**, *57*, 727-741.
[137] F. Yang, S. S. Teves, C. J. Kemp, S. Henikoff, *BBA-Rev. Cancer.* **2014**, *1845*, 84-89.
[138] S. E. Lipshultz, R. E. Scully, S. R. Lipsitz, S. E. Sallan, L. B. Silverman, T. L. Miller, E. V. Borry, B. L. Asselin, U. Athale, L. A. Clavell, E. Larsen, A. Moghrabi, Y. Samson, B. Michon, M. A. Schorin, H. J. Cohen, D. S. Neuberg, E. J. Orav, S. D. Colan, *Lancet Oncol.* **2010**, *11*, 950-961.
[139] C. D. Meyer, C. S. Joiner, J. F. Stoddart, *Chem. Soc. Rev.* **2007**, *36*, 1705-1723.
[140] T. Kubota, T. Furukawa, H. Tanino, A. Suto, Y. Otan, M. Watanabe, T. Ikeda, M. Kitajima, *Breast Cancer* **2001**, *8*, 333-338.
[141] R. Callaghan, F. Luk, M. Bebawy, *Drug Metab. Dispos.* **2014**, *42*, 623-631.
[142] Y. Mi, L. Lou, *Brit. J. Cancer* **2007**, *97*, 934-940.
[143] T. Yildirim, A. Traeger, E. Preussger, S. Stumpf, C. Fritzsche, S. Hoeppener, S. Schubert, U. S. Schubert, *Macromolecules* **2016**, *49*, 3856-3868.
[144] T. Yildirim, A. Traeger, P. Sungur, S. Hoeppener, C. Kellner, I. Yildirim, D. Pretzel, S. Schubert, U. S. Schubert, *Biomacromolecules* **2017**, *18*, 3280-3290.
[145] M. Fiallo, A. Laigle, M. N. Borrel, A. Garniersuillerot, *Biochem. Pharmacol.* **1993**, *45*, 659-665.
[146] P. Mohan, N. Rapoport, *Mol. Pharmaceutics* **2010**, *7*, 1959-1973.
[147] O. Sedlacek, B. D. Monnery, J. Mattova, J. Kucka, J. Panek, O. Janouskova, A. Hocherl, B. Verbraeken, M. Vergaelen, M. Zadinova, R. Hoogenboom, M. Hruby, *Biomaterials* **2017**, *146*, 1-12.
[148] J. H. Park, S. Kwon, M. Lee, H. Chung, J. H. Kim, Y. S. Kim, R. W. Park, I. S. Kim, S. B. Seo, I. C. Kwon, S. Y. Jeong, *Biomaterials* **2006**, *27*, 119-126.
[149] J. Wang, J. J. Masehi-Lano, E. J. Chung, *Biomater. Sci.* **2017**, *5*, 1450-1459.

List of abbreviations

AEMA	(2-Aminoethyl)-methacrylate
AF4	Asymmetric flow field-flow fractionation
AmOx	2-(4-Aminobutyl)-2-oxazoline
AmButOx	But-3-enyl-2-oxazoline functionalized via thiol-ene click with 2-aminoethane-1-thiol
ATRP	Atom transfer radical polymerization
BBB	Blood-brain barrier
BPEI	Branched poly(ethylene imine)
CC_{50}	Half-maximal cytotoxic concentration
CLSM	Confocal laser scanning microscopy
CROP	Cationic ring-opening polymerization
Cryo-TEM	Cryogenic transmission electron microscopy
DG	Degree of grafting
DLS	Dynamic light scattering
DMAEMA	*N*,*N*-Dimethyl-(2-aminoethyl)-methacrylate
DNA	Deoxyribonucleic acid
DOX	Doxorubicin
DP	Degree of polymerization
EGFP	Enhanced green fluorescence protein
EI	Ethylene imine
EMA	European Medicines Agency
EPR effect	Enhanced permeability and retention effect
EtOx	2-Ethyl-2-oxazoline
FDA	U. S. Food and Drug Administration
GSH	L-Glutathione
HAADF	High-angle annular dark-field
hCMEC	Human cerebral microvascular endothelial cells
HEK-293	Human embryonic kidney 293
HT-29	Human colorectal adenocarcinoma
LPEI	Linear poly(ethylene imine)
MALLS	Multi angle laser light scattering
MAEMA	*N*-Methyl-(2-aminoethyl)-methacrylate

MFI	Mean fluorescence intensity
MOTiF	Multi-organ-tissue-flow biochip
mRNA	Messenger RNA
NMR	Nuclear magnetic resonance spectroscopy
N/P ratio	Nitrogen (polymer) to phosphate (nucleic acid) ratio
PAMAM	Poly(amidoamine)
PAEMA	Poly(2-amino)ethyl methacrylate
PCL	Poly(ε-caprolactone)
PDMAEMA	Poly(2-dimethylamino)ethyl methacrylate
pDNA	Plasmid DNA
PDI	Polydispersity index
PEG	Poly(ethylene glycol)
PEI	Poly(ethylene imine)
PEtOx	Poly(2-ethyl-2-oxazoline)
PLA	Poly(lactic acid)
PLGA	Poly(lactic-*co*-glycolic acid)
PLL	Poly(L-lysine)
PMAEMA	Poly(2-methylamino)ethyl methacrylate
PMeOx	Poly(2-methyl-2-oxazoline)
PMMA	Poly(methyl methacrylate)
POx	Poly(2-oxazoline)
RAFT	Reversible addition-fragmentation chain-transfer
RNA	Ribonucleic acid
ROP	Ring-opening polymerization
SEC	Size exclusion chromatography
SIM	Structured illumination microscopy
siRNA	Small interfering RNA
STEM	Scanning transmission electron microscopy
TE	Transfection efficiency

Publication list

Peer-reviewed publications

T. Bus, A. Traeger, U. S. Schubert, The great escape: How cationic polyplexes overcome the endosomal barrier, *J. Mater. Chem. B* **2018**, *6*, 6904-6918.

A.-K. Trützschler, **T. Bus**, M. Sahn, A. Traeger, C. Weber, U. S. Schubert, The power of shielding: Low toxicity and high transfection performance of cationic graft copolymers containing poly(2-oxazoline) side chains, *Biomacromolecules* **2018**, *19*, 2759-2771.

A.-K. Trützschler,‡ **T. Bus**,‡ M. Reifarth, J. C. Brendel, S. Hoeppener, A. Traeger, U. S. Schubert, Beyond gene transfection with methacrylate-based polyplexes – The influence of the amino substitution pattern, *Bioconjugate Chem*. **2018**, *29*, 2181-2194.

D. Hoelzer,‡ M. N. Leiske,‡ M. Hartlieb, **T. Bus**, D. Pretzel, S. Hoeppener, K. Kempe, R. Thierbach, U. S. Schubert, Tumor targeting with pH-responsive poly(2-oxazoline)-based nanogels for metronomic doxorubicin treatment, *Oncotarget* **2018**, *9*, 22316-22331.

M. Pröhl, P. D. Moser, J. A. Czaplewska, P. Hoffmann, **T. Bus**, A. Traeger, H. Goerls, U. S. Schubert, M. Gottschaldt, Synthesis of D-fructose conjugated ligands via C6 and C1 and their corresponding $[Ru(bpy)_2(L)]Cl_2$ complexes, *Carbohydr. Res*. **2017**, *446-447*, 19-27.

M. Hartlieb,‡ **T. Bus**,‡ J. Kübel, D. Pretzel, S. Hoeppener, M. N. Leiske, K. Kempe, B. Dietzek, U. S. Schubert, Tailoring cellular uptake and fluorescence of poly(2-oxazoline)-based nanogels, *Bioconjugate Chem*. **2017**, *28*, 1229-1235.

T. Bus,‡ C. Englert,‡ M. Reifarth, P. Borchers, M. Hartlieb, A. Vollrath, S. Hoeppener, A. Traeger, U. S. Schubert, 3rd Generation poly(ethylene imine)s for gene delivery, *J. Mater. Chem. B* **2017**, *5*, 1258-1274.

I. Yildirim, **T. Bus**, M. Sahn, T. Yildirim, D. Kalden, S. Hoeppener, A. Traeger, M. Westerhausen, C. Weber, U. S. Schubert, Fluorescent amphiphilic heterografted comb polymers comprising biocompatible PLA and PEtOx side chains, *Polym. Chem*. **2016**, *7*, 6064-6074.

M. Pröhl, **T. Bus**, J. A. Czaplewska, A. Traeger, M. Deicke, H. Weiss, W. Weigand, U. S. Schubert, M. Gottschaldt, Synthesis and in vitro toxicity of D-glucose and D-fructose conjugated curcumin–ruthenium complexes, *Eur. J. Inorg. Chem*. **2016**, *33*, 5197-5204.

C. Englert,‡ A.-K. Trützschler,‡ M. Raasch, **T. Bus**, P. Borchers, A. S. Mosig, A. Traeger, U. S. Schubert, Crossing the blood-brain barrier: Glutathione-conjugated poly(ethylene imine) for gene delivery, *J. Control. Release* **2016**, *241*, 1-14.

C. von der Ehe, **T Bus**, C. Weber, S. Stumpf, P. Bellstedt, M. Hartlieb, U. S. Schubert, M. Gottschaldt, Glycopolymer-functionalized cryogels as catch and release devices for the pre-enrichment of pathogens, *ACS Macro Lett.* **2016**, *5*, 326-331.

S. Noack-Schönmann, **T. Bus**, R. Banasiak, N. Knabe, W. J. Broughton, H. Den Dulk-Ras, P. J. Hooykaas, A. A. Gorbushina, Genetic transformation of Knufia petricola A 95 – A model organism for biofilm-material interactions, *AMB Express* **2014**, *4*, 80-86.

Manuscripts in submission

N. Zabarska, J. A. Czaplweska, **T. Bus**, D. Sorsche, T. Kischkat-Grimm, U. S. Schubert, M. Gottschaldt, Synthesis and characterization of ruthenium(II)-sugar conjugates as potential agents for targeted photodynamic therapy, **2016**, submitted.

Poster presentations

T. Bus, M. Hartlieb, D. Pretzel, S. Hoeppener, U. S. Schubert, Poly(2-oxazoline)-based, doxorubicin-loaded nanogels for cancer drug delivery, *European Polymer Congress (EPF)* **2015**, Dresden, Germany.

T. Bus, C. Englert, A. Vollrath, A. Traeger, U. S. Schubert, Cationic poly(2-oxazoline)s as promising polymer platform for non-viral gene delivery, *European Polymer Congress (EPF)* **2015**, Dresden, Germany.

T. Bus, C. Englert, A. C. Rinkenauer, L. Tauhardt, A. Vollrath, A. Traeger, U. S. Schubert, Promising polymer library for non-viral gene delivery, *European Society for Animal Cell Technology (ESACT)* **2015**, Barcelona, Spain.

T. Bus, E. Schleussner, U. R. Markert, J. Pastuschek, Alterations in morphology and gene expression of the COV434 cell line by 3D cultivation techniques, *American Society for Reproductive Immunology (ASRI)* **2013**, Boston, USA.

Oral presentations

T. Bus, M. N. Leiske, A-K. Trützschler, E. Rudiseva, S. Klausing, C. Heinrich, A. Traeger, U. S. Schubert, The development of novel surfactants and their role in defined media, *European Society for Animal Cell Technology (ESACT)* **2017**, Lausanne, Switzerland.

T. Bus, C. Englert, M. Reifarth, P. Borchers, M. Hartlieb, A. Vollrath, S. Hoeppener, A. Traeger, U. S. Schubert, 3rd Generation poly(ethylene imine) combines biocompatibility and efficient gene delivery, *ESACT Frontiers Retreat* **2016**, Lyon, France.

† Equal contribution

Acknowledgement / Danksagung

Eine wissenschaftliche Arbeit ist nie das Werk einer einzelnen Person, daher möchte ich mich an dieser Stelle bei allen Personen bedanken, die mich während meiner Promotion und bei der Erstellung dieser Arbeit unterstützt haben.

An erster Stelle danke ich Prof. Dr. Ulrich S. Schubert für die Möglichkeit und das entgegengebrachte Vertrauen in seiner Arbeitsgruppe promovieren zu können. Für mich war es eine tolle und lehrreiche Erfahrung in dieser interdisziplinären Umgebung zusammen mit Chemikern, Biologen, Physikern und Materialwissenschaftlern an den spannendsten Fragestellungen zu arbeiten. Unter den besten Voraussetzungen durfte ich forschen, mich weiterentwickeln und über mich hinauswachsen. Das ist keine Selbstverständlichkeit und dafür bin ich sehr dankbar.

Ganz besonderem Dank verpflichtet bin ich meiner direkten Betreuerin Dr. Anja Träger für die vielen wissenschaftlichen Diskussionen, fachlichen und experimentellen Anregungen, Korrekturen in letzter Minute, Händchen-Halten bei Konferenzvorträgen, Kaffeeklatsch mit Kaffeeflecken überall und ihr entgegengebrachtes Vertrauen auch eigene Projekte angehen zu können.

Schön und herausfordernd waren die letzten Jahre, die dank vieler toller Kollegen unvergesslich bleiben werden. Anfangen möchte ich mit denjenigen, die ihren Doktortitel schon in der Tasche und Jena längst verlassen haben. Ein großes Dankeschön geht daher an Dr. Alexandra C. Rinkenauer und Dr. Michael Wagner, die mich in meinem ersten Jahr an die Hand genommen, eingearbeitet und in den Kosmos der Schubert Group eingeweiht haben.

Ein herzliches Dankeschön geht ebenso an Anne-Kristin Trützschler, meinem chemischen Pendant im „Vectura“-Projekt. Ich möchte mich bei dir, liebe Anne, für deine Freundschaft, deine Unterstützung und deinen Rat in allen möglichen wissenschaftlichen und persönlichen Dingen in den letzten Jahren bedanken. Wir hatten tolle und auch langwierige Projekte, bei denen nicht immer alles rund lief. Dennoch können wir auf das, was wir in unserer gemeinsamen Forschung erreicht haben, stolz sein. Daneben möchte ich mich auch für die unvergesslichen Escape-Spiele, Chemikerbälle, Volleyballspiele, Krimidinner und Mittagessen in der Rose mit dir, Meike, Tina, Robert, Jan, Tobi, Stefan, Simon, Christian, Martin, Thomas und, und, und…bedanken.

Ich danke der gesamten Biogruppe: Carolin Kellner, Elisabeth Preußger, Elisabeth Moek, Dr. Anja Träger und Dr. David Pretzel für die großartige Zusammenarbeit und Hilfe bei der Zellkultur und pipettieraufwändigen Assays, aber auch für die Organisation und die neu geschaffene Ordnung im Biolabor. Natürlich darf auch die neue Generation der Biogruppe nicht vergessen werden, auch wenn die Zeit zusammen kurz war: Friederike Richter, Franziska Hausig, Gauri Gangapurwala und Bärbel Beringer-Siemers.

Bei Dr. Uwe Köhn möchte ich mich ganz herzlich für seine Freundschaft und jahrelange Unterstützung in Form von „Motivasen“, aufmunternden Worten, hilfreichen Anregungen, wissenschaftlichen Diskussionen und konstruktiver Kritik während der gesamten Promotion und bei der Erstellung dieser Arbeit bedanken. Trotz deines vollen Arbeitspensums nimmst du dir immer Zeit für die kleinen und großen Sorgen der Mitarbeiter. Das schätze ich besonders an dir.

Natürlich bedanke ich mich bei vielen weiteren Kollegen der Arbeitsgruppe für die Unterstützung bei organisatorischen, fachlichen, technischen und experimentellen Fragen, für eine unglaubliche Atmosphäre und den Spaß, den wir nicht nur bei „GoT“-Abenden hatten: Franca Frister, Sylvia Braunsdorf, Dr. Meike N. Leiske, Blerina Shkodra-Pula, Dr. Stephanie Schubert, Dr. Antje Vollrath, Dr. Justyna Czaplewska, Dr. Jürgen Vitz, Dr. Anna Crecelius-Vitz, PD Dr. Stephanie Höppener, Steffi Stumpf, Pelin Sungur, Renzo Paulus, PD Dr. Ivo Nischang, Nicole Fritz, Grit Festag, …und allen anderen! Für die vielen Erklärungen und Diskussionen (auch während der Zugfahrt) rund um die Polymerchemie bedanke ich mich besonders bei Dr. Christine Weber, PD Dr. Michael Gottschaldt und Dr. Johannes C. Brendel. Weiterhin danke ich meinen Coautoren Dr. Christoph Englert, Dr. Matthias Hartlieb, Anne-Kristin Trützschler, Dr. Meike N. Leiske, Dr. Michael Pröhl, Martin Reifarth, Dr. Christian von der Ehe, Dr. Ilknur Yildirim und Dr. Dörte Hölzer für die tolle Zusammenarbeit.

Mein abschließender Dank gilt meinen Eltern Elke und Jarek Buś, meiner Schwester Corina sowie Hannes, die mich auf meinen Weg durch die Promotion begleitet haben. Euer Rückhalt, euer Verständnis, eure Motivation und Unterstützung in den letzten Jahren, insbesondere in den letzten Monaten und Wochen(!), trugen wesentlich zum Gelingen dieser Arbeit bei. Ich danke euch für Alles!

Declaration of authorship / Selbstständigkeitserklärung

Hiermit erkläre ich, dass ich die vorliegende Arbeit selbständig angefertigt, nicht anderweitig zu Prüfungszwecken vorgelegt und keine anderen als die angegebenen Hilfsmittel verwendet habe. Sämtliche wissentlich verwendete Textausschnitte, Zitate oder Inhalte anderer Verfasser wurden ausdrücklich als solche gekennzeichnet.

I certify that the work presented here is, to the best of my knowledge and belief, original and the result of my own investigations, except as acknowledged, and has not been submitted, either in part or whole, for a degree at this or any other university.

Jena, den

_____

Tanja Buś

Publications Pub1 to Pub8

Pub1 Reprodced from T. Bus, A. Traeger, U. S. Schubert, The great escape: How cationic polyplexes overcome the endosomal barrier, *J. Mater. Chem. B* 2018, *6*, 6904-6918 with permission from The Royal Society of Chemistry (RSC).

Pub2 Reprinted with permission from A.-K. Trützschler, T. Bus, M. Reifarth, J. C. Brendel, S. Hoeppener, A. Traeger, U. S. Schubert, Beyond gene transfection with methacrylate-based polyplexes – The influence of the amino substitution pattern, *Bioconjugate Chemistry* 2018, *29*, 2181-2194. Copyright 2018 American Chemical Society.

Pub3 Reprinted with permission from A.-K. Trützschler, T. Bus, M. Sahn, A. Traeger, C. Weber, U. S. Schubert, The power of shielding: Low toxicity and high transfection performance of cationic graft copolymers containing poly(2-oxazoline) side chains, *Biomacromolecules* 2018, *19*, 2759-2771. Copyright 2018 American Chemical Society.

Pub4 T. Bus, C. Englert, M. Reifarth, P. Borchers, M. Hartlieb, A. Vollrath, S. Hoeppener, A. Traeger, U. S. Schubert, *Journal of Materials Chemistry B* 2017, *5*, 1258-1274. Reproduced by permission of The Royal Society of Chemistry (RSC).

Pub5 Reprinted from *Journal of Controlled Release*, C. Englert, A.-K. Trützschler, M. Raasch, T. Bus, P. Borchers, A. S. Mosig, A. Traeger, U. S. Schubert, Crossing the blood-brain barrier: Glutathione-conjugated poly(ethylene imine) for gene delivery, *241*, 1-14. Copyright 2016 Elsevier.

Pub6 I. Yildirim, T. Bus, M. Sahn, T. Yildirim, D. Kalden, S. Hoeppener, A. Traeger, M. Westerhausen, C. Weber, U. S. Schubert, *Polym. Chem*. 2016, *7*, 6064-6074. Reproduced by permission of The Royal Society of Chemistry (RSC).

Pub7 Reprinted with permission from M. Hartlieb, T. Bus, J. Kübel, D. Pretzel, S. Hoeppener, M. N. Leiske, K. Kempe, B. Dietzek, U. Schubert, Tailoring cellular uptake and fluorescence of poly(2-oxazoline)-based nanogels, *Bioconjugate Chemistry* 2017, *28*, 1229-1235. Copyright 2017 American Chemical Society.

Pub8 Reprinted by permission of Oncotarg

Publication Pub1

The great escape: How cationic polyplexes overcome the endosomal barrier

T. Bus, A. Traeger, U. S. Schubert

J. Mater. Chem. B **2018**, *6*, 6904-6918.

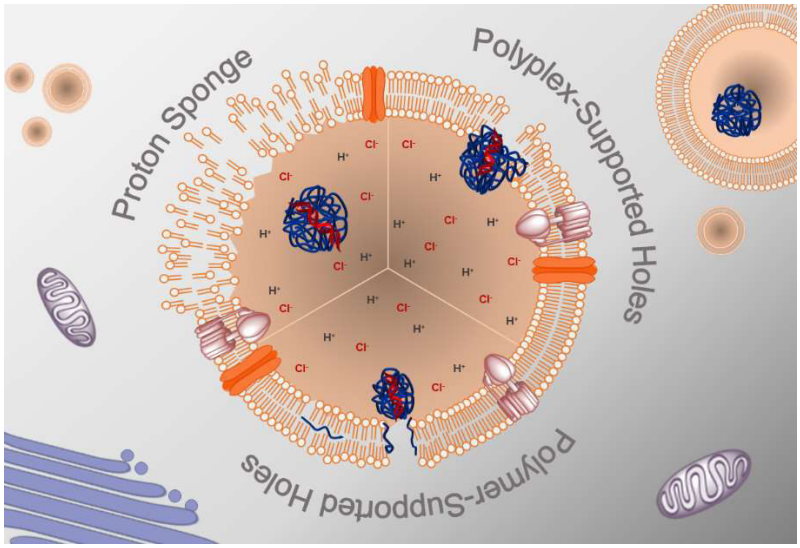

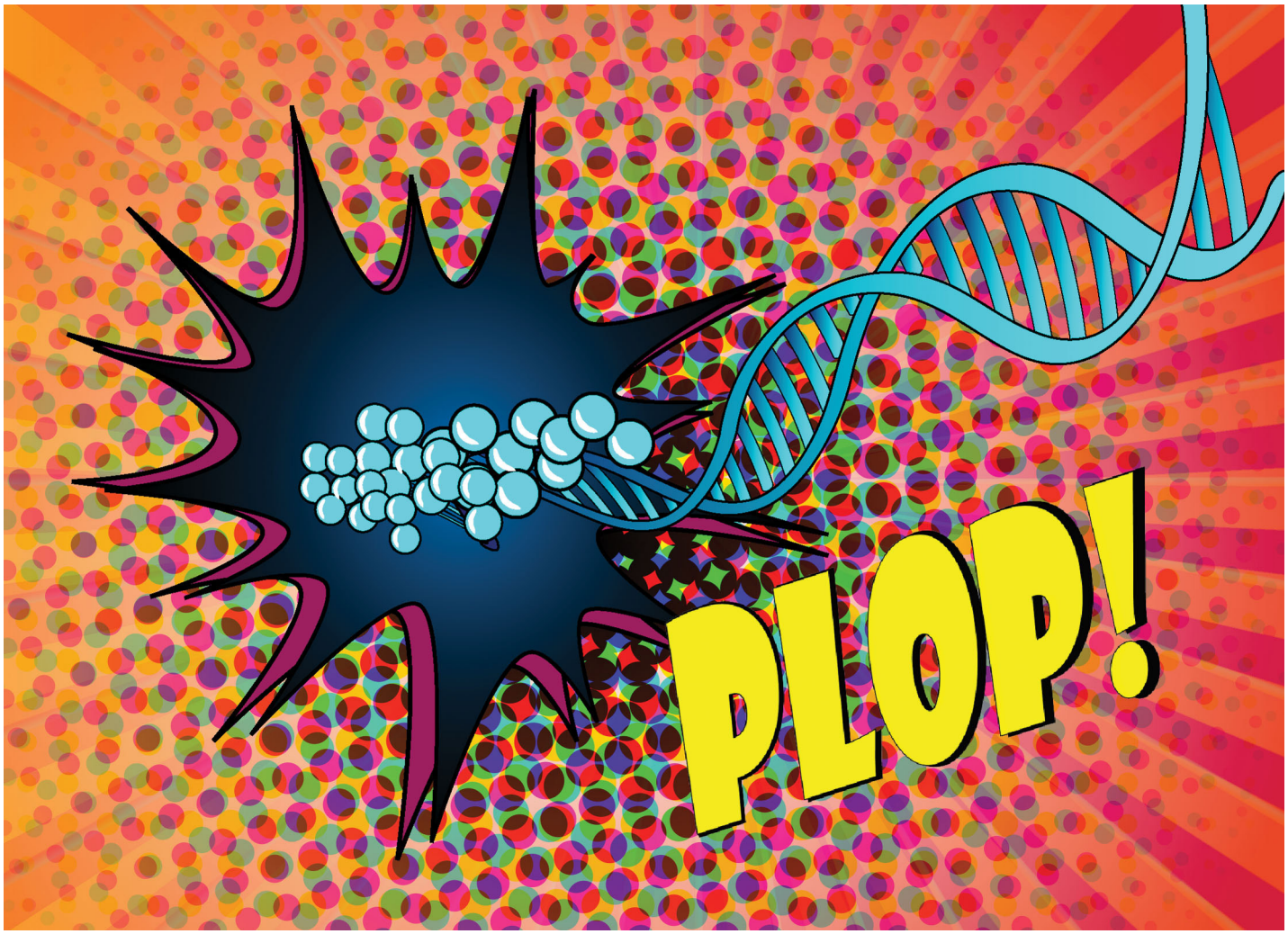

Highlighting research from the groups of Ulrich S. Schubert and Anja Traeger at the Friedrich Schiller University of Jena

The great escape: how cationic polyplexes overcome the endosomal barrier

This review highlights the findings of the endosomal release of genetic material complexed by polymers. Several obstacles on the molecular and cellular level along the gene delivery process are known. In particular, the efficient escape from endo-lysosomal compartments has been demonstrated to be a major barrier and its exact mechanism still remains unclear. This review addresses the different endosomal release theories and highlights their key mechanism.

As featured in:

See Anja Traeger, Ulrich S. Schubert *et al.*, *J. Mater. Chem. B*, 2018, **6**, 6904.

ROYAL SOCIETY OF CHEMISTRY

rsc.li/materials-b

Registered charity number: 207890

Journal of
Materials Chemistry B

REVIEW

View Article Online
View Journal | View Issue

Cite this: J. Mater. Chem. B, 2018, 6, 6904

The great escape: how cationic polyplexes overcome the endosomal barrier

Tanja Bus,[ab] Anja Traeger*[ab] and Ulrich S. Schubert *[ab]

Received 12th April 2018,
Accepted 11th September 2018

DOI: 10.1039/c8tb00967h

rsc.li/materials-b

The targeted and efficiency-oriented delivery of (therapeutic) nucleic acids raises hope for successful gene therapy, *i.e.*, for the local and individual treatment of acquired and inherited genetic disorders. Despite promising achievements in the field of polymer-mediated gene delivery, the efficiency of the non-viral vectors remains orders of magnitude lower than viral-mediated ones. Several obstacles on the molecular and cellular level along the gene delivery process were identified, starting from the design and formulation of the nano-sized carriers up to the targeted release to their site of action. In particular, the efficient escape from endo-lysosomal compartments was demonstrated to be a major barrier and its exact mechanism still remains unclear. Different hypotheses and theories of the endosomal escape were postulated. The most popular one is the so-called "proton sponge" hypothesis, claiming an escape by rupture of the endosome through osmotic swelling. It was the first effort to explain the excellent transfection efficiency of poly(ethylene imine). Moreover, it was thought that a unique mechanism based on the ability to capture protons and to buffer the endosomal pH is the basis of endosomal escape. Recent theories deal with the direct interaction of the cationic polyplex or free polymer with the exoplasmic lipid leaflet causing membrane destabilization, permeability or polymer-supported nanoscale hole formation. Both escape strategies are more related to viral-mediated escape compared to the "proton sponge" effect. This review addresses the different endosomal release theories and highlights their key mechanism.

Introduction

Non-viral gene delivery based on polymers remains in the focus of interdisciplinary research activities in macromolecular chemistry, pharmacy and medicine as well as biotechnology.[1–3] Polymers represent promising delivery vectors as they mimic the gene

[a] *Laboratory of Organic Chemistry and Macromolecular Chemistry (IOMC), Friedrich Schiller University Jena, Humboldtstrasse 10, 07743 Jena, Germany. E-mail: anja.traeger@uni-jena.de, ulrich.schubert@uni-jena.de*
[b] *Jena Center for Soft Matter (JCSM), Friedrich Schiller University Jena, Philosophenweg 7, 07743 Jena, Germany*

Tanja Bus

Tanja Bus was born in Hildburghausen (Germany) in 1989. She studied biotechnologies (BEng) at the University of Applied Sciences Jena and molecular life sciences (MSc) at the Friedrich Schiller University in Jena. After her graduation in 2014, she joined the research group of Prof. Ulrich S. Schubert at the Friedrich-Schiller University in Jena as a PhD student. Her research focused on the utilization of tailor-made synthetic polymers for gene and drug delivery in vitro.

Anja Traeger

Anja Traeger (née Schallon) was born in 1982 in Beeskow (Germany) and studied biochemistry at the University of Bayreuth (Germany; 2002–2007) with a stay at the University of York (UK). After her PhD studies (2007–2011) at the University of Bayreuth, she moved to the Friedrich Schiller University Jena to study at the Jena Center for Soft Matter (JCSM) supervised by Prof. Ulrich S. Schubert. In 2017 she started her independent research group financed by the BMBF "NanoMatFutur" program. Her research interests are the characterization and biological application of multi-functional polymer-based nanomaterials for gene delivery.

delivery performance of viruses but with additional safety benefits regarding pathogenicity and immunogenicity. Furthermore, they offer the opportunity for unlimited architecture designs with high chemical variations, large scale production and simple storage conditions. The understanding of the vector's chemistry as well as their structure–property relationship on the molecular and cellular level are central issues to evaluate their prospective biomedical or biotechnological potential. Several strategies or synthetic approaches for polymer-mediated gene delivery exist including the chemical conjugation of nucleic acids to the polymer backbone, electrostatic interactions, encapsulation and the adsorption onto micro or nano spheres.[4] Additionally, the polymers can be functionalized with targeting ligands, labels or dyes, shielding domains or endosomolytic units to improve their biological performance. Depending on the aim of approach it is possible to target different intracellular localizations, like the cytoplasm by small interfering RNA (siRNA)[5,6] and messenger RNA (mRNA),[7,8] the mitochondria by peptide nucleic acids (PNA)[9–11] or the cell nucleus by plasmid DNA (pDNA).[12] Attention was recently attracted to the power of genome editing systems (CRISPR/Cas9, zinc-finger nucleases) representing the next challenge for vector design.[13–16] The continuous development of polymeric structures increases the knowledge of the mechanism of transfection and identify several extra- and intracellular obstacles.[17,18] The most important gene delivery challenges were defined as (i) nucleic acid packaging and carrier stability to protect the nucleic acids against enzymatic degradation, (ii) the internalization mechanism and intracellular pathway, (iii) the endo-lysosomal escape and the transport to the site of action and finally, (iv) the release of the cargo from its vector. The intracellular fate of polyplexes, in particular the endo-lysosomal pathway, was found to be a critical rate-limiting step determining the success or failure of gene expression.

The scope of this review comprises the utilization of cationic polymers for the delivery of nucleic acids by complexation (polyplexes) with emphasis on the endosomal release as the main rate-limiting step in gene delivery. The first part covers a brief historical résumé about the development of cationic polymers used for nucleic acid delivery and describes the general delivery process. The main part of this review addresses the different endosomal release strategies that have been hypothesized and highlights their key mechanism. Finally, the validity of each theory is discussed in detail based on published studies and reports.

Ulrich S. Schubert

Ulrich S. Schubert was born in Tübingen (Germany) in 1969. He studied chemistry in Frankfurt and Bayreuth (both Germany) and at the Virginia Commonwealth University, Richmond (USA). His PhD studies were performed at the Universities of Bayreuth and South Florida. After a post-doctoral training with J.-M. Lehn at the University of Strasbourg (France), he moved to the TU Munich (Germany) and obtained his Habilitation in 1999. During 1999–2000 he was Professor at the University of Munich, and during 2000–2007 Full-Professor at the TU Eindhoven (the Netherlands). Since 2007, he is a Full-Professor at the Friedrich Schiller University Jena, Germany.

Cationic polymers in gene delivery

The idea to transport nucleic acids into cells in order to force the expression of a gene of interest is very ancient.[19] Early discoveries in the basics of molecular genetics, the gene transfer in bacteria and the recombinant DNA technology laid the foundation for the concept of treating diseases by introducing therapeutic genes into the organism, the so-called gene therapy.[19] Developments in this area have passed several milestones, including early successful transfection of mammalian cells *in vitro* and *in vivo*, the introduction of clinical trials, the completion of the Human Genome Project, the approval and launch of gene therapy products such as Glybera, as well as the modern vision of precision nano medicine.[20,21]

Historical overview of polymer-based gene delivery

The historical progress in polymer-based gene delivery is depicted in Fig. 1. The first successful mammalian gene delivery experiments based on polyamines were reported in the early 1960s by Szybalska and Szybalski using spermine in a phosphate buffer to transfer DNA.[22] Few years later, diethylaminoethyl (DEAE) dextran was applied for the delivery of viral RNA as well as DNA.[23,24] Due to further progress in mammalian gene delivery and continuos optimization of transfection protocols, several other natural and synthetic polycations were investigated in the following decades including poly(ornithine),[25,26] poly(brene),[27,28] poly(arginine)[25,29] and poly(L-lysine) (PLL).[25,30] Thereby, the use of mammalian DNA and plasmid DNA instead of viral gene constructs became the focus of research. Due to the high content of amino groups implicating positive charge densities, polycations were able to bind and condense DNA into small, compact structures varying in shape and size.[31,32] In this context it has to be mentioned that most of heretofore applied polymers, in particular PLL, required the supplementation of membrane-active agents or lysosomotrophic additives within the transfection protocol to promote the endosomal escape of the polyplex into the cytoplasm and to gain distinguishable gene expressions. Various substances were successfully utilized including solvents like DMSO,[28,33] weak bases as chloroquine[34] and ammonium chloride[33] or glycerol.[35] Another strategy to achieve successful transfection at that date was the conjugation of the polymer with ligands or fusion peptides.[30,36,37] Despite promising results the transfection efficiency remained relatively low, which led to the search for alternative polymers with improved performances. At that time different synthetic polymers with high amino

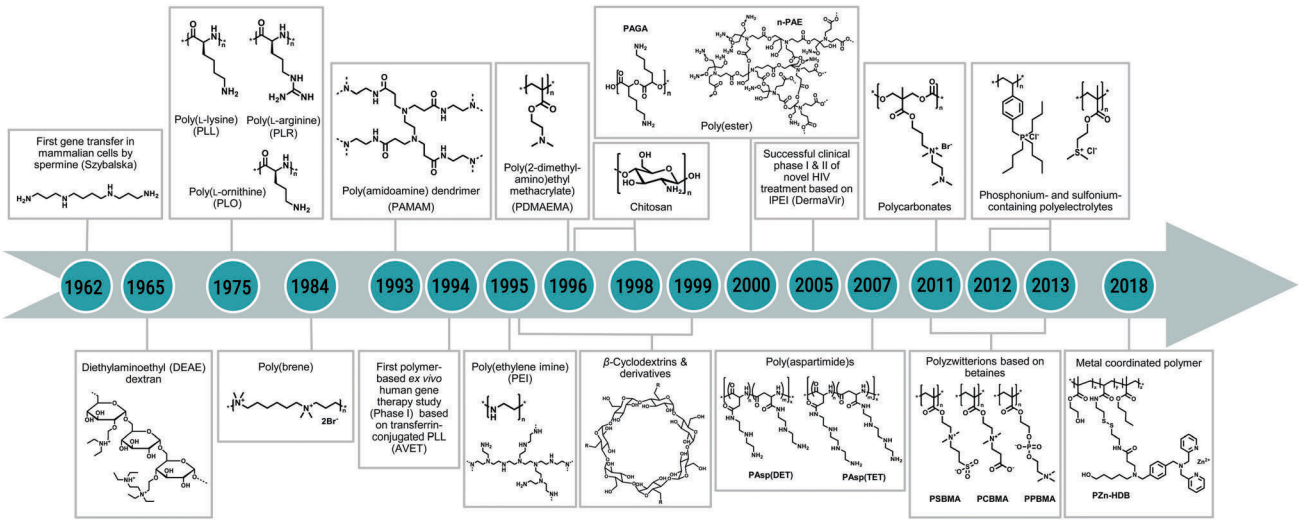

Fig. 1 Polycations and polymers used for gene delivery in the past 50 years.

group content and pH buffering properties were examined for gene delivery to avoid the usage of lysosomotrophic additives, cell targeting or membrane disruptive agents and to simplify the transfection protocol. In the early 1990s poly(amidoamine) (PAMAM) dendrimers were successfully applied for pDNA delivery without the need of additives. The polymer's performance was explained by its low pK_a values of primary amino groups (pK_a = 6.9) and tertiary amino moieties (pK_a = 3.9) responsible for endosomal buffering properties and lysosomotrophic effects.[38] A few years later, 1995, poly(ethylene imine) (PEI), a polymer applied as chelating agent or in the paper as well as the paint industry, was examined for gene delivery.[39] As the transfection efficiency of mammalian cells was markedly improved compared to other polycations used so far, this contributed largely to today's "gold standard" for gene delivery.[40,41] Also poly(methacrylate)s with favorable pH buffering capacities due to different amino moieties were evaluated. In particular, poly(*N*,*N*-dimethyl-(aminoethyl)methacrylate) (PDMAEMA) revealed enhanced transfection efficiencies.[42–45] Nevertheless, as these systems suffer from high cytotoxicity, the need for an alternative polymer with improved biocompatibility caused a rise in the design of new cationic polymers. Over the last 20 years, new generation of polymer classes were introduced to set a higher standard on safety and efficiency in gene delivery. The focus was directed towards biocompatible as well as biodegradable polymers including modified PEI derivatives,[46–48] chitosan and its derivatives,[49–52] cyclodextrins,[53–55] poly(amino ester)s,[56–58] poly(aspartimide)s[59,60] or poly(carbonate)s.[61,62] Since 2012, phosphonium and sulfonium containing macromolecules were investigated for non-viral gene delivery.[63–66] These polymers revealed DNA binding affinity and low toxicity making them promising alternatives to nitrogen-based systems. Besides polycations, also zwitterionic-based polymers, including polycarboxybetaines (PCB), polyphosphobetaines (PPB) and polysulfobetaines (PSB), have been investigated in the last years.[67–70] Recently, a zinc coordinated copolymer for non-viral gene delivery was introduced by Guo and colleagues.[71] The non-cationic polymer demonstrated a high affinity to phosphodiesters in nucleic acids, mediated by a zinc(II)–dipicolylamine moiety, but also promising transfection performances due to effective endosomal release properties as well as GSH triggered DNA release. As shown in Fig. 1, the development of polymers within the last 50 years reveals several optimizations, highlights and breakthroughs in the conception and the chemistry of non-viral gene delivery vectors. However, the efficiency of such vectors is still moderate and the search for a new "gold standard" far beyond from being completed. Continuous efforts and increasing knowledge in this area will encourage the progress of powerful tools for the delivery of nucleic acids.

The uptake mechanism of polyplexes

The popularity of cationic polymers for the transfer of nucleic acids is attributed to the simple formulation of gene carriers. In general, nucleic acids show a high affinity towards cationic polymers due to electrostatic interactions. Negatively charged phosphates within the nucleic acid backbone interact with the positively charged amino groups within the polymer backbone or the side chains leading to the spontaneous formation of polymer–nucleic acid complexes, known as polyplexes. An appropriate complexation, in particular the condensation of circular, large nucleic acids, leads to the formation of nanoscaled structures masking the charges of the nucleic acids and supporting the adsorption to the cell membrane followed by internalization. In principle, the uptake of cationic polyplexes is described by the process of endocytosis (Fig. 2), whereby the exact pathway strongly affects the intracellular trafficking of the cargo as well as the transfection efficiency. Endocytosis depends on various aspects of the nanocarrier such as its size, the polymer type and the cell type.[72–74] Several studies reported the cellular internalization of cationic polyplexes by means of clathrin-dependent as well as independent endocytosis, caveolae-mediated endocytosis and macropinocytosis.[47,75–78]

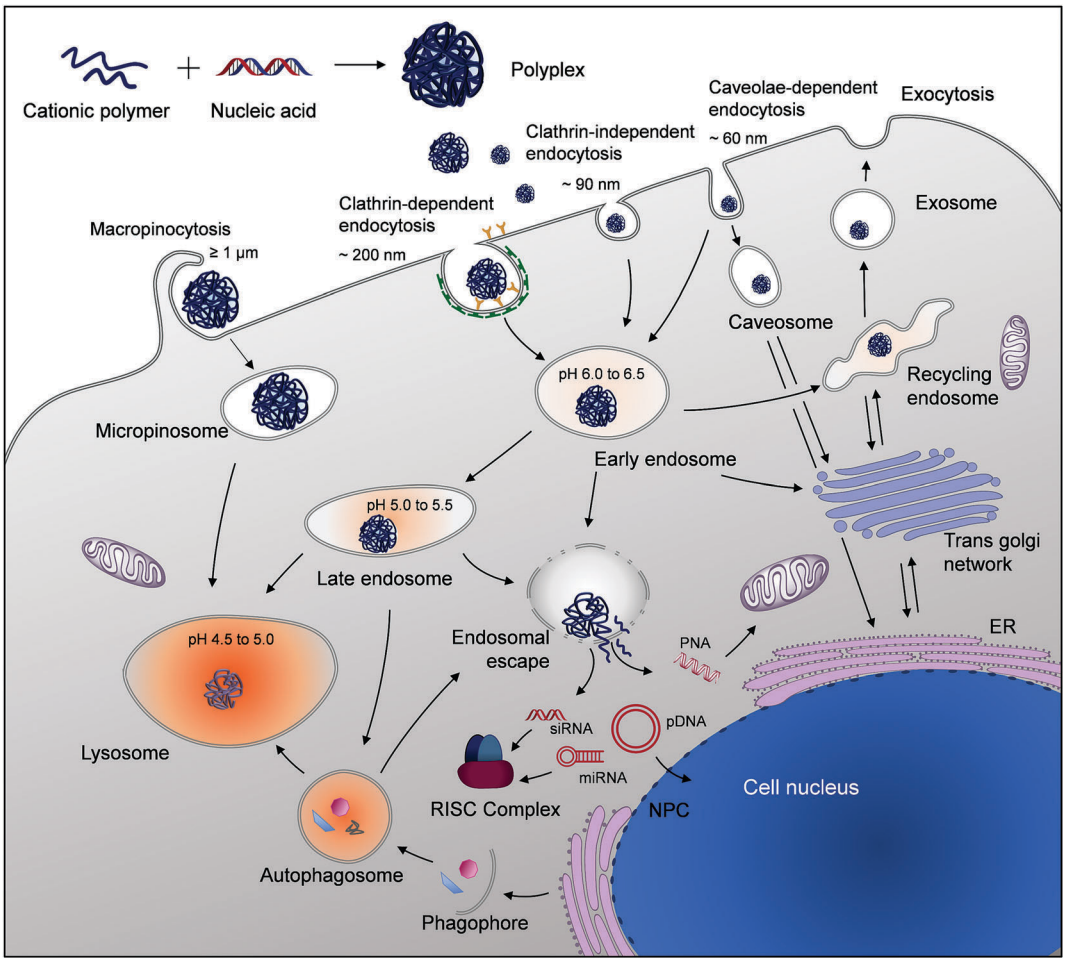

Fig. 2 The gene delivery process of cationic polymers including polyplex formation, intracellular uptake *via* various endocytosis pathways, intracellular polyplex trafficking, endosomal escape into the cytoplasm, release of the cargo from the polymer and transport to the site of action. Depending on the type of nucleic acid, the site of action is either located within the cytoplasm or in the nucleus. ER: endoplasmic reticulum; NPC: nuclear pore complex.

The mammalian cell membrane is predominantly composed of neutral lipids including glyocerophospholipids, sphingolipids and sterols (mostly cholesterol), which create the typical phospholipid bilayer structure.[79] The affinity of cationic polyplexes to the cell membrane is mostly facilitated by surface glycoproteins, *i.e.* anionic proteoglycans, or receptors (if ligands are involved like transferrin or folate *etc.*).[80,81] After attachment to the plasma membrane, the invagination of the plasma membrane leads to the entrapment of the polyplex into membrane-bound vesicles like coated vesicles, caveosomes or macropinosomes (Fig. 2). Both, clathrin-dependent as well as clathrin-independent endocytosis will result in the localization of polyplexes within early endosomes. Within these compartments the pH value quickly drops from neutral to lower pH values of 6.5 to 6.0 due to the activity of membrane-incorporated vacuolar-type ATPases (V-ATPase, proton pump). The early endosomes are directed to sorting endosomes. From there the content is recycled back to the extracellular milieu by exocytosis or other intracellular recycling circuits involving the trans-Golgi network. Apart from that, the cargo can be directed to the lysosomal pathway for degradation (Fig. 2). In the latter case, the endosomes will mature to late endosomes, in which the action of the membrane-bound V-ATPases will lead to a further decrease in pH value to approx. 5.5 to 5.0. Late endosomes are, furthermore, able to fuse with lysosomes, which contain a highly acidic milieu of pH 5.0 to 4.5 representing optimal conditions for the activity of degradative enzymes (lysosomal hydrolases). Autophagy is another lysosomal-mediated degradation pathway, which plays an important role in the clearance of damaged organelles, misfolded proteins as well as invaded foreign substances including pathogens[82,83] or nanomaterials.[84–87] Initiated by the formation of a phagophore, which derived from the endoplasmic reticulum (ER), maturated autophagosomes fuse with lysosomes to become an autolysosome responsible for degradation processes. Autophagy could be induced by nutrient starvation but also by endosomal membrane damage and, thus, represents a further barrier against the cytosolic release of polyplexes for successful gene delivery. However, both events (exocytosis as well as the lysosomal pathway) were reported to have a pivotal impact on transfection efficiency and should be overcome by the efficient escape from these compartments.[78,88,89] In contrast to this "classical" pathway, polyplexes that are internalized by caveolae-mediated

endocytosis are exposed to a neutral pH value within the caveosomes and, thus, to a less hostile environment (Fig. 2). By means of microtubules, the caveosomes and their cargo move on to the Golgi apparatus and the endoplasmic reticulum (ER).[74,90] Nevertheless, caveolae are able to interact with early endosomes, thus getting involved in acidification processes.[91] As the fate of the polyplexes and the related transfection efficiency strongly depends on the trafficking route, polyplexes should escape from endocytic vesicles at an early stage of endocytosis before intracellular expulsion or enzymatic degradation of the cargo. After successful endosomal escape, the cargo needs to be released from its carrier and transported to its site of action (Fig. 2). However, it is not yet clear if the cargo is completely released from its vector during the escape process or if the release occurs in the cytoplasm by means of anionic molecules, *e.g.* cytoplasmic RNA and heparin-like glycosaminoglycans,[92] or even in the nucleus. In the case of various RNA types, like siRNA and miRNA, the release within the cytoplasm is sufficient to enable interaction with the RNA-induced silencing complex (RISC) in order to exert their silencing activity. In contrast, pDNA has to cover a relatively long distance through the cytoplasm to reach the nucleus. Thereby, a complete release of the nucleic acid from its vector within the periphery of the cytoplasm leads to the loss of protection and increases the risk of enzymatic degradation by nucleases. Furthermore, the motion of the naked DNA to the nuclear envelope is characterized by Brownian movement and is thought to be highly inefficient depending on the site of release as well as the size of DNA. The release of pDNA or pDNA-based polyplexes in the perinuclear region is thought to be preferable compared to a release within the outer cellular regions of dense meshed cytoplasm.[93,94] Moreover, various studies discussed an active motion of dissociated pDNA or the intact polyplex along microtubules or motor proteins to the nucleus,[94–97] as common for viruses.[98,99] Besides the travelling of pDNA to the nuclear envelope, the nuclear translocation represents a further critical barrier towards efficient gene expression and, is frequently discussed with regard to cell-division dependency and nuclear pore complex involvement.[100–104] Nevertheless, the endosomal release is still seen as the major bottleneck for the delivery of all types of nucleic acids.[105–109] Several reviews outline strategies to overcome the endosomal entrapment by modifying the vector structure or composition, including fusogenic ligands, peptides, pH-sensitive polymer properties or photosensitive agents.[37,105,107,110,111] In the following sections we present and discuss the principles behind the escape of cationic polymers from endo-lysosomal compartments.

Endosomal escape theories

The proton sponge theory

The ability to act as a ''proton sponge'' within acidifying endosomes was a first attempt to explain the highly efficient transfection performance of PEI.[39,40] The original postulated ''proton sponge'' hypothesis implies that due to the protonation of the amino groups within the acidic endosomal lumen, a ''massive vesicular ATPase-driven proton accumulation followed by passive chloride influx into endosomes [...] should cause osmotic swelling and subsequent endosome disruption.''[39] To understand this pH-driven release model, one has to understand the nature of PEI. PEI is a polymers with the highest charge density due to its polyamine structure consisting of repeating units of two aliphatic carbons and an amino group, $-(CH_2-CH_2-NH)_n-$ (43 g mol^{-1}). There are two morphologies of PEI, the linear (lPEI) and the branched (bPEI) form commercially available with a broad molar mass range from 200 g mol^{-1} to 750 000 g mol^{-1} whereas the 25 000 g mol^{-1} PEI is the most utilized one in gene transfer. Both types are distinguishable by their synthesis and amino group functionalities.[112–116] LPEI bears solely secondary amino groups in the backbone, while bPEI possess primary, secondary as well as tertiary amino groups. Based on its structure, PEI is a weak-base buffering polyelectrolyte revealing a pH-dependent protonation behavior and charge-driven conformational changes.[117] Potentiometric titrations and computational approaches revealed that 50 to 55% of the PEI amino groups are protonated at physiological conditions independent of the structure of PEI.[118–122] The partially protonation behavior was explained by the electrostatic repulsion due to the close vicinity (7 Å distance between two charges) of the amino groups.[17,120,121] According to the pK_a value, the highest buffer capacities of PEI lies between pH 8 and 10, which is attributed to the secondary amino groups present in both polymer types. Nevertheless, PEI has a broad buffer capacity from the basic to the acidic range and show a second maximum at pH 4 to 7 (pK_a $\sim$ 4.5), which explains the buffering capacity in acidic environments such as within endo-lysosomes.[117,120] According to the ''proton sponge'' theory (Fig. 3), the remaining amino functionalities are further able to act as a buffering agent or so-called ''proton sponge'' within acidifying endo-lysosomal compartments. The acidification is achieved by the activity of the membrane-bound V-ATPase, as described in the section above. In general, this multi-subunit protein-complex translocate protons across the membrane into the interior of the vesicle by means of ATP hydrolysis, thus generating a transmembrane electrical potential difference.[123] Charge compensation is required to maintain the ATPase pumping activity and the acidification of the compartments. Counter-ion pathway like chloride channels (ClC) and transporters mediate the influx of anions (Cl^-) or efflux of cations (H^+) and, therefore, compensate for the accumulation of protons (see Fig. 2) in the natural state of the proton pumps.[123,124] Once, a PEI polyplex is entrapped within endo-lysosomes, the remaining non-protonated amino groups are further protonated, thus buffering and delaying the acidification within the vesicles, which is associated with an simultaneous influx of chloride ions. Moreover, the volume of the PEI molecule will be enlarged due to the stronger repulsion of the intramolecular positively charged amino groups, known as umbrella effect.[40,125] While, the V-ATPases try to maintain the proton gradient across the membrane as well as the acidification within the vesicle, the luminal chloride counter-ion concentration rises continuously. The evolving osmotic imbalance is, consequently, counteracted by the entrance of water. A critical

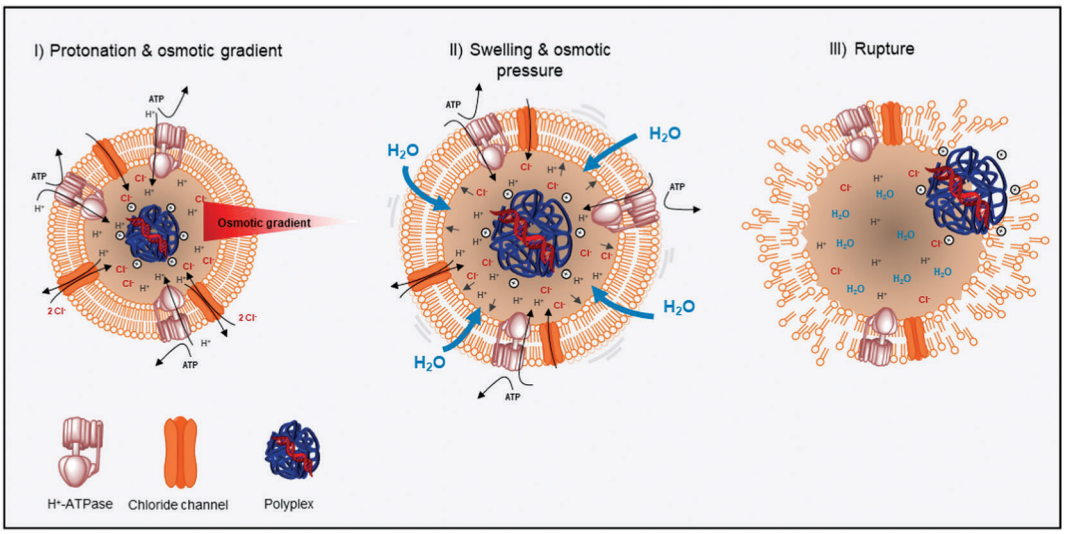

Fig. 3 Illustration of the "proton sponge" hypothesis. The cationic polyplex is located within an endo-lysosomes and will be further protonated due to its buffering capacity in the acidic lumen. Due to the high activity of the membrane-bound V-ATPase the enhanced influx of chloride ions causes an osmotic imbalance (I). This concentration gradient is counteracted by the entrance of water resulting in the swelling of the endo-lysosomal compartment (II) and finally to the endosomal burst and release of carrier and cargo (III).

membrane tension due to continuous swelling of the endosome and the expansion of the polymer itself finally results in the bursting of the endo-lysosomal compartment and the release of its cargo within the cytoplasm.

The ability of cationic polymers to act as a "proton sponge" was found for several other cationic polymers with high buffer capacities over a broad pH range (pH 5.0 to 8.0) including PAMAM[38] and PDMAEMA.[44] However, the "proton sponge" hypothesis is still highly debated in the scientific community, as experimental evidence is inconsistent. There are four key aspects discussed so far: (i) the endosomal buffering effect of cationic polymers and related to this (ii) the ability to prevent acidification within endo-lysosomal compartments and to avoid lysosomal involvement and (iii) the complete rupture or lysis of endo-lysosomes.

Evidence for the important role of endosomal acidification and buffering was provided by the study of Kichler *et al.* using the V-ATPase inhibitor Bafilomycin A1 that suppresses the acidification within endosomal compartments and, thus, prevent the protonation of PEI leading to a significant decrease in gene expression.[126] Sonawane and coworkers analyzed the kinetics of acidification and chloride accumulation in endosomes by utilizing dye-labeled cationic polymers sensitive to pH or chloride ions. They observed a reduced acidification and a high chloride content within swollen endosomes for the high buffering polymers PEI and PAMAM.[127] Other studies examined the buffering ability after chemical modification of PEI, *e.g.* by quaternization. Quaternized PEI was not able to buffer the acidification and to escape the endosome before lysosomal fusion. This clearly demonstrated that buffering is essential for PEI-mediated transfection.[128,129] The poor transfection ability of PLL was explained by the full protonation of the side chains' primary amino groups and the absent buffering capacity at a pH below 8.[121,130] Once PLL is entrapped within an endosome it is unable to buffer the acidification and to escape the hostile environment in a time-efficient manner to avoid an enzymatic degradation in the lysosomes. Another reason was associated to its tight DNA binding and the highly stable polyplex formation, showing weak polyplex dissociation by intracellular competitors required to release the nucleic acid.[130–133] Strategies for PLL-based delivery were based on the conjugation of functional moieties to the PLL backbone such as histidine, imidazole, transferrin or membrane-disruptive peptides providing the missing buffering capacities or an active membrane lysis mechanism to gain efficient release.[134–137] Besides chemical modification, the supplementation of chloroquine resulted in a significant enhancement of PLL's transfection efficiency as well.[128,138] The mode of action of chloroquine (pK_a values of 8.1 and 10.2)[139] was discussed to be a multi-step mechanism characterized by (i) an increased accumulation within acidic compartments and its entrapment after protonation, (ii) the buffering of the vesicles to promote escape and to prevent lysosomal degradation, (iii) the interaction with the endosomal membrane leading to membrane permeabilization and (iv) the dissociation of polyplexes and the direct interaction with the unpacked nucleic acids.[34,138,140] Recently, it was also demonstrated that a chloroquine analogue with a fluorine atom instead of the 7-Cl atom revealed ten times higher transfection efficiencies, thus making it a powerful alternative to chloroquine.[140]

The good performances of PAMAM (pK_a 3 to 6) and PDMAEMA ($pK_a \sim 7.5$) were also referred to the excellent buffer capacities of tertiary amino groups within the polymer structures. However, in the direct comparison to PEI, PDMAEMA reveal a five to ten fold lower endosomal escape as well as transfection efficiency.[141–143] This was explained by the fact that PEI revealed a higher buffering capacity as well as a stronger interaction with membranes.[141,144] An explanation for a weaker membrane interaction might be the decrease in size of PDMAEMA-based

polyplexes at low pH value, whereas PEI-polyplexes revealed swollen structures at similar conditions.[145] Furthermore, it was shown that PDMAEMA was unable to physically disrupt the endosomal membrane.[146] Funhoff *et al.* aimed to enhance the buffering capacity and, therefore, the endosomal escape of PDMAEMA by the conjugation of two tertiary amino groups per monomer unit.[147] This polymer had two pK_a values, one at pH 5.5 providing buffering capability at low pH as well as a second at pH 9.3 providing DNA binding and condensation properties. Despite its promising structure, the polymer did not achieve adequate transfection efficiencies and it was concluded that the ''proton sponge'' effect was not valid for this kind of polymer. Since poly(methacrylate)s provides the structural versatility of different amino moieties, they are preferable model systems to investigate the influence of primary, secondary and tertiary amino groups on the delivery performance. There are several studies dealing with the direct comparison of the different amino functionalities.[148–151] Interestingly, it was shown that homo- and copolymers bearing a higher content of primary amino groups led to the highest transfection efficiency compared to polymers with tertiary amino groups.[148,152] Based on their results the authors challenged a direct correlation between buffer capacity and transfection efficiency.[142,148,152] Despite tertiary amino groups with pK_a values close to endo-lysosomal pH, also PAMAM dendrimers showed much less proton buffering capacities as well as reduced transfection efficiencies compared to PEI.[153] Native PAMAM dendrimers of higher generations were found to be unsuccessful in endosomal release, whereas the insertion of additional functional groups enhanced the transfection efficiency due to improved buffering capacity.[153–155] Based on these outcomes we can conclude that different polymers bearing the same amino type, do not necessarily share the same H^+ absorbing ability. Titration studies demonstrated different protonation behavior between polymers and its corresponding monomers, as polymers showed slightly lower pK_a values.[17,44,148,156] Thus, indicating a strong influence of the chemical structure (amine spacing) on protonation. Therefore, the prediction of a polymer's escape and transfection performance based on the type of amino functionalities and the buffering capacity is not reliable.

Other doubts in the ''proton sponge'' hypothesis focused on the ability of polymers to prevent the acidification of endosomes and a lysosomal involvement. Previous publications interpreted this effect as an increase in pH value or almost neutralization.[41,127,157] The pH value of polyplex-containing endosomal vesicles were analyzed by labeling either the polymer or the nucleic acid with pH-sensitive fluorophores, or utilizing dyes selective for acidic organelles.[97,120,138] Most findings revealed an initial pH value decrease in endocytic vesicles bearing PEI polyplexes (pH $\sim$ 6) indicating their localization within early endosomes.[128,138] These findings indicate that PEI is able to delay the acidification but not to increase the luminal pH. The intracellular fate of PEI polyplexes evokes the question whether PEI acts only within endosomes or also within lysosomes. Godbey *et al.* and Akinc *et al.* reported a lack of lysosomal involvement in PEI-polyplex trafficking.[128,158] On the other side, subcellular fractioning by Lecocq as well as Klemm and coworkers revealed the accumulation of the polymer within lysosomal compartments.[159,160] Lysosomal involvement of PEI-polyplexes was further shown by the research of Kulkarni and colleagues as well as Benjaminsen *et al.* using pH-sensitive fluorophores to track PEI polyplexes within the endocytic pathways.[120,161] They did not recognize a change in the lysosomal pH value, thus concluding that the proton sponge might not be the dominating mechanism for endo-lysosomal release.[120] Lazebnik and Pack quantitatively determined the endocytic trafficking of PEI-siRNA polyplexes by a self-developed method based on a simple polymerization technique combined with a subcellular fractioning method.[162] The authors observed that PEI polyplexes initially appeared in early endosomes and moved further to other compartments, like late endosomes and lysosomes within the first 30 min of post-transfection. The largest amounts of polyplexes were detected in lysosomes one hour post-transfection. An explanation for the inconsistencies of the final intracellular distribution of polyplexes (early/late endosomes, lysosomes) might be explained by the complexity of the uptake mechanism for cationic gene delivery vehicles. Rejman and colleagues as well as Van der Aa *et al.* investigated the uptake mechanisms of PEI polyplexes and observed that the polyplexes were mainly internalized by two types of endocytosis. PEI-based polyplexes that were internalized *via* clathrin-mediated endocytosis, were mostly found within lysosomes but lead to poor transfection efficiencies probably due to degradation.[75,163] No lysosomal co-localization of polyplexes was observed by caveolae-mediated endocytosis, which, results in high gene expression.[75,77] It was shown that lysosomes could be involved in the trafficking of polyplexes but its consequence on transfection performance has to be examined individually for each polymer to be used. Hence, it has to be kept in mind that the internalization route of cationic polyplexes or nano-carriers is highly cell type dependent and may vary between different cell lines but also polymer type.[17,74,78,138,164]

The most discussed part of the ''proton sponge'' hypothesis is the lysis or the complete rupture of the endo-lysosomal membrane. It was questioned whether the binding of protons by PEI within the endosome is sufficient enough to cause an osmotic gradient against the V-ATPase activity. Thus, a critical PEI concentration was assessed to be necessary to achieve a critical membrane tension strong enough for rupture.[120,165,166] In mathematical calculations and computational modeling studies it was shown that the osmotic pressure, generated by the pH value drop from 7.4 to 5.0 as well as the protonation of the cationic polymer is insufficient for an endosomal membrane rupture.[17,120] The expansion of membrane during swelling, which was calculated to be approx. 1 to 2%, do not reach the critical area expansion of lipid vesicles (2 to 5% strain[167]) at which the membrane integrity gets lost.[17,120] This result indicated that a complete physically rupture is highly unlikely. Electron microscopy investigations by Bieber *et al.* demonstrated the attachment of PEI aggregates with the inner side of the lysosomal membrane causing partial membrane disruptions.[168] Similar observations were made in other TEM imaging studies analyzing

the trafficking of polyplexes based on PEI, cyclodextran or poly(methacrylate)s.[152,169,170] They typically showed a close vicinity of the polyplex to the endo-lysosomal membrane and local membrane deformations and disruptions. Live cell spinning disk confocal microscopy was further utilized to capture the dynamics in endosomal release and observed a release of nucleic acids within the cytoplasm by a transient local burst or through nanoscale holes.[171] Interestingly, the endosomes remained intact after the escape event and no complete endosomal lysis was observed. Summarizing these results, a local destabilization of the endosomal membrane integrity, which lead to a transient nanoscale hole formation, might explain the endosomal release.[171] Although several literature reports describe this phenomenon as "pore formation", we will continue to speak of "nanoscale hole formation" in order to avoid misunderstandings regarding protein-formed membrane pores mediating the passage of small molecules and ions.[172]

The polyplex-mediated membrane disruption

As a consequence, a new endosomal escape concept was proposed. In brief, the endosomal escape is mediated by a direct charge-driven polyplex–membrane interaction leading to local membrane destabilization, permeability or even nanoscale hole formation from where the polyplex can be released into the cytoplasm (Fig. 4).[108,168,171,173] A key characteristic is that the endo-lysosomal compartment is kept intact during and after escape compared to a complete lysis as suggested in the "proton sponge" hypothesis.

PEI and other amino-containing polymers provoke membrane damage or at worst cell lysis as indicated by various cytotoxicity studies.[174,175] These disruptive properties of polymers were also thought to be beneficial for transfection, thus generating an optimal balance between cytotoxicity and transfection efficiency. The principles of polymer–membrane interactions were fundamentally elucidated by the work of Banaszak Holl.[108,176,177] His group investigated a broad range of cationic polymers including PEI, PLL and PAMAM dendrimers and evaluated membrane damages or permeability of artificial lipid bilayers or cellular membranes by atomic force microscopy (AFM), enzymatic or protein leakage assays and flow cytometry experiments.[177–179] Different degrees of membrane damages like membrane thinning due to lipid reorientation or lipid removal, and transient membrane hole formation were identified, which was influenced by the polymer molar mass, charge density and concentration.[176,179–181] Interestingly, nanoscale membrane holes induced the leakage of intracellular molecules or dyes,[178,179] but did neither facilitate the cellular entry of polyplexes nor gene expression.[182] Since autophagy can be triggered by endosomal membrane damage,[183,184] a direct evidence for polyplex-mediated membrane disruption or nanoscale hole formation could be given by the detection of autophagy markers. Different studies described the utilization of fluorophore-tagged microtubule-associated protein 1 light chain 3 (LC3), galectin-8 (Gal8) and galectin-9 (Gal9) markers to assay endosomal escape and membrane damage, caused by non-viral gene delivery vectors, in real-time by live cell imaging.[85,87,185]

The charge-driven polymer–membrane interaction within membrane vesicles, as a key aspect of this theory, can be explained by the composition of the inner leaflet of the endo-lysosomal membrane. The membrane structure of early endosomes is rather similar to the plasma membrane and mainly composed of neutral lipids (sphingolipids, sterols, *etc.*). During the maturation to late endosomes the lipid composition changes

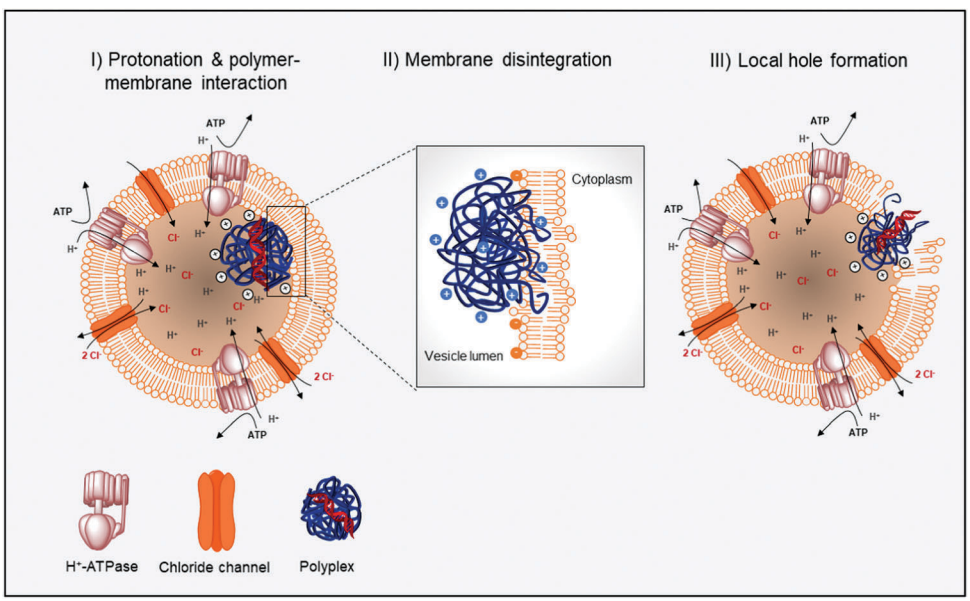

Fig. 4 Illustration of the polyplex-mediated escape theory. Once entrapped within an endo-lysosomal compartment, the cationic polyplexes will be protonated due to the activity of the membrane-bound ATPases. The polyplex with increasing charge density directly interacts with the anionic (phospho)lipids of the inner membrane leaflet. This interaction leads to membrane destabilization and to a local loss of membrane integrity, thus forming nanoscale holes within the membrane. The vector is able to escape the endo-lysosomal compartment through these holes. The compartment keeps intact and complete lysis or rupture does not occur.

towards anionic lipids as the amount of sterols decreases and the amount of anionic bis(monocylglycero)phosphate (BMP) increases.[79] Thus, cationic polymers with continuously increasing charge density will preferably interact with this kind of lipids due to electrostatically interactions as well as hydrogen bonding between the amino groups of the polymer and the phosphate groups of the lipids. Experimental and simulations studies reported that the interaction of PEI with anionic lipids enabled the polymer to intercalate into the hydrophobic core of the membrane bilayer, thus enhancing anionic lipid translocation (lipid "flip-flop") and facilitating the transport of charged molecules (nucleic acids) across the membrane.[186,187]

The polymer-mediated membrane disruption

On the basis of the above introduced theory a revised version was developed, which explains the endosomal escape of cationic polymeric vectors by the intercalation of free cationic polymer chains into the endosomal membrane.[108] As depicted in Fig. 5 the free polymer interacts with the membrane in terms of a "carpet structure" or polymer-supported membrane holes, thus, causing defects in the lipid layer, which leads to the leakage of molecules or nanosized particles. It was hypothesized that the dynamic equilibrium between dissociated polymer chains and polyplexes represents an essential mechanism behind this theory. It is assumed that the free polymer can already intercalate into the cell plasma membrane before endocytosis. Additionally, it is thought that the cell is unable to clear the polymer from the plasma membrane. Hence, the polymer keeps circulating in the membrane during the entire endocytosis and endosomal maturation process leading to membrane disintegration and supporting the subsequent membrane permeability or nanoscale hole formation through which the polyplex and/or nucleic acid can escape.[108,188] This model may also explain cytotoxic effects of cationic polymers, in particular of PEI, which was found to permeabilize lipid membranes of mitochondria or the endoplasmic reticulum.[189,190]

Evidence for a positive effect of free polymer chains on the transfection efficiency was previously reported by different research groups.[154,188,191–194] The authors observed that the addition of uncomplexed PEI, independent of the timing, significantly increased the transfection efficiency compared to the standard protocol of polyplex-mediated transfection.[154,192] It was also shown that the chain length play a more essential role for the enhancement of transfection than the chain topology.[195] Wu and colleagues hypothesized that free polymer chains are able to interfere with signal proteins (SNARE) on the inner cell membrane before or during endocytosis, thus, disturbing the fusion of endocytic vesicles with lysosomes.[195,196]

The excess of polymer during polyplex preparation indicated by high N/P ratios is thought to be beneficial for high transfection efficiencies. This was explained by the fact that only a small amount of PEI is sufficient for complex formation, whereas the majority of PEI (~70 to 80%) stays free in solution promoting the internalization and intracellular trafficking of the polyplexes independent of the molar mass.[191,197,198] Detailed studies on RNA-based polyplexes observed a rapid exchange between polyplexes of different sizes, free polymer and dissociated nucleic acids. Based on this a model of dynamic equilibrium was proposed, which describes the interplay of nucleic acid release and its protection from nuclease degradation as vital issue for successful escape and transfection.[199]

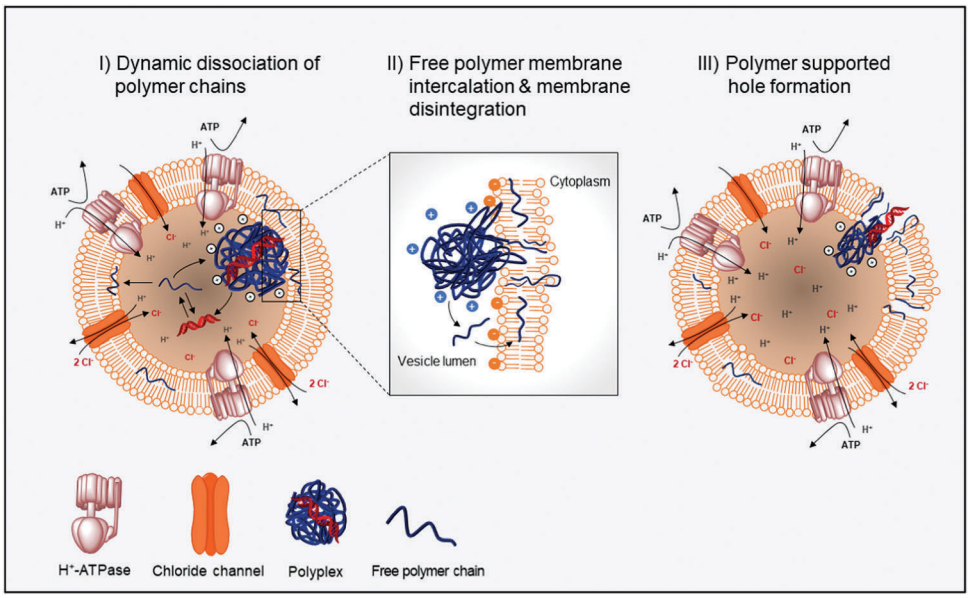

Fig. 5 Graphical illustration of the free polymer-mediated escape theory based on the dynamic release and reattachment of polymer chains as well as nucleic acids to the polyplexes. Free polymer chains intercalate within the membrane of endo-lysosomal compartments, which leads to membrane destabilization and to a local loss of membrane integrity. The polyplex escape the endo-lysosomal compartment through the polymer-supported holes within the membrane. The compartment keeps intact and complete lysis or rupture does not occur.

This theory is further supported by the work of Clark *et al.* using a simplified model of monolayers and vesicles consisting of a mixture of neutral and negative lipids (1,2-dipalmitoylphosphatidylcholine and bis(monoacylglycero)phosphate) to examine the interactions of PEI.[200] The authors observed that the adsorption of free PEI molecules causes deformation and permeabilization of vesicles resulting in the transmembranal diffusion of large molecules (Alexafluor dye) without a rupture of the vesicle. Quantitative analysis by patch clamp measurements of whole HEK cells elucidated a polymer-supported lipid intercalation (carpet structure) or nanoscale hole formation within the plasma membrane caused rather by free polymers than by polyplexes.[201] The behavior of polyelectrolytes, such as PEI, may provide an adequate explanation during the discussed progress. Detailed studies on the polyelectrolyte state of PEI in dependency of different salt and pH conditions revealed conformational changes at different protonation states.[117,202] At neutral pH value, PEI exhibits a more coiled or aggregated structure and predominately settles itself at the bilayer water interface, which do not cause disruption or hole formation. With decreasing pH value, PEI becomes elongated due to the electrostatic repulsion between charges of the protonated amino groups. Because of multiple cationic moieties within the polymer chains a polar environment is created, which provides optimal conditions for water molecules to pass through the lipid bilayer. Thus, the strong interaction and penetration of polymer chains through the membrane leads to the formation of (water) channels or nanoscale holes.[203]

Summary and concluding remarks

Cationic polymers used for the delivery of nucleic acids have to overcome several biological barriers to finally achieve their assignment. In particular, the escape from endo-lysosomal compartments was found to be a major critical step in this process. Once entrapped within the endocytosis pathway only a minority of delivery vectors ($\leq$1 to 2% or two to five bursts per cell) will overcome the endo-lysosomal barrier.[171,204,205] Interestingly, this seems to be sufficient for the transfection to be efficient. The remaining fraction is destined for recycling pathways (exocytosis) or enzymatic degradation (lysosome). To exploit the full potential of this promising technology we have to gain a deeper understanding in the chemistry and the property-relationship of polyplexes on the molecular as well as on the cellular level, since several essential information are

Table 1 Summary of endosomal escape strategies of cationic polymers and polyplexes

Endosomal strategy	Key aspects of mechanism	Studies/methods supporting the theory
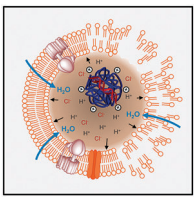	"Proton sponge" effect[39,40] (I) Protonation of polymers' amino groups in acidic endo-lysosomal compartment leads to enhanced chloride ion influx. (II) Osmotic imbalance causes water entrance and swelling of endo-lysosomal compartment. (III) Endo-lysosomal membrane rupture or lysis.	Inhibition of endo-lysosomal acidification by bafilomycin A1 treatment significantly decreases transfection efficiency.[126,128] Quantitatively measurement of chloride ion accumulation and acidification within endosomes by pH-sensing fluorescent probes.[127] Chemical modifications of amino functionalities of PEI directly influenced transfection efficiency due to alterations in the buffering capacity of the polymer.[128,129] Chloroquine treatment enhances transfection efficiency of PLL, PLL-conjugates and DEAE dextran, but not of PEI.[34,128,137,138]
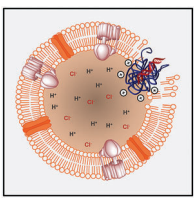	Polyplex-mediated membrane permeability and nanoscale hole formation[18,171] (I) Time-dependent protonation of amino groups in acidic endo-lysosomal compartment. (II) Charge-driven interaction of polyplex with endo-lysosomal membrane. (III) Membrane disintegration, permeability and local hole formation. Endo-lysosomes remain intact.	Qualitatively and quantitatively polyplex and pH tracking by confocal laser scanning microscopy and flow cytometry using pH-sensitive fluorophores.[120,138,161] Polymer–membrane interaction of lipid bilayers by AFM.[178–180] Quantifying endo-lysosomal disruption by calcein assay.[206] Assaying endo-lysosomal disruption by LC3- and Gal8-autophagy markers *via* live cell imaging.[85,87,185] Qualitatively detection of local membrane disruption by TEM imaging and live cell spinning disk confocal microscopy.[168,169,171] Computational modeling support polymer–membrane interactions.[203,207]
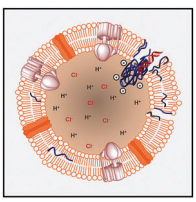	Free polymer-mediated membrane permeability and nanoscale hole formation[108] (I) Dynamic release and reattachment of polymer chains and nucleic acid to polyplex. (II) Free polymer chains intercalate in the plasma membrane or the membrane of endo-lysosomes. (III) Membrane disintegration by polymer intercalation or by polymer-supported hole formation. Endo-lysosomes remain intact. Feasible mechanism for nuclear entry.	Enhanced gene expression by the supplementation of free polymer to standard transfection protocol.[191–193] Quantification of the cell membrane permeability by cationic polymers *via* (whole-cell) patch clamp.[201] Quantification of the endo-lysosomal membrane disruption by calcein assay.[194] Membrane disruption through polymer interaction by dye, LDH and hemolysis leakage assay.[174,175,178,194] Qualitatively tracking of intact and cleaved nucleic acid by FRET confocal microscopy and FRET flow cytometry.[154] Computational modeling support polymer–membrane interactions.[203]

still missing.[17] If we know the key parameters for an efficient release, we can adapt strategies for the design of more powerful delivery vectors. During the past decades numerous studies were performed to explore the polyplex release mechanism. Thereby, a wide range of methods and techniques help to examine the performance and efficiency of the release.[109] The greatest knowledge on the endosomal release of cationic polymers was gained by the investigations of PEI-based polyplexes. Fewer insights on the release mechanism of other cationic polymers have been achieved with PLL, PDMAEMA or PAMAM. The most commonly discussed escape strategies based on the polymers mentioned above are summarized in Table 1. The "proton sponge" hypothesis was the first attempt to explain the excellent gene delivery performance of polymers with a high amino group content. Based on the protonation of the amino groups within the acidic endosomal lumen, it was thought that an osmotic imbalance causes membrane swelling and, finally, the rupture of the vesicle membrane. Nowadays, this theory is still popular and frequently used to explain the efficiency of new transfection vectors. Nevertheless, this hypothesis needs to be revised due to the lack of vital experimental data and various counterevidence. In particular, the endosomal membrane rupture or lysis was found to be highly improbable and was more or less disproved so far. Probably all amino-containing polymers will act as a "proton sponge" by capturing a high number of protons, but the general endosomal escape will not be triggered by a complete membrane rupture. Undoubtedly, pK_a values and high buffer capacities in the range of physiological and lysosomal pH value are important, but do not seem to be the predominant parameter for an efficient endosomal escape of polyplexes. It seems more likely that the charge-driven direct interaction of polyplexes or free polymer chains with the endosomal membrane leads to membrane disintegration, permeability or nanoscale hole formation. But in particular, the dynamic interplay between complexed and free polymer might be the secret of success for efficient polymer-mediated gene delivery. Thus, the underlying mechanism rather resembles a virus-mediated escape due to the similarity in membrane interaction and would not be as unique as previously thought. The viral vector escape mechanism was shown to be driven by the pH-dependent conformational or hydrophobicity change of peptides leading to the piercing of the vesicular membrane followed by fusion with the viral vector or membrane disruption.

Finally, we can conclude that several aspects have an essential impact on the overall endosomal escape of polymer-based vectors. These include (i) the polymer composition with type and content of amino functionalities, (ii) the cell type-specific internalization pathway and (iii) the polymer-specific interaction with lipid bilayers. However, there is no single truth regarding the cellular gene delivery mechanism covering all types of polymers. Consequently, the endosomal escape mechanism must be considered separately for each polymer to optimize its efficiency.

Conflicts of interest

The authors declare no conflicts of interest.

Acknowledgements

The authors would like to acknowledge the financial support by the German Federal Ministry of Education and Research (BMBF #031A518B Vectura, #13XP5034A PolyBioMik) and by the Carl Zeiss Foundation. Furthermore, funding of the collaborative research center PolyTarget (SFB 1278, project B06) by the Deutsche Forschungsgemeinschaft (DFG) is highly appreciated.

References

1 P. Zhang and E. Wagner, *Top. Curr. Chem.*, 2017, **375**, 26.
2 D. W. Pack, A. S. Hoffman, S. Pun and P. S. Stayton, *Nat. Rev. Drug Discovery*, 2005, **4**, 581–593.
3 U. Lachelt and E. Wagner, *Chem. Rev.*, 2015, **115**, 11043–11078.
4 S. Y. Wong, J. M. Pelet and D. Putnam, *Prog. Polym. Sci.*, 2007, **32**, 799–837.
5 E. Wagner, *Acc. Chem. Res.*, 2012, **45**, 1005–1013.
6 D. J. Gary, N. Puri and Y. Y. Won, *J. Controlled Release*, 2007, **121**, 64–73.
7 A. Yamamoto, M. Kormann, J. Rosenecker and C. Rudolph, *Eur. J. Pharm. Biopharm.*, 2009, **71**, 484–489.
8 C. Cheng, A. J. Convertine, P. S. Stayton and J. D. Bryers, *Biomaterials*, 2012, **33**, 6868–6876.
9 H. Fang, K. Zhang, G. Shen, K. L. Wooley and J.-S. A. Taylor, *Mol. Pharmaceutics*, 2009, **6**, 615–626.
10 P. E. Nielsen, *Q. Rev. Biophys.*, 2005, **38**, 345–350.
11 K. R. Beavers, T. A. Werfel, T. W. Shen, T. E. Kavanaugh, K. V. Kilchrist, J. W. Mares, J. S. Fain, C. B. Wiese, K. C. Vickers, S. M. Weiss and C. L. Duvall, *Adv. Mater.*, 2016, **28**, 7984–7992.
12 J. Luten, C. F. van Nostrum, S. C. De Smedt and W. E. Hennink, *J. Controlled Release*, 2008, **126**, 97–110.
13 H. Yin, K. J. Kauffman and D. G. Anderson, *Nat. Rev. Drug Discovery*, 2017, **16**, 387–399.
14 C. E. Nelson and C. A. Gersbach, *Annu. Rev. Chem. Biomol. Eng.*, 2016, **7**, 637–662.
15 L. Li, Z. Y. He, X. W. Wei, G. P. Gao and Y. Q. Wei, *Hum. Gene Ther.*, 2015, **26**, 452–462.
16 W. Sun, W. Ji, J. M. Hall, Q. Hu, C. Wang, C. L. Beisel and Z. Gu, *Angew. Chem., Int. Ed.*, 2015, **54**, 12029–12033.
17 Y. Y. Won, R. Sharma and S. F. Konieczny, *J. Controlled Release*, 2009, **139**, 88–93.
18 C. H. Jones, C.-K. Chen, A. Ravikrishnan, S. Rane and B. A. Pfeifer, *Mol. Pharmaceutics*, 2013, **10**, 4082–4098.
19 J. A. Wolff and J. Lederberg, *Hum. Gene Ther.*, 1994, **5**, 469–480.
20 T. Wirth, N. Parker and S. Ylä-Herttuala, *Gene*, 2013, **525**, 162–169.
21 S. J. Aronson and H. L. Rehm, *Nature*, 2015, **526**, 336.
22 E. H. Szybalska and W. Szybalski, *Proc. Natl. Acad. Sci. U. S. A.*, 1962, **48**, 2026–2034.
23 A. Vaheri and J. S. Pagano, *Virology*, 1965, **27**, 434–436.
24 J. H. McCutchan and J. S. Pagano, *J. Natl. Cancer Inst.*, 1968, **41**, 351–357.

25 F. E. Farber, J. L. Melnick and J. S. Butel, *Biochim. Biophys. Acta*, 1975, **390**, 298–311.
26 Y. Dong, A. I. Skoultchi and J. W. Pollard, *Nucleic Acids Res.*, 1993, **21**, 771–772.
27 W. G. Chaney, D. R. Howard, J. W. Pollard, S. Sallustio and P. Stanley, *Somatic Cell Mol. Genet.*, 1986, **12**, 237–244.
28 S. Kawai and M. Nishizawa, *Mol. Cell. Biol.*, 1984, **4**, 1172–1174.
29 N. Emi, S. Kidoaki, K. Yoshikawa and H. Saito, *Biochem. Biophys. Res. Commun.*, 1997, **231**, 421–424.
30 G. Y. Wu and C. H. Wu, *J. Biol. Chem.*, 1987, **262**, 4429–4432.
31 A. V. Kabanov, I. V. Astafyeva, M. L. Chikindas, G. F. Rosenblat, V. I. Kiselev, E. S. Severin and V. A. Kabanov, *Biopolymers*, 1991, **31**, 1437–1443.
32 V. A. Bloomfield, *Curr. Opin. Struct. Biol.*, 1996, **6**, 334–341.
33 M. A. Lopata, D. W. Cleveland and B. Sollner-Webb, *Nucleic Acids Res.*, 1984, **12**, 5707–5717.
34 P. Erbacher, A. C. Roche, M. Monsigny and P. Midoux, *Exp. Cell Res.*, 1996, **225**, 186–194.
35 W. Zauner, A. Kichler, W. Schmidt, A. Sinski and E. Wagner, *Biotechniques*, 1996, **20**, 905–913.
36 E. Wagner, M. Ogris and W. Zauner, *Adv. Drug Delivery Rev.*, 1998, **30**, 97–113.
37 E. Wagner, *Adv. Drug Delivery Rev.*, 1999, **38**, 279–289.
38 J. Haensler and F. C. Szoka, *Bioconjugate Chem.*, 1993, **4**, 372–379.
39 O. Boussif, F. Lezoualc'h, M. A. Zanta, M. D. Mergny, D. Scherman, B. Demeneix and J. P. Behr, *Proc. Natl. Acad. Sci. U. S. A.*, 1995, **92**, 7297–7301.
40 J.-P. Behr, *Chimia*, 1997, **51**, 34–36.
41 W. T. Godbey, K. K. Wu and A. G. Mikos, *J. Controlled Release*, 1999, **60**, 149–160.
42 J. Y. Cherng, P. vandeWetering, H. Talsma, D. J. A. Crommelin and W. E. Hennink, *Pharm. Res.*, 1996, **13**, 1038–1042.
43 P. van de Wetering, J. Y. Cherng, H. Talsma, D. J. A. Crommelin and W. E. Hennink, *J. Controlled Release*, 1998, **53**, 145–153.
44 P. van de Wetering, E. E. Moret, N. M. E. Schuurmans-Nieuwenbroek, M. J. van Steenbergen and W. E. Hennink, *Bioconjugate Chem.*, 1999, **10**, 589–597.
45 M. E. Favretto, A. Krieg, S. Schubert, U. S. Schubert and R. Brock, *J. Controlled Release*, 2015, **209**, 1–11.
46 H. L. Jiang, M. A. Islam, L. Xing, J. Firdous, W. Cao, Y. J. He, Y. Zhu, K. H. Cho, H. S. Li and C. S. Cho, *Top. Curr. Chem.*, 2017, **375**, 34.
47 T. Bus, C. Englert, M. Reifarth, P. Borchers, M. Hartlieb, A. Vollrath, S. Hoeppener, A. Traeger and U. S. Schubert, *J. Mater. Chem. B*, 2017, **5**, 1258–1274.
48 S. Taranejoo, J. Liu, P. Verma and K. Hourigan, *J. Appl. Polym. Sci.*, 2015, **132**, 42096.
49 J. Murata, Y. Ohya and T. Ouchi, *Carbohydr. Polym.*, 1996, **29**, 69–74.
50 P. Erbacher, S. M. Zou, T. Bettinger, A. M. Steffan and J. S. Remy, *Pharm. Res.*, 1998, **15**, 1332–1339.
51 S. C. W. Richardson, H. J. V. Kolbe and R. Duncan, *Int. J. Pharm.*, 1999, **178**, 231–243.
52 M. Köping-Höggård, I. Tubulekas, H. Guan, K. Edwards, M. Nilsson, K. M. Vårum and P. Artursson, *Gene Ther.*, 2001, **8**, 1108.
53 Q. Y. Zhao, J. Temsamani and S. Agrawal, *Antisense Res. Dev.*, 1995, **5**, 185–192.
54 C. O. Mellet, J. M. G. Fernandez and J. M. Benito, *Chem. Soc. Rev.*, 2011, **40**, 1586–1608.
55 H. Gonzalez, S. J. Hwang and M. E. Davis, *Bioconjugate Chem.*, 1999, **10**, 1068–1074.
56 Y. B. Lim, S. O. Han, H. U. Kong, Y. Lee, J. S. Park, B. Jeong and S. W. Kim, *Pharm. Res.*, 2000, **17**, 811–816.
57 Y. B. Lim, S. M. Kim, H. Suh and J. S. Park, *Bioconjugate Chem.*, 2002, **13**, 952–957.
58 A. Maheshwari, R. I. Mahato, J. McGregor, S. Han, W. E. Samlowski, J. S. Park and S. W. Kim, *Mol. Ther.*, 2000, **2**, 121–130.
59 K. Miyata, M. Oba, M. Nakanishi, S. Fukushima, Y. Yamasaki, H. Koyama, N. Nishiyama and K. Kataoka, *J. Am. Chem. Soc.*, 2008, **130**, 16287–16294.
60 H. Uchida, K. Miyata, M. Oba, T. Ishii, T. Suma, K. Itaka, N. Nishiyama and K. Kataoka, *J. Am. Chem. Soc.*, 2011, **133**, 15524–15532.
61 Y. Chuan, Z. Y. Ong, Y.-Y. Yang, P. L. R. Ee and J. L. Hedrick, *Macromol. Rapid Commun.*, 2011, **32**, 1826–1833.
62 Z. Y. Ong, K. Fukushima, D. J. Coady, Y.-Y. Yang, P. L. R. Ee and J. L. Hedrick, *J. Controlled Release*, 2011, **152**, 120–126.
63 S. T. Hemp, M. H. Allen, M. D. Green and T. E. Long, *Biomacromolecules*, 2012, **13**, 231–238.
64 S. T. Hemp, M. H. Allen, A. E. Smith and T. E. Long, *ACS Macro Lett.*, 2013, **2**, 731–735.
65 M. C. Mackenzie, A. R. Shrivats, D. Konkolewicz, S. E. Averick, M. C. McDermott, J. O. Hollinger and K. Matyjaszewski, *Biomacromolecules*, 2015, **16**, 236–245.
66 C. Ornelas-Megiatto, P. R. Wich and J. M. J. Fréchet, *J. Am. Chem. Soc.*, 2012, **134**, 1902–1905.
67 J. Zhang, Z. Wang, W. Lin and S. Chen, *Biomaterials*, 2014, **35**, 7909–7918.
68 F. Dai and W. Liu, *Biomaterials*, 2011, **32**, 628–638.
69 J. Sun, F. Zeng, H. Jian and S. Wu, *Biomacromolecules*, 2013, **14**, 728–736.
70 K.-M. Xiu, N.-N. Zhao, W.-T. Yang and F.-J. Xu, *Acta Biomater.*, 2013, **9**, 7439–7448.
71 S. Liu, H. Jia, J. Yang, J. Pan, H. Liang, L. Zeng, H. Zhou, J. Chen and T. Guo, *ACS Macro Lett.*, 2018, **7**, 868–874.
72 J. Rejman, V. Oberle, I. S. Zuhorn and D. Hoekstra, *Biochem. J.*, 2004, **377**, 159–169.
73 K. von Gersdorff, N. N. Sanders, R. Vandenbroucke, S. C. De Smedt, E. Wagner and M. Ogris, *Mol. Ther.*, 2006, **14**, 745–753.
74 P. Midoux, G. Breuzard, J. P. Gomez and C. Pichon, *Curr. Gene Ther.*, 2008, **8**, 335–352.
75 J. Rejman, A. Bragonzi and M. Conese, *Mol. Ther.*, 2005, **12**, 468–474.

76 Z. U. Rehman, D. Hoekstra and I. S. Zuhorn, *J. Controlled Release*, 2011, **156**, 76–84.
77 N. P. Gabrielson and D. W. Pack, *J. Controlled Release*, 2009, **136**, 54–61.
78 C. Gonçalves, E. Mennesson, R. Fuchs, J.-P. Gorvel, P. Midoux and C. Pichon, *Mol. Ther.*, 2004, **10**, 373–385.
79 G. van Meer, D. R. Voelker and G. W. Feigenson, *Nat. Rev. Mol. Cell Biol.*, 2008, **9**, 112–124.
80 C. K. Payne, S. A. Jones, C. Chen and X. W. Zhuang, *Traffic*, 2007, **8**, 389–401.
81 B. Yameen, W. I. Choi, C. Vilos, A. Swami, J. Shi and O. C. Farokhzad, *J. Controlled Release*, 2014, **190**, 485–499.
82 D. Glick, S. Barth and K. F. Macleod, *J. Pathol.*, 2010, **221**, 3–12.
83 M. Gannage and C. Munz, *Traffic*, 2009, **10**, 615–620.
84 N. Man, Y. Chen, F. Zheng, W. Zhou and L. P. Wen, *Autophagy*, 2010, **6**, 449–454.
85 A. Wittrup, A. Ai, X. Liu, P. Hamar, R. Trifonova, K. Charisse, M. Manoharan, T. Kirchhausen and J. Lieberman, *Nat. Biotechnol.*, 2015, **33**, 870–876.
86 T. Shintani, F. Yamazaki, T. Katoh, M. Umekawa, Y. Matahira, S. Hori, A. Kakizuka, K. Totani, K. Yamamoto and H. Ashida, *Biochem. Biophys. Res. Commun.*, 2010, **391**, 1775–1779.
87 W. Song, Z. Ma, Y. Zhang and C. Yang, *Acta Biomater.*, 2017, **58**, 196–204.
88 R. S. Shukla, A. Jain, Z. Zhao and K. Cheng, *Nanomedicine*, 2016, **12**, 1323–1334.
89 R. Wattiaux, N. Laurent, S. Wattiaux-De Coninck and M. Jadot, *Adv. Drug Delivery Rev.*, 2000, **41**, 201–208.
90 M. J. Reilly, J. D. Larsen and M. O. Sullivan, *Mol. Pharmaceutics*, 2012, **9**, 1280–1290.
91 R. G. Parton, *Dev. Cell*, 2004, **7**, 458–460.
92 I. Moret, J. Esteban Peris, V. M. Guillem, M. Benet, F. Revert, F. Dasí, A. Crespo and S. F. Aliño, *J. Controlled Release*, 2001, **76**, 169–181.
93 E. Dauty and A. S. Verkman, *J. Biol. Chem.*, 2005, **280**, 7823–7828.
94 E. E. Vaughan and D. A. Dean, *Mol. Ther.*, 2006, **13**, 422–428.
95 S. Grosse, Y. Aron, G. Thévenot, M. Monsigny and I. Fajac, *J. Controlled Release*, 2007, **122**, 111–117.
96 J. Suh, D. Wirtz and J. Hanes, *Proc. Natl. Acad. Sci. U. S. A.*, 2003, **100**, 3878–3882.
97 R. P. Kulkarni, D. D. Wu, M. E. Davis and S. E. Fraser, *Proc. Natl. Acad. Sci. U. S. A.*, 2005, **102**, 7523–7528.
98 B. Sodeik, *Trends Microbiol.*, 2000, **8**, 465–472.
99 U. F. Greber and M. Way, *Cell*, 2006, **124**, 741–754.
100 A. P. Lam and D. A. Dean, *Gene Ther.*, 2010, **17**, 439–447.
101 S. Brunner, E. Furtbauer, T. Sauer, M. Kursa and E. Wagner, *Mol. Ther.*, 2002, **5**, 80–86.
102 S. Grosse, G. Thevenot, M. Monsigny and I. Fajac, *J. Gene Med.*, 2006, **8**, 845–851.
103 R. L. Matz, B. Erickson, S. Vaidyanathan, J. F. Kukowska-Latallo, J. R. Baker, B. G. Orr and M. M. Banaszak Holl, *Mol. Pharmaceutics*, 2013, **10**, 1306–1317.
104 H. Pollard, J. S. Remy, G. Loussouarn, S. Demolombe, J. P. Behr and D. Escande, *J. Biol. Chem.*, 1998, **273**, 7507–7511.
105 A. K. Varkouhi, M. Scholte, G. Storm and H. J. Haisma, *J. Controlled Release*, 2011, **151**, 220–228.
106 C. M. Wiethoff and C. R. Middaugh, *J. Pharm. Sci.*, 2003, **92**, 203–217.
107 Y. W. Cho, J.-D. Kim and K. Park, *J. Pharm. Pharmacol.*, 2003, **55**, 721–734.
108 S. Vaidyanathan, B. G. Orr and M. M. Banaszak Holl, *Acc. Chem. Res.*, 2016, **49**, 1486–1493.
109 T. F. Martens, K. Remaut, J. Demeester, S. C. De Smedt and K. Braeckmans, *Nano Today*, 2014, **9**, 344–364.
110 M. Dominska and D. M. Dykxhoorn, *J. Cell Sci.*, 2010, **123**, 1183–1189.
111 P. K. Selbo, A. Weyergang, A. Høgset, O.-J. Norum, M. B. Berstad, M. Vikdal and K. Berg, *J. Controlled Release*, 2010, **148**, 2–12.
112 K. M. Kem, *J. Polym. Sci., Part A: Gen. Pap.*, 1979, **17**, 1977–1990.
113 B. Brissault, A. Kichler, C. Guis, C. Leborgne, O. Danos and H. Cheradame, *Bioconjugate Chem.*, 2003, **14**, 581–587.
114 L. Tauhardt, K. Kempe, K. Knop, E. Altuntas, M. Jager, S. Schubert, D. Fischer and U. S. Schubert, *Macromol. Chem. Phys.*, 2011, **212**, 1918–1924.
115 G. D. Jones, A. Langsjoen, S. M. M. C. Neumann and J. Zomlefer, *J. Org. Chem.*, 1944, **09**, 125–147.
116 M. Jager, S. Schubert, S. Ochrimenko, D. Fischer and U. S. Schubert, *Chem. Soc. Rev.*, 2012, **41**, 4755–4767.
117 K. A. Curtis, D. Miller, P. Millard, S. Basu, F. Horkay and P. L. Chandran, *PLoS One*, 2016, **11**, e0158147.
118 A. von Harpe, H. Petersen, Y. Li and T. Kissel, *J. Controlled Release*, 2000, **69**, 309–322.
119 J. D. Ziebarth and Y. Wang, *Biomacromolecules*, 2010, **11**, 29–38.
120 R. V. Benjaminsen, M. A. Mattebjerg, J. R. Henriksen, S. M. Moghimi and T. L. Andresen, *Mol. Ther.*, 2013, **21**, 149–157.
121 M. X. Tang and F. C. Szoka, *Gene Ther.*, 1997, **4**, 823–832.
122 C. Sun, T. Tang, H. Uludağ and J. E. Cuervo, *Biophys. J.*, 2011, **100**, 2754–2763.
123 J. E. DiCiccio and B. E. Steinberg, *J. Gen. Physiol.*, 2011, **137**, 385–390.
124 Y.-B. Hu, E. B. Dammer, R.-J. Ren and G. Wang, *Transl. Neurodegener.*, 2015, **4**, 18.
125 J. Nguyen and F. C. Szoka, *Acc. Chem. Res.*, 2012, **45**, 1153–1162.
126 A. Kichler, C. Leborgne, E. Coeytaux and O. Danos, *J. Gene Med.*, 2001, **3**, 135–144.
127 N. D. Sonawane, F. C. Szoka and A. S. Verkman, *J. Biol. Chem.*, 2003, **278**, 44826–44831.
128 A. Akinc, M. Thomas, A. M. Klibanov and R. Langer, *J. Gene Med.*, 2005, **7**, 657–663.
129 M. Thomas and A. M. Klibanov, *Proc. Natl. Acad. Sci. U. S. A.*, 2002, **99**, 14640–14645.
130 K. Itaka, A. Harada, Y. Yamasaki, K. Nakamura, H. Kawaguchi and K. Kataoka, *J. Gene Med.*, 2004, **6**, 76–84.

131 T.-M. Ketola, M. Hanzlíková, L. Leppänen, M. Raviña, C. J. Bishop, J. J. Green, A. Urtti, H. Lemmetyinen, M. Yliperttula and E. Vuorimaa-Laukkanen, *J. Phys. Chem. B*, 2013, **117**, 10405–10413.
132 M. Ruponen, S. Yla-Herttuala and A. Urtti, *Biochim. Biophys. Acta, Biomembr.*, 1999, **1415**, 331–341.
133 M. Ruponen, S. Ronkko, P. Honkakoski, J. Pelkonen, M. Tammi and A. Urtti, *J. Biol. Chem.*, 2001, **276**, 33875–33880.
134 M. Zenke, P. Steinlein, E. Wagner, M. Cotten, H. Beug and M. L. Birnstiel, *Proc. Natl. Acad. Sci. U. S. A.*, 1990, **87**, 3655–3659.
135 P. Midoux and M. Monsigny, *Bioconjugate Chem.*, 1999, **10**, 406–411.
136 P. Midoux, C. Pichon, J.-J. Yaouanc and P.-A. Jaffrès, *Br. J. Pharmacol.*, 2009, **157**, 166–178.
137 C. Plank, K. Zatloukal, M. Cotten, K. Mechtler and E. Wagner, *Bioconjugate Chem.*, 1992, **3**, 533–539.
138 M. L. Forrest and D. W. Pack, *Mol. Ther.*, 2002, **6**, 57–66.
139 J. L. Irvin and E. M. Irvin, *J. Am. Chem. Soc.*, 1947, **69**, 1091–1099.
140 J. Cheng, R. Zeidan, S. Mishra, A. Liu, S. H. Pun, R. P. Kulkarni, G. S. Jensen, N. C. Bellocq and M. E. Davis, *J. Med. Chem.*, 2006, **49**, 6522–6531.
141 P. Dubruel, B. Christiaens, B. Vanloo, K. Bracke, M. Rosseneu, J. Vandekerckhove and E. Schacht, *Eur. J. Pharm. Sci.*, 2003, **18**, 211–220.
142 P. Dubruel, B. Christiaens, M. Rosseneu, J. Vandekerckhove, J. Grooten, V. Goossens and E. Schacht, *Biomacromolecules*, 2004, **5**, 379–388.
143 A. Schallon, V. Jérôme, A. Walther, C. V. Synatschke, A. H. E. Müller and R. Freitag, *React. Funct. Polym.*, 2010, **70**, 1–10.
144 U. Rungsardthong, M. Deshpande, L. Bailey, M. Vamvakaki, S. P. Armes, M. C. Garnett and S. Stolnik, *J. Controlled Release*, 2001, **73**, 359–380.
145 P. Dubruel, V. Toncheva and E. H. Schacht, *J. Bioact. Compat. Polym.*, 2000, **15**, 191–213.
146 R. A. Jones, M. H. Poniris and M. R. Wilson, *J. Controlled Release*, 2004, **96**, 379–391.
147 A. M. Funhoff, C. F. van Nostrum, G. A. Koning, N. M. E. Schuurmans-Nieuwenbroek, D. J. A. Crommelin and W. E. Hennink, *Biomacromolecules*, 2004, **5**, 32–39.
148 D. Sprouse and T. M. Reineke, *Biomacromolecules*, 2014, **15**, 2616–2628.
149 H. B. Li, M. A. Cortez, H. R. Phillips, Y. Y. Wu and T. M. Reineke, *ACS Macro Lett.*, 2013, **2**, 230–235.
150 A. E. Smith, A. Sizovs, G. Grandinetti, L. Xue and T. M. Reineke, *Biomacromolecules*, 2011, **12**, 3015–3022.
151 C. H. Zhu, S. Jung, G. Y. Si, R. Cheng, F. H. Meng, X. L. Zhu, T. G. Park and Z. Y. Zhong, *J. Polym. Sci., Part A: Polym. Chem.*, 2010, **48**, 2869–2877.
152 A.-K. Trützschler, T. Bus, M. Reifarth, J. C. Brendel, S. Hoeppener, A. Traeger and U. S. Schubert, *Bioconjugate Chem.*, 2018, **29**, 2181–2194.
153 G. S. Yu, Y. M. Bae, H. Choi, B. Kong, I. S. Choi and J. S. Choi, *Bioconjugate Chem.*, 2011, **22**, 1046–1055.
154 S. Vaidyanathan, J. Chen, B. G. Orr and M. M. B. Holl, *Mol. Pharmaceutics*, 2016, **13**, 1967–1978.
155 J. F. Kukowska-Latallo, A. U. Bielinska, J. Johnson, R. Spindler, D. A. Tomalia and J. R. Baker, *Proc. Natl. Acad. Sci. U. S. A.*, 1996, **93**, 4897–4902.
156 H. Lee, S. H. Son, R. Sharma and Y.-Y. Won, *J. Phys. Chem. B*, 2011, **115**, 844–860.
157 A. Akinc and R. Langer, *Biotechnol. Bioeng.*, 2002, **78**, 503–508.
158 W. T. Godbey, M. A. Barry, P. Saggau, K. K. Wu and A. G. Mikos, *J. Biomed. Mater. Res.*, 2000, **51**, 321–328.
159 M. Lecocq, S. Wattiaux-De Coninck, N. Laurent, R. Wattiaux and M. Jadot, *Biochem. Biophys. Res. Commun.*, 2000, **278**, 414–418.
160 A. R. Klemm, D. Young and J. B. Lloyd, *Biochem. Pharmacol.*, 1998, **56**, 41–46.
161 R. P. Kulkarni, S. Mishra, S. E. Fraser and M. E. Davis, *Bioconjugate Chem.*, 2005, **16**, 986–994.
162 M. Lazebnik and D. W. Pack, *J. Controlled Release*, 2017, **247**, 19–27.
163 M. A. van der Aa, U. S. Huth, S. Y. Hafele, R. Schubert, R. S. Oosting, E. Mastrobattista, W. E. Hennink, R. Peschka-Suss, G. A. Koning and D. J. Crommelin, *Pharm. Res.*, 2007, **24**, 1590–1598.
164 A. Remy-Kristensen, J. P. Clamme, C. Vuilleumier, J. G. Kuhry and Y. Mely, *Biochim. Biophys. Acta*, 2001, **1514**, 21–32.
165 S. Yang and S. May, *J. Chem. Phys.*, 2008, **129**, 185105, DOI: 10.1063/1.3009263.
166 M. Ogris, P. Steinlein, M. Kursa, K. Mechtler, R. Kircheis and E. Wagner, *Gene Ther.*, 1998, **5**, 1425–1433.
167 D. Needham and R. S. Nunn, *Biophys. J.*, 1990, **58**, 997–1009.
168 T. Bieber, W. Meissner, S. Kostin, A. Niemann and H.-P. Elsasser, *J. Controlled Release*, 2002, **82**, 441–454.
169 S. Mishra, P. Webster and M. E. Davis, *Eur. J. Cell Biol.*, 2004, **83**, 97–111.
170 C. Jonker, C. de Heus, L. Faber, C. ten Brink, L. Potze, J. Fermie, N. Liv and J. Klumperman, *Matters*, 2017, 1–8, DOI: 10.19185/matters.201711000012.
171 Z. U. Rehman, D. Hoekstra and I. S. Zuhorn, *ACS Nano*, 2013, **7**, 3767–3777.
172 R. J. C. Gilbert, H. Bayley and G. Anderluh, *Philos. Trans. R. Soc., B*, 2017, **372**, 20160208.
173 R. Rattan, S. Vaidyanathan, G. S. H. Wu, A. Shakya, B. G. Orr and M. M. B. Holl, *Mol. Pharmaceutics*, 2013, **10**, 3013–3022.
174 D. Fischer, Y. Li, B. Ahlemeyer, J. Krieglstein and T. Kissel, *Biomaterials*, 2003, **24**, 1121–1131.
175 B. C. Evans, C. E. Nelson, S. S. Yu, K. R. Beavers, A. J. Kim, H. Li, H. M. Nelson, T. D. Giorgio and C. L. Duvall, *J. Visualized Exp.*, 2013, e50166, DOI: 10.3791/50166.
176 A. Mecke, I. J. Majoros, A. K. Patri, J. R. Baker, M. M. Banaszak Holl and B. G. Orr, *Langmuir*, 2005, **21**, 10348–10354.
177 P. R. Leroueil, S. Hong, A. Mecke, J. R. Baker, B. G. Orr and M. M. Banaszak Holl, *Acc. Chem. Res.*, 2007, **40**, 335–342.

178 S. P. Hong, A. U. Bielinska, A. Mecke, B. Keszler, J. L. Beals, X. Y. Shi, L. Balogh, B. G. Orr, J. R. Baker and M. M. B. Holl, *Bioconjugate Chem.*, 2004, **15**, 774–782.
179 S. P. Hong, P. R. Leroueil, E. K. Janus, J. L. Peters, M. M. Kober, M. T. Islam, B. G. Orr, J. R. Baker and M. M. Banaszak Holl, *Bioconjugate Chem.*, 2006, **17**, 728–734.
180 A. Mecke, S. Uppuluri, T. M. Sassanella, D.-K. Lee, A. Ramamoorthy, J. R. Baker, B. G. Orr and M. M. Banaszak Holl, *Chem. Phys. Lipids*, 2004, **132**, 3–14.
181 A. Mecke, D.-K. Lee, A. Ramamoorthy, B. G. Orr and M. M. Banaszak Holl, *Langmuir*, 2005, **21**, 8588–8590.
182 L. E. Prevette, D. G. Mullen and M. M. Banaszak Holl, *Mol. Pharmaceutics*, 2010, **7**, 870–883.
183 X. Chen, B. Khambu, H. Zhang, W. T. Gao, M. Li, X. Y. Chen, T. Yoshimori and X. M. Yin, *J. Biol. Chem.*, 2014, **289**, 11162–11174.
184 T. L. M. Thurston, M. P. Wandel, N. von Muhlinen, Á. Foeglein and F. Randow, *Nature*, 2012, **482**, 414.
185 K. V. Kilchrist, B. C. Evans, C. M. Brophy and C. L. Duvall, *Cell. Mol. Bioeng.*, 2016, **9**, 368–381.
186 C. Zhang, F.-G. Wu, P. Hu and Z. Chen, *J. Phys. Chem. C*, 2014, **118**, 12195–12205.
187 U. Kwolek, D. Jamróz, M. Janiczek, M. Nowakowska, P. Wydro and M. Kepczynski, *Langmuir*, 2016, **32**, 5004–5018.
188 Y. Yue, F. Jin, R. Deng, J. Cai, Z. Dai, M. C. M. Lin, H.-F. Kung, M. A. Mattebjerg, T. L. Andresen and C. Wu, *J. Controlled Release*, 2011, **152**, 143–151.
189 G. Grandinetti, N. P. Ingle and T. M. Reineke, *Mol. Pharmaceutics*, 2011, **8**, 1709–1719.
190 G. Grandinetti, A. E. Smith and T. M. Reineke, *Mol. Pharmaceutics*, 2012, **9**, 523–538.
191 Y. Yue, F. Jin, R. Deng, J. Cai, Y. Chen, M. C. Lin, H. F. Kung and C. Wu, *J. Controlled Release*, 2011, **155**, 67–76.
192 S. Boeckle, K. von Gersdorff, S. van der Piepen, C. Culmsee, E. Wagner and M. Ogris, *J. Gene Med.*, 2004, **6**, 1102–1111.
193 Z. Dai, T. Gjetting, M. A. Mattebjerg, C. Wu and T. L. Andresen, *Biomaterials*, 2011, **32**, 8626–8634.
194 D. K. Bonner, X. Zhao, H. Buss, R. Langer and P. T. Hammond, *J. Controlled Release*, 2013, **167**, 101–107.
195 J. Cai, Y. Yue, Y. Wang, Z. Jin, F. Jin and C. Wu, *J. Controlled Release*, 2016, **238**, 71–79.
196 Y. Yue and C. Wu, *Biomater. Sci.*, 2013, **1**, 152–170.
197 J. P. Clamme, J. Azoulay and Y. Mely, *Biophys. J.*, 2003, **84**, 1960–1968.
198 I. Y. Perevyazko, M. Bauer, G. M. Pavlov, S. Hoeppener, S. Schubert, D. Fischer and U. S. Schubert, *Langmuir*, 2012, **28**, 16167–16176.
199 A. Shakya, C. A. Dougherty, Y. Xue, H. M. Al-Hashimi and M. M. Banaszak Holl, *Biomacromolecules*, 2016, **17**, 154–164.
200 S. R. Clark, K. Y. Lee, H. Lee, J. Khetan, H. C. Kim, Y. H. Choi, K. Shin and Y.-Y. Won, *Acta Biomater.*, 2018, **65**, 317–326.
201 S. Vaidyanathan, K. B. Anderson, R. L. Merzel, B. Jacobovitz, M. P. Kaushik, C. N. Kelly, M. A. van Dongen, C. A. Dougherty, B. G. Orr and M. M. Banaszak Holl, *ACS Nano*, 2015, **9**, 6097–6109.
202 C. K. Choudhury and S. Roy, *Soft Matter*, 2013, **9**, 2269–2281.
203 C. K. Choudhury, A. Kumar and S. Roy, *Biomacromolecules*, 2013, **14**, 3759–3768.
204 A.-T. Dinh, C. Pangarkar, T. Theofanous and S. Mitragotri, *Biophys. J.*, 2007, **92**, 831–846.
205 T. Merdan, K. Kunath, D. Fischer, J. Kopecek and T. Kissel, *Pharm. Res.*, 2002, **19**, 140–146.
206 D. K. Bonner, C. Leung, J. Chen-Liang, L. Chingozha, R. Langer and P. T. Hammond, *Bioconjugate Chem.*, 2011, **22**, 1519–1525.
207 W.-d. Tian and Y.-q. Ma, *Soft Matter*, 2012, **8**, 6378–6384.

Publication Pub2

Beyond gene transfection with methacrylate-based polyplexes – The influence of the amino substitution pattern

A.-K. Trützschler, T. Bus, M. Reifarth, J. C. Brendel,
S. Hoeppener, A. Traeger, U. S. Schubert

Bioconjugate Chem. **2018**, *29*, 2181-2194.

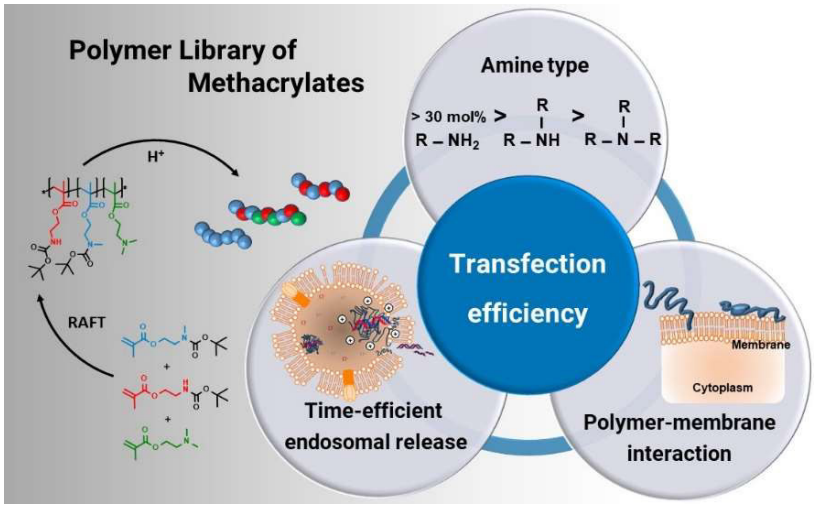

Bioconjugate Chemistry

Article

Cite This: *Bioconjugate Chem.* 2018, 29, 2181−2194

pubs.acs.org/bc

Beyond Gene Transfection with Methacrylate-Based Polyplexes—The Influence of the Amino Substitution Pattern

Anne-Kristin Trützschler,[‡,§,†] Tanja Bus,[‡,§,†] Martin Reifarth,[‡,§,#,∥] Johannes C. Brendel,[‡,§] Stephanie Hoeppener,[‡,§] Anja Traeger,*[,‡,§] and Ulrich S. Schubert*[,‡,§]

[‡]Institue for Organic Chemistry and Macromolecular Chemistry, Friedrich Schiller University Jena, Humboldtstrasse 10, 07743 Jena, Germany

[§]Jena Center for Soft Matter (JCSM), Friedrich Schiller University Jena, Philosophenweg 7, 07743 Jena, Germany

[#]Institute of Physical Chemistry and Abbe Center of Photonics, Friedrich Schiller University Jena, Helmholtzweg 4, 07743 Jena, Germany

[∥]Leibniz Institute of Photonic Technology, Albert-Einstein-Strasse 9, 07745 Jena, Germany

Supporting Information

ABSTRACT: Methacrylate-based polymers represent promising nonviral gene delivery vectors, since they offer a large variety of polymer architectures and functionalities, which are beneficial for specific demands in gene delivery. In combination with controlled radical polymerization techniques, such as the reversible addition−fragmentation chain transfer polymerization, the synthesis of well-defined polymers is possible. In this study we prepared a library of defined linear polymers based on (2-aminoethyl)-methacrylate (AEMA), *N*-methyl-(2-aminoethyl)-methacrylate (MAEMA), and *N*,*N*-dimethyl-(2-aminoethyl)-methacrylate (DMAEMA) monomers, bearing pendant primary, secondary, and tertiary amino groups, and investigated the influence of the substitution pattern on their gene delivery capability. The polymers and the corresponding plasmid DNA complexes were investigated regarding their physicochemical characteristics, cytocompatibility, and transfection performance. The nonviral transfection by methacrylate-based polyplexes differs significantly from poly(ethylene imine)-based polyplexes, as a successful transfection is not affected by the buffer capacity. We observed that polyplexes containing a high content of primary amino groups (AEMA) offered the highest transfection efficiency, whereas polyplexes bearing tertiary amino groups (DMAEMA) exhibited the lowest transfection efficiency. Further insights into the uptake and release mechanisms could be identified by fluorescence and transmission electron microscopy, emphasizing the theory of membrane-pore formation for the time-efficient endosomal release of methacrylate-based vectors.

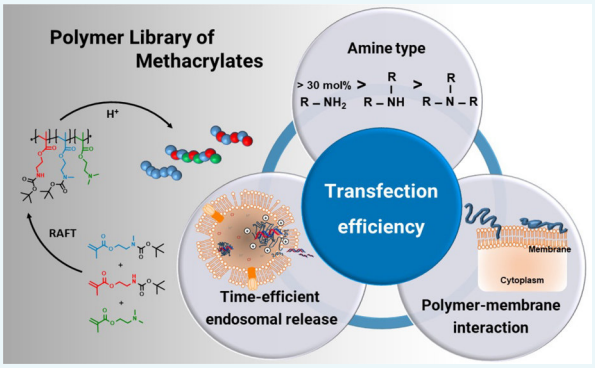

INTRODUCTION

In the last century the intensive research on major human diseases has shown that a wide variety of diseases originate from dysfunction in protein expression. With the increasing knowledge about gene regulation and the role of RNA, personalized therapies on the basis of nucleic acids became feasible. Due to the instability of naked nucleic acids against nucleases and the limited direct cellular uptake,[1] the use of delivery systems, called vectors, is essential for efficient therapeutic approaches. Besides viral vectors, synthetic systems gain increasing attention in the field of gene delivery. Despite the high transfection efficiency of viral gene delivery vectors,[2] the potential immune response on the natural viral proteins, the limitations in the size of the DNA and the difficulties in the scale-up of these systems make nonviral systems more favorable.[3] In accordance, the structures and efficiencies of polymeric delivery systems have constantly been improved, since the first polycation-mediated transfection in 1965[4] and the first polymer-targeted gene delivery in the late 1980s were introduced.[5,6] Different bottlenecks during the transfection processes have been described so far.[7] Thereby, a high molar mass, the presence of cationic charges, as well as a buffering capacity at low pH values were discussed to be beneficial for (i) the formation of the polymer/nucleic acid complex, (ii) the attachment of this complex to cellular membranes and the associated uptake by endocytosis, as well as (iii) the endosomal escape and dissociation of the cargo from the polymer. To date, linear poly(ethylene imine) (lPEI) represents the most frequently applied and most efficient polymer for gene delivery. The secondary amino groups along the backbone are partially

Received: January 28, 2018
Revised: April 12, 2018
Published: May 1, 2018

DOI: 10.1021/acs.bioconjchem.8b00074
Bioconjugate Chem. 2018, 29, 2181−2194

Scheme 1. Schematic Representation of the RAFT-Polymerization and Deprotection Reaction of the Terpolymer Containing Boc-Protected Primary (Red), Secondary (Blue), and Tertiary (Green) Amino Groups Containing Monomers

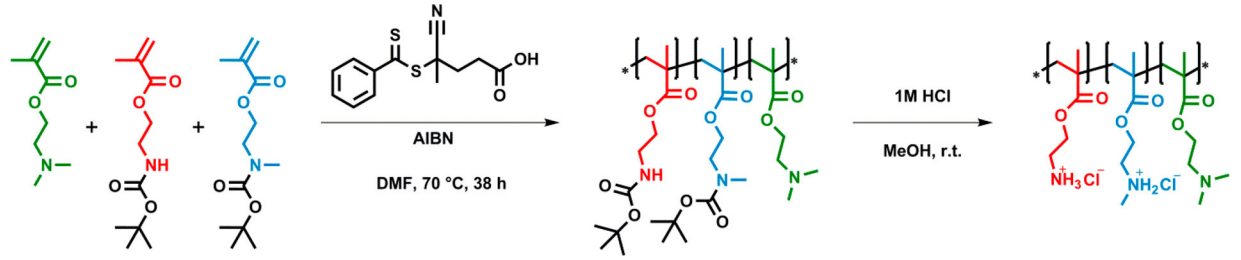

protonated at physiological conditions, which enable the binding of nucleic acids and the buffering of acidifying endosomes as postulated by the popular "proton sponge" hypothesis.[8,9] This theory describes a potential escape strategy from endolysosomes by the increase of the charge density due to further protonation leading to an enhanced influx of chloride ions and water. Consequently, the increasing osmotic pressure causes the rupture of the endosomal membrane and, hence, the release of the vector within the cytsoplasm. Besides lPEI, which comprises mainly secondary amino groups, other materials and amino functionalities have been studied regarding their transfection performance including polymers like poly(L-lysine) (PLL, primary amino groups), poly(*N*,*N*-dimethyl(aminoethyl) methacrylate) (PDMAEMA, tertiary amino groups), and branched PEI (bPEI, primary, secondary, and tertiary amino groups). To gain deeper insight into the impact of the different amino functionalities it is important to investigate the transfection performance with defined polymer architectures. As a consequence, the reversible addition−fragmentation chain transfer polymerization technique (RAFT), which tolerates a wide range of functional groups and enables the controlled synthesis of well-defined structures, represents a promising tool in polymer-based gene delivery.[10,11] In particular, the structural versatility of methacrylate-based polymers allows the introduction of all mentioned different amino moieties into a similar polymer structure and, thus, a direct comparison of the impact of primary, secondary, and tertiary amino groups. So far, only a few studies investigated the influence of this degree of substitution on the final transfection efficiency. Primary, secondary, as well as tertiary amino groups were studied separately on polymer structure and functionality use by groups such as Reineke and co-workers as well as by Zhu et al.[12−14] Palermo et al. revealed that primary and tertiary amino groups in methacrylate-based copolymers complex the phosphate head groups of an artificial lipid bilayer, showing higher membrane internalization of the primary amino groups.[15] This theory is supported by earlier findings of disruptive peptides, which evolve into the membrane to create pathways for other molecules to escape into the cytosol.[16−18] Nevertheless, a thorough comparison of structurally similar polymers comprising primary, secondary, and tertiary amino groups is still missing. To the best of our knowledge, previous reports included either additional functional domains or monomers, or lack at least one of the structural amino varieties.

Within this study we focused on the controlled RAFT synthesis of 2-(*N*,*N*-dimethylamino)ethyl methacrylate, *N*-methyl-*N*-*tert*-butyloxycarbonyl-(2-aminoethyl)-methacrylate (BocMAEMA), and *N*-*tert*-butyloxycarbonyl-(2-aminoethyl)-methacrylate (BocAEMA) to create a library of linear statistical homo- and copolymers with varying amino functionalities. Based on this library, we were able to investigate the influence of different compositions of primary, secondary, and tertiary amino groups in linear polymers on the transfection performance and to elucidate an optimal polymer composition. The polymers were characterized regarding their polyplex formation, cytocompatibility, and their extra- and intracellular fate focusing on uptake and endosomal release.

RESULTS AND DISCUSSION

Polymer Preparation and Characterization. To systematically investigate the influence of secondary amino groups in combination with primary and tertiary amino groups on the transfection efficiency, a library of linear statistical polymers was synthesized via RAFT polymerization.[10,19] The direct polymerization of AEMA with MAEMA and/or DMAEMA led to hydrogels during the polymerization process. This side reaction is probably caused by the basic effect of the amino groups containing methacrylate monomers, which resulted in the aminolysis of the esters or the RAFT group. The cycling or branching reaction induced by the aminolysis of the methacrylate ester unit was previously described and is commonly used for cross-linking of polymers.[20] Another possible reason for the gel formation might be the aminolysis of the RAFT end group causing intermolecular disulfide bridges.[21−23] Therefore, BocAEMA and BocMAEMA were synthesized starting with the Boc-protection of the corresponding ethanolamine according to literature reports.[24−27]

Due to the Boc-protection of the primary and secondary amino groups during synthesis, the hydrogel formation can be avoided during the polymerization process. The polymerization was performed in DMF at 70 °C for 40 h with a M/CTA feed of 240, with a CTA/*I* ratio of 4 and monomer ratios of the copolymers or terpolymers of 50:50 or 1/3, respectively (Scheme 1). The kinetics of the co- and terpolymerization revealed a controlled polymerization with narrow dispersity and a statistical distribution of the monomers (see SI Figures S1 and S2). For the copolymerization of BocAEMA and DMAEMA similar reactivity ratios were already described by Zhu et al.[12] The aim for the final molar mass of the synthesized polymers was at least 20 kDa, which represents a compromise considering the enhancement of the transfection efficiency versus an increasing toxicity with increasing molar mass and the opportunity for controlled polymer synthesis.[28,29]

An overview of the synthesized Boc-protected polymer library (**PBM** to **PBMA**) is provided in Table 1. In the following, the polymers are named using "P" for polymer, "B" for the presence of Boc-protected AEMA and/or MAEMA units, and the combination of letters "D", "M", and "A" for the presence of primary (A), secondary (M), or tertiary amino group containing monomers (D), respectively. All polymers

DOI: 10.1021/acs.bioconjchem.8b00074
Bioconjugate Chem. 2018, 29, 2181−2194

Table 1. Selected Characterization Data of the Boc-Protected Polymers

Polymer	M_n [a] [g mol^{-1}]	Đ	n [b] [mol %] DMAEMA	n [b] [mol %] BocMAEMA	n [b] [mol %] BocAEMA
PBM	35,600	1.08	-	100	-
PBA	33,800	1.10	-	-	100
PBDM	34,400	1.16	60	40	-
PBDA	49,800	1.19	57	-	43
PBMA	54,600	1.14	-	50	50
PBDMA	46,200	1.25	33	33	33

[a]Molar mass and dispersity were determined by size exclusion chromatography (DmAc, 0.21% LiCl, PMMA calibration). [b]Molar percentage was determined by ^{1}H NMR.

Table 2. Selected Characterization Data of the Co- and Homopolymers

Polymer	M_{nAF4} [a]	Đ$_{AF4}$ [a]	Mn_{SEC} [b]	Đ$_{SEC}$ [b]	DP [d]	pK_a
PD	26,200	1.09	29,000[c]	1.09[c]	185	7.45
PM	24,000	1.21	13,400	2.04	167	8.40
PA	21,400	1.10	11,700	1.98	163	8.19
PDM	31,500	1.14	17,900	2.15	208	7.97
PDA	37,000	1.12	16,500	2.19	249	7.83
PMA	46,000	1.28	20,000	2.26	348	8.29
PDMA	36,000	1.27	21,800	2.35	250	8.03

[a]Molar masses and dispersities were determined by AF4 using the MALLS detector. [b]Molar mass was determined by size exclusion chromatography (0.1% TFA, 0.1 M NaCl, dextran calibration). [c]Molar mass was determined by size exclusion chromatography (DmAc, 0.21% LiCl, PMMA calibration). [d]The degree of polymerization was calculated from AF4 results and ^{1}H NMR determining the ratio of monomers. pK_a value was calculated from the titration curves (see SI Figure S5).

featured molar masses in the range of 33 to 54 kDa and narrow distributions (see Figure 1A). In the ^{1}H NMR spectra of the homo- and copolymers characteristic methylene signals of the protection group can be observed at 1.43 ppm (see SI Figure S3). The resulting compositions were calculated from ^{1}H NMR using the ratio of the specific signals of the secondary (δ 2.93 ppm) and tertiary amine (δ 2.25 ppm) containing units, which are assigned to the methyl groups at the amino function. The ratio of those methyl signals to the methylene signal (δ 4.02 ppm) of all units neighboring the ester function in the backbone provides the mole fraction of each monomer.

As no Boc-protection is required, the polymerization of the PDMAEMA homopolymer (**PD**) was directly performed in ethanol using 4,4′-azobis(4-cyanopentanoic acid) as initiator at 70 °C for 20 h. The other Boc-protected polymers of the library (**PBM** to **PBDMA**) were finally deprotected using 1 M hydrochloric acid in methanol. A complete deprotection of the polymers was confirmed by HSQC-NMR at a polymer concentration of 200 mg mL^{-1}, which did not show any residual ^{1}H-signal in the typical range at 1.44 ppm for the methyl groups of the Boc-protection group and no corresponding ^{13}C signal (see SI Figure S4). The results of the characterization experiments are summarized in Table 2. The characterization of the water-soluble deprotected library was performed by size exclusion chromatography on an Appli-Chrom ABOA CatPhil system, which revealed only small interactions with the cationic polymers (Figure 1B). The determination of the molar masses was conducted by asymmetric flow field-flow fractionation (AF4) coupled with multiangle laser light scattering (MALLS) detection showing narrow distributions and molar masses in the range of 21 to 37 kDa. With regard to the missing appropriate size exclusion standards (dextrane used for aqueous SEC) for cationic methacrylate systems the determination of the molar masses and the dispersities is more accurate by utilizing the MALLS detection.[30] However, the AF4 measurement will always tend to underestimate the values for dispersitiy in comparison with other MALLS coupled techniques due to the architecture of the AF4 channel including a membrane with a cutoff of 10 kDa.[31]

In additional titration experiments, the pK_a values of the homo- and copolymers **PD** to **PDMA** were determined to be in the range from pH 7.45 to 8.40 (Table 2). The later used physiological ionic strength was mimicked by the addition of 150 mM NaCl. In Figure S5, the titration curves are shown starting at around pH 2 and plotted against the volume of 0.1 M NaOH solution added to the polymer solution of 10 mg mL^{-1}. The calulation of the pK_a value was performed by fitting the obtained curves with a FTT fit after smoothing the plot to avoid artifacts. The turning points were determined by the differentiation of the fitted curves and the pK_a value was calculated by the Henderson−Hasselbalch eq 2 (see Experimental Section). For PDMAEMA the pK_a was previously described to be 7.5 by van de Wetering et al., which is in

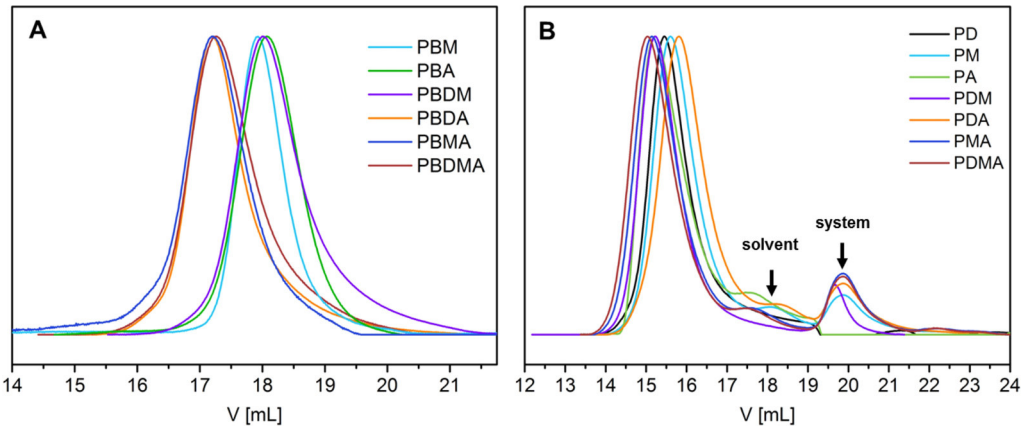

Figure 1. (A) Size exclusion chromatography curves (DmAc, 0.21% LiCl, PMMA calibration) of the Boc-protected polymer library showing narrow dispersities. (B) SEC curves (water, 0.1% trifluoroacetic acid, 0.1 M NaCl, system peak @ 20 mL) of deprotected polymer library showing monomodal distributions.

DOI: 10.1021/acs.bioconjchem.8b00074
Bioconjugate Chem. 2018, 29, 2181−2194

accordance with our result for the **PD** polymer (pK_a = 7.45).[32] These results confirm that at typical cell culture conditions at a pH value of 7.2 to 7.4, at least half of the amino functions of the polymers are in a protonated state and can, therefore, bind and condense negatively charged nucleic acids, thus forming polyplexes.

The calculation of the buffer capacity was performed for qualitative comparison from the titration data according to eq 1 and was plotted as a function of the pH value (Figure S6). For the calculation of β, d(pH) was set to 1 as defined from IUPAC. $Dn(OH^-)$ was calculated from the volume of sodium hydroxide solution used for the change of 1 pH unit.[33]

$$\beta = \frac{dn(OH^-)}{d\,pH} \quad (1)$$

Tested polymers revealed buffer capacities in the range of pH 6.0 to 10.0. Homo- or copolymers with a high content of primary and secondary amino groups (**PM**, **PA**, **PMA**, and **PDMA**) exhibited good buffer capacities at more basic conditions of pH 8.0 and above, while polymers with increasing content of tertiary amino groups (**PD**, **PDM**, **PDA**) tend to show also buffer capacities from neutral to acidic conditions in agreement with the increase in DMAEMA content. In particular, for **PD**, increased buffer capacities over the whole range from pH 6 to pH 8 could be observed. With regard to the "proton sponge" theory, it can be assumed that the sample **PD** most probably possesses the highest potential of enhancing endosomal release. Therefore, we examined the transfection potential of the methacrylate-based polymer library with a particular focus on the influence of different amino functionalities in the following studies, which includes cytocompatibility, cellular uptake, and polymer-mediated escape.

Cytocompatibility. The success of newly designed synthetic transfection vectors crucially depends on their interaction with cellular membranes, the first biological barrier along the intracellular uptake process, which correlates with the overall cell viability. To investigate the cytotoxic potential of the methacrylate-based homo- and copolymers in vitro, we performed a resazurin-based cell viability assay with L929 cells, as recommended by ISO10993-5. Due to high cationic charge densities within the polymer structure, cytotoxic effects, as known from the literature, can be expected.[34,35] As depicted in Figure 2, a concentration-dependent cytotoxicity of all polymers was observed after 24 h. The lowest cell viability was observed for the homo polymers **PD**, **PM**, and **PA** as well as for the copolymer **PDM** revealing CC_{50} values (half-maximal cytotoxic concentration) of 23 μg mL^{-1} for **PM** and 19 μg mL^{-1} for the remaining polymers. Whereas, the co- and terpolymers containing primary amino groups showed moderate cytotoxicities with CC_{50} values of 62 μg mL^{-1} (**PDA**), 38 μg mL^{-1} (**PMA**), and 31 μg mL^{-1} (**PDMA**), respectively. The CC_{50} values of the polymers, except **PDA**, are within the range of linear polyethylene imine (lPEI 25 kDa, CC_{50} = 25 μg mL^{-1}), which is the most prominent polymer-based vector used for gene delivery. The molar mass-dependent cytotoxicity of lPEI can be explained by its high cationic charge density, but it should be considered that the polymer-mediated gene delivery mostly correlates with the cytotoxicity of polyamines, which is the main issue in transfection.

In addition to that, the membrane activity of the polymers was investigated using erythrocytes suspended in PBS (Figure 3A and B). All polymers revealed a strong interaction with cellular membranes as indicated by the increased hemolytic activity (Figure 3A) and erythrocyte aggregation (Figure 3B). The membrane activity was higher for polymers containing primary amino groups. As a significantly higher erythrocyte damage was observed at transfection relevant concentration (see values for 10 μg mL^{-1}). Membrane destabilization and rupture indicate a strong membrane activity resulting in a severe cytotoxicity.[13,29]

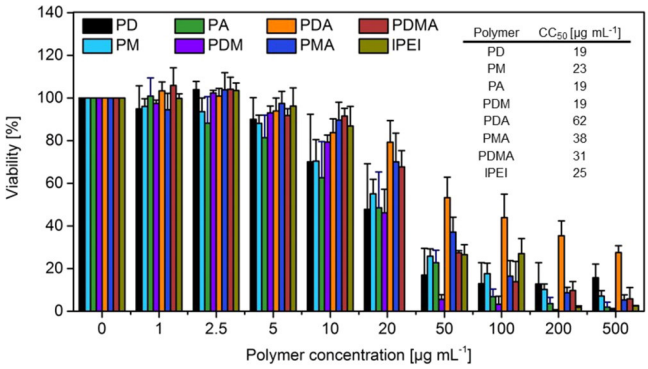

Figure 2. Cytotoxicity evaluation of the methacrylate-based homo- and copolymers **PD** to **PDMA** including lPEI 25 kDa (as control) at indicated concentrations after 24 h. CC_{50} values represented in the table were calculated applying the Boltzman fit (see Figure S7). Values represent the mean ± SD (n = 3).

Methacrylate-Based Polyplexes. In order to examine the binding affinity of all polymers to nucleic acids, the ethidium bromide quenching assay (EBA) was performed using pDNA (4.8 kb) as genetic material to be transfected.[36,37] Different nitrogen (polymer) to phosphate (DNA) ratios (N/P) were used for the polyplex preparation in order to assess the optimal conditions for a stable polyplex formation. All tested polymers revealed the ability to condense pDNA and to form polyplexes with increasing N/P ratios (Figure 4A). This was indicated by the decrease in fluorescence intensities, as a result of the exclusion of ethidium bromide from its binding site within the pDNA. At higher N/P ratios (10 to 20) a plateau of constant fluorescence values is formed in all cases, which indicates a stable polyplex formation. However, the overall fluorescence intensities vary depending on the type of composition of the polymers. Homo- and copolymers based on DMAEMA (**PD**, **PDM**, **PDA**) displayed higher relative fluorescence intensities between 60% and 45%. Those polymers demonstrated only a reduced ability for pDNA condensation, which can be related to the sterically hindered tertiary amino groups. The presence of primary and secondary amino groups (**PM**, **PA**, **PMA**, and **PDMA**) resulted in improved DNA condensation properties (fluorescence intensities below 40%). These observations clearly confirmed the trend for an improved DNA complexation by primary and secondary amino groups.[13,28,38]

Despite differences in the complexation behavior and the resulting relative fluorescence intensities, all polyplexes featured comparable sizes below 200 nm at N/P 20 with a high cationic surface charge between 35 and 39 mV (Table 3), which is typical for cationic methacrylates.[39−41] Nevertheless, the prepared polyplexes exhibited a broad size distribution as indicated by the relatively high PDI values. This fact indicates the presence of a disperse polyplex population and suggests the formation of aggregates, which is a consequence of the preparation method as well as the complexation buffer used.

DOI: 10.1021/acs.bioconjchem.8b00074
Bioconjugate Chem. 2018, 29, 2181−2194

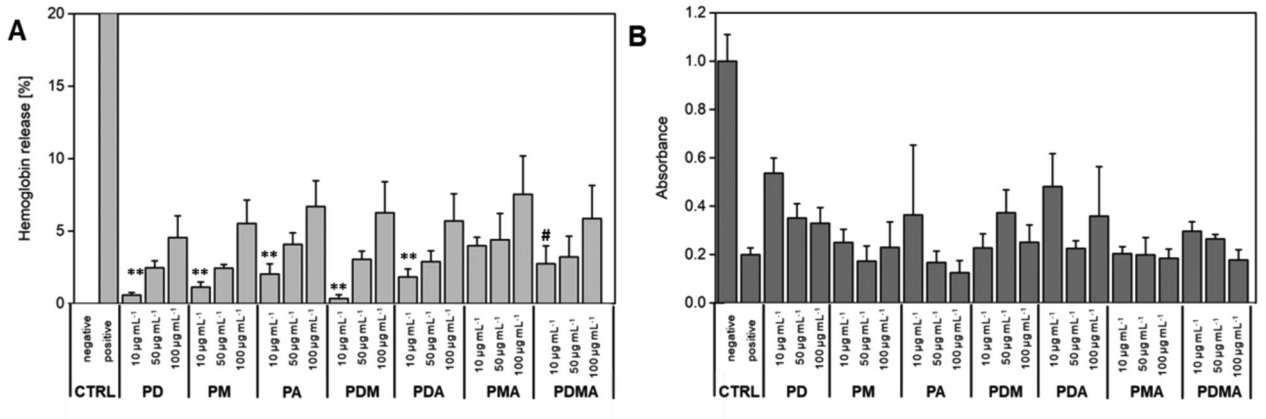

Figure 3. Hemocompatibility studies of methacrylate-based homo- and copolymers **PD** to **PDMA**. (A) Erythrocyte hemolysis assay of polymers at indicated concentrations. Triton X-100 served as positive control (99,8% hemolysis) and PBS as negative control (0%). A value less than 2% hemoglobin release was classified as nonhemolytic and values >5% as hemolytic. *t* test of the hemolysis values at 10 μg mL^{-1} in comparison to PMA; $^{**}P \leq 0.005$; # $P > 0.05$. (B) Aggregation of erythrocytes after polymer treatment at indicated concentrations. PBS was used as negative control and bPEI (25 kDa) as postitive control. Values represent the mean ± SD (n = 3).

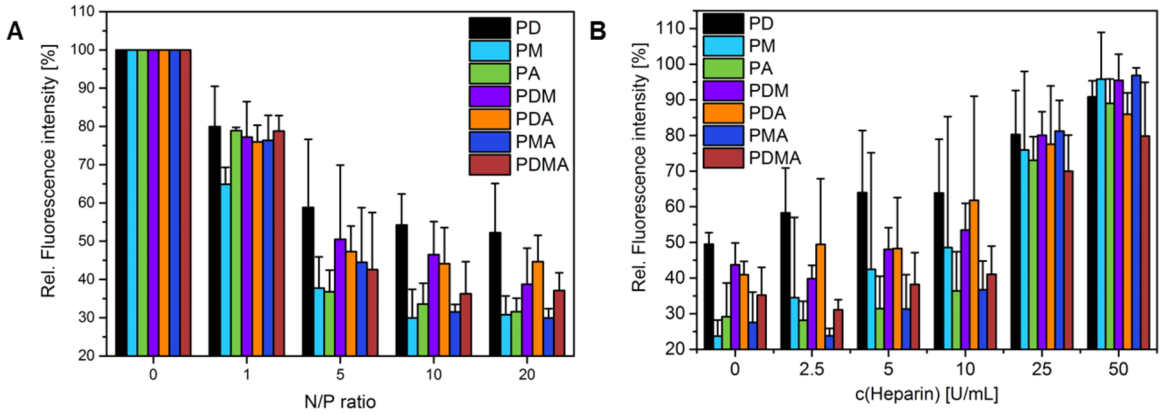

Figure 4. Polyplex stability: (A) Ethidium bromide quenching assay with polyplexes of **PD** to **PDMA** prepared at different N/P ratios (pDNA). (B) Dissociation assay of polyplexes **PD** to **PDMA** (N/P 20) using heparin at different concentrations. Values represent the mean ± SD (n = 3).

Table 3. Size and Zeta Potential of pDNA-Polyplexes Prepared with PD to PDMA at N/P 20[a]

polyplexes of	*Z*-average [d.nm]	PDI	ζ (zeta potential) [mV]
PD	84	0.4	37
PM	97	0.4	37
PA	180	0.4	39
PDM	138	0.3	37
PDA	144	0.4	35
PMA	115	0.4	38
PDMA	148	0.3	39

[a]Polyplexes were measured in 20 mM 4-(2-hydroxethyl) piperazine-1-ethanesulfonic acid (HEPES) and 5% (w/v) glucose, at pH 7.2, by dynamic and electrophoretic light scattering.

The high dispersity is most likely caused by the preparation of polyplexes with higher N/P ratios than necessary for neutralization of the pDNA charges. However, this method (vigorous mixing of pDNA and polymer) is known to show improved polyplex stability and transfection performance.[42]

The dissociation capability of the genetic material from the polymer was investigated by the heparin dissociation assay (Figure 4B).[43] The previously formed polyplexes were treated with different concentrations of heparin to provoke the release of pDNA within the polymer complex acting as competitor to the polymer. Hence, ethidium bromide will be able to intercalate into the displaced nucleic acid once more, leading to an increase in fluorescence intensity. The tested methacrylate-based polymers seem to force a strong condensation of pDNA, since very high concentrations of heparin (50 U mL^{-1}) were required to reach a (almost) full release of the pDNA from the polyplexes. The swiftest release was achieved with **PD**, **PDM**, and **PDA**, although such copolymers comprising DMAEMA units only revealed reduced pDNA dissociation rates (80% to 85%).

Polyplex Performance. Since various studies reported good transfection efficiencies (TE) of methacrylate-based polymers or particles,[12,44,45] the transfection capability of the polymer library was evaluated at various conditions. For this purpose, HEK-293 cells were transfected with pDNA encoding the enhanced green fluorescence protein (EGFP). The transfection efficiency was determined by flow cytometry (Figure 5) analyzing all viable cells (counterstaining with propidium iodide, red) successfully expressing EGFP (green). Despite the fact that **PD** possessed the highest buffer capacity at slightly acidic conditions, which is expected to be beneficial for endosomal release, it demonstrated the lowest transfection levels (<20% TE) at different N/P ratios independent of serum-reduced or serum-containing cell media. Similar observations were reported previously.[40,46] The best trans-

DOI: 10.1021/acs.bioconjchem.8b00074
Bioconjugate Chem. 2018, 29, 2181−2194

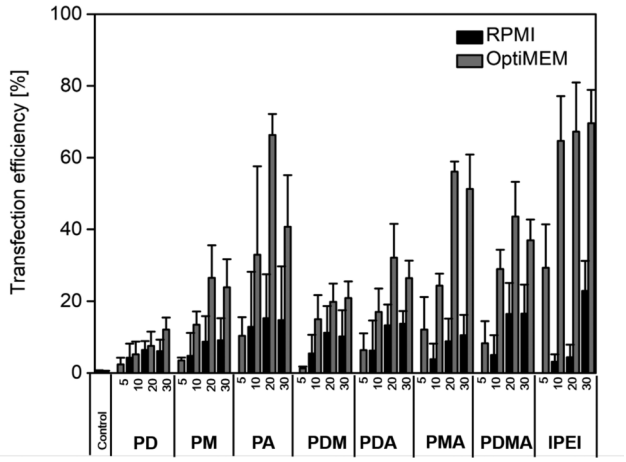

Figure 5. Transfection study of adherent HEK-293 cells in serum-reduced (OptiMEM, light gray) and serum-containing media (RPMI + 10% FCS, black) with all polymers of the library and commercial 25 kDa lPEI as positive control at different N/P ratios after 24 h. Values represent the mean ± SD (n = 3).

fection efficiencies were achieved with **PA** (66% TE) and **PMA** (56% TE) revealing comparable gene expression to lPEI, the standard of transfection (25 kDa, Polysciences) at a N/P ratio of 20. The terpolymer **PDMA** showed also good transfection levels (43% TE) at N/P 20, while **PM**, **PDM**, and **PDA** revealed moderate TEs between 20% and 30%. A concentration-dependent impairment of the overall cell viability during transfection in serum-reduced medium was observed (Figure S8) and showed similar tendencies compared to the cytotoxicity profile of the polymers (see Figure 2). It has to be mentioned, that the assessment of the viability by flow cytometry (PI staining) is based on membrane leakage and, therefore, not directly comparable to the alamarBlue assay. Nevertheless, it is known that polyplexes revealed decreased cytotoxicity compared to free polymers, as the cationic charge is partially masked upon complexation with nucleic acids.[47] In the presence of serum proteins, the intracellular level of EGFP decreases drastically, resulting in maximum TEs below 20% for all methacrylate-based polymers as well as lPEI. Furthermore, improved cell viabilities for tested polyplexes at these conditions were observed (Figure S8). Due to their strong cationic character, negatively charged proteins may aggregate with the polyplexes, which causes an alteration in the surface charges and the sizes of the complex, finally leading to the formation of larger structures and the masking of the positive net charge.[48,49] This effect, in turn, may lead to a reduced affinity to cell membranes (polymer-membrane interaction), diminished uptake of polyplexes and, consequently, to a reduction in transfection efficiencies.[50,51]

Based on the results obtained from flow cytometry experiments, we conclude that polymers with tertiary amino groups and an average molar mass in the range of 20 kDa are not beneficial for transfection, whereas primary amino groups have a substantial impact on the successful delivery of nucleic acids, as the highest transfection efficiency was observed for the polymer with the highest primary amine content (serum-reduced conditions). It should be mentioned that the transfection efficiency of PDMAEMA was previously shown to increase with the increase of the molar mass.[52] The best polymer for transfection was **PA**, which comprises 100% AEMA units. Polymers including additional secondary amino groups (**PMA** and **PDMA**) also demonstrated improved outcomes compared to polymers without any primary amino groups. Homopolymers with 100 mol % tertiary or secondary amino groups as well as copolymers consisting of varying ratios of the corresponding monomers lacked the ability to efficiently transfect HEK-293 cells. Despite the beneficial buffer capability based on the presence of tertiary amino groups, various studies have been questioning the endosomal escape mechanism of PDMAEMA by the "proton sponge" effect.[16,53,54] Our results further undermine this theory, since the buffer capacities of the methacrylate-based polymers do not correlate with their ability for gene expression.[55,56]

To gain a deeper insight of the differences in the gene delivery performance of the methacrylates, we investigated the uptake behavior of the polyplexes. It has been reported that

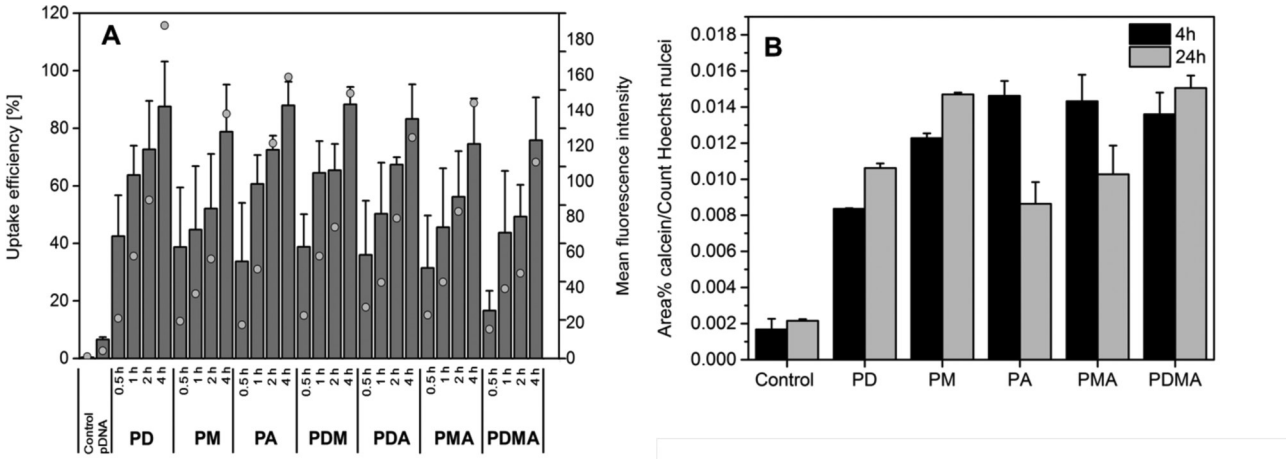

Figure 6. (A) Polyplex uptake of adherent HEK-293 cells in serum-reduced media using YOYO-1 labeled pDNA. The uptake efficiency (columns) and the mean fluorescence intensity of all viable cells (dots) measured by flow cytometry after certain time points. Values represent the mean ± SD (n = 3). (B) Quantification of endosomal release by the calcein release assay. HEK-293 cells were treated with **PD**, **PM**, **PA**, **PMA**, and **PDMA** polyplexes and simultaneous supplementation of calcein (25 μM). After 4 and 24 h the endosomal release of polyplexes was evaluated by the release of calcein from endosomes into the cytoplasm of the cells, leading to high fluorescence signals. Ratio of green fluorescent calcein area in % over the number of detected Hoechst stained nuclei in HEK-293 cells were detected by fluorescence microscopy and quantified using ImageJ.

DOI: 10.1021/acs.bioconjchem.8b00074
Bioconjugate Chem. 2018, 29, 2181−2194

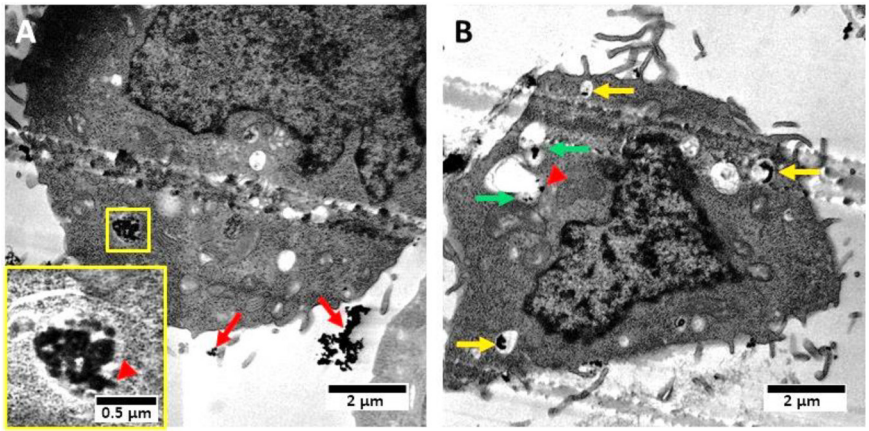

Figure 7. HAADF-STEM images of polyplex treated HEK-293 cells for 4 h in OptiMEM. Polyplexes can be observed as electron dense structures (black). (A,B) **PMA** polyplex treated cells: Red arrows indicate polyplex aggregation in the extracellular environment. Yellow arrows indicate interaction of polyplexes with the membrane of endolysosomal vesicles. Green arrows indicate deformed membrane structures of endolysosomes caused by polylpex interaction. Red arrowheads indicated disturbed membrane integrity of polyplex-containing vesicles and potential membrane disruption or pore formation. Polyplex structures (black) seems to pass from endosomes to cytoplasm.

cationic polyplexes are internalized into cells by endocytosis.[57,58] Since we obtained polyplexes with favorable sizes below 200 nm and cationic net charges, their cellular uptake was investigated by flow cytometry measurements using YOYO-1 labeled pDNA and bafilomycin, a vacuolar type H^+-ATPase inhibitor (see SI Figure S9A,B). Uptake studies at 4 °C confirmed an energy-dependent internalization pathway via endocytosis, shown by the inhibition of the polyplex uptake into HEK-293 cells (Figure S9A). Furthermore, results obtained by the treatment of cells with bafilomycin further support an uptake by endocytosis, since an almost complete inhibition of EGFP transfection was observed (Figure S9B). This effect is caused by the inhibition of the acidification of endolysosomal organelles, which prevents the endosomal release of polyplexes into the cytoplasm, and thus, a successful transfection. This experiment further supports the requirement of polymer protonation through acidification to achieve sufficient endosomal escape.

In contrast, uptake studies at 37 °C revealed a time-dependent uptake of YOYO-1 labeled polyplexes, where about 80% of HEK-293 cells presented internalized polyplexes after 4 h (Figure 6A). In particular, the homopolymers **PD** (MFI = 188) and **PA** (MFI = 159) followed by **PDM** (MFI ∼ 150) revealed the highest amount of YOYO-1 positive cells.

Our results indicate that a high uptake is not the limiting step for high transfection levels,[59] since the endosomal release represents a further critical hindrance in the gene delivery process.[29,60] Therefore, the endosomal escape of the homopolymers **PD**, **PM**, and **PA** as well as the best performing copolymer **PMA** and terpolymer **PDMA** was further examined via a calcein release assay after 4 and 24 h (see Figure 6B and SI Figures S10 and S11). Calcein is a membrane impermeable fluorophore, which is not able to enter cells by diffusion, but by fluid-phase endocytosis. As calcein is, therefore, trapped within the endolysosomes, it can only escape by membrane disruption, which leads to a bright fluorescence in the cytosol by the distribution of calcein throughout the whole cell.[54,61] Since our polymers and polyplexes revealed increased interaction with cellular membranes (see hemolysis and aggregation data), they may promote the release of calcein from endolysosomes within the cytoplasm compared to untreated cells. This experimental setup is designed to model the potential release mechanisms hypothesized by earlier studies on methacrylates with artificial membranes.[15] Representative images of HEK-293 cells with calcein remaining captured within the endolysosomes (control) as well as images of successfully released calcein (**PMA**) are provided within the Supporting Information (Figures S10 and S11). After endosomal release of the dye into the cytosol, the fluorescent area of the calcein signal should increase while the relative fluorescence intensity should decrease in comparison to the stained cell nuclei. The evaluation of the endosomal release was conducted by image analysis of the captured fluorescence pictures using the ImageJ software as described in the Experimental Section focusing on the increase in the relative fluorescent area to the number of stained nuclei. The differentiation between endosomal and cytosolic fluorescence was limited using fluorescence microscopy regarding spatial information and resolution quality. Therefore, the overall fluorescent area was plotted against the number of Hoechst stained nuclei. The results revealed an increased fluorescent area of HEK-293 cells treated with methacrylate-based polyplexes compared to cells treated only with calcein (control). The methacrylate-based polyplexes showed an up to eight-times higher relative fluorescent area after 4 h in contrast to the control, which provides a hint for an early endosomal escape by membrane disruptive activity. In particular, **PA**, **PMA**, and **PDMA** showed the fastest endosomal release, whereas **PD** revealed a lower ratio of escape after 4 h. This trend may relate to its poor transfection performance. **PD** seems to be unable to escape the endosomes in a time efficient manner as, for instance, **PA**, thus being kept entrapped within endolysosomes despite its high buffer capacity. As mentioned earlier, various studies have been questioning the endosomal escape of PDMAEMA by the "proton sponge" effect.[16,53,54] For example, Jones et al. reported the lack of an endosome disruptive activity of PDMAEMA as an explanation for its diminished transfection performance.[54] After 24 h, the fluorescence area of **PA** and **PMA** treated cells decreases compared to the other measured polyplexes, which indicates a fast release within a few hours. A decrease in calcein fluorescence intensity after 4 h was also reported by others and explained by the activity of P-glycoprotein pumps, which might transport calcein out of the cell.[62] A rapid endosomal release of polyplexes within the first hours during the

DOI: 10.1021/acs.bioconjchem.8b00074
Bioconjugate Chem. 2018, 29, 2181−2194

transfection process seems to correlate with high transfection efficiency, as the highest transfection levels were observed for **PA** and **PMA**.

In order to elucidate the location and membrane interaction of the polyplexes, high-angle annular dark-field scanning transmission electron microscopy (HAADF-STEM) was applied. This method provides a resolution down to a few nanometers and combines it with the capability to reveal the ultrastructure of the cellular interior. Figure 7 shows representative images of HEK-293 cells, embedded into an Epon-based resin, after exposure to polyplexes based on **PMA** after 4 h incubation time. In addition to the cellular organelle structures (i.e., mitochondria, vesicles, nucleus), structures of high electron density (dark/black) were observed. We attribute these structures to polymer−DNA complexes, since the functional groups of the polyplex (amines and phosphates) exhibit a strong chemical affinity to the standard staining reagents (OsO_4 and uranyl acetate) resulting in an efficient staining of polyplexes. This staining ability of mentioned reagents has been observed for a variety of different polyplexes so far.[63] In Figure 7A and B, **PMA** polyplexes are located within endosomal structures and, partially, a high number of polyplexes is observed within these structures. In the periphery of the cells the formation of aggregates is evident (red arrow); however, smaller aggregates are also observed to approach the cells. Next to completely filled endosomal structures, some intracellular vesicles are filled with a low number of densely packed polyplexes next to a large amount of intracellular fluids. In Figure 7B an increased interaction of the polyplexes with the endosomal membrane is observed in some cases (yellow arrows), which can be explained by the electrostatic interaction between the positively charged polyplexes and the negatively charged membranes. A close vicinity of the polyplexes to the endosomal membrane was also observed for PEI-based polyplexes.[64] Moreover, in some cases alterations of the endosomal membrane structures become evident. Here, the polyplexes are partially observed in close vicinity to the endosomal structure, which are associated with deformed membranes (green arrows). These structural changes can be attributed to endosomal escape events. An alternative escape strategy to the "proton sponge" effect might be induced by the direct interaction of methacrylate-based polyplexes with the endolysosomal membrane causing a membrane destabilization and a subsequent release due to pore formation without complete rupture. This effect was previously reported for cationic polymers.[59,60,65−67] A disturbed membrane integrity of polyplex-containing vesicles was observed, as parts of the electron dense structures were detected outside of the vesicular membrane reaching into the cytoplasm of HEK-293 cells (indicated by red arrow heads). This observation, as well as our previous results (hemolysis and calcein assay), support an endosomal escape by pore formation due to an increased tension on the membrane rather than a complete osmotic rupture of the endosome.

CONCLUSION

In an effort to understand the influence of different amino functionalities in methacrylate-based polymers on their transfection efficiency, we have synthesized a library of defined linear homo- and copolymers bearing primary, secondary, and tertiary amino groups. The polymers were prepared using the RAFT process and revealed similar molar masses with a DP of 163 to 250 and narrow dispersities (Đ = 1.09 to 1.28) as well as varying compositions of DMAEMA, MAEMA, and AEMA monomers. pK_a values between 7.45 and 8.40 were observed, leading to partial protonation of all polymers at physiological conditions. The buffer capacities, in particular, for **PD**, are in the pH range of endosomal environments, which is supposed to be beneficial for transfection. All synthesized polymers were able to bind and condense pDNA resulting in the formation of stable, nanosized polyplexes (<200 nm). Furthermore, the performance of these polymers as gene delivery vehicles was examined at different conditions by microscopic techniques (fluorescence and scanning transmission electron microscopy) as well as flow cytometry measurements. It was found that several parameters (Figure 8) show a relevant impact on the

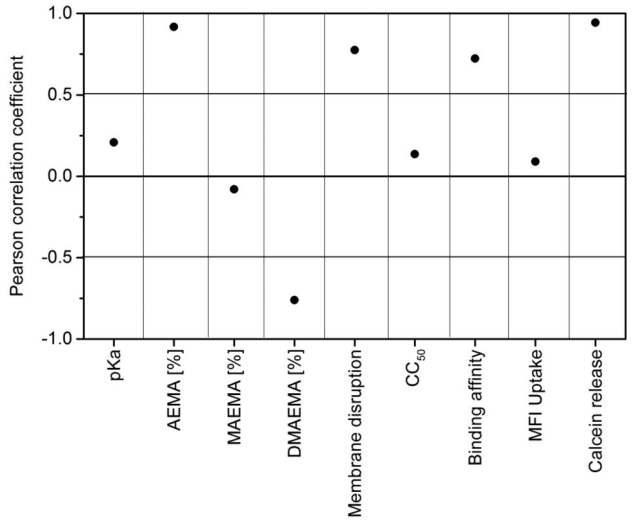

Figure 8. Overview of factors (main polyplex properties) with impact on the transfection efficiency using the Pearson correlation coefficient. Highest proportional correlation is represented by 1.0, whereas −1.0 means the highest inverse proportional correlation. Values around zero indicate no correlation. For membrane disruption, the hemoglobin release at 10 μg mL^{-1} polymer concentration was used. For cytotoxicity the half-maximal (50%) cytotoxic concentration (CC_{50}) was used. The binding affinity represents the measured relative fluorescence of ethidium bromide at N/P 20. To compare the mean fluorescence intensity (MFI) of polyplex uptake, the time (min) that was needed to reach 100 relative MFI (where the control is 1) was determined. The calcein release represents the ratio of green fluorescent calcein area in % over the number of detected Hoechst stained nuclei of the polymers after 4 h.

successful transfection: most importantly, (i) the type and content of the amino group, (ii) the interaction of the polymer with the membrane, and (iii) a rapid endosomal release. However, the size of polyplexes, their uptake rate, and, interestingly, the buffer capacity revealed no direct correlation with the observed transfection levels. Based on our results, the transfection efficiency of such polymers can be summarized regarding their amino functionalities as follows: Primary amino groups > Secondary amino groups > Tertiary amino groups. High contents of primary amino groups in homo- (**PA**) and copolymers (**PMA**) resulted in an improved transfection efficiency, whereas higher amounts of tertiary amino groups within the polymer structure seem to hamper the transfection process (**PD** and **PDM**). A primary amino content of at least ∼40 to 50 mol % was found to be necessary for efficient transfection, since already the copolymer **PDA** ($AEMA_{30\%}$-$DMAEMA_{70\%}$) comprising ∼70 mol % of tertiary amino groups

DOI: 10.1021/acs.bioconjchem.8b00074
Bioconjugate Chem. 2018, 29, 2181−2194

showed reduced results. With the addition of 30 mol % secondary amino groups, the transfection performance of the terpolymer **PDMA** ($AEMA_{30\%}$-$MAEMA_{30\%}$-$DMAEM_{40\%}$) in contrast, significantly increased compared to **PDA**. This effect was only observed for copolymers of MAEMA, since the homopolymer **PM** also demonstrated reduced transfection levels. The good performance of the presented homo- and copolymers could furthermore be explained by a strong polymer−membrane interaction rather than by a rupture mediated by osmotic swelling, as postulated for the "proton sponge" effect. However, it is demonstrated that the endosomal acidification is still required for further protonation of the polymers and therefore for their sufficient interaction with the endolysosomal membrane (see bafilomycin treatment). In fact, all polymers exhibited high hemoglobin release and erythrocyte aggregation, indicating their ability to destabilize membranes and to cause a partial rupture. Despite the fact that such a high membrane interaction leads to an increased cytotoxicity, this property seemed to be beneficial for a fast endosomal release. This assumption is in accordance with the results of our calcein release assay, which revealed a fast endosomal escape, in particular, for **PA** and **PMA**. Based on these investigations, we conclude that the mechanisms for endosomal escape during transfection of methacrylate based polymers differ significantly from PEI, as they are unaffected by the respective buffer capacity and support the theory of the disruptive formation of pores.

EXPERIMENTAL SECTION

Materials. Unless otherwise stated, the chemicals were used without further purification. 2-(*N*,*N*-Dimethylamino)ethyl methacrylate (DMAEMA), methacryloyl chloride, anhydrous triethylamine, 4-cyano-4-(phenylcarbonothioylthio) pentanoic acid (CPDB-COOH), neutral aluminum oxide and 2-(methylamino)ethanol, propidium iodide, and calcein were purchased from Sigma-Aldrich (Merck). The inhibitor removal for DMAEMA was performed using the inhibitor remover from Sigma-Aldrich. Linear and branched poly(ethylene imine) (lPEI/bPEI, 25 kDa) was obtained from Polysciences. Di-*tert*-butyldicarbonate for the protection was from Alfa Aesar and 2-aminoethanol was purchased by TCI. 2-Bisazobutyronitile was received from Acros and recrystallized from methanol prior to use. Hydrochloric acid, dimethylformamide, and tetrahydrofuran were purchased from VWR Chemicals; all other solvents used were obtained from standard suppliers. Ethidium bromide solution (1%, 10 mg mL^{-1}) was obtained from Carl Roth. AlamarBlue, YOYO-1 iodide, and Hoechst 33342 (10 mg mL^{-1} solution) were obtained from Life Technologies (Thermo Fisher). If not stated otherwise, cell culture consumables, cell culture media, and supplements (L-Glutamin, antibiotics) were obtained from Greiner Bio-One, Lonza, and Biochrom (Merck Millipore), respectively. Plasmid pEGFP-N1 (4.7 kb, Clontech, USA) encoding green fluorescent protein (EGFP) was isolated with the Giga Plasmid Kit provided by Qiagen. Double-stranded DNA (dsDNA, 23 nucleotides) was purchased from Jena Bioscience.

Synthesis of *N*-*tert*-Butyloxycarbonyl-(2-aminoethyl)-methacrylate (BocAEMA). *N*-*tert*-Butyloxycarbonyl-(2-aminoethyl)-methacrylate was synthesized according to a procedure of Kuroda et al.[24] 10 g of 2-aminoethanol was dissolved in 120 mL THF and 200 mL of a 1 M aqueous sodium hydroxide solution were added. 35.28 g of di-*tert*-butyldicarbonate in 80 mL THF was added dropwise while cooling the reaction mixture in an ice bath and stirred overnight. The mixture was diluted with ethyl acetate and washed with water, $NaHCO_3$, and brine and the aqueous phase was reextracted with ethyl acetate, dried over sodium sulfate, and the solvent removed under reduced pressure. Without further purification 18.5 g of *N*-*tert*-butyloxycarbonyl-2-aminoethanol was diluted with 30 mL dry dichloromethane under Schlenk conditions and 22.6 mL of dry triethylamine was added while cooling the mixture in an ice bath. Fifteen milliliters of methacryloyl chloride were added dropwise and the reaction was stirred overnight. The mixture was washed with water, brine, and sodium hydrogen carbonate and dried over sodium sulfate. The crude off-white product was finally recrystallized from *n*-hexane. ^{1}H NMR (300 MHz, $CDCl_3$): δ [ppm] = 1.42 (s, 9H), 1.93 (s, 3H), 3.43 (m, 2H), 4.18 (t, 2H), 4.8 (br. s, 1H), 5.57 (s, 1H), 6.10 (s, 1H). ^{13}C NMR (75 MHz, $CDCl_3$): δ [ppm] = 18.2 (CH_3), 28.3 (CH_3), 39.6 (CH_2), 63.9 (CH_2), 79.5 (CH_2), 125.8 (C_{quart}), 136.0 (C_{quart}), 155.7 (C_{quart}), 167.2 (C_{quart}).

Synthesis of *N*-Methyl-*N*-*tert*-butyloxycarbonyl-(2-aminoethyl)-methacrylate (BocMAEMA). *N*-Methyl-*N*-*tert*-butyloxycarbonyl-(2-aminoethyl)-methacrylate was synthesized according to a procedure of Sinclair et al.[25] Ten grams of *N*-methylaminoethanol, dissolved in 80 mL chloroform was cooled in an ice bath and 29 g di-*tert*-butylcarbonate in 80 mL was added dropwise and stirred at room temperature for 1 h. The solvent was removed under reduced pressure and the mixture was purified by distillation (30 mbar, 180 °C). Under Schlenk conditions 21.4 g of *N*-methyl-*N*-*tert*-butyloxycarbonyl-2-aminoethanol were diluted with 100 mL dry dichloromethane, 49.4 mL triethylamine was added, and the reaction mixture cooled in an ice bath. 17.7 mL methacryloyl chloride in 100 mL dichloromethane were added dropwise and the reaction was stirred at room temperature overnight. The mixture was washed with water and brine and dried over sodium sulfate. Further purification was done by column chromatography using a mixture of cyclohexane an ethyl acetate (9:1−3:1). ^{1}H NMR (300 MHz, $CDCl_3$): δ [ppm] = 1.96 (s, 9H), 2.76 (m, 3H), 3.30 (m, 2H), 4.56 (m, 2H), 5.65 (s, 1H), 6.30 (s, 1H). ^{13}C NMR (75 MHz, $CDCl_3$): δ [ppm] = 18.2 (CH_3), 28.3 (CH_3), 35.2 (CH_2), 47.9 (CH_3), 62.7 (CH_2), 79.7(CH_2), 126.0 (C_{quart}), 136.1 (C_{quart}), 155.8 (C_{quart}), 167.1 (C_{quart}).

Synthesis of Homo- and Copolymers. Homo- and copolymers of BocAEMA, BocMAEMA and DMAEMA were prepared by the reversible addition−fragmentation chain transfer (RAFT) polymerization method.[10] In a typical RAFT copolymerization experiment, 0.735 g of BocAEMA (3.18×10^{-3} mol), 0,773 g of BocMAEMA (3.18×10^{-3} mol), 0.98 mg of AIBN initiator (5.96×10^{-5} mol), 5.68 mg of CPDB-COOH RAFT agent (20.33×10^{-5} mol) and 5.03 mL DMF were mixed together with anisole as internal standard (0.347 mL) in a 25 mL reaction vial. The monomer concentration was kept at 1 mol L^{-1}. The reaction mixture was degassed with argon for at least 30 min and, subsequently, the reaction solution was placed in a preheated oil bath at 70 °C for 38 h. The copolymer was purified by two times precipitation from THF into a minimum of 10-fold volume of *n*-hexane and dried under reduced pressure. Conversion was measured by ^{1}H NMR spectroscopy using anisole as internal standard.

The RAFT polymerization of the DMAEMA homopolymers was carried out in ethanol in 1.73 molar solution. 1.572 g DMAEMA (0.01 mol), 2.8 mg 4,4′-azobis(4-cyanovaleric acid) (0.001 mmol), and 11.1 mg 4-cyano-4-(phenylcarbonothioylth-

DOI: 10.1021/acs.bioconjchem.8b00074
Bioconjugate Chem. 2018, 29, 2181−2194

io) pentanoic acid (0.004 mmol) were dissolved in 3.3 mL of ethanol, and 0.77 mL DMF were added as internal standard. The reaction mixture was degassed with argon for 10 min and heated to 70 °C for 10 h. The resulting polymer was purified via precipitation from THF in *n*-hexane twice and dried at high vacuum. Conversion was measured by ^{1}H NMR.

Deprotection of Boc-Protected Polymers. Boc-protected homo- and copolymers were deprotected using diluted hydrochloric acid in methanol. In a typical procedure, 300 mg polymer was dissolved in 10 mL methanol and 1 mL of concentrated hydrochloric acid was added dropwise and stirred at room temperature overnight. The solvent was removed under reduced pressure, dissolved in water, and freeze-dried.

Asymmetric Flow Field-Flow Fractionation (AF4). Asymmetric flow field-flow fractionation (AF4) was performed on an AF2000 MT system (Postnova Analytics, Landberg, Germany) coupled to an UV (PN3211, 260 nm), RI (PN3150), and MALLS (PN3070, 633 nm) detector. The eluent is delivered by two different pumps (tip and focus-flow) and the sample is injected by an autosampler (PN5300) into the channel. The channel has a trapezoidal geometry and an overall area of 31.6 cm^2. The nominal height of the spacer was 500 μm and a regenerated cellulose membrane with a molar mass cutoff of 10,000 g mol^{-1} was used as the accumulation wall. All experiments were carried out at 25 °C and the eluent was 20 mM NaCl in 25 mM sodium acetate buffer at pH 3.5. The detector flow rate was set to 0.5 mL min^{-1} for all samples and a sample volume of 50 μL (10 mg mL^{-1}) was injected with an injection flow rate of 0.2 mL min^{-1} for 7 min. For all samples the cross-flow was set to 2 mL min^{-1}. After the focusing period and a transition time of 1 min, the cross-flow was kept constant for 1 min and then decreased under a power function gradient 0.40 to zero within 15 min. Afterward the cross-flow was kept constant at zero for 20 min to ensure complete elution. For calculation of the molar mass a Zimm plot was used. The refractive index increment (dn/dc) of all samples was measured by manual injection of a known concentration directly into the channel without any focusing or cross-flow. The dn/dc was calculated as the average of at least three injections from the area under the RI curve.

NMR Spectrometry. NMR spectra were recorded on a Bruker AC 300 MHz or on a Bruker AC 250 MHz spectrometer.

Titration. The titration for the detection of the pK_a value of the polymers was performed with the automated titrator 765 Dosimat (Metrohm, Herisau, Swiss) and the pH detector GMH3530 (GHM Messtechnik GmbH Standort Greisinger, Regenstauf, Germany). For a typical measurement the polymer in aqueous 150 mM NaCl solution (10 mg mL^{-1}) was acidified by 10 μL hydrochloric acid and stirred while titrated against a 0.1 M sodium hydroxide solution (0.1 mL min^{-1}) to a pH value of 12. The pK_a value was calculated using the Henderson–Hasselbalch eq 2 by determining the equivalence point from the titration diagram.

$$\mathrm{pH} = p\mathrm{K}_a + \log\frac{[\mathrm{A}^-]}{[\mathrm{HA}]} \tag{2}$$

Size Exclusion Chromatography (SEC). Size exclusion chromatography (SEC) was measured on a Agilent 1200 series system equipped with a PSS degasser, a G1310A pump, a G1362A refractive index detector, and a PSS GRAM guard column running with dimethylacetamide (DmAc) with 0.21% of lithium chloride. The Techlab oven was set to 50 °C and the molar masses were calculated using a poly(methyl methacrylate) (PMMA) standard. For the water-soluble polymers a SEC system of Jasco was used with a DG-980-50 degasser, a PU-980 pump, equipped with a RI-930 RI detector and Jasco oven set to 50 °C. The column used was AppliChrom ABOA CatPhil, which is operated with a water solution with 0.1% trifluoric acid and 0.1 M NaCl.

Polyplex Preparation. Polyplexes of plasmid DNA (pDNA) and polymers were prepared by mixing stock solutions of 15 μg mL^{-1} pDNA and different amounts of polymers (1 mg mL^{-1}) to obtain various N/P ratios (nitrogen of polymer to phosphate of pDNA) in HBG buffer (20 mM 4-(2-hydroxethyl) piperazine-1-ethanesulfonic acid (HEPES) and 5% (w/v) glucose, pH 7.2). The solutions were vortexed for 10 s at maximal speed and incubated at room temperature for 15 min to ensure complex formation.

Ethidium Bromide Quenching Assay. The formation of polyplexes with pDNA was examined by quenching of the ethidium bromide fluorescence. Briefly, 15 μg mL^{-1} pDNA in a total volume of 100 μL HBG buffer were incubated with ethidium bromide (0.4 μg mL^{-1}) for 10 min at room temperature. Subsequently, polyplexes with different amounts of polymer (various N/P ratios) were prepared in black 96-well plates (Nunc Thermo Fisher) and incubated at room temperature for 15 min before the fluorescence measurements. The fluorescence of the samples was measured at an excitation wavelength of 525 nm and an emission wavelength of 605 nm using a Tecan microplate reader. A sample containing only pDNA and ethidium bromide was used to calibrate the device to 100% fluorescence against a background of 0.4 μg mL^{-1} of ethidium bromide in HBG solution. The percentage of dye displaced upon polyplex formation was calculated using eq 3:

$$\mathrm{RFU}[\%] = \frac{F_{\mathrm{sample}} - F_0}{F_{\mathrm{pDNA}} - F_0} \times 100 \tag{3}$$

Here, RFU is the relative fluorescence and F_{sample}, F_0, and F_{pDNA} represents the fluorescence intensities of a given sample, the ethidium bromide in HBG alone, and the ethidium bromide intercalated into pDNA alone.

Heparin Dissociation Assay. Polyplexes with an N/P ratio of 20 were prepared as described above in a total volume of 100 μL HBG buffer containing ethidium bromide (0.4 μg mL^{-1}). After incubation in the dark at room temperature for 15 min, polyplexes were transferred into a black 96-well plate, and heparin of indicated concentrations was added. The solution was mixed and incubated for further 30 min at 37 °C in the dark. The fluorescence of ethidium bromide was measured at Ex 525 nm/Em 605 nm with a Tecan microplate reader. The percentage of intercalated ethidium bromide was calculated as described before.

Dynamic and Electrophoretic Light Scattering. Dynamic light scattering (DLS) was performed on a Zetasizer Nano ZS (Malvern Insturments, Herrenberg) with a He–Ne laser operating at a wavelength of λ = 633 nm. All measurements (30 runs, triplicate) were carried out at 25 °C after an equilibration time of 120 s. The counts were detected at an angle of 173°. The mean particle size was approximated as the effective (z-average) diameter and the width of the distribution as the polydispersity index of the particles (PDI) obtained by the cumulants method assuming a spherical shape. Electrophoretic light scattering (ELS) was used to measure the zeta potential (ζ). The measurement was performed on a

DOI: 10.1021/acs.bioconjchem.8b00074
Bioconjugate Chem. 2018, 29, 2181–2194

Zetasizer Nano ZS (Malvern Instruments, Herrenberg, Germany) by applying laser Doppler velocimetry. For each measurement, 20 runs were carried out using the slow-field reversal and the fast-field reversal mode at 150 V. Each experiment was performed in triplicate a 25 °C. The zeta potential was calculated from the electrophoretic mobility (μ) according to the Henry Equation. Henry coefficient f(ka) was calculated according to Oshima. For size determination of polyplexes a pDNA concentration of 15 μg mL^{-1} was used for preparation at N/P 20 in HBG buffer.

Determination of Cytotoxicity. Cytotoxicity studies were performed with the mouse fibroblast cell line L929 (CCL-1, ATCC), as recommended by ISO10993-5. The cells were cultured in Dulbecco's modified eagle's medium (DMEM, Biochrom) supplemented with 10% fetal calf serum (FCS), 100 U mL^{-1} penicillin, and 100 μg mL^{-1} streptomycin at 37 °C in a humidified 5% (v/v) CO_2 atmosphere. In detail, cells were seeded at 10^4 cells per well in a 96-well plate and incubated for 24 h. Afterward, the testing substances (polymers) at different concentrations, ranging from 1 μg mL^{-1} to 500 μg mL^{-1}, were added to the cells and the plates were incubated for further 24 h. Subsequently, the medium was replaced by a mixture of fresh culture medium and alamarBlue solution, prepared according to the manufacturer's instructions. After a further incubation of 4 h at 37 °C, the fluorescence was measured at Ex 570 nm/Em 610 nm, with untreated cells on the same well plate serving as negative controls. The negative control was standardized as 0% of metabolism inhibition and referred as 100% viability. Data are expressed as mean ± SD of three independent determinations.

Hemolysis Assay. The interaction of polymers with cellular membranes was examined by analyzing the release of hemoglobin from erythrocytes. Blood from sheep, collected in heparinized tubes, were provided by the Institute of Animal Science and Animal Welfare, Friedrich Schiller University Jena. The blood was centrifuged at 4500 × g for 5 min, and the pellet was washed three times with cold 1.5 mM phosphate buffered saline (PBS, pH 7.4). After dilution with PBS in a ratio of 1:7, aliquots of erythrocyte suspension were mixed 1:1 with the polymer solution and incubated in a water bath at 37 °C for 60 min. After centrifugation at 2400 × g for 5 min, the hemoglobin release into the supernatant was determined spectrophotometrically using a microplate reader at 544 nm wavelength. Complete hemolysis (100%) was achieved using 1% Triton X-100 serving as positive control. Pure PBS was used as negative control (0% hemolysis). The hemolytic activity of the polycations was calculated as follows (eq 4):

$$\%\text{Hemolysis} = 100 \times \frac{(A_{\text{Sample}} - A_{\text{Negative control}})}{A_{\text{Positive control}}} \quad (4)$$

A value less than 2% hemolysis rate were classified as nonhemolytic, 2 to 5% as slightly hemolytic and values >5% as hemolytic. Experiments were run in triplicates and were performed with three different blood donors.

Erythrocyte Aggregation. Erythrocytes were isolated as described above. The erythrocyte suspension was mixed 1:1 with the polymer solutions (100 μL total volume) in a clear flat bottomed 96-well plate. The cells were incubated at 37 °C for 2 h, and the absorbance was measured at 645 nm in a microplate reader. Cells which were treated with PBS, which served as negative control and 25 kDa bPEI (50 μg mL^{-1}, Sigma-Aldrich) was used as positive control. Absorbance values of the test solutions lower than the negative control were regarded as aggregation. Experiments were run in triplicates and were performed with three different donor bloods from sheep.

Polyplex Uptake. HEK-293 cells (CRL-1573, ATCC) were routinely cultured in RPMI 1640 medium supplemented with 10% FCS, 100 μg mL^{-1} streptomycin, 100 IU mL^{-1} penicillin, and 2 mM L-glutamine at 37 °C in a humidified 5% (v/v) CO_2 atmosphere.

For kinetic uptake studies of polyplexes, cells were seeded at a density of 10^5 cells per mL in 24-well plates and cultured for 24 h. One hour prior to the addition of polyplexes, the medium was changed to OptiMEM (Thermo Fisher). The pDNA was labeled with YOYO-1 iodide prior to polyplex preparation. For labeling of 1 μg pDNA, 0.026 μL of 1 M YOYO-1 solution was mixed with pDNA and incubated for 15 min at 4 °C protected from light. Afterward HBG buffer and polymers were added at the indicated N/P ratio and polyplexes were formed as described previously. At least 50 μL polyplexes in solution were added to the cells. The cells were harvested 0.5, 1, 2, 4, and 24 h after polyplex addition and 10% trypan blue was added to quench the outer fluorescence of cells. For energy-dependent uptake studies, cells were equilibrated in OptiMEM at 4 °C 30 min prior to polyplex addition. The plates were further incubated at 4 °C for 4 h. To determine the relative uptake of polyplexes, 10^4 cells were measured by flow cytometry using a Cytomics FC 500 (Beckman Coulter) and the amount of viable cells (propidium iodide counterstaining, red) showing YOYO-1 signal (green) were gated.

Calcein Assay. Endosomal escape was evaluated by the calcein quenching assay, as reported earlier using dsDNA (Jena Bioscience) for polyplex preparation.[61] The calcein solution (25 μM final concentration, dissolved in ultrapure water), and polyplexes (N/P 20, 50 μL) were simultaneously added to HEK-293 cells supplemented in OptiMEM for 4 h. Subsequently, cells were washed three times with PBS to remove remaining calcein and free polyplexes. 250 μL phenol-free growth medium supplemented with Hoechst 33342 (1:1000) was added to cells for a further incubation period of 20 min prior to imaging analysis. To examine calcein release after 24 h, cells were cultured in fresh growth media without calcein after the washing steps for further 20 h. Imaging was performed with a fluorescence microscope (Axio Observer Z1, Carl Zeiss, Jena, Germany) equipped with a mercury arc UV lamp and the appropriate filter combinations for excitation and detection of emission (Hoechst 33342: Ex 405 nm/BP 435−490 nm; Calcein: Ex 458 nm/BP 510−550 nm). Five images of random well plate localizations per sample were captured with a Plan-Apochromat 10 × 0.45 air objective while identical instrument settings (camera gain, integration time, UV lamp power). Image analysis was performed with the freely available ImageJ software. Therefore, the images of Hoechst counterstained cell nuclei were processed using the "subtract background" command (10 pixels, separate colors). Afterward the "threshold" was set using the "Otsu" method in black and white (color space HSB, dark background) and the brightness was set to 5/255. The image type was set to 8-bit and converted "to Mask" and the "watershed" method was applied to avoid overlapping of the cell nuclei by an automated manner. Finally the "analyze particles" option was used (21-infinity pixel units, circularity 0.5−1.0, show outlines, display results, exclude edges, and summarize) for particle counting of the cell nuclei. For the calcein images, the analysis was performed in the same manner, but instead of the "watershed" method, the "dilate"

DOI: 10.1021/acs.bioconjchem.8b00074
Bioconjugate Chem. 2018, 29, 2181−2194

method was used. For determination of fluorescent area the "analyze particles" protocol (0 to infinity pixels, circularity 0 to 1.0, and no outlines) was applied.

Transfection of Adherent Cells. For transfection studies, cells were seeded at a density of 10^5 cells per mL in 24-well plates and incubated for 24 h at 37 °C, 5% CO_2. One hour prior to transfection, cells were supplemented with 0.5 mL OptiMEM or fresh serum containing growth medium. Polyplexes were prepared as described above, and were added to the cells (50 μL per well). After an incubation time of 4 h at 37 °C, the supernatant was replaced by fresh growth medium and the cells were further incubated for 20 h. Regarding Bafilomycin experiments, 175 nM Bafilomycin was added to the cells and incubated for 20 min, prior to the polyplex supplementation. For analysis via flow cytometry (Cytomics FC 500, Beckman Coulter), cells were harvested by trypsinization. Dead cells were identified via counterstaining with propidium iodide. For determination of transfection efficiency, 10^4 viable cells expressing EGFP (green) were gated. The experiments were performed independently three times.

Transmission Electron Microscopy. For electron microscopy investigations, HEK-293 cells were seeded on 6-well plates with a cell density of 2×10^6 cells mL^{-1} and incubated with the respective polyplex (N/P 20) in OptiMEM for 4 h. Subsequently, cells were detached with trypsin and the resulting cell suspension was centrifuged, washed (PBS 1×), and fixed for 2 h with glutaraldehyde (2% in PBS 1×, prepared from 8% EM grade stock solution, purchased from EMS, Hatfield) on ice. After glutaraldehyde fixation, the cells were again washed with PBS and post-fixed for 1 h with osmium tetroxide (1% in PBS, prepared from 4% EM grade stock solution, purchased from EMS, Hatfield). After washing with pure water, the cell suspension was stained for 1 h with uranyl actetate solution in the dark (1% in solution in ultrapure water prepared from depleted uranyl acetate dihydrate purchased from EMS, Hatfield). Subsequently, the sample was again washed with pure water prior to dehydration by an ethanol/water series (50%, 70%, 90%, 2 × 100% dry EtOH, purified with a Solvent Purification System, stored over molecular sieves). The dehydrated samples were then transferred into BEEM capsules (Plano, Wetzlar). After removal of the ethanol, the cell suspension was immersed in mixtures of Embed 812 (EMS, Hatfield) and ethanol (Embed/EtOH = 1:1 v/v for 1 h, 2:1 v/v for 12 h) and prior to embedding in pure Embed 812 for 4 h. After a further change of the embedding medium, the resin was allowed to harden in an oven at 70 °C for 24 h. From the resin block, ultrathin sections of 80 nm were cut with an ultramicrotome (PT-XL PowerTome, RMC, Tucson) using a diamond knife (RMC, Tucson). The ultrathin resin sections were captured, deposited on a carbon supported copper grid (400 mesh, Quantifoil, Jena), and imaged with a Technai G2 system (FEI), with 120 kV acceleration voltage in STEM mode (HAADF detection).

Statistical Analysis. The result values represent the mean ± SD ($n \geq 3$). To determine the Pearson correlation, the PEARSON function in Excel was used. Each parameter was compared to the transfection efficiency at N/P 20. The *t* test calculation was done using the *t* test function in excel. The hemolysis data of the library at 10 μg mL^{-1} was compared with the values of PMA.

■ ASSOCIATED CONTENT

Supporting Information

The Supporting Information is available free of charge on the ACS Publications website at DOI: 10.1021/acs.bioconjchem.8b00074.

Supporting NMR spectra, titration curves, buffer capacity plot, example for a Boltzmann fit for CC_{50} calculation, energy dependent uptake studies, and example of the ImageJ analysis of the fluorescence microscopy pictures (PDF)

■ AUTHOR INFORMATION

Corresponding Authors

*E-mail: anja.traeger@uni-jena.de.
*E-mail: ulrich.schubert@uni-jena.de.

ORCID

Ulrich S. Schubert: 0000-0003-4978-4670

Author Contributions

†Anne-Kristin Trützschler and Tanja Bus contributed equally to this work

Notes

The authors declare no competing financial interest.

■ ACKNOWLEDGMENTS

The authors like to thank the Bundesministerium für Bildung und Forschung (BMBF, Germany, #031A518B Vectura, #13N13416 smart-dye-livery, #13XP5034A PolyBioMik) for financial support. Furthermore, funding of the collaborative research center PolyTarget (SFB 1278) by the Deutsche Forschungsgemeinschaft (DFG) is highly acknowledged. A. Traeger acknowledges the Carl Zeiss Foundation for funding. M. Reifarth is grateful for financial support in the frames of "Carl-Zeiss-Strukturmaßnahme" as well as the ProExzellenzII initiative "Nanopolar" of the Federal State of Thuringia. J. C. Brendel thanks the Deutsche Forschungsgemeinschaft (DFG) for generous funding in the Emmy-Noether Programm (BR 4905/3-1). The authors furthermore acknowledge Elisabeth Preußger and Carolin Kellner for assistance with cell experiments. TEM investigations were performed at the electron microscopy facilities of the Jena Center for Soft Matter (JCSM), which was established with grants from the Deutsche Forschungsgemeinschaft (DFG) and the European Fund for Regional Development (EFRE). The LSM880 ELYRA PS.1 was further funded with a grant from the DFG.

■ ABBREVIATIONS

AEMA, (2-Aminoethyl)-methacrylate; MAEMA, *N*-Methyl-(2-aminoethyl)-methacrylate; DMAEMA, *N,N*-Dimethyl-(2-aminoethyl)-methacrylate; pDNA, Plasmid DNA; lPEI, Linear poly(ethylene imine); bPEI, Branched poly(ethylene imine); RAFT, Reversible addition−fragmentation chain transfer; Boc, *tert*-Butyloxycarbonyl; CTA, Chain transfer agent; I, Initiator; M, Monomer; PD, Poly(DMAEMA); PM, Poly(MAEMA); PA, Poly(AEMA); PDM, Poly(DMAEMA-*co*-MAEMA); PDA, Poly(DMAEMA-*co*-AEMA); PMA, Poly(MAEMA-*co*-AEMA); PDMA, Poly(DMAEMA-*co*-MAEMA-*co*-AEMA); M_n, Number-average molar mass; PMMA, Poly(methyl methacrylate); DmAc, Dimethyl acetamid; HSQC, Heteronuclear single quantum coherence; AF4, Asymmetric flow field-flow fractionation; MALLS, Multiangle laser light scattering; SEC, Size exclusion chromatography; TFA, Trifluoroacetic acid; CC_{50},

DOI: 10.1021/acs.bioconjchem.8b00074
Bioconjugate Chem. 2018, 29, 2181−2194

50% Cytotoxic concentration; SD., Standard deviation; TE, Half-maximal cytotoxic concentration; EGFP, Enhanced green fluorescence protein; FCS, Fetal calf serum; HEK, Human embryonic kidney cells; MFI, Mean fluorescence intensity; HAADF-STEM, High-angle annular dark-field scanning transmission electron microscopy

REFERENCES

(1) Lechardeur, D., Sohn, K.-J., Haardt, M., Joshi, P. B., Monck, M., Graham, R. W., Beatty, B., Squire, J., O'Brodovich, H., and Lukacs, G. L. (1999) Metabolic instability of plasmid DNA in the cytosol: a potential barrier to gene transfer. *Gene Ther. 6*, 482−497.

(2) Kealy, B., Liew, A., McMahon, J. M., Ritter, T., O'Doherty, A., Hoare, M., Greiser, U., Vaughan, E. E., Maenz, M., O'Shea, C., et al. (2009) Comparison of viral and nonviral vectors for gene transfer to human endothelial progenitor cells. *Tissue Eng., Part C 15*, 223−231.

(3) Nayerossadat, N., Maedeh, T., and Ali, P. (2012) Viral and nonviral delivery systems for gene delivery. *Adv. Biomed. Res. 1*, 27−27.

(4) Vaheri, A., and Pagano, J. S. (1965) Infectious poliovirus RNA: A sensitive method of assay. *Virology 27*, 434−6.

(5) De Smedt, S. C., Demeester, J., and Hennink, W. E. (2000) Cationic polymer based gene delivery systems. *Pharm. Res. 17*, 113−126.

(6) Wu, G. Y., and Wu, C. H. (1987) Receptor-mediated in vitro gene transformation by a soluble DNA carrier system. *J. Biol. Chem. 262*, 4429−32.

(7) Wong, S. Y., Pelet, J. M., and Putnam, D. (2007) Polymer systems for gene delivery—Past, present, and future. *Prog. Polym. Sci. 32*, 799−837.

(8) Boussif, O., Lezoualc'h, F., Zanta, M. A., Mergny, M. D., Scherman, D., Demeneix, B., and Behr, J. P. (1995) A versatile vector for gene and oligonucleotide transfer into cells in culture and in vivo: polyethylenimine. *Proc. Natl. Acad. Sci. U. S. A. 92*, 7297−301.

(9) Behr, J. P. (1997) The proton sponge: A trick to enter cells the viruses did not exploit. *Chimia 51*, 34−36.

(10) Ahmed, M., and Narain, R. (2013) Progress of RAFT based polymers in gene delivery. *Prog. Polym. Sci. 38*, 767−790.

(11) Xu, F. J., Neoh, K. G., and Kang, E. T. (2009) Bioactive surfaces and biomaterials via atom transfer radical polymerization. *Prog. Polym. Sci. 34*, 719−761.

(12) Zhu, C., Jung, S., Si, G., Cheng, R., Meng, F., Zhu, X., Park, T. G., and Zhong, Z. (2010) Cationic methacrylate copolymers containing primary and tertiary amino side groups: Controlled synthesis via RAFT polymerization, DNA condensation, and in vitro gene transfection. *J. Polym. Sci., Part A: Polym. Chem. 48*, 2869−2877.

(13) Sprouse, D., and Reineke, T. M. (2014) Investigating the effects of block versus statistical glycopolycations containing primary and tertiary amines for plasmid DNA delivery. *Biomacromolecules 15*, 2616−2628.

(14) Smith, A. E., Sizovs, A., Grandinetti, G., Xue, L., and Reineke, T. M. (2011) Diblock glycopolymers promote colloidal stability of polyplexes and effective pDNA and siRNA delivery under physiological salt and serum conditions. *Biomacromolecules 12*, 3015−3022.

(15) Palermo, E. F., Lee, D.-K., Ramamoorthy, A., and Kuroda, K. (2011) Role of cationic group structure in membrane binding and disruption by amphiphilic copolymers. *J. Phys. Chem. B 115*, 366−375.

(16) Funhoff, A. M., van Nostrum, C. F., Koning, G. A., Schuurmans-Nieuwenbroek, N. M. E., Crommelin, D. J. A., and Hennink, W. E. (2004) Endosomal escape of polymeric gene delivery complexes is not always enhanced by polymers buffering at low pH. *Biomacromolecules 5*, 32−39.

(17) Nakase, I., Kobayashi, S., and Futaki, S. (2010) Endosome-disruptive peptides for improving cytosolic delivery of bioactive macromolecules. *Biopolymers 94*, 763−770.

(18) Murthy, N., Robichaud, J. R., Tirrell, D. A., Stayton, P. S., and Hoffman, A. S. (1999) The design and synthesis of polymers for eukaryotic membrane disruption. *J. Controlled Release 61*, 137−143.

(19) Lowe, A. B., and McCormick, C. L. (2007) Reversible addition−fragmentation chain transfer (RAFT) radical polymerization and the synthesis of water-soluble (co)polymers under homogeneous conditions in organic and aqueous media. *Prog. Polym. Sci. 32*, 283−351.

(20) Fixe, F., Dufva, M., Telleman, P., and Christensen, C. B. V. (2004) Functionalization of poly(methyl methacrylate) (PMMA) as a substrate for DNA microarrays. *Nucleic Acids Res. 32*, e9.

(21) Moad, G., Chong, Y. K., Postma, A., Rizzardo, E., and Thang, S. H. (2005) Advances in RAFT polymerization: the synthesis of polymers with defined end-groups. *Polymer 46*, 8458−8468.

(22) Thomas, D. B., Convertine, A. J., Hester, R. D., Lowe, A. B., and McCormick, C. L. (2004) Hydrolytic susceptibility of dithioester chain transfer agents and implications in aqueous RAFT polymerizations. *Macromolecules 37*, 1735−1741.

(23) Xu, J., He, J., Fan, D., Wang, X., and Yang, Y. (2006) Aminolysis of polymers with thiocarbonylthio termini prepared by RAFT polymerization: The difference between polystyrene and polymethacrylates. *Macromolecules 39*, 8616−8624.

(24) Sinclair, A., Bai, T., Carr, L. R., Ella-Menye, J.-R., Zhang, L., and Jiang, S. (2013) Engineering buffering and hydrolytic or photolabile charge shifting in a polycarboxybetaine ester gene delivery platform. *Biomacromolecules 14*, 1587−1593.

(25) Kuroda, K., and DeGrado, W. F. (2005) Amphiphilic polymethacrylate derivatives as antimicrobial agents. *J. Am. Chem. Soc. 127*, 4128−4129.

(26) Palermo, E. F., Vemparala, S., and Kuroda, K. (2012) Cationic spacer arm design strategy for control of antimicrobial activity and conformation of amphiphilic methacrylate random copolymers. *Biomacromolecules 13*, 1632−1641.

(27) Li, H., Cortez, M. A., Phillips, H. R., Wu, Y., and Reineke, T. M. (2013) Poly(2-deoxy-2-methacrylamido glucopyranose)-b-Poly(methacrylate amine)s: Optimization of diblock glycopolycations for nucleic acid delivery. *ACS Macro Lett. 2*, 230−235.

(28) Rinkenauer, A. C., Schubert, S., Traeger, A., and Schubert, U. S. (2015) The influence of polymer architecture on in vitro pDNA transfection. *J. Mater. Chem. B 3*, 7477−7493.

(29) Layman, J. M., Ramirez, S. M., Green, M. D., and Long, T. E. (2009) Influence of polycation molecular weight on poly(2-dimethylaminoethyl methacrylate)-mediated DNA delivery in vitro. *Biomacromolecules 10*, 1244−1252.

(30) Wagner, M., Pietsch, C., Tauhardt, L., Schallon, A., and Schubert, U. S. (2014) Characterization of cationic polymers by asymmetric flow field-flow fractionation and multi-angle light scattering—A comparison with traditional techniques. *J. Chromatogr. A 1325*, 195−203.

(31) Perevyazko, I., Trützschler, A.-K., Gubarev, A., Lebedeva, E., Traeger, A., Schubert, U. S., and Tsvetkov, N. (2017) Molecular and structural analysis via hydrodynamic methods: Cationic poly(2-aminoethyl-methacrylate)s. *Polymer 131*, 252−262.

(32) van de Wetering, P., Zuidam, N. J., van Steenbergen, M. J., van der Houwen, O. A. G. J., Underberg, W. J. M., and Hennink, W. E. (1998) A mechanistic study of the hydrolytic stability of poly(2-(dimethylamino)ethyl methacrylate). *Macromolecules 31*, 8063−8068.

(33) Chiriac, V., and Balea, G. (1997) Buffer index and buffer capacity for a simple buffer solution. *J. Chem. Educ. 74*, 937.

(34) Fischer, D., Li, Y., Ahlemeyer, B., Krieglstein, J., and Kissel, T. (2003) In vitro cytotoxicity testing of polycations: influence of polymer structure on cell viability and hemolysis. *Biomaterials 24*, 1121−1131.

(35) Kleinberger, R. M., Burke, N. A. D., Zhou, C., and Stöver, H. D. H. (2016) Synthetic polycations with controlled charge density and molecular weight as building blocks for biomaterials. *J. Biomater. Sci., Polym. Ed. 27*, 351−369.

(36) Lepecq, J. B., and Paoletti, C. (1967) A fluorescent complex between ethidium bromide and nucleic acids. *J. Mol. Biol. 27*, 87−106.

(37) Geall, A. J., and Blagbrough, I. S. (2000) Rapid and sensitive ethidium bromide fluorescence quenching assay of polyamine conjugate−DNA interactions for the analysis of lipoplex formation in gene therapy. *J. Pharm. Biomed. Anal. 22*, 849−859.

DOI: 10.1021/acs.bioconjchem.8b00074
Bioconjugate Chem. 2018, 29, 2181−2194

(38) Rinkenauer, A. C., Tauhardt, L., Wendler, F., Kempe, K., Gottschaldt, M., Traeger, A., and Schubert, U. S. (2015) A cationic poly(2-oxazoline) with high in vitro transfection efficiency identified by a library approach. *Macromol. Biosci. 15*, 414−425.
(39) You, Y.-Z., Manickam, D. S., Zhou, Q.-H., and Oupický, D. (2007) Reducible poly(2-dimethylaminoethyl methacrylate): Synthesis, cytotoxicity, and gene delivery activity. *J. Controlled Release 122*, 217−225.
(40) Agarwal, S., Zhang, Y., Maji, S., and Greiner, A. (2012) PDMAEMA based gene delivery materials. *Mater. Today 15*, 388−393.
(41) van de Wetering, P., Moret, E. E., Schuurmans-Nieuwenbroek, N. M. E., van Steenbergen, M. J., and Hennink, W. E. (1999) Structure−activity relationships of water-soluble cationic methacrylate/methacrylamide polymers for nonviral gene delivery. *Bioconjugate Chem. 10*, 589−597.
(42) Pezzoli, D., Giupponi, E., Mantovani, D., and Candiani, G. (2017) Size matters for in vitro gene delivery: investigating the relationships among complexation protocol, transfection medium, size and sedimentation. *Sci. Rep. 7*, 44134.
(43) Kwok, A., and Hart, S. L. (2011) Comparative structural and functional studies of nanoparticle formulations for DNA and siRNA delivery. *Nanomedicine 7*, 210−219.
(44) Jain, R., Dandekar, P., Loretz, B., Koch, M., and Lehr, C.-M. (2015) Dimethylaminoethyl methacrylate copolymer-siRNA nanoparticles for silencing a therapeutically relevant gene in macrophages. *MedChemComm 6*, 691−701.
(45) Xu, F. J., and Yang, W. T. (2011) Polymer vectors via controlled/living radical polymerization for gene delivery. *Prog. Polym. Sci. 36*, 1099−1131.
(46) Schallon, A., Jérôme, V., Walther, A., Synatschke, C. V., Müller, A. H. E., and Freitag, R. (2010) Performance of three PDMAEMA-based polycation architectures as gene delivery agents in comparison to linear and branched PEI. *React. Funct. Polym. 70*, 1−10.
(47) Cherng, J.-Y., van de Wetering, P., Talsma, H., Crommelin, D. J. A., and Hennink, W. E. (1996) Effect of size and serum proteins on transfection efficiency of poly ((2-dimethylamino)ethyl methacrylate)-plasmid nanoparticles. *Pharm. Res. 13*, 1038−1042.
(48) Ogris, M., Brunner, S., Schuller, S., Kircheis, R., and Wagner, E. (1999) PEGylated DNA/transferrin-PEI complexes: reduced interaction with blood components, extended circulation in blood and potential for systemic gene delivery. *Gene Ther. 6*, 595−605.
(49) Monopoli, M. P., Walczyk, D., Campbell, A., Elia, G., Lynch, I., Baldelli Bombelli, F., and Dawson, K. A. (2011) Physical−chemical aspects of protein corona: Relevance to in vitro and in vivo biological impacts of nanoparticles. *J. Am. Chem. Soc. 133*, 2525−2534.
(50) Ogris, M., Brunner, S., Schüller, S., Kircheis, R., and Wagner, E. (1999) PEGylated DNA/transferrin−PEI complexes: reduced interaction with blood components, extended circulation in blood and potential for systemic gene delivery. *Gene Ther. 6*, 595.
(51) Forrest, M. L., Meister, G. E., Koerber, J. T., and Pack, D. W. (2004) Partial acetylation of polyethylenimine enhances in vitro gene delivery. *Pharm. Res. 21*, 365−371.
(52) van de Wetering, P., Cherng, J.-Y., Talsma, H., and Hennink, W. E. (1997) Relation between transfection efficiency and cytotoxicity of poly(2-(dimethylamino)ethyl methacrylate)/plasmid complexes. *J. Controlled Release 49*, 59−69.
(53) Dubruel, P., Christiaens, B., Vanloo, B., Bracke, K., Rosseneu, M., Vandekerckhove, J., and Schacht, E. (2003) Physicochemical and biological evaluation of cationic polymethacrylates as vectors for gene delivery. *Eur. J. Pharm. Sci. 18*, 211−220.
(54) Jones, R. A., Poniris, M. H., and Wilson, M. R. (2004) pDMAEMA is internalised by endocytosis but does not physically disrupt endosomes. *J. Controlled Release 96*, 379−391.
(55) Forrest, M. L., and Pack, D. W. (2002) On the kinetics of polyplex endocytic trafficking: implications for gene delivery vector design. *Mol. Ther. 6*, 57−66.
(56) Kulkarni, R. P., Mishra, S., Fraser, S. E., and Davis, M. E. (2005) Single cell kinetics of intracellular, nonviral, nucleic acid delivery vehicle acidification and trafficking. *Bioconjugate Chem. 16*, 986−994.
(57) Vercauteren, D., Rejman, J., Martens, T. F., Demeester, J., De Smedt, S. C., and Braeckmans, K. (2012) On the cellular processing of non-viral nanomedicines for nucleic acid delivery: Mechanisms and methods. *J. Controlled Release 161*, 566−581.
(58) Rejman, J., Bragonzi, A., and Conese, M. (2005) Role of clathrin- and caveolae-mediated endocytosis in gene transfer mediated by lipo- and polyplexes. *Mol. Ther. 12*, 468−474.
(59) Bieber, T., Meissner, W., Kostin, S., Niemann, A., and Elsasser, H.-P. (2002) Intracellular route and transcriptional competence of polyethylenimine−DNA complexes. *J. Controlled Release 82*, 441−454.
(60) Rehman, Z. U., Hoekstra, D., and Zuhorn, I. S. (2013) Mechanism of polyplex- and lipoplex-mediated delivery of nucleic acids: Real-time visualization of transient membrane destabilization without endosomal lysis. *ACS Nano 7*, 3767−3777.
(61) Bonner, D. K., Leung, C., Chen-Liang, J., Chingozha, L., Langer, R., and Hammond, P. T. (2011) Intracellular trafficking of polyamidoamine−poly(ethylene glycol) block copolymers in DNA delivery. *Bioconjugate Chem. 22*, 1519−1525.
(62) Salomone, F., Cardarelli, F., Di Luca, M., Boccardi, C., Nifosì, R., Bardi, G., Di Bari, L., Serresi, M., and Beltram, F. (2012) A novel chimeric cell-penetrating peptide with membrane-disruptive properties for efficient endosomal escape. *J. Controlled Release 163*, 293−303.
(63) Reifarth, M., Hoeppener, S., and Schubert, U. S. (2018) Uptake and intracellular fate of engineered nanoparticles in mammalian cells: Capabilities and limitations of transmission electron microscopy—polymer-based nanoparticles. *Adv. Mater. 30*, 1703704.
(64) Bus, T., Englert, C., Reifarth, M., Borchers, P., Hartlieb, M., Vollrath, A., Hoeppener, S., Traeger, A., and Schubert, U. S. (2017) 3rd generation poly(ethylene imine)s for gene delivery. *J. Mater. Chem. B 5*, 1258−1274.
(65) Palermo, E. F., Sovadinova, I., and Kuroda, K. (2009) Structural determinants of antimicrobial activity and biocompatibility in membrane-disrupting methacrylamide random copolymers. *Biomacromolecules 10*, 3098−3107.
(66) Vaidyanathan, S., Chen, J., Orr, B. G., and Banaszak Holl, M. M. (2016) Cationic polymer intercalation into the lipid membrane enables intact polyplex DNA escape from endosomes for gene delivery. *Mol. Pharmaceutics 13*, 1967−1978.
(67) Vaidyanathan, S., Anderson, K. B., Merzel, R. L., Jacobovitz, B., Kaushik, M. P., Kelly, C. N., van Dongen, M. A., Dougherty, C. A., Orr, B. G., and Banaszak Holl, M. M. (2015) Quantitative measurement of cationic polymer vector and polymer-pDNA polyplex intercalation into the cell plasma membrane. *ACS Nano 9*, 6097−109.

DOI: 10.1021/acs.bioconjchem.8b00074
Bioconjugate Chem. 2018, 29, 2181−2194

SUPPORTING INFORMATION

Beyond Gene Transfection with Methacrylate-based Polyplexes – The Influence of the Amino Substitution Pattern

Anne-Kristin Trützschler,[‡,§,†] Tanja Bus[‡,§,†] Martin Reifarth,[‡,§,#,$] Johannes C. Brendel,[‡,§] Stephanie Hoeppener,[‡,§] Anja Traeger,[‡,§,] Ulrich S. Schubert[‡,§,*]*

[‡] *Laboratory of Organic and Macromolecular Chemistry (IOMC), Friedrich Schiller University Jena, Humboldtstrasse 10, 07743 Jena, Germany*

[§] *Jena Center for Soft Matter (JCSM), Friedrich Schiller University Jena, Philosophenweg 7, 07743 Jena, Germany*

[#] *Institute of Physical Chemistry and Abbe Center of Photonics, Friedrich Schiller University Jena, Helmholtzweg 4, 07743 Jena, Germany*

[$] *Leibniz Institute of Photonic Technology, Albert-Einstein-Strasse 9, 07745 Jena, Germany*

[†] *The authors contributed equally to this work*

Email: ulrich.schubert@uni-jena.de, anja.traeger@uni-jena.de

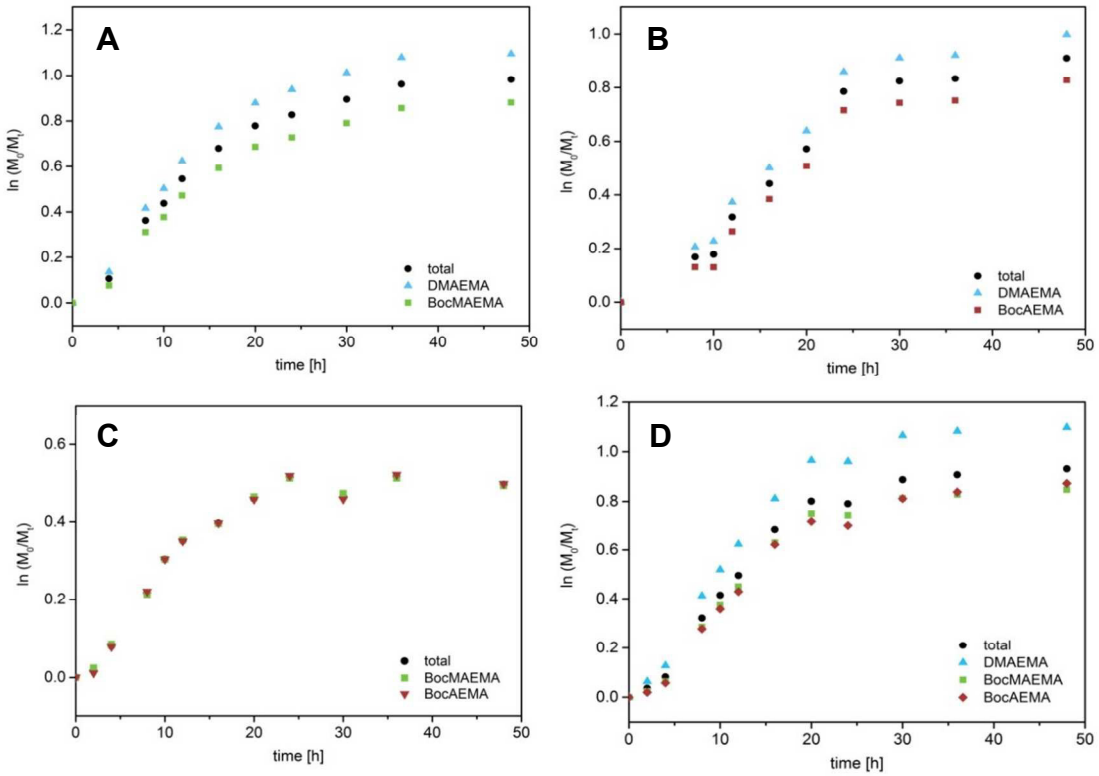

Figure S1. Kinetic plot of ln (M0/Mt) over time for the Boc protected copolymers **PDM** (A), **PDA** (B), **PMA** (C), **PDMA** (D).

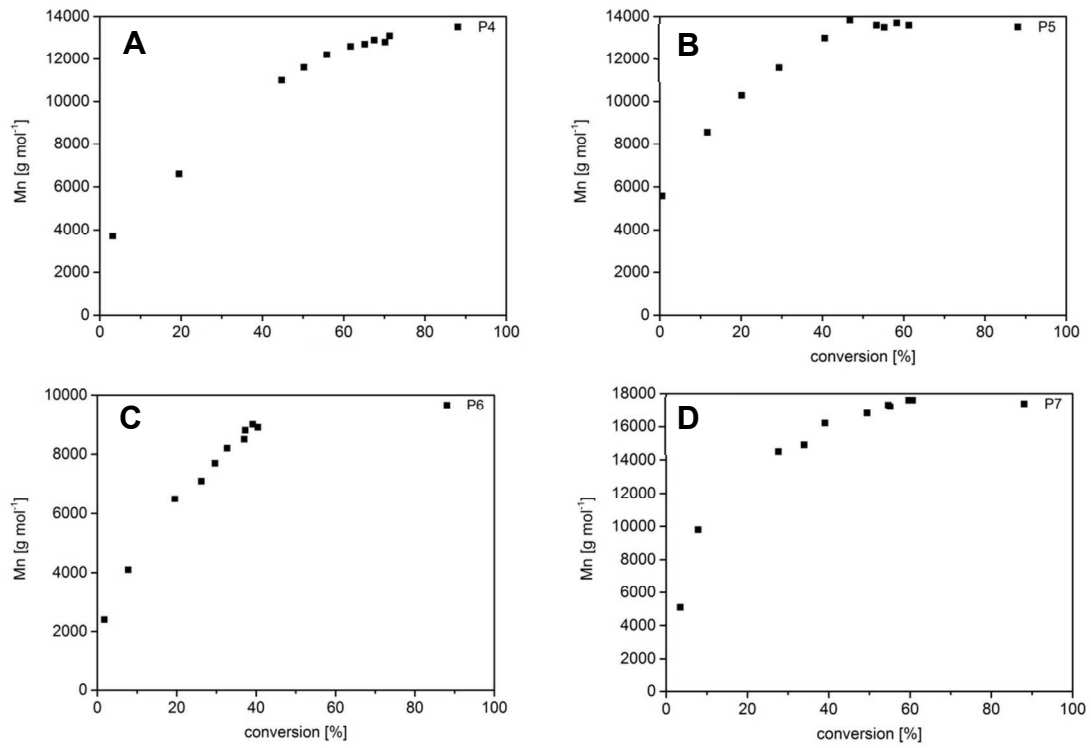

Figure S2. Kinetic plot of the molar mass over the conversion of **PDM** (A), **PDA** (B), **PMA** (C) and **PDMA** (D).

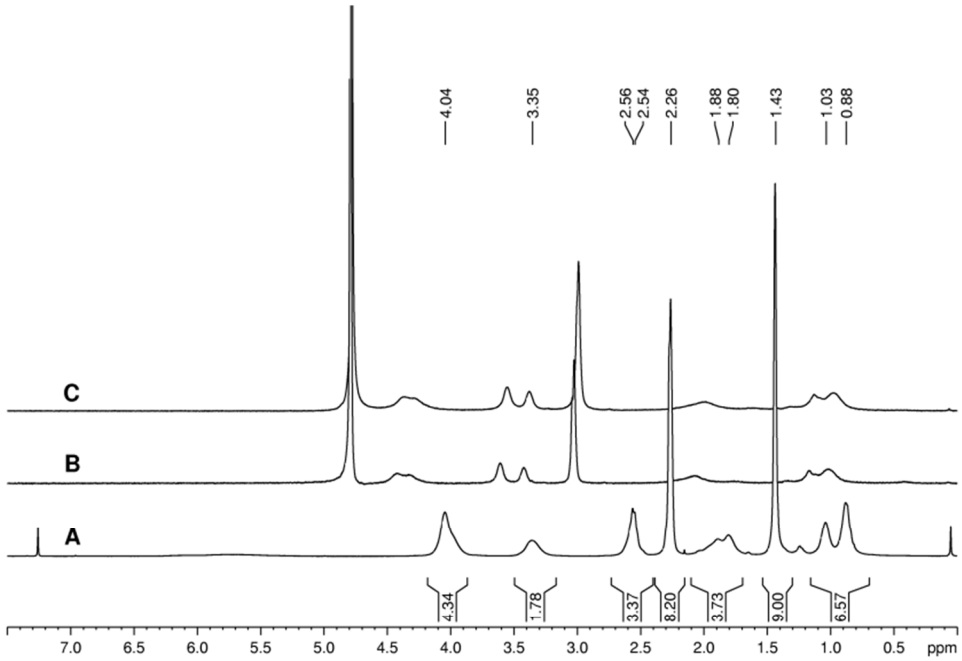

Figure S3. (A) ^{1}H-NMR spectra of the Boc-protected of **PDA** in $CDCl_3$, **(B)** ^{1}H-NMR spectra deprotection of **PDA** with trifluoroacetic acid in D_2O, **(C)** ^{1}H-NMR spectra deprotection of **PDA** with 1M HCl in methanol in D_2O.

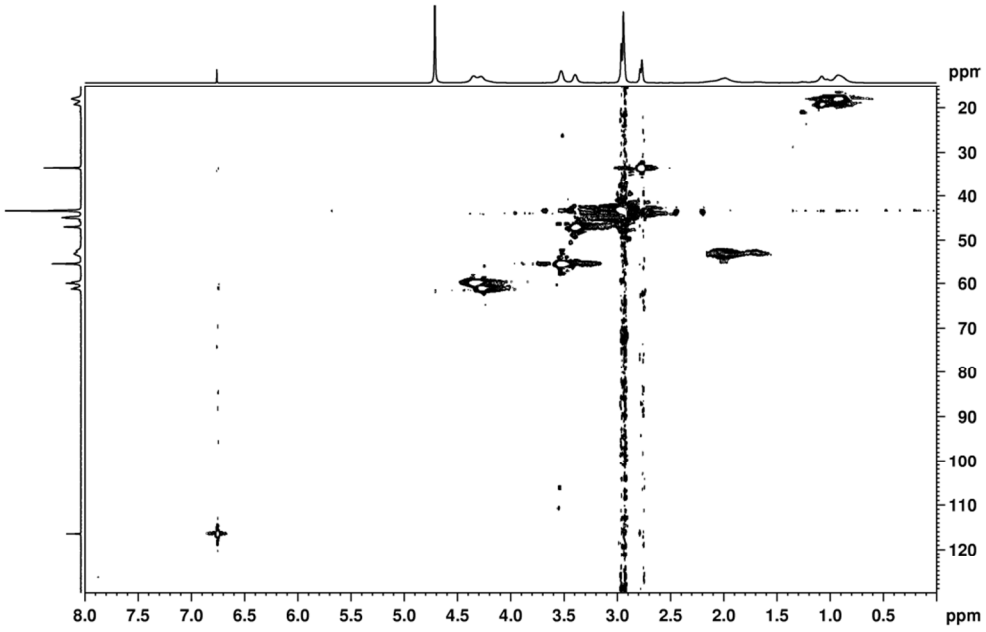

Figure S4. HSQC-NMR of **PDM** (100 mg) showing no methyl signals of the corresponding Boc-protection group. Spectrum on to ^{1}H-NMR, spectrum left ^{13}C-NMR in D_2O.

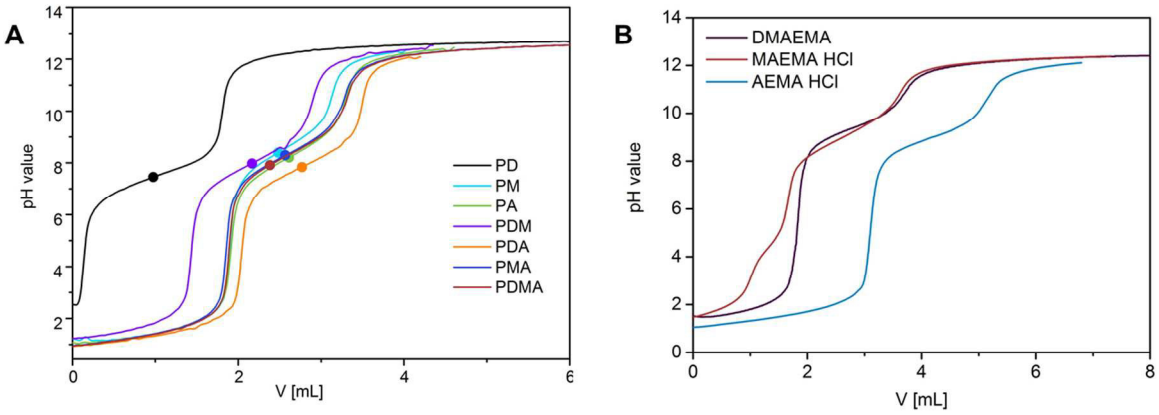

Figure S5: Titration curves of the deprotected polymer library 10 mg mL^{-1} in 150 mM NaCl in water **(A)**, methacrylate monomers DMAEMA, AEMA and MAEMA 10 mg mL^{-1} in pure water **(B)**, the calculated pK_as are shown in bold dots.

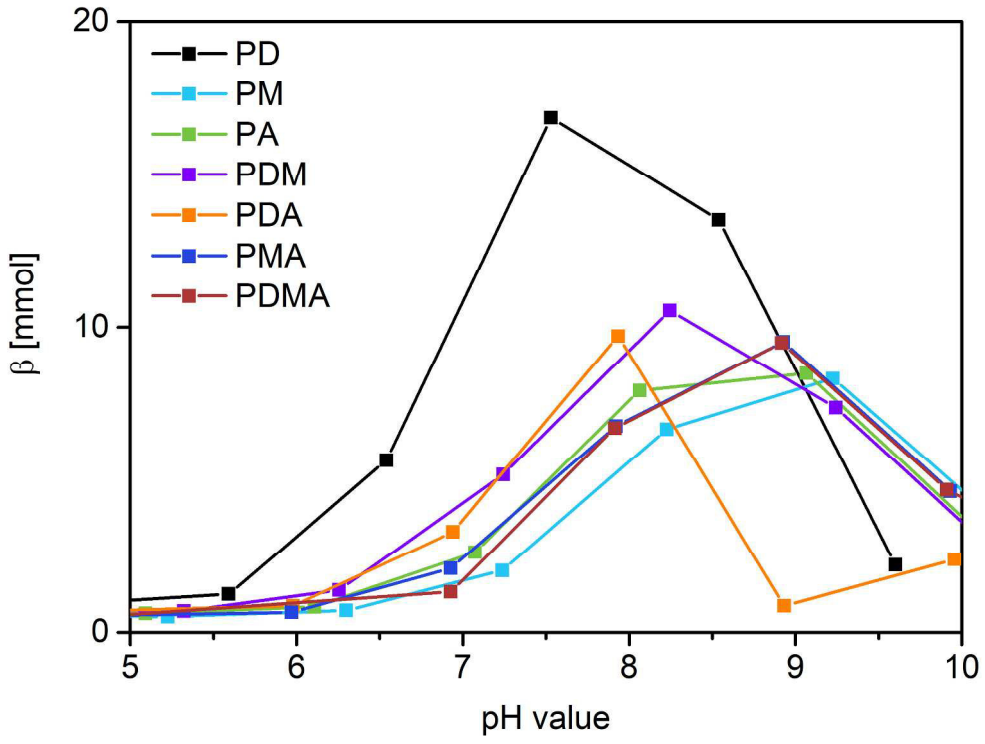

Figure S6. Buffer capacity of the deprotected polymer library calculated with equation (1) from titration over the pH range. **PMA** (dark blue) and **PDMA** (red) are strongly overlapping. Connecting lines do not represent actual data points; for visual support.

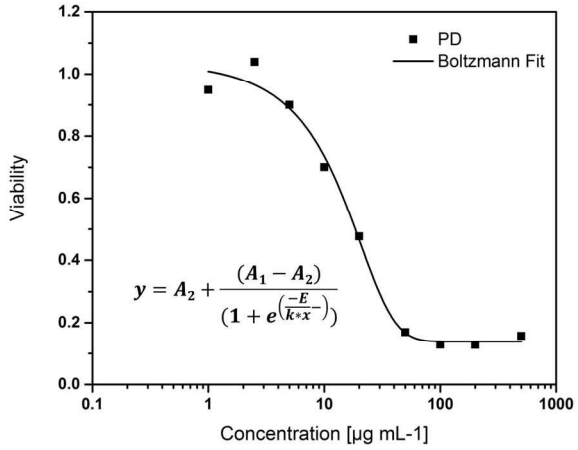

Figure S7. Example of dose-response curves of L929 mouse fibroblasts after polymer treatment for 24 h with **PD**. CC_{50} values were calculated with Origin software (Botzman fit) from cytotoxicity data.

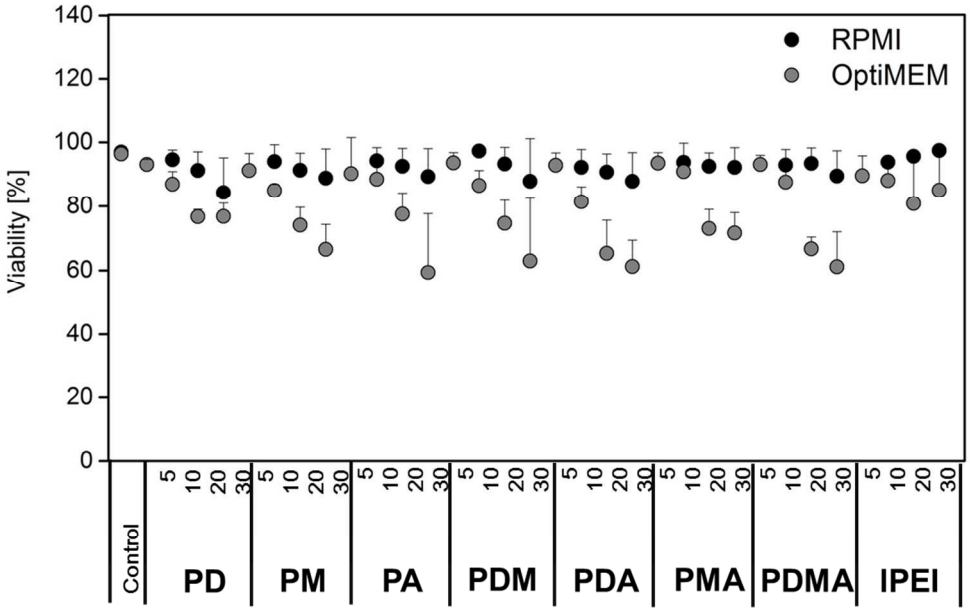

Figure S8. Viability data of the corresponding transfection experiments (Figure 5) using polymethacrylate library at various N/P ratios. Cell viability was determined by propidium iodide staining and flow cytometry. Values represent the mean ± S.D. (n=3).

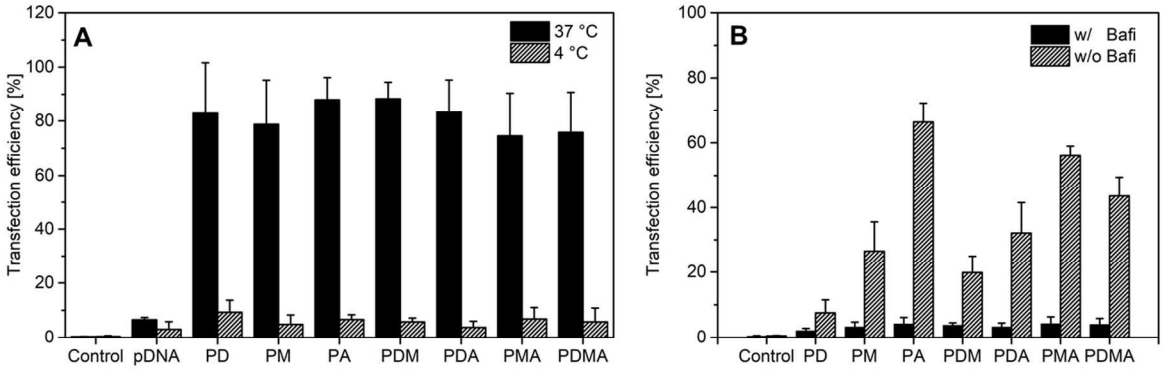

Figure S9. (A) Energy-dependent uptake study on HEK-293 cells. Amount of cells [%], which internalized polyplexes (**PD** to **PDMA**) with YOYO-1 labeled pDNA after 4 h at 37 °C and 4 °C. **(B)** Transfection efficiency of **PD** to **PDMA** (N/P 20) after treatment with bafilomycin (proton pump inhibitor). Cells were analyzed 24 h post-transfection. Values represent the mean ± S.D. (n=3).

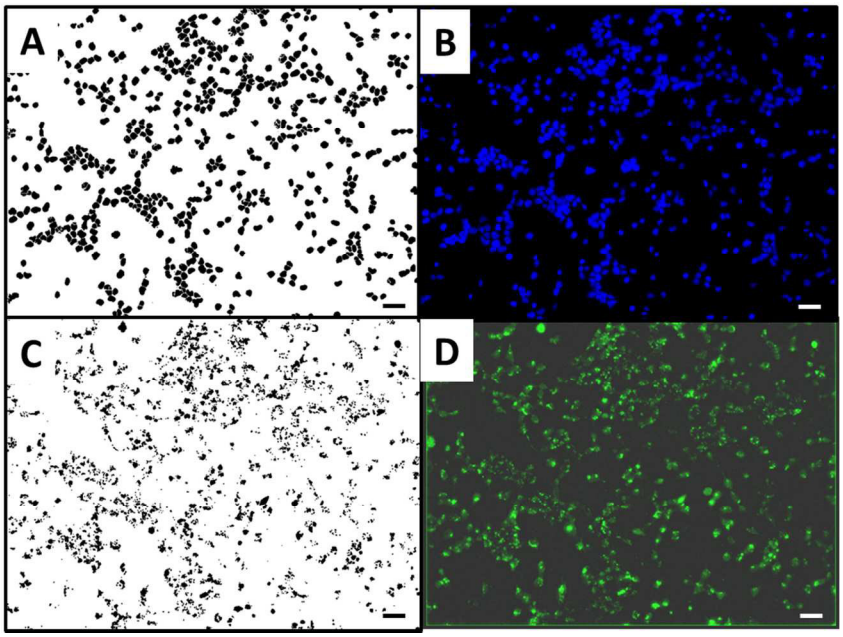

Figure S10. Fluorescence image of HEK-293 cells treated with **PMA** in the calcein quenching assay (see experimental part). **(A)** and **(C)** ImageJ processed images for nucleus count and fluorescence area determination. **(B)** and **(D)** fluorescence images stained with Hoechst or calcein at corresponding wavelength (Hoechst 33342: Ex 405 nm/BP 435-490 nm; Calcein: Ex 458 nm/BP 510-550 nm) after background correction. Scale bar black or white corresponds to 50µm.

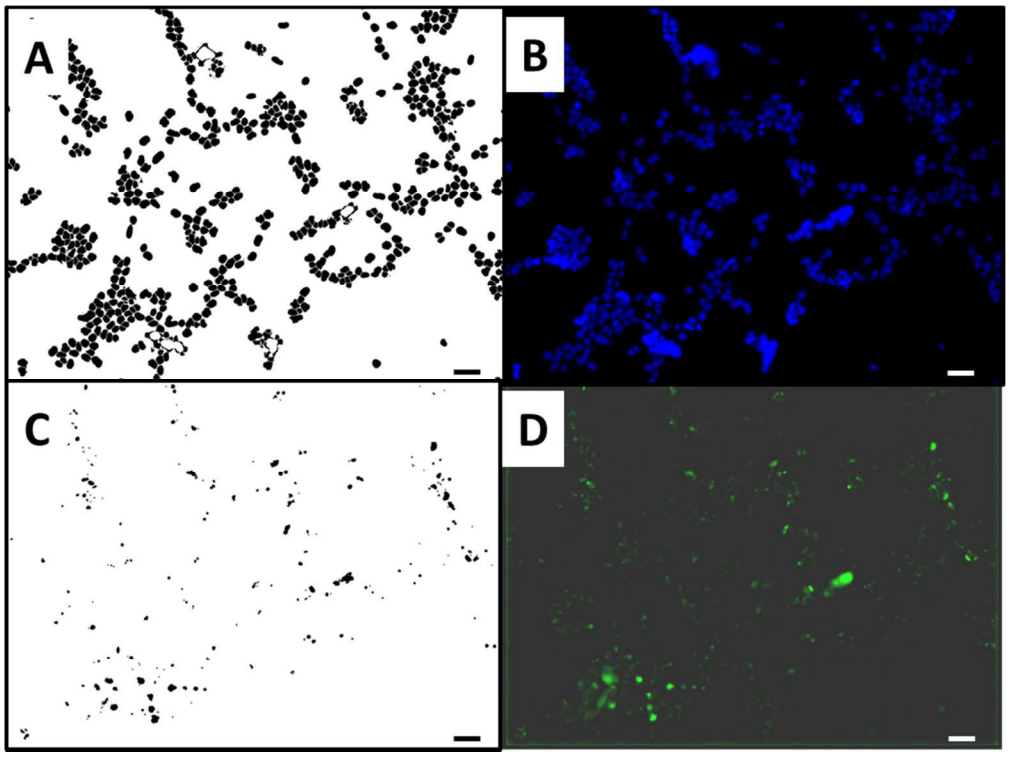

Figure S11. Fluorescence image of HEK-293 cells treated only with calcein serving as control in the calcein quenching assay (see experimental part). **(A)** and **(C)** ImageJ processed images for nucleus count and fluorescence area determination. **(B)** and **(D)** fluorescence images stained with Hoechst or calcein at corresponding wavelength (Hoechst 33342: Ex 405 nm/BP 435-490 nm; Calcein: Ex 458 nm/BP 510-550 nm) after background correction. Scale bar black or white corresponds to 50µm.

Publication Pub3

The power of shielding: Low toxicity and high transfection performance of cationic graft copolymers containing poly(2-oxazoline) side chains

A.-K. Trützschler, T. Bus, M. Sahn, A. Traeger, C. Weber, U. S. Schubert

Biomacromolecules **2018**, *19*, 2759-2771.

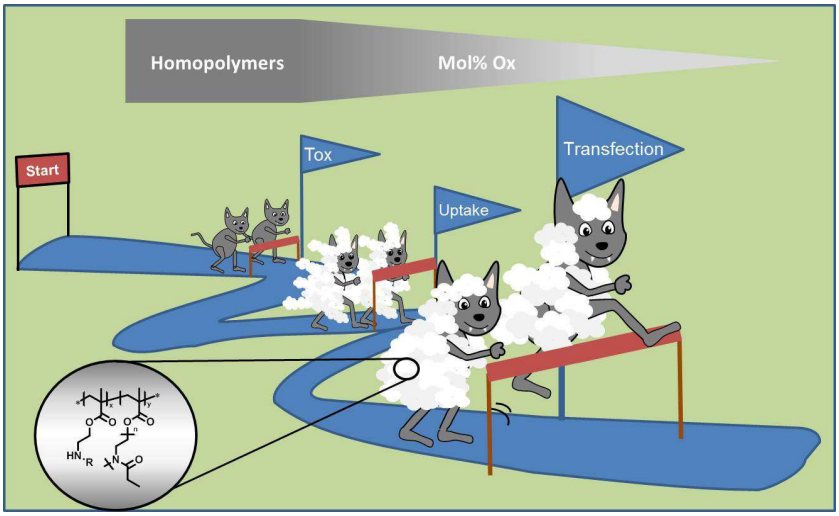

Biomacromolecules

Article

Cite This: Biomacromolecules 2018, 19, 2759−2771

pubs.acs.org/Biomac

The Power of Shielding: Low Toxicity and High Transfection Performance of Cationic Graft Copolymers Containing Poly(2-oxazoline) Side Chains

Anne-Kristin Trützschler,[†,‡] Tanja Bus,[†,‡] Martin Sahn,[†,‡] Anja Traeger,[†,‡] Christine Weber,[†,‡] and Ulrich S. Schubert*[,†,‡]

[†]Laboratory of Organic and Macromolecular Chemistry (IOMC), Friedrich Schiller University Jena, Humboldtstrasse 10, 07743 Jena, Germany

[‡]Jena Center for Soft Matter (JCSM), Friedrich Schiller University Jena, Philosophenweg 7, 07743 Jena, Germany

Supporting Information

ABSTRACT: We show the potential of oligo(2-ethyl-2-oxazoline) (Ox_n)-shielded graft copolymers of (2-aminoethyl)-methacrylate and *N*-methyl-(2-aminoethyl)-methacrylate for pDNA delivery in HEK cells. For the effect of grafting density and side chain length concerning improved transfection properties through the concept of shielding to be investigated, copolymers were synthesized via the macromonomer method using a combination of cationic ring opening polymerization and reversible addition−fragmentation chain transfer polymerization to vary the degree of grafting (DG = 10 and 30%) as well as the side chain degree of polymerization (DP = 5 and 20). Investigations of the polyplex formation, in vitro flow cytometry, and confocal laser scanning microscopy measurements on the copolymer library revealed classical shielding properties of the Ox side chains, including highly reduced cytotoxicity and a partial decrease in transfection efficiency, as also reported for polyethylene glycol shielding. In terms of the transfection efficiency, the best performing copolymers (**A-*g*-Ox$_5$(10)** and **M-*g*-Ox$_5$(10)**) revealed equal or better performances compared to those of the corresponding homopolymers. In particular, the graft copolymers with low DG and side chain DP transfected well with over 10-fold higher IC_{50} values. In contrast, a DG of 30% resulted in a loss of transfection efficiency due to missing ability for endosomal release, and a side chain DP of 20 hampered the cellular uptake.

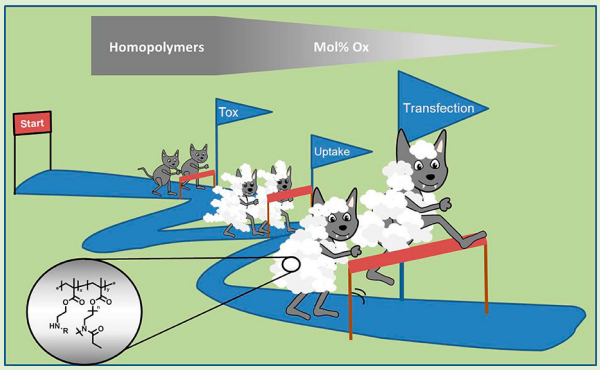

INTRODUCTION

Vectors for gene delivery can be divided into two major groups: viral and nonviral carrier systems. Even though the most efficient vectors are still viral vectors, their small size prohibits the use of large genetic material. In addition, safety issues cannot be neglected due to the use of recombinant viruses.[1] The group of nonviral vectors includes liposomes as well as natural and synthetic polymers. Advantages of polymeric carriers comprise tailored variation in size and structure, low immunologic interaction, and straightforward upscaling possibilities.[2] However, nonviral systems still reveal lower transfection efficiencies in comparison to viruses. Despite their fundamentally different structures, liposomes and cationic polymers have to overcome the same obstacles of transfection: (1) reversible binding of genetic material, (2) intracellular uptake across the cell membrane into endosomes, and (3) the endosomal escape and release of the nucleic acids.[2,3]

Polymeric carrier systems often consist of cationically charged monomers providing the possibility to complex the anionically charged genetic material (e.g., pDNA, siRNA).[2] In addition, cationically charged moieties enable an electrostatic interaction with the partially anionically charged cell membranes.[4,5] This interaction enables the polymers to enter eukaryotic cells via endocytosis and might also be beneficial for escape from the formed endosomes. Different theories regarding the endosomal escape of cationic polymers were hypothesized. The proton sponge effect is one theory, explaining the escape by a burst of the endosome due to osmotic pressure.[6] However, vectors with a high buffer capacity do not always feature enhanced transfection performance.[7,8]

An intercalation of the polymer into the membrane could provide an alternative explanation: Channels may be formed in the endosomal membrane through which the genetic material or the polyplex can escape the endosome.[9,10] This theory is supported by in-depth investigations using disruptive peptides, highly cationic charged poly(amidoamine) (PAMAM) dendrimers, and poly(allyl ammonium) derivatives.[8,9,11]

Received: March 1, 2018
Revised: May 14, 2018
Published: May 23, 2018

DOI: 10.1021/acs.biomac.8b00362
Biomacromolecules 2018, 19, 2759−2771

Scheme 1. Schematic Representation of the RAFT Copolymerization of the Boc-Protected Monomers BocA and BocM with the OEtOxMA Macromonomers Ox_5 (DP = 5) and Ox_{20} (DP = 20) to Obtain the Boc-Protected Graft Copolymers BocA-*g*-$Ox_{5/20}$(10/30) and BocM-*g*-$Ox_{5/20}$(10/30), Respectively, and Subsequent Deprotection Yielded the Graft Copolymers with a Cationic Backbone A-*g*-$Ox_{5/20}$(10/30) and M-*g*-$Ox_{5/20}$(10/30)[a]

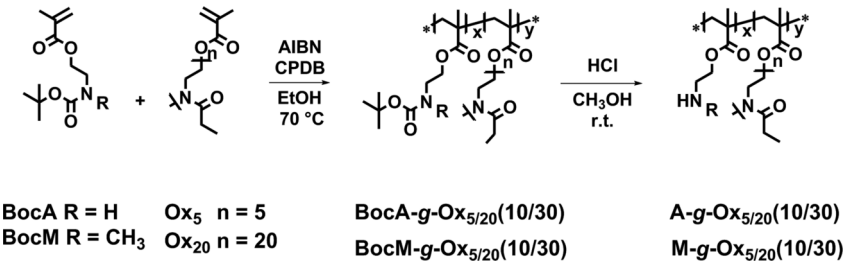

[a]Numbers in brackets indicate the degree of grafting, i.e., 10 or 30, respectively.

Polymethacrylates containing tertiary amines have been used for gene delivery since 1996.[12] Despite relatively low transfection performance, poly(2-(*N*,*N*-dimethylamino)ethyl methacrylate (PDMAEMA) represents the most common polymer in this respect. The replacement of DMAEMA by *N*-methyl-(2-aminoethyl)-methacrylate (MAEMA) or (2-aminoethyl)-methacrylate (AEMA) resulted in higher transfection efficiencies but also higher toxicities of the polymers.[13,14] Despite the latter, PAEMA revealed excellent performance for luciferase expression, as reported by Ming et al. in 2010.[15] Recently, our group investigated the delivery performance of homo- and statistical copolymers of all three monomers, demonstrating the essential need for primary and secondary amines for sufficient transfection performance.[16]

In general, the fine balance between cytotoxicity and transfection efficiency still remains a critical obstacle for the application of densely charged polymers for transfection processes. For all homopolymers bearing primary and secondary amines (such as PAEMA and PMAEMA), high transfection efficiencies are accompanied by high toxicity on eukaryotic cells.[17] The ability to permeate cellular membranes is closely connected to the toxic effects from membrane disruption.[18] The incorporation of glucopyranose into PAEMA- and PMAEMA-based polymers resulted in lowered toxicity maintaining reasonable transfection efficiencies, as reported by Reineke et al.[13,19]

Shielding with neutral polymers such as poly(ethylene glycol) (PEG) is a more classical approach.[20] The polymer decreases the surface charges and sterically hinders access to the functional groups. In turn, this results in a reduction of cytotoxicity, lower aggregation rates, reduced unspecific interaction with phagocytes, and a high circulation time in vivo.[20] For this reason, PEG is well approved, applied in several drugs as well as transfection vectors, and included in FDA approvals.[21,22] However, a reduced transfection efficiency is observed for shielded gene carriers compared to unshielded ones as a side effect.[22] For instance, PDMAEMA-*g*-PEG did not efficiently transfect for a degree of grafting (DG) higher than 30%.[23] For ABA block copolymers, a minimum degree of polymerization (DP) was beneficial (110 for PDAEMA and 15 for the PEG blocks).[24] An increasing number of patients showing immunological response to PEG has driven the search for alternative shielding polymers.[25,26] Since the 1980s, the number of untreated patients expressing anti-PEG antibodies has increased from 0.2 to 25% in 2008.[25,27] This results in earlier blood clearance due to the immune system, thereby obliterating PEG's benefits such as prolonged circulation time.[28]

Hydrophilic poly(2-oxazoline)s (POx) represent an alternative for PEG that has come into focus lately.[29,30] In particular, poly(2-ethyl-2-oxazoline)s (PEtOx) feature a high biocompatibility (up to 20 g L^{-1} in vitro and up to 2 g kg^{-1} in rats).[31] POx can be synthesized by living cationic ring-opening polymerization (CROP), providing a multitude of possibilities for obtaining building blocks suitable for incorporation into polymeric gene vectors.[32] In 2014, Correia et al. combined PEtOx with poly(D,L-lactic acid) and polyethylene imine (PEI) to form micelles for microcircle DNA delivery, representing an exemplary use of the shielding properties of PEtOx for linear polymeric vectors.[33,34] In 2011, Erlach et al. showed a strong dependency of the transfection efficiency on the DG and DP of shielding side chains for graft copolymers with a poly(L-lysine) backbone, which were synthesized via a grafting-onto approach.[35,23]

In particular, POx macromonomers with a methacrylate functionality represent valuable components for the design of cationic polymers synthesized by reversible addition−fragmentation chain transfer (RAFT) polymerization.[36] The macromonomers offer the opportunity to incorporate shielding moieties into cationic vectors to potentially improve viability as well as transfection efficiency. In this study, we exploit a library of graft copolymers for pDNA delivery. For this purpose, the primary and secondary amino group bearing monomers AEMA and MAEMA were copolymerized with PEtOx-based macromonomers via RAFT polymerization to shield the cationic graft copolymer backbone (Scheme 1). For the optimum copolymer composition to be identified, the side chain DP was varied, and DG values from 10 to 30% were targeted. In comparison with the PAEMA and PMAEMA homopolymers, the masking regarding biocompatibility and transfection was investigated in vitro supported by means of flow cytometry and CLSM measurements on HEK cells.

EXPERIMENTAL SECTION

Materials. Unless stated otherwise, all chemicals were used without further purification and purchased from standard suppliers. Methacryloyl chloride, anhydrous triethylamine (NEt_3), 2-cyano-2-propyl benzodithioate (CPDB), neutral aluminum oxide, and 2-(methylamino)ethanol were purchased from Sigma-Aldrich. Di-*tert*-butyldicarbonate was obtained from Alfa Aesar, and 2-aminoethanol was purchased from TCI. 2,2′-Azobis(2-methylpropionitrile) (AIBN) was received from Acros and recrystallized from methanol prior to use. 2-Ethyl-2-oxazoline (EtOx, Acros Organics) and methyl *p*-toluenesulfonate (MeOTs, Sigma-Aldrich) were dried over barium oxide, distilled, and stored under an argon atmosphere. Acetonitrile (ACN, Sigma-Aldrich) was dried in a solvent purification system (Pure Solv EN,

DOI: 10.1021/acs.biomac.8b00362
Biomacromolecules 2018, 19, 2759−2771

InnovativeTechnology) before used as a polymerization solvent. Hydrochloric acid (HCl), *N,N*-dimethylformamide (DMF), and tetrahydrofuran (THF) were purchased from VWR Chemicals. Linear poly(ethylene imine) (lPEI, 25 kDa) and branched PEI (bPEI, 25 kDa) were obtained from Polysciences. Ethidium bromide solution (1%, 10 mg mL^{-1}) was purchased from Carl Roth (Karlsruhe, Germany). AlamarBlue, YOYO-1 iodide, Hoechst 33342 (10 mg mL^{-1} solution) as well as LysoTracker Red DND-99 were obtained from Life Technologies (Thermo Fisher, Germany). If not stated otherwise, cell culture media and supplements (antibiotics) were obtained from Biochrom (Merck Millipore, Germany) and Thermo Fischer (Germany). Plasmid pEGFP-N1 (4.7 kb, Clontech, USA) encoding green fluorescent protein (EGFP) was isolated with the Giga Plasmid Kit provided by Qiagen (Hilden, Germany).

Instruments. The polymerization of EtOx was performed in a Biotage Initiator Sixty microwave synthesizer.

NMR spectra were recorded on a Bruker AC 300 MHz or on a Bruker AC 250 MHz spectrometer in $CDCl_3$ or D_2O at room temperature.

Size exclusion chromatography (SEC) was measured on an Agilent 1200 series system equipped with a PSS degasser, a G1310A pump, a G1362A refractive index detector, and a PSS GRAM guard/30/10 Å column series running with *N,N*-dimethylacetamide (DMAc) with 0.21% of lithium chloride. The Techlab oven was set to 50 °C, and the molar masses were calculated using a poly(methyl methacrylate) (PMMA) standard (505−981,000 g mol^{-1}). For the water-soluble polymers, a Jasco SEC system was used comprising a DG-980-50 degasser, a PU-980 pump, a RI-930 RI detector, and a column oven set to 50 °C. The system was equipped with AppliChrom ABOA CatPhil guard/200/350 Å column set and run with an aqueous eluent containing 0.1% trifluoroacetic acid and 0.1 M NaCl. Poly(2-vinylpyridine) (P2VP) (1,300−81,000 g mol^{-1}) calibration was used for the graft copolymers. The PAEMA and PMAEMA homopolymers were analyzed using dextran calibration (180−277,000 g mol^{-1}) as previously published.[16] The macromonomers were analyzed on a Shimadzu SEC system equipped with an SCL-10A VP system controller, a LC-10AD VP pump, and an RID-10A refractive index detector using a solvent mixture containing chloroform, triethylamine, and isopropanol (94:4:2) at a flow rate of 1 mL min^{-1} on a PSS-SDV-linear S 5 μm column (PSS GmbH Mainz, Germany) at 40 °C. The system was calibrated with polystyrene standards (370−128,000 g mol^{-1}).

Batch dynamic light scattering (DLS) was performed on a Zetasizer Nano ZS (Malvern Instruments, Herrenberg, Germany). All measurements were performed in folded capillary cells (DTS1070, Malvern Instruments, Herrenberg, Germany). After an equilibration time of 120 s, 3 × 15 s runs were carried out at 25 °C (λ_{Ex} = 633 nm). Scattered light was detected at an angle of 173°. Each measurement was performed in triplicate. Electrophoretic light scattering (ELS) was used to measure the zeta potential (ζ). The measurement was also performed on the Zetasizer Nano ZS by applying laser Doppler velocimetry. For each measurement, 3 runs were carried out using the slow-field reversal and the fast-field reversal mode at 150 V. Each experiment was performed in triplicate at 25 °C. The zeta potential was calculated from the electrophoretic mobility (l) according to the Henry equation. Henry coefficients f(ka) were calculated according to Ohshima.[37]

Titration. The titration for the determination of the pK_a values of the polymers was performed with an automated titrator 765 Dosimat (Metrohm, Herisau, Swiss) and a pH detector GMH3530 (GHM Messtechnik GmbH Standort Greisinger, Regenstauf, Germany). For a typical measurement, the polymer in ultrapure water (10 mg mL^{-1}) was acidified by addition of 10 μL of 6 M hydrochloric acid and stirred while titrated against a 0.1 M sodium hydroxide solution (0.1 mL min^{-1}) to a pH value of 12. The titration curves were analyzed via an FTT fit using a 20 points smoothing. The pK_a values were estimated using the Henderson−Hasselbalch equation (eq 1) by determining the equivalence point from the titration diagram.

$$\mathrm{pH} = \mathrm{p}K_a + \log \frac{[A^-]}{[HA]} \quad (1)$$

Monomer Synthesis. *N-tert-Butyloxycarbonyl-(2-aminoethyl)-methacrylate (BocAEMA, BocA).* BocAEMA was synthesized according to a procedure by Kuroda et al.[38] Ten grams (0.162 mol) of 2-aminoethanol was dissolved in 120 mL of THF and 200 mL of a 1 M sodium hydroxide solution were added. Then, 35.28 g (0.162 mol) of di-*tert*-butyldicarbonate in 80 mL of THF was added dropwise while cooling the reaction mixture in an ice bath. Subsequent to stirring overnight at room temperature, the mixture was diluted with ethyl acetate and washed with water, aqueous sodium bicarbonate solution, and brine. The aqueous phase was re-extracted with ethyl acetate and dried over sodium sulfate, and the solvent was removed under reduced pressure. Without further purification, 18.5 g (0.114 mol) of *N-tert*-butyloxycarbonyl-2-aminoethanol was diluted with 30 mL of dry dichloromethane under Schlenk conditions, and 22.6 mL (0.167 mol) of dry NEt_3 was added while cooling the mixture in an ice bath. Fifteen milliliters (0.155 mol) of methacryloyl chloride was added dropwise, and the reaction was stirred overnight. The mixture was washed with water, brine, and aqueous sodium bicarbonate solution and dried over sodium sulfate. The crude off white product was finally recrystallized from *n*-hexane.

^{1}H NMR (300 MHz, $CDCl_3$): δ [ppm] 1.42 (*s*, 9H), 1.93 (*s*, 3H), 3.43 (*m*, 2H), 4.18 (*t*, J^2= 5.33 Hz 2H), 4.8 (br. *s*, 1H), 5.57 (*s*, 1H), 6.10 (*s*, 1H). ^{13}C NMR (75 MHz, $CDCl_3$): δ [ppm] 18.2 (CH_3), 28.3 (CH_3), 39.6 (CH_2), 63.9 (CH_2), 79.5 (CH_2), 125.8 (C_{quart}), 136.0 (C_{quart}), 155.7 (C_{quart}), 167.2 (C_{quart}). Yield: 60%, 15.67 g.

N-Methyl-N-tert-butyloxycarbonyl-(2-aminoethyl)-methacrylate (BocMAEMA, BocM). BocMAEMA was synthesized according to a procedure by Sinclair et al.[39] Ten grams (0.133 mol) of *N*-methylaminoethanol was dissolved in 80 mL of chloroform and cooled in an ice bath. Twenty-nine grams (0.113 mol) of di-*tert*-butylcarbonate in 80 mL of chloroform was added dropwise and stirred at room temperature for 1 h. The solvent was removed under reduced pressure, and the mixture was purified by distillation (30 mbar, 180 °C). Under Schlenk conditions, 21.4 g (0.122 mol) of *N*-methyl-*N-tert*-butyloxycarbonyl-2-aminoethanol was diluted in 100 mL of dry dichloromethane. Then, 49.4 mL (0.366 mol) of triethylamine was added, and the reaction mixture was cooled in an ice bath. Then, 17.7 mL (0.183 mol) of methacryloyl chloride in 100 mL of dichloromethane was added dropwise. Subsequent to stirring at room temperature overnight, the mixture was washed with water as well as brine and dried over sodium sulfate. Further purification was performed by column chromatography using a mixture of cyclohexane and ethyl acetate (9:1−3:1; v/v, R_f = 0.18, 10:1).

^{1}H NMR (300 MHz, $CDCl_3$): δ [ppm] 1.96 (*s*, 9H), 2.76 (*m*, 3H), 3.30 (*m*, 2H), 4.56 (*m*, 2H), 5.65 (*s*, 1H), 6.30 (*s*, 1H). ^{13}C NMR (75 MHz, $CDCl_3$): δ [ppm] 18.2 (CH_3), 28.3 (CH_3), 35.2 (CH_2), 47.9 (CH_3), 62.7 (CH_2), 79.7 (CH_2), 126.0 (C_{quart}), 136.1 (C_{quart}), 155.8 (C_{quart}), 167.1 (C_{quart}). Yield: 77%, 22.84 g.

Oligo(2-ethyl-2-oxazoline)methacrylate. The oligo(2-ethyl-2-oxazoline) methacrylates $\mathbf{Ox_5}$ and $\mathbf{Ox_{20}}$ were synthesized as described in the literature.[40]

According to a [M]/[I] of 20 for $\mathbf{Ox_{20}}$ and an initial monomer concentration of 4 mol L^{-1}, 0.559 g (3 mmol) of MeTos, 5.954 g (60 mmol) of EtOx, and 9 mL of acetonitrile were transferred to a predried microwave vial under an argon atmosphere. The closed vial was transferred to the autosampler of the microwave. After a prestirring period of 30 s, the solution was heated to a temperature of 140 °C for 2 min. The reaction vessel was cooled to room temperature by pressurized air. The living polymer chains were quenched by addition of 0.34 mL (4.5 mmol) of methacrylic acid and 0.84 mL (6 mmol) of NEt_3. The reaction solution was heated at 50 °C for 20 h. After cooling to room temperature, 300 mL of dichloromethane was added. The organic phase was washed with saturated aqueous sodium bicarbonate solution and brine. The organic layers were dried over sodium sulfate and filtered, and the solvent was evaporated under reduced pressure ($T \leq 26$ °C).

The degree of polymerization was calculated from ^{1}H NMR spectroscopy by comparison of the proton signal of the initiating methyl group at 2.95 to 3.05 ppm to the backbone signal from 3.51 to 4.28 ppm (see Figure S1) and the dispersity was determined via SEC (see Figure S2) using polystyrene calibration.

The resulting polymers were stored at −18 °C.

DOI: 10.1021/acs.biomac.8b00362
Biomacromolecules 2018, 19, 2759−2771

Table 1. Synthesis and Characterization Data of the Boc-Protected Graft Copolymers BocA-*g*-Ox$_{5/20}$(10/30) and BocM-*g*-Ox$_{5/20}$(10/30) with the Overall [M]/[CTA] Ratio Kept as 200 for All RAFT Polymerizations

	n_{EtOx}	feed MA/Ox$_n$ [%]	conv.$_{NMR}$ [a] [%]	DP$_{Theo}$ [b]	MA/Ox$_n$ [c] $_{NMR}$ [%]	M$_{nTheo}$ [d] [g mol^{-1}]	M$_{nSEC}$ [e] [g mol^{-1}]	Đ [e]
BocA-*g*-Ox$_5$(30)	5	70:30	>98	196	55:45	105,300	74,200	1.27
BocA-*g*-Ox$_{20}$(30)	20	70:30	>90	180	70:30	121,900	75,000	1.23
BocA-*g*-Ox$_5$(10)	5	90:10	>90	180	83:17	112,800	56,000	1.26
BocA-*g*-Ox$_{20}$(10)	20	90:10	>90	180	85:15	114,600	81,900	1.36
BocM-*g*-Ox$_5$(30)	5	70:30	>90	184	59:41	103,700	66,100	1.33
BocM-*g*-Ox$_{20}$(30)	20	70:30	97	198	69:31	128,900	80,000	1.24
BocM-*g*-Ox$_5$(10)	5	90:10	90	180	86:14	116,400	42,400	1.38
BocM-*g*-Ox$_{20}$(10)	20	90:10	93	186	90:10	125,700	65,100	1.25

[a]Determined by ^{1}H NMR spectroscopy from the reaction mixtures. [b]Calculated from the initial [M]/[CTA] ratio and overall monomer conversion. [c]Determined by ^{1}H NMR spectroscopy of the purified polymers. [d]Calculated from conversion and copolymer composition (amino group-containing monomer MA/macromonomer Ox$_n$). [e]Determined by SEC (DMAc, 0.21% LiCl, PMMA calibration).

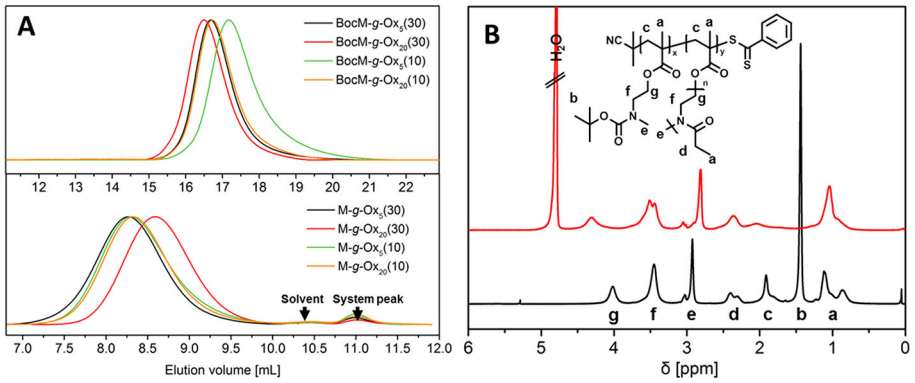

Figure 1. (A) Size exclusion chromatograms of the Boc-protected MAEMA-based graft copolymers **BocM-*g*-Ox$_{5/20}$(10/30)** (top, DMAc, 0.21% LiCl, RI detection) and of the unprotected MAEMA-based graft copolymers **M-*g*-Ox$_{5/20}$(10/30)** (bottom, water, 0.1% trifluoroacetic acid, 0.1 M NaCl). (B) ^{1}H NMR spectra of the protected graft copolymer **BocM-*g*-Ox$_5$(10)** (black, in $CDCl_3$) and the respective deprotected graft copolymer **M-*g*-Ox$_5$(10)** (red in D_2O) including assignment of the peaks to the schematic representation of the structure of **BocM-*g*-Ox$_5$(10)**.

^{1}H NMR (300 MHz, $CDCl_3$): δ [ppm] 1.11 (*s*, 15H), 1.91 (*s*, 3H), 2.38 (*m*, 10H), 3.01 (*m*, 3H), 3.48 (*m*, 18H), 4.28 (*s*, 2H), 5.60 (*s*, 1H), 6.06 (*s*, 1H).

Ox$_{20}$: M_n (NMR) 2,100 g mol^{-1}, M_n (SEC): 2,800 g mol^{-1} (PS calibration), DF 96%, Đ = 1.08. For the synthesis of **Ox$_5$**, MeTos (12 mmol, 2.234 g), EtOx (60 mmol, 5.966 g), and 9 mL of acetonitrile were reacted in the microwave for 30 s as described above. The functionalization was performed as described above using 1.550 mL (18 mmol) of methacrylic acid and 3.4 mL (24 mmol) of NEt_3. **Ox$_5$**: M_n (NMR): 600 g mol^{-1}, M_n (SEC): 900 g mol^{-1} (PS calibration), DF 94%, Đ = 1.20.

RAFT Copolymerization. Copolymers of BocAEMA or BocMAEMA and **Ox$_5$** or **Ox$_{20}$** were obtained by RAFT polymerization. In a typical RAFT copolymerization experiment for **BocA-*g*-Ox$_5$(30)**, 1.00 g of **Ox$_5$** (1.08 mmol), 0.586 g of BocAEMA (2.53 mmol), 0.74 mg of AIBN (4.51 μmol), 3.99 mg of CPDB (18.00 μmol), and 3.61 mL DMF were mixed with anisole as internal standard (0.118 mL) in a 10 mL reaction vial. The monomer concentration was kept at 1 mol L^{-1}. The reaction mixture was degassed with argon for at least 10 min, a t_0 sample was taken, and subsequently, the reaction solution was placed in a preheated oil bath at 70 °C for 21 h. A t_e sample for determination of monomer conversion was taken. Conversion was measured by ^{1}H NMR spectroscopy in $CDCl_3$ using anisole as an internal standard. The copolymer was precipitated from THF into a large volume of *n*-hexane twice, and size exclusion chromatography on Biobeads SX1 column in THF was performed. Afterward, the clean product was dried under reduced pressure. The reaction time was 16.5 h for **BocA-*g*-Ox$_{20}$(30)**, **BocA-*g*-Ox$_5$(10)**, and **BocA-*g*-Ox$_{20}$(10)** and 15.25 h for the BocMAEMA copolymers (**BocM-*g*-Ox$_{5/20}$(10/30)**). Additional dialysis was performed against ultrapure water for 4 weeks using a regenerated cellulose membrane with a cutoff of 3.5 kg mol^{-1} for **BocA-*g*-Ox$_{20}$(30)**, **BocA-*g*-Ox$_{20}$(10)**, and **BocM-*g*-Ox$_{5/20}$(10/30)**. The feed ratios of the copolymers can be found in Table 1.

BocA-g-Ox$_{5/20}$(10/30). ^{1}H NMR (300 MHz, $CDCl_3$): δ [ppm] 0.87 (H_a), 1.44 (H_b), 1.82–2.09 (H_c), 2.31–2.40 (H_d), 3.04 (H_e, 3H), 3.37–3.45 (H_f), 3.99 (H_g), see Figure S3.

M_n (SEC, DMAc with 0.21% of lithium chloride, PMMA calibration): **BocA-*g*-Ox$_5$(30)**, 74,200 g mol^{-1} (Đ = 1.27); **BocA-*g*-Ox$_{20}$(30)**, 75,000 g mol^{-1} (Đ = 1.23); **BocA-*g*-Ox$_5$(10)**, 56,000 g mol^{-1} (Đ = 1.26); **BocA-*g*-Ox$_{20}$(10)**, 81,900 g mol^{-1} (Đ = 1.36).

BocM-g-Ox$_{5/20}$(10/30). ^{1}H NMR (300 MHz, $CDCl_3$): δ [ppm] 0.87 (H_a), 1.44 (H_b), 1.91 (H_c), 2.30–2.40 (H_d), 2.92–3.03 (H_e), 3.45 (H_f), 4.02 (H_g), see Figure S4.

M_n (SEC, DMAc with 0.21% of lithium chloride, PMMA calibration): **BocM-*g*-Ox$_5$(30)**, 66,100 g mol^{-1} (Đ = 1.33); **BocM-*g*-Ox$_{20}$(30)**, 80,000 g mol^{-1} (Đ = 1.24); **BocM-*g*-Ox$_5$(10)**, 42,400g mol^{-1} (Đ = 1.38); **BocM-*g*-Ox$_{20}$(10)PB8**, 65,100 g mol^{-1} (Đ = 1.25).

Deprotection of the Boc-Protected Graft Copolymers. The Boc-protected copolymers were deprotected using diluted hydrochloric acid in methanol. In a typical procedure, 300 mg of the polymer was dissolved in 10 mL of methanol, and 1 mL of hydrochloric acid was added dropwise. The reaction mixture was stirred at room temperature overnight. The volatiles were removed under reduced pressure, and the polymer was dissolved in water and freeze-dried.

A-g-Ox$_{5/20}$(10/30). ^{1}H NMR (300 MHz, D_2O): δ [ppm] 1.05 (CH_3 backbone + CH_3 side chain EtOx), 1.50–2.09 (CH_2 backbone), 2.31–2.40 (CH_2 side chain EtOx), 2.91 (CH_3 EtOx initiator), 3.37–3.52 (CH_2–N side chain), 4.28 (CH_2–O side chain), see Figure S6.

M_n (SEC, H_2O, 0.1% trifluoric acid and 0.1 M NaCl, P2VP calibration): **A-*g*-Ox$_5$(30)**, 18,400 g mol^{-1} (Đ = 1.49); **A-*g*-Ox$_{20}$(30)**, 17,300 g mol^{-1} (Đ = 1.54); **A-*g*-Ox$_5$(10)**, 16,700 g mol^{-1} (Đ = 1.44); **A-*g*-Ox$_{20}$(10)**, 22,800 g mol^{-1} (Đ = 1.48).

DOI: 10.1021/acs.biomac.8b00362
Biomacromolecules 2018, 19, 2759–2771

M-g-Ox$_{5/20}$(10/30). ^{1}H NMR (300 MHz, $CDCl_3$): δ [ppm] 1.05 (CH_3 backbone + CH_3 side chain EtOx), 1.50−2.09 (CH_2 backbone), 2.31−2.40 (CH_2 side chain EtOx), 2.70−2.91(CH_3 EtOx initiator + N−CH_3), 3.37−3.52 (CH_2−N side chain), 4.28 (CH_2−O side chain), see Figure 1.

M_n (SEC, H_2O, 0.1% trifluoric acid and 0.1 M NaCl, P2VP calibration): **M-*g*-Ox$_5$(30)**, 20,200 g mol^{-1} (Đ = 1.42); **M-*g*-Ox$_{20}$(30)**, 13,400 g mol^{-1} (Đ = 1.30); **M-*g*-Ox$_5$(10)**, 17,300 g mol^{-1} (Đ = 1.43); **M-*g*-Ox$_{20}$(10)**, 17,500 g mol^{-1} (Đ = 1.40).

SEC and NMR results are also summarized in Table 2.

Table 2. Characterization of Deprotected Polymers A-*g*-Ox$_{5/20}$(10/30) and M-*g*-Ox$_{5/20}$(10/30)

polymer	n_{EtOx}	DG[a] [%]	M_n[b] [g mol^{-1}]	Đ[d]	pK_a[c]	mol% Ox[e]	DP[f]$_{Theo}$
A-*g*-Ox$_5$(30)	5	41	18,400	1.49	7.60	77	196
A-*g*-Ox$_{20}$(30)	20	41	17,300	1.54	7.36	88	180
A-*g*-Ox$_5$(10)	5	16	16,700	1.44	7.42	53	180
A-*g*-Ox$_{20}$(10)	20	10	22,800	1.48	7.41	82	180
M-*g*-Ox$_5$(30)	5	40	20,200	1.42	7.60	77	184
M-*g*-Ox$_{20}$(30)	20	31	13,400	1.30	7.42	82	198
M-*g*-Ox$_5$(10)	5	17	17,300	1.43	7.91	56	180
M-*g*-Ox$_{20}$(10)	20	16	17,500	1.40	7.56	72	186
PA[d]	0	0	11,700	1.98	7.71	0	163
PM[d]	0	0	13,400	2.04	7.01	0	167

[a]Degree of grafting determined from the ^{1}H NMR spectra. [b]Determined by SEC (water, 0.1% trifluoroacetic acid, 0.1 M NaCl, RI detection, P2VP calibration). [c]Calculated from the titration curve of the acidified polymers (10 mg mL^{-1} in water) against 0.1 M NaOH solution. [d]PAEMA and PMAEMA data previously published, DP_{AF4} 163/167.[16] Dextran calibration was used for SEC. [e]Calculated from the ^{1}H NMR spectra of the corresponding Boc-protected copolymers. [f]Calculated from the initial [M]/[CTA] ratio and overall monomer conversion.

PAEMA and PMAEMA Homopolymers. The synthesis of PAEMA (PA) and PMAEMA (PM) is described in an earlier publication.[16]

Polyplex Preparation. Following an adjusted method by Pezzoli et al.,[41] polyplexes of pDNA and polymers were prepared by mixing stock solutions of 15 μg mL^{-1} of pDNA and different amounts of polymers (1 mg mL^{-1}) to obtain various N*/P ratios in HBG buffer (20 mM 4-(2-hydroxethyl) piperazine-1-ethanesulfonic acid (HEPES) and 5% (w/v) glucose, pH 7.2). N* is referred to the number of transfection-relevant potentially protonatable nitrogen atoms (i.e., amine nitrogen atoms) to exclude amide nitrogen atoms within the polymer structure and P the number of phosphates from the pDNA in mixture. The solutions were vortexed for 10 s at maximal speed and incubated at room temperature for 15 min to ensure complex formation.

Ethidium Bromide Quenching Assay. The formation of polyplexes with pDNA was examined by quenching of the ethidium bromide fluorescence. Briefly, 15 μg mL^{-1} of pDNA in a total volume of 100 μL of HBG buffer was incubated with ethidium bromide (0.4 μg mL^{-1}) for 10 min at room temperature. Subsequently, polyplexes with different amounts of polymer (various N*/P ratios) were prepared in black 96-well plates (Nunc Thermo Fisher) and incubated at room temperature for 15 min before the fluorescence measurements. The fluorescence of the samples was measured at an excitation wavelength of λ = 525 nm and an emission wavelength of λ = 605 nm using a Tecan microplate reader. A sample containing only pDNA and ethidium bromide was utilized to calibrate the device to 100% fluorescence against a background of 0.4 μg mL^{-1} of ethidium bromide in HBG solution. The percentage of dye displaced upon polyplex formation was calculated using eq 2

$$\text{RFU}\,[\%] = \frac{F_{\text{sample}} - F_0}{F_{\text{pDNA}} - F_0} * 100 \quad (2)$$

where RFU is the relative fluorescence and F_{sample}, F_0, and F_{pDNA} are the fluorescence intensities of a given sample, the ethidium bromide in HBG alone, and the ethidium bromide intercalated into pDNA alone.

Heparin Dissociation Assay. Polyplexes with an N*/P ratio of 30 were prepared as described above in a total volume of 100 μL of HBG buffer containing ethidium bromide (0.4 μg mL^{-1}). After incubation in the dark at room temperature for 15 min, the polyplexes were transferred into a black 96-well plate, and heparin of indicated concentrations was added. The solution was mixed and incubated for a further 30 min at 37 °C in the dark. The fluorescence of ethidium bromide was measured at λ_{Ex} = 525 nm/λ_{Em} = 605 nm with a Tecan microplate reader. The percentage of intercalated ethidium bromide was calculated as described before.

Determination of Cytotoxicity. Cytotoxicity studies were performed with the mouse fibroblast cell line L929 (CCL-1, ATCC) as recommended by ISO10993-5. The cells were cultured in Dulbecco's modified Eagle's medium (DMEM, Biochrom) supplemented with 10% fetal calf serum (FCS), 100 U mL^{-1} penicillin, and 100 μg mL^{-1} of streptomycin at 37 °C in a humidified 5% (v/v) CO_2 atmosphere. In detail, cells were seeded at 10^4 cells per well in a 96-well plate and incubated for 24 h. Afterward, the polymers at different concentrations, ranging from 5 to 330 μg mL^{-1}, were added to the cells, and the plates were incubated for additional 24 h. Subsequently, the medium was replaced by a mixture of fresh culture medium and alamarBlue solution (Life Technologies, Germany) prepared according to the manufacturer's instructions. After a further incubation of 4 h at 37 °C, the fluorescence was measured at λ_{Ex} = 570/λ_{Em} = 610 nm with untreated cells on the same well plate serving as negative controls. The negative control was standardized as 0% of metabolism inhibition and referred to as 100% viability. Data are expressed as mean ± SD of three independent determinations.

Hemolysis Assay. The interaction of polymers with cellular membranes was examined by analyzing the release of hemoglobin from erythrocytes. Blood from sheep, collected in heparinized tubes, was provided by the Institute of Animal Science and Animal Welfare, Friedrich Schiller University Jena. The blood was centrifuged at 4,500 *g* for 5 min, and the pellet was washed three times with cold 1.5 mM phosphate-buffered saline (PBS, pH 7.4). After dilution with PBS in a ratio of 1:7, aliquots of erythrocyte suspension were mixed 1:1 with the polymer solution and incubated in a water bath at 37 °C for 60 min. After centrifugation at 2,400 *g* for 5 min, the hemoglobin release into the supernatant was determined spectrophotometrically using a microplate reader at 544 nm wavelength. Complete hemolysis (100%) was achieved using 1% Triton X-100 serving as positive control. Pure PBS was used as negative control (0% hemolysis). The hemolytic activity of the polycations was calculated as follows (eq 3)

$$\%\text{hemolysis} = 100 * \frac{(A_{\text{sample}} - A_{\text{negative control}})}{A_{\text{positive control}}} \quad (3)$$

A value less than 2% hemolysis rate was classified as nonhemolytic, 2−5% as slightly hemolytic, and values >5% as hemolytic. Experiments were run in triplicate and were performed with three different blood donors.

Erythrocyte Aggregation. Erythrocytes were isolated as described above. The erythrocyte suspension was mixed 1:1 with the polymer solutions (100 μL total volume) in a clear flat-bottomed 96-well plate. The cells were incubated at 37 °C for 2 h, and the absorbance was measured at λ = 645 nm in a microplate reader. Cells, which were treated with PBS, served as negative control, and 25 kDa bPEI (50 μg mL^{-1}, Polysciences) was used as positive control. Absorbance values of the test

DOI: 10.1021/acs.biomac.8b00362
Biomacromolecules 2018, 19, 2759−2771

solutions lower than the negative control were regarded as aggregation. Experiments were run in triplicate and were performed with three different donor bloods from sheep.

Polyplex Uptake. HEK-293 cells (CRL-1573, ATCC) were routinely cultured in DMEM medium (1 g L^{-1} glucose) supplemented with 10% FCS, 100 μg mL^{-1} of streptomycin, 100 IU mL^{-1} of penicillin, and at 37 °C in a humidified 5% (v/v) CO_2 atmosphere.

For kinetic studies of polyplexes, cells were seeded at a density of 10^5 cells per mL in 24-well plates and cultured for 24 h. One hour prior to the addition of polyplexes, the medium was changed to serum-reduced OptiMEM or replaced by fresh growth medium (DMEM). The pDNA was labeled with YOYO-1 iodide prior to polyplex preparation in HBG buffer. For labeling of 1 μg pDNA, 0.026 μL of 1 M YOYO-1 solution was mixed with pDNA and incubated for 15 min at 4 °C protected from light. Subsequently, the polymers were added at the indicated N*/P ratio, and polyplexes were formed as described previously. At least 50 μL of polyplexes in solution were added to the cells. The cells were harvested 4 h after polyplex addition. For the relative uptake of polyplexes to be determined, 10^4 cells were measured by flow cytometry using a Cytomics FC 500 (Beckman Coulter), and the amount of viable cells showing YOYO-1 signal (green) were gated.

Regarding the uptake studies via confocal laser scanning microscopy, HEK-293 cells were seeded and cultured as described above in glass-bottomed microscopy dishes (CELLSTAR FourWell Plate, Greiner BioOne, Germany). Prior to polyplex addition, medium was replaced by fresh DMEM. Polyplexes containing YOYO-1-labeled pDNA was incubated for 4 h at 37 °C. Afterward, medium was replaced by fresh DMEM supplemented with Hoechst 3342 for nucleus staining and LysoTracker Red DND-99 for lysosomal staining. Additionally, 10% trypan blue solution was added to quench the fluorescence of not completely internalized polyplexes. Imaging was performed with LSM880, Elyra PS.1 system (Zeiss, Germany) applying a 63× 1.4 NA plan apochromat oil objective. Colocalization studies were analyzed using the ZEN software (Zeiss, Germany) of five images per experiment. The experiments were performed independently at least three times.

Transfection of Adherent Cells. For transfection studies, HEK-293 cells were seeded at a density of 10^5 cells per mL in 24-well plates and incubated for 24 h at 37 °C in 5% CO_2. One hour prior to transfection, medium was replaced by 0.5 mL of OptiMEM. Polyplexes were prepared as described above and were added to the cells (50 μL per well). After an incubation time of 4 h at 37 °C, the supernatant was replaced by fresh growth medium, and the cells were further incubated for 20 h. For analysis via flow cytometry (Cytomics FC 500, Beckman Coulter), cells were harvested at least 24 h post-transfection by trypsinization. Dead cells were identified via counterstaining with propidium iodide. For determination of transfection efficiency, 10^4 viable cells were measured and cells expressing EGFP (green) were gated. The experiments were performed independently three times.

RESULTS AND DISCUSSION

Polymer Synthesis and Characterization. Within this study, the potential shielding effect of hydrophilic PEtOx side chains in methacrylate-based cationic graft copolymers and their reduction of cytotoxic effects was investigated. As long side chains may hinder the polyplex formation, we selected to investigate graft copolymers with side chain DPs of 5 and 20, respectively. The corresponding Ox_n macromonomers **Ox_5** with a DP of 5 and **Ox_{20}** with a DP of 20 were synthesized via CROP as described previously.[42] Therefore, the living polymer chains were quenched using methacrylic acid and triethylamine to introduce the methacrylate functionality at the ω-chain ends.[40] The degree of functionalization was found to be nearly quantitatively as determined by ^{1}H NMR spectroscopy (see Supporting Information).

Primary as well as secondary amino moieties are suitable for the complexation of nucleic acids. As a direct comparison for graft copolymer architectures is missing to date, we included both into the graft copolymer backbone. For aminolysis-induced gelation reaction during RAFT polymerization to be avoided, the amino group containing methacrylates were polymerized as Boc-protected monomers **BocA** and **BocM** according to the literature.[38,39]

It is known from the literature that the transfection efficiency of linear PDMAEMA is negligible up to a molar mass of ~60 kDa.[43] Comparable studies on the influence of other functionalities in copolymer vectors revealed improved transfection efficiencies using molar masses in the range of 10−40 kDa.[3,23,44,45] Therefore, the overall [monomer] to [chain transfer agent] ratio was set to 200 for all RAFT polymerizations to reach reasonable molar masses. In particular, the balance between efficient transfection and cytotoxicity seems to be one of the major issues in vector synthesis. We therefore aimed at graft copolymers featuring DGs of 10 and 30%, respectively. Hence, the ratio of amino group-functionalized monomer and macromonomer was kept 7:3 or 9:1 for both Ox_n macromonomers (DP 5, 20). The combination of the four comonomers ratios resulted in a library of eight copolymers covering a broad range of ratios of transfection amine units to shielding units (Ox_n) (Table 1).

The copolymerizations were performed at 70 °C in DMF. After a reaction time between 15 and 21 h, monomer conversions above 90% were achieved, resulting in theoretical DP values in the range of 180−196 as intended. Residual macromonomer was completely removed by a combination of precipitation, size exclusion chromatography on a Biobeads SX1 column, and dialysis against water (see Experimental Section for details). Accordingly, the SEC elugrams of the purified graft copolymers revealed monomodal molar mass distributions with Đ values between 1.23 and 1.38 (Figure 1A and Figure S5). Molar masses between 42 and 81 kDa were estimated using PMMA calibration, which are, however, of little significance due to the graft architecture of the polymers.

The composition of the graft copolymers was determined by means of ^{1}H NMR spectroscopy using isolated characteristic signals of the repeating units (see Figure 1B and Figure S6). For the graft copolymers containing the protected primary amino moieties **BocA-*g*-$Ox_{5/20}$(10/30)**, the methyl signal integral of the Boc protection group at 1.45 ppm and the methyl end group of the $Ox_{5/20}$ side chains at 3.0 ppm were well suited (signals "b" and "e" in Figure S6). Because of the overlapping methyl signal of the secondary amino moiety with signal "e", the composition of **BocM-*g*-$Ox_{5/20}$(10/30)** was calculated from the ratio of the Boc signal and the methylene signal of the $Ox_{5/20}$ side chains at 2.42 ppm (signals "b" and "d" in Figure 1B). The composition of the graft copolymers comprising **Ox_{20}** (i.e., with a side chain DP of 20) is in good agreement with the comonomer feed ratio. In contrast, the graft copolymers with a side chain DP of 5 featured a slightly decreased molar fraction of Boc-protected amino methacrylate compared to the feed ratio.

The whole library of Boc-protected polymers was deprotected using 1 M hydrochloric acid in methanol. Complete deprotection was proven by the disappearance of the methyl signals at 1.44 ppm in ^{1}H NMR spectra that are assigned to the Boc protection group (see Figure 1B and Figure S6, Table 2). The composition of all deprotected graft copolymers was again evaluated from suitable signals in the ^{1}H NMR spectra and found to be in reasonable agreement with that of the deprotected polymers (signals "e" and "g" in Figure 1 were used for this purpose). In addition, the SEC elugrams of all deprotected graft copolymers revealed monomodal molar mass distributions. It is thus to be

DOI: 10.1021/acs.biomac.8b00362
Biomacromolecules 2018, 19, 2759−2771

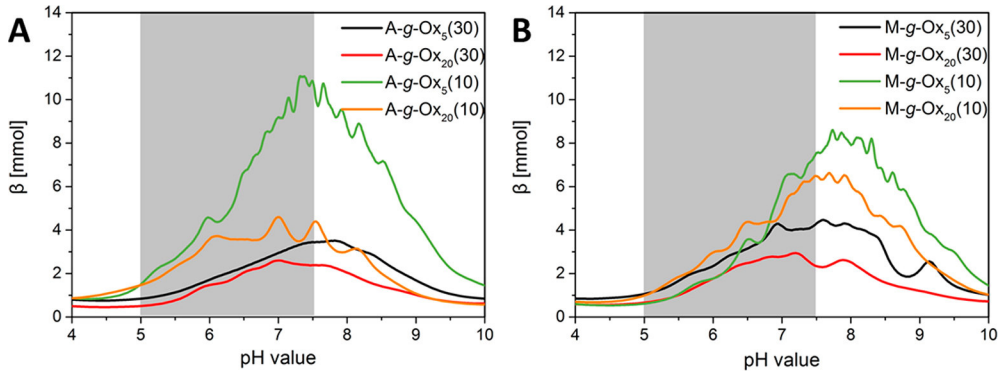

Figure 2. Buffer capacity of the deprotected graft copolymers calculated with eq 4 from titration over pH range for copolymers containing (A) AEMA and (B) MAEMA.

expected that no undesired degradation occurred during the deprotection step, and the initial DG was maintained. In conclusion, our experimental setup provided a series of eight graft copolymers with tailored variation and arrangement of building blocks to introduce shielding of cytotoxic segments within the polymer architectures. For the comparison of the graft copolymers with the homopolymers of AEMA (**PA**) and MAEMA (**PM**), homopolymers with comparable DPs of 163 and 167, respectively, were used (see Table 2).[16]

As the endosomal release is usually influenced by the pH value change in the endosome, the pK_a values of the amine-functional graft copolymers were determined by half-automated titration from acidic to alkaline conditions using 0.1 M NaOH solution (see Table 2, Figure S7). For this purpose, the turning points were determined by differentiation of the fitted titration curves. Afterward, the pK_a values were calculated by the Henderson–Hasselbalch equation (eq 1). The pK_a values between 7.36 and 7.91 are in a comparable range to those of the homopolymers **PM** (pK_a = 7.01) and **PA** (pK_a = 7.71) (Table 2). These results confirmed that at least half of the amino moieties of the polymers are in a protonated state at pH values between 7.2 and 7.4, as typical for cell culture. As a general trend, the pK_a values of the graft copolymer series comprising secondary amino moieties **M-*g*-Ox$_n$** are slightly higher than those of the graft copolymers comprising primary amino groups **A-*g*-Ox$_n$**.

Although it is not commonly believed anymore that the proton-sponge effect is the only reason for efficient gene delivery, the buffering ability still seems to severely impact the performance of vectors.[6] In other studies, we experienced a trend of the buffer capacity linked to the endosomal escape performance of polymeric vectors from which we would assume that the polymers with the highest buffer capacities show the highest potential in transfection performance. Therefore, the buffer capacities were calculated from the FTT-smoothed curves of the titration using eq 4. The titration of HCl against NaOH solution as reference for low buffer capacity of maximum of 0.7×10^{-4} mol can be found in the literature.[46]

$$\beta = \frac{\mathrm{d}\, n(\mathrm{OH}^-)}{\mathrm{d\ pH}} \qquad (4)$$

The buffer capacities are plotted as a function of the pH value in the pH range from 4 to 10 in Figure 2. In particular, the graft copolymers featuring a low DG and side chain DP revealed high buffer capacities in the relevant pH range from 7.4 to 5. The buffer capacity decreased with increasing side chain DP.

Biocompatibility and Polyplex Properties. The aim of the combination of PEtOx-based and cationic building blocks in graft copolymer architectures was to increase the biocompatibility of the corresponding cationic homopolymers with high charge density, i.e., PAEMA (**PA**) and PMAEMA (**PM**). For the cytotoxicity of the copolymers to be examined, an alamarBlue assay was performed with polymer concentrations up to 330 μg mL^{-1} for 24 h (Figure 3A). Furthermore, the polymers were incubated with erythrocytes obtained from sheep blood to test membrane destabilization and aggregation of the blood cells to obtain further information about the polymers' biocompat-

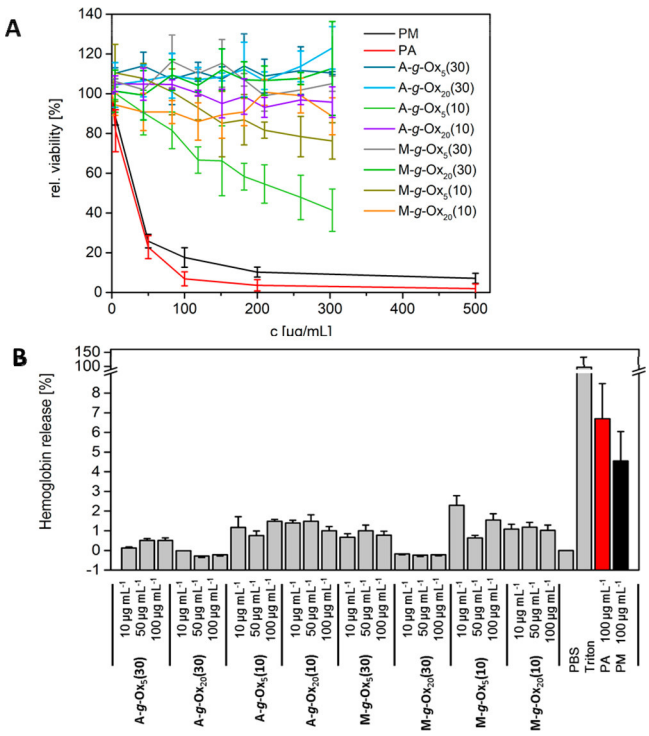

Figure 3. Bio- and hemocompatibility of the library. (A) Relative viability of L929 cells after 24 h incubation with the amino-functional graft copolymers and the homopolymers **PM** and **PA** at indicated concentrations as recommended by ISO10993-5. (B) Hemolysis assay of erythrocytes after incubation with the polymers at indicated concentrations. Triton X-100 was used as positive and phosphate-buffered saline (PBS) as negative controls. A value less than 2% hemolysis is classified as nonhemolytic, 2 to 5% as slightly hemolytic, and values >5% as hemolytic. Values represent the mean ± SD (n = 3).

DOI: 10.1021/acs.biomac.8b00362
Biomacromolecules 2018, 19, 2759–2771

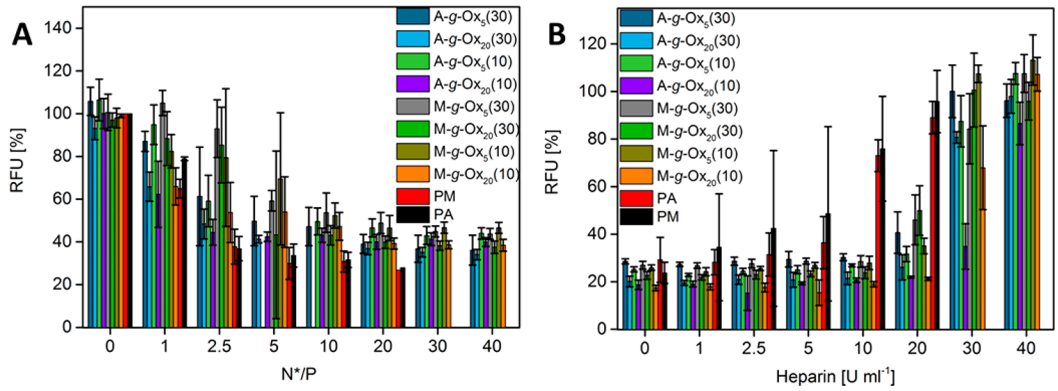

Figure 4. Polyplex formation and stability studies with pDNA using the graft copolymers **A-*g*-Ox$_{5/20}$(10/30)** and **M-*g*-Ox$_{5/20}$(10/30)** and the homopolymers **PM** and **PA**. (A) Complexation affinity (ethidium bromide quenching assay) of respective polymers at indicated N*/P ratios. N* is the number of amines, and P is the number of phosphate groups of the pDNA. (B) Dissociation assay of polyplexes formed at N*/P 30 using heparin (0−40 U mL^{-1}). Values represent the mean ± SD (n = 3).

ibility (Figure 3B). For all experiments, the homopolymers **PA** and **PM** are included as unshielded references (red or black, Figure 3A).

As known from the literature, primary and secondary amino groups show disruptive effects on cellular membranes, which support the endosomal escape but in turn can lead to harsh membrane damage.[47,48] Surprisingly, the six graft copolymers comprising Ox$_n$ side chains with a DP of 20 or featuring a DG of 30% showed no toxic effects at all in the concentration range from 5 to 330 μg mL^{-1}, yielding viabilities of around 100%. **M-*g*-Ox$_5$(10)** revealed only slightly toxic effects decreasing the viability to 80%, whereas the viability of cells incubated with **A-*g*-Ox$_5$(10)** decreased to 41% at 330 μg mL^{-1}, i.e., the highest concentration tested. Apparently, a DG of 10% in combination with the rather short Ox$_5$ side chains is not sufficient to completely shield the high amount of primary and secondary amino groups. In addition, the toxicity of polymers containing MAEMA (IC$_{50}$ = 23 μg mL^{-1}) is slightly lower than for AEMA-based polymers (IC$_{50}$ = 19 μg mL^{-1}).[16] The same trend can also be seen in Figure 3A for the homopolymers **PA** and **PM** showing an exponential decrease of the viability at low concentrations (c < 50 μg mL^{-1}). The fact that the viability of the copolymers was improved by a factor of 10 and higher points toward the shielding effect of the oligomeric oxazoline side chains, as known from PEG shielding.[21,49] In the case of erythrocyte hemolysis, no to low hemolytic activity was detected up to 2% with PBS as negative control at 0% and Triton X-100 as positive control. In comparison with the homopolymers **PA** and **PM**, a significant reduction of the hemolysis at 100 μg mL^{-1} can be seen. It is known that a high charge density can result in high erythrocyte aggregation and membrane disruption.[17,50] A high rate of aggregation occurred (see Figure S8) for all copolymers, slightly lower or comparable to commercial bPEI 25 kDa. These results lead to the conclusion that the membrane activity is still potent for aggregation but that the graft copolymers do not induce membrane disruption.

In the next step, polyplex formation and DNA dissociation were investigated via a competitive assay using ethidium bromide as intercalation dye into the pDNA (Figure 4A) and heparin as competitor for the pDNA in the release study (see Figure 4B). Therefore, polyplexes of all graft copolymers were prepared by mixing polymer and pDNA at certain N*/P ratios at room temperature (N* is the number of transfection relevant amines, and P is the number of phosphates from the pDNA in the mixture).

All polymers revealed a good binding affinity, in particular at higher N*/P ratios, indicated by the reduction of ethidium fluorescence intensity from 100 to 40%. The complex formation is almost entirely reversible up to a fluorescence intensity of 100% (Figure 4B). In contrast to the homopolymers, an effective pDNA dissociation from the copolymers was only observed at very high heparin concentrations starting at 30 μg mL^{-1}. Apparently, the Ox$_n$ side chains of the graft copolymers impede the displacement by heparin and thus protect the nucleic acid. In particular, the copolymers **A-*g*-Ox$_{20}$(10)** and **M-*g*-Ox$_{20}$(10)** revealed high polyplex stability against anionic competitor molecules because they required more than 4-times higher heparin supplementation compared to the homopolymers to achieve 100% release. An explanation for the delayed dissociation could be the increased DP of the side chains, hampering the action of heparin as a competitor for the pDNA. Nevertheless, the reason for the enhanced dissociation properties of the polymers comprising a DG of 30% remains unclear. DLS measurements of the copolymers in aqueous 0.1 M NaCl and 0.1 M HCl solution revealed hydrodynamic diameters from 8 to 14 nm (number weighted values, see Figures S9−11).[51] The unexpectedly small number-weighted size average of some of the polyplexes is potentially due to the overestimation of small uncomplexed polymer chains in the polyplex solution. The zeta potential and size distribution of the polyplexes were measured in HBG buffer, revealing positively charged complexes (9−21 mV) of increased size and dispersity (see Table S1). This further indicates the successful masking (and condensation) of the anionically charged pDNA within the polyplex at N*/P 30, which is beneficial for the affinity to the cell plasma membrane and the intracellular uptake process.

Uptake and Transfection. After successful polyplex formation, the properties concerning uptake and transfection efficiency were the focus of further studies. For this purpose, uptake experiments using YOYO-1-labeled pDNA were performed at 37 °C for 4 h with HEK cells. The repellent properties of PEG-shielded vectors reported so far reveal no influence of serum proteins, showing the same efficiencies in reduced as well as serum-containing medium.[52] Such effects have been reported also for the more hydrophilic poly(2-methyl-oxazoline).[53] For investigating if PEtOx exhibits a similar effect in our graft copolymers, the uptake experiments were performed in

DOI: 10.1021/acs.biomac.8b00362
Biomacromolecules 2018, 19, 2759−2771

serum-reduced OptiMEM and media or serum-containing growth medium (Figure 5).

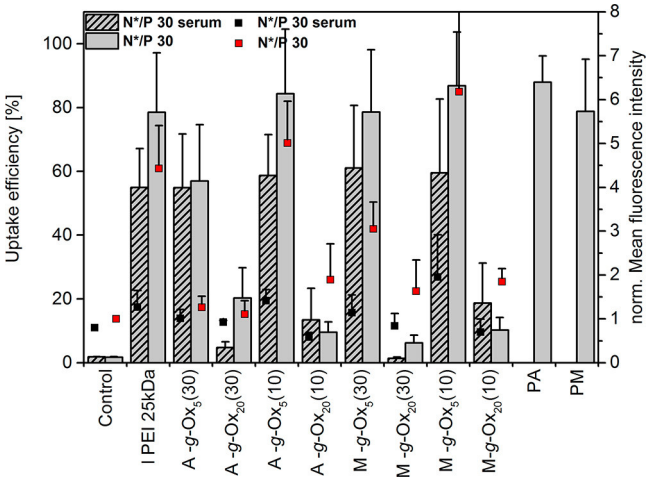

Figure 5. Cellular uptake study of **A-*g*-Ox$_{5/20}$(10/30)** and **M-*g*-Ox$_{5/20}$(10/30)** polyplexes (N*/P 30) using YOYO-1-labeled pDNA. HEK cells were treated with polyplexes for 4 h at 37 °C, and uptake was analyzed via flow cytometry showing the uptake efficiency (bars) in serum-reduced (plane) and full growth medium (striped) and the MFI (dots) in serum-reduced (red) and full growth medium (black). Values represents the mean ± SD (n = 3). Data for PA and PM polyplexes at an N*/P value of 20 are taken from ref 16.

In comparison to commercial PEI, stated as the gold standard for non-viral transfection, the four polymers comprising PEtOx side chains with a DP of 5 showed comparable uptake efficiencies to PEI, reaching levels from ≈ 60 to over 80% after 4 h according to transfection standard protocol. Polyplexes formed from graft copolymers with longer PEtOx side chains (**Ox$_{20}$**) revealed no or only low uptake efficiencies. In contrast, the degree of grafting did not influence the uptake. Presumably, the longer Ox$_{20}$ chains hamper the interaction of the amines with the cellular membrane. Furthermore, an influence of serum proteins on the uptake performance could be observed (in particular for MFI values). The shielding property of PEtOx does not seem to be sufficient for a complete repellent effect of proteins, as an accumulation of proteins to the polyplex can hinder the internalization. After successful uptake studies, transfection experiments in HEK cells were also performed in OptiMEM. Figure 6 shows the transfection efficiency (TE, bars) as well as the mean fluorescence intensity (MFI, dots).

Surprisingly, the transfection performance differed from the uptake efficiency of pDNA-based polyplexes. As expected from the previous experiments, copolymers containing side chains with a DP of 20 (**Ox$_{20}$**) showed no transfection efficiencies. In contrast to the cellular uptake, the transfection efficiency is influenced by the degree of grafting: **A-*g*-Ox$_5$(30)** and **M-*g*-Ox$_5$(30)** revealed no transfection efficiency. Those copolymers with a DG of ∼30% seem to be unable to escape the endosomes even though they have been internalized with high efficiencies. This might be because the higher amount of side chains decreases the polymer-membrane interaction inside the endosomes and thereby limits the endosomal escape. The hemocompatibility tested before (Figure 3B) supports this assumption. The highest membrane interaction was found for the copolymers **A-*g*-Ox$_5$(10)** and **M-*g*-Ox$_5$(10)**. Copolymers **A-*g*-Ox$_5$(10)** and **M-*g*-Ox$_5$(10)** showed maximum buffer capacities of 11.05 and 8.60

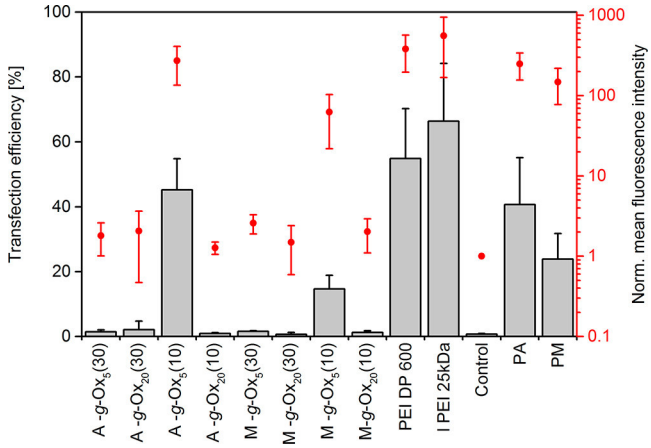

Figure 6. Transfection efficiency (black y-axis, bars) and MFI over all cells (red y-axis, dots) regarding tested graft copolymers in comparison to the homopolymers **PA** and **PM** for adherent HEK cells in OptiMEM at N*/P 30 after 24 h. The control represents untreated HEK; lPEI 25 kDa was purchased from Polysciences, and lPEI DP 600 was self-synthesized lPEI with a DP of 600. Values represent the mean ± SD (n = 3). Data for **PA** and **PM** polyplexes at N*/P value of 20 are taken from ref 16, and the data for PEI DP 600 are taken from Bus et al.[54]

mmol between pH values 5 and 9 in contrast to the other copolymers featuring reduced buffer capacities in the range of 6.61 to 2.59 mmol. The maximum buffer capacity range of the best performer **A-*g*-Ox$_5$(10)** is shifted to lower pH values compared to **M-*g*-Ox$_5$(10)**. The improved TE of the AEMA-based graft copolymer leads to the assumption that the buffer capacity may influence the endosomal escape. CLSM measurements conducted on HEK cells transfected using the graft copolymers with a side chain DP of 5 further supported this hypothesis (Figure 7).

Images of YOYO-1-stained pDNA complexed with the indicated polymers revealed localization within HEK cells. For proving whether the endosomal escape of polymers **A-*g*-Ox$_5$(10)** and **M-*g*-Ox$_5$(10)**, showing transfection, differs from **A-*g*-Ox$_5$(30)** and **M-*g*-Ox$_5$(30)**, showing no transfection but good uptake, a colocalization experiment was performed. Therefore, the polyplexes, including the references **PA**, **PM**, and lPEI (YOYO-1-labeled), and LysoTracker Red-labeled endolysosomes were investigated regarding their colocalization after 4 h. A colocalization of both signals (yellow signals) indicates that the pDNA is located inside the endolysosomes. Green signals (YOYO-1) refer to pDNA located outside the endolysosomes and might indicate an efficient release from the endosome. Polyplexes of **A-*g*-Ox$_5$(10)** and **M-*g*-Ox$_5$(10)** revealed a reduced correlation factor of 0.25 to 0.26 compared to the polyplexes formed with **A-*g*-Ox$_5$(30)** and **M-*g*-Ox$_5$(30)** (0.41 and 0.35). This correlates well with the observed transfection efficiency of **A-*g*-Ox$_5$(10)** and **M-*g*-Ox$_5$(10)** and might be linked to a more efficient endosomal release, mandatory for a successful transfection. In comparison to lPEI (R = 0.17), both best performers showed slightly higher correlation factors, which is in agreement with the transfection efficiencies obtained. The homopolymers **PA** and **PM** exhibited low correlation factors, indicating a superior release capability, which is in accordance with the previously reported data.[16]

Structure Correlation. Up to this point, the polymers' properties have only been discussed concerning their DG or side chain DP. By increasing both, the fraction of shielding units is increased. For further investigating if simply the overall molar

DOI: 10.1021/acs.biomac.8b00362
Biomacromolecules 2018, 19, 2759−2771

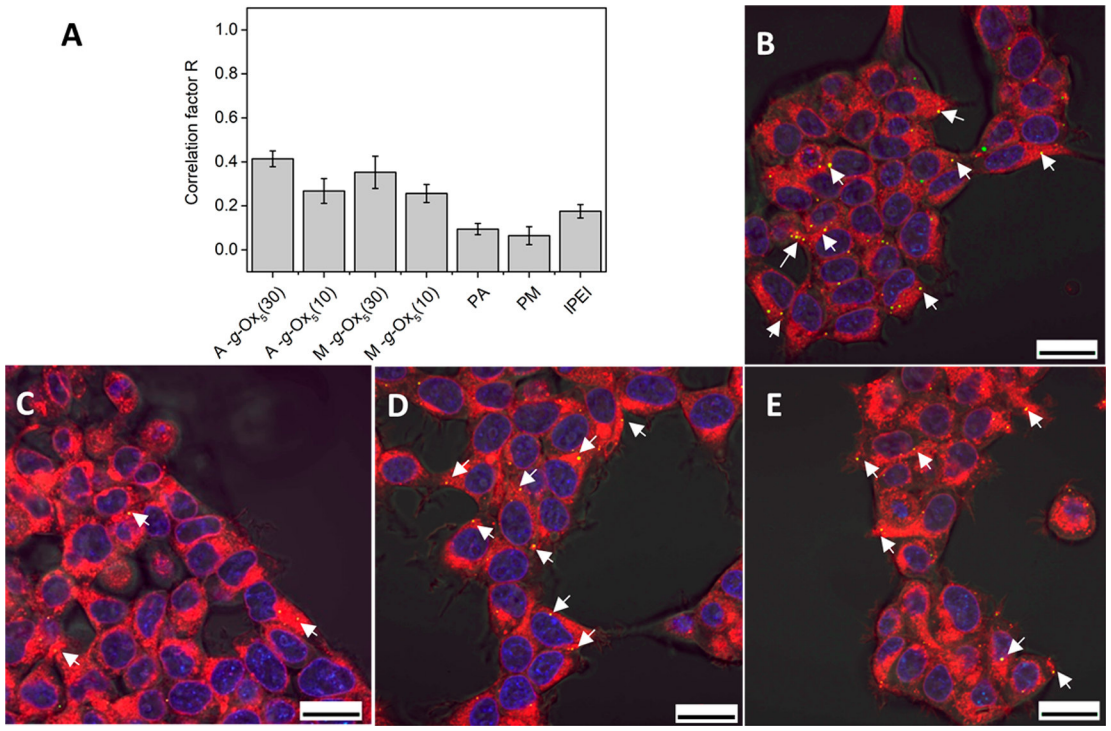

Figure 7. Imaging of HEK cells transfected with the indicated polymers in growth media for 4 h and stained with Hoechst (blue) for the cell nuclei, LysoTracker Red (red) for endolysosomes, and YOYO-1-labeled pDNA (green). Outer fluorescence was quenched with trypan blue. (A) Correlation factor of LysoTracker Red and YOYO-1 for polyplexes in endolysosomes. (B–E) Representative images of polyplexes formed with **A-*g*-Ox$_5$(10)** (B), **A-*g*-Ox$_5$(30)** (C), **M-*g*-Ox$_5$(10)** (D), and **M-*g*-Ox$_5$(30)** (E). Scale bar represents 20 μm. Data represent mean ± SEM of five technical and at least three biological replicates. White arrows indicate examples of colocalized pDNA polymer complexes in endolysosomes.

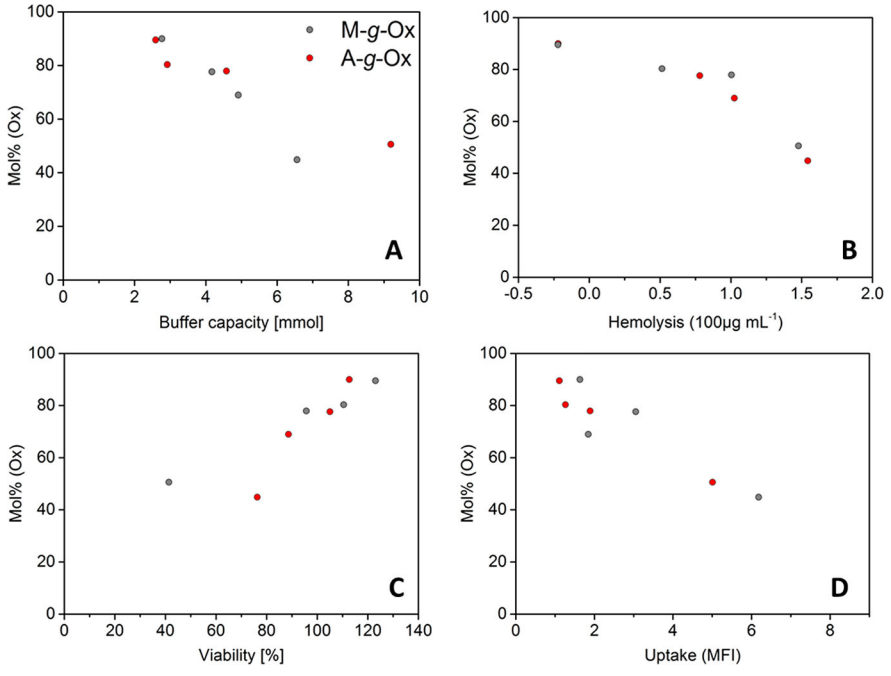

Figure 8. Structure–property relation of (A) the buffer capacity at pH 6, (B) uptake MFI, (C) viability at 500 μg mL^{-1}, and (D) hemolysis rate at 100 μg mL^{-1} against the mol% of 2-oxazoline moieties (see Table 2). Graft copolymers based on AEMA are depicted in red, and MAEMA-based polymers are depicted in gray.

fraction of Ox moieties is directly influencing the tranfection-related properties such as buffer capacity, hemolysis activity, viability, and uptake efficiency, those properties were plotted against the Ox mol% in Figure 8. The buffer capacity at pH 7 decreases with increasing molar fraction of Ox (Figure 8A). This is expected as the graft copolymers with higher Ox content feature fewer amino moieties. The hemolysis rate, and thereby the strong membrane interaction, is increasing with decreasing Ox content (Figure 8B). This is in good agreement with the results obtained for the viability, as we often observe a

DOI: 10.1021/acs.biomac.8b00362
Biomacromolecules 2018, 19, 2759–2771

dependency of the biocompatibility on the hemolytic properties. Indeed, the viability is increasing with the molar Ox fraction, i.e., with decreasing number of amino moieties (Figure 8C). Furthermore, the uptake is directly dependent on the molar fraction of Ox: It is increasing with decreasing Ox content. In general, it can be summarized that these poperties of the graft copolymers are independent from the DG or the side chain DP and only dependent on the overall number of shielding repeating units, i.e., the molar Ox fraction.

SUMMARY AND CONCLUSIONS

An eight membered library of graft copolymers comprising PAEMA as well as PMAEMA backbones and PEtOx side chains with a DP of 5 or 20 was successfully obtained. They were fully characterized using SEC and NMR spectroscopy and featured pK_a values between 7.39 and 7.9. Biocompatibility tests revealed that already a DG of 10 and a side chain DP of 5 led to a significant reduction of cytotoxic effects with regards to viability and hemolytic activity with the PEARSON correlation (calculation model for the significance of correlations between two factors; correlation $0.6 < x > -0.6$) of 0.88 and −0.91, respectively (see Table S2). All graft copolymers were able to complex pDNA in a sufficient and reversible manner. Polyplexes formed from graft copolymers with a side chain DP of 5 were efficiently internalized into HEK cells. The uptake of these graft copolymers was dependent on the use of serum-enriched medium with regards to the MFI after 4 h. This is in contrast to the shielding properties reported for PEG, which is known for serum-independent uptake and transfection.[29] However, only the copolymers **A-*g*-Ox$_5$(10)** and **M-*g*-Ox$_5$(10)** with low side chain DP and low DG achieved reasonable transfection efficiencies. This leads to the hypothesis that the degree of shielding (DG of 30 and side chain DP of 20) was too high for the endosomal escape and, as a consequence, for efficient transfection. Although PEG shielding is usually reported to reduce the transfection efficiency in comparison to the unshielded polymers, the transfection efficiency of **PA** (45%) was retained in the graft copolymer **A-*g*-Ox$_5$(10)** (Figure 9). Even though a reduction of the transfection efficiency of **M-*g*-Ox$_5$(10)** compared to **PM** was observed, a strong improvement in the biocompatibility was revealed. In comparison to the shielded methacrylate copolymers, the transfection standard lPEI revealed high transfection efficiency but results simultaneously in significantly reduced cell viability.

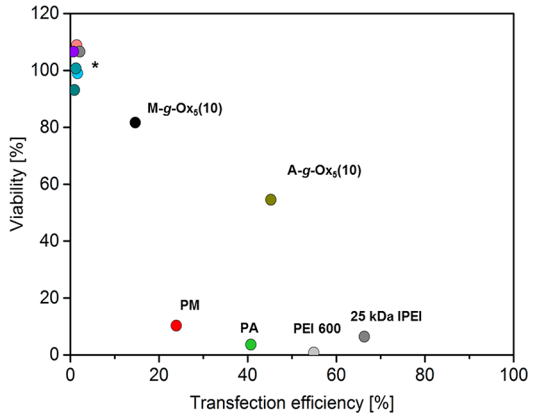

Figure 9. Depiction of viability (at 200 μg mL^{-1} polymer addition) of L929 cells vs transfection efficiency for adherent HEK cells in OptiMEM (at N*/P 30) after 24 h for living cells of the methacrylate-based polyplexes of **PM** (black), **PA** (red), **A-*g*-Ox$_5$(10)**, and **M-*g*-Ox$_5$(10)** as assigned, ***A-*g*-Ox$_{5/20}$(10/30)** and **M-*g*-Ox$_{5/20}$(10/30)**, and the self-synthesized lPEI DP 600[54] (dark gray) as well as the commercial lPEI 25 kDa (light gray) from Polyscience.

In fact, the commercial gold standard lPEI includes ∼11% unhydrolized EtOx units, serving as shielding moieties,[55,56] which is obvious from the comparison with the previously published data for self-synthesized lPEI 600 with a hydrolysis degree of >98%.[57] Figure 9 clearly demonstrates the strong reduction of the cytotoxic effects of **A-*g*-Ox$_5$(10)** and **M-*g*-Ox$_5$(10)** while the transfection efficiency of the primary amine-bearing polymer **A-*g*-Ox$_5$(10)** improved against the homopolymer **PA**.

Our future research will concentrate on further decreasing the PEtOx content of the graft copolymers to explore if the transfection efficiency can be further improved while maintaining the beneficial significantly reduced cytotoxicity that is induced by the PEtOx side chains.

ASSOCIATED CONTENT

Supporting Information

The Supporting Information is available free of charge on the ACS Publications website at DOI: 10.1021/acs.biomac.8b00362.

Additional NMR spectra and SEC elugrams, tritration curves, erythrocyte aggregation test, zeta potentials, DLS size distributions, and PEARSON correlation factors (PDF)

AUTHOR INFORMATION

Corresponding Author

*E-mail: ulrich.schubert@uni-jena.de.

ORCID

Ulrich S. Schubert: 0000-0003-4978-4670

Notes

The authors declare no competing financial interest.

ACKNOWLEDGMENTS

The authors gratefully acknowledge the Bundesministerium für Bildung und Forschung (BMBF, Germany, #031A518B Vectura, #13XP5034A PolyBioMik) and the support by the DFG-funded Collaborative Research Centre PolyTarget (SFB 1278, projects Z01, B06). The authors thankfully acknowledge Elisabeth Preußger for the conduction of uptake experiments, Carolin Kellner for alamarBlue, hemolysis, and aggregation assays, and Michael Dirauf for support with macromonomer synthesis. The LSM880 ELYRA PS.1 was further funded with a grant from the DFG.

REFERENCES

(1) Lehn, P.; Fabrega, S.; Oudrhiri, N.; Navarro, J. Gene delivery systems: Bridging the gap between recombinant viruses and artificial vectors. *Adv. Drug Delivery Rev.* **1998**, *30* (1), 5−11.

(2) Mintzer, M. A.; Simanek, E. E. Nonviral vectors for gene delivery. *Chem. Rev.* **2009**, *109* (2), 259−302.

(3) Rinkenauer, A. C.; Schubert, S.; Traeger, A.; Schubert, U. S. The influence of polymer architecture on in vitro pDNA transfection. *J. Mater. Chem. B* **2015**, *3* (38), 7477−7493.

(4) Jones, C. H.; Chen, C.-K.; Ravikrishnan, A.; Rane, S.; Pfeifer, B. A. Overcoming nonviral gene delivery barriers: Perspective and future. *Mol. Pharmaceutics* **2013**, *10* (11), 4082−4098.

(5) Aied, A.; Greiser, U.; Pandit, A.; Wang, W. Polymer gene delivery: Overcoming the obstacles. *Drug Discovery Today* **2013**, *18* (21), 1090−1098.

DOI: 10.1021/acs.biomac.8b00362
Biomacromolecules 2018, 19, 2759−2771

(6) Behr, J.-P. The proton sponge: A trick to enter cells the viruses did not exploit. *Chimia* **1997**, *51* (1−2), 34−36.
(7) Forrest, M. L.; Pack, D. W. On the kinetics of polyplex endocytic trafficking: Implications for gene delivery vector design. *Mol. Ther.* **2002**, *6* (1), 57−66.
(8) Funhoff, A. M.; van Nostrum, C. F.; Koning, G. A.; Schuurmans-Nieuwenbroek, N. M. E.; Crommelin, D. J. A.; Hennink, W. E. Endosomal escape of polymeric gene delivery complexes is not always enhanced by polymers buffering at low pH. *Biomacromolecules* **2004**, *5* (1), 32−39.
(9) Wilkosz, N.; Jamróz, D.; Kopeć, W.; Nakai, K.; Yusa, S.-i.; Wytrwal-Sarna, M.; Bednar, J.; Nowakowska, M.; Kepczynski, M. Effect of Polycation Structure on Interaction with Lipid Membranes. *J. Phys. Chem. B* **2017**, *121* (30), 7318−7326.
(10) Vaidyanathan, S.; Orr, B. G.; Banaszak Holl, M. M. Role of Cell Membrane−Vector Interactions in Successful Gene Delivery. *Acc. Chem. Res.* **2016**, *49* (8), 1486−1493.
(11) Nakase, I.; Kobayashi, S.; Futaki, S. Endosome-disruptive peptides for improving cytosolic delivery of bioactive macromolecules. *Biopolymers* **2010**, *94* (6), 763−770.
(12) Pack, D. W.; Hoffman, A. S.; Pun, S.; Stayton, P. S. Design and development of polymers for gene delivery. *Nat. Rev. Drug Discovery* **2005**, *4* (7), 581−593.
(13) Li, H.; Cortez, M. A.; Phillips, H. R.; Wu, Y.; Reineke, T. M. Poly(2-deoxy-2-methacrylamido glucopyranose)-b-poly(methacrylate amine)s: Optimization of diblock glycopolycations for nucleic acid delivery. *ACS Macro Lett.* **2013**, *2* (3), 230−235.
(14) Smith, A. E.; Sizovs, A.; Grandinetti, G.; Xue, L.; Reineke, T. M. Diblock glycopolymers promote colloidal stability of polyplexes and effective pDNA and siRNA delivery under physiological salt and serum conditions. *Biomacromolecules* **2011**, *12* (8), 3015−3022.
(15) Ma, M.; Li, F.; Yuan, Z.-f.; Zhuo, R.-x. Influence of hydroxyl groups on the biological properties of cationic polymethacrylates as gene vectors. *Acta Biomater.* **2010**, *6* (7), 2658−2665.
(16) Trützschler, A.-K.; Bus, T.; Reifarth, M.; Brendel, J. C.; Höppener, S.; Traeger, A.; Schubert, U. S. Beyond gene transfection with methacrylate-based polyplexes − The influence of the amino substitution pattern. *Bioconjugate Chem.* **2018**, DOI: 10.1021/acs.bioconjchem.8b00074.
(17) Fischer, D.; Li, Y.; Ahlemeyer, B.; Krieglstein, J.; Kissel, T. In vitro cytotoxicity testing of polycations: Influence of polymer structure on cell viability and hemolysis. *Biomaterials* **2003**, *24* (7), 1121−1131.
(18) Godbey, W. T.; Wu, K. K.; Mikos, A. G. Poly(ethylenimine) and its role in gene delivery. *J. Controlled Release* **1999**, *60* (2), 149−160.
(19) Sprouse, D.; Reineke, T. M. Investigating the effects of block versus statistical glycopolycations containing primary and tertiary amines for plasmid DNA delivery. *Biomacromolecules* **2014**, *15* (7), 2616−2628.
(20) Veronese, F. M.; Pasut, G. PEGylation, successful approach to drug delivery. *Drug Discovery Today* **2005**, *10* (21), 1451−1458.
(21) Choi, Y. H.; Liu, F.; Kim, J.-S.; Choi, Y. K.; Park, J. S.; Kim, S. W. Polyethylene glycol-grafted poly-l-lysine as polymeric gene carrier. *J. Controlled Release* **1998**, *54* (1), 39−48.
(22) Ogris, M.; Walker, G.; Blessing, T.; Kircheis, R.; Wolschek, M.; Wagner, E. Tumor-targeted gene therapy: Strategies for the preparation of ligand−polyethylene glycol−polyethylenimine/DNA complexes. *J. Controlled Release* **2003**, *91* (1), 173−181.
(23) Üzgün, S.; Akdemir, Ö.; Hasenpusch, G.; Maucksch, C.; Golas, M. M.; Sander, B.; Stark, H.; Imker, R.; Lutz, J.-F.; Rudolph, C. Characterization of tailor-made copolymers of oligo(ethylene glycol) methyl ether methacrylate and N,N-dimethylaminoethyl methacrylate as nonviral gene transfer agents: Influence of macromolecular structure on gene vector particle properties and transfection efficiency. *Biomacromolecules* **2010**, *11* (1), 39−50.
(24) Hinton, T. M.; Guerrero-Sanchez, C.; Graham, J. E.; Le, T.; Muir, B. W.; Shi, S.; Tizard, M. L. V.; Gunatillake, P. A.; McLean, K. M.; Thang, S. H. The effect of RAFT-derived cationic block copolymer structure on gene silencing efficiency. *Biomaterials* **2012**, *33* (30), 7631−7642.
(25) Armstrong, J. K. The occurance, induction, specifity and potential effect of antibodies against poly(ethylene glycol). In *PEGylated Protein Drugs: Basic Science and Clinical Applications*; Veronese, F. M., Ed.; Birkhäuser Verlag: Switzerland, 2009; p 287.
(26) Richter, A. W.; Akerblom, E. Polyethylene glycol reactive antibodies in man: Titer distribution in allergic patients treated with monomethoxy polyethylene glycol modified allergens or placebo, and in healthy blood donors. *Int. Arch. Allergy Immunol.* **2004**, *74* (1), 36−39.
(27) Garay, R. P.; El-Gewely, R.; Armstrong, J. K.; Garratty, G.; Richette, P. Antibodies against polyethylene glycol in healthy subjects and in patients treated with PEG-conjugated agents. *Expert Opin. Drug Delivery* **2012**, *9* (11), 1319−1323.
(28) Ganson, N. J.; Kelly, S. J.; Scarlett, E.; Sundy, J. S.; Hershfield, M. S. Control of hyperuricemia in subjects with refractory gout, and induction of antibody against poly(ethylene glycol) (PEG), in a phase I trial of subcutaneous PEGylated urate oxidase. *Arthritis Res. Ther.* **2006**, *8* (1), R12.
(29) Knop, K.; Hoogenboom, R.; Fischer, D.; Schubert, U. S. Poly(ethylene glycol) in drug delivery: Pros and cons as well as potential alternatives. *Angew. Chem., Int. Ed.* **2010**, *49* (36), 6288−6308.
(30) Bauer, M.; Lautenschlaeger, C.; Kempe, K.; Tauhardt, L.; Schubert, U. S.; Fischer, D. Poly(2-ethyl-2-oxazoline) as alternative for the stealth polymer poly(ethylene glycol): Comparison of in vitro cytotoxicity and hemocompatibility. *Macromol. Biosci.* **2012**, *12* (7), 986−998.
(31) Luxenhofer, R.; Han, Y.; Schulz, A.; Tong, J.; He, Z.; Kabanov, A. V.; Jordan, R. Poly(2-oxazoline)s as polymer therapeutics. *Macromol. Rapid Commun.* **2012**, *33* (19), 1613−1631.
(32) Sedlacek, O.; Monnery, B. D.; Filippov, S. K.; Hoogenboom, R.; Hruby, M. Poly(2-Oxazoline)s − Are they more advantageous for biomedical applications than other polymers? *Macromol. Rapid Commun.* **2012**, *33* (19), 1648−1662.
(33) Gaspar, V. M.; Gonçalves, C.; de Melo-Diogo, D.; Costa, E. C.; Queiroz, J. A.; Pichon, C.; Sousa, F.; Correia, I. J. Poly(2-ethyl-2-oxazoline)−PLA-g−PEI amphiphilic triblock micelles for co-delivery of minicircle DNA and chemotherapeutics. *J. Controlled Release* **2014**, *189*, 90−104.
(34) Gaspar, V. M.; Baril, P.; Costa, E. C.; de Melo-Diogo, D.; Foucher, F.; Queiroz, J. A.; Sousa, F.; Pichon, C.; Correia, I. J. Bioreducible poly(2-ethyl-2-oxazoline)−PLA−PEI-SS triblock copolymer micelles for co-delivery of DNA minicircles and doxorubicin. *J. Controlled Release* **2015**, *213*, 175−191.
(35) von Erlach, T.; Zwicker, S.; Pidhatika, B.; Konradi, R.; Textor, M.; Hall, H.; Lühmann, T. Formation and characterization of DNA-polymer-condensates based on poly(2-methyl-2-oxazoline) grafted poly(l-lysine) for non-viral delivery of therapeutic DNA. *Biomaterials* **2011**, *32* (22), 5291−5303.
(36) Ahmed, M.; Narain, R. Progress of RAFT based polymers in gene delivery. *Prog. Polym. Sci.* **2013**, *38* (5), 767−790.
(37) Ohshima, H. A Simple Expression for Henry's Function for the Retardation Effect in Electrophoresis of Spherical Colloidal Particles. *J. Colloid Interface Sci.* **1994**, *168* (1), 269−271.
(38) Palermo, E. F.; Vemparala, S.; Kuroda, K. Cationic spacer arm design strategy for control of antimicrobial activity and conformation of amphiphilic methacrylate random copolymers. *Biomacromolecules* **2012**, *13* (5), 1632−1641.
(39) Sinclair, A.; Bai, T.; Carr, L. R.; Ella-Menye, J.-R.; Zhang, L.; Jiang, S. Engineering buffering and hydrolytic or photolabile charge shifting in a polycarboxybetaine ester gene delivery platform. *Biomacromolecules* **2013**, *14* (5), 1587−1593.
(40) Weber, C.; Becer, C. R.; Hoogenboom, R.; Schubert, U. S. Lower critical solution temperature behavior of comb and graft shaped poly[oligo(2-ethyl-2-oxazoline)methacrylate]s. *Macromolecules* **2009**, *42* (8), 2965−2971.
(41) Pezzoli, D.; Giupponi, E.; Mantovani, D.; Candiani, G. Size matters for in vitro gene delivery: investigating the relationships among complexation protocol, transfection medium, size and sedimentation. *Sci. Rep.* **2017**, *7*, 44134.

DOI: 10.1021/acs.biomac.8b00362
Biomacromolecules 2018, 19, 2759−2771

(42) Weber, C.; Krieg, A.; Paulus, R. M.; Lambermont-Thijs, H. M. L.; Becer, C. R.; Hoogenboom, R.; Schubert, U. S. Thermal properties of oligo(2-ethyl-2-oxazoline) containing comb and graft copolymers and their aqueous solutions. *Macromol. Symp.* **2011**, *308* (1), 17−24.
(43) Agarwal, S.; Zhang, Y.; Maji, S.; Greiner, A. PDMAEMA based gene delivery materials. *Mater. Today* **2012**, *15* (9), 388−393.
(44) Layman, J. M.; Ramirez, S. M.; Green, M. D.; Long, T. E. Influence of polycation molecular weight on poly(2-dimethylaminoethyl methacrylate)-mediated DNA delivery in vitro. *Biomacromolecules* **2009**, *10* (5), 1244−1252.
(45) Venkataraman, S.; Ong, W. L.; Ong, Z. Y.; Joachim Loo, S. C.; Rachel Ee, P. L.; Yang, Y. Y. The role of PEG architecture and molecular weight in the gene transfection performance of PEGylated poly-(dimethylaminoethyl methacrylate) based cationic polymers. *Biomaterials* **2011**, *32* (9), 2369−2378.
(46) Benjaminsen, R. V.; Mattebjerg, M. A.; Henriksen, J. R.; Moghimi, S. M.; Andresen, T. L. The possible 'proton sponge' effect of polyethylenimine (PEI) does not include change in lysosomal pH. *Mol. Ther.* **2013**, *21* (1), 149−157.
(47) Palermo, E. F.; Lee, D.-K.; Ramamoorthy, A.; Kuroda, K. Role of cationic group structure in membrane binding and disruption by amphiphilic copolymers. *J. Phys. Chem. B* **2011**, *115* (2), 366−375.
(48) Murthy, N.; Robichaud, J. R.; Tirrell, D. A.; Stayton, P. S.; Hoffman, A. S. The design and synthesis of polymers for eukaryotic membrane disruption. *J. Controlled Release* **1999**, *61* (1−2), 137−143.
(49) Luong, D.; Kesharwani, P.; Deshmukh, R.; Mohd Amin, M. C. I.; Gupta, U.; Greish, K.; Iyer, A. K. PEGylated PAMAM dendrimers: Enhancing efficacy and mitigating toxicity for effective anticancer drug and gene delivery. *Acta Biomater.* **2016**, *43*, 14−29.
(50) Mecke, A.; Majoros, I. J.; Patri, A. K.; Baker, J. R.; Banaszak Holl, M. M.; Orr, B. G. Lipid bilayer disruption by polycationic polymers: The roles of size and chemical functional group. *Langmuir* **2005**, *21* (23), 10348−10354.
(51) Weber, C.; Rogers, S.; Vollrath, A.; Hoeppener, S.; Rudolph, T.; Fritz, N.; Hoogenboom, R.; Schubert, U. S. Aqueous solution behavior of comb-shaped poly(2-ethyl-2-oxazoline). *J. Polym. Sci., Part A: Polym. Chem.* **2013**, *51* (1), 139−148.
(52) Hoffmann, J.; Groll, J.; Heuts, J.; Rong, H.; Klee, D.; Ziemer, G.; Moeller, M.; Wendel, H. P. Blood cell and plasma protein repellent properties of star-PEG-modified surfaces. *J. Biomater. Sci., Polym. Ed.* **2006**, *17* (9), 985−996.
(53) Konradi, R.; Pidhatika, B.; Mühlebach, A.; Textor, M. Poly-2-methyl-2-oxazoline: A peptide-like polymer for protein-repellent surfaces. *Langmuir* **2008**, *24* (3), 613−616.
(54) Bus, T.; Englert, C.; Reifarth, M.; Borchers, P.; Hartlieb, M.; Vollrath, A.; Hoeppener, S.; Traeger, A.; Schubert, U. S. 3rd generation poly(ethylene imine)s for gene delivery. *J. Mater. Chem. B* **2017**, *5* (6), 1258−1274.
(55) Tauhardt, L.; Kempe, K.; Knop, K.; Altuntaş, E.; Jäger, M.; Schubert, S.; Fischer, D.; Schubert, U. S. Linear polyethyleneimine: Optimized synthesis and characterization − On the way to "pharmagrade" batches. *Macromol. Chem. Phys.* **2011**, *212* (17), 1918−1924.
(56) Thomas, M.; Lu, J. J.; Ge, Q.; Zhang, C.; Chen, J.; Klibanov, A. M. Full deacylation of polyethylenimine dramatically boosts its gene delivery efficiency and specificity to mouse lung. *Proc. Natl. Acad. Sci. U. S. A.* **2005**, *102* (16), 5679−5684.
(57) Englert, C.; Trützschler, A.-K.; Raasch, M.; Bus, T.; Borchers, P.; Mosig, A. S.; Traeger, A.; Schubert, U. S. Crossing the blood-brain barrier: Glutathione-conjugated poly(ethylene imine) for gene delivery. *J. Controlled Release* **2016**, *241* (Supplement C), 1−14.

DOI: 10.1021/acs.biomac.8b00362
Biomacromolecules 2018, 19, 2759−2771

Supporting Information

The Power of Shielding – Low Toxicity and High Transfection Performance of Cationic Graft Copolymers Containing Poly(2-oxazoline) Side Chains

Anne-Kristin Trützschler,[a,b] Tanja Bus,[a,b] Martin Sahn,[a,b] Anja Traeger,[a,b] Christine Weber,[a,b] Ulrich S. Schubert[a,b]*

[a]Laboratory of Organic and Macromolecular Chemistry (IOMC), Friedrich Schiller University Jena, Humboldtstrasse 10, 07743 Jena, Germany.

[b]Jena Center for Soft Matter (JCSM), Friedrich Schiller University Jena, Philosophenweg 7, 07743 Jena, Germany.

*Correspondence to U. S. Schubert (ulrich.schubert@uni-jena.de)

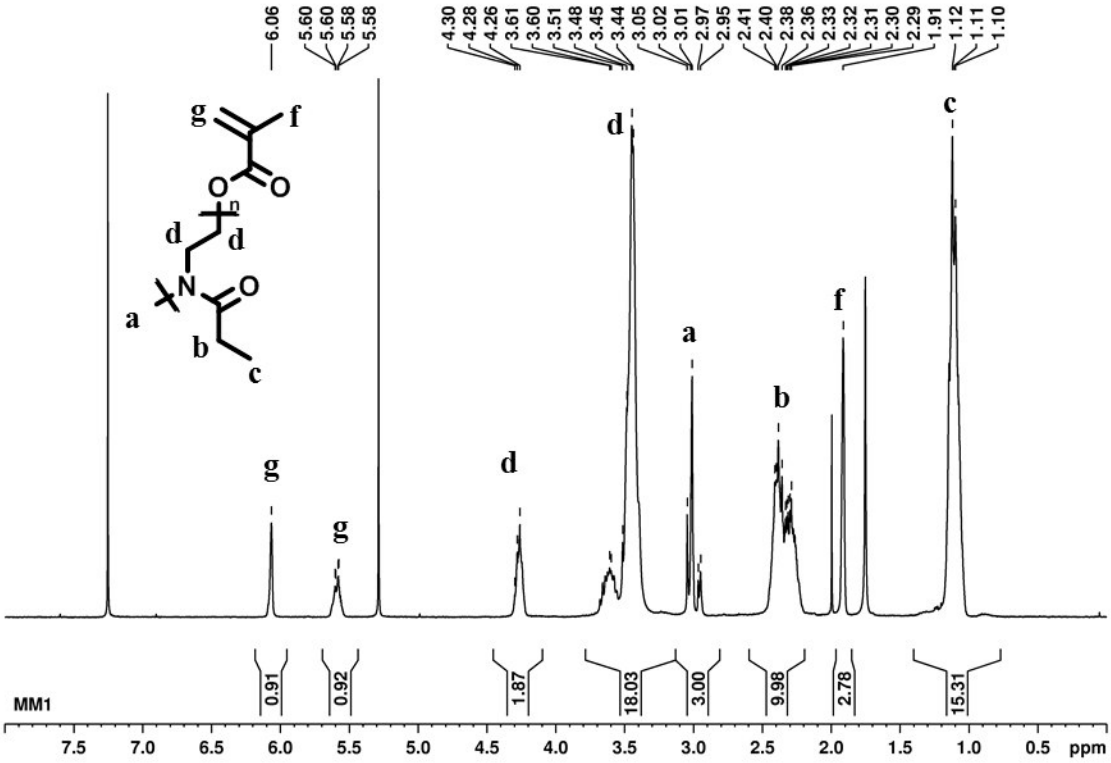

Figure S1: ^{1}H-NMR spectrum (300 MHz, $CDCl_3$) of the macromonomer **Ox_5** (DP = 5). The spectrum was calibrated to the initiating methyl group signal at 3.01 ppm. The unmarked signals belong to solvent residues of acetonitrile and dichlorormethane, respectively.

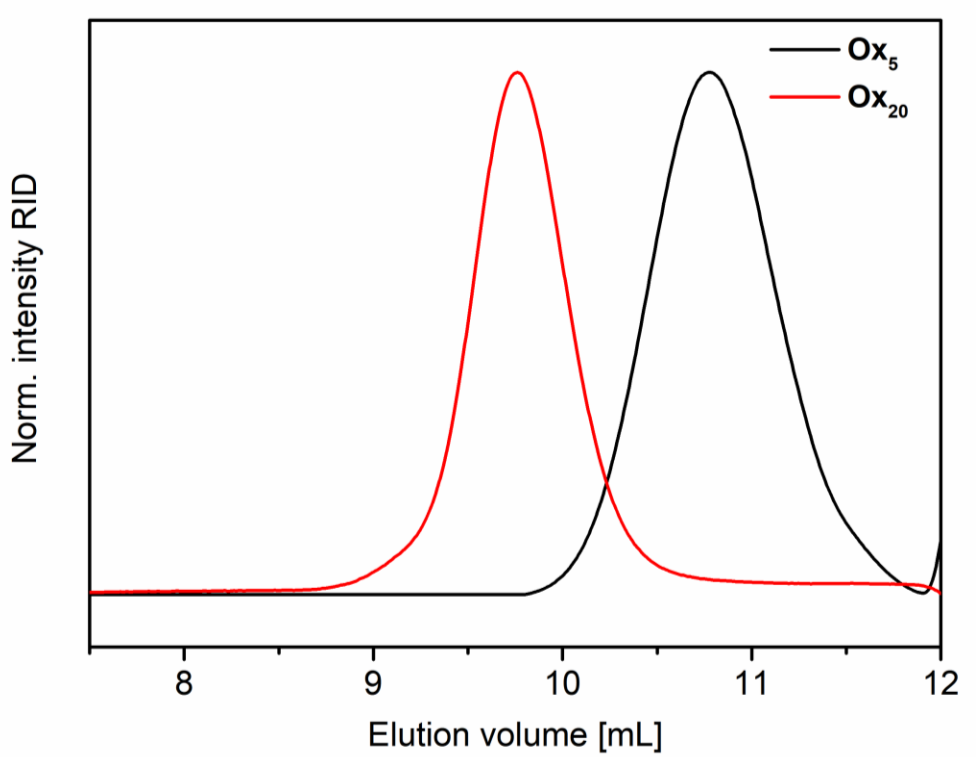

Figure S2: Size exclusion chromatograms of the macromonomers **Ox_5** and **Ox_{20}** ($CHCl_3$, triethylamine, isopropanol (94:4:2)), system signal at 12 min.

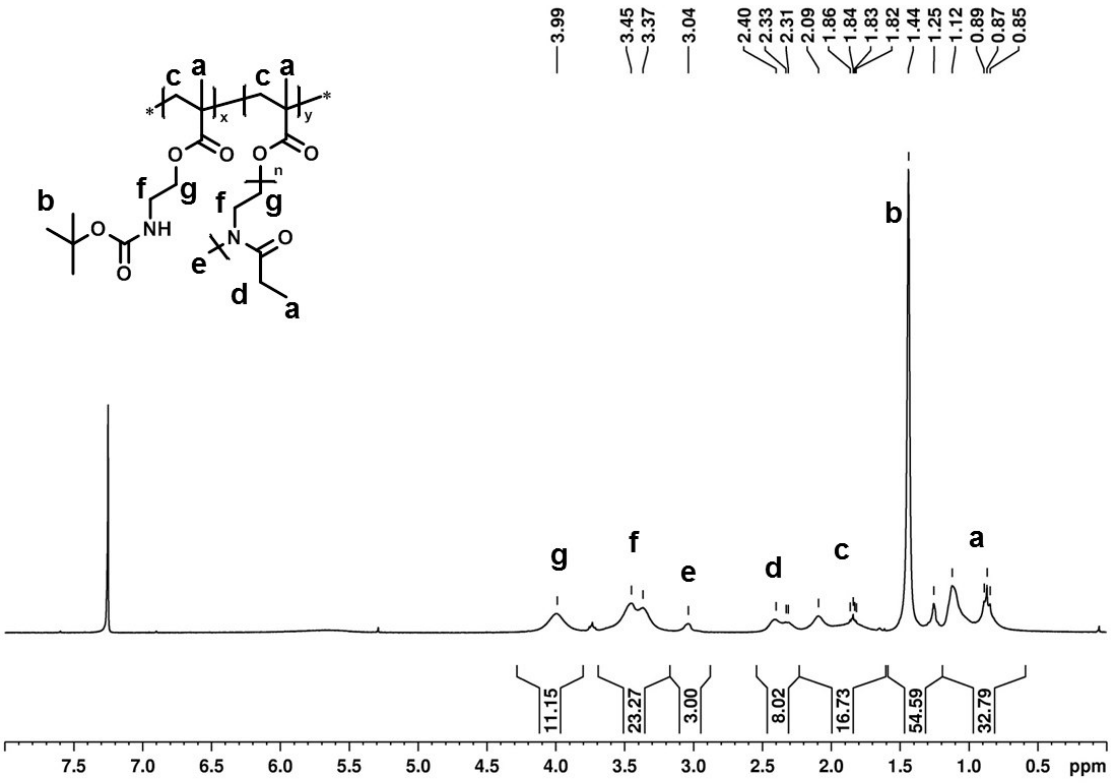

Figure S3: ^{1}H-NMR spectrum (300 MHz, $CDCl_3$) of the protected graft copolymer **BocA-*g*-Ox$_5$(10)** and assignment of the signals to the polymer structure.

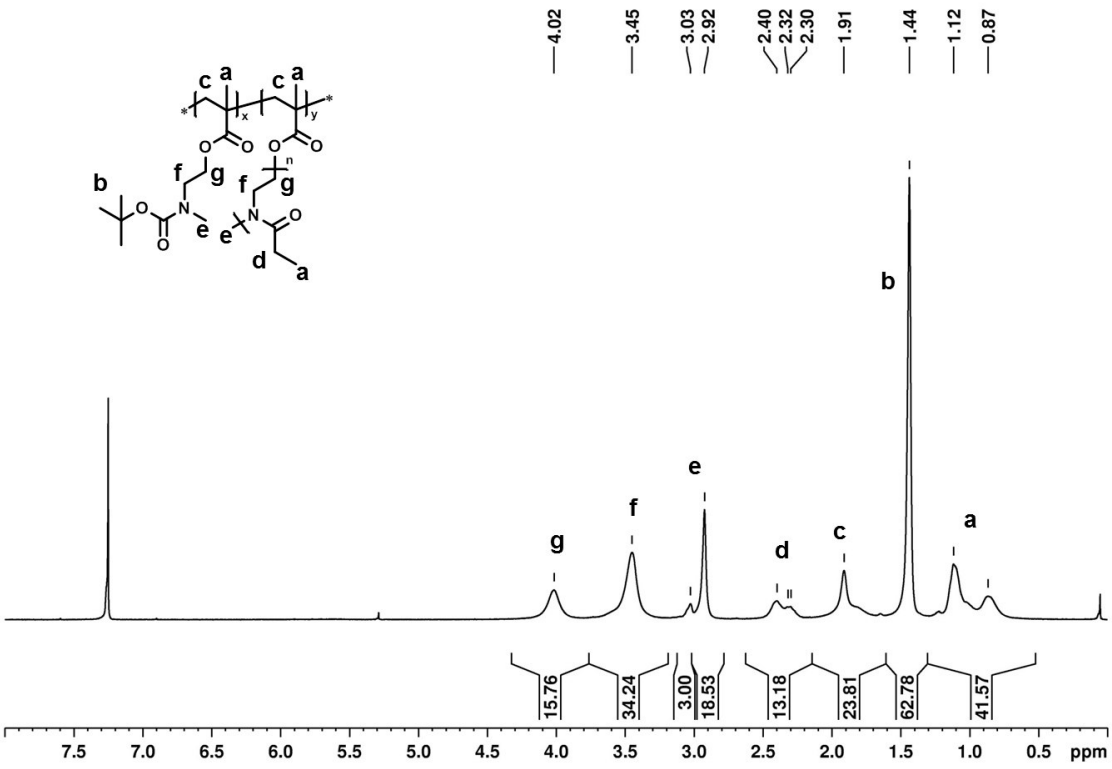

Figure S4: ^{1}H-NMR spectrum (300 MHz, $CDCl_3$) of the protected graft copolymer **M-*g*-Ox$_5$(10)** and assignment of the signals to the polymer structure.

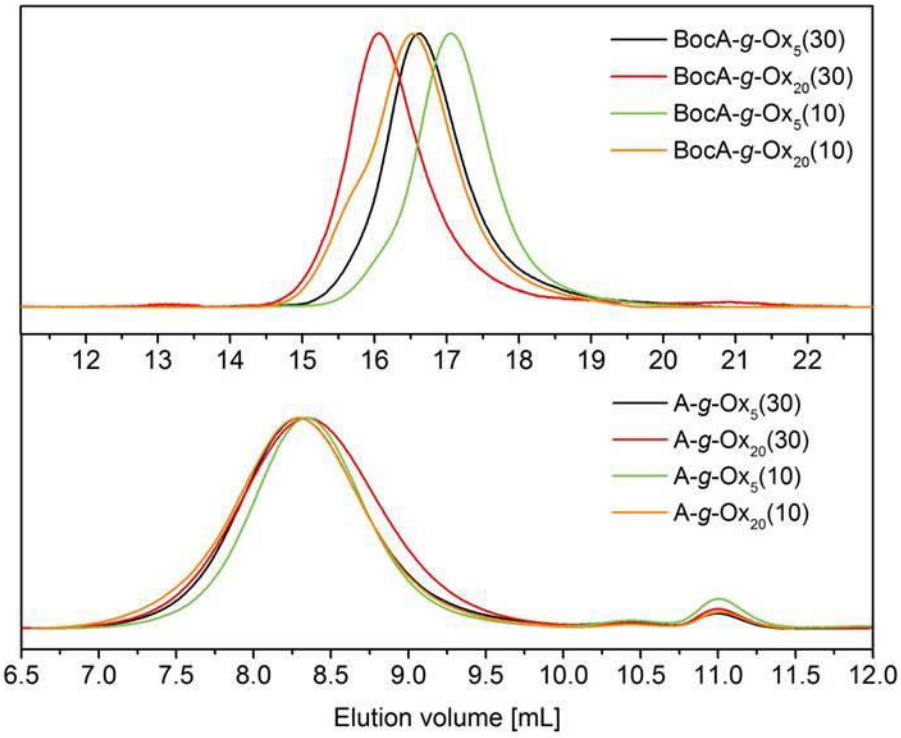

Figure S5: Top: Size exclusion chromatogram of the Boc-protected AEMA based graft-copolymers (DMAc, 0.21% LiCl, RI detection). Bottom: SEC elugrams of the deprotected AEMA based graft copolymers (water, 0.1% trifluoroacetic acid, 0.1 M NaCl). Solvent signal at 10 mL and system peak at 11 mL.

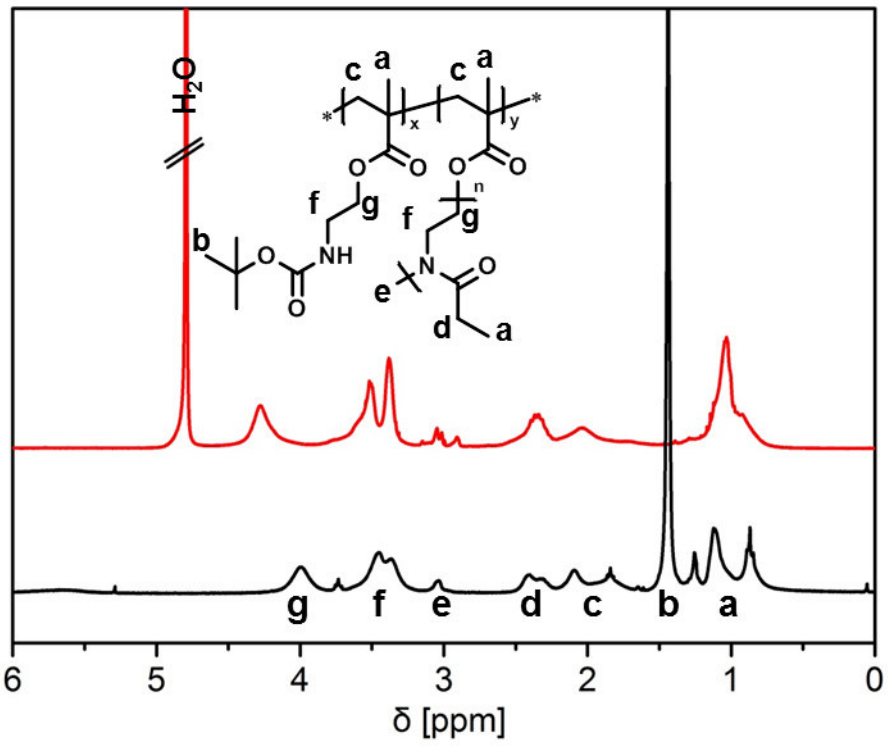

Figure S6: ^{1}H-NMR spectra of **BocA-*g*-Ox$_5$(10)** (black in $CDCl_3$) and **A-*g*-Ox$_5$(10)** (red in D_2O) and assignment of the peaks to the structure of the polymers.

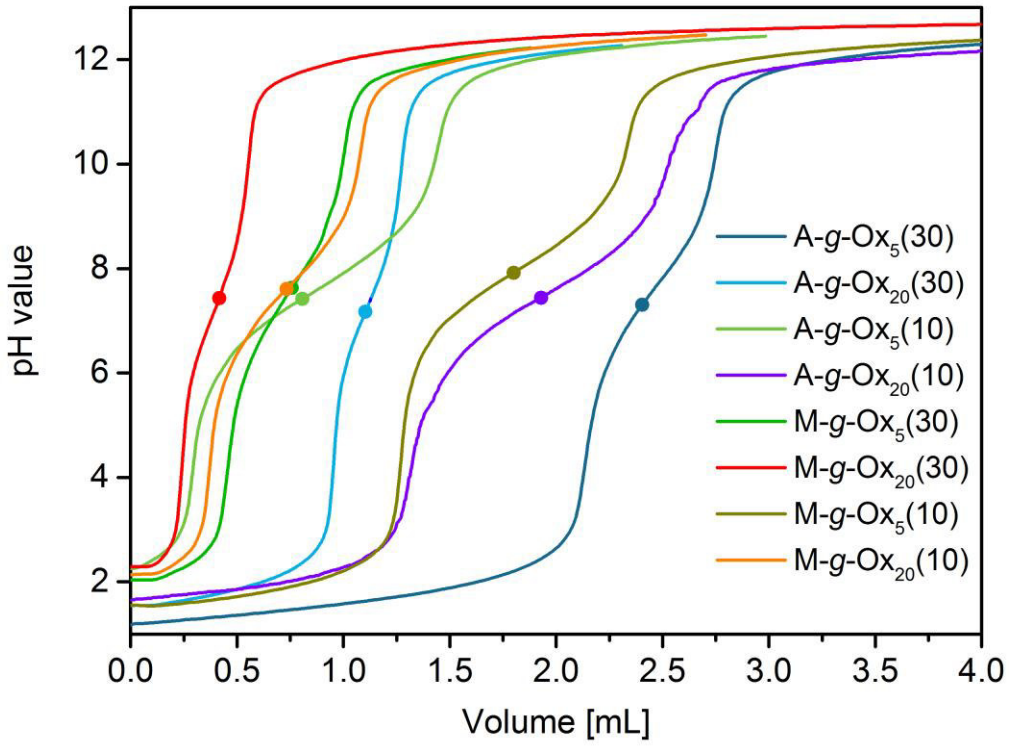

Figure S7: Titration curves of the deprotected graft copolymers (10 mg mL^{-1} in water) against 0.1 M NaOH solution. Calculated pK_a values are highlighted by a filled circle.

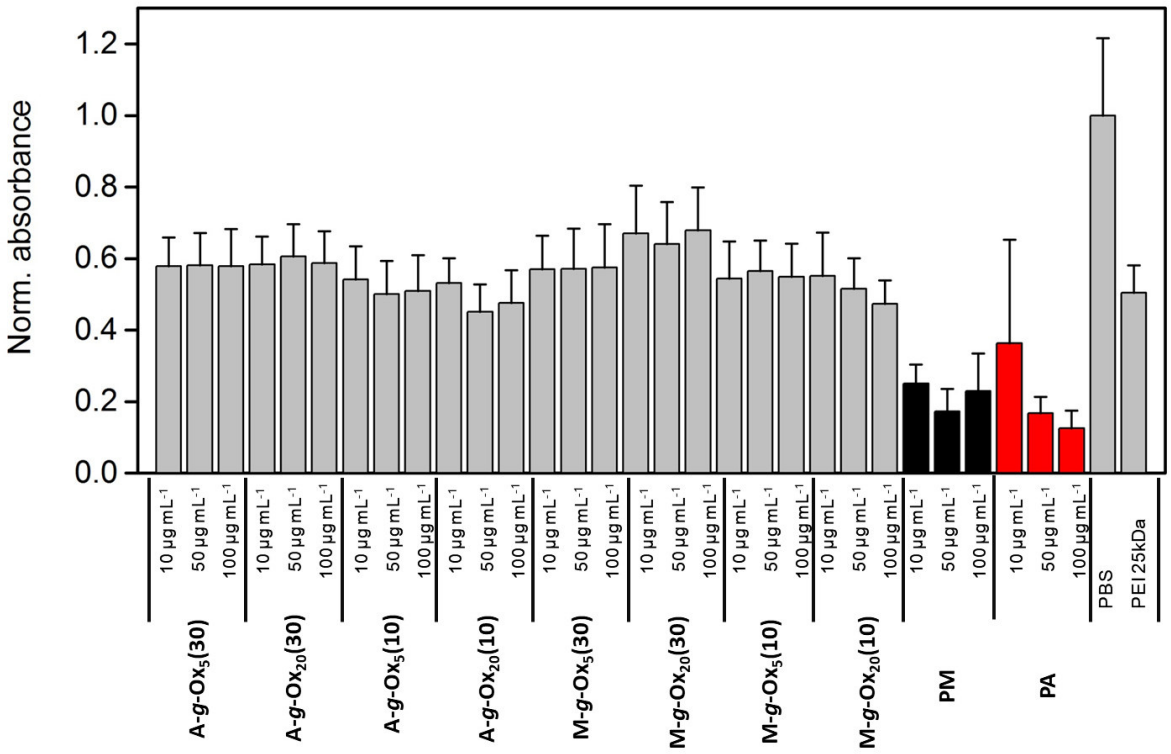

Figure S8: Erythrocyte aggregation assay of **A-g-Ox$_{5/20}$(10/30)** and **M-g-Ox$_{5/20}$(10/30)** at indicated concentrations. BPEI with a molar mass of 25 kDa served as positive control and PBS as negative control.

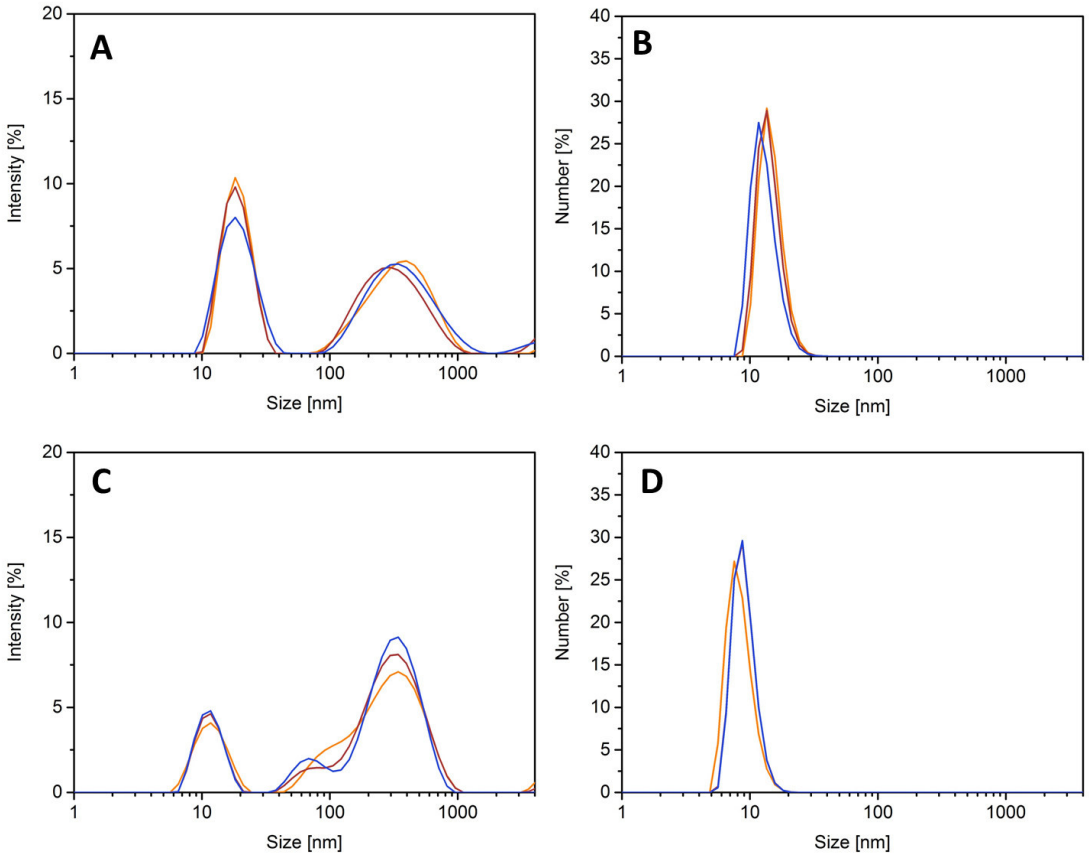

Figure S9: Intensity-weighted (A, C) and number-weighted (B, D) size distributions of **A-*g*-Ox$_{20}$(30)** (**A-B**) and **A-*g*-Ox$_5$(10)** (**C-D**) observed by DLS measurements in 0.1M NaCl solution (c(polymer) = 2 mg mL^{-1}). All measurements were conducted n = 3.

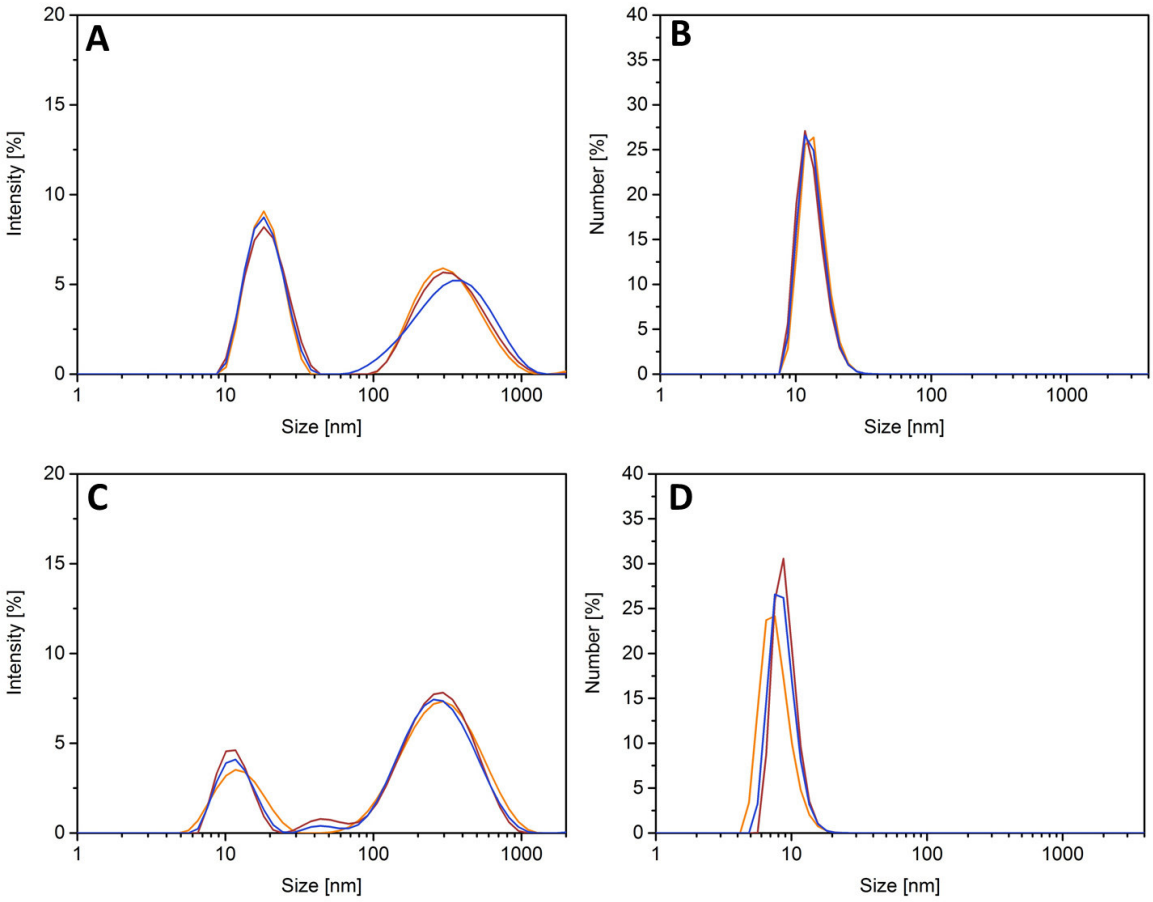

Figure S10: Intensity-weighted (**A**, **C**) and number-weighted (**B**, **D**) size distribution of **A-*g*-Ox$_{20}$(30)** (**A-B**) and **A-*g*-Ox$_5$(10)** (**C-D**) observed by DLS measurements in 0.1M HCl solution. (c(polymer) = 2 mg mL^{-1}). All measurements were conducted n = 3.

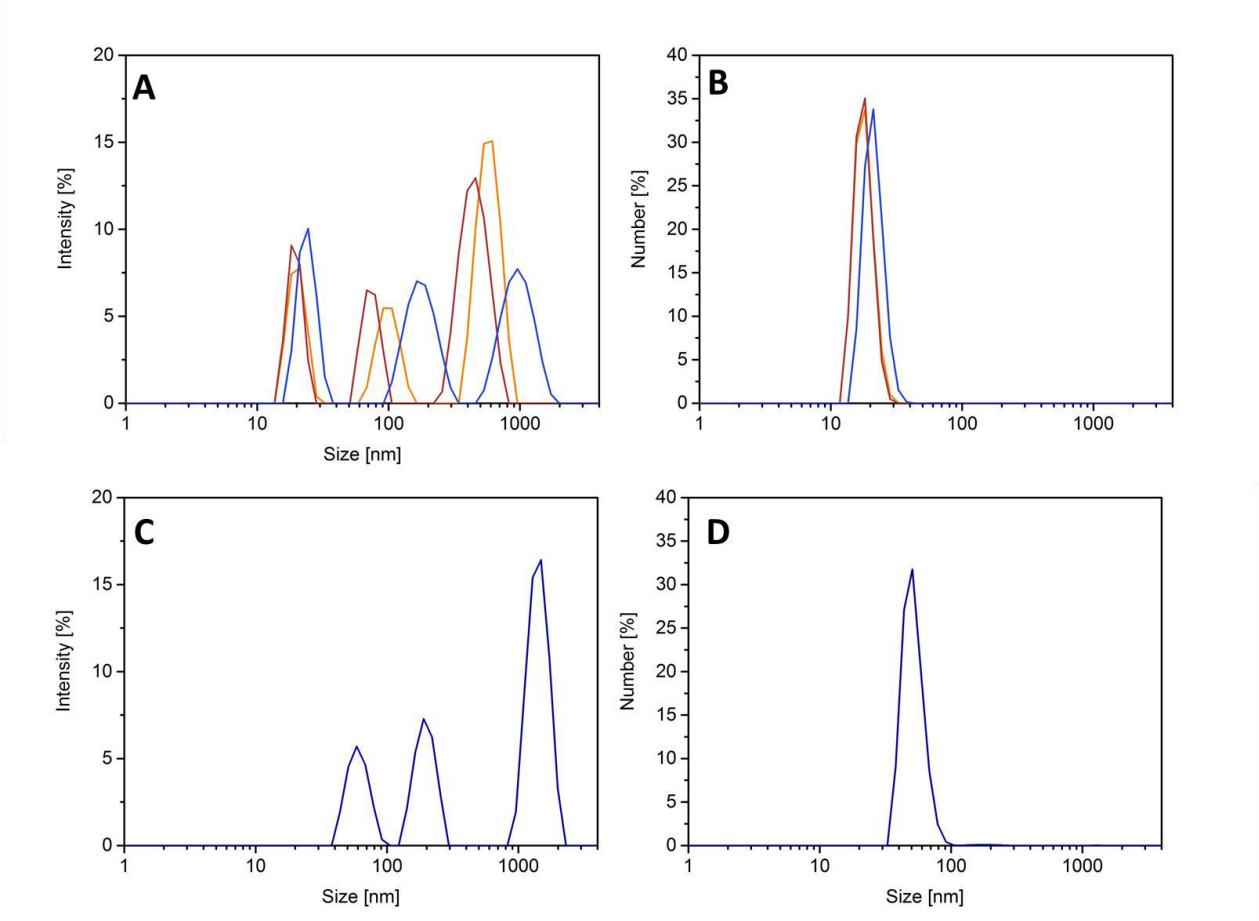

Figure S11: Intensity-weighted (**A**, **C**) and number-weighted (**B**, **D**) size distribution of polyplexes of **A-*g*-Ox$_{20}$(30)** (**A-B**) and **A-*g*-Ox$_5$(10)** (**C-D**) at N*/P 30 observed by DLS measurements in 20 mM 4-(2-hydroxethyl) piperazine-1-ethanesulfonic acid (HEPES) and 5% (w/v) glucose, pH 7.2. All measurements were conducted n = 3.

Table S1: Zeta potentials of the pDNA complexes with **A-*g*-Ox$_{5/20}$(10/30)** and **M-*g*-Ox$_{5/20}$(10/30)** at N*/P 30 measured by electrophoretic mobility measurements (20 mM 4-(2-hydroxethyl) piperazine-1-ethanesulfonic acid (HEPES) and 5% (w/v) glucose, pH 7.2). All measurements were conducted n = 3 separately (15 measurements each).

Polymer sample	Number weighted size polymer, (0.1M NaCl) d [nm]	Number weighted size polymer, (0.1M HCl) d [nm]	Zeta potential [mV]	Number weighted size polyplex, d [nm]
A-*g*-Ox$_5$(30)	11	12	17.6	51
A-*g*-Ox$_{20}$(30)	15	14	19.1	18
A-*g*-Ox$_5$(10)	8	8	15.7	52
A-*g*-Ox$_{20}$(10)	11	12	21.3	50
M-*g*-Ox$_5$(30)	10	11	19.5	71
M-*g*-Ox$_{20}$(30)	12	11	13.2	20
M-*g*-Ox$_5$(10)	11	10	10.4	59
M-*g*-Ox$_{20}$(10)	11	11	15.2	55

Table S2: PEARSON correlation factor, where 0.4 to 0.59 indicates moderate correlation, 0.6 to 0.79 strong correlation and 0.8 to 1 very strong correlation.

	Mol%Ox	Viability (500 µg/mL)	Uptake (MFI) NP30	Transfection (MFI) NP30	Buffer capacity (pH 7)	Hemolysis (100 µg/mL)
Mol%Ox		0.88	-0.92	-0.68	-0.90	-0.91
Viability (500 µg/Ml)	0.88		-0.78	-0.89	-0.99	-0.84
Uptake (MFI) NP30	-0.92	-0.78		0.66	0.83	0.78
Transfection (MFI) NP30	-0.68	-0.89	0.66		0.89	0.55
Buffer capacity (pH 7)	-0.90	-0.99	0.83	0.89		0.85
Hemo (100 µg/mL)	-0.91	-0.84	0.78	0.55	0.85	

No correlation	0.00
Direct correlation	1.00
Invers correlation	-1.00

Publication Pub4

3rd Generation poly(ethylene imine)s for gene delivery

T. Bus, C. Englert, M. Reifarth, P. Borchers, M. Hartlieb, A. Vollrath, S. Hoeppener, A. Traeger, U. S. Schubert

J. Mater. Chem. B **2017**, *5*, 1258-1274.

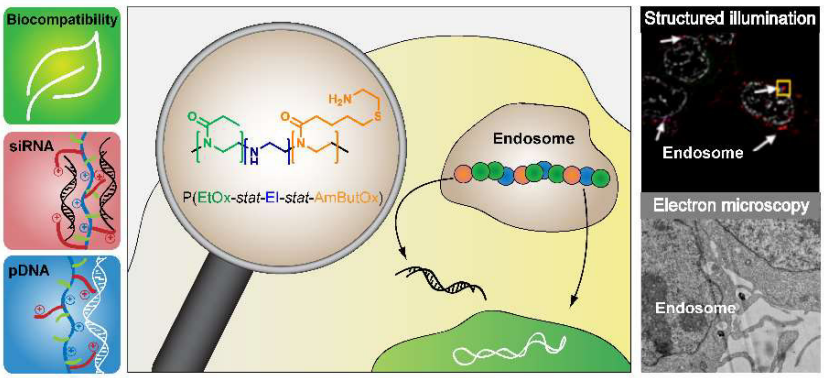

Journal of Materials Chemistry B

PAPER

View Article Online
View Journal | View Issue

Cite this: J. Mater. Chem. B, 2017, 5, 1258

3rd generation poly(ethylene imine)s for gene delivery†

Tanja Bus,‡[ab] Christoph Englert,‡[ab] Martin Reifarth,[abcd] Philipp Borchers,[ab] Matthias Hartlieb,§[ab] Antje Vollrath,[ab] Stephanie Hoeppener,[ab] Anja Traeger*[ab] and Ulrich S. Schubert*[ab]

Received 4th October 2016,
Accepted 20th December 2016

DOI: 10.1039/c6tb02592g

www.rsc.org/MaterialsB

Cationic polymers play a crucial role within the field of gene delivery offering the possibility to circumvent (biological) barriers in an elegant way. However, polymers are accompanied either by a high cytotoxicity or low efficiency. In this study, a series of high molar mass poly(2-oxazoline)-based copolymers was synthesized introducing 2-ethyl-2-oxazoline, ethylene imine, and primary amine bearing monomer units representing a new generation of poly(ethylene imine) (PEI). The potential of these modified PEIs as non-viral gene delivery agents was assessed and compared to linear PEI by studying the cytotoxicity, the polyplex characteristics, the transfection efficiency, and the cellular uptake using plasmid DNA (pDNA) as well as small interfering RNA (siRNA). High transfection efficiencies, even in serum containing media, were achieved using pDNA without revealing any cytotoxic effects on the cell viability at concentrations up to 1 mg mL^{-1}. The delivery potential for siRNA was further investigated showing the importance of polymer composition for different genetic materials. To elucidate the origins for this superior performance, super-resolution and electron microscopy of transfected cells were used, identifying the endosomal release of the polymers as well as a reduced protein interaction as the main difference to PEI-based transfection processes. In this respect, the investigated copolymers represent remarkable alternatives as non-viral gene delivery agents.

Introduction

Within the last decades synthetic polymers emerged as versatile tools in the field of gene delivery.[1] They represent promising alternatives to viral vectors or lipid-based, non-viral transfection agents, since they combine the advantages of large scale production, simple storage conditions, and the availability of a variety of architectures with tailored properties, *e.g.* defined molar masses, end groups, and functionalities.[2] The most prominent representative of synthetic, cationic polymers utilized for nucleic acid delivery is the gold standard poly(ethylene imine) (PEI).[3,4] Subdivided into a linear (lPEI) and a branched (bPEI) topology, it reveals one of the highest cationic-charge-densities of all organic macromolecules.[5] Under physiological conditions, every sixth nitrogen (N) is protonated[6] and able to interact with the phosphate groups (P) of deoxyribonucleic acid (DNA) as well as ribonucleic acid (RNA) to form nanoscale interelectrolyte complexes, so-called polyplexes.[7–9]

lPEI offers the benefit to be synthesized by hydrolysis of poly(2-alkyl-2-oxazoline)s (POx) using a living polymerization process resulting in well-defined structures.[10] However, these advantages are accompanied by a severe cytotoxicity and undesired non-specific interactions with cellular and non-cellular components, both *in vitro* and *in vivo*.[11–13] Various attempts have been made to optimize PEI by focusing on the design of biodegradable[14–16] and biocompatible[17,18] derivatives, which represent the 2nd generation of PEI-based polymers. Carbohydrates, *e.g.* dextran[19] or hydroxyethyl starch (HES),[20] as well as stealth polymers like poly(ethylene glycol) (PEG)[21,22] are extensively studied.[23] Approaches as the introduction of biodegradable linkers, such as disulfide bonds,[24–26] the combination with liposomes[27,28] or the utilization of micelles or nanoparticles in combination with PEI[29,30] are further concepts partially fulfilling the complex requirements. Besides the post-modification of the PEI backbone, the partial hydrolysis of POx, resulting in P(Ox-*stat*-EI) copolymers, represents a

[a] Laboratory of Organic and Macromolecular Chemistry (IOMC), Friedrich Schiller University Jena, Humboldtstrasse 10, 07743 Jena, Germany. E-mail: ulrich.schubert@uni-jena.de, anja.traeger@uni-jena.de
[b] Jena Center for Soft Matter (JCSM), Friedrich Schiller University Jena, Philosophenweg 7, 07743 Jena, Germany
[c] Institute of Physical Chemistry and Abbe Center of Photonics, Friedrich Schiller University Jena, Helmholtzweg 4, 07743 Jena, Germany
[d] Leibniz Institute of Photonic Technology, Albert-Einstein-Strasse 9, 07745 Jena, Germany

† Electronic supplementary information (ESI) available: Fig. S1–S21. See DOI: 10.1039/c6tb02592g

‡ The authors contributed equally to this work.

§ Current address: Department of Chemistry, University of Warwick, Gibbet Hill Road, Coventry, CV4 7AL, UK.

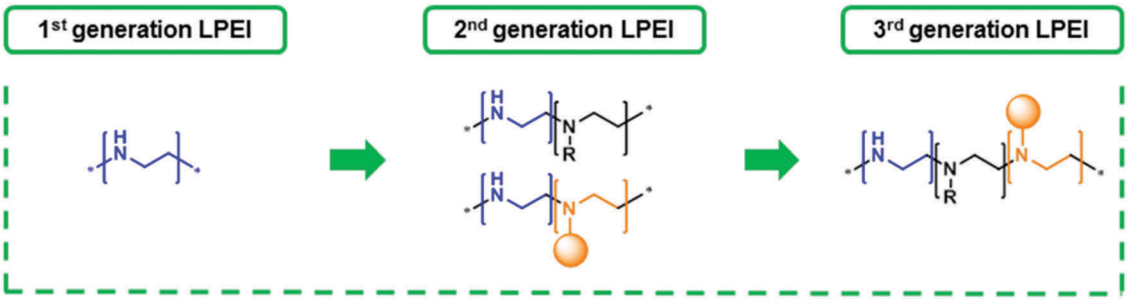

Fig. 1 Overview of different generations of linear poly(ethylene imine) (lPEI). Compared to the original lPEI (1st generation), which has been established over the last decades, the 2nd generation lPEI contains functional monomer units (black or orange) besides the present ethylene imine units (blue). The 3rd generation lPEI describes the presence of multiple functional units comprising cationic functionalities (blue), functional groups to increase cell viability (black) as well as a third group of functionalities (orange, *e.g.* primary amine functionalities or targeting molecules).

promising approach.[31,32] The "stealth behavior" of POx, comparable to PEG, facilitates a reduction of cytotoxicity.[32,33] Although the cytotoxicity problem might be solved, the modifications often result in inefficient gene delivery presumably due to weak DNA complexation and decreased cell interaction.[34] Hence, the design criteria for a perfect polymeric vector are still unknown and other polymer characteristics, *i.e.* the degree of hydrophobicity or synergistic effects of different polycationic species within one polymeric vector, have to be considered.[17,35]

The present contribution focusses on the synthesis of high molar mass copolymers of lPEI and POx. A combination of primary and secondary amines as well as non-charged 2-ethyl-2-oxazoline (EtOx) units was aspired. While different amine species were used to support the polyplex formation, biocompatibility is achieved *via* the integration of EtOx. To realize the synthesis of the targeted polymer structure, a post-polymerization functionalization of partially hydrolyzed high molar mass poly(2-ethyl-2-oxazoline) (PEtOx) was used. The insertion of alkenes is followed by the functionalization *via* thiol–ene click chemistry. This extraordinary combination of modification techniques offers a new platform of copolymers which marks the beginning of a new generation – the 3rd generation of PEI (see Fig. 1).

The designed copolymers were investigated concerning their *in vitro* transfection potential including polyplex characterization, competitor/serum interaction and the cellular uptake mechanism using plasmid DNA as well as siRNA. For a detailed understanding of the mechanism during the gene delivery process super-resolution fluorescence as well as electron microscopy were utilized.

Materials and methods

Materials

2-Ethyl-2-oxazoline (EtOx) and methyl tosylate were obtained from Acros Organics, distilled to dryness (over barium oxide in the case of EtOx), and stored under argon atmosphere. Pyridine, methanol, dichloromethane, 4-*N*,*N*-dimethylaminopyridine (DMAP), 2-(boc-amino)ethanethiol, 2,2-dimethoxy-2-phenylacetophenone (DMPA), trifluoroacetic acid and Amberlyst® A21 (free base) were obtained from Sigma Aldrich (Steinhausen, Germany) and are of analytical grade and were used without further purification. Acetonitrile was purified on a MBraun solvent purification system (MB SPS-800). The dye Cy5 was purchased from Lumiprobe GmbH (Hannover, Germany). *N*-Succinimidyl-4-pentenate was prepared according to literature procedures.[36] The commercially available poly(ethylene imine)s, both the branched (bPEI) as well as the linear (lPEI) type, were purchased from Polysciences (USA). Poly(methacrylic acid) (PMAA, DP = 200) was synthesized according to literature procedures.[37] The transfection reagent jetPRIME, used as positive control for siRNA delivery, was obtained from Polyplus (Polyplus transfection SA, USA). 5-(*N*-Ethyl-*N*-isopropyl)amiloride (EIPA) was purchased from Sigma-Aldrich (Merck, Darmstadt). Ethidium bromide solution (1%, 10 mg mL^{-1}) was purchased from Carl Roth (Karlsruhe, Germany). AlamarBlue, YOYO-1 iodide, Hoechst 33342 trihydrochloride as well as all other indicated CLSM dyes were obtained from Life Technologies (Thermo Fisher Scientific, Germany). If not stated otherwise, cell culture media and solutions (L-glutamine, antibiotics) were obtained from Biochrom (Berlin, Germany). Plasmid pEGFP-N1 (4.7 kb, Clontech, USA) encoding green fluorescent protein (EGFP) was isolated with the Giga Plasmid Kit provided by Qiagen (Hilden, Germany). The siRNA negative controls (scrambled siRNA, 21 nucleotides, double-stranded) and the siRNA against *egfp* (sense 5′-GCAAGCTGACCCTGAAGTTCAT-3′, antisense 5′-ATGAACTTCAGGGTCAGCTTGC-3′) were purchased from Eurogentech (Seraing, Belgium).

General methods and instrumentation

An Initiator Sixty single-mode microwave synthesizer from Biotage, equipped with a noninvasive IR sensor (accuracy: 2%), was used for polymerizations and hydrolyses under microwave irradiation.

Proton (^{1}H) nuclear magnetic resonance (NMR) spectra were acquired in deuterated methanol, at room temperature using a Bruker AC 300 MHz spectrometer; chemical shifts (δ) are expressed in parts per million relative to TMS.

Size exclusion chromatography (SEC) was performed using an Agilent Technologies 1200 Series gel permeation chromatography system equipped with a G1329A auto sampler, a G131A isocratic pump, a G1362A refractive index detector, and both a PSS Gram 30 and a PSS Gram 1000 column placed in series. As eluent a 0.21% LiCl solution in *N*,*N*-dimethylacetamide (DMAc) was used at 1 mL min^{-1} flow rate and a column oven temperature of 40 °C. Molar masses were calculated using a poly(styrene) calibration.

Asymmetric flow field-flow fractionation (AF4) was performed on an AF2000 MT System (Postnova Analytics, Landsberg, Germany) coupled to an UV (PN3211, 260 nm (Postnova)), RI (PN3150), multi-angle light scattering (MALLS, PN3070, 633 nm (Postnova)) and DLS (ZetaSizer Nano ZS; Malvern) detector. The eluent was delivered by three different pumps (tip, focus, cross-flow) and the sample was injected by an autosampler (PN5300) into the channel. The channel has a trapezoidal geometry and an overall area of 31.6 cm^2. The nominal height of the spacer was 500 μm. A regenerated cellulose membrane with a molar mass cut-off of 10 kDa served as accumulation wall. All experiments were carried out at 25 °C with pure water as eluent. A sample of 10 μL (1 mg mL^{-1}) was injected with an injection flow rate of 0.2 mL min^{-1} and a cross-flow rate of 1.2 mL min^{-1} for 7 min (detector flow rate 0.5 ml min^{-1}, focus flow rate 1.5 mL min^{-1}). After the focusing step, the cross-flow rate was reduced under an exponential gradient (0.4) within 10 min to 0 mL min^{-1}. The cross-flow was kept constant at 0 mL min^{-1} for 40 min to ensure complete elution. All measurements were in triplicate.

For the acid/base titration the copolymers **P1** to **P3** ($m \sim 20$ mg) were dissolved in 4 mL deionized water, and 20 μL conc. hydrochloric acid were added (0.06 M). The titration was performed against 0.1 M aqueous sodium hydroxide solution using a 765 Dosimat from Metrohm, a digital pH/mV-thermometer GMH 3530 from Greisinger electronic, and the EBS9 M Recorder software.

Synthesis of poly(2-ethyl-2-oxazoline) (PEtOx)

The monomer 2-ethyl-2-oxazoline (3.965 g) and the initiator methyl tosylate (12.42 mg, 0.067 mmol) were dissolved in dry acetonitrile (6.0 mL) in a microwave vial within a glovebox under nitrogen atmosphere. After stirring for 2 minutes the vessel was transferred to a microwave synthesizer and heated for 128 min at 140 °C. After cooling to room temperature, a sample was taken to determine the chain length by ^{1}H NMR. The polymerization mixture was diluted with 5 mL of dichloromethane, followed by precipitation in 250 mL ice-cold diethyl ether. The precipitate was filtered off, dissolved in deionized water and lyophilized (yield: 3.720 g, 94%).

PEtOx. DP = 575. ^{1}H NMR (300 MHz, D_2O): δ 3.70–3.20 (–NR–CH_2–CH_2), 2.41–2.08 (CH_2–CH_3), 1.09–0.79 (CH_2–CH_3) ppm. SEC (DMAc, LiCl): M_n = 69 000 g mol^{-1}, $Đ$ = 1.3. AF4: M_n = 57 000 g mol^{-1}, $Đ$ = 1.23.

Synthesis of poly(2-ethyl-2-oxazoline-*stat*-ethylene imine) (P(EtOx-*stat*-EI))

To obtain a specific degree of hydrolysis of **P(EtOx-*stat*-EI)**, kinetic studies were performed previously according to literature procedures.[38] The results were used to synthesize PEtOx with defined degree of hydrolysis in larger scale. Accordingly, **PEtOx** (3.510 g, 0.062 mmol) was dissolved in 6 M hydrochloric acid (36 mL). The reaction mixture was heated in a microwave synthesizer at 100 °C for 100 min. Subsequently, the excess of HCl and the resulting propionic acid were distilled off and the residue was dissolved in 15 mL water. The obtained solution was neutralized with 3 M aqueous NaOH to a pH value >8, and the remaining solvent was removed under reduced pressure. The residue was dissolved in DMF and the filtered polymer solution was precipitated two times in 500 mL cold diethyl ether. The obtained product was dried at 85 °C under reduced pressure. ^{1}H NMR spectroscopy was used to determine the conversion of the PEtOx to lPEI. Therefore, the signals from the released lPEI backbone and the signals from the remaining CH_3 group in the side chain of PEtOx were used (yield: 2.350 g, 91%).

P(EtOx-*stat*-EI). EtOx : EI [%] = 54 : 46. ^{1}H NMR (300 MHz, MeOD): δ 3.69–3.41 (NR–CH_2–CH_2), 2.93–2.63 (NH–CH_2–CH_2), 2.55–2.31 (CH_2–CH_3), 1.19–1.03 (CH_2–CH_3) ppm. SEC (DMAc, LiCl): M_n = 48 000 g mol^{-1}, $Đ$ = 1.28. AF4: M_n = 31 300 g mol^{-1}, $Đ$ = 1.03.

Synthesis of P(EtOx-*stat*-EI-*stat*-ButEnOx) (preP1 to preP3)

The partially hydrolyzed PEtOx, **P(EtOx-*stat*-EI)** (**1**: 659 mg, **2**: 654 mg, **3**: 647 mg), and the catalyst 4-*N*,*N*-dimethylaminopyridine (DMAP, 100 mg, 0.82 mmol) were dissolved in a microwave vial in pyridine (V = 8 mL) at 80 °C. In a second vial, a defined quantity of *N*-succinimidyl-4-pentenate (645 mg, 483 mg, 318 mg) was dissolved in the same solvent (4 mL) and heated up to 80 °C. The two solutions were combined and solvent was added (3 mL) to yield a 4 wt% mixture of **P(EtOx-*stat*-EI)**. The reaction mixture was stirred for 20 h at 80 °C. After cooling to room temperature the sample was filtered and precipitated into 400 mL ice-cold diethyl ether. The copolymer was filtered off and washed with 40 mL of diethyl ether. Due to the negligible effect of the side product *N*-hydroxysuccinimide on subsequent reaction steps, no further purification steps were required. The residue was dried under reduced pressure to constant weight (yield: **1**: 619 mg, 68%, **2**: 650 mg, 75%, **3**: 625 mg, 77%).

preP1. EtOx : EI : ButEnOx = 54 : 12 : 34%. ^{1}H NMR (300 MHz, MeOD): δ 6.00–5.77 (*H*C═CH_2), 5.18–4.95 (HC═CH_2), 3.81–3.40 (NR–CH_2–CH_2), 3.00–2.74 (NH–CH_2–CH_2), 2.67 (NHS), 2.60–2.20 (CH_2–CH_3, CH_2–CH_2–C$_2$H$_3$), 1.20–0.97 (CH_2–CH_3) ppm. SEC (DMAc, LiCl): M_n = 36 000 g mol^{-1}, $Đ$ = 2.12. AF4: M_n = 25 500 g mol^{-1}, $Đ$ = 1.41.

preP2. EtOx : EI : ButEnOx = 54 : 17 : 29%. ^{1}H NMR (300 MHz, MeOD): δ 6.00–5.78 (*H*C═CH_2), 5.17–4.95 (HC═CH_2), 3.81–3.40 (NR–CH_2–CH_2), 2.95–2.68 (NH–CH_2–CH_2), 2.59 (NHS), 2.57–2.21 (CH_2–CH_3, CH_2–CH_2–C$_2$H$_3$), 1.21–1.00 (CH_2–CH_3) ppm. SEC (DMAc, LiCl): M_n = 34 500 g mol^{-1}, $Đ$ = 1.63. AF4: M_n = 30 900 g mol^{-1}, $Đ$ = 1.33.

preP3. EtOx : EI : ButEnOx = 54 : 23 : 23%. ^{1}H NMR (300 MHz, MeOD): δ 5.99–5.76 (*H*C═CH_2), 5.19–4.96 (HC═CH_2), 3.81–3.40 (NR–CH_2–CH_2), 2.94–2.66 (NH–CH_2–CH_2), 2.57 (NHS), 2.55–2.25 (CH_2–CH_3, CH_2–CH_2–C$_2$H$_3$), 1.22–0.99 (CH_2–CH_3) ppm. SEC (DMAc, LiCl): M_n = 36 000 g mol^{-1}, $Đ$ = 1.55. AF4: M_n = 30 400 g mol^{-1}, $Đ$ = 1.33.

Synthesis of P(EtOx-*stat*-EI-*stat*-bocAmButOx) *via* thiol–ene functionalization (*boc*P1 to *boc*P3)

In a microwave vial, **P(EtOx-*stat*-EI-*stat*-ButEnOx)** (**preP1**: 253 mg, **preP2**: 351 mg, **preP3**: 360 mg) was dissolved in methanol (2 mL). In a second vial, the photoinitiator 2,2-dimethoxy-2-phenylacetophenone (DMPA, 49 ± 0.5 mg, 0.19 mmol) and a 1.3-fold excess per double bond of 2-(boc-amino)ethanethiol (193 μL, 239 μL, 205 μL)

were dissolved in methanol (2 mL), likewise. The combined solutions (10 wt%) were degassed with nitrogen for 20 min and the clear solution was stirred in a UV chamber (λ = 365 nm) overnight. Subsequently, the copolymer was precipitated in 200 mL ice-cold diethyl ether. After filtration, the copolymer was dried under reduced pressure for two days (yield: ***boc*P1**: 361 mg, 89%, ***boc*P2**: 493 mg, 92%, ***boc*P3**: 476 mg, 92%).

***boc*P1.** EtOx : EI : bocAmButOx = 54 : 12 : 34%. ^{1}H NMR (300 MHz, MeOD): δ 3.81–3.40 (NR–CH_2–CH_2), 3.27–3.16 (S–CH_2–CH_2), 3.00–2.74 (NH–CH_2–CH_2), 2.64 (NHS), 2.63–2.55 (S–CH_2–CH_2), 2.54–2.27 (CH_2–CH$_3$, CH_2–C$_2$H$_4$–CH_2), 1.82–1.57 (CH$_2$–C$_2$H$_4$–CH$_2$), 1.55–1.39 (C(CH_3)$_3$), 1.21–1.00 (CH$_2$–CH_3) ppm.

***boc*P2.** EtOx : EI : bocAmButOx = 54 : 17 : 29%. ^{1}H NMR (300 MHz, MeOD): δ 3.81–3.41 (NR–CH_2–CH_2), 3.28–3.16 (S–CH_2–CH_2), 2.92–2.72 (NH–CH_2–CH_2), 2.69–2.59 (S–CH_2–CH$_2$), 2.58 (NHS), 2.54–2.29 (CH_2–CH$_3$, CH_2–C$_2$H$_4$–CH_2), 1.82–1.56 (CH$_2$–C$_2$H$_4$–CH$_2$), 1.55–1.39 (C(CH_3)$_3$), 1.21–1.03 (CH$_2$–CH_3) ppm.

***boc*P3.** EtOx : EI : bocAmButOx = 54 : 23 : 23%. ^{1}H NMR (300 MHz, MeOD): δ 3.79–3.41 (NR–CH_2–CH_2), 3.27–3.17 (S–CH_2–CH_2), 2.91–2.71 (NH–CH_2–CH_2), 2.67–2.59 (S–CH_2–CH$_2$), 2.58 (NHS), 2.54–2.29 (CH_2–CH$_3$, CH_2–C$_2$H$_4$–CH_2), 1.80–1.56 (CH$_2$–C$_2$H$_4$–CH$_2$), 1.55–1.39 (C(CH_3)$_3$), 1.20–1.02 (CH$_2$–CH_3) ppm.

Synthesis of P(EtOx-*stat*-EI-*stat*-AmButOx) *via* deprotection (P1 to P3)

The copolymer **P(EtOx-*stat*-EI-*stat*-bocAmButOx)** (***boc*P1**: 321 mg, ***boc*P2**: 402 mg, ***boc*P3**: 420 mg) was dissolved in dichloromethane (3 mL). Trifluoroacetic acid was added (5 mL) and the reaction mixture was stirred overnight at room temperature. The copolymer was precipitated in 400 mL ice-cold diethyl ether. The precipitate was filtered, washed with 40 mL diethyl ether, dissolved in methanol and shaken overnight with Amberlyst A21 (free base) ($\sim$0.5 g). The solvent was removed and the copolymer lyophilized (yield: **P1**: 240 mg, 95%, **P2**: 293 mg, 91%, **P3**: 330 mg, 95%).

P1. EtOx : EI : bocAmButOx = 54 : 12 : 34%. ^{1}H NMR (300 MHz, MeOD): δ 3.76–3.29 (NR–CH_2–CH_2), 3.11–2.98 (S–CH_2–CH_2), 2.84–2.65 (NH–CH_2–CH_2), 2.58 (NHS), 2.57–2.46 (S–CH_2–CH$_2$), 2.45–2.16 (CH_2–CH$_3$, CH_2–C$_2$H$_4$–CH_2), 1.83–1.44 (CH$_2$–C$_2$H$_4$–CH$_2$), 1.10–0.89 (CH$_2$–CH_3) ppm. SEC (DMAc, LiCl): M_n = 30 500 g mol^{-1}, $Đ$ = 1.60. AF4: M_n = 35 300 g mol^{-1}, $Đ$ = 1.74.

P2. EtOx : EI : bocAmButOx = 54 : 17 : 29%. ^{1}H NMR (300 MHz, MeOD): δ 3.68–3.21 (NR–CH_2–CH_2), 3.01–2.87 (S–CH_2–CH_2), 2.72–2.56 (NH–CH_2–CH_2), 2.50 (NHS), 2.48–2.37 (S–CH_2–CH$_2$), 2.37–2.08 (CH_2–CH$_3$, CH_2–C$_2$H$_4$–CH_2), 1.70–1.36 (CH$_2$–C$_2$H$_4$–CH$_2$), 1.03–0.82 (CH$_2$–CH_3) ppm. SEC (DMAc, LiCl): M_n = 39 000 g mol^{-1}, $Đ$ = 1.58. AF4: M_n = 43 700 g mol^{-1}, $Đ$ = 1.72.

P3. EtOx : EI : bocAmButOx = 54 : 23 : 23%. ^{1}H NMR (300 MHz, MeOD): δ 3.87–3.40 (NR–CH_2–CH_2), 3.23–3.03 (S–CH_2–CH_2), 2.97–2.75 (NH–CH_2–CH_2), 2.74–2.57 (S–CH_2–CH$_2$), 2.56–2.28 (CH_2–CH$_3$, CH_2–C$_2$H$_4$–CH_2), 1.88–1.56 (CH$_2$–C$_2$H$_4$–CH$_2$), 1.22–0.98 (CH$_2$–CH_3) ppm. SEC (DMAc, LiCl): M_n = 31 500 g mol^{-1}, $Đ$ = 1.45. AF4: M_n = 30 500 g mol^{-1}, $Đ$ = 1.62.

Copolymer labeling with Cy5

Copolymer **P3** (40 mg) and triethylamine (150 μL) were dissolved in DMF (10 mL). After addition of the cyanine-5-NHS-ester (0.4 mg) the reaction was stirred at room temperature overnight. The labeled copolymer was precipitated in 500 mL ice-cold diethyl ether, filtered and re-dissolved in H_2O (15 mL). Further purification was performed by dialysis against water using a Spectra/Por 3 dialysis membrane (3500 g mol^{-1} cut-off). Finally, the product was lyophilized and obtained as a blue powder. The calculated labeling efficiency (*via* UV-Vis) for conjugation was 65% for **P3–Cy5** (yield: 27 mg, 67%). **lPEI** was treated likewise but dialyzed against a water/methanol mixture and dried under reduced pressure, subsequently (yield: 2.6 mg, 26%; labeling efficiency: 2%).

Synthesis of linear poly(ethylene imine) (lPEI)

The synthesized copolymer **P(EtOx-*stat*-EI)** (DP = 575, 100 mg) was treated with an excess of 6 M aqueous hydrochloric acid (1.5 mL) for 2 hours at 100 °C in a microwave synthesizer to yield a hydrolyzed linear poly(ethylene imine) (DP = 575). Neutralization and purification *via* precipitation were performed analogous to the described synthesis of **P(EtOx-*stat*-EI)** (see above). The product **lPEI** was dried at 85 °C under high vacuum for 2 days and the degree of hydrolysis was determined by ^{1}H NMR by correlating the integrals of the PEI backbone and the remaining methyl group of the PEtOx side chain (yield: 51 mg, 87%).

lPEI. EtOx : EI [%] = 5 : 95. ^{1}H NMR (300 MHz, MeOD): δ 3.58–3.41 (NR–CH_2–CH_2), 2.91–2.61 (NH–CH_2–CH_2), 2.56–2.36 (CH_2–CH$_3$), 1.18–1.06 (CH$_2$–CH_3) ppm.

Polyplex preparation

Polyplexes of pDNA and polymers were prepared by mixing stock solutions of 15 μg mL^{-1} pDNA and different amounts of polymers (1 mg mL^{-1}) to obtain various N/P ratios (nitrogen of polymer to phosphate of pDNA) in HBG buffer (20 mM 4-(2-hydroxyethyl)piperazine-1-ethanesulfonic acid (HEPES) and 5% (w/v) glucose, pH 7.2). The solutions were vortexed for 10 s at maximal speed and incubated at room temperature for 20 min to ensure complex formation. For the preparation of polyplexes with siRNA, 1 μM siRNA (final concentration) was used as described above.

Ethidium bromide quenching assay

The formation of polyplexes with pDNA as well as siRNA was examined by quenching of the ethidium bromide fluorescence. Briefly, pDNA (15 μg mL^{-1}) or siRNA (1 μM) in a total volume of 100 μL HBG buffer were incubated with ethidium bromide (0.4 μg mL^{-1}) for 10 min at room temperature. Subsequently, polyplexes with different amounts of polymer (various N/P ratios) were prepared in black 96-well plates (Nunc Thermo Fisher). The samples were incubated at room temperature for 15 min. The fluorescence of the samples was measured at an excitation wavelength of 525 nm and an emission wavelength of 605 nm using a microplate reader (TECAN Infinite M200 Pro, Crailsheim, Germany). A sample containing only pDNA and ethidium bromide was used to calibrate the device to 100% fluorescence against a background of 0.4 μg mL^{-1} of ethidium bromide in

HBG solution. The percentage of dye displaced upon polyplex formation was calculated using eqn (1):

$$\mathrm{RFU}[\%] = \frac{F_{\mathrm{sample}} - F_0}{F_{\mathrm{pDNA}} - F_0} \times 100 \quad (1)$$

Here, RFU is the relative fluorescence and F_{sample}, F_0, and F_{pDNA} are the fluorescence intensities of a given sample, the ethidium bromide in HBG alone, and the ethidium bromide intercalated into pDNA alone.

Heparin dissociation assay

To investigate the release of pDNA from polyplexes, the heparin dissociation assay was performed. Polyplexes with an N/P ratio of 30 were prepared as described above in a total volume of 100 μL HBG buffer containing ethidium bromide (0.4 μg mL^{-1}). After incubation in the dark at room temperature for 15 min, the polyplexes were transferred into a black 96-well plate, and heparin of indicated concentrations was added. The solution was mixed and incubated for further 30 min at 37 °C in the dark. The fluorescence of ethidium bromide was measured at Ex 525 nm/Em 605 nm with a Tecan microplate reader. The percentage of intercalated ethidium bromide was calculated as described before.

Dynamic and electrophoretic light scattering

Dynamic light scattering (DLS) was performed on a Zetasizer Nano ZS (Malvern Instruments, Herrenberg) with a He–Ne laser operating at a wavelength of λ = 633 nm. All measurements (30 runs, triplicate) were carried out at 25 °C after an equilibration time of 120 s. The counts were detected at an angle of 173°. The mean particle size was approximated as the effective (*z*-average) diameter and the width of the distribution as the polydispersity index of the particles (PDI) obtained by the cumulants method assuming a spherical shape. Electrophoretic light scattering (ELS) was used to measure the zeta potential (ζ). The measurement was performed on a Zetasizer Nano ZS (Malvern Instruments, Herrenberg, Germany) by applying laser Doppler velocimetry. For each measurement, 20 runs were carried out using the slow-field reversal and the fast-field reversal mode at 150 V. Each experiment was performed in triplicate a 25 °C. The zeta potential was calculated from the electrophoretic mobility (μ) according to the Henry equation. Henry coefficient f(ka) was calculated according to Oshima.

Determination of the cytotoxicity

Cytotoxicity studies were performed with the mouse fibroblast cell line L929 (CCL-1, ATCC), as recommended by ISO10993-5. The cells were routinely cultured in Dulbecco's modified eagle's medium (DMEM, Lonza, Basel) supplemented with 10% fetal calf serum (FCS), 100 U mL^{-1} penicillin and 100 μg mL^{-1} streptomycin at 37 °C in a humidified 5% (v/v) CO_2 atmosphere.

In detail, cells were seeded at 10^4 cells per well in a 96-well plate and incubated for 24 h, whereas no cells were seeded in the outer wells. Subsequently, the testing substances (polymers) at indicated concentrations (from 0.25 μg mL^{-1} to 1 mg mL^{-1}) were added to the cells and the plates were incubated for further 24 h. Control cells were incubated with fresh culture medium. Subsequently, the medium was replaced by a mixture of fresh culture medium and Alamar-Blue solution (Life technologies, Darmstadt, Germany), prepared according to the manufacturer's instructions. After a further incubation of 4 h at 37 °C, the fluorescence was measured at Ex 570/Em 610 nm, with untreated cells on the same well plate serving as negative controls. The negative control was standardized as 0% of metabolism inhibition and referred as 100% viability. Cell viability below 70% was considered indicative of cytotoxicity. Data are expressed as mean ± SD of three determinations.

Hemolysis assay

The interaction of polymers with cellular membranes was investigated by analyzing the release of hemoglobin from erythrocytes. Blood from sheep, collected in heparinized tubes, was provided by the Institute of Laboratory Animal Science and Animal Welfare, Friedrich-Schiller University Jena. The blood was centrifuged at 4500 × *g* for 5 min, and the pellet was washed three times with cold 1.5 mM phosphate buffered saline (PBS, pH 7.4). After dilution with PBS in a ratio of 1 : 7, aliquots of erythrocyte suspension were mixed 1 : 1 with the polymer solution and incubated in a water bath at 37 °C for 60 min. After centrifugation at 2400 × *g* for 5 min, the hemoglobin release into the supernatant was determined spectrophotometrically using a microplate reader (TECAN Infinite M200 Pro, Crailsheim, Germany) at a wavelength of 544 nm. Complete hemolysis (100%) was achieved using 1% Triton X-100 serving as positive control. Pure PBS was used as negative control (0% hemolysis). The haemolytic activity of the polycations was calculated as follow (2):

$$\%\ \mathrm{Hemolysis} = 100 \times \frac{\left(A_{\mathrm{Sample}} - A_{\mathrm{Negative\ control}}\right)}{A_{\mathrm{Positive\ control}}} \quad (2)$$

A value less than 2% hemolysis rate were classified as non-hemolytic, 2 to 5% as slightly haemolytic and values >5% as hemolytic. Experiments were run in triplicates and were performed with three different batches of donor blood.

Erythrocyte aggregation

Erythrocytes were isolated as described above. The erythrocyte suspension were mixed 1 : 1 with the polymer solutions (100 μL total volume) in a clear flat bottomed 96-well plate. The cells were incubated at 37 °C for 2 h, and the absorbance was measured at 645 nm in a microplate reader. Cells, which were treated with PBS served as negative control and 25 kDa bPEI (50 μg mL^{-1}, Polysciences) was used as positive control. Absorbance values of the test solutions lower than the negative control were regarded as aggregation. Experiments were run in triplicates and were performed with three different batches of donor blood.

Polyplex uptake

HEK-293 cells (CRL-1573, ATCC) were cultured in RPMI 1640 medium (Lonza, Basel) supplemented with 10% FCS, 100 μg mL^{-1} streptomycin, 100 U mL^{-1} penicillin and 2 mM L-glutamine at 37 °C in a humidified 5% CO_2 (v/v) atmosphere.

For uptake studies, cells were seeded at a density of 10^5 cells per mL in 24-well plates and cultured for 24 h. One hour prior to the addition of the polyplexes, the medium was changed to OptiMEM (Life Technologies, Darmstadt, Germany). The polyplexes were prepared as described above and at least 50 μL polyplexes in solution were added to the cells. The plates were incubated for 4 h at 37 °C, 5% CO_2.

For kinetic studies of the polyplex uptake within 4 h, pDNA was labeled with YOYO-1 iodide prior to the polyplex preparation. For labeling of 1 μg pDNA, 0.026 μL of 1 M YOYO-1 solution was mixed with pDNA and incubated for 20 min at 4 °C protected from light. Afterwards, HBG buffer and polymers were added at the indicated N/P ratio and the polyplexes were formed as described previously. The cells were harvested 0.5, 1, 2 and 4 h after polyplex addition and 10% trypan blue was added to quench the outer fluorescence of the cells. For energy-dependent uptake studies, cells were equilibrated in OptiMEM at 4 °C 1 h prior polyplex addition. The plates were incubated at 4 °C for 4 h. To determine the relative uptake of the polyplexes, 10^4 cells were measured by flow cytometry using a Cytomics FC 500 (Beckman Coulter) and the amount of viable cells showing YOYO-1 signal were gated. Dead cells were identified *via* counterstaining with propidium iodide (PI). The experiments were performed at least three times independently.

For inhibition experiments, cells were treated with 100 μM 5-(*N*-ethyl-*N*-isopropyl)amiloride (EIPA) in standard culture media 30 min prior to polyplex addition. Subsequently, **P3** and **lPEI** polyplexes were added to the cells and incubated for further 4 h. Afterwards, the cells were harvested and analyzed as described above *via* flow cytometry or were further prepared for STEM imaging.

Transfection of adherent cells

For transfection of adherent HEK-293 cells, the cells were seeded at a density of 10^5 cells per mL in 24-well plates and incubated for 24 h at 37 °C, 5% CO_2. One hour prior to transfection, the cells were washed with PBS and supplemented with 0.5 mL OptiMEM or fresh serum containing growth medium (RPMI 1640). The polyplexes were prepared as described above, and were added to the cells (50 μL per well). After an incubation time of 4 h at 37 °C, the supernatant was replaced by fresh growth medium and the cells were incubated for further 20 h. For analysis *via* flow cytometry (Cytomics FC 500, Beckman Coulter), cells were harvested by trypsinization. For determination of the viability during flow cytometry, dead cells were identified *via* counterstaining with propidium iodide. For determination of the transfection efficiency, 10^4 viable cells expressing EGFP were gated. The experiments were performed three times independently. Regarding the Bafilomycin experiments, 175 nM Bafilomycin was added to the cells in OptiMEM and incubated for 20 min, prior to the polyplex addition. The knockdown studies were performed with stable EGFP expressing CHO cells (CCL-61, ATCC, stable transfected with pEGFP-N1) and the corresponding siRNA (against *egfp*, riboxx, Germany). The polyplexes were incubated in OptiMEM for 6 h and measured after 72 h *via* flow cytometry.

Electron microscopy

Scanning transmission electron microscopy with high-angle annular dark-field detection (STEM-HAADF) was carried out using a Technai G^2 system (FEI), with 120 kV or 200 kV acceleration voltage on ultrathin slices of resin-embedded cell samples.

For cell preparation, HEK-293 cells (10^5 cells mL^{-1}) were seeded on 6-well plates and incubated for 4 h at 37 °C with the respective polyplex samples (N/P 30). The cells were harvested, washed with PBS and fixed for 2 h with glutaraldehyde (2% in PBS, prepared from 8% EM grade stock solution) on ice. Subsequent to aldehyde fixation, the cells were washed with PBS prior to the fixation with OsO_4 for 1 h (1% in PBS, prepared from 4% EM grade stock solution, both purchased from EMS, Hatfield). After this, the cells were washed with MilliQ water and staining with uranyl acetate solution was carried out for 1 h and protected from light (1% in solution in MilliQ water prepared from depleted uranyl acetate dihydrate purchased from EMS, Hatfield). Subsequently, the sample was washed with pure water prior to dehydration by an ethanol/water series (50%, 70%, 90%, 2 × 100% dry EtOH, purified with a Solvent Purification System and stored over molecular sieves). Thereafter, the cells were transferred into BEEM capsules (Plano, Wetzlar), in which the cell suspension was immersed in mixtures of Embed 812 (EMS, Hatfield) and ethanol (Embed/EtOH = 1 : 1 v/v for 1 hour, 2 : 1 v/v for 12 h, pure Embed 812 for 4 h). Subsequent to a further exchange of the embedding medium, the resin was allowed to harden at 70 °C for 24 h. From the resin block, ultrathin sections with a thickness of 80 nm were cut with an ultramicrotome (PT-XL PowerTome, RMC, Tucson) using a diamond knife (RMC, Tucson). The ultrathin resin sections were applied on a carbon supported copper grid (400 mesh, Quantifoil, Jena).

Confocal microscopy and structured illumination microscopy

Live cell imaging was performed for uptake studies. In detail, HEK cells (10^5 cells mL^{-1}) were seeded on glass-bottomed dishes (ibidi, Germany, thickness 170 ± 5 μm for high-resolution fluorescence microscopy) and cultivated for 24 h in a humidified atmosphere. One hour prior to the polymer addition, the cells were rinsed with phosphate buffered saline (PBS) and the medium was changed to OptiMEM. The polyplexes were formed with Cy5-labeled **P3** and YOYO-labeled pDNA or Cy3-labeled siRNA, added to the cells and incubated for further 4 h. Subsequently, medium was replaced by fresh culture medium or PBS supplemented with Hoechst 33342 for nucleus staining, LysoTracker Red DND-99 or LysoTracker Green DND-26 (all from Thermo Fisher Scientific) for lysosome staining.

Imaging was performed with LSM880, Elyra PS.1 system (Zeiss, Oberkochen, Germany) applying a 63× 1.4 NA plan apochromat oil objective. For SIM imaging, cells were grown on high precision cover glasses (Marienfeld-Superior, 18 × 18 mm, 170 ± 5 μm certified thickness) at a density of 5×10^4 cells mL^{-1}, fixed with paraformaldehyde (2% in PBS) and embedded in prolong gold antifading reagent (Thermo Fisher Scientific). Regarding the SIM performance, excitation wavelengths of 405 nm

(exc. grating 28.0 μm), 488 nm (exc. grating 34.0 μm), 561 nm (exc. grating 42.0 μm) and 642 nm (exc. grating 42.0 μm resp. 51.0 μm) were used. The following four color channels were used for both microscopy techniques: Nucleus (Hoechst 33342 staining, excitation wavelength 405 nm, BP 420–480 + LP 750, grey), pDNA (YOYO-1 Iodide, excitation wavelength 488 nm, BP 495–550 + LP 750, green), polymer **P3** (Cy-5 labeling, excitation wavelength 642 nm, LP 655, blue) and lysosome (CellLight Lysosomes-RFP BacMam 2.0, excitation wavelength 561 nm, BP 570–620 + LP 750, red). The grating position and axial position of the sample table were controlled by piezo controllers. Images were recorded with a sCMOS camera (pco.edge, Kehlheim, German), cooled to 5 °C. Reconstructions and deconvolution were performed with the commercial ZEN2 software installed on the system (Zeiss, Oberkochen, Germany).

Statistical analysis

The values represent the mean ± SD. For the calculation of the standard derivation of two or more different groups, the two sample *t*-test (student's *t*-test) or the ANOVA was used. Statistical significance was defined as * for *p*-values of <0.05 and # for *p*-values <0.005.

Results and discussion

Polymer synthesis

As chain transfer reactions are more likely to occur during polymerization of 2-methyl-2-oxazoline,[39] 2-ethyl-2-oxazoline was used as monomer for the polymerization of the precursor homopolymer, being able to decrease cytotoxicity of aspired copolymers.[40]

PEtOx was synthesized according to a literature procedure by microwave supported cationic ring-opening polymerization (CROP).[41] The degree of polymerization of 575 was calculated from the tosylate ^{1}H NMR signals of MeOTos before purification. In order to ensure the absence of water, the polymerization solutions were prepared in a glove box under nitrogen atmosphere yielding **PEtOx** with a dispersity *Đ* of 1.3 (SEC: DMAc, 0.21% LiCl, standard: PS, Table 1). This homopolymer served as precursor for the subsequent copolymer synthesis.

PEtOx was hydrolyzed in a microwave synthesizer (Scheme 1a) to yield the copolymer poly(2-ethyl-2-oxazoline-*stat*-ethylene imine) (**P(EtOx-*stat*-EI)**) with an EtOx content of 54% (calc. from ^{1}H NMR).[38]

To introduce primary amines to the polymers, a fraction of the ethyleneimine units was functionalized with *N*-succinimidyl-4-pentenate to introduce alkene functionalities (Scheme 1b).[42] While the synthesis of poly(2-butenyl-2-oxazoline) is possible *via* the polymerization of the respective monomers,[36] these units do not withstand the conditions of the acidic hydrolysis of PEtOx. Three different copolymers of P(EtOx-*stat*-EI-*stat*-ButEnOx) (**preP1** to **preP3**) with varying ratios of secondary amines and 2-(3-butenyl-2-oxazoline)s (1 : 3, 1 : 2, 1 : 1) were synthesized while maintaining a constant EtOx content of 54% (Table 1). The introduction of primary amines was performed by thiol–ene photoaddition. Hence, the copolymers P(EtOx-*stat*-EI-*stat*-AmButOx) (**P1** to **P3**) were synthesized by reaction of the corresponding precursor copolymers (**preP1** to **preP3**) with a protected aminothiol under UV irradiation and subsequent deprotection to yield the primary amine group (Scheme 1c and d).

Characterization by ^{1}H NMR spectroscopy confirms the presence of 2-ethyl-2-oxazoline (EtOx) as well as ethylene imine (EI) units (Fig. 2, **PEtOx** and **P(EtOx-*stat*-EI)**). The integrals of the signals of the EtOx side chain (A, B) as well as the signals of the backbone (C) remain constant during further reactions and are, therefore, used as reference.

The successful functionalization with the activated acid *N*-succinimidyl-4-pentenate is exemplified by the proton signals of the double bond (ButEnOx) that appear at 5.9 ppm (–*H*C═CH_2, H) and 5.1 ppm (–HC═CH_2, I) for the copolymer **preP3**. The first signal is used to calculate the composition of the formed copolymer by comparing the signals of the ethylene imine backbone (between 3.00 to 2.66, NH–CH_2–CH_2, D) and the methyl protons of the EtOx side chain (between 1.22 to 0.97, CH_2–CH_3, A). The successful functionalization of **preP1** to **preP3** with the thiol is shown by the disappearance of the double bond signals after the photoaddition (***boc*P3**). The signals of the newly formed CH_2 groups appear at 2.40 (I′) and 1.70 ppm (H′), respectively. Furthermore, a singlet of the *tert*-butyloxycarbonyl (boc) protecting group is obtained at 1.50 ppm (L). After treatment with

Table 1 Composition and molar masses for **PEtOx**, **P(EtOx-*stat*-EI)**, **preP1** to **preP3** and **P1** to **P3**

		Composition[a]		Amine ratio	NMR[b]	AF4		SEC	
Abbr.	Name	*X* [%]	*Y* [%]	$sec_X : prim_Y$	M_n [g mol^{-1}]	M_n [g mol^{-1}]	*Đ*	M_n [g mol^{-1}]	*Đ*
PEtOx	$PEtOx_{575}$	—	—	—	57 000	57 000	1.2	69 000	1.3
P(EtOx-*stat*-EI)	$P(EtOx_{54\%}$-*stat*-$EI_X)$	46	—	—	42 100	31 300	1.3	48 000	1.3
preP1	$P(EtOx_{54\%}$-*stat*-EI_X-$ButEnOx_Y)$	12	34	—	58 100	25 500	1.4	36 000	2.1
preP2	$P(EtOx_{54\%}$-*stat*-EI_X-$ButEnOx_Y)$	17	29	—	55 800	30 900	1.3	34 500	1.6
preP3	$P(EtOx_{54\%}$-*stat*-EI_X-$ButEnOx_Y)$	23	23	—	53 000	30 400	1.3	36 000	1.6
P1	$P(EtOx_{54\%}$-*stat*-EI_X-$AmButOx_Y)$	12	34	1 : 2.8	73 200	35 300	1.7	30 500	1.6
P2	$P(EtOx_{54\%}$-*stat*-EI_X-$AmButOx_Y)$	17	29	1 : 1.7	68 600	43 700	1.7	39 000	1.6
P3	$P(EtOx_{54\%}$-*stat*-EI_X-$AmButOx_Y)$	23	23	1 : 1	63 100	30 500	1.6	31 500	1.5

[a] Determined by ^{1}H NMR (calculated from the ratio of EtOx, ButEnOx signals and EI backbone). [b] Determined by ^{1}H NMR (calculated from tosylate signals of MeOTos before purification).

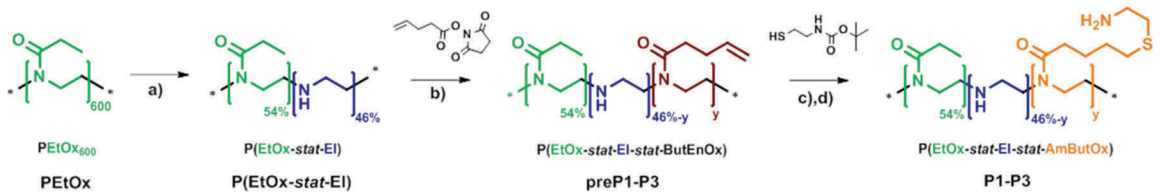

Scheme 1 Schematic representation of the synthesis of cationic copolymers. (a) Partial hydrolysis of poly(2-ethyl-2-oxazoline) in a microwave synthesizer, (b) post-polymerization functionalization with *N*-succinimidyl-4-pentenate, (c) thiol–ene photo-addition of 2-(boc-amino)ethanethiol at 365 nm and (d) deprotection using trifluoroacetic acid.

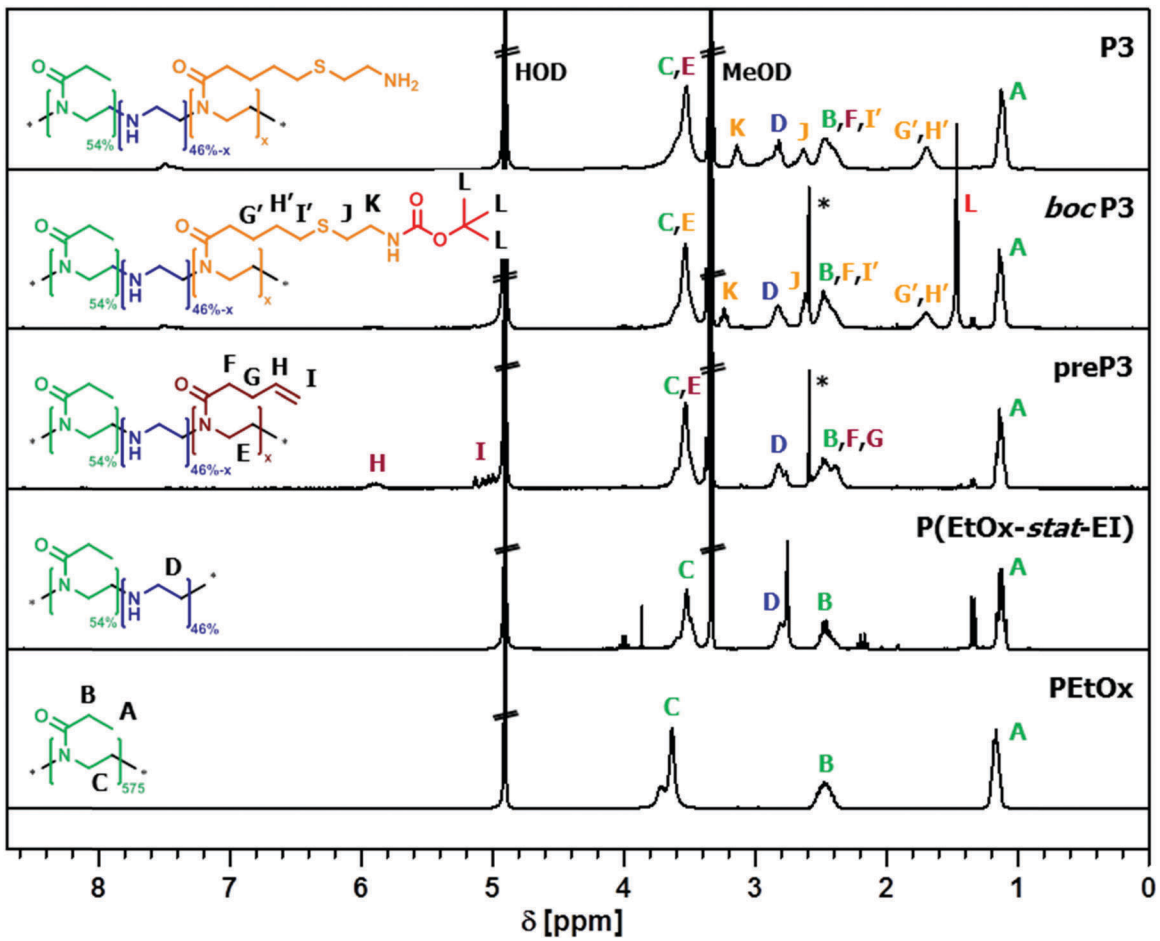

Fig. 2 Comparison of ^{1}H NMR spectra of **PEtOx**, **P(EtOx-*stat*-EI)**, **preP3**, ***boc*P3** and the final product **P3** (* side product *N*-hydroxysuccinimide) (300 MHz, MeOD).

trifluoroacetic acid (TFA) and precipitation into diethyl ether, the signal of the protecting group disappears, indicating the successful deprotection of ***boc*P1** to **bocP3** and, consequently, the synthesis of P(EtOx-*stat*-EI-*stat*-AmButOx) (**P1** to **P3**).

A comparison of the composition and molar masses of the prepared copolymers obtained by asymmetric flow field-flow fractionation (AF4) and size exclusion chromatography (SEC) is shown in Table 1. Although a trend is clearly visible, the obtained values should be handled with care due to the fact that the introduction of double bond containing ButEnOx units as well as the cationic amine units (primary and secondary) could lead to undesired column and membrane interactions and, hence, to a change in the elution behavior. SEC traces, exemplified for the synthesis of **P2**, are depicted in the ESI† (Fig. S1).

To enable *in vitro* imaging, copolymer **P3** was labeled using one equivalent of Cy5–NHS per polymer chain. Successful dye functionalization and purification *via* dialysis (3500 g mol^{-1} cut-off) was verified by size exclusion chromatography (SEC), revealing no trace of unbound dye (ESI,† Fig. S2).

Bio- and hemocompatibility

Biocompatibility represents a critical parameter for PEI based polymers. One option to reduce the known cytotoxicity of PEI[12,13,43]

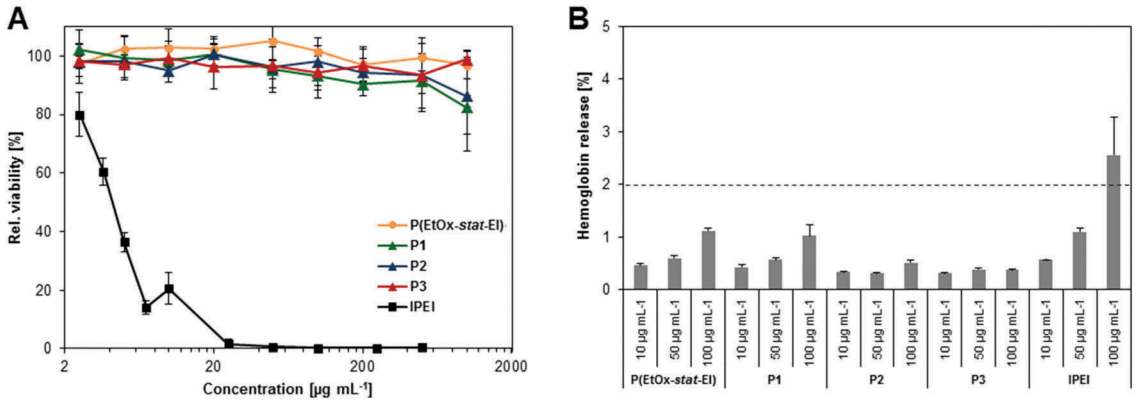

Fig. 3 Determination of bio- and hemocompatibility. (A) Relative viability of L929 cells after 24 h incubation with the polymers at different concentrations according to ISO10993-5. (B) Hemolysis assay of erythrocytes after incubation with polymers at the indicated concentrations. Triton X-100 served as positive control (98.8% hemolysis) and PBS as negative control (0.2%). A value less than 2% hemolysis rate was classified as non-hemolytic, 2 to 5% as slightly hemolytic and values >5% as hemolytic. Values represent the mean ± S.D. (n = 3).

is the introduction of EtOx units.[31] The copolymers introduced here (**P1** to **P3**) possess an oxazoline content of 54%, expected to decrease severe cytotoxic effects. The cytotoxicity of **P1** to **P3** was investigated in comparison to **lPEI** (Fig. 3A), obtained by full hydrolysis of **P(EtOx-*stat*-EI)**. Besides **lPEI**, commercial available linear poly(ethylene imine) (**comlPEI**, 25 kDa, Polyscience) was used as internal control. The results of the following *in vitro* experiments performed with **comlPEI** are summarized in the ESI† (Fig. S18–S20).

As assumed, **lPEI** leads to a significant reduction of cell viability at low concentrations (IC_{50} of 3.6 µg mL^{-1}), which is in accordance to literature data.[3] Despite a high molar mass (>25 kDa), **P(EtOx-*stat*-EI)** as well as **P1** to **P3** showed no cytotoxicity after 24 h using polymer concentrations up to 1 mg mL^{-1} (IC_{50} > 1 mg mL^{-1}, Fig. 3A). This improvement on cell viability is attributed to the introduced EtOx content of 54% within the copolymers and is consistent with literature reports on partially hydrolyzed POx.[32]

The blood compatibility of the copolymers was further investigated by assessment of the hemolytic activity (Fig. 3B) as well as the aggregation of erythrocytes. The treatment of **P(EtOx-*stat*-EI)** and **P1** to **P3** did not show any hemolytic activity in a concentration range from 10 to 50 µg mL^{-1}. A slight hemolysis (~1% hemoglobin release) could be revealed at higher concentrations of **P(EtOx-*stat*-EI)** and **P1** (100 µg mL^{-1}). In contrast, **lPEI** revealed an increased interaction with the cellular membranes of the blood cells resulting in hemoglobin releases above 2% (100 µg mL^{-1}) and, moreover, in a strong agglomeration of erythrocytes (see ESI,† Fig. S3 and S4). The later was not observed with EtOx containing copolymers (**P(EtOx-*stat*-EI)**, **P1** to **P3**) indicating a good hemo- and biocompatibility.

Characterization of the polyplexes

Despite the beneficial impact of EtOx on the biocompatibility of the polymers, their impact on the polyplex formation was investigated. For this purpose, the ethidium bromide quenching assay (EBA) was used to investigate the condensation of plasmid DNA (pDNA) by **P1** to **P3** as well as **P(EtOx-*stat*-EI)**, at different nitrogen (polymer) to phosphate (DNA) ratios (N/P). Ethidium bromide is excluded from its binding sites within the oligonucleotides because of the electrostatic and hydrophobic interactions between polymer and the nucleic acid, leading to a reduction in fluorescence that can be correlated to the affinity of the complexation.[44,45] All copolymers (**P1** to **P3**) revealed decreasing fluorescence intensities below 40% relative fluorescence units (RFU, Fig. 4A). Stable polyplexes indicated by a plateau were reached at higher N/P ratios 5 to 40, whereby no significant differences between **P1**, **P2**, **P3** and **lPEI** were observed. In contrast, the precursors **PEtOx** (data not shown) and **P(EtOx-*stat*-EI)** did not form appropriate polyplexes. It can be assumed that the EtOx units prevent a strong binding of the DNA to the secondary amines of the PEI backbone. This reduced complexation affinity is compensated by the introduction of the more flexible side chains consisting of AmButOx (primary amines) within **P1** to **P3**, which apparently are essential for the polyplex formation. Interestingly, the combination of EI and AmButOx seems to be beneficial, since a comparable copolymer **P(MeOx-*stat*-AmButOx)** without ethylene imine units revealed reduced pDNA complexation around 60% RFU in a previous study.[17] A synergistic effect between both, primary amines in the side chain and secondary amines in the backbone, leads to an improved binding of DNA despite an EtOx content of 54%. The following studies of **P1** to **P3** were performed with polyplexes formed at N/P 30 as this guarantees stable polyplex formation.

To analyze the stability and the dissociation properties of the formed polyplexes, the heparin dissociation assay was performed.[46–48] Heparin, a sulfated glycosaminoglycan, has an anionic character and competes with the nucleic acid of the polyplex. With increasing amount of heparin, the pDNA dissociates from the polymer and the polyplex dissolves. As indicated in Fig. 4B, polyplexes formed with partially hydrolyzed PEtOx (**P(EtOx-*stat*-EI)**) as well as **P2** and **P3** polymers revealed a reversible binding, achieving 80% dissociation at 5 U mL^{-1} heparin. A higher heparin concentration (20 U mL^{-1}) was required for **P1** reaching 80% dissociation. One reason for

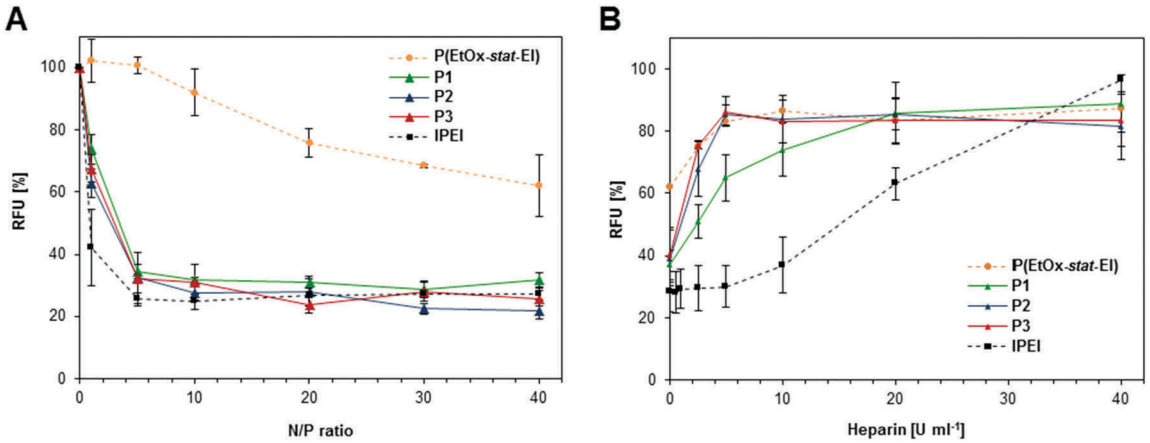

Fig. 4 Polyplex formation and stability with pDNA using the polymers **P(EtOx-*stat*-EI)**, **P1**, **P2**, **P3** as well as **lPEI**, which was used as positive control. (A) Complexation affinity (ethidium bromide quenching assay) of all polymers at the indicated N/P ratios. (B) Dissociation assay of polyplexes formed at N/P 30 using heparin. Values represent the mean ± S.D. (n = 3).

this might be the higher amount of AmButOx, responsible for an enhanced binding to the genetic material. However, a full release from the copolymers **P1** to **P3** could not be achieved using heparin. Therefore, another polyanion, namely poly(methacrylic acid) (PMAA, DP = 200), was successfully used as competitor (Fig. S5, ESI†). **lPEI** required an increased amount of heparin (40 U mL^{-1}) as compared to the copolymers. These results confirm the weakening of the electrostatic interactions caused by the presence of EtOx units, which are beneficial for a fast release of the genetic material.

As polyplexes are usually internalized into cells *via* endocytic pathways, the size as well as the charge of the complexes is of crucial importance. For efficient delivery, critical sizes of polymeric nanocarriers up to 200 nm are recommended.[33,49] As depicted in Table 2, the polyplexes formed with **P1** to **P3** at N/P 30 exhibit a favorable size of approximately 150 nm with a positive net charge, as determined by dynamic and electrophoretic light scattering. **P(EtOx-*stat*-EI)** formed complexes with a z-average of 242 ± 73.4 nm and high polydispersity (0.46) supporting the inefficient polyplex formation as observed by EBA.[50] Polyplexes formed with **lPEI** revealed a smaller complex size of 80 nm with a positive net charge comparable to previous studies.[46] These results support our assumption that the EtOx units impede the compact packaging of the genetic material into small polyplexes. This can be compensated by the presence of AmButOx units resulting in polyplex sizes between **lPEI** and loosely bound **P(EtOx-*stat*-EI)** polyplexes. Therefore, the tailored combination of EtOx and AmButOx units within the copolymer structure can be used to design polyplexes with required properties.

Table 2 Size and surface charge (zeta potential) of pDNA complexes at N/P 30 measured *via* dynamic light as well as electrophoretic light scattering

Polymeric system	z-Average [d, nm]	PDI	Zeta potential [mV]
P(EtOx-*stat*-PEI)	242 ± 73.4	0.46	20 ± 0.44
P1	158 ± 1.0	0.23	27 ± 0.25
P2	143 ± 1.4	0.21	23 ± 0.11
P3	154 ± 1.4	0.23	23 ± 0.12
lPEI	80 ± 2.3	0.17	33 ± 4.23

Transfection efficiency

Based on the previous results, the polymers **P1** to **P3** appear to be promising candidates as non-viral gene delivery agents and were, therefore, analyzed regarding their transfection efficiency (TE) using human embryonic kidney (HEK) cells and pDNA containing a enhanced green fluorescence protein reporter gene (*egfp*). The TE was determined by flow cytometry analyzing all viable cells (PI staining) which successfully express EGFP (see ESI,† Fig. S6 and S7). To investigate the interaction with serum proteins, a side effect of cationic polymers, the cells were transfected in serum reduced media (OptiMEM) and in serum containing media (RPMI1640 supplemented with 10% FCS) (Fig. 5). The use of serum offers test conditions more comparable to an *in vivo* situation and represents a known challenge for the performance of the polymers due to the inhibitory effect of serum proteins on the cellular uptake process.[51,52]

It should be noted that higher N/P ratios were required for the copolymers as all nitrogen atoms were taken into account for the N/P calculations. This includes also the amide functionalities of EtOx and AmButOx although they are not capable to interact with the pDNA. **P1**-based polyplexes were less efficient as indicated by a TE below 50%. High TEs over 60% were achieved in serum reduced conditions for **P2** and **P3** polyplexes at N/P 30 to 50. Comparable TEs were obtained for **lPEI** at N/P20. Compared to the transfection in OptiMEM, the EGFP transfection level of **P1** to **P3** at N/P 50 in serum containing media did not change considerably. Due to the cytotoxic effect of **lPEI** and the influence of serum proteins the cell viability as well as the TE decreased rapidly with increasing N/P ratios.

The combination of high cell viability (no cyto-/hemotoxicity) and formidable transfection performance even in the presence of proteins underlines the potential of **P2** and, in particular, **P3** as preferable gene delivery vectors. Moreover, **P3** also withstands

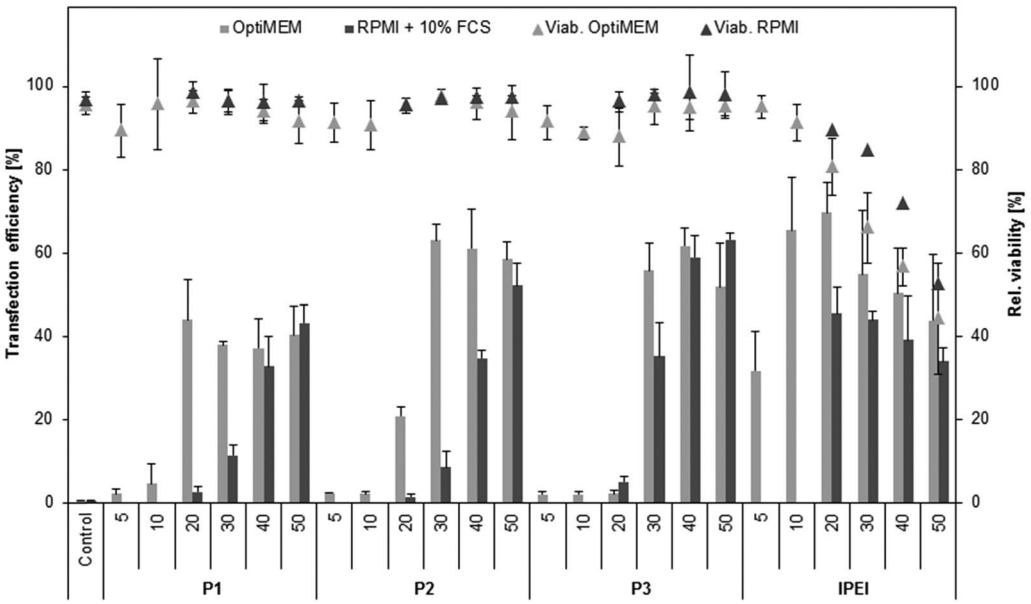

Fig. 5 Transfection efficiency of copolymers **P1** to **P3** and **lPEI** for adherent HEK cells in serum reduced (OptiMEM, light grey) and serum containing media (RPMI + 10% FCS, dark grey) at different N/P ratios after 24 h. Values represent the mean ± S.D. (n = 3).

a comparison to **lPEI** and the literature known 'gold standard for transfection', **comlPEI** (see ESI,† Fig. S18).

Uptake mechanism

For cationic polyplexes, the internalization into cells by endocytosis followed by the endosomal release of the pDNA into the cytosol and the subsequent transport into the nucleus is reported.[53,54] To clarify this process and to understand the excellent transfection performance of the copolymers, the uptake mechanism was investigated. An uptake kinetic using polyplexes formed with YOYO-1 labeled pDNA was performed to detect the internalization within cells by flow cytometry (Fig. 6). All tested polymers exhibited a fast and time-dependent cellular uptake. In detail, almost 90% of measured cells internalized polyplexes after 4 h when medium is changed

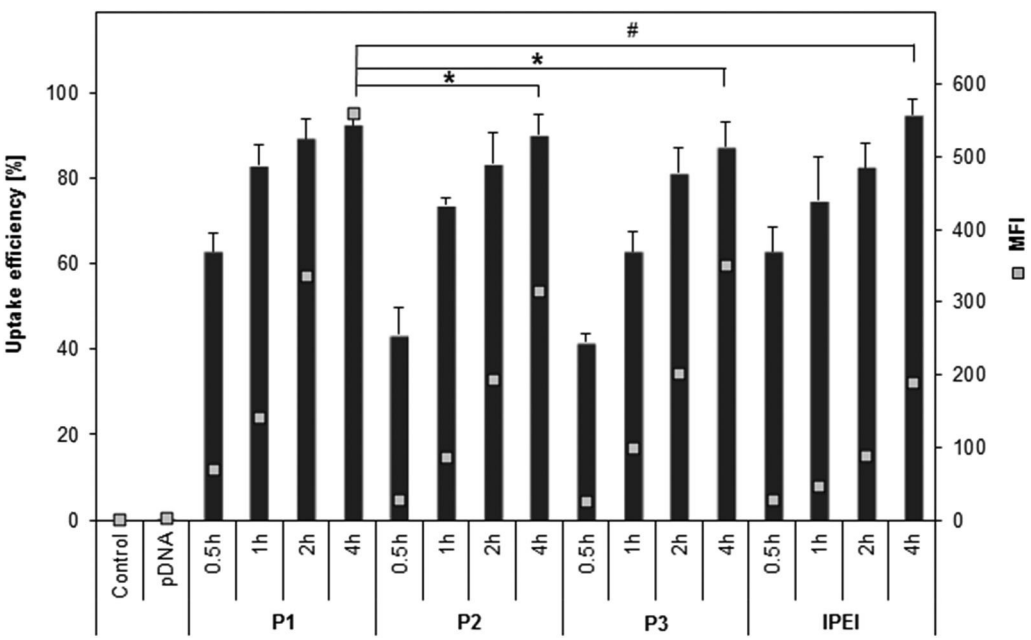

Fig. 6 Uptake study. Polyplexes formed with YOYO-1 labeled pDNA were incubated with HEK cells in OptiMEM for indicated time points using the copolymers **P1** to **P3** and **lPEI** (N/P ratio 30) as control. Statistical analysis (t-test) was used to compare the MFI after 4 h of **P1** with **P3** and **lPEI**, * represents $p < 0.05$ and # $p < 0.005$ of MFI values using student's t-test. Values represent the mean ± S.D. (n = 3).

according to standard transfection protocol. In particular, **P1** as well as **lPEI** showed an enhanced uptake efficiency after 30 min (~60%) compared to **P2** and **P3** (40%). Although most of the cells internalized polyplexes, the quantities (mean fluorescence intensities, MFI) differ significantly after 4 h (Fig. 6). Higher internalized polyplex concentrations were detected in cells using **P2**, **P3** (twofold) and **P1** (threefold) compared to **lPEI**. An explanation might be the introduction of AmButOx to the copolymers for enhanced complexation with the genetic material and cellular uptake, while the EtOx content possessing reduced membrane disruption.

To preclude an uptake by passive membrane diffusion, the uptake of YOYO-1 stained polyplexes was performed at 4 °C and 37 °C, respectively (Fig. S8B, ESI†). Polyplexes of all tested polymers were internalized into cells at 37 °C with approximately 90% efficiency. In contrast, the uptake efficiency was significantly decreased to approximately 10% at 4 °C for all samples. This indicates an energy-dependent uptake (endocytotic process). Furthermore, bafilomycin, a proton pump (H^+-ATPase) inhibitor, was used to prevent endosomal release caused by acidification (Fig. S8A, ESI†). The inhibition of an endosomal escape prevents the release of pDNA into the cytoplasm, the transfer into the nucleus and the EGFP expression. As expected, the TE significantly decreased after treatment with bafilomycin for all tested polymers to <5%. This indicates the involvement of the endosomal uptake and release as critical steps during the transfection mechanism, as it is reported for PEI.[43,55]

High resolution microscopy of polyplex–cell interactions

Deeper insights into the uptake mechanism and the fate of polyplexes within the cells were obtained with microscopic studies including confocal microscopy, structured illumination microscopy (SIM) and high-angular annular dark-field scanning transmission electron microscopy (HAADF-STEM).

Confocal microscopy as well as SIM studies were performed with HEK cells and polyplexes based on YOYO-1 labeled pDNA and Cy5-labeled **P3** representing the polymer with the overall highest transfection efficiency compared to **lPEI**. Fluorescence imaging of cells, in particular SIM images, revealed a co-localization of pDNA-bound **P3** polyplexes (blue) within the lysosomes/late endosomes (red, RFP labeling, Fig. 7 and Fig. S9 and S10, ESI†). The detection of the YOYO-signal within the cytoplasm that was not co-localized with lysosomal structures reveals that pDNA is released from the polyplex itself. Considering the low concentration of heparin required to destabilize the polyplex, an efficient release of pDNA into the cytoplasm can be assumed. As SIM provides a resolution of approx. 100 nm, a more detailed insight into the polyplex behavior within the lysosomes/late endosomes was obtained compared to conventional confocal imaging. A non-centrically localization of **P3** polyplexes

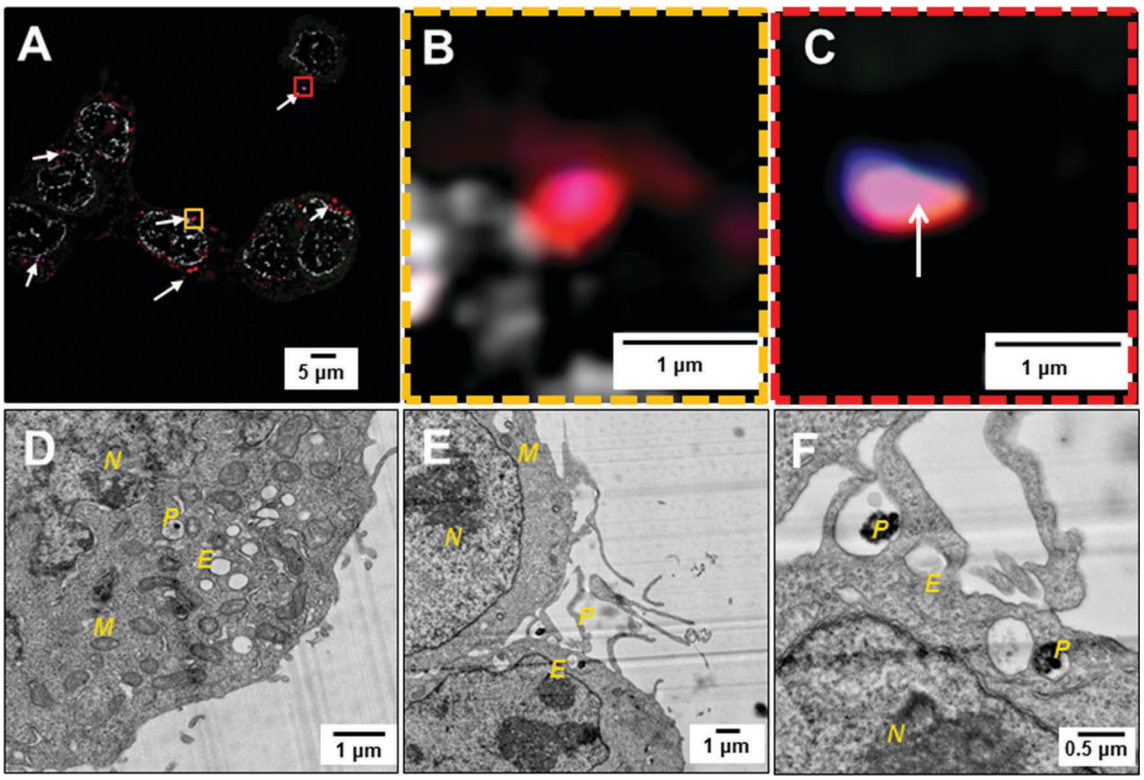

Fig. 7 High resolution imaging. (A) Structured illumination image of **P3**-based polyplexes within cells (deconvolved data). White arrows indicate co-localization of **P3**-pDNA polyplexes within lysosomes. (B and C) Magnified view of the yellow and red, dash-lined frame in (A): **P3**-Cy5 polyplex within the endosome. 63× Oil Obj. 1.4 NA. Grey: Hoechst 33342. Red: lysosomal membrane (RFP). Green: plasmid DNA labeling (YOYO-1). Blue: polymer labeling (Cy-5). (D–F) HAADF-STEM images of **P3**-based polyplexes taken up by HEK cells. The following letters correspond to cell organelles: N = cell nucleus, M = mitochondria, E = endosomal compartment, P = polyplex.

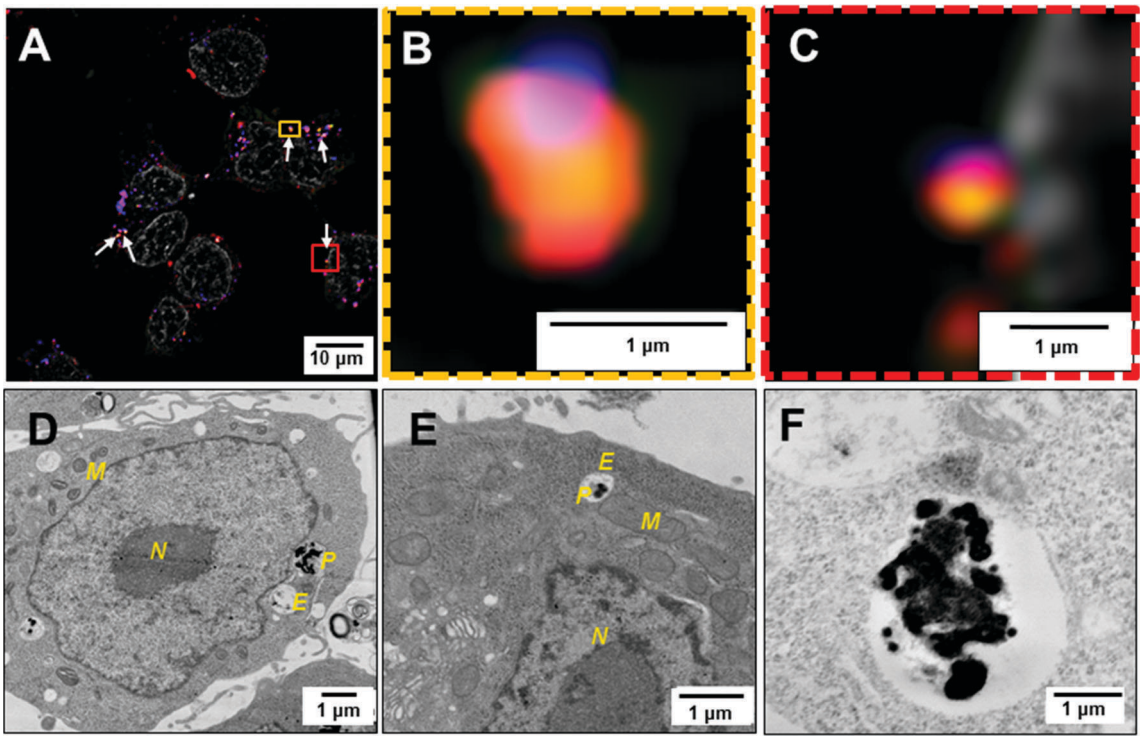

Fig. 8 High resolution imaging. (A) Structured illumination image of **lPEI**-based polyplexes within HEK cell, white arrows indicates full co-localization (deconvolved data). (B and C) Magnified zoom of yellow and red, dash-lined frame in (A): **lPEI-Cy5** polyplex within the endosome. 63× oil obj. 1.4 NA. Grey: Hoechst 33342. Red: lysosomal membrane (RFP). Green: plasmid DNA labeling (YOYO-1). Blue: polymer labeling (Cy-5). (D–F) HAADF-STEM images of **lPEI**-based polyplex taken up by HEK-293 cell. The following letters correspond to cellular structures: N = cell nucleus, M = mitochondria, E = endosomal compartment, P = polyplex.

(Cy5 and YOYO-1 signal) within the endosome (red) was observed, being in close vicinity to the endosomal membrane (Fig. 7A and zoom-in Fig. 7B and C, single channel splitting: Fig. S11, ESI†). This could be attributed to a strong interaction between the polyplex and the cytoplasmic membrane at the time of the cellular uptake or a strong interaction of the polyplex with the endosomal membrane caused by acidification. However, also **lPEI** polyplexes (Cy5 and YOYO-1 signal) were localized in close vicinity to the endosomal membrane (Fig. 8A and zoom-in Fig. 8B and C, single channel splitting: Fig. S12, ESI†). Interestingly, a higher number of larger endosomes bearing polyplex signals with an apparent larger spatial dimension was found for **lPEI** in contrast to **P3**. To study the interaction of both polymers with the endosomal membrane in more detail, STEM on embedded sections was carried out to confirm this assumption. STEM provides a resolution in the low nanometer range, elucidating the subcellular ultrastructural context, and particularly, highlighting membrane structures. EM images revealed an uptake of single **P3** polyplexes into vesicles with sizes of 200 to 500 nm ($n > 10$ vesicles of different sections were analyzed, Fig. S13, ESI†). Although, the polyplexes themselves provide only poor electron contrast, their structures were highlighted efficiently within the cellular environment (Fig. 7D–F) in the sample by sample staining. This can be explained by the strong affinity of the amines of the polymer and phosphates of the DNA to the heavy metal stains (OsO_4 and uranylacetate, respectively). The close vicinity between **P3** polyplex and the endosomal membrane was confirmed. We attribute this observation to a preceding active cell membrane-driven uptake event, initiated by strong interaction of a single polyplex with the membrane. We observed an uptake event involved by membrane ruffles and lamellipodia-like structures (Fig. 7E and F), supporting our previous findings concerning an energy-dependent uptake, such as by macropinocytosis. We therefore investigated cells after incubation with **P3** polyplexes in the presence of the inhibitor, 5-(*N*-ethyl-*N*-isopropyl)amiloride (EIPA, 100 µM). Our experiments support the assumption, since only 25% of the cells internalized **P3** polyplexes after 4 h (see ESI,† Fig. S14). Performing STEM imaging, we observed no **P3** polyplexes within the cytoplasm (see ESI,† Fig. S15A and B). This underlines an uptake mechanism *via* macropinocytosis.

STEM images of **lPEI** polyplexes revealed larger endosomes with sizes of 500 to 1500 nm ($n > 10$ vesicles of different sections were analyzed, Fig. S16, ESI†) bearing more than a single polyplex as well as increased cellular membrane rupture (Fig. 8D–F). The presence of multiple polyplexes within large endosomes explains the large spatial dimension of the polyplex signals as being found in SIM images (Fig. 8F). STEM images of cells, which were incubated with **lPEI** polyplexes in the presence of a macropinocytosis inhibitor (EIPA), revealed indeed a cellular internalization (see ESI,† Fig. S15C and D). However, the uptake efficiency was apparently lower compared to the

standard uptake protocol (~65% YOYO-positive cells after 4 h) and hints towards alternative uptake mechanisms in addition to macropinocytosis. It was already demonstrated that **lPEI** possesses a high membrane activity (see erythrocyte aggregation, Fig. S3 and S4, ESI†), which is in association with polymer aggregation in serum containing media[5] and could lead to enhanced uptake of multiple polyplexes within single endosomes. Aggregated polyplexes could be also responsible for a reduced uptake because of a size-limited uptake mechanism, *e.g.* endocytosis. The presence of EtOx subunits within **P3** shields the formed polyplexes from aggregation caused by protein interaction prior to uptake. This might be a reason for a more efficient cellular uptake and the high transfection efficiency of the respective copolymer. Based on this data, the efficient endosomal release of single **P3** polyplexes is impressive compared to agglomerated **lPEI** polyplexes. Due to the high buffer capacity of **lPEI**, an enhanced protonation of amines followed by the swelling of the endosomes might occur, as it is hypothesized for the "proton sponge" effect.[6,51,53,54,56] In case of **P3**, the full protonation of the primary/secondary amines could lead to a destabilization of the membrane indicating a membrane rupture and the subsequent release of the cargo into the cytosol. A previous study of Zuhorn and co-workers describes a similar process for PEI polyplexes supporting these findings.[52] Additionally, the authors showed that the release did not come along with a complete rupture of the endosome. As the polymers **P1** to **P3** possess a content of 12 to 23% secondary amines and a content of primary amines of 34 to 23%, they do not show such a severe swelling of endosomal compartments like **lPEI** polyplexes. Nevertheless, it can be assumed that a protonation of the primary amines in the side chain within the endosomal compartments forces the interaction of the polymers with the endosomal membrane leading to an efficient endosomal release. These results indicate that not only the buffer capacity and the swelling of endosomal compartments but also the interaction of the polymer with the endosomal membrane facilitate the escape from the endosome, which is in accordance to literature data and visualized in detail.[51,52]

siRNA delivery

To further investigate the potential of the modified PEI copolymers, the delivery efficiency for siRNA was determined. Although DNA and siDNA represent genetic material they differ in certain characteristics. Most importantly, siRNA is smaller (<30 base pairs (bp) compared to 4700 bp pDNA) and more rigid. From a biological point of view, pDNA has to be transferred across the nuclear barrier to the cell nuclei, whereas siRNA has to be released from the polyplex in the cytoplasm to form the RNA-induced silencing complex (RISC).[57]

The copolymers **P1** to **P3** were further investigated regarding the influence of primary and secondary amines for siRNA delivery. High binding affinity to siRNA (<40%) of all tested polymers was observed by EBA (Fig. 9A). Positively charged polyplexes with a size of <200 nm were formed, whereas **lPEI** polyplexes exhibited a compact size of around 83 nm (Table 3). This trend was also observed for the pDNA based polyplexes (see Table 2).

A GFP-expressing CHO cell line was used to estimate the knockdown efficiency (Fig. 9B). Interestingly, **P1** showed superior knockdown efficiency for siRNA (244 ± 50.3 MFI), compared to **P3** (317 ± 19.3 MFI), which was identified as best performer for pDNA transfection. Both, **P1** and **P2**, led to a significant reduction of around 40% of the fluorescence intensity of EGFP-expressing cells. In contrast, **P3** showed only 10 to 20% reduction of MFI. Interestingly, **lPEI** as well as branched PEI

Table 3 Size and surface charge (zeta potential) of the siRNA complexes at N/P 30 measured *via* dynamic light as well as electrophoretic light scattering in water-based HBG buffer

Polymeric system	*z*-Average [d, nm]	PDI	Zeta potential [mV]
P1	102 ± 1.2	0.15	21 ± 1.2
P2	124 ± 1.5	0.13	25 ± 1.0
P3[a]	149 ± 12.6	0.49	22 ± 0.1
lPEI	83 ± 2.3	0.23	33 ± 1.6

[a] Intensity weighted size distribution revealed a mean peak of 257 nm (68%).

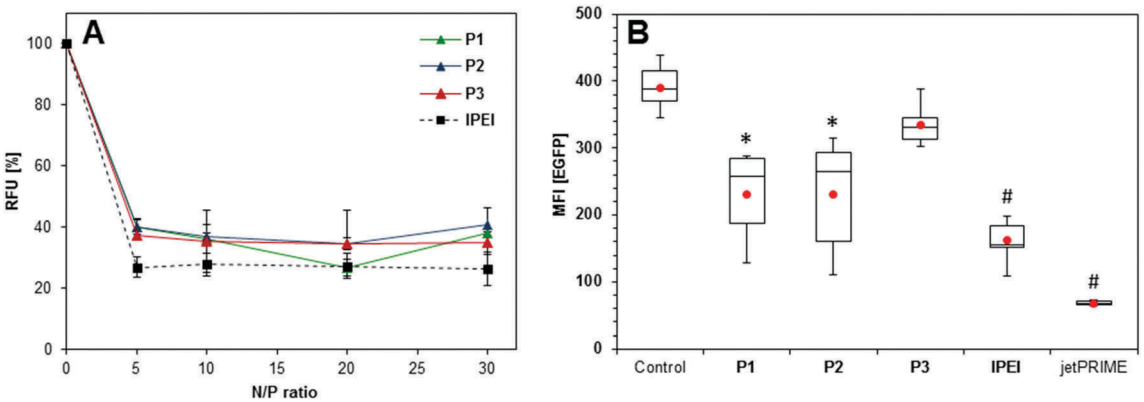

Fig. 9 Investigations of the siRNA delivery. (A) Binding affinity of siRNA to **P1** to **P3** and **lPEI** at different N/P ratios measured by the fluorescence quenching of ethidium bromide. The fluorescence of pure siRNA represents 100% RFU. (B) siRNA knockdown mediated by **P1** to **P3**, **lPEI** and jetPRIME polyplexes at N/P 30 after 72 h. Stable EGFP-expressing CHO cells were transfected with polyplexes formed using siRNA able to knock down *egfp*. Statistical analysis (*t*-test) was used to compare the mean fluorescence intensity (MFI) of the control with **P1** to **P3** and **lPEI**, * represents $p < 0.05$ and # $p < 0.005$. The values represent the mean ± S.D. ($n \geq 3$).

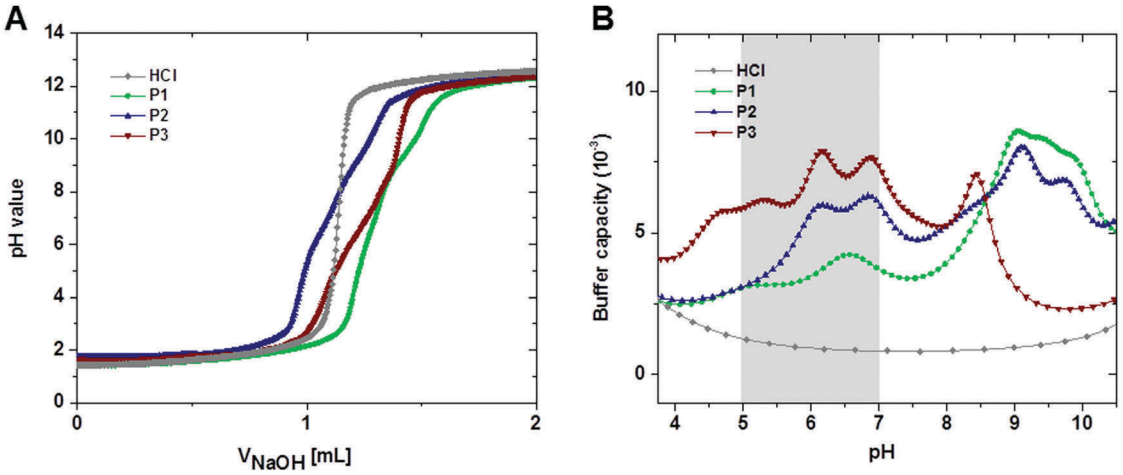

Fig. 10 (A) Acid–base titration curves of an acidified solution of the cationic copolymers **P1** to **P3** (~5 mg mL^{-1}) dissolved in 4 mL hydrogen chloride (HCl, 0.06 M) and neutralized with sodium hydroxide (0.1 M). For comparison, 0.06 M HCl was titrated accordingly. Precipitation of **lPEI** at pH 7 prevents the interpretation of the respective titration curve. (B) The buffer capacities of the cationic copolymers **P1** to **P3** were calculated from A utilizing the relation $\beta = dn(OH^-)/dpH$ and presented as a function of the pH value. For comparison, the buffer capacity of HCl is included.

(**bPEI**) revealed high knockdown potentials of around 60% (Fig. 9B). **ComlPEI** was less efficient and exhibited comparable efficiencies to the copolymers **P1** and **P2** (Fig. S20, ESI†). However, the highest knockdown (>80%, ~68 ± 3.9 MFI) was achieved with the positive control jetPRIME (cationic, polymeric transfection reagent, Polyplus). The fluorescence intensities were not reduced when using scrambled siRNA (negative control, see ESI,† Fig. S17). The polymers **P1** and **P2** revealed adequate knockdown levels, but are not as effective as commercially available siRNA transfection agents. Nevertheless, the promising performance and high biocompatibility of these 3rd generation PEIs could be developed in future studies by optimizing the polymeric design and composition as a higher AmOx content shows improved performance.

To understand the different performances of the copolymers depending on the genetic material, the endosomal release has to be considered. For successful delivery of siRNA a fast and efficient release from the endosome into the cytosol is beneficial, whereas the transfection efficiency of pDNA is increased, when it is transported to the perinuclear region inside endosomal compartments.[58]

From the titration of the polymers **P1** to **P3** (Fig. 10A) the buffer capacities of the respective copolymers were calculated ($\beta = dn(OH^-)/dpH$) and expressed as a function of the pH value (Fig. 10B). The copolymers show considerable higher buffer capacities with increasing EI content for pH values between 5 and 7 (endosomal release environment). As **P3** revealed the

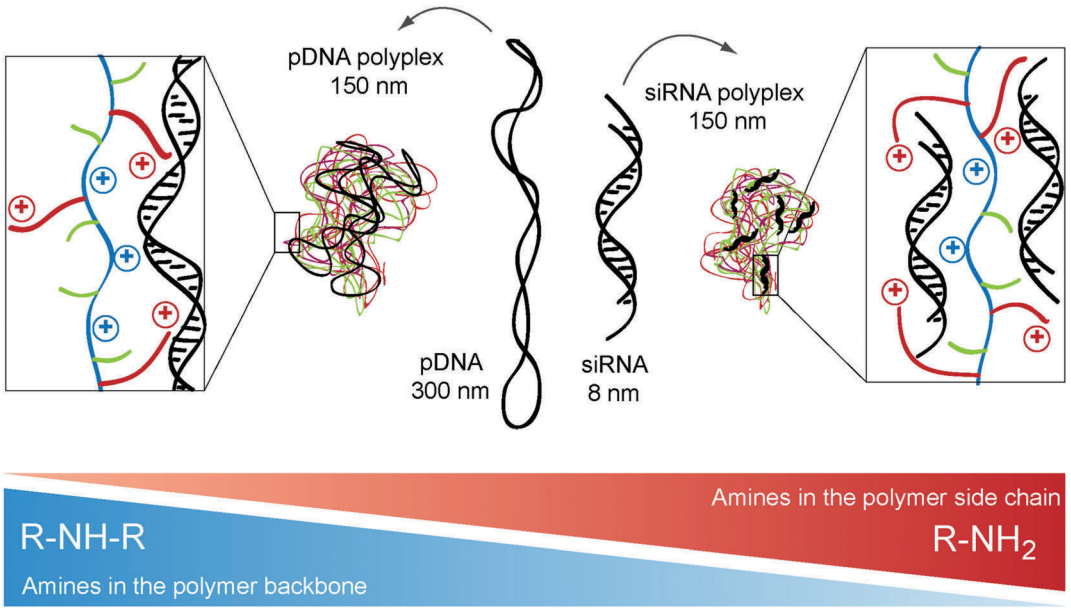

Fig. 11 Schematic representation of the polyplex formation illustrating the interaction of 3rd generation poly(ethylene imine) with pDNA or siRNA.

highest buffer capacity at acidic conditions, this could be an explanation for the diminished performance for siRNA delivery due to a delayed endosomal escape. In contrast, **P1** showed the highest degree of protonation at endosomal pH values facilitating a faster endosomal release into the cytosol by interaction of the charged amines with the endosomal membrane. It should be kept in mind, that **P1** and **P2** revealed also a high buffer capacity at a pH value around 9, in contrast to **P3**, which could be a hint for different performances.

Moreover, it could be assumed that the different physicochemical parameters of the genetic material (size, topology) play a crucial role for the interaction with the 3rd generation PEIs (Fig. 11). siRNA is small and stiff preferentially interacting with the primary amines in the polymer side chain. In contrast to that, the large pDNA requires the interaction with the primary amines (flexible side chains) as well as the secondary amines (backbone). This enabled an tremendous enhancement of pDNA delivery compared to literature reported polymer systems, *e.g.* P(EtOx-*stat*-MeOx).[17]

Conclusion

The introduced 3rd generation PEI copolymers has shown to present several advantages in contrast to 1st (PEI) and 2nd (single PEI modifications) generation approaches in terms of efficient polymeric gene delivery. Starting from high molar mass PEtOx, partially hydrolyzed **P(EtOx-*stat*-EI)** copolymers were synthesized. Subsequently, different amounts of the ethylene imine subunits were functionalized, introducing alkene groups which, in turn, could be used to attach primary amine groups in the side chains using thiol–ene chemistry. While the EtOx content of these polymers remained constant, the ratio between primary and secondary amine groups was varied to obtain a series of copolymers. It should be highlighted that no adverse effects on the cell viability was observed for polymer concentrations up to 1 mg mL^{-1} in contrast to **lPEI** (IC_{50} = 3.6 μg mL^{-1}). Remarkably, these 3rd generation PEIs were, in contrast to the 2nd generation **P(EtOx-*stat*-EI)**, able to form well-defined complexes with various genetic materials, in detail pDNA and siRNA. Besides a fast uptake, the delivery of pDNA revealed comparable transfection efficiencies to **lPEI**. In serum containing media, the performance of copolymer-based polyplexes could even exceed the efficiency of **lPEI**. Furthermore, the copolymers (in particular **P1** and **P2**) revealed siRNA delivery capability as well. Nevertheless, an optimization of this approach should be further pursued in future studies. Noteworthy, a different ratio of primary to secondary amines is required to form appropriate polyplexes with siRNA emphasizing the multivalence and potential of the presented polymeric system.

Using live cell confocal microscopy, super-resolution microscopy as well as transmission electron microscopy of ultrathin sections of embedded cell samples, the transfection mechanism was elucidated in more detail. In contrast to **lPEI**, where endosomes contained multiple polyplexes in swollen endosomes, copolymer based polyplexes present themselves individually within the endosomal compartments. This was attributed to a lower protein interaction of **PEtOx** containing vectors, preventing agglomeration in serum containing media prior to uptake as well as to a diminished membrane interaction. This feature also leads to a release process based on membrane interactions of the described polyplexes in contrast to the ''proton sponge'' effect hypothesized for PEI. The 3rd generation PEI outperforms PEI of former generations (1st and 2nd) concerning an overall concept in terms of toxicity as well as transfection efficiency for a wide range of genetic materials. Thus, it represents a promising alternative for more complex transfection approaches including hard-to-transfect cells or *in vivo* studies.

Acknowledgements

The authors would like to thank Dr. Michael Wagner for AF4 measurements and Carolin Fritzsche for support of the cyto- and hemocompatibility assays. This project was funded by the German Federal Ministry of Education & Research (BMBF, #031A518B Vectura, #13N13416 smart-dye-livery), the Thüringer Ministerium für Wirtschaft, Wissenschaft, und Digitale Gesellschaft (TMWWDG, ProExzellenzI, NanoConSens; ProExzellenzII, NanoPolar). The funding of the collaborative research center ChemBioSys (SFB 1127) by the Deutsche Forschungsgemeinschaft (DFG) is highly acknowledged. MR and AT are grateful for the financial support in the frameworks of ''Carl-Zeiss-Strukturmaßnahme'' and the Carl-Zeiss Stiftung. MH gratefully acknowledges the DFG (GZ: HA 7725/1-1) for funding. The LSM880 ELYRA PS.1 was further funded with a grant from the DFG. The transmission electron microscope was obtained with a grant from the European Funds for Regional Developments (EFRE) and the DFG.

References

1 U. Laechelt and E. Wagner, *Chem. Rev.*, 2015, **115**, 11043–11078.
2 A. C. Rinkenauer, S. Schubert, A. Traeger and U. S. Schubert, *J. Mater. Chem. B*, 2015, **3**, 7477–7493.
3 U. Lungwitz, M. Breunig, T. Blunk and A. Göpferich, *Eur. J. Pharm. Biopharm.*, 2005, **60**, 247–266.
4 M. A. Mintzer and E. E. Simanek, *Chem. Rev.*, 2009, **109**, 259–302.
5 M. Neu, D. Fischer and T. Kissel, *J. Gene Med.*, 2005, **7**, 992–1009.
6 O. Boussif, F. Lezoualc'h, M. A. Zanta, M. D. Mergny, D. Scherman, B. Demeneix and J. P. Behr, *Proc. Natl. Acad. Sci. U. S. A.*, 1995, **92**, 7297–7301.
7 W. T. Godbey, M. A. Barry, P. Saggau, K. K. Wu and A. G. Mikos, *J. Biomed. Mater. Res.*, 2000, **51**, 321–328.
8 S. De Smedt, J. Demeester and W. Hennink, *Pharm. Res.*, 2000, **17**, 113–126.
9 I. Y. Perevyazko, M. Bauer, G. M. Pavlov, S. Hoeppener, S. Schubert, D. Fischer and U. S. Schubert, *Langmuir*, 2012, **28**, 16167–16176.
10 M. Jager, S. Schubert, S. Ochrimenko, D. Fischer and U. S. Schubert, *Chem. Soc. Rev.*, 2012, **41**, 4755–4767.

11 P. Chollet, M. C. Favrot, A. Hurbin and J.-L. Coll, *J. Gene Med.*, 2002, **4**, 84–91.
12 J. H. Jeong, S. H. Song, D. W. Lim, H. Lee and T. G. Park, *J. Controlled Release*, 2001, **73**, 391–399.
13 Y. Yue, F. Jin, R. Deng, J. Cai, Z. Dai, M. C. M. Lin, H.-F. Kung, M. A. Mattebjerg, T. L. Andresen and C. Wu, *J. Controlled Release*, 2011, **152**, 143–151.
14 M. Thomas, Q. Ge, J. J. Lu, J. Chen and A. Klibanov, *Pharm. Res.*, 2005, **22**, 373–380.
15 W. Y. Seow, K. Liang, M. Kurisawa and C. A. E. Hauser, *Biomacromolecules*, 2013, **14**, 2340–2346.
16 C. Englert, M. Hartlieb, P. Bellstedt, K. Kempe, C. Yang, S. K. Chu, X. Ke, J. M. García, R. J. Ono, M. Fevre, R. J. Wojtecki, U. S. Schubert, Y. Y. Yang and J. L. Hedrick, *Macromolecules*, 2015, **48**, 7420–7427.
17 A. C. Rinkenauer, L. Tauhardt, F. Wendler, K. Kempe, M. Gottschaldt, A. Traeger and U. S. Schubert, *Macromol. Biosci.*, 2015, **15**, 414–425.
18 S. Taranejoo, J. Liu, P. Verma and K. Hourigan, *J. Appl. Polym. Sci.*, 2015, 132.
19 S. Ochrimenko, A. Vollrath, L. Tauhardt, K. Kempe, S. Schubert, U. S. Schubert and D. Fischer, *Carbohydr. Polym.*, 2014, **113**, 597–606.
20 M. Noga, D. Edinger, E. Wagner, G. Winter and A. Besheer, *J. Biomater. Sci., Polym. Ed.*, 2014, **25**, 855–871.
21 M. Ogris, S. Brunner, S. Schuller, R. Kircheis and E. Wagner, *Gene Ther.*, 1999, **6**, 595–605.
22 H. Petersen, P. M. Fechner, D. Fischer and T. Kissel, *Macromolecules*, 2002, **35**, 6867–6874.
23 K. Knop, R. Hoogenboom, D. Fischer and U. S. Schubert, *Angew. Chem., Int. Ed.*, 2010, **49**, 6288–6308.
24 J. Liu, X. Jiang, L. Xu, X. Wang, W. E. Hennink and R. Zhuo, *Bioconjugate Chem.*, 2010, **21**, 1827–1835.
25 N. Zhao, S. Roesler and T. Kissel, *Int. J. Pharm.*, 2011, **411**, 197–205.
26 G. Zhang, J. Liu, Q. Yang, R. Zhuo and X. Jiang, *Bioconjugate Chem.*, 2012, **23**, 1290–1299.
27 Y. Yamazaki, M. Nango, M. Matsuura, Y. Hasegawa, M. Hasegawa and N. Oku, *Gene Ther.*, 2000, **7**, 1148–1155.
28 A. Sato, S. Kawakami, M. Yamada, F. Yamashita and M. Hashida, *J. Drug Targeting*, 2001, **9**, 201–207.
29 X. Wang, D. Niu, C. Hu and P. Li, *Curr. Pharm. Des.*, 2015, **21**, 6140–6156.
30 A. T. Press, A. Traeger, C. Pietsch, A. Mosig, M. Wagner, M. G. Clemens, N. Jbeily, N. Koch, M. Gottschaldt, N. Bézière, V. Ermolayev, V. Ntziachristos, J. Popp, M. M. Kessels, B. Qualmann, U. S. Schubert and M. Bauer, *Nat. Commun.*, 2014, **5**, 5565–5577.
31 H. P. C. Van Kuringen, J. Lenoir, E. Adriaens, J. Bender, B. G. De Geest and R. Hoogenboom, *Macromol. Biosci.*, 2012, **12**, 1114–1123.
32 R. Shah, Z. Kronekova, A. Zahoranová, L. Roller, N. Saha, P. Saha and J. Kronek, *J. Mater. Sci.: Mater. Med.*, 2015, **26**, 1–12.
33 R. Luxenhofer, G. Sahay, A. Schulz, D. Alakhova, T. K. Bronich, R. Jordan and A. V. Kabanov, *J. Controlled Release*, 2011, **153**, 73–82.
34 S.-D. Li and L. Huang, *J. Controlled Release*, 2010, **145**, 178–181.
35 A. C. Rinkenauer, A. Schallon, U. Günther, M. Wagner, E. Betthausen, U. S. Schubert and F. H. Schacher, *ACS Nano*, 2013, **7**, 9621–9631.
36 A. Gress, A. Völkel and H. Schlaad, *Macromolecules*, 2007, **40**, 7928–7933.
37 A. Krieg, C. Pietsch, A. Baumgaertel, M. D. Hager, C. R. Becer and U. S. Schubert, *Polym. Chem.*, 2010, **1**, 1669–1676.
38 H. M. L. Lambermont-Thijs, F. S. van der Woerdt, A. Baumgaertel, L. Bonami, F. E. Du Prez, U. S. Schubert and R. Hoogenboom, *Macromolecules*, 2010, **43**, 927–933.
39 M. Litt, A. Levy and J. Herz, *J. Macromol. Sci., Chem. A*, 1975, **9**, 703–727.
40 M. Bauer, S. Schroeder, L. Tauhardt, K. Kempe, U. S. Schubert and D. Fischer, *J. Polym. Sci., Part A: Polym. Chem.*, 2013, **51**, 1816–1821.
41 M. Bauer, C. Lautenschlaeger, K. Kempe, L. Tauhardt, U. S. Schubert and D. Fischer, *Macromol. Biosci.*, 2012, **12**, 986–998.
42 C. Englert, L. Tauhardt, M. Hartlieb, K. Kempe, M. Gottschaldt and U. S. Schubert, *Biomacromolecules*, 2014, **15**, 1124–1131.
43 T. Bieber, W. Meissner, S. Kostin, A. Niemann and H. P. Elsasser, *J. Controlled Release*, 2002, **82**, 441–454.
44 J. B. Lepecq and C. Paoletti, *J. Mol. Biol.*, 1967, **27**, 87–106.
45 A. J. Geall and I. S. Blagbrough, *J. Pharm. Biomed. Anal.*, 2000, **22**, 849–859.
46 A. Kwok and S. L. Hart, *Nanomedicine*, 2011, **7**, 210–219.
47 M. Ruponen, S. Ylä-Herttuala and A. Urtti, *Biochim. Biophys. Acta*, 1999, **1415**, 331–341.
48 S. Sundaram, S. Viriyayuthakorn and C. M. Roth, *Biomacromolecules*, 2005, **6**, 2961–2968.
49 J. Rejman, V. Oberle, I. S. Zuhorn and D. Hoekstra, *Biochem. J.*, 2004, **377**, 159–169.
50 R. V. Benjaminsen, M. A. Mattebjerg, J. R. Henriksen, S. M. Moghimi and T. L. Andresen, *Mol. Ther.*, 2013, **21**, 149–157.
51 M. Wagner, A. C. Rinkenauer, A. Schallon and U. S. Schubert, *RSC Adv.*, 2013, **3**, 12774–12785.
52 Z. U. Rehman, D. Hoekstra and I. S. Zuhorn, *ACS Nano*, 2013, **7**, 3767–3777.
53 A. M. Funhoff, C. F. van Nostrum, G. A. Koning, N. M. E. Schuurmans-Nieuwenbroek, D. J. A. Crommelin and W. E. Hennink, *Biomacromolecules*, 2004, **5**, 32–39.
54 A. Akinc, M. Thomas, A. M. Klibanov and R. Langer, *J. Gene Med.*, 2005, **7**, 657–663.
55 J. Rejman, A. Bragonzi and M. Conese, *Mol. Ther.*, 2005, **12**, 468–474.
56 J. P. Behr, *Acc. Chem. Res.*, 2012, **45**, 980–984.
57 A. T. Da Poian, F. A. Carneiro and F. Stauffer, *Braz. J. Med. Biol. Res.*, 2005, **38**, 813–823.
58 C. Scholz and E. Wagner, *J. Controlled Release*, 2012, **161**, 554–565.

Electronic Supplementary Material (ESI) for Journal of Materials Chemistry B.

SUPPORTING INFORMATION:

3rd Generation Poly(ethylene imine)s for Gene Delivery

Tanja Bus,[a,b,†] Christoph Englert,[a,b,†] Martin Reifarth,[a,b,c,d] Philipp Borchers,[a,b]
Matthias Hartlieb,[a,b,#] Antje Vollrath,[a,b] Stephanie Hoeppener,[a,b]
Anja Traeger,[a,b,] Ulrich S. Schubert[a,b,]**

[a] *Laboratory of Organic and Macromolecular Chemistry (IOMC), Friedrich Schiller University Jena, Humboldtstrasse 10, 07743 Jena, Germany*

[b] *Jena Center for Soft Matter (JCSM), Friedrich Schiller University Jena, Philosophenweg 7, 07743 Jena, Germany*

[c] *Institute of Physical Chemistry and Abbe Center of Photonics, Friedrich Schiller University Jena, Helmholtzweg 4, 07743 Jena, Germany*

[d] *Leibniz Institute of Photonic Technology, Albert-Einstein-Strasse 9, 07745 Jena, Germany*

[†] *The authors contributed equally to this work*

[#] *Current address: Department of Chemistry, University of Warwick, Gibbet Hill Road, Coventry, CV4 7AL, UK.*

Email: ulrich.schubert@uni-jena.de, anja.traeger@uni-jena.de

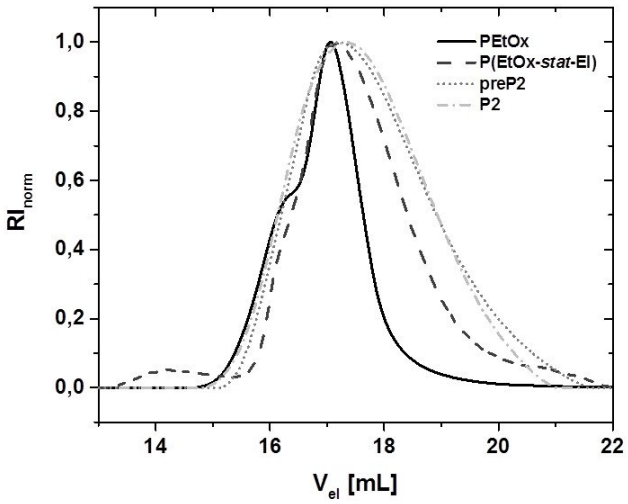

Figure S1. Size exclusion chromatography traces of the starting homopolymer **PEtOx** and the copolymers **P(EtOx-*stat*-EI)**, **preP2** and **P2** (*N*,*N*-dimethylacetamide, 0.21% LiCl, calibration: polystyrene).

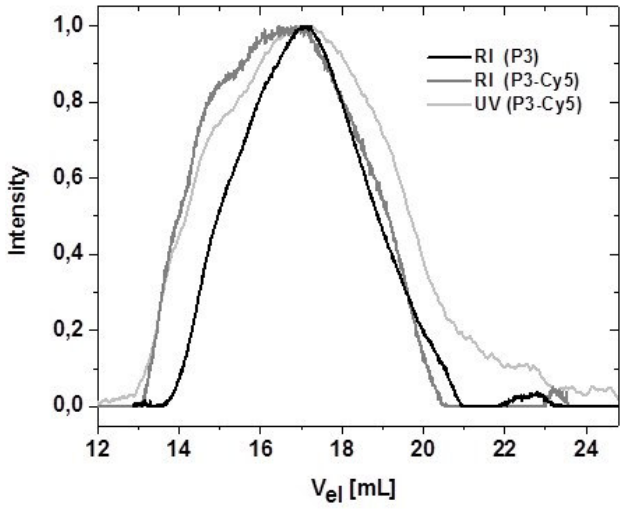

Figure S2. Size exclusion chromatography elugrams of the labeled copolymer **P3** (**P3-Cy5**) in comparison to the unlabeled starting material (**P3**) (*N*,*N*-dimethylacetamide, 0.21% LiCl, calibration: polystyrene).

Hemocompatibility of PEI-based polyplexes

The erythrocyte aggregation of the PEI copolymers was performed in parallel with high molar mass lPEI polymers as positive controls. **lPEI** show membrane-perturbing activity at high concentrations (100 µg mL^{-1}) leading to the aggregation of erythrocytes as indicated in the photospectrometrically measurement and by light microscopy. This effect was not seen with the copolymers **P1** to **P3**.

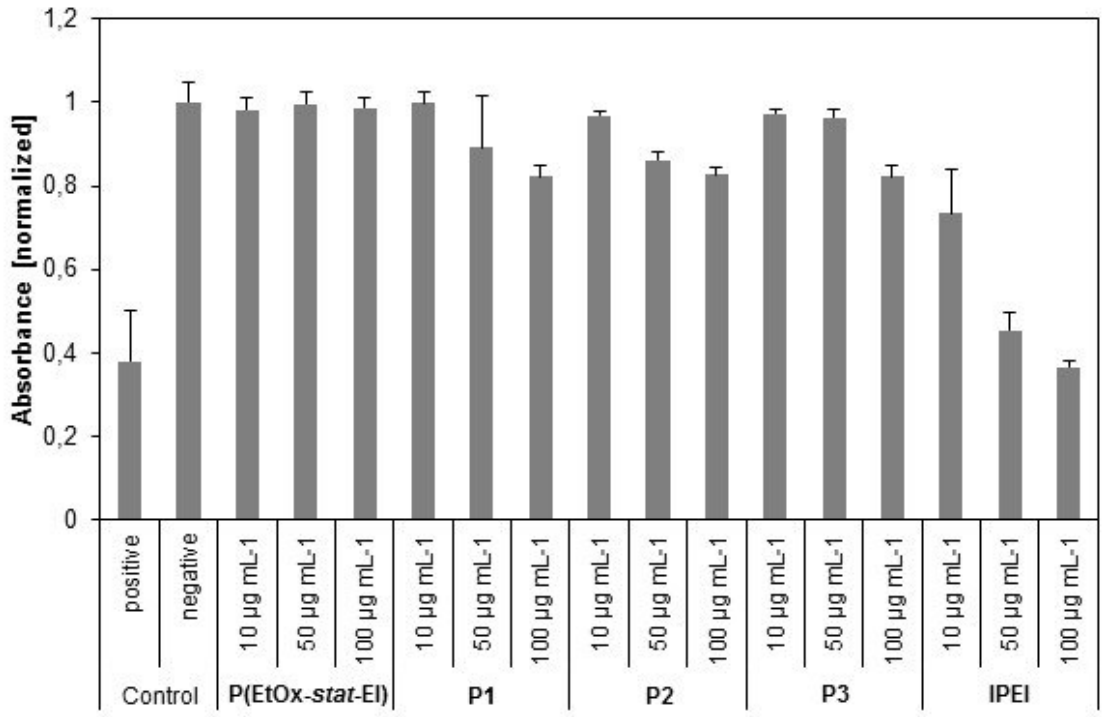

Figure S3. Erythrocyte aggregation of the tested polymers at indicated concentrations. bPEI (25 kDa) served as positive control resulting in high aggregation formation and PBS as negative control. Values represent the mean ± S.D. (n=3).

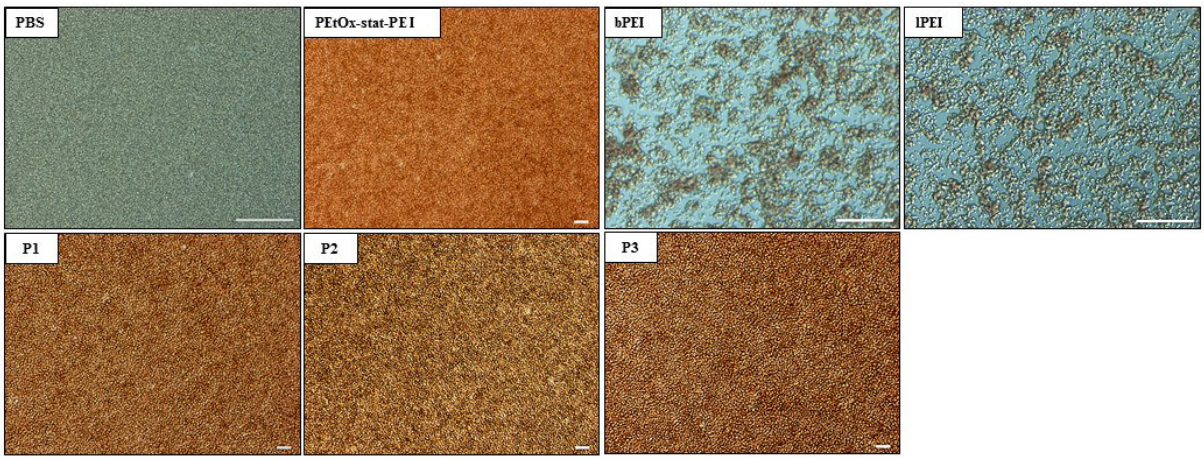

Figure S4. Light microscopy of erythrocyte aggregation of the polymers **P1** to **P3**, **PEtOx** and both **lPEI** polymers. PBS served as negative control, while bPEI (25kDa) was served as positive control. Scale bar = 50 µm.

Interaction of polymers with genetic material

The polyplex dissociation assay was performed aside from heparin with poly(methacrylic acid) (PMAA) (DP = 200) as competing factor. To keep equal conditions, same PMAA concentrations as for heparin were used during the measurement.

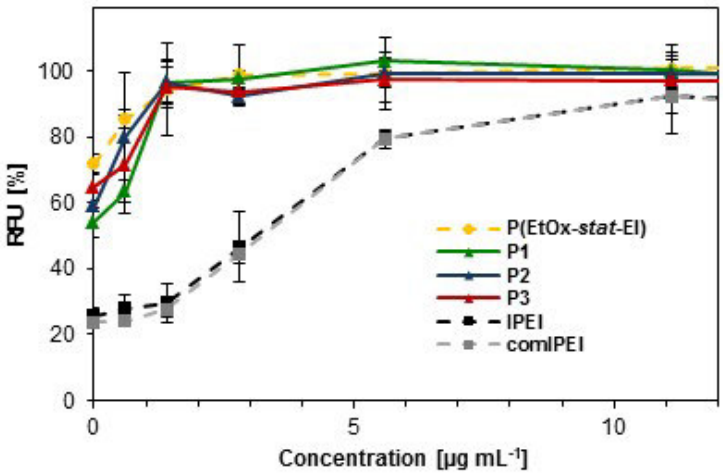

Figure S5. Dissociation assay of polyplexes formed with pDNA at N/P 30 and with increasing PMAA concentrations, which correlates to heparin concentrations.

Analysis of polyplex uptake and transfection of cells

The uptake and transfection studies were performed with HEK cells and pDNA encoding the EGFP (enhanced green fluorescence protein) or with YOYO-labeled pDNA. Transfection efficiency was determined by measuring the amount of viable cells (PI stained) expressing EGFP after 24 h *via* flow cytometry, whereas non-transfected cells served as negative control. To determine the amount of EGFP expressing cells, the histogramm of control cells was used and the percentage of cells within the gated area was defined as transfection efficiency in percentage.

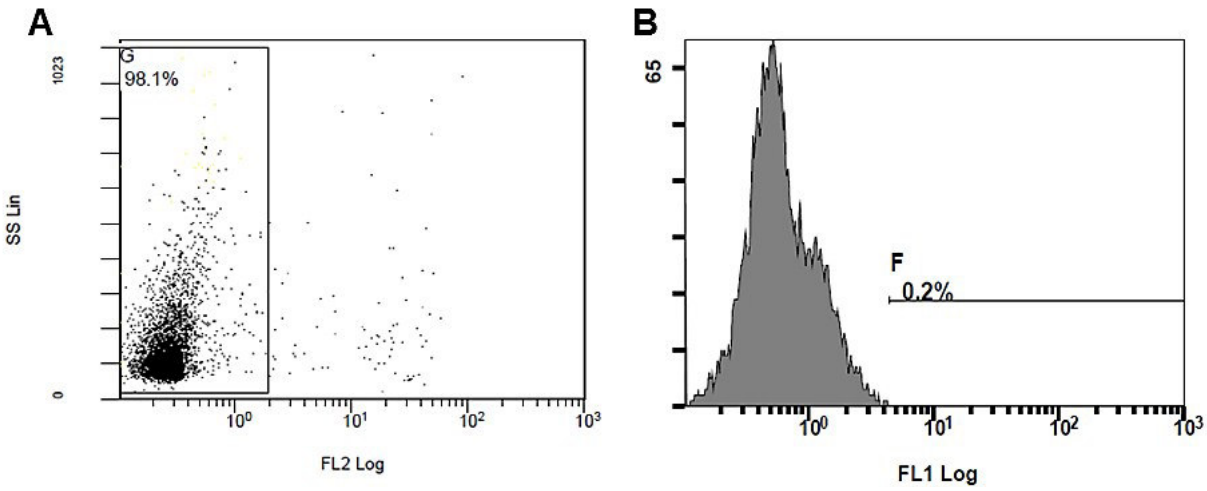

Figure S6. Flow cytometry measurements. A) Dot-plot of PI stained HEK cells for determining cell viability. FL2 Log represents red fluorescence of PI stained cells. All cells within the specified area G represent all measured viable cells. B) Histogramm of non-transfected cells served as control. FL1 Log represents green fluorescence by EGFP expression.

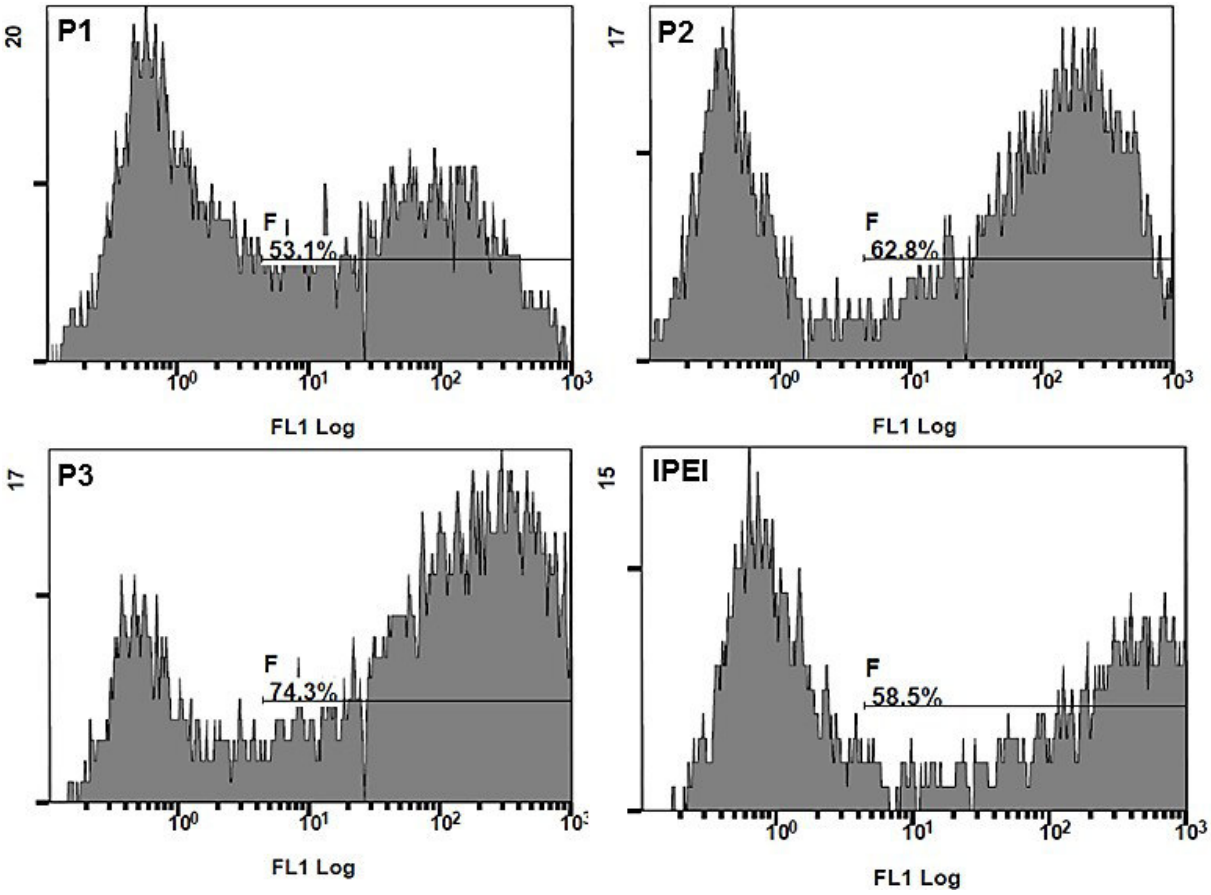

Figure S7. Histograms of flow cytometry measurements determining positive EGFP-expressing HEK cells after 24 h post-transfection with **P1** to **P3** and lPEI (N/P 30). Only viable HEK cells (PI staining) were gated. FL1 Log represents green fluorescence by EGFP expression.

To investigate the uptake mechanism in detail, cells were treated at different conditions with bafilomycin (proton pump inhibitor) or at 4 °C and 37 °C.

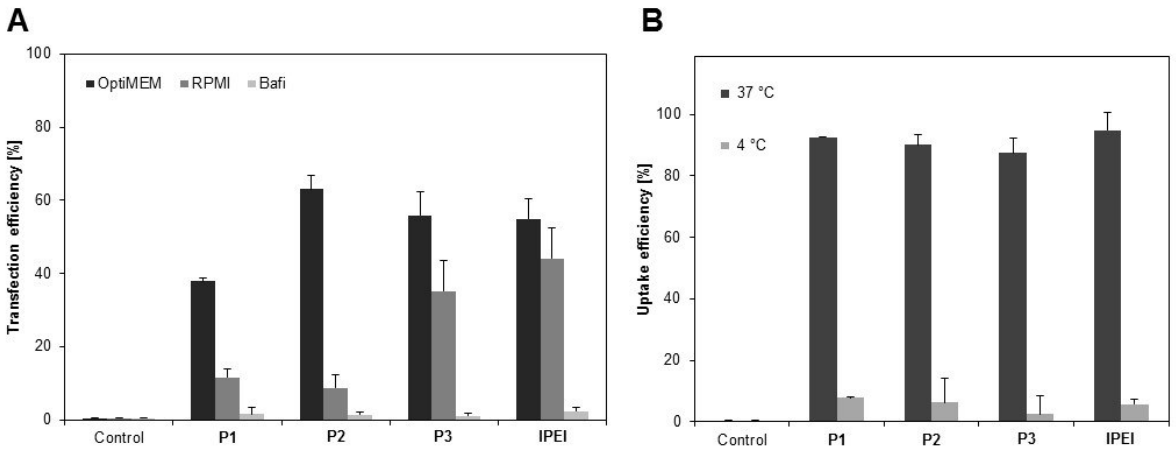

Figure S8. A) Uptake study: amount of cells taken up YOYO-1 labeled pDNA after 4 h at different temperatures (4 °C and 37 °C) using the copolymers **P1** to **P3** and **lPEI** (N/P ratio 30) as controls. Values represent the mean (n = 3). B) Comparison of the transfection efficiency of **P1** to **P3** and **lPEI** for adherent HEK cells in serum reduced (OptiMEM) and serum containing media (RPMI + 10% FCS) as well as after bafilomycin treatment at N/P 30. Values represent the mean (n = 3).

Live cell imaging

Confocal as well as structured illumination microscopy were used to investigate the uptake process of polyplexes in more detail and for visualization purposes. Therefore, non-treated control HEK cells as well as **P3** polyplexes added to HEK cells in serum reduced media were analyzed.

Control: pDNA transfection

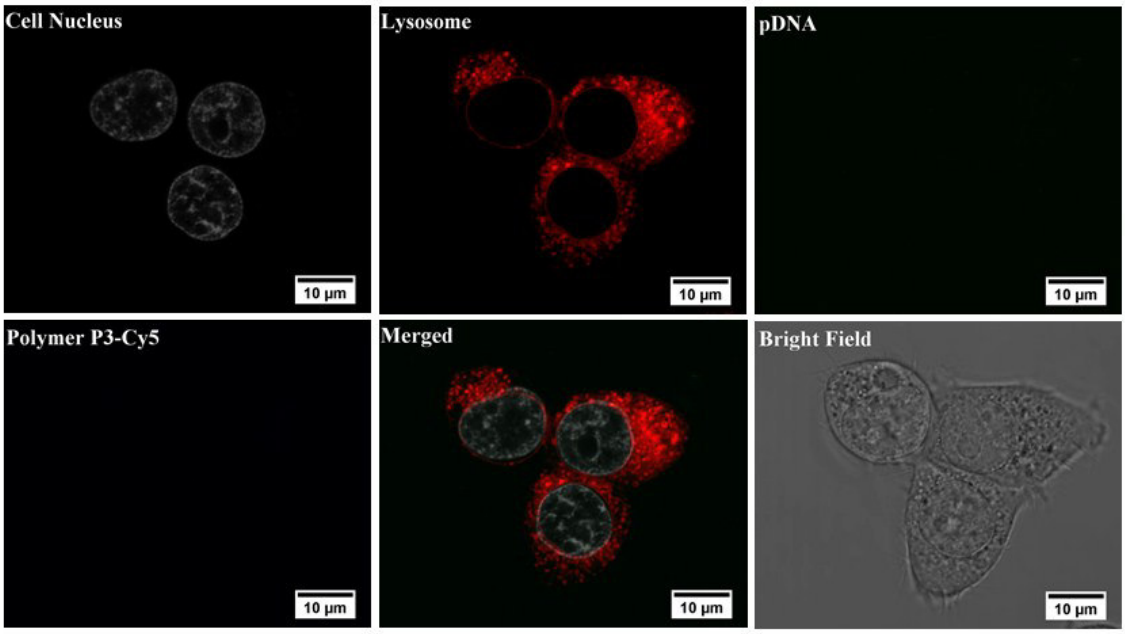

Figure S9. Uptake studies: HEK cells in serum reduced media without polyplexes served as negative controls. The cells were analyzed after 4 h *via* confocal laser scanning microscopy. The cell nucleus was stained with Hoechst 33342, the lysosomes with LysoTracker Red.

P3-Cy5: pDNA transfection

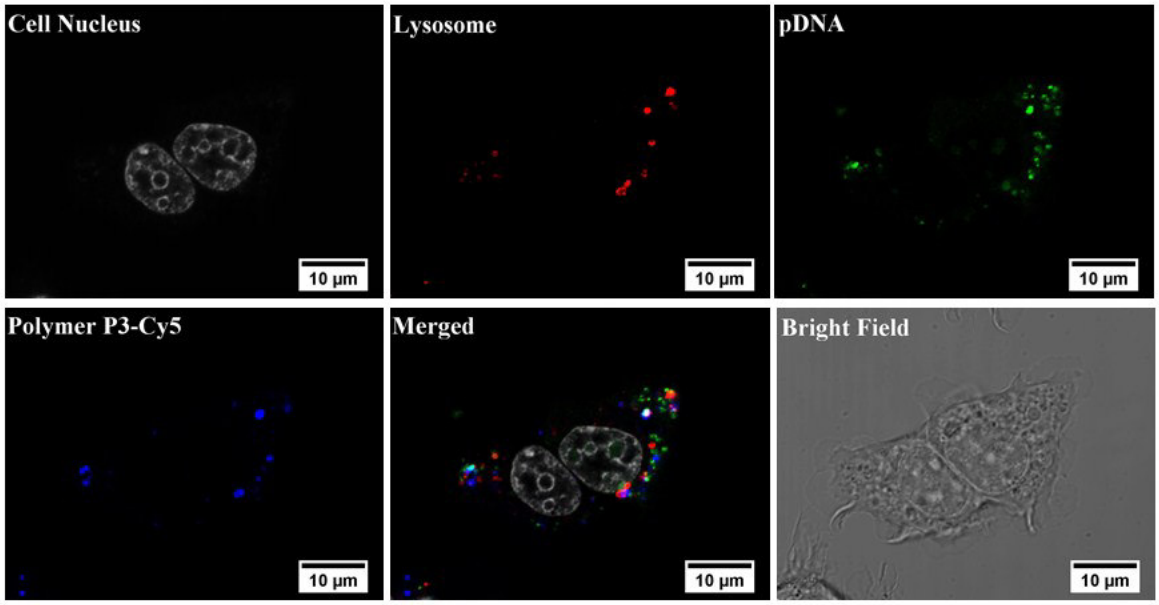

Figure S10. Uptake studies: Pure YOYO-labeled pDNA was added to HEK cells in serum reduced media. The cells were analyzed after 4 h *via* confocal laser scanning microscopy. The cell nucleus was stained with Hoechst 33342, the lysosomes with LysoTracker Red.

Structured illumination microscopy (SIM)

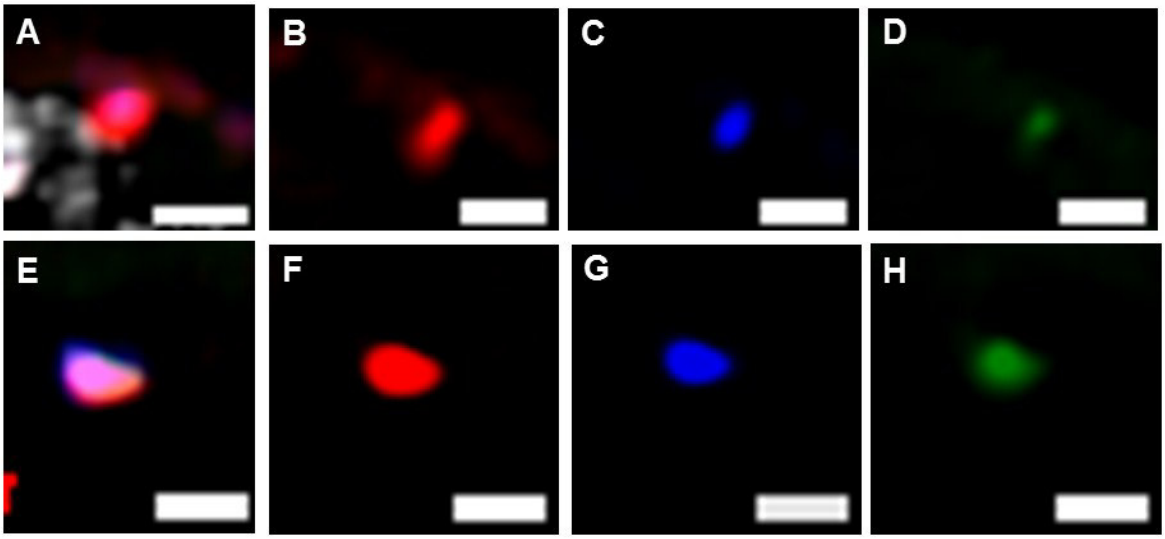

Figure S11. Magnified SIM images of endosome bearing polyplexes formed with **P3** in the presence of DNA (SIM data, deconvolved, acquired with 63x Oil Obj. 1.4 NA). Red; Lysosomal membrane (RFP). Green: pDNA labeling (YOYO-1). Blue: Polymer labeling (Cy5). A and E: Merged channels. B-D, F-H: split channels. Scale bars = 1 µm,

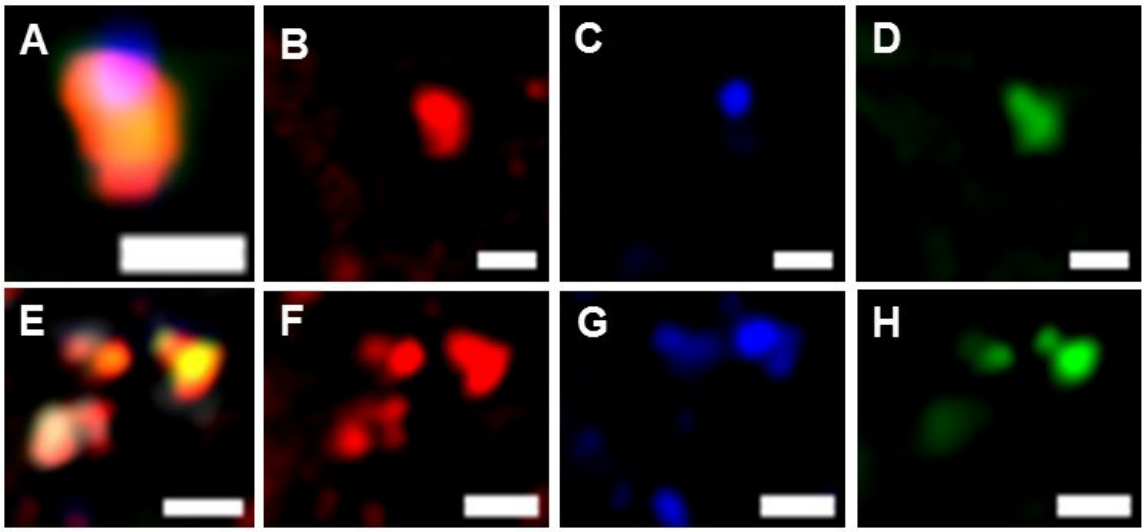

Figure S12. Magnified SIM images of endosome bearing polyplexes formed with **lPEI** in the presence of DNA (SIM data, deconvolved, acquired with 63x Oil Obj. 1.4 NA). Red; Lysosomal membrane (RFP). Green: pDNA labeling (YOYO-1). Blue: Polymer labeling (Cy5). A and E: Merged channels. B-D, F-H: split channels. Scale bars = 1 µm,

Scanning transmission electron microscopy (STEM)

To obtain deeper insights into the uptake mechanism and the fate of polyplexes inside the cell as well as the endosomal environment, scanning transmission electron microscopy (STEM) were performed. The images display a section (thickness of the resin slice: 80 nm) through the cell and sizes are determined by a two-dimensional section through the cell. This can only conditionally make a statement of the actual size of the three-dimensional vesicle. More than 5 sections (and ~ 10 vesicles) of different cells were analyzed to evaluate our findings.

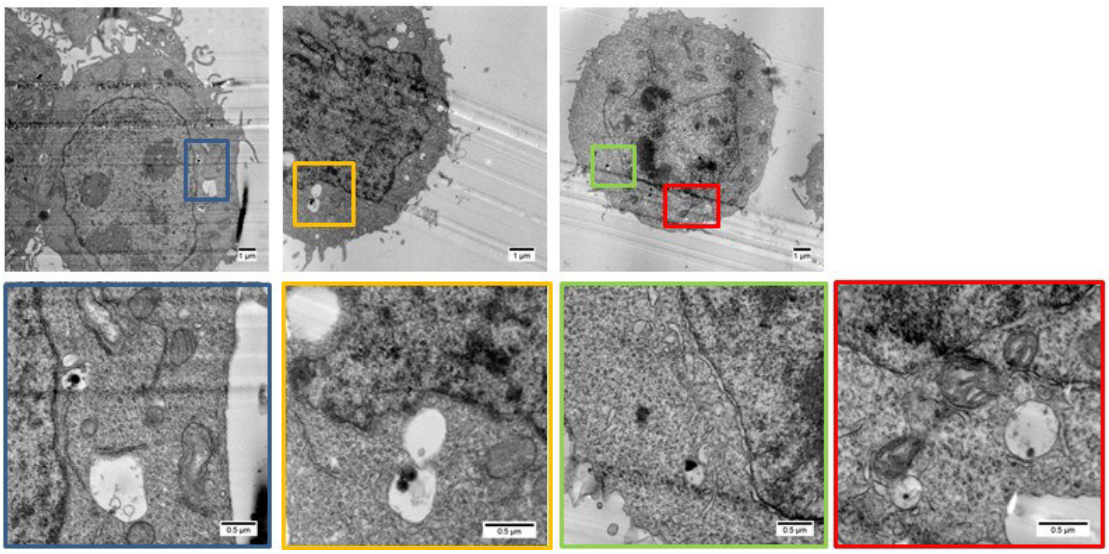

Figure S13. STEM images of polyplex uptake in HEK cells at standard conditions. Polyplexes were formed with **P3** and pDNA. Cells were harvested after 4 h.

Macropinocytosis inhibitor

For inhibition experiments, cells were treated with 100 µM 5-(*N*-ethyl-*N*-isopropyl)amiloride (EIPA) in standard culture media 30 min prior to polyplex addition. Subsequently, **P3** and lPEI polyplexes were added to the cells and incubated for further 4 h. Afterwards, the cells were harvested and analyzed as described above *via* flow cytometry or were further prepared for STEM imaging.

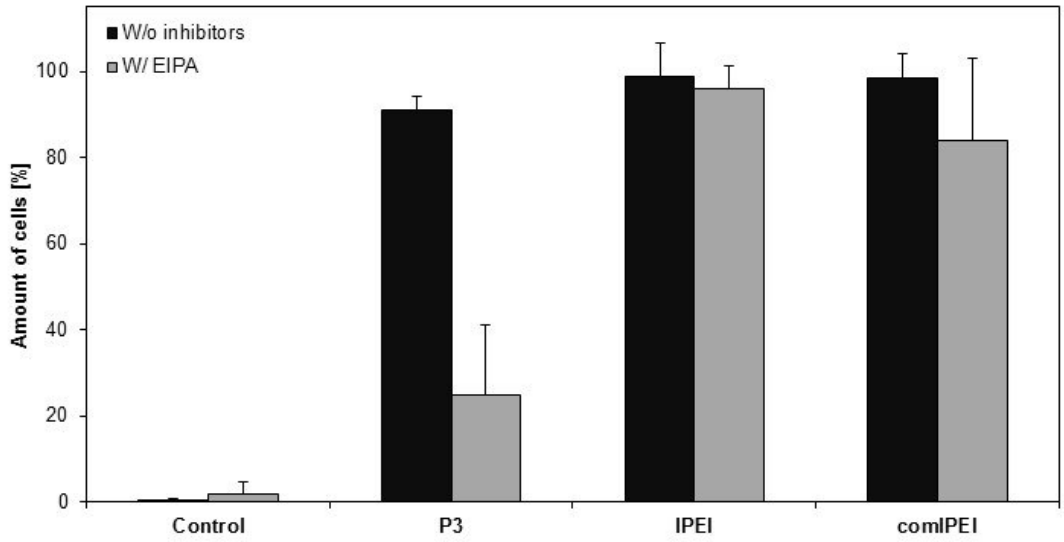

Figure S14. Polyplex uptake (YOYO-labeled pDNA) in HEK cells after treatment with EIPA (macropinocytosis inhibitor).

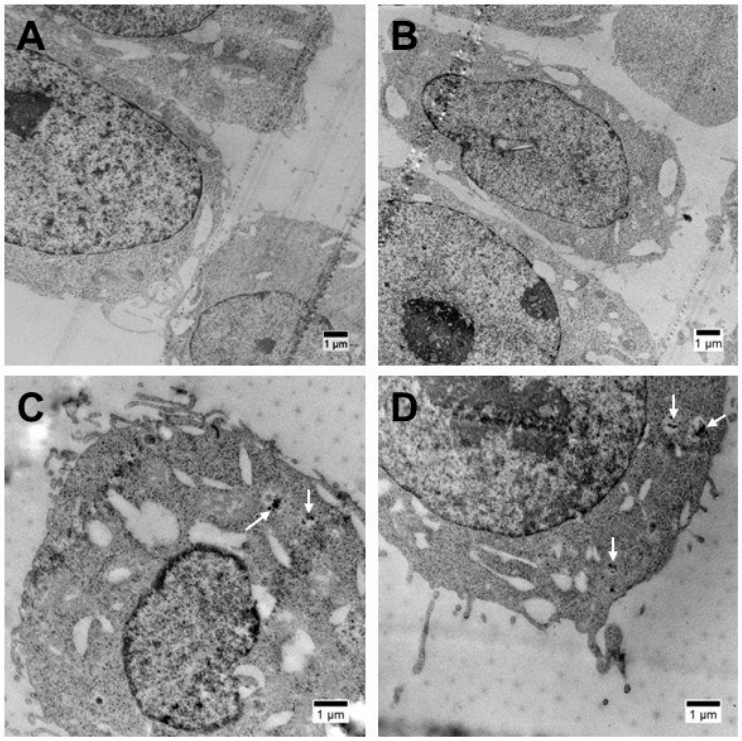

Figure S15. STEM images of polyplex uptake in HEK cells after treatment with EIPA (macropinocytosis inhibitor). A-B) Uptake of **P3** polyplexes. C-D) Uptake of **lPEI** polyplexes. White arrows indicate vesicles with polyplexes.

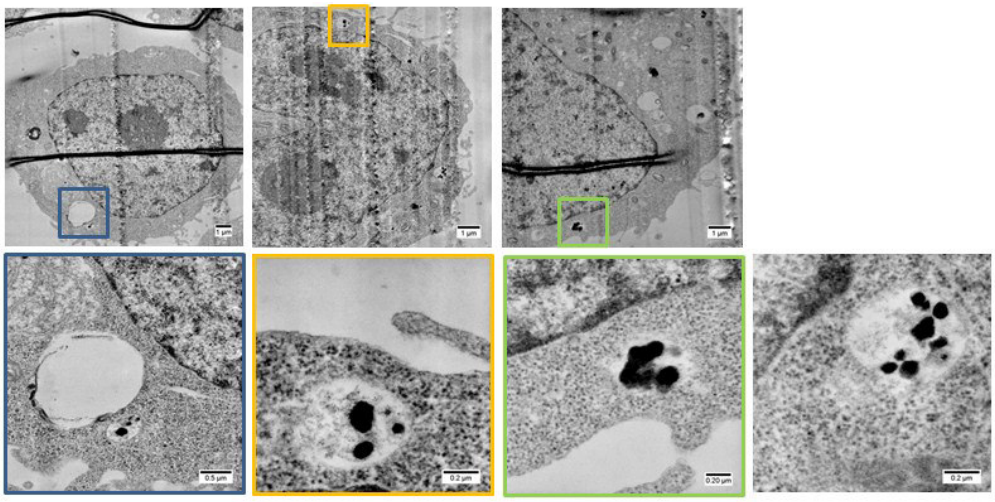

Figure S16. STEM images polyplex uptake in HEK cells at standard conditions. Polyplexes were formed with **lPEI** and pDNA. Cells were harvested after 4 h.

siRNA delivery

A stable GFP-expressing CHO cell line was transfected with the polymers **P1** to **P3** as well as PEI using scrambled siRNA as negative control. The knockdown of EGFP was analyzed *via* flow cytometry by measuring the MFI of all viable cells (PI staining).

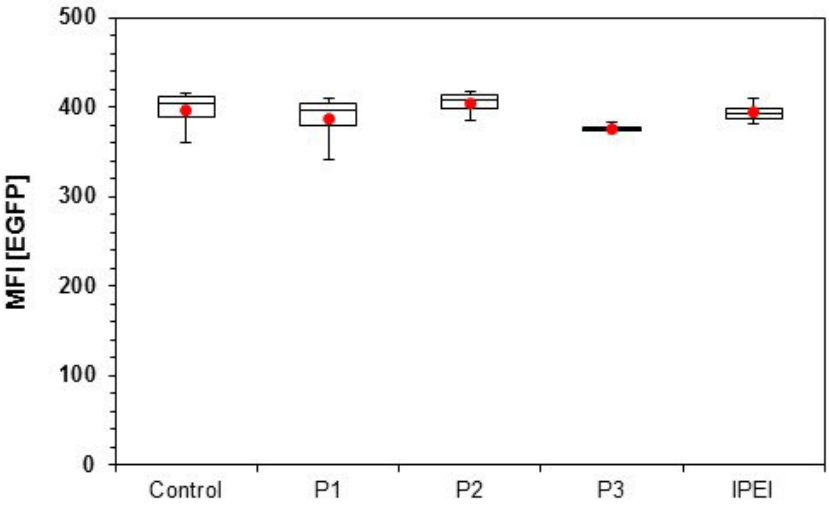

Figure S17. siRNA transfection efficiency mediated by **P1** to **P3** as well as PEI polyplexes at N/P 30 after 72 h. Stable EGFP-expressing CHO cells were transfected with scrambled siRNA served as negative control. The values represent the mean ± S.D., $n \geq 3$.

Comparison of lPEI and commercial lPEI25k (comlPEI, Sigma Aldrich)

The cytotoxicity tests of the PEI copolymers were performed in parallel with high molar mass lPEI polymers as positive controls. Fully hydrolyzed PEtOx, thus lPEI as well as the commercially available lPEI (25 kDa, **comlPEI**) obtained from Polysciences were used. The synthesized lPEI shows a higher cytotoxicity (IC_{50} at ~ 4 µg mL^{-1}), whereas the commercial PEI reaches 50% cell viability at 25 µg mL^{-1}. The reduced cytotoxicity could be attributed to residual, N-acyl groups from polymerization, which is also stated by the supplier.[39] Furthermore, the hemolysis and the erythrocyte aggregation assay were performed with both PEIs. Both polymers show membrane-perturbing activity at high concentrations (100 µg mL^{-1}) leading to hemoglobin release and the aggregation of erythrocytes. This effect was not seen with the copolymers **P1** to **P3**.

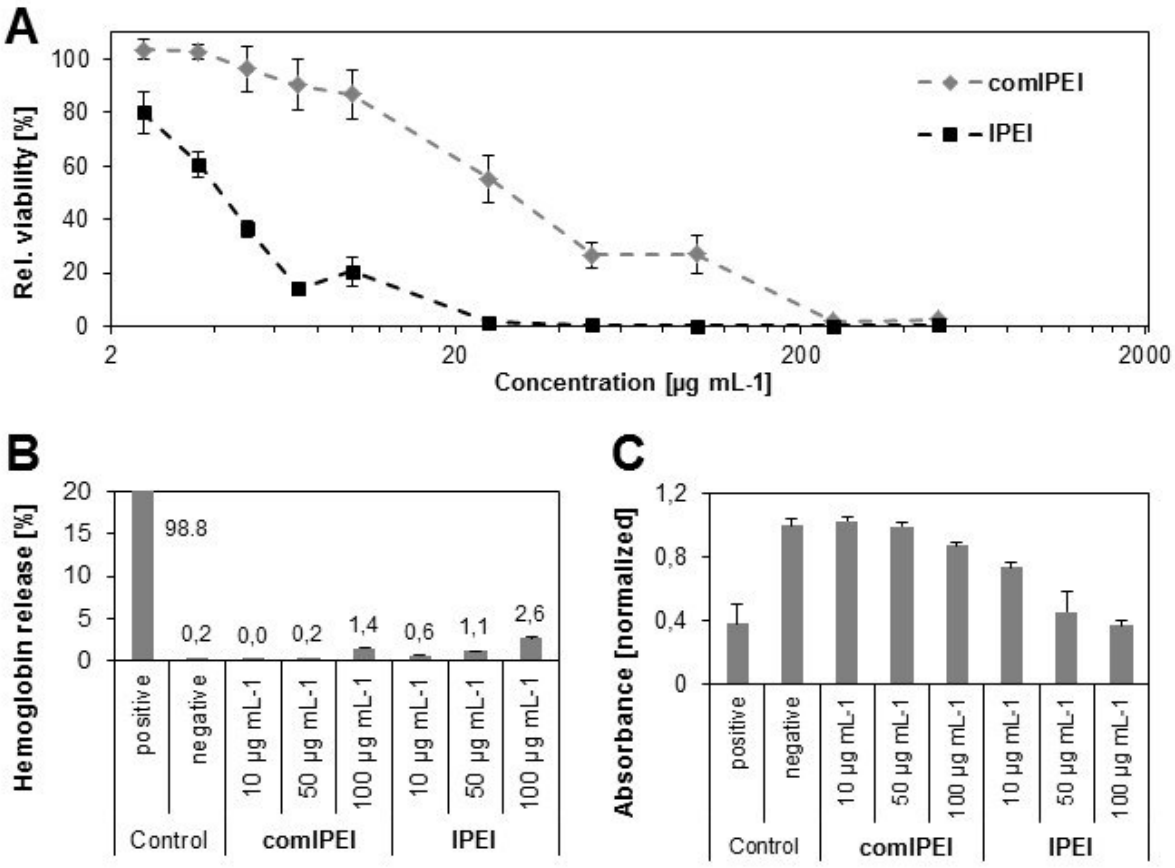

Figure S18. Comparison of **lPEI** and commercially available PEI (**comlPEI**, Polysciences). A) Cytotoxicity assay treating L929 cells with the synthesized **lPEI** as well as **comlPEI** at indicated concentrations. B) Hemolysis assay of erythrocytes after incubation with polymers at indicated concentrations. Triton X-100 served as positive control (100% hemolysis) and PBS as negative control. C) Erythrocyte aggregation of the tested polymers at indicated concentrations. bPEI (25 kDa) served as negative control resulting in high aggregation formation and PBS as negative control. Values represent the mean ± S.D. (n=3).

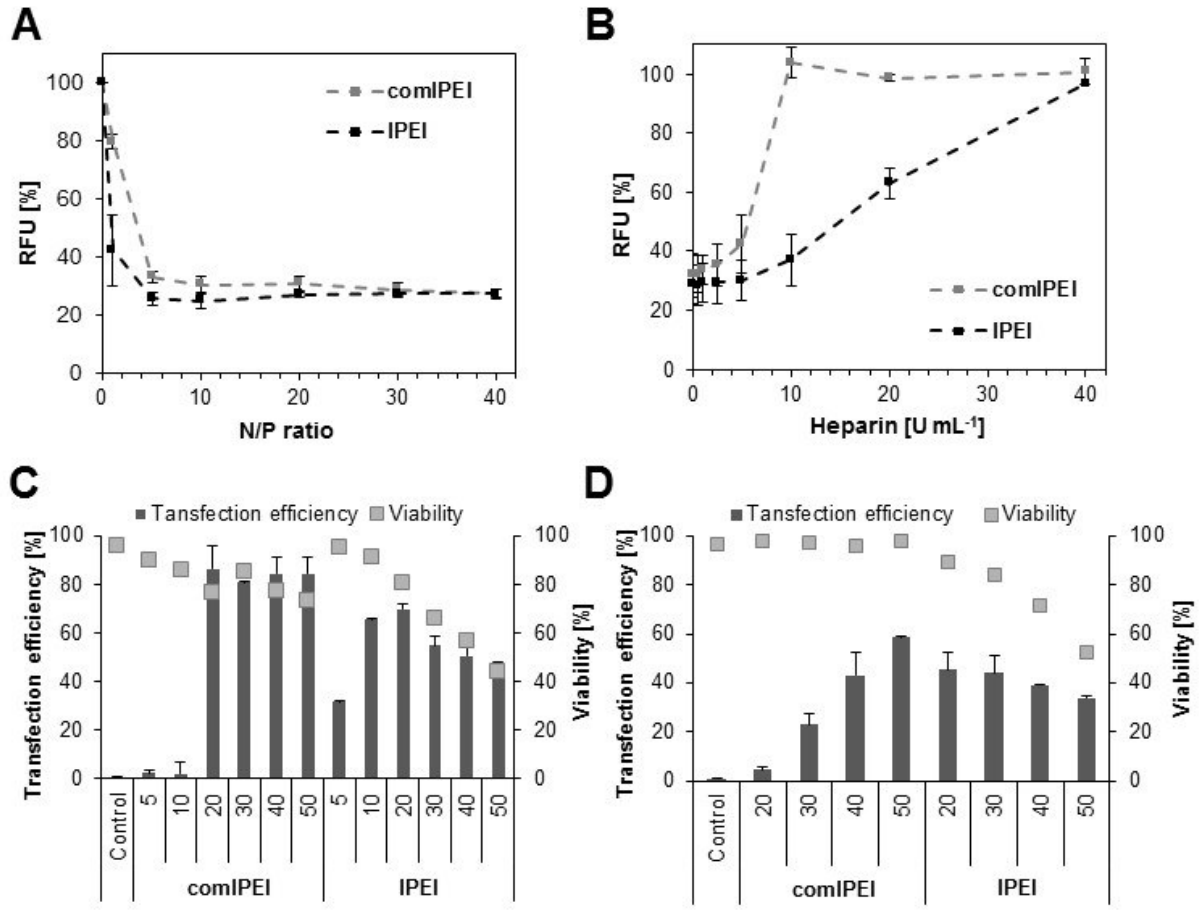

Figure S19. Comparison of **lPEI** and commercially available PEI (**comlPEI**, Polysciences). A) Complexation affinity (EBA) of mentioned polymers using pDNA at the indicated N/P ratios. B) Dissociation assay with heparin of polyplexes formed with pDNA at N/P 30. C-D) Transfection efficiency of both PEI polymers for adherent HEK cells in serum reduced (C) as well as serum containing (D) media at different N/P ratios after 24 h. Values represent the mean ± S.D. (n=3).

Besides the synthesized lPEI, comlPEI was used as control for the ethidium bromide quenching assay (Figure S18A). Both polymers show a high complexation affinity with pDNA, while a faster polyplex formation of lPEI could be detected at N/P 5. Regarding the heparin dissociation assay, comlPEI achieved a full decomplexation of genetic material at a heparin concentration of 10 U mL^{-1} (Figure S19B). For the complete release of pDNA (100% RFU) from lPEI polyplexes, 40 U mL^{-1} heparin was required. The uptake and transfection studies were

performed with HEK cells and pDNA encoding the EGFP (enhanced green fluorescence protein). Transfection efficiency was determined by measuring the amount of cells expressing EGFP after 24 h *via* flow cytometry. ComlPEI shows high TE > 80% at N/P ratios of 20 to 50 in serum reduced media, which is comparable to other studies. It has to be mentioned that with increasing N/P ratio, i.e. the polyplex concentration, the cell viability is reduced. This effect could be prevented using serum containing media for transfection, whereas a significant reduction of up to 70% (at N/P 20) of TE is occured.

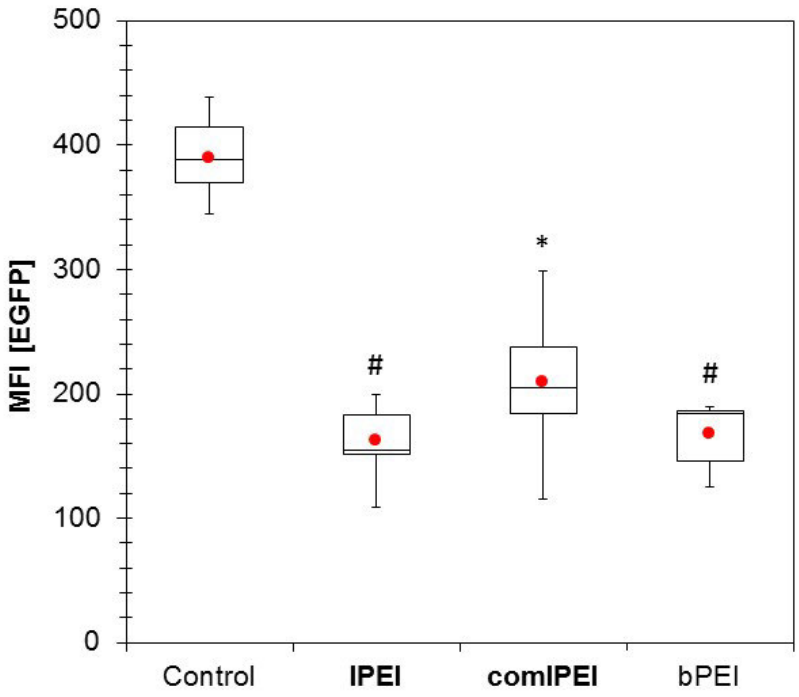

Figure S20. siRNA transfection efficiency mediated by PEI polyplexes at N/P 30 after 72 h. Stable EGFP-expressing CHO cells were transfected with polyplexes formed using siRNA able to knock down *egfp*. Statistical analysis (t-test) was used to compare the MFI of the control with PEI, * represents $p < 0.05$ and # $p < 0.005$. The values represent the mean ± S.D., n ≥

Publication Pub5

Crossing the blood-brain barrier: Glutathione-conjugated poly(ethylene imine) for gene delivery

C. Englert, A.-K. Trützschler, M. Raasch, T. Bus, P. Borchers, A. S. Mosig, A. Traeger, U. S. Schubert

J. Control. Release **2016**, *241*, 1-14.

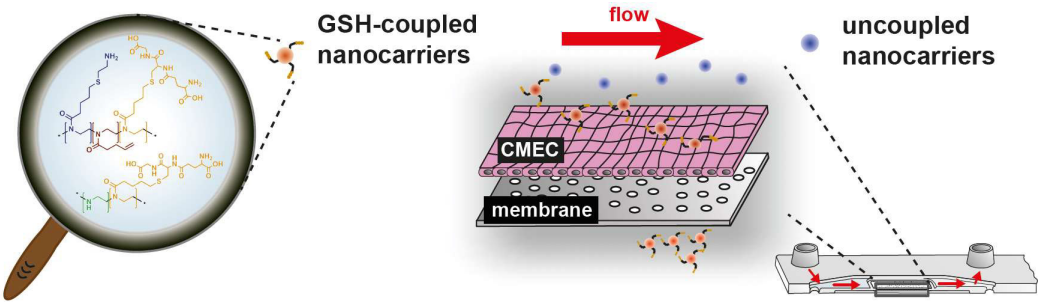

Journal of Controlled Release 241 (2016) 1–14

Contents lists available at ScienceDirect

Journal of Controlled Release

journal homepage: www.elsevier.com/locate/jconrel

Crossing the blood-brain barrier: Glutathione-conjugated poly(ethylene imine) for gene delivery

Christoph Englert [a,b,1], Anne-Kristin Trützschler [a,b,1], Martin Raasch [c,d], Tanja Bus [a,b], Philipp Borchers [a,b], Alexander S. Mosig [b,c,d,*], Anja Traeger [a,b,**], Ulrich S. Schubert [a,b,***]

[a] Laboratory of Organic and Macromolecular Chemistry (IOMC), Friedrich Schiller University Jena, Humboldtstrasse 10, 07743 Jena, Germany
[b] Jena Center for Soft Matter (JCSM), Friedrich Schiller University Jena, Philosophenweg 7, 07743 Jena, Germany
[c] Institute of Biochemistry II, Jena University Hospital, Nonnenplan 2-4, 07743 Jena, Germany
[d] Center for Sepsis Control and Care, Jena University Hospital, Erlanger Allee 101, 07747 Jena, Germany

ARTICLE INFO

Article history:
Received 29 June 2016
Received in revised form 24 August 2016
Accepted 28 August 2016
Available online 30 August 2016

Keywords:
Poly(ethylene imine)
Blood-brain barrier
Microfluidic biochip
L-Glutathione
Non-viral gene delivery

ABSTRACT

The targeted drug delivery to the central nervous system represents one of the major challenges in pharmaceutical formulations since it is strictly limited through the highly selective blood-brain barrier (BBB). L-Glutathione (GSH), a tripeptide and well-known antioxidant, has been studied in the last years as potential candidate to facilitate the receptor-mediated transcytosis of nanocarriers. We thus tested whether GSH decoration of a positively charged polymer, poly(ethylene imine), with this vector enables the transport of genetic material and, simultaneously, the passage through the BBB. In this study, we report the synthesis of GSH conjugated cationic poly(ethylene imine)s *via* ecologically desirable thiol-ene photo-addition. The copolymers, containing 80% primary or secondary amine groups, respectively, were investigated concerning their bio- and hemocompatibility as well as their ability to cross a hCMEC/D3 endothelial cell layer mimicking the BBB within microfluidically perfused biochips. We demonstrate that BBB passage depends on the used amino-groups and on the GSH ratio. Thereby the copolymer containing secondary amines showed an enhanced performance. We thus conclude that GSH-coupling represents a feasible and promising approach for the functionalization of nanocarriers intended to cross the BBB for the delivery of drugs to the central nervous system.

1. Introduction

Discovered by Paul Ehrlich in 1885 and named by Max Lewandowsky in 1900, the blood-brain barrier (BBB) is known as one of the most challenging obstacles concerning the delivery of drugs and therapeutic nucleic acids [1,2]. Within the BBB, specialized endothelial cells of the cerebral vasculature (cerebral microvascular endothelial cell, CMEC) form an endothelial layer that strictly regulates the passage of small molecules. The tightness of the BBB is furthermore regulated by astrocytes and pericytes that are in direct contact with the CMECs [3]. The BBB passage of molecules depends on several parameters, including the molecular size, lipid solubility, hydrophilicity, and the degree of dissociation. The passage of macromolecules as well as of 98% of small molecules (<400 g mol^{-1}) is prevented under physiological conditions [4]. Besides the passive transport, which comprises the diffusion of small molecules [5], the active transport of amino acids and macromolecules such as transferrin is described to be mediated by carrier proteins or transcytosis [6]. While the transport of different amino acids is well-investigated [7], the transport of L-glutathione (GSH), a tripeptide which is known as antioxidant that lowers the oxidative stress level within the brain, is currently under investigation [8–10].

In order to circumvent the BBB, several methods including the invasive direct injection into the central nervous system (CNS) and the non-invasive nasal delivery of nanoparticular and liposomal carriers as well as of covalently targeted small molecules have been investigated [11,12]. However, nasal delivery possesses the difficulty to adjust the therapeutic delivery due to individually varying absorption profiles, limited volume and long term side effects [11].

Introducing targeting molecules to nanocarriers is the key to benefit from the active transporting systems and to enable also the passage of larger drugs. Non-viral receptor- and adsorptive-initiated transcytosis, as well as carrier-mediated transport can be used for an active transcellular vector-based drug delivery. By using larger biomolecules like antibodies and peptides [13,14], additional surface modifications like PEGylation and polysorbate 80 ("Tween 80" or polyoxyethylene(20)

* Correspondence to: A.S. Mosig, Center for Sepsis Control and Care, Jena University Hospital, Erlanger Allee 101, 07747 Jena, Germany.
** Correspondence to: A. Traeger, Jena Center for Soft Matter (JCSM), Friedrich Schiller University Jena, Philosophenweg 7, 07743 Jena, Germany.
*** Correspondence to: U.S. Schubert, Laboratory of Organic and Macromolecular Chemistry (IOMC), Friedrich Schiller University Jena, Humboldtstrasse 10, 07743 Jena, Germany.
E-mail addresses: alexander.mosig@med.uni-jena.de (A.S. Mosig), anja.traeger@uni-jena.de (A. Traeger), ulrich.schubert@uni-jena.de (U.S. Schubert).
[1] The authors contributed equally to this work.

http://dx.doi.org/10.1016/j.jconrel.2016.08.039
0168-3659/

sorbitan monooleate) [15] or small molecule conjugation (such as GSH), BBB passage could be revealed successfully [16–19]. The latter has been successfully used to modify nanoparticles for drug delivery resulting in an enhanced passaging ability of the BBB [20,21]. Recently, Grover et al. combined two known techniques to create a novel nanoparticle system (PEGylation and GSH coating), while Gaillard *et al.* showed the improvement of the BBB passage using liposomal carrier systems [20,21]. The 2-BBB company has already started with two clinical trials regarding liposomal based PEGylated and GSH decorated particles bearing doxorubicin and methylprednisolone [22]. At the end of 2014 positive results from phase 1 were announced showing a BBB passage and anti-tumor properties. This reveals that the decoration with GSH seems to be a promising targeting approach also for other carrier systems. While the choice of targeting molecules influences the transcytosis efficiency, the nanocarrier material should be adopted to the transported drug. Therefore, synthetic as well as natural polymers (*e.g.* polysaccharides, proteins) have been used for the transport of drugs and genetic material [23]. Among others, polybutylacrylate (polysorbate 80) [24] and PLA/PGA or PLGA (TAT [25] or polysorbate 80 [26]) have been successfully established in *in vivo* tests for the encapsulation of hydrophobic drugs. In order to enable nucleic acid delivery to the central nervous system (as novel treatment option of neuronal-related diseases), there is an urgent need for appropriate binding nanocarriers. Cationic polymers, in particular poly(ethylene imine) (PEI), represent a class of suitable candidates for the complexation of genetic material by electrostatic interactions [27]. Due to its superior buffering ability enabling endosomal escape, PEI is known as the gold standard of polymeric carriers for gene delivery *in vitro* [28]. However, its potential is accompanied with high cytotoxicity and non-biodegradability [29]. The functionalization of the linear PEI backbone [30] and the addition of side chains, creating copolymers, represent a powerful strategy to overcome these limitations and have been extensively studied attaching various carbohydrates [31–33] or polymers like poly(ethylene glycol) [34].

However, these *in vitro* studies were based on standard cell culture techniques under static culture conditions. Shear forces as observed *in vivo* and their impact on endothelial cells [35] as first cells to come in contact with administered drugs have not been addressed. Microfluidics can serve as a tool to reduce this transferability gap. Recently, we reported a microfluidically supported biochip model of the BBB with the proof-of-concept of the modulation of the BBB permeability by inflammatory cytokines [36]. To mimic the cerebral endothelial cell layer of the BBB, hCMEC/D3 cell layers have been used that specifically express cerebral endothelial marker proteins including cell adhesion and tight junction proteins as well as CNS related transporter proteins. *In vitro* the cell line forms a tight endothelial cell layer that shows similarities with the BBB even in the absence of astrocytes or pericytes [37–39]. Thus HCEMC/D3 cells were already used in various BBB models [40,41] for mechanistically studies on leukocyte transmigration [42], nanoparticle uptake and transcytosis [43,44].

In this study, we describe for the first time a nanocarrier design that combines vector as well as charge optimized properties for crossing the BBB and that enables complexation of nucleic acids. We focused on the installation of GSH moieties on the backbone of high molar mass linear PEI. A post-polymerization functionalization process was applied to obtain double bond functionalities and defined quantities of cationic ethylene imine units. Since reduced GSH provides a free thiol end group, thiol-ene photo-addition was used to modify the PEI backbone avoiding potentially hazardous metal catalysts. Comparable amounts of primary amine groups in the polymer side chain were installed in a second approach on the PEI backbone for an enhanced polyplex stability. The copolymers were characterized concerning their polyplex formation, toxicity, hemocompatibility and their potential to deliver nucleic acids across the BBB. We want to demonstrate that polyplexes, formed by GSH-modified PEI-based polymers and plasmid DNA, are able to cross an endothelial cell model of the BBB under physiological shear stress of 4 dyn cm^{-2}.

2. Results and discussion

To conjugate GSH to a cationic polymer backbone (using a poly(ethylene imine)-derivative), the thiol-ene photo-addition reaction was utilized. It can be performed under mild conditions (no thermal energy, no toxic metal catalysts) without generating harmful side products. The solubility properties of GSH limits the click reaction to water. To investigate the influence of different amine functionalities on the balance between stable polyplex formation and BBB passage, materials either containing solely secondary amines or bearing additional primary amines were synthesized.

2.1. Polymer synthesis

The homopolymer poly(2-ethyl-2-oxazoline) (PEtOx) was synthesized according to literature procedure [9]. For this purpose, the cationic ring-opening polymerization (CROP) of the monomer 2-ethyl-2-oxazoline was performed in a microwave reactor. The precursor revealed a degree of polymerization of 575 (calculated from the tosylate ^{1}H-NMR signal integrals of MeOTos before purification) and a dispersity of 1.3 (SEC: DMAc, 0.21% LiCl, calibration: polystyrene). PEtOx was further treated with half-concentrated hydrochloric acid and heated to reflux overnight [45]. The resulting linear poly(ethylene imine) (**P1**) exhibited a degree of hydrolysis of > 95% (calculated from ^{1}H-NMR). **P1** served as the main polymer for the installation of all functionalities including the GSH moieties. To investigate the influence of different cationic charges on the biocompatibility and the DNA binding affinity, primary as well as secondary amine functionalities were introduced to the polymer backbone besides the GSH functionalities [46]. This versatile approach required two different synthesis pathways (see Scheme 1).

The first one comprises of the partial functionalization of linear poly(ethylene imine) (**P1**) with *N*-succinimidyl-4-pentenate to introduce double bond functionalities yielding the P(EI-*stat*-ButEnOx) copolymer (**P2**) (see Scheme 1a, strategy I) [47]. Since the homopolymer poly(2-butenyl-2-oxazoline) (which can be synthesized by a CROP of the respective monomers) does not withstand the conditions of acidic or basic hydrolysis, the mentioned post-polymerization modification strategy was applied. Preliminary studies of copolymers consisting of varying contents of ethylene imine (EI) and 2-butenyl-2-oxazoline units (ButEnOx) resulted in a critical amount of EI units required for the formation of stable polyplexes [47]. Therefore, a ButEnOx content of 27% was installed onto the backbone of **P1**, resulting in an EI content of 78% (**2**) (see Table 1). The introduction of GSH (reduced state, for the schematic representation of the structure see Scheme 1) was performed by a thiol-ene photoaddition while maintaining a constant EI content of 78% (Scheme 1c). Since GSH shows only limited solubility properties, the click reaction was performed in water utilizing the photoinitiator Irgacure® 2959. The full conversion resulted in the copolymer P($EI_{73\%}$-*stat*-$GluButOx_{27\%}$) (**3**).

In a second approach primary amine moieties were installed on the polymer backbone to investigate their influence on the interaction with DNA. While primary amine groups are known to promote superior complexation of nucleic acids [48,49], secondary amines reveal an enhanced buffer capacity resulting in a fast endosomal release [50]. The previously mentioned modification strategy was used (Scheme 1a, strategy II) to synthesize a fully functionalized poly(2-butenyl-2-oxazoline) (**P4**). Subsequently, the protected aminothiol was added to **P4** under UV irradiation (Scheme 1b) to yield the copolymer P(*boc*$AmButOx_{82\%}$-*stat*-$ButEnOx_{18\%}$) (**P5**) (Table 1). In a second photo-addition step, reduced GSH was introduced to the backbone of **P5** analog to the previously described first synthesis route (Scheme 1c, strategy II). Under these conditions, the conversion of the double bonds was incomplete (56% of the origin double bond functionalities remained), even after an additional functionalization step. Almost certainly, the content of flexible side chains containing sterically demanding protection groups hinders the full modification. Furthermore, the introduction of a defined amount

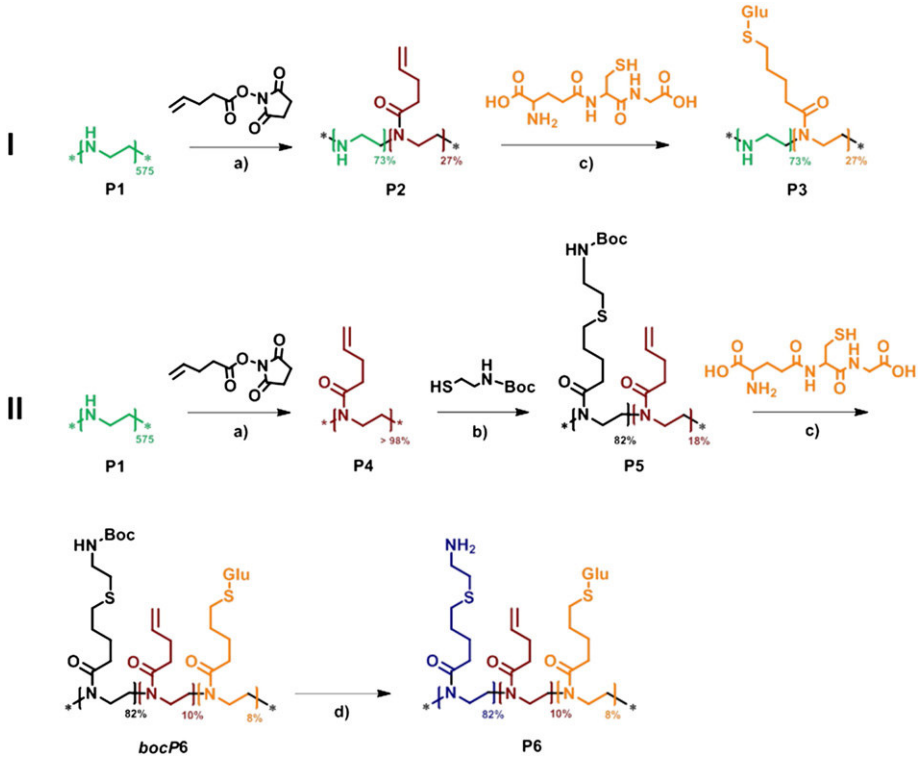

Scheme 1. Schematic representation of the synthesis of I) P(EI-*stat*-GluButOx) (**P3**) and II) P(AmButOx-*stat*-ButEnOx-*stat*-GluButOx) (**P6**), respectively. a) Functionalization of linear poly(ethylene imine) (**P1**). b) Thiol-ene photo-addition of *tert*-butyl-(2-mercaptoethyl)carbamate to the copolymer backbone. c) Thiol-ene photo-addition of L-glutathione to the copolymer backbone. d) Deprotection of primary amine side chains.

of bulky GSH (~8%) could result in an additional hindrance, which limits the degree of functionalization. The deprotection of ***boc*P6** (Scheme 1d) resulted in the final polymer P(AmButOx$_{82\%}$-*stat*-ButEnOx$_{10\%}$-*stat*-GluButOx$_{8\%}$) (**P6**). Focusing on the amount of amine groups within the copolymers, a comparison of **P3** and **P6** concerning this point is part of further investigations.

Characterization by ^{1}H-NMR spectroscopy (Fig. 1) confirmed the almost complete hydrolysis of PEtOx revealing one main signal for the backbone of **P1** between 3.70 and 3.20 ppm (NR—C*H*$_2$—C*H*$_2$, A). In addition, 5% remaining 2-ethyl-2-oxazoline units can be found. The appearance of the double bond signals for **P2** at 5.81 ppm (*CH*$_2$═C*H*—, E) and 4.95 ppm (*CH*$_2$═CH—, F) confirm the successful functionalization with *N*-succinimidyl-4-pentenate. The former signal is compared to the unaffected ethylene imine backbone to determine the composition of the formed copolymer **P2** (degree of functionalization: 27%). The disappearance of the double bond signals after the thiol-ene photoaddition confirmed the complete functionalization with GSH. Besides the additional protons observed after the click reaction (E′ and F′), the signals of GSH can be assigned to the respective protons (see Fig. 1). The very specific GSH signal for the CH group of the cysteine unit appears at 4.54 ppm (NR—*CH*—CH$_2$—S, H).

The complete functionalization of **P1** resulted in polymer **P4**, indicated by the disappearance of the signals assigned to the ethylene imine backbone (between 3.70 and 3.20 ppm) (see Fig. 2). Instead, the signals assigned to the double bonds at 5.8 ppm (*CH*$_2$═C*H*—, D) and 4.96 ppm (*CH*$_2$═CH—, E) as well as to the backbone (3.45–3.53, NR—*CH*$_2$—*CH*$_2$, A) could be observed. The successful attachment of side chains bearing primary amine groups and GSH moieties is shown by the CH$_2$ signals nearby the amine group around 2.8 ppm (NH$_2$—*CH*$_2$—*CH*$_2$), the signal of the *boc*-protecting group which disappears after deprotection (1.4 ppm, *CH*$_3$ boc) and the specific GSH protons of **P6**.

The composition of the prepared polymers (and respective intermediates) is depicted in Table 1. Asymmetric flow field-flow fractionation (AF4) was utilized to determine the molar masses of the starting polymer **P1** and the final products **P3** and **P6**. Since the intermediates reveal different solubility behaviors, another characterization method had to be chosen. Therefore, size exclusion chromatography (SEC) was used to determine the molar masses of **P2**, **P4**, **P5** and ***boc*P6**. However, in both cases the presence of cationic amine units (primary or secondary) and/or double bond functionalities resulted in undesired column and membrane interactions and, therefore, a change in the elution behavior (increased dispersities) [51,52]. Although the obtained values indicate lower molar masses compared to the calculated values, a trend is visible.

To confirm the successful photo-addition of GSH and the formation of a single (polymeric) species (**P3**, **P6**), diffusion-ordered NMR spectroscopy (DOSY NMR) was performed. GSH clearly revealed a higher diffusion coefficient compared to the polymeric species. The decreasing values for the GSH decorated **P2** indicate an increase of the hydrodynamic radius of **P3** in solution (Fig. 3A). This can be explained by the bulky GSH moiety. Comparable results are obtained for **P6** (Fig. 3B).

2.2. Bio- and hemocompatibility

Biocompatibility represents a critical parameter for potential non-viral vectors in biomedical applications. *In vitro* studies were performed using the precursor **P2** and the final GSH-conjugated polymers **P3** and **P6** in comparison to the linear PEI (**P1**) to evaluate their bio- and hemocompatibility (Fig. 4A and Supporting information Fig. S1). **P4** and **P5** were excluded due to their insolubility in aqueous media. **P1** exhibited a high cytotoxicity at low polymer concentrations (IC_{50} of ~4 μg mL^{-1}) because of its high molar mass and cationic charge density (leading to membrane damages followed by the possible initiation of apoptosis [53,54]). Interestingly, the attachment of 27% GSH resulted in a strong reduction of the cytotoxicity. **P3** revealed an IC_{50} value of

Table 1
Composition and molar masses for (*co*-)polymers **P1** to **P6**.

		Composition[a]			NMR[b]	AF4		SEC[c,d]	
		X	Y	Z	Mn	Mn	Đ	Mn	Đ
Abr.	**Name**	[%]	[%]	[%]	[gmol^{-1}]	[gmol^{-1}]		[gmol^{-1}]	
P1	$LPEI_x$	>98	0	0	24,800	9900	1.4	n.d.	n.d.
P2	$P(EI_x$–*stat*–$ButEnOx_y)$	73	27	0	37,500	n.d.	n.d.	31,400[c]	1.2
P3	$P(EI_x$–*stat*–$GluButOx_z)$	73	0	27	85,200	21,000	2.0	n.d.	n.d.
P4	$PButEnOx_y$	0	>98	0	71,900	n.d.	n.d.	44,000[c]	1.5
P5	$P(bocAmButOx_x$–*stat*–$ButEnOx_y)$	82	18	0	155,300	n.d.	n.d.	23,400[d]	1.9
bocP6	$P(bocAmButOx_x$–*stat*–$ButEnOx_y$–*stat*–$GluButOx_z)$	82	10	8	169,500	n.d.	n.d.	38,400[d]	1.7
P6	$P(AmButOx_x$–*stat*–$ButEnOx_y$–*stat*–$GluButOx_z)$	82	10	8	122,300	63,300	1.8	n.d.	n.d.

[a] Determined by ^{1}H NMR (calculated from the ratio of x, y and z signals)

[b] Determined by ^{1}H NMR (calculated from tosylate signals of MeOTos before purification)

[c] SEC 1: $CHCl_3$/*i*PrOH/NEt_3 94:2:4, polystyrene calibration

[d] SEC 2: DMAc, 0.21% LiCl, polystyrene calibration

n.d. – not determined. All polymers soluble in aqueous media and /or insoluble in organic solvents were measured at AF4 – MALS system.

~270 μg mL^{-1} and even polymer concentrations up to 150 μg mL^{-1} revealed nearly no cytotoxic effects (relative viability ≥ 85%). The precursor **P2** also exhibited a lower cytotoxicity compared to **P1** (see Supporting information Fig. S1A). The replacement of the ethylene imine units by flexible primary amine containing side chains for **P6** led to an increased cytotoxicity (IC_{50} value of ~44 μg mL^{-1}) compared to **P3**. Furthermore, the incomplete thiol-ene photoaddition resulted in a lower content of GSH and, likewise, unmodified double bond functionalities, which could both influence the biocompatibility. However,

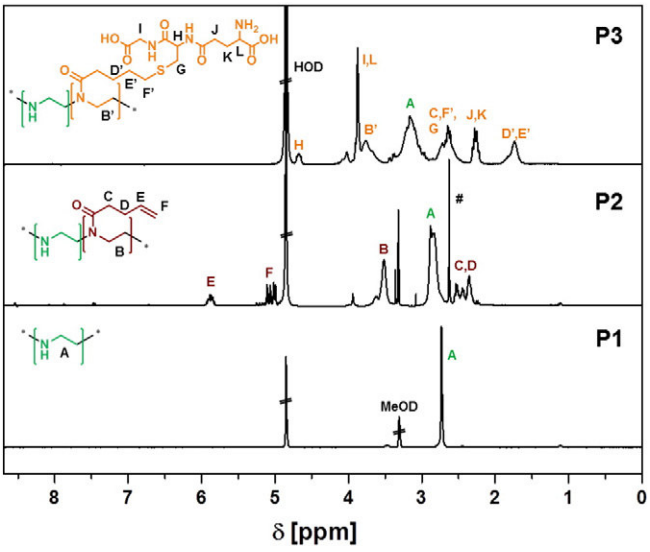

Fig. 1. Comparison of ^{1}H-NMR spectra of **P1** to **P3** (# side product *N*-hydroxysuccinimide) (400 MHz, D_2O/MeOD).

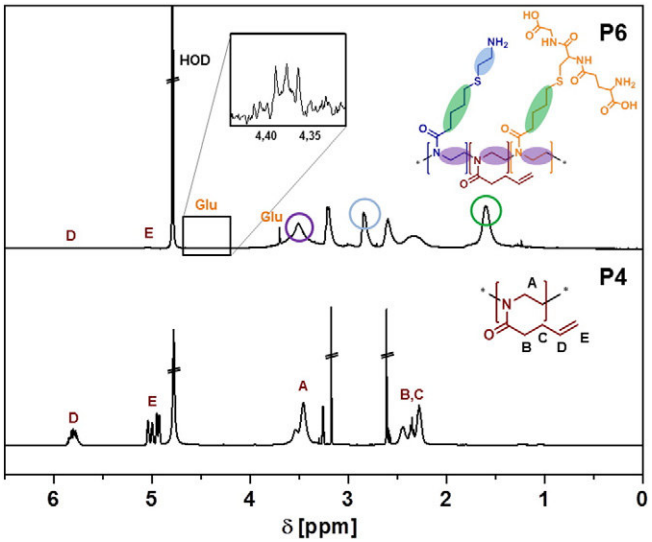

Fig. 2. Comparison of ^{1}H-NMR spectra of **P4** and **P6** (400 MHz, D_2O/MeOD and D_2O).

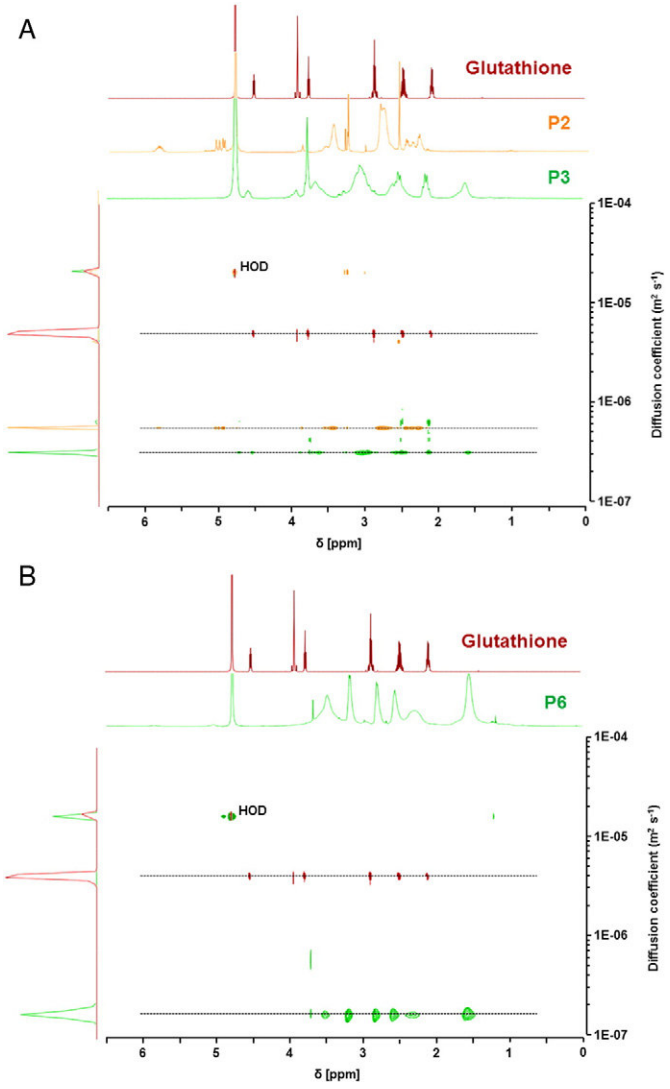

Fig. 3. Diffusion ordered NMR spectra of: A) **P2**, **P3** and L-glutathione and B) **P6** and L-glutathione (400 MHz, D_2O).

polymer concentrations of **P3** and **P6** from 2 to 5 μg mL^{-1} were used for the preparation of polyplexes, which are in an acceptable range beyond the cytotoxicity-inducing concentrations. The cytotoxicity test was not only performed with L292 cells according to the ISO protocol 10993-5 but the assay was also performed with HEK as well as hCMEC/3D cells for a detailed determination of the causal relation of toxicity and related interactions (see Supporting information Fig. S2 A). In static culture the hCMEC revealed a different performance during cytotoxicity tests and showed only 10% relative viability for **P1** at a concentration of 2 μg mL^{-1} and also a decreased viability for **P6** whereas **P3** revealed no cytotoxic effects up to 500 μg mL^{-1}. While the IC_{50} values of **P1** and **P6** decreased up to a 2-fold higher concentration, **P3** showed no cytotoxic effect at all independent of the used cell line (Fig. S2B).

To investigate the blood compatibility of **P2**, **P3** and **P6**, the hemolytic activity as well as the aggregation of erythrocytes was assessed (Fig. 4B, Supporting information Figs. S3 and S4). All investigated copolymers did not show any hemolytic activity in a concentration range from 10 to 100 μg mL^{-1}. **P1** as well as **P2** (SI Fig. S1B) revealed a slightly hemolytic activity at higher concentrations (50 to 100 μg mL^{-1}) indicated by a hemoglobin releases of 2% as well as strong agglomeration of erythrocytes (see Supporting information, Fig. S3). While no agglomeration for **P3** was observed, indicating a good hemocompatibility, **P6** showed distinct interactions with cellular membranes of erythrocytes leading to aggregation. Obviously, the type of amines within the polymer side chain represents a crucial factor for the interaction with cells, in particular with the plasma membrane, and is therefore linked to the biocompatibility properties. This fact was also assumed by Dekie et al. concluding this from glutamic acid derivatives [55]. However, Fischer et al. mentioned that these effects have to be mentioned relative to the polymer class and can also be influenced by factors like charge density (number of amines and three dimensional arrangements) [54].

As reported earlier, primary amines revealed an increased affinity to cellular membranes compared to secondary amines, indicated by a higher toxicity [56]. Tripathi et al. demonstrated the successful reduction of the cytotoxicity by pyridoxyl derivatization of primary amines of branched PEI [57]. This behavior supports the findings observed for **P3** and **P6**.

2.3. Characterization of the polyplexes

An efficient delivery of nucleic acids, like plasmid DNA, into cells depends on several parameters. They comprise of the compact condensation of the genetic material, the masking of negative charges, the prevention of degradation and the efficient dissociation from the vector after transfer into the cellular cytoplasm or nucleus. PEI derivatives, in particular PEI disulfide linked rabies virus glycoprotein, have been shown to enable the delivery of neurogenic microRNA into the brain [58]. To investigate the binding affinity of **P1**, **P2** (SI Fig. S1C), **P3** as

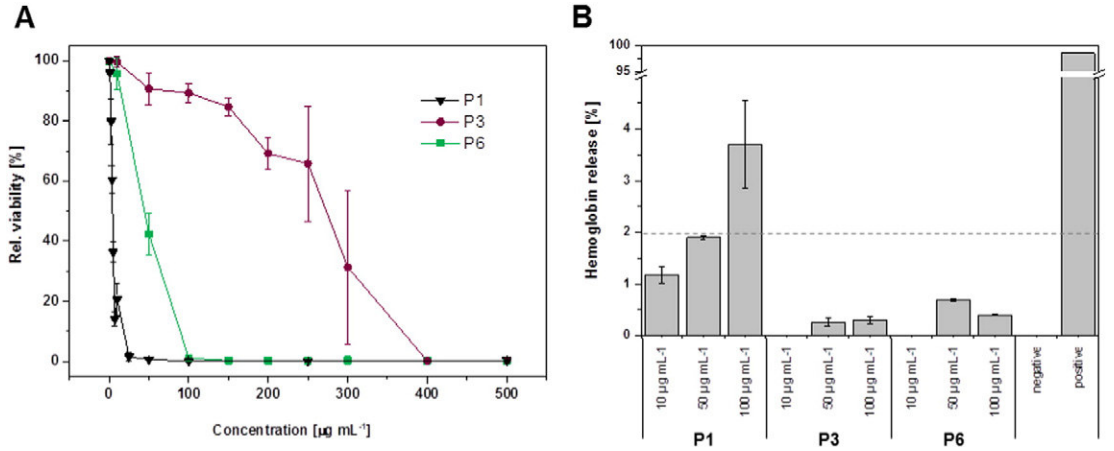

Fig. 4. Bio- & hemocompatibility. A) Relative viability of L929 cells after 24 h incubation with the respective polymers at indicated concentrations. B) Hemolysis assay of erythrocytes after incubation with polymers at indicated concentrations. Triton X-100 was used as positive and PBS as negative control. A value < 2% hemolysis is classified as non-hemolytic, 2–5% as slightly hemolytic and values > 5% as hemolytic. Values represent the mean ± S.D. (n = 3).

well as **P6** with plasmid DNA as model system, the ethidium bromide quenching assay (EBA) was utilized. Polyplexes were formed at different nitrogen (polymer) to phosphate (DNA) ratios (N/P). Due to the electrostatic and hydrophobic interactions between the polymer and the pDNA, ethidium bromide is excluded from its binding sites within the oligonucleotides resulting in a reduction of fluorescence intensity [59,60].

All polymers revealed a decreasing fluorescence intensity with increasing N/P ratios that resulted in a plateau, indicating stable polyplex formation (Fig. 5A and Supporting information Fig. S1D). While the positive control **P1** exhibited a fast polyplex formation starting at N/P 5, **P2**, **P3** and **P6** revealed a stable polyplex formation at higher N/Ps from 20 to 40 reaching 60%, 45% and 30% relative fluorescence units (RFU), respectively. A possible explanation for the slightly lower binding affinity could be the ethylene imine units which are shielded by the bulky GSH moieties as well as a lower zeta potential of **P3** (4.06 mV) compared to **P6** (28.4 mV) (see Table S5). For **P6**, primary amine groups are attached through flexible side chains, which are easier accessible for the pDNA. Additionally primary amines are known to promote pDNA compensation [61].

The heparin dissociation assay was used to analyze the stability and the dissociation behavior of the formed polyplexes [62,63]. Heparin is a natural polyanion with one of the highest density of negative charges and can effectively bind to the positive charged polymers **P3** and **P6**. It competes with the pDNA within the polyplex and forces the release of the nucleic acid. The free nucleic acid is able to rebind free ethidium bromide (added in the same concentration as for the EBA) causing an increase of the fluorescence intensity (Fig. 5B). In the case of the **P3** and **P6** polyplexes, the pDNA was released very fast at low heparin concentrations. While **P3** revealed a reversible binding, reaching 90% dissociation at 10 U mL^{-1} heparin, **P6** showed full dissociation (~100% RFU at 10 U mL^{-1}). In contrast, **P1** required higher concentrations of heparin (40 U mL^{-1}) for almost full release (~95% RFU), which underlines the stability of **P1**/pDNA polyplexes and is in accordance to literature data [46].

An efficient delivery, comprising of the internalization of polyplexes into cells *via* endocytic pathways, requires defined sizes and charges of the complexes. Therefore, critical sizes of polymeric carriers up to 200 nm are recommended [64]. As shown in Table 2, the formed polyplexes of **P3** and **P6** revealed z-averages of 282 nm and 117 nm at a N/P ratio of 20, respectively, which are calculated from the correlation function. Since the intensity of the particle scattering is proportional to the sixth power of its diameter (Rayleigh approximation), larger particles or agglomerates of free polymer chains result in comparatively more light scattering and higher intensity than smaller ones. Therefore, the intensity-weighted diameters (z-averages) determined by dynamic light scattering are supplemented by the number-weighted sizes revealing a calculated number percentage over 95. Although the calculated sizes can only be seen as informative basis, they are in good agreement with the favorable size of polyplexes. The zeta potential changes during the synthesis from well-known positive charged **P1** (28.4 mV) to the GSH bearing conjugate **P3** (−6.9 mV). In this case, a potential explanation could be that the positive charge of the former PEI backbone is complexing the DNA meanwhile the GSH carboxylic acid moieties are present at the outside of the polyplex resulting in a negative value of −6.9 mV while the precursor **P2** showed comparable size and zeta potential as **P1**. The results of **P2** can be found in the Supporting information, Table S6. The change in charge cannot be observed in the case of **P6**. Here, the lower content of GSH and the side chains with more flexible primary amines reduce the effect of the GSH functionalities.

Table 2
Size and zeta potential measured in 20 mM 4-(2-hydroxethyl) piperazine-1-ethanesulfonic acid (HEPES) and 5% (w/v) glucose, pH 7.2 of pDNA complexes of **P1**, **P3** and **P6** at N/P 20 measured by dynamic light scattering.

Polymeric system	z-Average [d/nm]	PDI	Number-weighted size [d/nm]	Zeta potential [mV]
P1	132 ± 28	0.24	61 ± 18	28.4 ± 2.7
P3	282 ± 5	0.38	109 ± 18	−6.9 ± 0.1
P6	117 ± 1	0.31	61 ± 16	33.2 ± 1.5

2.4. Uptake efficiency

To investigate the potential of the different polymers to deliver nucleic acids, cellular uptake studies were performed with adherent human embryonic kidney (HEK) cells as well as hCMEC/3D in OptiMEM and EndoGro media (see Supporting information, Figs. S7 and S8). For this purpose, YOYO-1 labeled pDNA was used for the polyplex formation at N/P 20 to detect the time-depended cellular internalization by flow cytometry. A fast polyplex uptake in HEK cells was revealed for **P6** polyplexes exhibiting ~50% internalization after 15 min, >80% internalization after 1 h, and a nearly complete uptake of polyplexes after 2 to 4 h similar to **P1**. Taking the aggregation data of **P6** into account, the strong interaction with the cellular membrane, led to enhanced uptake efficiency. In contrast, **P3** polyplexes exhibited only poor uptake efficiencies with <10% of HEK cells positive for internalized **P3** polyplexes (Fig. 6A). These results were also confirmed by life cell imaging after 1 h (Fig. 6B). Interestingly, the precursor of **P3** without GSH, **P2**, exhibited

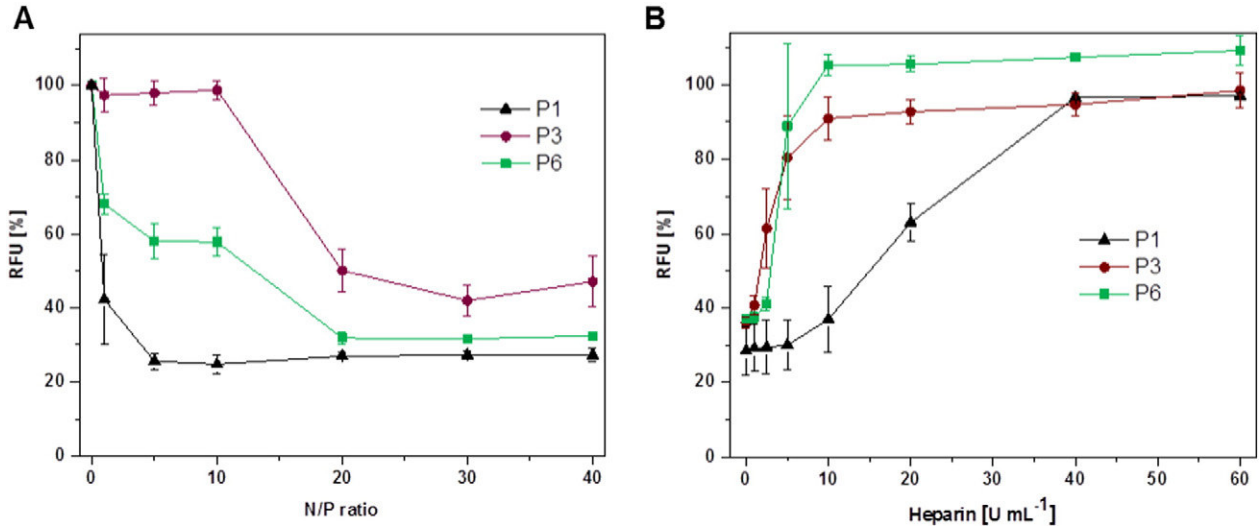

Fig. 5. Polyplex formation and stability with pDNA using the polymers **P1**, **P3** and **P6**. A) Complexation affinity (ethidium bromide quenching assay) of respective polymers at indicated N/P ratios. B) Dissociation assay of polyplexes formed at N/P 40 using heparin (0 to 60 U mL^{-1}). Values represent the mean ± S.D. (n = 3).

an enhanced polyplex uptake comparable to **P6** (see Supporting information, Fig. S1E). Compared to HEK cell experiments the uptake of **P6** decreased in hCMEC/3D cells independently from the culture media used to 20 to 40%. In contrast, the results of **P1** and **P3** uptake did not changed significantly.

Taking the MFI of uptaken pDNA into account, comparable results were also obtained for the transfection efficiencies of the polymers **P1**, **P3** and **P6 in HEK cells**. A transfection efficiency of over 60% of HEK cells was achieved for **P1**, whereas reduced transfection efficiencies were found for **P3** and **P6** of around 30% and 5%, respectively (see Supporting information, Fig. S9).

2.5. Blood-brain barrier passaging performance within the biochip approach

The GSH modified polyplexes were subsequently investigated towards their ability to cross the endothelial layer of the BBB. HCMEC/D3 cells resembling the cerebral endothelial cell layer of the BBB were cultured on a suspended membrane within MOTiF biochips that were recently shown to enable an improved culture of endothelial cells under physiological perfusion conditions [65]. Here, the membrane serves as a cell substrate that is perfused from the apical side of the endothelial cell layer. The cells were grown until full confluence to form a densely packed layer (see Supporting information, Fig. S10). Additionally, immunofluorescence staining for characteristic adherens and tight junction proteins was performed to confirm the integrity of the microvascular endothelial layer before perfusion (see Fig. 7, first row). HCMEC exhibit prominent staining of VE-Cadherin, a key component of adherens endothelial junction and mediator of Claudin-5 expression [66]. Claudin-5 is the main claudin-class protein expressed in BBB endothelial cells and a key regulator of its permeability [67]. Another VE-Cadherin regulated protein is β-Catenin, which plays an important role in maintenance of the BBB integrity and related signaling [68,69]. In addition, we investigated the distribution of occludin, another protein important for tight junction formation and for regulating paracellular permeability [70]. Occludin is associated with cytoplasmic scaffolding and regulatory protein ZO-1 [3]. Claudin-5, β-Catenin, ZO-1 and occludin were found all expressed and localized to intercellular junctions formed by hCMEC. Perfusion with precursor polymer **P1** resulted in a significant loss of endothelial junctional markers (see Fig. 7). Arrowheads indicate a reduced staining of the proteins at the intercellular contacts. This observation is in accordance to the results obtained for the biocompatibility of **P1** on L929 cells (see Fig. 4A) as well as on hCMEC (see Supporting information S2). In flow experiments hCMEC seem to be rendered more susceptible to PEI uptake since already a concentration of 0.1 μg mL^{-1} revealed a strong impact on the cell viability (see Fig. 4A). In 2006 Mennesson et al. already showed that an increase in the polyplex-cell membrane interaction and binding capabilities under flow conditions is altered by shear and sedimentation velocity forces [71]. As demonstrated in hemocompatibility tests, **P1** leads to erythrocyte aggregation and, therefore, to strong membrane interactions. We speculate that in the presence of flow this interaction could

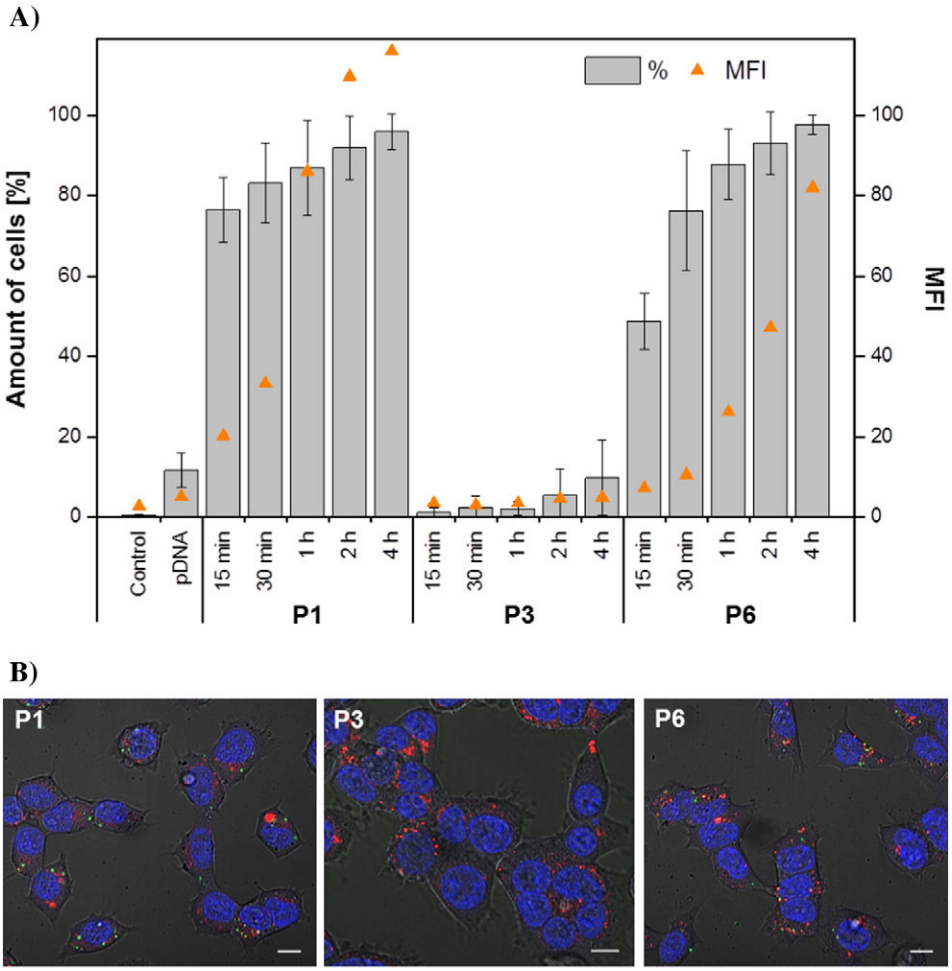

Fig. 6. Cellular uptake study of **P1**, **P3** and **P6** polyplexes (N/P 20) using YOYO-1 labeled pDNA. A) HEK cells were treated with polyplexes for 15 min to 4 h and uptake was analyzed *via* flow cytometry (MFI – mean fluorescence intensity). Values represents the mean ± S.D. (n = 3). B) Confocal microscopy of HEK cells, which were incubated for 1 h with polyplexes (green). Cell nuclei were stained with Hoechst (blue), lysosomes with LysoTracker Red (red). Scale bar = 10 μm.

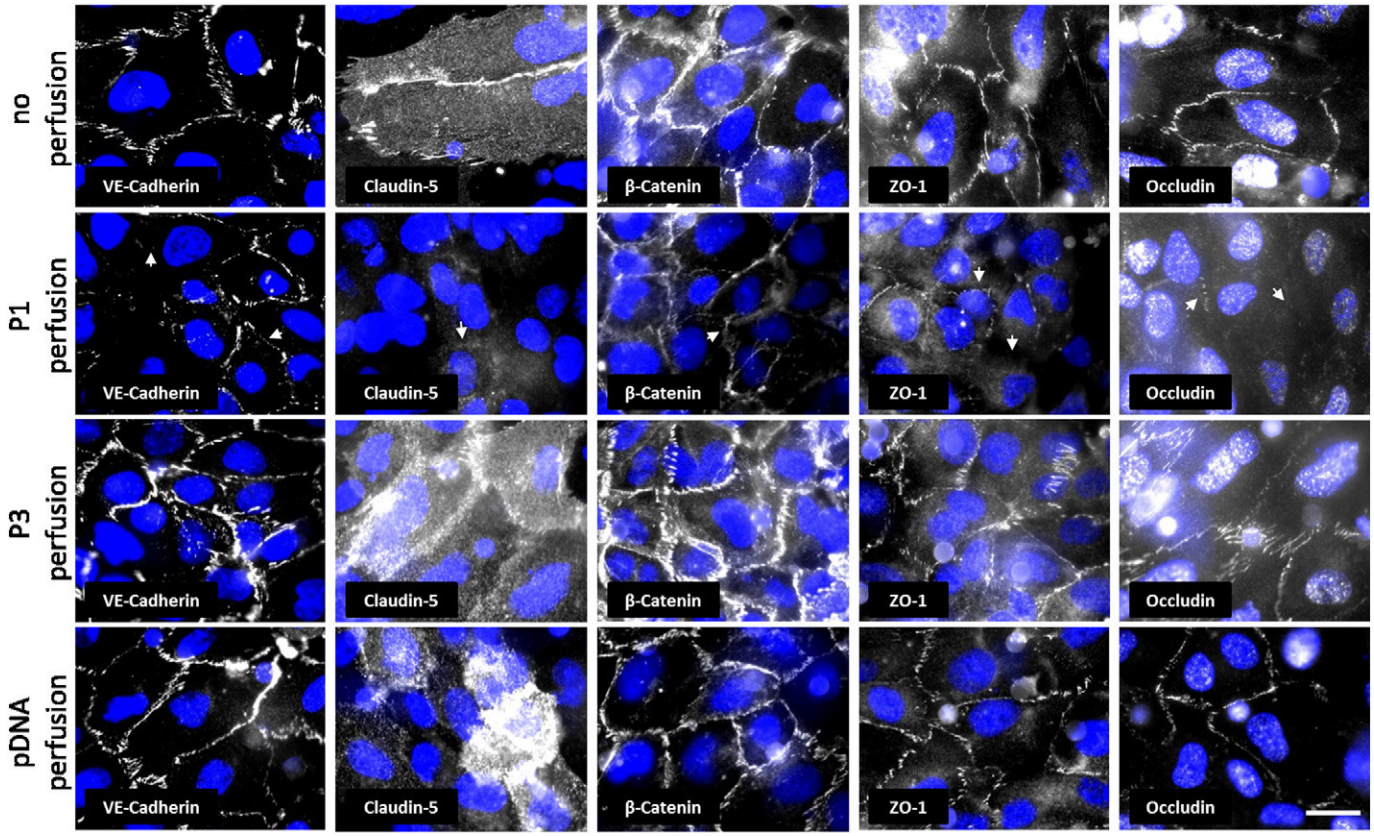

Fig. 7. Expression of BBB relevant junctional marker proteins before and after polyplex perfusion. pDNA served as control group. Arrowheads show breakdown or diminished expression of adherens (VE-Cadherin) and tight junction components evoked by polyplex **P1**. Nuclei are stained in blue (scale bar 20 nm, n = 3).

be promoted which results in a disruption of tight junctions and increased cytotoxicity. In contrast, perfusion with polyplex **P3** as well as free pDNA, serving as control, revealed no impact on adherens or tight junction formation (see Fig. 7). We thus conclude that under flow conditions the tightness of the hCMEC layers is not impaired by the polyplexes, except for polyplex **P1**.

The biochip design allows the quantification of nanoparticles taken up by the endothelial layer through fluorescence measurements as well as the exact determination of the total amount of polyplexes that crossed the endothelial barrier. The imperviousness of the model system, in particular for the endothelial cell layer, was proven for YOYO-1 labeled pDNA without nanocarrier (see Supporting information, Fig. S11). In order to demonstrate the need of glutathione moieties for a successful passage, the precursor **P2** was investigated for comparison reasons. For the polyplex **P6**, we observed the highest uptake into the endothelial cell layer that was associated with a polyplex aggregation (Fig. 8A; see also Supporting information Fig. S3), which was also observed in kinetic studies using HEK cells. In contrast, polyplexes **P1** and **P2** show a lower enrichment at the endothelial layer. **P3** exhibited the weakest enrichment within the endothelial layer compared to other polymers. An image analysis of the quantitative uptake revealed that the internalization of the polyplex **P6** within the endothelial barrier was significantly higher compared to the internalization of the polyplexes **P1** and **P2**, respectively (Fig. 8B). Interestingly, the highest difference in the endothelial uptake of all polyplexes tested was observed for **P3,** even with a significant difference regarding the GSH free precursor **P2** (see Fig. S12).

To further elucidate the trans-endothelial transport of the different polyplexes, we measured its enrichment in the lower chamber underneath the endothelial barrier of the biochip (Fig. 8C). GSH was reported to facilitate a crossing of the nanocarriers through the BBB [21]. We thus tested whether pDNA bound to **P3** could be delivered through the endothelial barrier more efficiently than polyplexes **P1**, **P2** or **P6** (high uptake efficiency and strong interaction with endothelial layer). After 30 min of perfusion we observed a significant increase of polyplex **P1** translocation through the endothelial that remained at this level up to 60 min of perfusion. A viability test revealed that **P1** was toxic already at low concentrations (Fig. 4A). A similar effect was further confirmed by immunofluorescence staining of several endothelial adherens and tight junction proteins involved in maintenance of barrier integrity. Accordingly, **P1** induced a leakage of hCMEC/D3 cell layers under flow conditions. The difference in our observations under flow conditions compared to static culture conditions, where the final concentration of 0.5 μg mL^{-1} was still in an acceptable range, can likely be explained by a significantly increased total amount of polyplexes presented to the cells within the similar incubation time compared to the static cell culture. This could be an explanation to the unexpected polyplex passage after 30 min. In contrast, we observed a continuously increasing transport of the polyplex **P3** through the endothelial layer reaching a maximum at 60 min. Indeed, a significantly difference is observed compared to the non-passaging precursor polyplex **P2** without glutathione modification. Taking the results of the uptake studies into account, a highly "active" polymer like **P6** within HEK cells can perform in a different way compared to microvascular endothelial cell interactions. It is not beneficial for a passage through the BBB due to its strong interaction with any kind of cells, independent of proper uptake or not. These results indicate that *in vivo* **P6** would probably adhere to and might be partly internalized by endothelial blood vessel cells, followed by cargo release instead of passing the cell layer. Importantly, the pure pDNA, the precursor polyplex using **P2** without GSH and **P6** containing only 8%

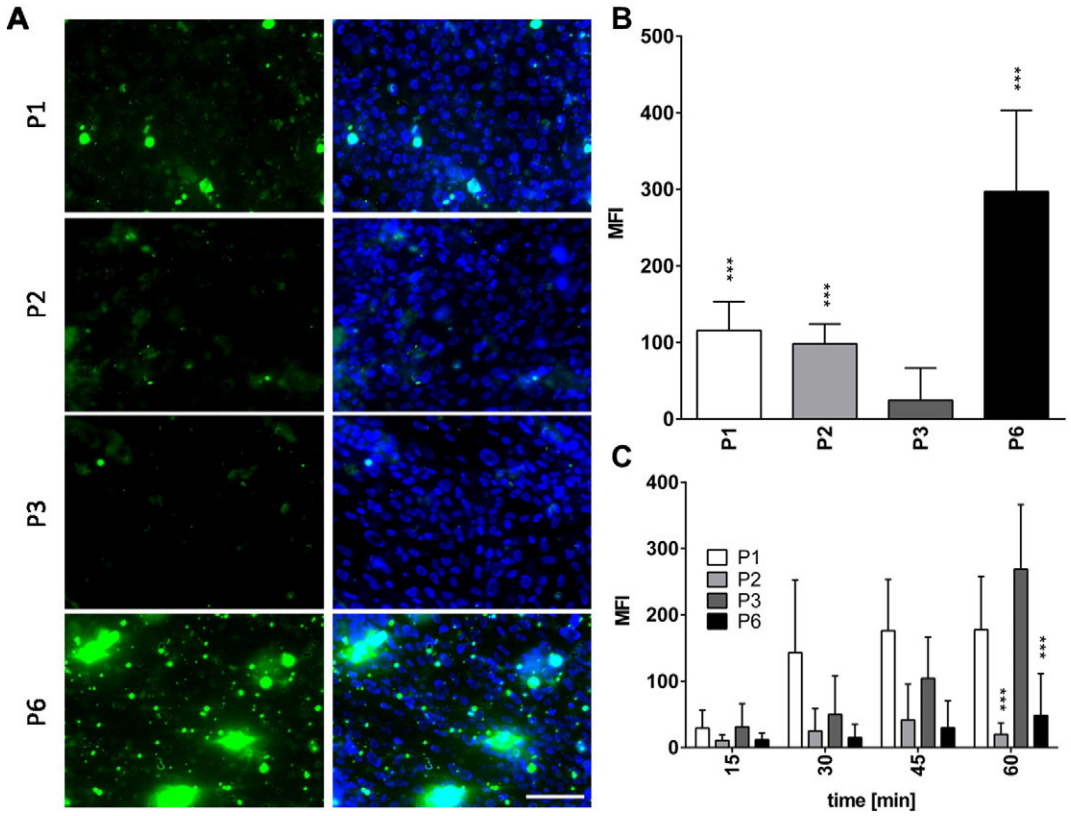

Fig. 8. Performance of the GSH-conjugated polyplexes **P1**, **P2**, **P3** and **P6** in a microfluidically supported biochip assay mimicking permeability of the BBB. A) Microscopic images display polyplex uptake (green) with the hCMEC/D3 cells (nuclei stained with DAPI (blue)) under a physiologic shear stress of 4 dyn cm^{-2}. B) Quantificational analysis of polyplexes at the cellular barrier. C) Passage of polyplexes **P1**, **P2**, **P3** and **P6** through BBB-like hCMEC/D3 cell layer over time. * significances *vs.* **P3**; ***$p < 0.001$; $n = 3$; scale bar 100 nm.

coupled GSH were virtually prevented from crossing the endothelial layer. Only **P3** showed no interaction neither with HEK cells nor endothelia cells, but was able to pass the BBB and, therefore, was identified as a promising candidate as BBB nanocarrier. These results further indicate the strong influence of the polymer design/composition for a BBB carrier balancing the GSH content, DNA binding potential and cellular interactions.

3. Conclusion

In this study, the synthesis of L-glutathione (GSH) bearing cationic polymers is described. To enable the transport of genetic material, ~80% amine functionalities of different nature (primary amines in side chains and secondary amine groups in polymer backbones) were installed within a poly(ethylene imine) derivative. A post-polymerization modification technique followed by a thiol-ene photo-addition in water was used to attach the GSH moieties. The cationic polymers investigated in this study exhibited cytotoxic side effects. The insertion of different types of amines in combination with GSH improved the cell viability compared to poly(ethylene imine). While the presence of primary amines in **P6** still revealed adverse effects on the cell viability combined with a strong interaction with cellular membranes, **P3** exhibited a superior cell viability as well as a good hemocompatibility. Despite the functionalization with negatively charged GSH, the copolymers were able to bind and release plasmid DNA. These features supported the potential application as attractive gene delivery agents for the passage of the BBB.

Studies with biochip embedded cerebral microvascular endothelial cell layers perfused under physiological shear stress conditions revealed a significantly enhanced passage of the BBB for the GSH modified candidate containing secondary amine functionalities. Interestingly, the primary amines led to strong interactions with cells combined with remarkable high uptake efficiency independent of the utilized cell types. However, this functionalization likely mediates an intracellular incorporation within the BBB and, thus, renders the nanocarriers (**P6**) unsuitable to efficiently cross the endothelial layer of the BBB. While **P1** showed an unexpected cell layer passaging effect which is probably due to a reduced tightness of the cell layer, the nanocarrier precursor (**P2**) as well as the uncomplexed plasmid DNA nanocarriers revealed significantly reduced ability to cross the endothelial BBB compared to GSH-coupled nanocarriers with higher GSH amounts (**P3**). The GSH-coupling of nanocarriers thus represents a promising approach to efficiently cross the BBB while avoiding cellular toxicity as shown in this first proof-of-concept study *in vitro*. However, follow-up studies are required to further characterize trans-endothelial transport across the BBB. To proof the feasibility of GSH-coupled nanocarriers as novel therapeutic option for drug-delivery to the CNS also more complex *in vivo* models will be investigated in the future.

4. Experimental part

4.1. Materials

Unless otherwise stated, the chemicals were used without further purification. Trifluoroacetic acid, ethanol, methanol, Irgacure® 2959, *tert*-butyl-(2-mercaptoethyl)carbamate and reduced L-glutathione were purchased from Sigma Aldrich. The following chemicals were ordered from the suppliers in brackets: 2-Ethylen-2-oxazoline (Acros Organics), 4-dimethylaminopyridine (Merck Millipore), 2,2-dimethoxy-1,2-diphenylethan-1-one (TCI America), hydrochloric acid (VWR Chemicals). *N*-succinimidyl-4-pentenate was synthesized according to literature procedures [72]. AlamarBlue, YOYO-1 iodide, Hoechst 33342 trihydrochloride (10 mg mL^{-1} solution) as well as LysoTracker Red

DND-99 were obtained from Life Technologies (Thermo Fisher, Germany). If not stated otherwise, cell culture media and supplements (L-glutamine, antibiotics) were obtained from Lonza (Basel, Switzerland) and Biochrom (Merck Millipore, Germany), respectively. All other chemicals were purchased from standard suppliers and used without further purification.

4.2. General methods and instrumentation

An Initiator Sixty single-mode microwave synthesizer from Biotage, equipped with a noninvasive IR sensor (accuracy: 2%), was used for polymerization under microwave irradiation.

Proton (^{1}H) nuclear magnetic resonance (NMR) spectra were recorded in deuterated water or methanol, at room temperature using a Bruker Advance I (300 MHz) or a Bruker Advance III HD (400 MHz) spectrometer; chemical shifts (δ) are expressed in parts per million relative to TMS. Size exclusion chromatography (SEC) was measured on a Agilent 1200 series system equipped with a PSS degasser, a G1310A pump, a G1362A refractive index detector and a PSS GRAM guard column running with dimethylacetamide (DmAc) with 0.21% of lithium chloride. For further measurements a Shimadzu system using a SCL-10A VP controller equipped with a DGU-14A degasser, a LC-10AD VP pump, a RID-10A refractive index detector and a PSS SDV guard and linear S column running with chloroform/*iso*-propanol/triethylamine (94:2:4) was utilized. The Techlab oven used for both systems was set to 40 °C and the molar masses were calculated using polystyrene (PS) standards. Asymmetric flow field-flow fractionation (AF4) was performed on an AF2000 MT system (Postnova Analytics, Landberg, Germany) coupled to an UV (PN3211, 260 nm), RI (PN3150), MALS (PN3070, 633 nm) detector. The eluent is delivered by two different pumps (tip and focus-flow) and the sample is injected by an autosampler (PN5300) into the channel. The channel has a trapezoidal geometry and an overall area of 31.6 cm^2. The nominal height of the spacer was 500 μm and a regenerated cellulose membrane with a molar mass cut-off of 10,000 g mol^{-1} (M_n) was used as the accumulation wall. All experiments were carried out at 25 °C and the eluent was 20 mM NaCl in 25 mM sodium acetate buffer at pH 3.5. The detector flow rate was set to 0.5 mL min^{-1} for all samples and 50 μL (10 mg mL^{-1}) were injected with an injection flow rate of 0.2 mL min^{-1} for 7 min. For all samples the cross-flow was set to 2 mL min^{-1}. After the focusing period and a transition time of 1 min, the cross flow was kept constant for 1 min and was then decreased under a power function gradient 0.40 to zero within 15 min. Afterwards the cross-flow was kept constant at zero for 20 min to ensure complete elution. For the calculation of the molar mass a Zimm plot was used. The refractive index increment (d*n*/d*c*) of all samples was measured by manual injection of a known concentration directly into the channel without any focusing or cross-flow. The d*n*/d*c* was calculated as the average of at least three injections from the area under the RI curve. The cytotoxicity studies as well as ethidium bromide and heparin assays were performed using a microplate reader (Tecan Infinite M200 Pro, Crailsheim, Germany). For the uptake studies of HEK-293 and hCMEC/D3 cells a flow cytometer, Cytomics FC 500 (Beckman Coulter, Krefeld, Germany) and a confocal laser scanning microscope LSM880 (Carl Zeiss, Jena, Germany) were used (see below).

4.3. Synthesis of linear poly(ethylene imine) (**P1**)

The polymerization of the monomer 2-ethyl-2-oxazoline using the initiator methyl tosylate was performed in a microwave synthesizer according to literature procedures [9]. The resulting poly(2-ethyl-2-oxazoline) (**PEtOx**, DP = 575, 5.0 g) was further hydrolyzed in 6 M hydrochloric acid (HCl) at 100 °C for 16 h under heating to reflux [73]. The excess of HCl and formed propionic acid was removed under reduced pressure. After dissolving in water, the solution was neutralized by the addition of 3 M sodium hydroxide (pH > 8). The precipitated linear poly(ethylene imine) was filtered off and, subsequently, redissolved in 15 mL *N*,*N*-dimethylformamide to remove the formed salt. After repeated precipitation in 400 mL ice-cold diethyl ether, the obtained product was dried under reduced pressure at 85 °C for three days. ^{1}H-NMR was used to determine the degree of hydrolysis of the resulting polymer **1** (yield: 1.85 g, 85%).

PEtOx: DP = 575. ^{1}H-NMR (300 MHz, D_2O): δ 3.70–3.20 (—NR—CH_2—CH_2), 2.41–2.08 (CH_2—CH_3), 1.09–0.79 (CH_2—CH_3) ppm.
P1: EtOx:EI [%] = 5:95. ^{1}H-NMR (300 MHz, MeOD): δ 3.58–3.41 (NR—CH_2—CH_2), 2.91–2.61 (NH—CH_2—CH_2), 2.56–2.36 (CH_2—CH_3), 1.18–1.06 (CH_2—CH_3) ppm. AF4: M_n = 9900 g mol^{-1}, Đ = 1.4.

4.4. Synthesis of P(EI-stat-ButEnOx) (**P2**, **P4**)

Double bond functionalities were installed on the backbone of **P1** by a post-polymerization modification process. For this purpose, **P1** (for **P2**: 751 mg, for **P4**: 765 mg) and the catalyst 4-*N*,*N*-dimethylaminopyridine (DMAP, for **P2**: 120 mg, 0.98 mmol, for **P4**: 360 mg, 2.95 mmol) were dissolved in pyridine (V = 5 mL) at 80 °C. In a second vial, *N*-succinimidyl-4-pentenate (for **P2**: 707 mg, for **P4**: 4.012 g) was dissolved in pyridine (V = 5 mL) and heated to 80 °C. The two solutions were combined to a 5 wt% mixture (5 mL pyridine were added) of **P1**. The reaction mixture was stirred for 21 h at 80 °C. The polymer solution was precipitated in 500 mL ice-cold diethyl ether. The filtered product was washed with 50 mL diethyl ether and dried under reduced pressure to constant weight (yield: **P2**: 0.83 g, 73%, **P4**: 1.29 g, 58%).

P2: EI:ButEnOx [%] = 73:27. ^{1}H-NMR (400 MHz, D_2O): δ 2.28–2.46 (m, CH_2 ButEnOx), 2.63–2.85 (m, NH—CH_2—CH_2), 3.35–3.62 (m, NR—CH_2—CH_2), 4.9–5.0 (dd, CH_2═CH—), 5.76–5.86 (m, CH_2═CH—) ppm. SEC ($CHCl_3$/*i*PrOH/NEt_3): M_n = 31,400 g mol^{-1}, Đ = 1.20.
P4: EI:ButEnOx [%] = 0:100. ^{1}H-NMR (400 MHz, D_2O): δ 2.27–2.44 (m, CH_2 ButEnOx), 3.45–3.53 (m, NR—CH_2—CH_2), 4.92–5.04 (dd, CH_2═CH), 5.76–5.84 (m, CH_2═CH) ppm. SEC ($CHCl_3$/*i*PrOH/NEt_3): M_n = 44,000 g mol^{-1}, Đ = 1.53.

4.5. Synthesis of P(EI-stat-GluButOx) via thiol-ene photo-addition (**P3**)

In a microwave vial, P($EI_{73\%}$-*stat*-ButEnO$x_{27\%}$) (**P2**: 740 mg) and a 1.2-fold excess per double bond of reduced L-glutathione (1.11 g, 3.6 mmol) were dissolved in 15 mL Milli-Q water (5 wt% of **P2**). The radical photoinitiator Irgacure® 2959 (100 mg, 0.45 mmol) was added and the reaction mixture was degassed with argon for 30 min. The clear solution was stirred in a UV-chamber (λ = 365 nm) for 17 h and, subsequently, dialyzed against water using Spectra/Por 1 dialysis membrane (6000 to 8000 g mol^{-1} cut-off). The product **P3** was lyophilized and obtained as a yellowish powder (yield: 770 mg, 44%).

P3: EI:GluButOx [%] = 73:27. ^{1}H-NMR (400 MHz, D_2O): δ 1.60–1.71 (m, CH_2—CH_2—S—), 2.12 (q, NCH—CH_2—CH_2—C═O), 2.45–2.64 (m, NCH—CH_2—CH_2—C═O, CH_2 ButOx), 2.87–3.30 (m, CH_2—S—CH_2—CH_2, NH—CH_2—CH_2), 3.63–3.95 (m, NR—CH_2—CH_2, NR—CH_2—COOH, NH_2—CH), 4.54 (m, NR—CH—CH_2—S) ppm. AF4: M_n = 21,000 g mol^{-1}, Đ = 2.0.

4.6. Synthesis of P(bocAmButOx-stat-ButEnOx) via thiol-ene photo-addition (**P5**)

In a similar procedure, PButEnOx (**P4**, 1.13 g) and 2-(*boc*-amino)ethanethiol (1.19 g, 6.7 mmol) were dissolved in 15 mL methanol (7.5 wt% of **P4**). 2,2-Dimethoxy-2-phenylacetophenone (DMPA, 88 mg, 0.40 mmol) was added as photoinitiator and the reaction

mixture was degassed with argon for 30 min. Subsequently, the solution was stirred in a UV-chamber (λ = 365 nm) for 17 h. Precipitation in 400 mL ice-cold diethyl ether, washing with 50 mL of diethyl ether and drying under reduced pressure for three days resulted in a yellowish powder **P5** (yield: 1.94 g, 80%).

P5: *boc*AmButOx:ButEnOx [%] = 82:18. ^{1}H-NMR (300 MHz, MeOD): δ 1.42 (s, CH_3 boc), 1.65 (s, CH_2—S—CH_2—CH_2—NR), 2.37–2.63 (m, m, CH_2 ButEnOx, S—CH_2—CH_2—NR), 3.50 (m, NR—CH_2—CH_2, S—CH_2—CH_2—NR), 4.96–5.09 (dd, CH_2═CH), 5.84 (m, CH_2═CH) ppm. SEC (DMAc, 0.21% LiCl): M_n = 23,400 g mol^{-1}, Đ = 1.86.

4.7. Synthesis of P(bocAmButOx-stat-ButEnOx-stat-GluButOx) via thiol-ene photo-addition (boc**P6**)

The conjugation of reduced L-glutathione (GSH) to the copolymer **P5** was performed similar to the conjugation to **P3**. For this purpose, **P5** (1.01 g) was dissolved in 17 mL ethanol (6 wt% of **P5**). The photoinitiator Irgacure® 2959 (321 mg, 1.4 mol) and a 1.2-fold excess per double bond of GSH (252 mg, 0.82 mmol) was added, the reaction mixture was degassed with argon for 30 min and stirred in a UV-chamber (λ = 365 nm) for 48 h. An aliquot of 50 μL was taken and characterized *via* ^{1}H-NMR. Due to still incomplete photo-addition, additional GSH (150 mg, 0.49 mmol) was added to the reaction mixture and irradiated for further 48 h. The copolymer was purified by dialysis against ethanol using Spectra/Por 1 dialysis membrane (6000 to 8000 g mol^{-1} cut-off) and dried under reduced pressure for four days (yield: 735 mg, 67%).

***boc*P6**: *boc*AmButOx:ButEnOx:GluButOx [%] = 82:10:8. ^{1}H-NMR (300 MHz, MeOD): δ 1.32–1.48 (s, CH_3 boc), 1.67 (m, CH_2—S—CH_2—CH_2—NR), 2.20 (m, NCH—CH_2—CH_2—C═O), 2.17–2.60 (m, NCH—CH_2—CH_2—C═O, CH_2 ButOx), 3.08–3.91 (m, CH_2—S—CH_2—CH_2, NR—CH_2—CH_2, NR—CH_2—COOH, NH_2—CH), 4.58 (m, NR—CH—CH_2—S), 5.02 (CH_2═CH), 5.34 (CH_2═CH) ppm. SEC (DMAc, 0.21% LiCl): M_n = 38,400 g mol^{-1}, Đ = 1.74.

4.8. Synthesis of P(AmButOx-stat-ButEnOx-stat-GluButOx) via deprotection (***P6***)

The protected copolymer ***boc*P6** (615 mg) was dissolved in dichloromethane (24 mL) and trifluoroacetic acid (40 mL) was added. The reaction mixture was stirred for 20 h at room temperature and, subsequently, precipitated in 300 mL ice-cold diethyl ether. The residue was filtered off, washed with 30 mL diethyl ether, re-dissolved in methanol and shaken overnight with Amberlyst® A21 (free base) (~0.5 mg). After filtration, the solvent was removed and the copolymer **P6** lyophilized.

P6: AmButOx:ButEnOx:GluButOx [%] = 82:10:8. ^{1}H-NMR (400 MHz, D_2O): δ 1.60 (CH_2—S—CH_2—CH_2—NR), 2.05 (NCH—CH_2—CH_2—C═O), 2.32–3.73 (NCH—CH_2—CH_2—C═O, CH_2 ButOx, CH_2—S—CH_2—CH_2, NR—CH_2—CH_2, NR—CH_2—COOH, NH_2—CH_2—CH_2), 4.38 (NR—CH—CH_2—S), 5.06 (CH_2═CH), 5.84 (CH_2═CH) ppm. AF4: M_n = 63,300 g mol^{-1}, Đ = 1.82.

4.9. Determination of the cytotoxicity

Cytotoxicity studies were performed with the mouse fibroblast cell line L929 (CCL-1, ATCC), as recommended by ISO10993-5 as well as with HEK-293 and hCMECs/D3 cells. The cells were routinely cultured in Dulbecco's modified eagle's medium (DMEM, Lonza) supplemented with 10% fetal calf serum (FCS), 100 U mL^{-1} penicillin and 100 μg mL^{-1} streptomycin at 37 °C in a humidified 5% (v/v) CO_2 atmosphere. In detail, cells were seeded at 10^4 cells per well in a 96-well plate and incubated for 24 h, whereas no cells were seeded in the outer wells. Afterwards, the substances to be tested (polymers) at indicated concentrations (from 10 μg mL^{-1} to 500 μg mL^{-1}) were added to the cells and the plates were incubated for further 24 h. Control cells were incubated with fresh culture medium. Subsequently, the medium was replaced by a mixture of fresh culture medium and Alamar-Blue solution, prepared according to the manufacturer's instructions. After an additional incubation of 4 h at 37 °C, the fluorescence was measured at Ex 570/Em 610 nm, with untreated cells on the same well plate serving as negative controls. The negative control was standardized as 0% of metabolism inhibition and referred as 100% viability. Cell viability below 70% was considered indicative of cytotoxicity. Data are expressed as mean ± S.D. of three determinations.

4.10. Hemolysis assay

The interaction of polymers with cellular membranes was examined by analyzing the release of hemoglobin from erythrocytes. Blood from sheep, collected in heparinized tubes, were provided by the Institute of Laboratory Animal Science and Animal Welfare, Friedrich Schiller University Jena. The blood was centrifuged at 4500 × *g* for 5 min, and the pellet was washed three times with cold 1.5 mM phosphate buffered saline (PBS, pH 7.4). After dilution with PBS in a ratio of 1:7, aliquots of erythrocyte suspension were mixed 1:1 with the polymer solution and incubated in a water bath at 37 °C for 60 min. After centrifugation at 2400 × *g* for 5 min, the hemoglobin release into the supernatant was determined spectrophotometrically using a microplate reader at 544 nm wavelength. Complete hemolysis (100%) was achieved using 1% Triton X-100 serving as positive control. Pure PBS was used as negative control (0% hemolysis). The hemolytic activity of the polycations was calculated as follow (Eq. (1)):

$$\%\text{Hemolysis} = 100 * \frac{(A_{Sample} - A_{Negative\ \ control})}{A_{Positive\ \ control}} \quad (1)$$

A value < 2% hemolysis rate was considered as non-hemolytic, 2 to 5% as slightly hemolytic and values > 5% as hemolytic. Experiments were run in triplicates and were performed with three different batches of donor blood.

4.11. Erythrocyte aggregation

The erythrocyte suspension was mixed 1:1 with the polymer solutions (100 μL total volume) in a clear flat bottomed 96-well plate. The cells were incubated at 37 °C for 2 h, and the absorbance was measured at 645 nm in a microplate reader. Cells, which were treated with PBS served as negative control and 25 kDa bPEI (50 μg mL^{-1}, Polyscience) was used as positive control. Absorbance values of the test solutions lower than the negative control were regarded as aggregation. Experiments were run in triplicates and were performed with three different charges of donor blood from sheep.

4.12. Polyplex preparation

Polyplexes of pDNA and polymers were prepared by mixing stock solutions of 15 μg mL^{-1} pDNA and different amounts of polymers (1 mg mL^{-1}) to obtain various N/P ratios (nitrogen of polymer to phosphate of pDNA) in HBG buffer (20 mM 4-(2-hydroxethyl) piperazine-1-ethanesulfonic acid (HEPES) and 5% (w/v) glucose, pH 7.2). The solutions were vortexed for 10 s at maximal speed and incubated at room temperature for 20 min to ensure complex formation.

4.13. Ethidium bromide quenching assay

The formation of polyplexes with pDNA was examined by quenching of the ethidium bromide fluorescence as described previously [56]. Briefly, 15 μg mL^{-1} pDNA in a total volume of 100 μL HBG buffer

(HEPES buffered glucose) were incubated with ethidium bromide (0.4 μg mL^{-1}) for 10 min at room temperature. Afterwards, polyplexes with increasing amounts of indicated polymers (regarding N/P ratio) were prepared in black 96-well plates (Nunc Thermo Fisher). The samples were incubated at room temperature for 15 min before fluorescence measurements. The fluorescence of the samples was measured at an excitation wavelength of 525 nm and an emission wavelength of 605 nm using a microplate reader. A sample solely containing pDNA and EtBr was used to calibrate the device to 100% fluorescence against a background of 0.4 μg mL^{-1} of EtBr in HBG solution. The percentage of dye displaced upon polyplex formation was calculated using Eq. (2):

$$\mathrm{RFU}\,[\%] = \frac{F_{sample} - F_0}{F_{pDNA} - F_0} * 100 \quad (2)$$

RFU is defined as the relative fluorescence and F_{sample}, F_0, and F_{pDNA} are the fluorescence intensities of a given sample, the ethidium bromide in HBG alone, and the ethidium bromide intercalated into pDNA alone.

4.14. Heparin dissociation assay

To investigate the release of pDNA from the polyplexes, the heparin dissociation assay was performed. Polyplexes with a N/P ratio of 40 were prepared as described above in a total volume of 100 μL HBG buffer containing ethidium bromide (0.4 μg mL^{-1}). After incubation in the dark at room temperature for 15 min, the polyplexes were transferred into a black 96-well plate, and heparin of indicated concentrations was added. The solution was mixed and incubated for further 30 min at 37 °C in the dark. The fluorescence of ethidium bromide was measured at Ex 525 nm/Em 605 nm with a Tecan microplate reader. The percentage of intercalated ethidium bromide was calculated as described before.

4.15. Dynamic and electrophoretic light scattering

Dynamic light scattering (DLS) was performed on a Zetasizer Nano ZS (Malvern Instruments, Herrenberg) with a He-Ne laser operating at a wavelength of $\lambda = 633$ nm. All measurements (30 runs, triplicate) were carried out at 25 °C after an equilibration time of 120 s. The counts were detected at an angle of 173°. The mean particle size was approximated as the effective (z-average) diameter and the width of the distribution as the polydispersity index of the particles (PDI) obtained by the cumulants method assuming a spherical shape. Electrophoretic light scattering (ELS) was used to measure the zeta potential (ζ). The measurement was performed on a Zetasizer Nano ZS (Malvern Instruments, Herrenberg, Germany) by applying laser Doppler velocimetry. For each measurement, 20 runs were carried out using the slow-field reversal and the fast-field reversal mode at 150 V. Each experiment was performed in triplicate a 25 °C. The zeta potential was calculated from the electrophoretic mobility (μ) according to the Henry Equation. Henry coefficient f(ka) was calculated according to Oshima.

4.16. Polyplex uptake

HEK-293 cells (CRL-1573, ATCC) were cultured in RPMI 1640 medium supplemented with 10% FCS, 100 μg mL^{-1} streptomycin, 100 IU mL^{-1} penicillin and 2 mM L-glutamine at 37 °C in a humidified 5% (v/v) CO_2 atmosphere. For uptake studies, cells were seeded at a density of 10^5 cells per mL in 24-well plates and cultured for 24 h. One hour prior to the addition of the polyplexes, the medium was changed to OptiMEM (Thermo Fisher, Germany). For the uptake kinetic study within 4 h, pDNA was labeled with YOYO-1 iodide prior to the polyplex preparation. For labeling of 1 μg pDNA, 0.026 μL of 1 M YOYO-1 solution was mixed with pDNA and incubated for 20 min at 4 °C protected from light. Afterwards, HBG buffer and the polymers were added at the indicated N/P ratio and the polyplexes were formed as described previously. The cells were harvested 15 min, 30 min, 1 h, 2 h and 4 h after polyplex addition and 10% trypan blue was added to quench the outer fluorescence of the cells. To determine the relative uptake of the polyplexes, 10,000 cells were measured by flow cytometry using a Cytomics FC 500 (Beckman Coulter) and the amount of viable cells showing YOYO-1 signal were gated. Dead cells were identified *via* counterstaining with propidium iodide. The experiments were performed at least three times independently. The uptake studies of hCMECs were performed in OptiMEM and EndoGro media, respectively. For live cell imaging HEK cells (10^5 cells mL^{-1}) were seeded in glass-bottomed, 4-chamber dishes (CELLVIEW, Greiner Bio-One, Germany) and cultured for 24 h. One hour prior to polymer addition, the cells were rinsed with phosphate buffered saline (PBS) and the media were changed to OptiMEM. Polyplexes were prepared at N/P 20 as described above and incubated for further 1 h. Afterwards, the media were replaced with fresh culture media supplemented with LysoTracker Red DND-99 and Hoechst 33342 for lysosome and nucleus staining, respectively. The living cells were imaged with a LSM880 using the following excitation wavelengths/laser lines 405 nm (for Hoechst), 488 nm (for YOYO-1) and 561 nm (for LysoTracker Red).

4.17. Transfection of adherent cells

For transfection of adherent HEK-293 cells, the cells were seeded at a density of 10^5 cells mL^{-1} in 24-well plates and incubated for 24 h at 37 °C, 5% (v/v) CO_2. One hour prior to transfection, the cells were washed with PBS and supplemented with serum-reduced media (OptiMEM). Polyplexes were prepared as described above, and were added to the cells (50 μL per well). After an incubation time of 4 h at 37 °C, the supernatant was replaced by fresh growth medium and the cells were further incubated for 20 h. For analysis *via* flow cytometry (Cytomics FC 500, Beckman Coulter), the cells were harvested by trypsinization and 10^4 cells were analyzed. For determination of the viability during flow cytometry, dead cells were identified *via* counterstaining with propidium iodide. For determination of the transfection efficiency, viable cells expressing EGFP were gated. The experiments were performed independently three times.

4.18. Immunofluorescence microscopy.

Cells were fixed with ice cold methanol for 10 min at −20 °C, permeabilized with 0.1% Saponin and blocking was done with 3% normal donkey serum. Antibody staining was performed using mouse-anti-human VE-Cadherin, mouse-anti-human β-Catenin (both BD Biosciences, Heidelberg, Germany), mouse-anti-human Claudin-5, rabbit-anti-human ZO-1 and rabbit-anti-human Occludin (all Life Technologies, Karlsruhe, Germany) overnight. Secondary antibodies donkey-anti-rabbit Cy3 (Dianova, Hamburg, Germany) and donkey-anti-mouse AlexaFluor647 (Life Technologies) as well as DAPI (Life Technologies) were applied for 1 h at room temperature. Samples were embedded in fluorescence mounting medium (Dako, Hamburg, Germany) and imaged on an Axio Observer.Z1 fluorescence microscope (Carl Zeiss AG, Jena, Germany). Image analysis was performed using ImageJ2 software (Fiji).

4.19. Dynamic cell culture assay

MOTiF biochips were made by injection moulding of polystyrene and manufactured by microfluidic Chip Shop (Jena, Germany) as described previously [65]. Chip geometry and embedded structures are shown in Supporting information, Fig. S10. The human cerebral microvascular endothelial cell line hCMEC/D3 (BIOZOL, Eching, Germany) was cultured in EndoGRO-MV Basal Medium supplemented with 5% (v/v) FCS, 0.2% (v/v) EndoGRO-LS supplement, 5 ng/mL recombinant human epidermal growth factor, 10 mM L-glutamine, 1 μg mL^{-1} hydrocortisone-hemisuccinate, 0.75 U mL^{-1} heparin-sulfate, 50 μg mL^{-1}

ascorbic acid (all additives were obtained from Merck-Millipore, Darmstadt, Germany), and 100 U mL^{-1} penicillin and 100 μg mL^{-1} streptomycin at 37 °C in a humidified 5% (v/v) CO_2 atmosphere. The membrane within the biochip was coated with 150 μg mL^{-1} collagen A (Biochrom, Berlin, Germany) for at least 1 h prior to cell seeding. hCMEC/D3 were seeded at a density of 0.75×10^5 cm^{-2} in the upper channel to grow on top of the membrane. Cells were cultured until fully confluent after four to five days. Afterwards, biochips were connected to an Ismatec peristaltic pump (Cole Parmer, Wertheim, Germany) *via* gas permeable silicon tubing (Cole Parmer and microfluidic Chip Shop) at 37 °C in a humidified 5% (v/v) CO_2 atmosphere and accustomed to flow conditions with a flow rate of 175 μL min^{-1} (corresponding shear stress of 2 dyn cm^2) for 30 min. Meanwhile polyplex formation at a N/P ratio of 20 was performed in hCMEC/D3 cell culture medium as stated above with additionally applying YOYO-1 as reporter dye. As corresponding controls polyplex solutions without dye were used. Subsequently shear stress was increased to 4 dyn cm^2 and polyplex solutions were applied for 1 h. For sampling 30 μL from the lower channel system were taken whereas the first 15 μL were discarded to ensure sampling from under the membrane and not just from the microchannels. Samples were taken every 15 min. Afterwards, cells were washed gently by flushing the upper and lower microchannels three times with PBS. Nuclei were stained with Hoechst 33342. Membranes and supernatants were analyzed using an Axio Observer.Z1 fluorescence microscope (Carl Zeiss AG, Jena, Germany) applying a filter with 470 nm excitation and 525 nm emission wave lengths. At least three images per sample were taken. Fluorescence images were analyzed with the ImageJ2 software whereas controls were subtracted for quantification.

4.20. Statistical analysis

The values represent the mean ± S.D. Direct comparison of two different groups was done with two-tailed, non-paired student's test. For multiple comparisons analysis by two-way ANOVA was performed using Turkey's multiple testing as post-test. Statistical significant was defined with p-values of <0.05.

Acknowledgment

The authors would like to thank Carolin Fritzsche for the support with the bio assays and Gabriele Sentis and Dr. Peter Bellstedt for nuclear magnetic resonance measurements. We gratefully acknowledge Dr. Johannes C. Brendel for helpful discussions. The funding of the collaborative research center ChemBioSys (SFB 1127) by the Deutsche Forschungsgemeinschaft (DFG), the Carl Zeiss Foundation (scholarship for AT), the German Federal Ministry of Education and Research (BMBF # 031A518B Vectura) and the German Federal Institute of Risk Assessment (grant number 1329-533) are highly acknowledged. The LSM880 ELYRA PS.1 was further founded with a grant from the DFG.

Appendix A. Supplementary data

Supplementary figures and tables S1–S12. This material is available free of charge *via* the Internet at http://pubs.acs.org. Supplementary data associated with this article can be found in the online version, at http://dx.doi.org/10.1016/j.jconrel.2016.08.039.

References

[1] P. Ehrlich, Das Sauerstoffbedürfnis des Organismus, eine farbenanalytische Studie, Hirschwald, Berlin, 1885.
[2] M. Lewandowsky, Zur Lehre von der Cerebrospinalflüssigkeit, Z. Klin. Med. 40 (1900) 480–494.
[3] N.J. Abbott, A.A.K. Patabendige, D.E.M. Dolman, S.R. Yusof, D.J. Begley, Structure and function of the blood–brain barrier, Neurobiol. Dis. 37 (2010) 13–25, http://dx.doi.org/10.1016/j.nbd.2009.07.030.
[4] V.A. Levin, Relationship of octanol/water partition coefficient and molecular weight to rat brain capillary permeability, J. Med. Chem. 23 (1980) 682–684, http://dx.doi.org/10.1021/jm00180a022.
[5] X. Liu, M. Tu, R.S. Kelly, C. Chen, B.J. Smith, Development of a computional approach to predict blood-brain barrier permeability, Drug Metab. Dispos. 32 (2004) 132–139, http://dx.doi.org/10.1124/dmd.32.1.132.
[6] C.C. Visser, L.H. Voorwinden, D.J.A. Crommelin, M. Danhof, A.G. de Boer, Characterization and modulation of the transferrin receptor on brain capillary endothelial cells, Pharm. Res. 21 (2004) 761–769, http://dx.doi.org/10.1023/B:PHAM.0000026425.69874.8e.
[7] B.V. Zlokovic, The blood-brain barrier in health and chronic neurodegenerative disorders, Neuron 57 (2008) 178–201, http://dx.doi.org/10.1016/j.neuron.2008.01.003.
[8] R. Kannan, R. Chakrabarti, D. Tang, K.J. Kim, N. Kaplowitz, GSH transport in human cerebrovascular endothelial cells and human astrocytes: evidence for luminal localization of Na+-dependent GSH transport in HCEC1, Brain Res. 852 (2000) 374–382, http://dx.doi.org/10.1016/S0006-8993(99)02184-8.
[9] M. Bauer, C. Lautenschlaeger, K. Kempe, L. Tauhardt, U.S. Schubert, D. Fischer, Poly(2-ethyl-2-oxazoline) as alternative for the stealth polymer poly(ethylene glycol): comparison of in vitro cytotoxicity and hemocompatibility, Macromol. Biosci. 12 (2012) 986–998, http://dx.doi.org/10.1002/mabi.201200017.
[10] R. Kannan, J.F. Kuhlenkamp, E. Jeandidier, H. Trinh, M. Ookhtens, N. Kaplowitz, Evidence for carrier-mediated transport of glutathione across the blood-brain barrier in the rat, J. Clin. Invest. 85 (1990) 2009–2013, http://dx.doi.org/10.1172/JCI114666.
[11] C.M. Berlin, D.G. May-McCarver, D.A. Notterman, R.M. Ward, D.N. Weismann, G.S. Wilson, J.T. Wilson, Alternative routes of drug administration—advantages and disadvantages, Pediatrics 100 (1997) 143–152, http://dx.doi.org/10.1542/peds.100.1.143.
[12] A. Mistry, S. Stolnik, L. Illum, Nanoparticles for direct nose-to-brain delivery of drugs, Int. J. Pharm. 379 (2009) 146–157, http://dx.doi.org/10.1016/j.ijpharm.2009.06.019.
[13] X. Wen, K. Wang, Z. Zhao, Y. Zhang, T. Sun, F. Zhang, J. Wu, Y. Fu, Y. Du, L. Zhang, Y. Sun, Y. Liu, K. Ma, H. Liu, Y. Song, Brain-targeted delivery of trans-activating transcriptor-conjugated magnetic PLGA/lipid nanoparticles, PLoS One 9 (2014) e106652, http://dx.doi.org/10.1371/journal.pone.0106652.
[14] B. Oller-Salvia, M. Sanchez-Navarro, E. Giralt, M. Teixido, Blood-brain barrier shuttle peptides: an emerging paradigm for brain delivery, Chem. Soc. Rev. (2016), http://dx.doi.org/10.1039/C6CS00076B.
[15] J. Kreuter, Nanoparticulate systems for brain delivery of drugs, Adv. Drug Deliv. Rev. 47 (2001) 65–81, http://dx.doi.org/10.1016/S0169-409X(00)00122-8.
[16] L. Nobs, F. Buchegger, R. Gurny, E. Allémann, Surface modification of poly(lactic acid) nanoparticles by covalent attachment of thiol groups by means of three methods, Int. J. Pharm. 250 (2003) 327–337, http://dx.doi.org/10.1016/S0378-5173(02)00542-2.
[17] K. Kafedjiiski, M. Werle, F. Föger, A. Bernkop-Schnürch, Synthesis and in vitro characterization of a novel poly(acrylic acid)-glutathione conjugate, J. Drug. Deliv. Sci. Tech. 15 (2005) 411–417, http://dx.doi.org/10.1016/S1773-2247(05)50081-9.
[18] S.S. More, R. Vince, Design, synthesis and biological evaluation of glutathione peptidomimetics as components of anti-parkinson prodrugs, J. Med. Chem. 51 (2008) 4581–4588, http://dx.doi.org/10.1021/jm800239v.
[19] N. Raval, T. Mistry, N. Acharya, S. Acharya, Development of glutathione-conjugated asiatic acid-loaded bovine serum albumin nanoparticles for brain-targeted drug delivery, J. Pharm. Pharmacol. 67 (2015) 1503–1511, http://dx.doi.org/10.1111/jphp.12460.
[20] A. Grover, A. Hirani, V. Sutariya, Blood-barin barrier permeation of glutathione-coated nanoparticle, J. Pharm. Pharm. Sci 1 (2014), http://dx.doi.org/10.15226/2374-6866/1/1/00103.
[21] P.J. Gaillard, C.C.M. Appeldoorn, J. Rip, R. Dorland, S.M.A. van der Pol, G. Kooij, H.E. de Vries, A. Reijerkerk, Enhanced brain delivery of liposomal methylprednisolone improved therapeutic efficacy in a model of neuroinflammation, J. Control. Release 164 (2012) 364–369, http://dx.doi.org/10.1016/j.jconrel.2012.06.022.
[22] P.J. Gaillard, C.C.M. Appeldoorn, R. Dorland, J. van Kregten, F. Manca, D.J. Vugts, B. Windhorst, G.A.M.S. van Dongen, H.E. de Vries, D. Maussang, O. van Tellingen, Pharmacokinetics, brain delivery, and efficacy in brain tumor-bearing mice of glutathione pegylated liposomal doxorubicin (2B3-101), PLoS One 9 (2014) e82331, http://dx.doi.org/10.1371/journal.pone.0082331.
[23] T. Patel, J. Zhou, J.M. Piepmeier, W.M. Saltzman, Polymeric nanoparticles for drug delivery to the central nervous system, Adv. Drug Deliv. Rev. 64 (2012) 701–705, http://dx.doi.org/10.1016/j.addr.2011.12.006.
[24] J. Kreuter, R.N. Alyautdin, D.A. Kharkevich, A.A. Ivanov, Passage of peptides through the blood-brain barrier with colloidal polymer particles (nanoparticles), Brain Res. 674 (1995) 171–174, http://dx.doi.org/10.1016/0006-8993(95)00023-J.
[25] K.S. Rao, M.K. Reddy, J.L. Horning, V. Labhasetwar, TAT-conjugated nanoparticles for the CNS delivery of anti-HIV drugs, Biomaterials 29 (2008) 4429–4438, http://dx.doi.org/10.1016/j.biomaterials.2008.08.004.
[26] S.A. Kulkarni, S.-S. Feng, Effects of surface modification on delivery efficiency of biodegradable nanoparticles across the blood–brain barrier, Nanomedicine 6 (2011) 377–394, http://dx.doi.org/10.2217/nnm.10.131.
[27] J. Wang, Z. Lu, M.G. Wientjes, J.L.-S. Au, Delivery of siRNA therapeutics: barriers and carriers, AAPS J. 12 (2010) 492–503, http://dx.doi.org/10.1208/s12248-010-9210-4.
[28] M.A. Mintzer, E.E. Simanek, Nonviral vectors for gene delivery, Chem. Rev. 109 (2009) 259–302, http://dx.doi.org/10.1021/cr800409e.
[29] J.H. Jeong, S.H. Song, D.W. Lim, H. Lee, T.G. Park, DNA transfection using linear poly(ethylenimine) prepared by controlled acid hydrolysis of poly(2-ethyl-2-oxazoline), J. Control. Release 73 (2001) 391–399, http://dx.doi.org/10.1016/S0168-3659(01)00310-8.
[30] C. Englert, M. Hartlieb, P. Bellstedt, K. Kempe, C. Yang, S.K. Chu, X. Ke, J.M. García, R.J. Ono, M. Fevre, R.J. Wojtecki, U.S. Schubert, Y.Y. Yang, J.L. Hedrick, Enhancing the biocompatibility and biodegradability of linear poly(ethylene imine) through con-

trolled oxidation, Macromolecules 48 (2015) 7420–7427, http://dx.doi.org/10.1021/acs.macromol.5b01940.
[31] K. Kunath, A. von Harpe, D. Fischer, T. Kissel, Galactose-PEI–DNA complexes for targeted gene delivery: degree of substitution affects complex size and transfection efficiency, J. Control. Release 88 (2003) 159–172, http://dx.doi.org/10.1016/S0168-3659(02)00458-3.
[32] W. Cheng, C. Yang, J.L. Hedrick, D.F. Williams, Y.Y. Yang, P.G. Ashton-Rickardt, Delivery of a granzyme B inhibitor gene using carbamate-mannose modified PEI protects against cytotoxic lymphocyte killing, Biomaterials 34 (2013) 3697–3705, http://dx.doi.org/10.1016/j.biomaterials.2013.01.090.
[33] C. Englert, M. Fevre, R.J. Wojtecki, W. Cheng, Q. Xu, C. Yang, X. Ke, M. Hartlieb, K. Kempe, J.M. García, R.J. Ono, U.S. Schubert, Y.Y. Yang, J.L. Hedrick, Facile carbohydrate-mimetic modifications of poly(ethylene imine) carriers for gene delivery applications, Polym. Chem. (2016), http://dx.doi.org/10.1039/c6py00940a (in press).
[34] M. Ogris, S. Brunner, S. Schüller, R. Kircheis, E. Wagner, PEGylated DNA/transferrin-PEI complexes: reduced interaction with blood components, extended circulation in blood and potential for systemic gene delivery, Gene Ther. 6 (1999) 595–605.
[35] B.J. Ballermann, A. Dardik, E. Eng, A. Liu, Shear stress and the endothelium, Kidney Int. 54 (1998) 100–108, http://dx.doi.org/10.1046/j.1523-1755.1998.06720.x.
[36] M. Raasch, K. Rennert, T. Jahn, C. Gärtner, G. Schönfelder, O. Huber, A. Seiler, A. Mosig, An integrative microfluicically supported in vitro model of an endothelial barrier combined with cortical spheroids simulates effects of neuroinflammation in neocortex development, Biomicrofluidics 10 (2016), http://dx.doi.org/10.1063/1.4955184 (in press).
[37] B.B. Weksler, E.A. Subileau, N. Perrière, P. Charneau, K. Holloway, M. Leveque, H. Tricoire-Leignel, A. Nicotra, S. Bourdoulous, P. Turowski, D.K. Male, F. Roux, J. Greenwood, I.A. Romero, P.O. Couraud, Blood-brain barrier-specific properties of a human adult brain endothelial cell line, FASEB J. 19 (2005) 1872–1874, http://dx.doi.org/10.1096/fj.04-3458fje.
[38] B. Weksler, I.A. Romero, P.-O. Couraud, The hCMEC/D3 cell line as a model of the human blood brain barrier, Fluids Barriers CNS 10 (2013) 1–10, http://dx.doi.org/10.1186/2045-8118-10-16.
[39] B. Poller, H. Gutmann, S. Krähenbühl, B. Weksler, I. Romero, P.-O. Couraud, G. Tuffin, J. Drewe, J. Huwyler, The human brain endothelial cell line hCMEC/D3 as a human blood-brain barrier model for drug transport studies, J. Neurochem. 107 (2008) 1358–1368, http://dx.doi.org/10.1111/j.1471-4159.2008.05730.x.
[40] L. Cucullo, P.-O. Couraud, B. Weksler, I.-A. Romero, M. Hossain, E. Rapp, D. Janigro, Immortalized human brain endothelial cells and flow-based vascular modeling: a marriage of convenience for rational neurovascular studies, J. Cereb. Blood Flow Metab. 28 (2008) 312–328, http://dx.doi.org/10.1038/sj.jcbfm.9600525.
[41] L.M. Griep, F. Wolbers, B. de Wagenaar, P.M. ter Braak, B.B. Weksler, I.A. Romero, P.O. Couraud, I. Vermes, A.D. van der Meer, A. van den Berg, BBB on chip: microfluidic platform to mechanically and biochemically modulate blood-brain barrier function, Biomed. Microdevices 15 (2013) 145–150, http://dx.doi.org/10.1007/s10544-012-9699-7.
[42] B.P. Daniels, L. Cruz-Orengo, T.J. Pasieka, P.-O. Couraud, I.A. Romero, B. Weksler, J.A. Cooper, T.L. Doering, R.S. Klein, Immortalized human cerebral microvascular endothelial cells maintain the properties of primary cells in an in vitro model of immune migration across the blood brain barrier, J. Neurosci. Methods 212 (2013) 173–179, http://dx.doi.org/10.1016/j.jneumeth.2012.10.001.
[43] D. Ye, M.N. Raghnaill, M. Bramini, E. Mahon, C. Aberg, A. Salvati, K.A. Dawson, Nanoparticle accumulation and transcytosis in brain endothelial cell layers, Nanoscale 5 (2013) 11153–11165, http://dx.doi.org/10.1039/C3NR02905K.
[44] D. Ye, K.A. Dawson, I. Lynch, A TEM protocol for quality assurance of in vitro cellular barrier models and its application to the assessment of nanoparticle transport mechanisms across barriers, Analyst 140 (2015) 83–97, http://dx.doi.org/10.1039/C4AN01276C.
[45] H.M.L. Lambermont-Thijs, F.S. van der Woerdt, A. Baumgaertel, L. Bonami, F.E.D. Prez, U.S. Schubert, R. Hoogenboom, Linear poly(ethylene imine)s by acidic hydrolysis of poly(2-oxazoline)s: kinetic screening, thermal properties, and temperature-induced solubility transitions, Macromolecules 43 (2010) 927–933, http://dx.doi.org/10.1021/ma9020455.
[46] T. Bus, C. Englert, M. Reifarth, P. Borchers, M. Hartlieb, A. Vollrath, S. Hoeppener, A. Traeger, U.S. Schubert, 3rd Generation Poly(ethylene imine)s for Gene Delivery, 2016 (submitted).
[47] C. Englert, L. Tauhardt, M. Hartlieb, K. Kempe, M. Gottschaldt, U.S. Schubert, Linear poly(ethylene imine)-based hydrogels for effective binding and release of DNA, Biomacromolecules 15 (2014) 1124–1131, http://dx.doi.org/10.1021/bm4017572.
[48] M. Neu, D. Fischer, T. Kissel, Recent advances in rational gene transfer vector design based on poly(ethylene imine) and its derivatives, J. Gene Med. 7 (2005) 992–1009, http://dx.doi.org/10.1002/jgm.773.
[49] S.K. Samal, M. Dash, S. Van Vlierberghe, D.L. Kaplan, E. Chiellini, C. van Blitterswijk, L. Moroni, P. Dubruel, Cationic polymers and their therapeutic potential, Chem. Soc. Rev. 41 (2012) 7147–7194, http://dx.doi.org/10.1039/C2CS35094G.
[50] J.C. Sunshine, D.Y. Peng, J.J. Green, Uptake and transfection with polymeric nanoparticles are dependent on polymer end-group structure, but largely independent of nanoparticle physical and chemical properties, Mol. Pharm. 9 (2012) 3375–3383, http://dx.doi.org/10.1021/mp3004176.
[51] B. Wittgren, A. Welinder, B. Porsch, Molar mass characterization of cationic methyl methacrylate–ethyl acrylate copolymers using size-exclusion chromatography with online multi-angle light scattering and refractometric detection, J. Chromatogr. A 1002 (2003) 101–109, http://dx.doi.org/10.1016/S0021-9673(03)00729-5.
[52] R. Roemling, K. Tokunaga, H. Monyama, Analysis of cationic polymers by size exclusion chromatography (SEC), LC-GC Europe (2008) 47–48.
[53] S.M. Moghimi, P. Symonds, J.C. Murray, A.C. Hunter, G. Debska, A. Szewczyk, A two-stage poly(ethylenimine)-mediated cytotoxicity: implications for gene transfer/therapy, Mol. Ther. 11 (2005) 990–995, http://dx.doi.org/10.1016/j.ymthe.2005.02.010.
[54] D. Fischer, Y. Li, B. Ahlemeyer, J. Krieglstein, T. Kissel, In vitro cytotoxicity testing of polycations: influence of polymer structure on cell viability and hemolysis, Biomaterials 24 (2003) 1121–1131, http://dx.doi.org/10.1016/S0142-9612(02)00445-3.
[55] L. Dekie, V. Toncheva, P. Dubruel, E.H. Schacht, L. Barrett, L.W. Seymour, Poly-L-glutamic acid derivatives as vectors for gene therapy, J. Control. Release 65 (2000) 187–202, http://dx.doi.org/10.1016/S0168-3659(99)00235-7.
[56] A.C. Rinkenauer, L. Tauhardt, F. Wendler, K. Kempe, M. Gottschaldt, A. Traeger, U.S. Schubert, A cationic poly(2-oxazoline) with high in vitro transfection efficiency identified by a library approach, Macromol. Biosci. 15 (2015) 414–425, http://dx.doi.org/10.1002/mabi.201400334.
[57] S.K. Tripathi, N. Gupta, M. Mahato, K.C. Gupta, P. Kumar, Selective blocking of primary amines in branched polyethylenimine with biocompatible ligand alleviates cytotoxicity and augments gene delivery efficacy in mammalian cells, Colloids Surf. B 115 (2014) 79–85, http://dx.doi.org/10.1016/j.colsurfb.2013.11.024.
[58] D.W. Hwang, S. Son, J. Jang, H. Youn, S. Lee, D. Lee, Y.-S. Lee, J.M. Jeong, W.J. Kim, D.S. Lee, A brain-targeted rabies virus glycoprotein-disulfide linked PEI nanocarrier for delivery of neurogenic microRNA, Biomaterials 32 (2011) 4968–4975, http://dx.doi.org/10.1016/j.biomaterials.2011.03.047.
[59] J.B. Lepecq, C. Paoletti, Federation of european biochemical societies 3rd meeting: a fluorescent complex between ethidium bromide and nucleic acids, J. Mol. Biol. 27 (1967) 87–106, http://dx.doi.org/10.1016/0022-2836(67)90353-1.
[60] A.J. Geall, I.S. Blagbrough, Rapid and sensitive ethidium bromide fluorescence quenching assay of polyamine conjugate–DNA interactions for the analysis of lipoplex formation in gene therapy, J. Pharm. Biomed. Anal. 22 (2000) 849–859, http://dx.doi.org/10.1016/S0731-7085(00)00250-8.
[61] A.C. Rinkenauer, S. Schubert, A. Traeger, U.S. Schubert, The influence of polymer architecture on in vitro pDNA transfection, J. Mater. Chem. B 3 (2015) 7477–7493, http://dx.doi.org/10.1039/C5TB00782H.
[62] S. Sundaram, S. Viriyayuthakorn, C.M. Roth, Oligonucleotide structure influences the interactions between cationic polymers and oligonucleotides, Biomacromolecules 6 (2005) 2961–2968, http://dx.doi.org/10.1021/bm0502314.
[63] A. Kwok, S.L. Hart, Comparative structural and functional studies of nanoparticle formulations for DNA and siRNA delivery, Nanomed. Nanotechnol. 7 (2011) 210–219, http://dx.doi.org/10.1016/j.nano.2010.07.005.
[64] R. Luxenhofer, G. Sahay, A. Schulz, D. Alakhova, T.K. Bronich, R. Jordan, A.V. Kabanov, Structure-property relationship in cytotoxicity and cell uptake of poly(2-oxazoline) amphiphiles, J. Control. Release 153 (2011) 73–82, http://dx.doi.org/10.1016/j.jconrel.2011.04.010.
[65] R. Martin, R. Knut, J. Tobias, P. Sven, H. Thomas, H. Otmar, S. Ingo, B. Holger, L. Stefan, F. Harald, M. Alexander, Microfluidically supported biochip design for culture of endothelial cell layers with improved perfusion conditions, Biofacrication 7 (2015) 015013, http://dx.doi.org/10.1088/1758-5090/7/1/015013.
[66] J. Gavard, J.S. Gutkind, VE-cadherin and claudin-5: it takes two to tango, Nat. Cell Biol. 10 (2008) 883–885, http://dx.doi.org/10.1038/ncb0808-883.
[67] W. Jia, R. Lu, T.A. Martin, W.G. Jiang, The role of claudin-5 in blood-brain barrier (BBB) and brain metastases (review), Mol. Med. Rep. 9 (2014) 779–785, http://dx.doi.org/10.3892/mmr.2013.1875.
[68] E. Dejana, F. Orsenigo, M.G. Lampugnani, The role of adherens junctions and VE-cadherin in the control of vascular permeability, J. Cell Sci. 121 (2008) 2115–2122, http://dx.doi.org/10.1242/jcs.017897.
[69] S. Liebner, M. Corada, T. Bangsow, J. Babbage, A. Taddei, C.J. Czupalla, M. Reis, A. Felici, H. Wolburg, M. Fruttiger, M.M. Taketo, H. von Melchner, K.H. Plate, H. Gerhardt, E. Dejana, Wnt/β-catenin signaling controls development of the blood–brain barrier, J. Cell Biol. 183 (2008) 409–417, http://dx.doi.org/10.1083/jcb.200806024.
[70] T. Hirase, J.M. Staddon, M. Saitou, Y. Ando-Akatsuka, M. Itoh, M. Furuse, K. Fujimoto, S. Tsukita, L.L. Rubin, Occludin as a possible determinant of tight junction permeability in endothelial cells, J. Cell Sci. 110 (1997) 1603–1613 (doi:).
[71] E. Mennesson, P. Erbacher, M. Kuzak, C. Kieda, P. Midoux, C. Pichon, DNA/cationic polymer complex attachment on a human vascular endothelial cell monolayer exposed to a steady laminar flow, J. Control. Release 114 (2006) 389–397, http://dx.doi.org/10.1016/j.jconrel.2006.06.006.
[72] A. Gress, A. Völkel, H. Schlaad, Thio-click modification of poly[2-(3-butenyl)-2-oxazoline], Macromolecules 40 (2007) 7928–7933, http://dx.doi.org/10.1021/ma071357r.
[73] J.C. Fernandes, X. Qiu, F.M. Winnik, M. Benderdour, X. Zhang, K. Dai, Q. Shi, Linear polyethylenimine produced by partial acid hydrolysis of poly(2-ethyl-2-oxazoline) for DNA and siRNA delivery in vitro, Int. J. Nanomedicine 8 (2013) 4091–4102, http://dx.doi.org/10.2147/IJN.S47413.

SUPPORTING INFORMATION:

Glutathione-conjugated Poly(ethylene imine) for Passage of Blood-Brain Barrier

Christoph Englert,[a,b,†] Anne-Kristin Trützschler,[a,b,†] Martin Raasch,[c,d] Tanja Bus,[a,b] Philipp Borchers,[a,b] Alexander S. Mosig,[b,c,d,] Anja Traeger,[a,b,*] Ulrich S. Schubert[a,b,*]*

[a] *Laboratory of Organic and Macromolecular Chemistry (IOMC), Friedrich Schiller University Jena, Humboldtstrasse 10, 07743 Jena, Germany*

[b] *Jena Center for Soft Matter (JCSM), Friedrich Schiller University Jena, Philosophenweg 7, 07743 Jena, Germany*

[c] *Institute of Biochemistry II, Jena University Hospital, Nonnenplan 2-4, 07743 Jena, Germany*

[d] *Center for Sepsis Control and Care, Jena University Hospital, Erlanger Allee 101, 07747 Jena*

[†] *The authors contributed equally to this work*

Email: ulrich.schubert@uni-jena.de, anja.traeger@uni-jena.de, alexander.mosig@med.uni-jena.de

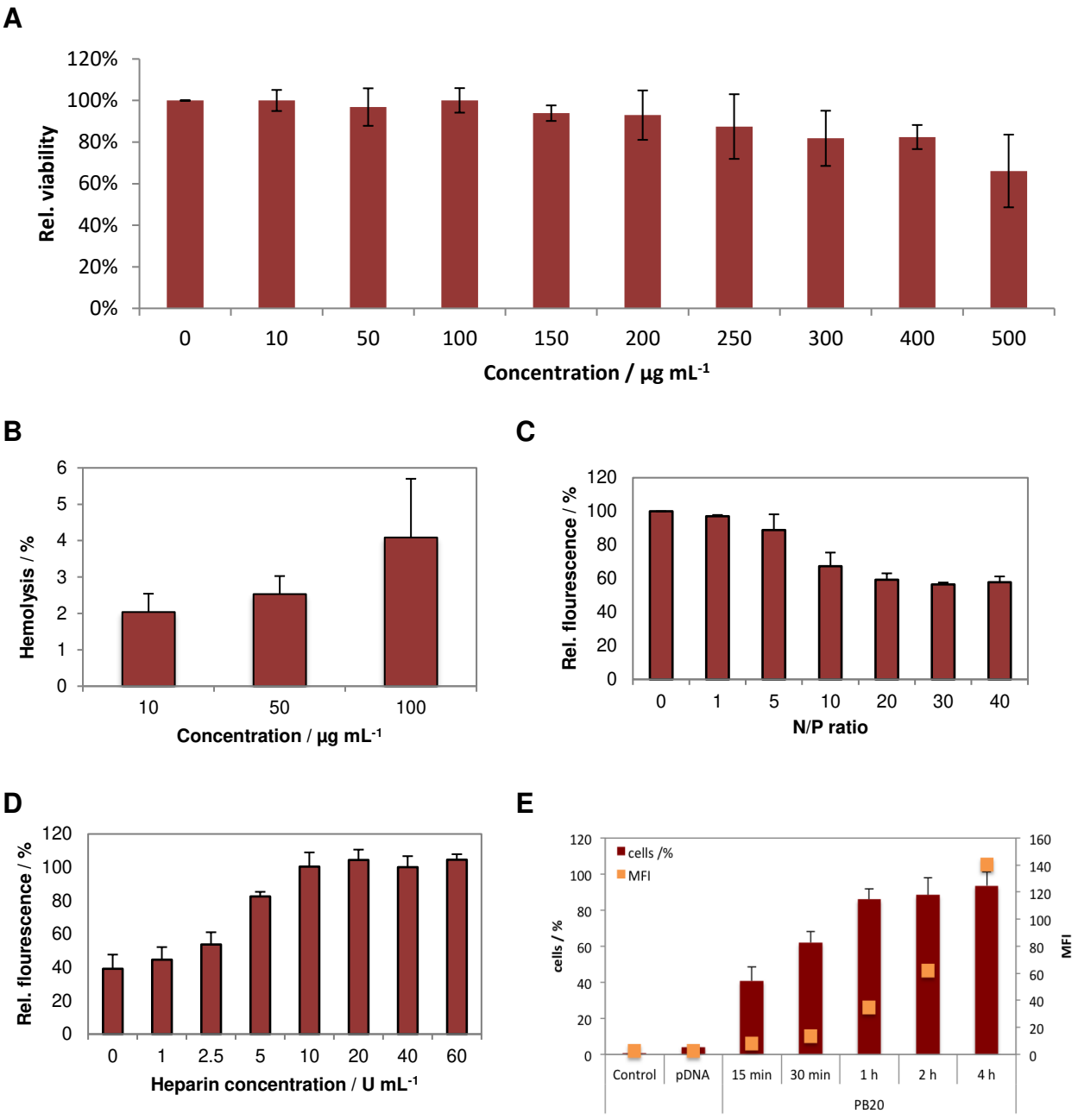

Figure S1. A) Cytotoxicity assay of **P2** using alarmaBlue. Non-treated cells served as 100% relative viability. B) Erythrocyte aggregation assay of **P2** at indicated concentrations. BPEI served as positive control and PBS as negative control. C) Hemolysis assay of erythrocytes after incubation with **P2** at indicated concentrations. Triton X-100 served as positive control (100% hemolysis) and PBS as negative control (1.99%). A value less than 2% hemolysis rate was classified as non-hemolytic, 2 to 5% as slightly hemolytic and values > 5% as hemolytic. Values represent the mean ± S.D. (n=3). D) Complexation affinity of **P2** with plasmid DNA at indicated N/P ratios (ethidium bromide quenching

assay). E) Dissociation assay of **P2** polyplexes formed at N/P 20 using heparin (0 to 60 U mL^{-1}). Values represent the mean ± S.D. (n=3).

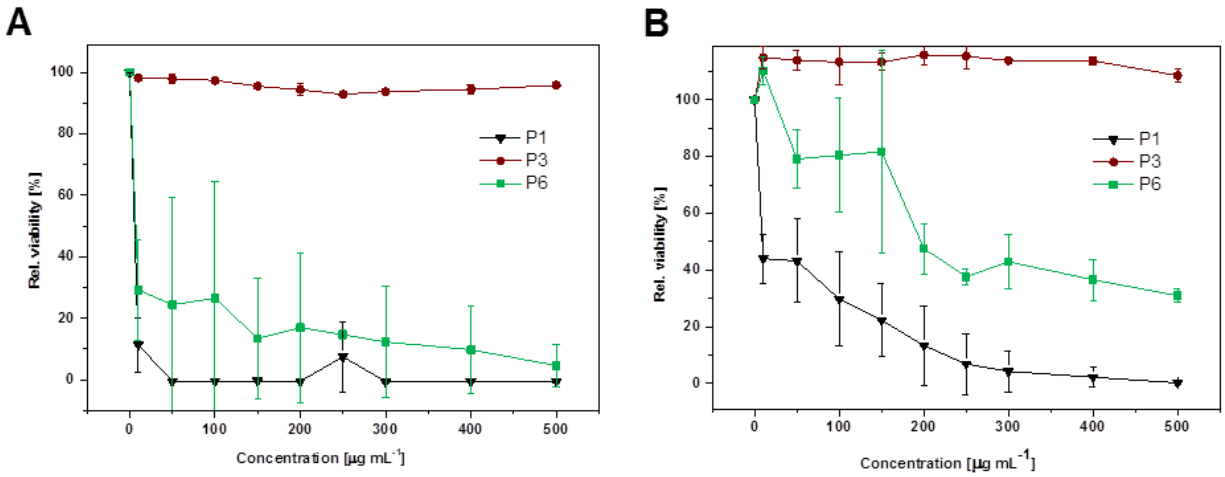

Figure S2. Biocompatibility. A) Relative viability of hCMEC cells after 24 h incubation with the respective polymers at indicated concentrations. B) Relative viability of HEK cells after 24 h incubation with the respective polymers at indicated concentrations.

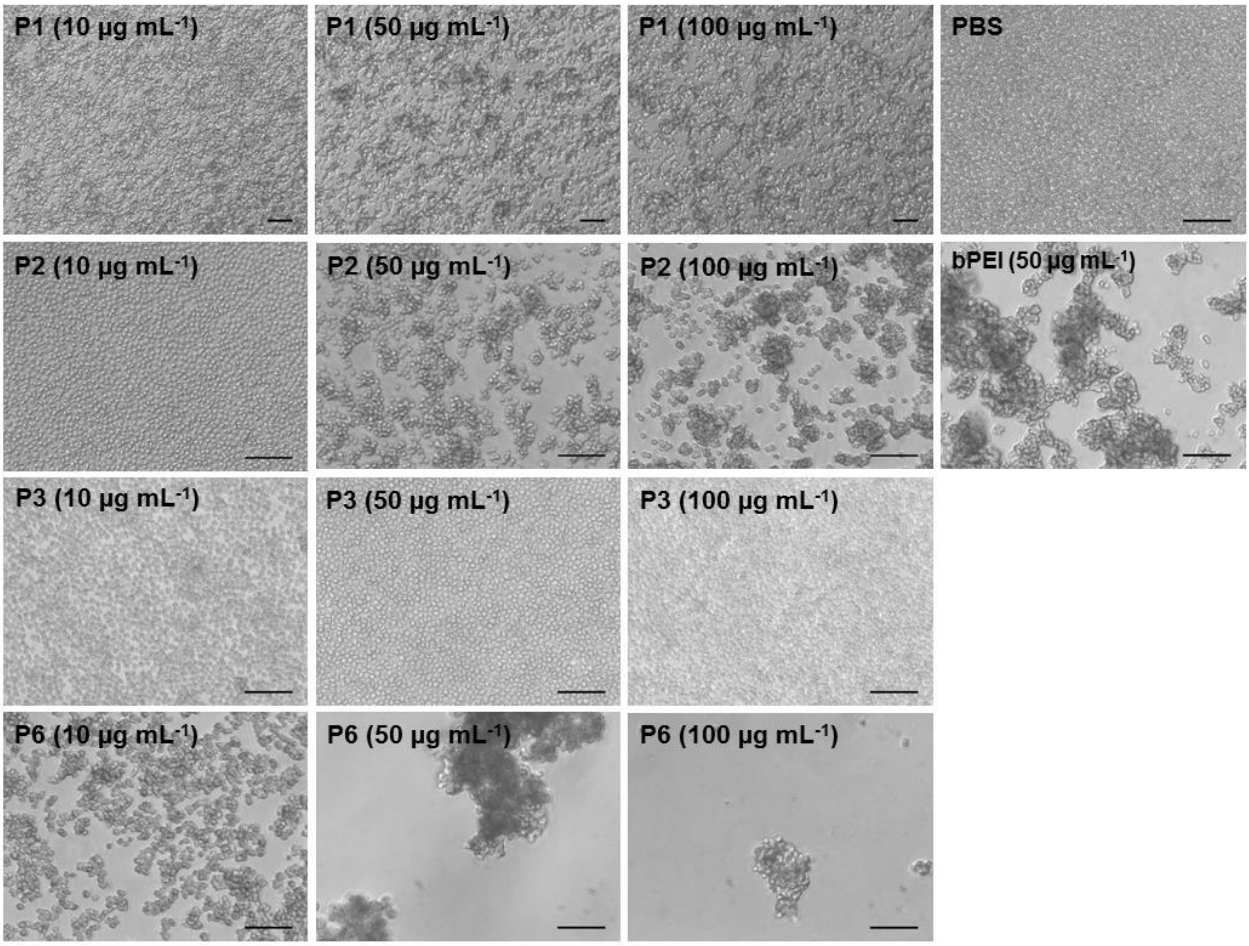

Figure S3. Light microscopy of erythrocyte aggregation of the polymers **P1**, **P3** and **P6**. PBS served as negative control, while bPEI (25kDa) was served as positive control. Scale bar = 20 μm.

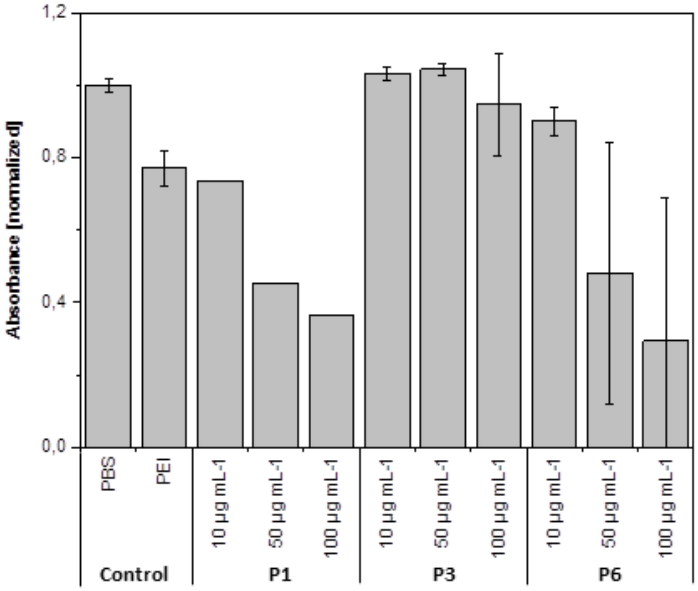

Figure S4. A) Hemolysis assay of erythrocytes after incubation with polymers at the indicated concentrations. Triton X-100 served as positive control and PBS as negative control. A value less than 2% hemolysis rate was classified as non-hemolytic, 2 to 5% as slightly hemolytic and values >5% as hemolytic. Values represent the mean ± S.D. (n=3). B) Erythrocyte aggregation of the tested polymers at indicated concentrations. bPEI (25 kDa) served as positive control resulting in high aggregation formation and PBS as negative control. Values represent the mean ± S.D. (n=3).

Table S5. Size and zeta potential of polymer **P1**, **P2**, **P3** and **P6** in HBG buffer measured by dynamic and electrophoretic light scattering.

Polymeric system	z-Average [d/nm]	PDI	Number-weighted size [d/nm]	Zeta potential [mV]
P1	450 ± 7	0.51	< 1	10.4 ± 0.5
P2	328 ± 27	0.66	< 1	4.9 ± 0.4
P3	233 ± 11	0.40	< 1	4.0 ± 1.4
P6	140 ± 23	0.58	26	28.4 ± 0.6

Table S6. Size and zeta potential of pDNA complexes of **P2** at N/P 20 in HBG buffer measured by dynamic and electrophoretic light scattering.

Polymeric system	z-Average [d/nm]	PDI	Number-weighted size [d/nm]	Zeta potential [mV]
P2	264 ± 11	0.35	109 ± 33	24.3 ± 1.1

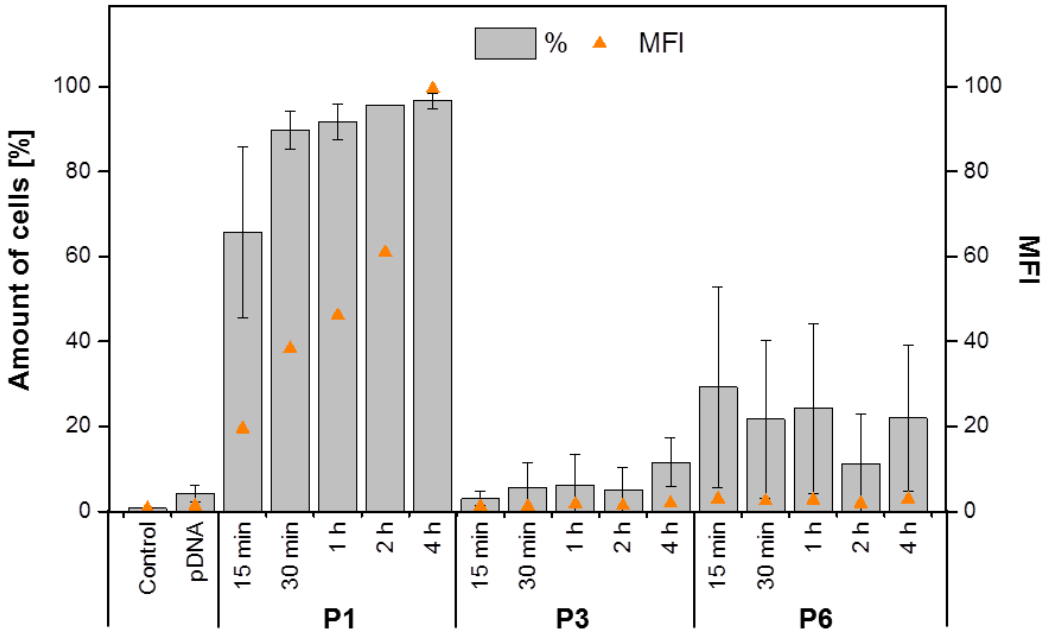

Figure S7. Cellular uptake study of **P1**, **P3** and **P6** polyplexes (N/P 20) using YOYO-1abeled pDNA. hCMEC cells were treated in EndoGro media with polyplexes for 4 h and uptake was analyzed via flow cytometry (MFI – Mean fluorescence intensity). Values represents the mean ± S.D. (n=3).

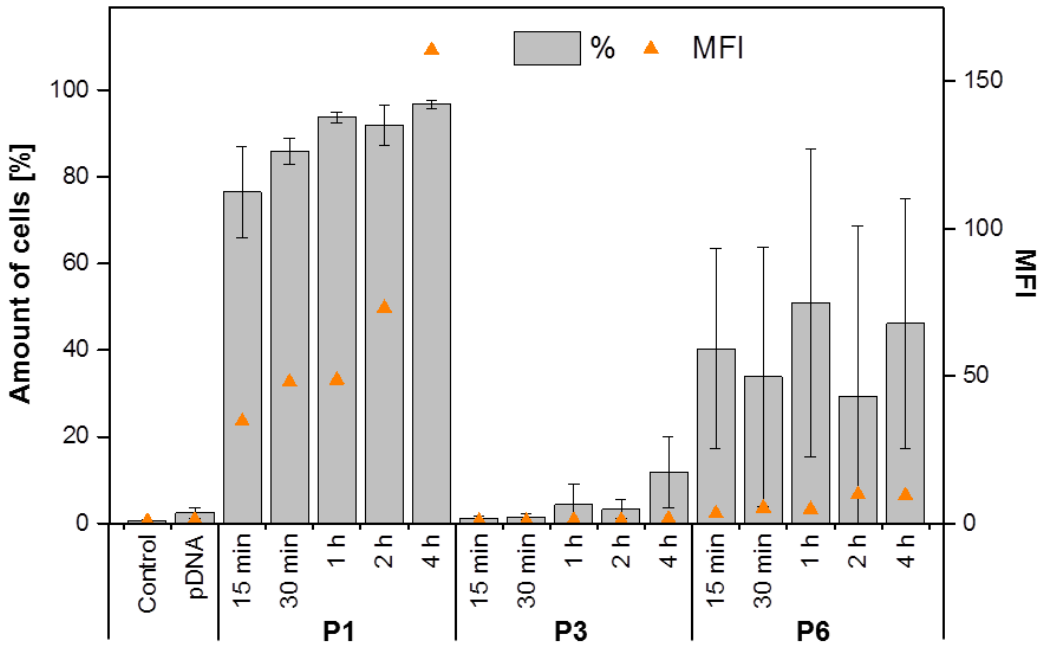

Figure S8. Cellular uptake study of **P1**, **P3** and **P6** polyplexes (N/P 20) using YOYO-1abeled pDNA. hCMEC cells were treated in OptiMEM with polyplexes for 4 h and uptake was analyzed via flow cytometry (MFI – Mean fluorescence intensity). Values represents the mean ± S.D. (n=3).

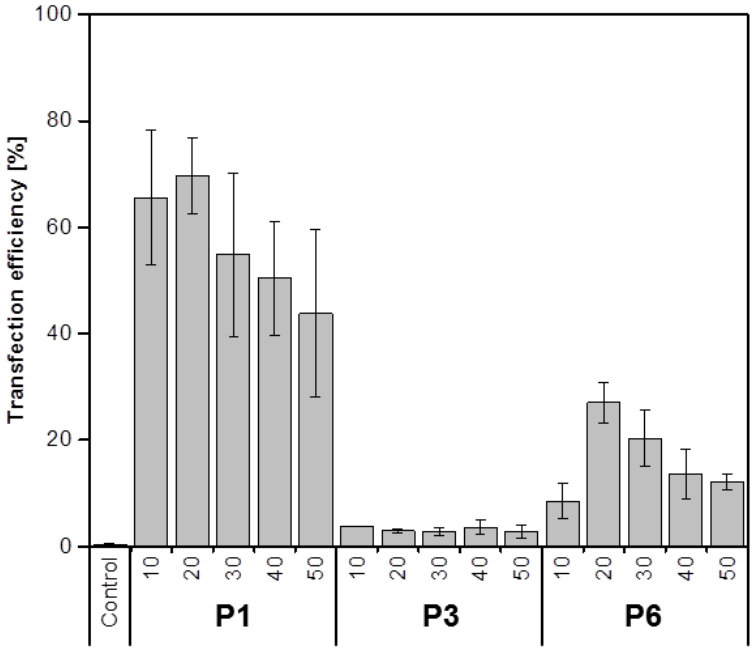

Figure S9. Transfection efficiency of copolymers **P1** to **P3** and **P6** for adherent HEK cells in OptiMEM at different N/P ratios after 24 h. Values represent the mean ± S.D. (n = 3).

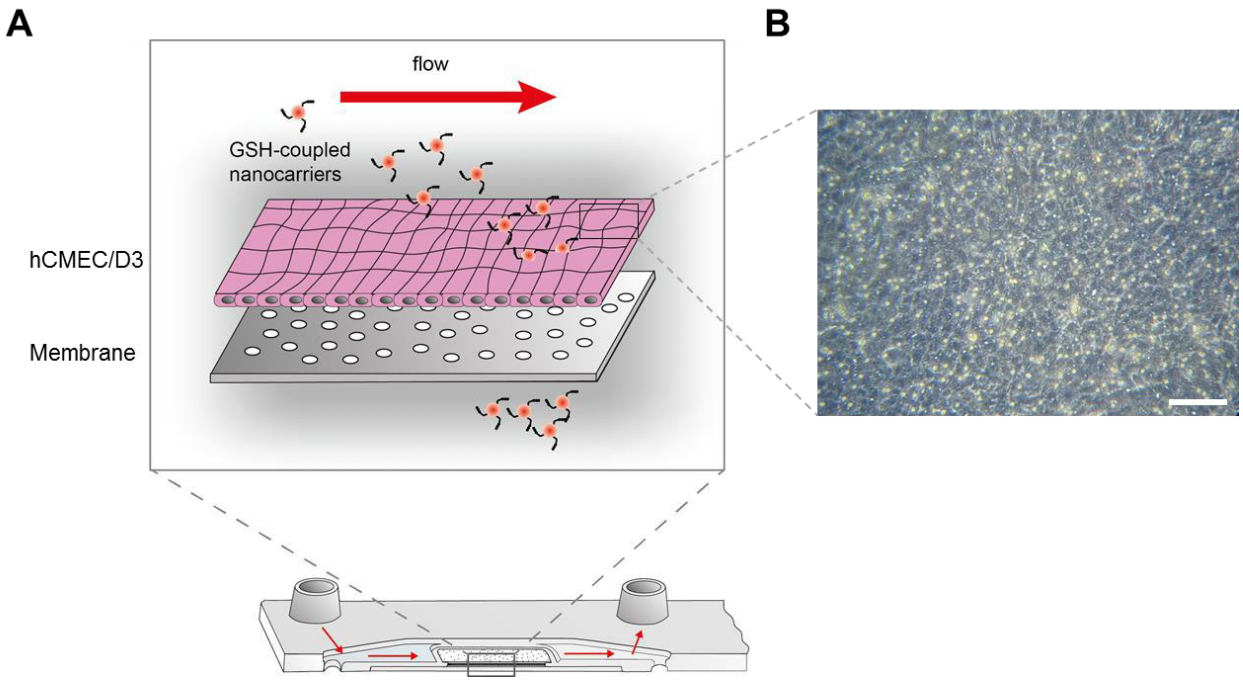

Figure S10. Chip geometry and dynamic cell culture setting. A) Schematic illustration of hCMEC/D3 cultured on top of a porous membrane within the chip. GSH-coupled nanocarriers are perfused on the apical side and passage through the cell layer was investigated basolateral. B) Microscopic image of confluent and tight hCMEC/D3 layer cultured within the chip. Membrane pores appear as bright round spots shining through the cell layer (scale bar 100 nm).

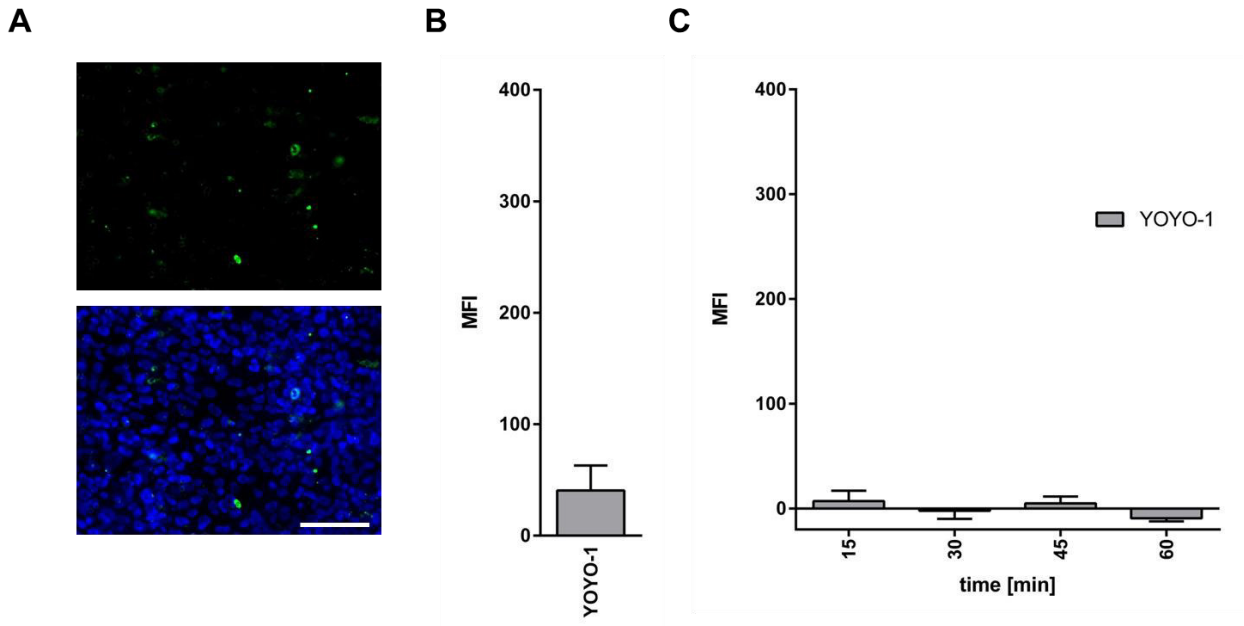

Figure S11. Negative control without polymer induced polyplex formation. A) Fluorescence images of YOYO-1 residues (green) on hCMEC/D3 (nuclei in blue). Only slight interaction can be observed. B) Quantification of YOYO 1 residues on hCMEC/D3 layer. C) Analysis of possible passage through hCMEC/D3 layer over time. No markable fluorescence was detectable. (scale 100 nm; n=3)

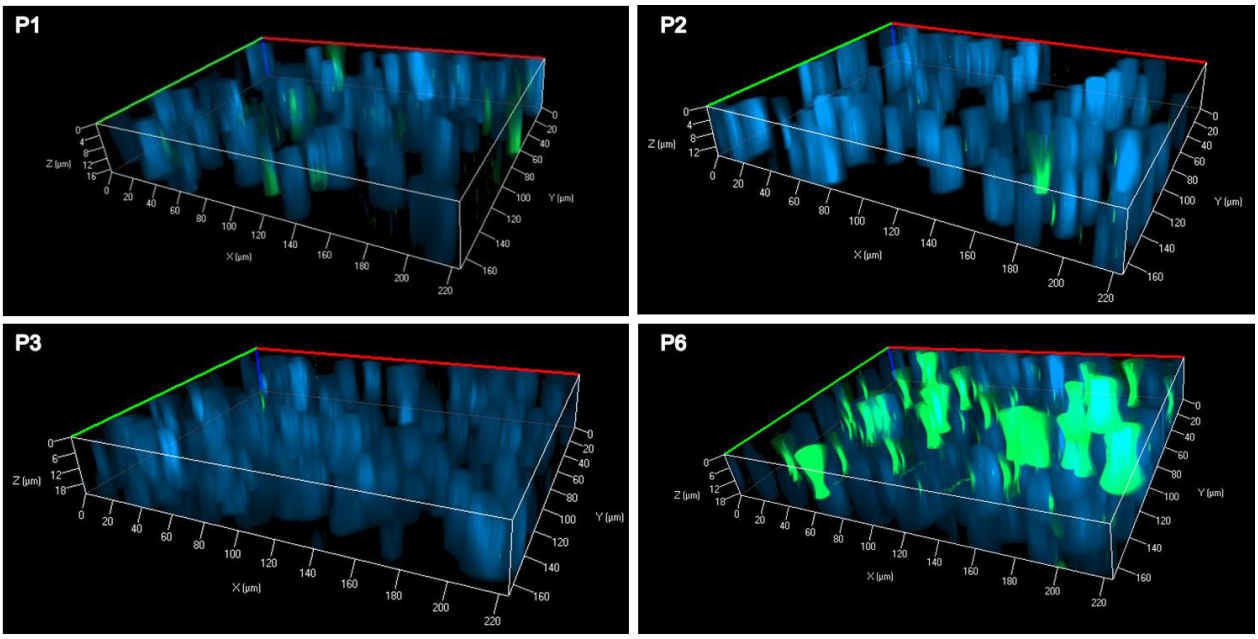

Figure S12. Three dimensional projection of z-stack images showing polyplex uptake (green) through localization at same levels as cell nuclei (blue) can be observed.

Publication Pub6

Fluorescent amphiphilic heterografted comb polymers comprising biocompatible PLA and PEtOx side chains

I. Yildirim, T. Bus, M. Sahn, T. Yildirim, D. Kalden, S. Hoeppener, A. Traeger, M. Westerhausen, C. Weber, U. S. Schubert

Polym. Chem. **2016**, *7*, 6064-6074.

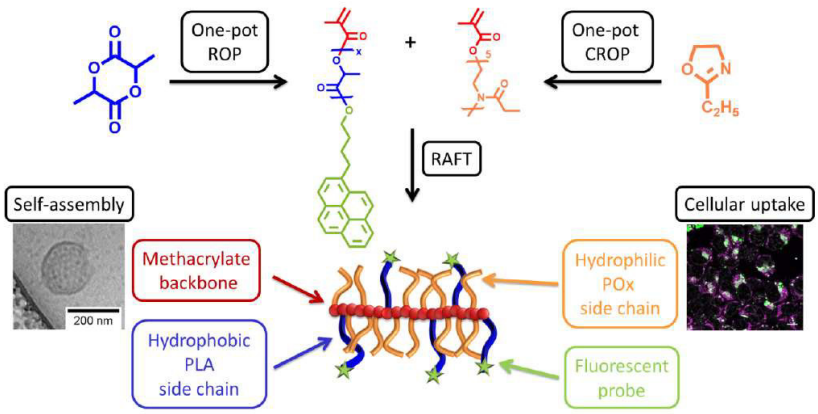

Polymer Chemistry

PAPER

View Article Online
View Journal | View Issue

Cite this: *Polym. Chem.*, 2016, **7**, 6064

Fluorescent amphiphilic heterografted comb polymers comprising biocompatible PLA and PEtOx side chains†

Ilknur Yildirim,[a,b] Tanja Bus,[a,b] Martin Sahn,[a,b] Turgay Yildirim,[a,b] Diana Kalden,[c] Stephanie Hoeppener,[a,b] Anja Traeger,[a,b] Matthias Westerhausen,[c] Christine Weber[a,b] and Ulrich S. Schubert*[a,b]

Received 29th June 2016,
Accepted 4th September 2016

DOI: 10.1039/c6py01130f

www.rsc.org/polymers

A series of amphiphilic heterografted comb polymers comprising various ratios of oligomeric polylactide (PLA) and poly(2-ethyl-2-oxazoline) (PEtOx) side chains was synthesized *via* the grafting-through method employing the reversible addition–fragmentation chain transfer copolymerization. Two well-defined PLA macromonomers were prepared *via* ring opening polymerization (ROP) of L-lactide using a calcium-based pre-catalyst, pyrenebutanol as an initiator and methacryloyl chloride as an end-capping agent. The PEtOx macromonomer was obtained from the cationic ROP of EtOx and end-capping with methacrylic acid. The amphiphilic comb polymers self-assembled in aqueous solution to form spherical and worm-like micelles, vesicles and more complex morphologies as a function of the composition, as is evident from dynamic light scattering and cryo-transmission electron microscopy studies. All polymers were found to be non-toxic to L929 cells up to a concentration of 200 μg mL^{-1}. Cellular uptake studies with HEK-293 cells by live cell confocal fluorescence microscopy revealed localization in the cytosol after 4 h and suggest an energy-driven cellular uptake mechanism.

Introduction

Certain polymer classes are often associated with distinct properties, such as biodegradability, hydrophilicity, charge or crystallinity. Although such properties can mostly be adjusted by the use of appropriate monomer types, the combination of several polymer classes that are obtained *via* completely different synthetic routes is advantageous, in particular when rather conservative application fields are in focus. As an example, the polyester polylactide (PLA) is the current gold standard as a biodegradable polymer from renewable resources to serve for encapsulation of hydrophobic guest molecules or many other applications in the bio-medical field.[1,2] PLA is obtained by the ring-opening polymerization (ROP) of lactide, however monomers which would add hydrophilic properties to a polyester are not commercially available. Hence, poly(ethylene glycol) (PEG) is often applied as a macroinitiator for the ROP due to its hydrophilic nature and stealth effect.[3]

Modern polymer chemistry offers a rich set of other hydrophilic polymers to prepare amphiphilic PLA-based macromolecules, taking into account the prerequisite that they can be obtained with well-defined end groups. This is the case for poly(2-oxazoline)s (POx)[4,5] since they can be polymerized by a living cationic ROP mechanism. POx that feature ethyl- and methyl-substituents are hydrophilic, and are candidates to replace PEG since they exhibit similar properties in biological systems: biocompatibility, protein repellency and prolonged blood circulation, *i.e.* the "stealth effect".[6]

Besides using hydroxyl end-functional macroinitiators to prepare linear block copolymers comprising PLA,[7,8] polymers with more sophisticated topologies endow further synthetic possibilities to the structural design.[9,10] Among these, comb-shaped and graft copolymers open avenues for further variations, taking into account additional factors such as main chain topology, grafting density, and the chemical composition of the backbone and the side chains. These additional factors offer the possibility to include further functionalities, but can also result in altered physicochemical properties since

[a]*Laboratory of Organic and Macromolecular Chemistry (IOMC), Friedrich Schiller University Jena, Humboldtstr. 10, 07743 Jena, Germany. E-mail: ulrich.schubert@uni-jena.de*
[b]*Jena Center for Soft Matter (JCSM), Friedrich Schiller University Jena, Philosophenweg 7, 07743 Jena, Germany*
[c]*Institute of Inorganic and Analytical Chemistry (IAAC), Friedrich Schiller University Jena, Humboldtstr. 8, 07743 Jena, Germany*

†Electronic supplementary information (ESI) available: Additional UV-vis absorption and fluorescence emission spectra, ^{1}H NMR spectra, hydrodynamic radii obtained from DLS measurements, and images from confocal microscopy. See DOI: 10.1039/c6py01130f

excluded volume interactions between grafted side chains[11,12] may lead to morphology diversification in self-assembled aggregates.[13]

A heterografted comb polymer is a special type of comb polymer[11–13] that contains two different side chain types, thus, representing a flexible means to combine the properties of distinct polymer types by an appropriate selection of polymer backbones and side chains. However, examples of heterografted comb polymers remain scarce to date, mostly due to demanding synthetic approaches as a result of the several consecutive reactions to be performed on the same polymer backbone, which is required in many synthetic approaches.[14–17] As an alternative, the copolymerization of macromonomers *via* the grafting through method comprises three independent steps: the synthesis of the two macromonomers and subsequent copolymerization.[12,13]

Aside from ring opening metathesis polymerization,[18] free radical[19–22] and controlled radical polymerization[23,24] are the most commonly utilized techniques for the polymerization of macromonomers. However, at least one macromonomer is often based on a linear polymer without substituents (such as PEG or PCL),[19–21,23] thereby decreasing the steric demand during the backbone formation. In fact, the copolymerization of PLA macromonomers with a different type of macromonomer (*i.e.* PEG,[25] poly(dimethylsiloxane)[26] and poly(*n*-butylacrylate)[18]) yielding heterografted copolymers has been rarely reported.

Herein, we present the copolymerization of a methacrylate ω-end-functional hydrophobic PLA macromonomer with a corresponding methacrylate functional macromonomer based on hydrophilic poly(2-ethyl-2-oxazoline) (PEtOx)[24,27] *via* reversible addition fragmentation chain transfer (RAFT) polymerization in order to obtain a series of amphiphilic heterografted comb polymers (Scheme 1). The hydrophilic/hydrophobic balance of the comb polymers was changed by altering the feed ratio of both macromonomers as well as the degree of polymerization (DP) of the PLA-based macromonomer to study the self-assembly behavior in water by means of dynamic light scattering (DLS) and cryo-transmission electron microscopy (cryo-TEM).

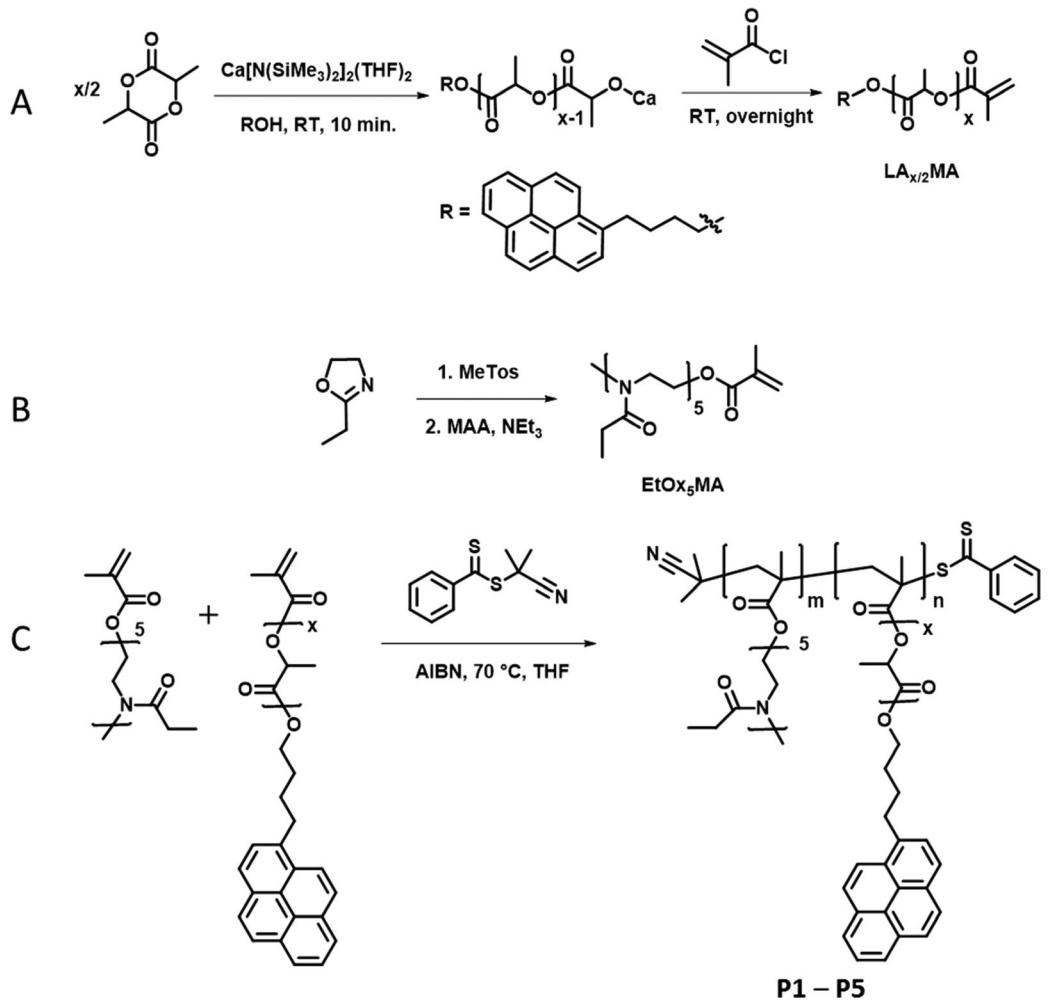

Scheme 1 Schematic representation of the synthesis of (A) the PLA macromonomer *via* ROP of L-lactide and *in situ* end capping with methacryloyl chloride, (B) the POx macromonomer *via* microwave assisted CROP of 2-ethyl-2-oxazoline, and (C) the heterografted comb polymers *via* RAFT polymerization.

Since both components represent biocompatible polymers, pyrene was attached as a fluorescent probe[28] to enable detailed studies regarding the cytotoxicity as well as the cellular uptake behavior. For this purpose, 1-pyrenebutanol was applied as an initiator during the calcium alkoxide initiated ROP of L-lactide,[29] which was converted to a macromonomer *via* end-capping with methacryloyl chloride.[30]

Experimental section

Materials

L-Lactide (98%) was purchased from Sigma-Aldrich and purified by recrystallization from dry toluene and dried under vacuum. Bis(tetrahydrofuran)calcium bis[bis(trimethylsilyl) amide] ($Ca[N(SiMe_3)_2]_2(THF)_2$) was synthesized according to previously reported procedures that are valued in several reviews.[31–34] 1-Pyrenebutanol (99%) and methacryloyl chloride (97%) were purchased from Sigma-Aldrich and used without further purification. Tetrahydrofuran (THF) was dried by refluxing over sodium/benzophenone. 2-Ethyl-2-oxazoline (99%, Acros, EtOx) was dried over barium oxide and distilled under argon prior to use. Methyl tosylate (98%, Aldrich) was distilled under reduced pressure and stored under argon. Acetonitrile (extra dry, Acros) was stored under argon. Methacrylic acid (99%, Aldrich) was used as received. Triethylamine was dried over potassium hydroxide and distilled under argon. 2,2′-Azobis(2-methylpropionitrile) (98%, Acros, AIBN) was recrystallized from methanol, and the chain transfer agent 2-cyanoprop-2-yl dithiobenzoate (CPDB) was purchased from Strem Chemicals. AlamarBlue, YOYO-1 iodide, NucRed Live 647 as well as LysoTracker Green DND-26 were obtained from Life Technologies (Thermo Fisher, Germany). Consumables for cell culture, like pipettes and cell culture plates (96 well), were obtained from Corning (USA) and Greiner Bio-one (Austria/Germany). If not stated otherwise, cell culture media and supplements (L-glutamin, antibiotics) were obtained from Biochrom (Merck Millipore, Germany). All other chemicals were purchased from standard suppliers and used without further purification. For the purification of the comb polymers a column filled with BioBeads S-X1 (exclusion limit 14 000 Da) with THF or toluene as an eluent was used.

Instruments

The ROP of L-lactide was carried out under nitrogen in an MBraun UNILab glove box workstation. The polymerization of EtOx was performed in a Biotage Initiator Sixty microwave synthesizer. Proton nuclear magnetic resonance (^1H NMR) spectra were recorded at room temperature in $CDCl_3$ on a Bruker Avance 300 MHz using the residual solvent resonance as an internal standard. The chemical shifts are given in ppm relative to tetramethylsilane (TMS). Size-exclusion chromatography (SEC) measurements were performed on two different setups. SEC in $CHCl_3$: Shimadzu system equipped with an SCL-10A system controller, an LC-10AD pump, a RID-10A refractive index detector, an SPD-10AD VP UV detector, and a PSSSDV-linear S column (5 mm particle size; Polymer Standards Service (PSS) GmbH, Mainz, Germany) at 40 °C using a chloroform, triethylamine, and 2-propanol (94 : 4 : 2) mixture as an eluent at a flow rate of 1 mL min^{-1}. The system was calibrated with PMMA standards (410 to 88 000 g mol^{-1}); SEC in THF: a Shimadzu system equipped with an SCL-10A system controller, an LC-10AD pump, an RID-10A refractive index detector, an SPD-10AD UV detector and an SDV linear M column from PSS at 40 °C using THF as an eluent at a flow rate of 1 mL min^{-1}. The system was calibrated against PLA standards (144 to 101 000 g mol^{-1}), which were purchased from PSS. For the measurements of the matrix-assisted laser desorption/ionization (MALDI) spectra, an Ultraflex III ToF/ToF instrument (Bruker Daltonics, Bremen, Germany) was used. The instrument is equipped with a Nd-YAG laser. All spectra were measured in the positive reflector mode. The instrument was calibrated prior to each measurement with an external PMMA standard from PSS. For the MALDI-ToF-MS sample preparation, separate solutions of polymer (10 mg mL^{-1} in THF), 2-(4′-hydroxybenzeneazo)benzoic acid (HABA, 30 mg mL^{-1} in THF), and doping of sodium chloride (NaCl, 100 mg mL^{-1} in acetone) were prepared and mixed following the dried droplet spotting technique. 1 μL of the mixture was spotted onto the target plate. For the ESI-Q-ToF-MS measurements, samples were analyzed by a microToF Q-II (Bruker Daltonics) mass spectrometer equipped with an automatic syringe pump from KD Scientific for sample injection. The ESI-Q-ToF mass spectrometer was operated at 4.5 kV, at a desolvation temperature of 180 °C. The mass spectrometer was operated in the positive ion mode. Nitrogen was used as the nebulizer and drying gas. The ESI-Q-ToF-MS instrument was calibrated in the m/z range from 50 to 3000 using a calibration standard (Tunemix solution) supplied from Agilent. All data were processed *via* Bruker Data Analysis software version 4.2. UV-Vis absorption measurements were performed using an Analytik Jena SPECORD 250 spectrometer (Analytik Jena, Jena, Germany). The fluorescence spectra were recorded on a Jasco FP-6500 spectrofluorometer. Dynamic light scattering was performed on a Zetasizer Nano ZS (Malvern Instruments, Herrenberg, Germany). After an equilibration time of 120 s, 3 × 12 runs were carried out at 25 °C (λ = 633 nm). The counts were detected at an angle of 173°. Each measurement was performed in triplicate. The size distribution of the particles was calculated applying the non-linear least squares fitting method. The mean particle size was approximated as the effective (Z-average) diameter and the width of the distribution as the polydispersity index (PDI) of the particles obtained by the cumulants method assuming a spherical shape of the particles. Cryo-transmission electron microscopy (cryo-TEM) investigations were performed on a Tecnai G^2 20 (FEI) equipped with an Olympus Soft Imaging Solutions MegaView and a 4 × 4k Eagle CCD camera system. Quantifoil grids (R2/2 Quantifoil, Germany) were cleaned by plasma treatment prior to use. Cryo sample preparation was conducted utilizing a FEI Vitrobot Mark IV system. 6 μL of the sample solution was de-

posited onto the grid, equilibrated shortly, and blotted for 1 s. The grids were immediately plunged into liquid ethane to obtain vitrification, and samples were stored at liquid nitrogen temperature until being transferred to the TEM utilizing a Gatan cryo transfer system.

For cytotoxicity and cellular uptake studies, a microplate reader (Tecan Infinite M200 Pro, Switzerland) and a confocal laser scanning microscope LSM880 (Carl Zeiss, Germany) were used (see below).

Synthesis

Cationic ring-opening polymerization. Oligo(2-ethyl-2-oxazoline) methacrylate ($EtOx_5MA$) was synthesized as reported previously.[27] Briefly, 1.383 g (7.44 mmol) of MeTos and 3.60 g (36.31 mmol) of EtOx were dissolved in 5.41 mL of acetonitrile and polymerized in a microwave synthesizer for 1 minute at 140 °C. 1.84 mL (21.8 mmol) of MAA and 6.04 mL (46.6 mmol) of triethyl amine were added. Subsequent to heating at 50 °C overnight, the macromonomer was dissolved in chloroform and purified by extraction with aqueous sodium bicarbonate solution and brine. The volatiles were removed under reduced pressure. $M_{n,\ NMR}$ = 600 g mol^{-1}, $M_{n,\ SEC}$ = 500 g mol^{-1}, $Đ$ = 1.17 (SEC in $CHCl_3$, PMMA calibration), DP = 5, DF = 96%.

ROP of L-lactide. The ROP of L-lactide was carried out in a glove box, at room temperature under a nitrogen atmosphere (<1 ppm H_2O, <1 ppm O_2), using THF as the solvent.

$LA_{15}MA$ 1: $Ca[N(SiMe_3)_2]_2(THF)_2$ (0.23 mmol, 116 mg) was dissolved in 1.0 mL of THF. This solution was added under vigorous stirring to a solution of L-lactide (1.0 g, 6.94 mmol) and 1-pyrene butanol (126.2 mg, 0.46 mmol) in 5.94 mL of THF in a microwave vial. This corresponds to a molar ratio of [L-lactide]/[1-pyrenebutanol]/[Ca] of 15/1/0.5 and an initial monomer concentration of $[L\text{-lactide}]_0$ of 1 mol L^{-1}. After 10 minutes, a sample was taken from the mixture and analyzed by ^{1}H NMR spectroscopy in order to determine the monomer conversion. The vial was capped, taken out of the glove box, and immersed in an ice bath. Subsequently, methacryloyl chloride (223 μL, 2.30 mmol) was added dropwise into the polymerization mixture through the septum of the vial. After 10 minutes, the ice bath was removed and the mixture was kept at room temperature for 24 hours under vigorous stirring. The excess of acid chloride was removed *via* precipitation in methanol and the purified product was dried under reduced pressure until a constant weight (yield: 0.8 g, 80%). ^{1}H NMR (300 MHz, $CDCl_3$): δ/ppm = 1.57 (d, –C(O)CH(C**H**$_3$)O–), 1.96 (s, –C(O)CH(CH$_3$)OC(C**H**$_3$)CH$_2$), 3.37 (t, $C_{16}H_9C\mathbf{H}_2C_3H_6OC(O)$–), 4.21 (t, $C_{16}H_9C_3H_6C\mathbf{H}_2OC(O)$–), 5.16 (q, –C(O)C**H**(CH$_3$)O–), 5.63 (s, –C(O)C(CH$_3$)C**H**$_2$), 6.20 (s, –C(O)C(CH$_3$)C**H**$_2$) 7.80–8.30 (m, $C_{16}\mathbf{H}_9C_4H_8OC(O)$–). The macromonomer was characterized by means of SEC (THF, RI detection, PLA calibration), MALDI-ToF-MS, and ESI-ToF-MS (see Results and discussion).

$LA_{10}MA$ 2 was obtained in an analogous fashion. 1.0 g of L-lactide (6.94 mmol), 175 mg of $Ca[N(SiMe_3)_2]_2(THF)_2$ (0.34 mmol), 190 mg of 1-pyrene butanol (0.69 mmol), 338 μL of methacryloyl chloride (3.40 mmol) and 5.94 mL of THF were used.

RAFT polymerization. Five different comb polymers were prepared by changing the ratios of the EtOx and PLA macromonomers. The $[M]_{total}$/[CPDB]/[AIBN] ratio was kept at 60/1/0.25 with an overall monomer concentration of 0.3 mol L^{-1}. In a representative RAFT copolymerization for **P1**, $LA_{15}MA$ (0.590 g, 0.19 mmol), $EtOx_5MA$ (0.562 g, 0.94 mmol), CPDB (4.2 mg, 0.019 mmol), and AIBN (0.77 mg, 0.0047 mmol) were dissolved in 3.8 mL of THF. After gently purging with argon for 30 minutes to remove the oxygen from the reaction mixture, the t_0 sample was taken for the determination of the monomer conversions. The polymerization was conducted in a pre-heated oil bath at 70 °C for 24 hours. The polymerization was stopped by cooling to room temperature and exposing the solution to air. The macromonomer conversions were calculated by comparing the integral values of the vinylic peaks in ^{1}H NMR spectra of the samples taken before and after polymerization. The comb polymers were purified by precipitation in methanol and subsequent preparative SEC on a BioBeads-SX-1 column, respectively. THF or toluene was used as the eluent based on the solubility of the comb polymers. Fractions (*ca.* 2 mL) were collected and analyzed by SEC with UV and RI detection. The desired fractions were combined and the volatiles were removed under reduced pressure.

Sample preparation for DLS and Cryo-TEM analysis

5 mg of comb polymer were dissolved in 500 μL of THF. The solution was dropped into 1 mL of deionized water in aliquots of 5 μL under vigorous stirring. THF was evaporated by stirring the open vial for at least two days to yield aqueous suspensions with a final polymer concentration of 5 mg mL^{-1}.

Determination of cytotoxicity

Cytotoxicity studies were performed with the mouse fibroblast cell line L929 (CCL-1, ATCC), as recommended by ISO10993-5. The cells were routinely cultured in Dulbecco's modified Eagle's medium supplemented with 10% fetal calf serum (FCS, Capricorn Scientific, Germany), 100 U mL^{-1} penicillin and 100 μg mL^{-1} streptomycin at 37 °C in a humidified 5% (v/v) CO_2 atmosphere. In detail, cells were seeded at 10^4 cells per well in a 96-well plate and incubated for 24 hours. No cells were seeded in the outer wells. Afterwards, the testing substances (polymers) were added to the cells at the indicated concentrations (from 5 μg mL^{-1} to 200 μg mL^{-1}) and the plates were incubated for additional 24 hours. Subsequently, the medium was replaced by a mixture of fresh culture medium and the assay reagent alamarBlue (resazurin based solution, Thermo Fisher, Germany, prepared according to manufacturer's instructions). After a further incubation of 4 hours at 37 °C in a humidified 5% (v/v) CO_2 atmosphere, the fluorescence was measured at Ex 570/Em 610 nm, with untreated cells on the same well plate serving as negative controls. The negative control was standardized as 0% of metabolism inhibition and referred to as 100% viability. Cell viability below 70% was considered indicative of cytotoxicity. Data are

expressed as mean ± standard deviation (SD) of three independent determinations.

Cellular uptake

Live cell imaging was performed using HEK-293 cells (CRL-1573, ATCC) for analyzing the cellular uptake of the comb polymers. For this purpose, HEK cells (10^5 cells per mL) were seeded in glass-bottomed, 4-chamber dishes (CELLVIEW, Greiner Bio-One, Germany) and cultured for 24 hours in RPMI 1640 medium (Lonza, Switzerland) supplemented with 10% FCS, 100 μg mL^{-1} streptomycin, 100 U mL^{-1} penicillin and 2 mM L-glutamine at 37 °C in a humidified 5% CO_2 atmosphere. One hour prior to polymer addition, the cells were rinsed with phosphate buffered saline (PBS) and the media were changed to OptiMEM (Gibco, Thermo Fisher, USA). The polymers were added to cells with a final concentration of 50 μg mL^{-1} and incubated for an additional 4 hours. Afterwards, the media were replaced with fresh culture media supplemented with LysoTracker Green DND-26 and NucRed Live 647 for lysosome and nucleus staining, respectively. The living cells were imaged with a LSM880 (Carl Zeiss, Germany) using the following excitation wavelengths/laser lines 405 nm (for pyrene), 488 nm (for lysosomes) and 633 nm (for nucleus).

Results and discussion

Macromonomer syntheses

In order to prepare heterografted comb polymers comprising hydrophilic and hydrophobic side chains, macromonomers based on PEtOx and PLA had to be prepared with methacrylate end groups. To facilitate reasonable conversions during the subsequent RAFT polymerization, the degree of polymerization (DP) of both macromonomers was kept low (DP = 5 to 15). Since several RAFT (co)polymerizations of $EtOx_5MA$ have been successfully established in our laboratories,[24,27,35] a DP of 5 was selected for the hydrophilic macromonomer. Hence, $EtOx_5MA$ was obtained by CROP of EtOx using MeTos as an initiator and subsequent end-capping with methacrylic acid using triethyl amine as a base to produce methacrylate anions *in situ*. For detailed information about the synthesis and characterization of $EtOx_5MA$, the reader is referred to the literature.[27]

So far, the catalyst $Ca[N(SiMe_3)_2]_2(THF)_2$ has proven powerful for the preparation of well-defined α-end-functional PLAs using various alcohols as initiators for the ROP of L-lactide at room temperature.[29] However, direct ω-end-functionalization of the resulting anionic PLA species has not been attempted yet. An electrophile such as methacryloyl chloride is necessary[30] to introduce a methacrylate end functionality *via* this direct end-capping route. Among the multitude of suitable alcohols that can be used as initiators for the ROP, 1-pyrenebutanol was selected for this study because of its fluorescence that makes it a suitable label for cellular uptake studies. To facilitate a similar reactivity of both macromonomer types during the subsequent RAFT copolymerization, the DP of the hydrophobic PLA macromonomers was kept low as well. Both polymerizations were driven to quantitative conversion prior to end-capping with a 10-fold excess of methacryloyl chloride. Hence, two different α,ω-end functional PLA macromonomers with a DP of 10 and 15, respectively, were prepared by ROP of L-lactide in a one-pot procedure. Table 1 summarizes the characterization results of the fluorescent PLA-based hydrophobic macromonomers $LA_{15}MA$ and $LA_{10}MA$ by means of SEC, ^1H NMR spectroscopy and mass spectrometry.

Due to the absorbance of the pyrene moieties at 340 nm, SEC analysis with UV detection provides a simple tool to confirm the covalent attachment of the initiator at the macromonomers. As is evident from the overlapping RI and UV signals in the elugrams of both macromonomers, the pyrene functionality is distributed evenly throughout the resulting PLA's, hinting at the absence of chain transfer reactions during the ROP (Fig. SI 1†). Moreover, the monomodal SEC traces and narrow molar mass distributions indicate that the quenching of the polymerization with methacryloyl chloride did not induce chain coupling or even autopolymerization of the methacrylate ω-end functionalities, neither during the course of the reaction nor during the purification.

SEC alone is incapable of providing a structural proof for a successful end-capping of the PLA chains. However, the ^1H NMR spectra of the resultant PLA macromonomers clearly reveal the presence of both pyrene and methacrylate moieties (Fig. 1). The fact that the separate integration of these signals was possible enabled the estimation of the degree of polymerization (DP) and the degree of functionalization at the ω-chain end (DF). For the former, the peak integrals corresponding to pyrene moieties (peak "g" in Fig. 1) and the methine proton of the lactide repeating units (peak "a" in Fig. 1) were used. The resulting molar masses are in good agreement with the values obtained from SEC analysis with PLA calibration as well as with the targeted molar mass for both macromonomers.

Table 1 Characterization data of the PLA macromonomers[a]

	M/I	Conv.[b] [%]	DP[c]	DF[c] [%]	$M_{n,\,theo}$[d] [g mol^{-1}]	$M_{n,\,NMR}$[c] [g mol^{-1}]	$M_{n,\,SEC}$[e] [g mol^{-1}]	$Đ_{SEC}$[e]	$M_{n,\,MALDI}$ [g mol^{-1}]	$Đ_{MALDI}$
$LA_{15}MA$	15	100	15	93	2500	2500	2300	1.24	2200	1.09
$LA_{10}MA$	10	100	10	90	1800	1800	1500	1.32	2000	1.13

[a] $[1\text{-Pyrenebutanol}]_0/[Ca]_0/[\text{methacryloyl chloride}] = 1/0.5/5$, $[\text{L-lactide}]_0 = 1$ M in THF, $t_{pol} = 10$ min, $T = 25$ °C. [b] Determined by ^1H NMR spectroscopy from the polymerization mixtures. [c] Degree of polymerization (DP) and degree of functionalization (DF) obtained from ^1H NMR spectra of the purified macromonomers. [d] Calculated from M/I and conversion. [e] Determined by SEC (THF, RI detection, PLA calibration).

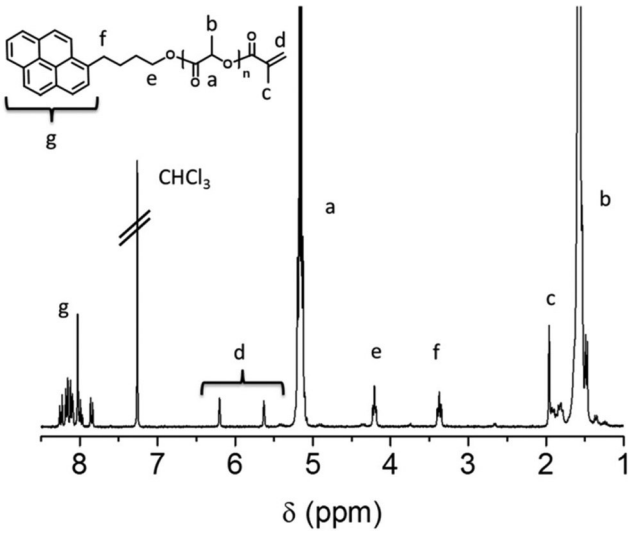

Fig. 1 ^{1}H NMR spectrum (300 MHz, $CDCl_3$) of the PLA macromonomer $LA_{15}MA$ and structural assignment of the observed peaks.

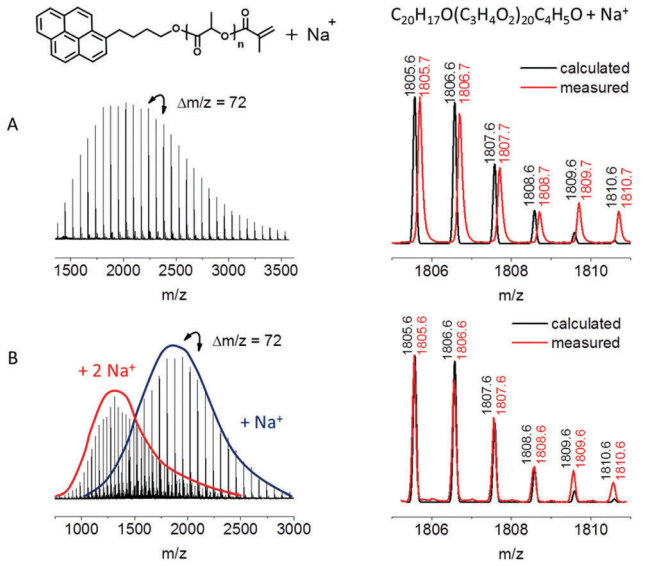

Fig. 2 Mass spectra of the PLA macromonomer $LA_{15}MA$ and the overlay of the isotopic patterns for the structural assignment of the peaks. (A) MALDI-ToF (HABA, NaCl) and (B) ESI-Q-ToF. Both spectra show an overlapping *m/z* series of the same PLA species that are either ionized with one (*z* = 1) or two (*z* = 2) sodium cations, respectively.

By comparison of the signals derived from both end groups, the DF was calculated. Therefore, the vinylic protons of the methacrylate moiety (peak "d") and either the pyrene signals in the aromatic region (peaks "g") or the benzylic methylene protons (peak "e") were used. The resulting DF varies between 84% and quantitative functionalization, based on the selected peak for integration due to the small intensity of the end group peaks. Hence, average values from four different integrations are reported in Table 1.

The excellent end group fidelity of the PLA macromonomers was further confirmed by mass spectrometric measurements. Fig. 2 shows the MALDI-ToF and ESI-Q-ToF MS of the PLA macromonomer $LA_{15}MA$. Both spectra reveal a single distribution of peaks at regular intervals spaced by $\Delta m/z$ = 72 between two neighboring peaks. The experimental isotopic patterns exactly overlap with the corresponding patterns calculated for the pyrene butanol α- and methacrylate ω-end functional PLA chains, which are ionized with a sodium cation. As often observed for ESI-Q-TOF analysis of polymers, this singly charged *m/z* distribution is overlaid with a second (doubly charged) *m/z* distribution, which corresponds to the same species ionized with two sodium cations. Although a $\Delta m/z$ = 72 (instead of $\Delta m/z$ = 144) in the mass spectra of PLA is often attributed to the presence of transesterification reactions in the literature,[30] it should be clearly stated that an intramolecular rearrangement at the active catalyst center is the reason for this observation in our case. This statement is based on our detailed previous research on this calcium alkoxide initiator system,[29] and sophisticated mechanistic studies are currently ongoing in our laboratories.

Grafting-through *via* RAFT copolymerization

Using both macromonomer types, *i.e.* hydrophilic $EtOx_5MA$ and hydrophobic LA_nMA, a series of heterografted comb polymers was prepared by RAFT copolymerization *via* the grafting through method. Thereby, the overall [monomer] to [CTA] ratio was kept constant at 60 using AIBN as an initiator and CPDB as a chain transfer agent in THF at 70 °C. In order to obtain comb polymers with varying hydrophilicity, the feed ratio of the $EtOx_5MA$ and $LA_{10}MA$ macromonomer was changed, however keeping a high molar fraction of the hydrophilic $EtOx_5MA$ throughout the series **P2–P5** because of the doubled DP of the hydrophobic $LA_{10}MA$. To elucidate the influence of the DP of the hydrophobic side chains, **P1** was synthesized using $LA_{15}MA$ while keeping the same feed ratio as for **P2**. As is often observed for grafting-through approaches, the macromonomer conversions were lower in this case due to the increased steric hindrance induced by the longer side chains.[27] For all comb polymers, complete removal of residual macromonomers was ensured by successive precipitation in methanol and preparative SEC using a BioBeads column. Table 2 summarizes the polymerization conditions and the characterization results of all purified comb polymers obtained by ^{1}H NMR spectroscopy and SEC analysis.

Fig. 3 shows an overlay of the SEC traces obtained from the comb polymers and the macromonomers with RI and UV detection at 340 nm. As can be clearly seen, all comb polymers elute earlier than the corresponding macromonomers due to the increased hydrodynamic volume of **P1** to **P5**. The fact that unimodal SEC traces are obtained confirms the complete removal of residual macromonomers during the purification process. The molar masses determined by SEC are similar for **P1** to **P4**, which is reasonable because the same [M]/[CTA] ratio was kept throughout the complete polymer series, and the conversions from all RAFT polymerizations were in a comparable

Table 2 Characterization results of the comb polymers **P1** to **P5**

	LA_nMA	$EtOx_5MA$/LA_nMA/CTA/AIBN	[$EtOx_5MA$]/[LA_nMA] (feed)	Conv.[a] [%]		$M_{n,theo}$[b] [g mol^{-1}]	$M_{n,SEC}$[c] [g mol^{-1}]	$Đ_{SEC}$[c]	[$EtOx_5MA$]/[LA_nMA] (NMR)[d]	EtOx/LA (NMR)[e]
				$EtOx_5MA$	LA_nMA					
P1	$LA_{15}MA$	42/18/1/0.25	71/29	32	25	20 600	27 500	1.17	70/30	45/55
P2	$LA_{10}MA$	42/18/1/0.25	71/29	90	85	50 000	28 200	1.37	65/35	50/50
P3	$LA_{10}MA$	50/10/1/0.25	83/17	75	73	35 600	29 000	1.25	80/20	65/35
P4	$LA_{10}MA$	53/7/1/0.25	88/12	95	90	41 000	26 300	1.25	85/15	70/30
P5	$LA_{10}MA$	54/6/1/0.25	90/10	85	75	36 800	19 500	1.23	90/10	80/20

[a] Conversion values determined by ^{1}H NMR spectroscopy from the polymerization mixtures. [b] Calculated from feed and conversion. [c] Determined by SEC ($CHCl_3$, RI detection, PMMA calibration). [d] Macromonomer molar ratio calculated from suitable signal integrals in the ^{1}H NMR spectra of the purified polymers. [e] Molar ratio of EtOx and LA repeating units calculated from suitable signal integrals in the ^{1}H NMR spectra of the purified polymers.

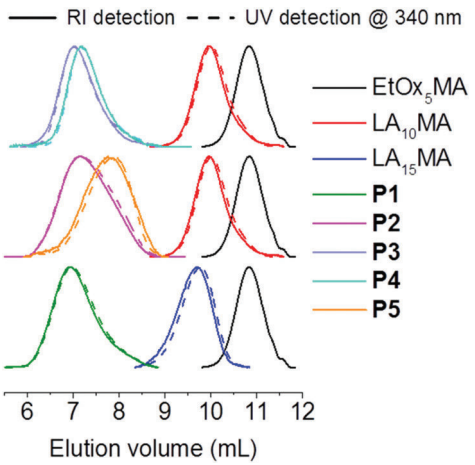

Fig. 3 Normalized SEC traces ($CHCl_3$) of the macromonomers and comb polymers **P1** to **P5**.

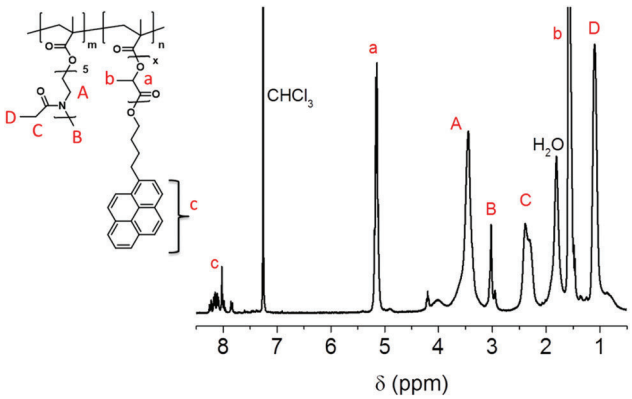

Fig. 4 ^{1}H NMR spectrum (300 MHz, $CDCl_3$) of **P3** together with the structural assignment of the observed peaks.

range (see Table 2). However, it has to be considered that SEC represents a relative method for molar mass determination and relies on the calibration with linear standard polymers, whose hydrodynamic volume strongly differs from that of comb-shaped polymers in general. Hence, SEC underestimates the molar masses of **P1** to **P5**. All comb polymers elute at similar retention times, revealing that the hydrodynamic volume of the polymeric architectures is not influenced by the side chain composition in chloroform, which represents a good solvent for both side chain types, *i.e.* PLA as well as PEtOx. In addition, the signals from UV and RI detection overlap for all polymers, confirming the incorporation of the respective PLA-based macromonomers, since $EtOx_5MA$ does not absorb at the wavelength selected for the UV detector.

Analysis of the purified comb polymers by means of ^{1}H NMR spectroscopy clearly reveals that both PLA and POx macromonomers were incorporated into the comb polymers as the signals derived from both polymer types can be clearly distinguished (Fig. 4). The signal corresponding to the methyl end groups of the PEtOx side chains (peak "B" in Fig. 4) was used to calculate the copolymer composition. Therefore, its integral was compared with the integral value of the methine proton peak of the PLA side chains (peak "a" in Fig. 4). The ratio of the two side chain types in the comb polymers is in excellent agreement with the feed ratio of both macromonomers, showing that LA_nMA was successfully incorporated during the RAFT copolymerization, despite its higher DP in comparison with $EtOx_5MA$ (compare Table 2). In addition, the aromatic protons of the pyrene unit (peak "c" in Fig. 4), which represent the end groups of the PLA side chains, are clearly visible, confirming the observations from SEC with UV detection (see above).

Fig. SI 3† depicts an overlay of the ^{1}H NMR spectra of **P1** to **P5** together with the structural assignment of the observed peaks used to estimate the copolymer composition. All spectra were normalized according to the peak maxima of the methine protons of the PLA side chains to underline the increasing PEtOx content throughout the polymer series from **P1** to **P5**. As the PEtOx content in the copolymer increases, so does the intensity of the respective signals assigned to this type of side chain. Although the ratio of the distinct side chain types was apparently not widely varied, the copolymer composition covers a broader range when the ratio of the EtOx and lactide repeating units is taken into account. This is due to the increased DP of the PLA-based side chains (DP = 10 and 15) compared with the DP of the PEtOx-based side chains (DP = 5).

Self-assembly behavior in aqueous media

To investigate the self-assembly behavior of the amphiphilic comb polymers **P1–P5** in water, aqueous suspensions were prepared by dropping THF polymer solutions into water. During the evaporation of THF, the formed structures were aged for a minimum of two days at room temperature. Subsequently, DLS and cryo-TEM measurements were performed.

Fig. 5 shows the resulting size distributions obtained from DLS of the copolymer assemblies **P2–P5**, *i.e.* the heterografted comb polymers synthesized using the macromonomers $LA_{10}MA$ and $EtOx_5MA$ along with representative cryo-TEM micrographs. Only in the case of the most hydrophilic copolymer **P5**, DLS revealed a bimodal size distribution of the self-assembled polymer structures, as is apparent by the overlay of the intensity, volume, and number weighted size distributions. Obviously, larger aggregates are visible in the intensity weighted distributions. Cryo-TEM measurements confirmed the presence of smaller (*ca.* 10 nm) and larger (*ca.* 40–50 nm) structures, which is in accordance with the DLS results. Presumably, the weight fraction of the hydrophilic EtOx is too high (w_{EtOx} = 0.73) in the case of **P5** and capable of shielding the hydrophobic PLA segments even without the formation of defined copolymer assemblies.

Monomodal size distributions were evident from DLS for the suspensions of the comb polymers **P3** and **P4** with a lower EtOx weight fraction of w_{EtOx} around 0.6. Homogeneous and densely packed spherical micelles with diameters around 15 nm were visualized by cryo-TEM analysis. This value roughly corresponds to the double length of a PLA with a DP of 10 in the all-*trans* conformation. Hence, one might assume that the micelles are formed by a spherical arrangement of several macromolecules with the PLA chains pointing towards the inside and the PEtOx side chains pointing to the outside. Already a slight increase in the weight fraction of hydrophobic PLA side chains resulted in spherical micelles with increased diameters of around 30 nm in the case of **P3**. Both observations are in accordance with the hydrodynamic diameters obtained from DLS measurements.

Further decrease of the EtOx content (**P2**, w_{EtOx} = 0.4) resulted in a mixture of self-assembled structures: spherical and worm-like micelles as well as large vesicles were found in the cryo-TEM micrographs. Accordingly the hydrodynamic diameters from DLS are increased with a rather high polydispersity index (PDI = 0.27, compare Table S1†). The diameter of the spherical and worm-like micelles (17 and 14 nm, respectively) corresponds well with the length of the PLA side chains of the comb polymer, as does the bilayer thickness of the vesicles (13 nm).

A similar variety of self-assembled structures was found by investigation of **P1** (Fig. 6), which is in good agreement with the bimodal intensity size distribution from DLS. In terms of the macromonomer mol fraction, this comb polymer has a similar composition as **P2**. However, the PLA side chains feature an increased DP of 15 since $LA_{15}MA$ was used during its synthesis, resulting in a further decreased w_{EtOx} of 0.36. In agreement with the length of the respective hydrophobic PLA side chains of the heterografted comb polymer **P1**, the micelles revealed slightly increased diameters (around 19 nm) in comparison to the structures formed by **P2**. Also the membrane thickness of the vesicular structures is slightly increased (21 nm). In addition, more complex morphologies were visualized by cryo-TEM investigations (Fig. 6b–d), which may be due to a hampered phase ordering due to the fact that hydrophilic and hydrophobic segments are covalently bound to the same comb polymer backbone. This would restrict the side chain mobility when compared with simple linear block copolymers.

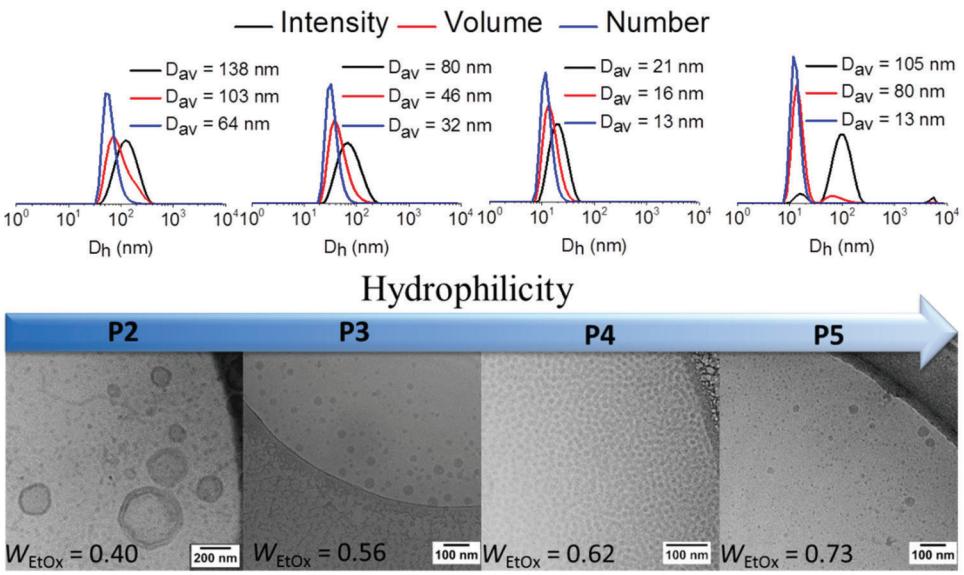

Fig. 5 DLS plots and cryo-TEM images of the suspensions obtained from **P2** to **P5** in water (c = 5 mg mL^{-1}).

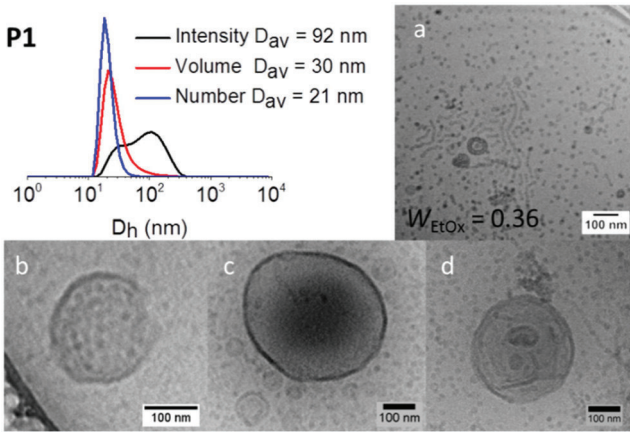

Fig. 6 DLS plots and cryo-TEM images of the suspensions formed by **P1** in water (c = 5 mg mL^{-1}; scale bars show 100 nm).

Fig. 6 shows examples of structures found for **P1**. In particular the large aggregates (up to 400 nm in diameter) featured different morphologies; however, no clearly defined structure can be elucidated in this case. Structures vary from segmented vesicles (b) (as reported by Mansfeld *et al.*[36] or Parry *et al.*[37]), distorted vesicles (c) as well as lamellar vesicles (d).

The transition from spherical micelles to vesicles has been predicted for heterografted comb polymers, and experimental confirmation has recently been provided by Luo *et al.* for heterografts with PEG and PLA side chains.[38,39] However, researchers in this field rather concentrate on an alteration of the side chain lengths of the comb polymers in analogy to variation of the block lengths in linear diblock copolymers. In fact, in these cases the only difference with linear block copolymers is the covalent junction at the comb polymer backbone (Fig. 7). We found that similar transitions are possible by keeping the DP of the side chains constant but altering the fraction of each type of side chain in the heterografted comb polymer.

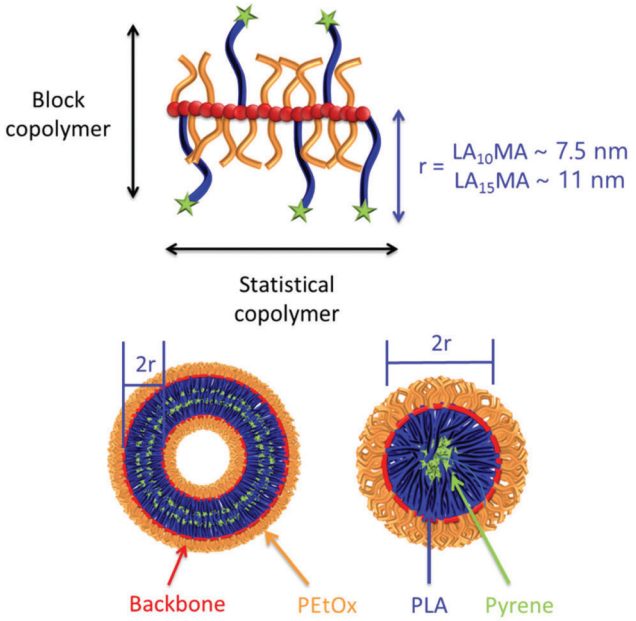

Fig. 7 Formation of spherical and worm-like micelles from comb polymers with mixed PEtOx and PLA side chains.

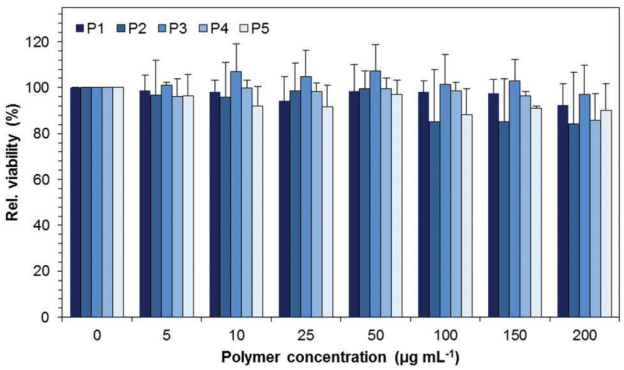

Fig. 8 Relative viability of L929 cells after 24 hours of incubation with heterografted comb polymers (**P1** to **P5**) at the indicated concentrations. Values represent the mean ± S.D. (n = 3).

Cytotoxicity and cellular uptake

As both segments of the comb polymers, *i.e.* the hydrophilic PEtOx and the hydrophobic PLA represent non-toxic polymers it was expected that the comb polymers **P1–P5** are highly biocompatible as well. Hence, an assay based on resazurin was performed to measure the metabolic activity of L929 mouse fibroblast cells after addition of polymer suspensions in water at varying concentrations. As depicted in Fig. 8, all polymers showed no significant reduction in cell viability after 24 hours at the tested conditions. Moreover, no influence of the different structural compositions of the polymers was observed. Due to the hydrophobic nature, it could be assumed that the PLA-pyrene side chains are located in the core of the self-assembled structure encompassed by the methacrylate backbone and PEtOx side chains (Fig. 7). Hence, the hydrophilic PEtOx arms, which shape the outer part of the self-assembled structures, indeed promote a high biocompatibility of the systems. A degradation of PLA combined with the release of pyrene would result in severe lethal effects, as this highly hydrophobic molecule would intercalate into cellular membranes.[40,41]

Based on these promising results, further biological investigations concerning the cellular uptake were performed. Since the pyrene at the end groups of the PLA side chains of the comb polymers enables easy detection of the polymeric structures,[42,43] it was possible to examine their intracellular distribution without the need to encapsulate any fluorescent probe. A representative UV-vis fluorescence emission spectrum is provided in Fig. S2† for **P4**. The ratio of the emission bands caused by the vibrational fine structure of pyrene corresponds very well to that of pyrene encapsulated into PLA-based nanocarriers,[44] confirming the assumption that the only potentially

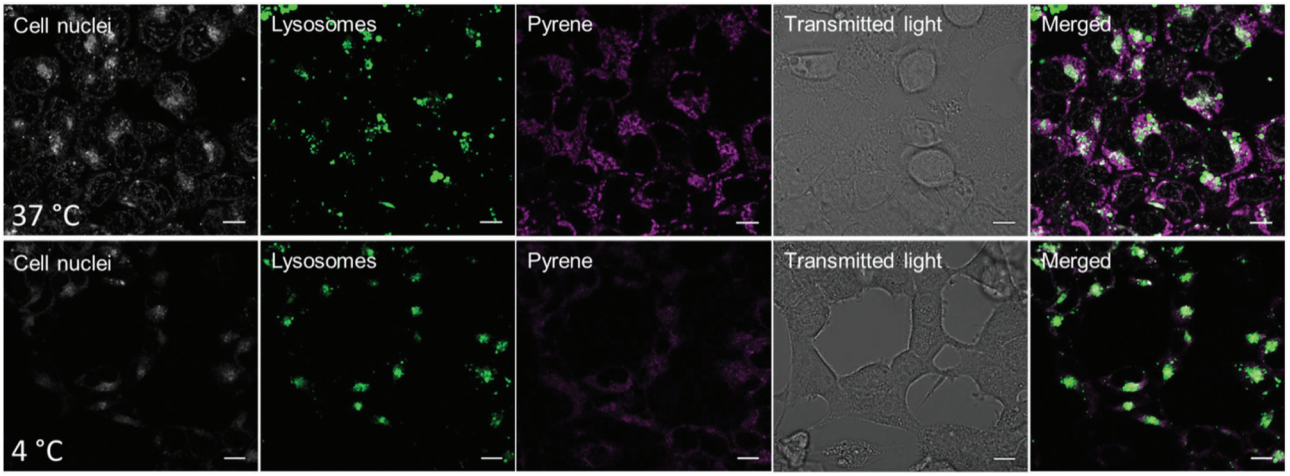

Fig. 9 Confocal live cell imaging of HEK-293 cells incubated with the suspension of **P1** in water (50 μg mL^{-1}) for 4 h at 37 °C (top) and 4 °C (bottom). The cell nucleus was stained with NucRed (grey) and the lysosomes/late endosomes with LysoTracker Green (green); pyrene is depicted in magenta (scale bars represent 10 μm).

toxic compound is not exposed to the surface of any polymeric structures formed in aqueous media. Therefore, HEK cells were incubated with **P1** to **P5** for 4 hours. Confocal live cell imaging revealed a high cellular internalization for all tested polymers at 37 °C (Fig. 9, top and Fig. SI 4 to SI 8†). The detected pyrene signal (magenta) was equally distributed within the cytosol, but was just rarely co-localized within the lysosomes (green) and not detectable within the nucleus. This could indicate either a fast endosomal release or cellular uptake *via* translocation through the cell membrane.

It is known that nanocarriers or nanoparticles possessing diameters from 20 to 500 nm enter cells in an active manner, mainly through endocytosis.[45,46] Furthermore, it is assumed that particles smaller than 20 nm may also internalize by passive diffusion[47] through channels, protein carriers or by translocation. Uptake studies of **P1** were performed at 4 °C, to investigate if the polymers are internalized into the cells by a passive process. Compared to the uptake at 37 °C, decreased pyrene fluorescence was detected within the cells. This indicates that a minor fraction of comb polymers is able to enter the cells by passive penetration. However, the predominant uptake mechanism for **P1** is an energy-driven process.

Conclusions

We present a convenient synthetic strategy for a series of fluorescent amphiphilic heterografted comb polymers comprising oligomeric biocompatible side chains *via* combination of ROP, CROP, and RAFT polymerizations. For this purpose, well-defined methacrylate ω-end-functional macromonomers based on PLA and PEtOx were prepared in separate one-pot procedures and were subsequently copolymerized *via* RAFT to obtain comb polymers with varying hydrophilicity simply by altering the feed ratio of both macromonomers. Cryo-TEM studies of the heterografted comb polymers in water revealed morphologies ranging from vesicular structures to spherical micelles. The morphology of the self-assembled structures correlated well with the hydrophilic character of the comb polymers. The fluorescent pyrene moieties attached to the PLA side chains of the comb polymers enabled performing cellular uptake studies without the need of encapsulation of any tracker molecules revealing that only a slight fraction is localized inside late endosomes/lysosomes. This is favorable for delivery applications, which will be in the focus of our future research as the PLA part of the polymer is biodegradable and a hydrophobic drug could be encapsulated into the self-assembled structures to be slowly released by degradation of the hydrophobic segments.

Acknowledgements

This project was funded by the German Federal Ministry of Education & Research (BMBF, #031A518B Vectura), the Thüringer Ministerium für Wirtschaft, Wissenschaft, und Digitale Gesellschaft (Thuringian Ministry for Economic Affairs, Science and Digital Society, ProExzellenzII, NanoPolar). AT and CW gratefully acknowledge the CarlZeiss Stiftung for funding. The LSM880 ELYRA PS.1 was further funded with a grant from the German Research Council (DFG). The transmission electron microscope was obtained with a grant from the European Funds for Regional Developments (EFRE) and the DFG. The authors wish to thank Nicole Fritz and Annett Urbanek for the mass spectrometry analysis and Carolin Fritzsche for the cytotoxicity studies.

Notes and references

1 O. Dechy-Cabaret, B. Martin-Vaca and D. Bourissou, *Chem. Rev.*, 2004, **104**, 6147–6176.

2 A. P. Gupta and V. Kumar, *Eur. Polym. J.*, 2007, **43**, 4053–4074.
3 K. Knop, R. Hoogenboom, D. Fischer and U. S. Schubert, *Angew. Chem., Int. Ed.*, 2010, **49**, 6288–6308.
4 O. Sedlacek, B. D. Monnery, S. K. Filippov, R. Hoogenboom and M. Hruby, *Macromol. Rapid Commun.*, 2012, **33**, 1648–1662.
5 R. Hoogenboom, *Angew. Chem., Int. Ed.*, 2009, **48**, 7978–7994.
6 N. Adams and U. S. Schubert, *Adv. Drug Delivery Rev.*, 2007, **59**, 1504–1520.
7 S. C. Lee, Y. Chang, J.-S. Yoon, C. Kim, I. C. Kwon, Y.-H. Kim and S. Y. Jeong, *Macromolecules*, 1999, **32**, 1847–1852.
8 C.-H. Wang and G.-H. Hsiue, *Biomacromolecules*, 2003, **4**, 1487–1490.
9 L. Zhao and Z. Lin, *Soft Matter*, 2011, **7**, 10520–10535.
10 Z. Ge and S. Liu, *Macromol. Rapid Commun.*, 2009, **30**, 1523–1532.
11 H. Shi, Y. Zhao, X. Dong, Y. Zhou and D. Wang, *Chem. Soc. Rev.*, 2013, **42**, 2075–2099.
12 S. S. Sheiko, B. S. Sumerlin and K. Matyjaszewski, *Prog. Polym. Sci.*, 2008, **33**, 759–785.
13 M. Zhang and A. H. E. Moeller, *J. Polym. Sci., Part A: Polym. Chem.*, 2005, **43**, 3461–3481.
14 H.-i. Lee, K. Matyjaszewski, S. Yu-Su and S. S. Sheiko, *Macromolecules*, 2008, **41**, 6073–6080.
15 M. Hans, H. Keul, A. Heise and M. Moeller, *Macromolecules*, 2007, **40**, 8872–8880.
16 A. Dag, H. Durmaz, E. Demir, G. Hizal and U. Tunca, *J. Polym. Sci., Part A: Polym. Chem.*, 2008, **46**, 6969–6977.
17 N. Cakir, M. Yavuzarslan, H. Durmaz, G. Hizal and U. Tunca, *J. Polym. Sci., Part A: Polym. Chem.*, 2013, **51**, 899–907.
18 Y. Xia, B. D. Olsen, J. A. Kornfield and R. H. Grubbs, *J. Am. Chem. Soc.*, 2009, **131**, 18525–18532.
19 K. Ishizu, N. Sawada, J. Satoh and A. Sogabe, *J. Mater. Sci. Lett.*, 2003, **22**, 1219–1222.
20 K. Ishizu, N. Okamoto, T. Murakami, S. Uchida and S. Nojima, *Macromol. Chem. Phys.*, 2009, **210**, 1717–1725.
21 H. Zhu, G. Deng and Y. Chen, *Polymer*, 2008, **49**, 405–411.
22 T. Stephan, S. Muth and M. Schmidt, *Macromolecules*, 2002, **35**, 9857–9860.
23 D. Neugebauer, Y. Zhang, T. Pakula and K. Matyjaszewski, *Macromolecules*, 2005, **38**, 8687–8693.
24 C. Weber, M. Wagner, D. Baykal, S. Hoeppener, R. M. Paulus, G. Festag, E. Altuntas, F. H. Schacher and U. S. Schubert, *Macromolecules*, 2013, **46**, 5107–5116.
25 M. Bagheri and E. Bigdeli, *J. Polym. Res.*, 2013, **20**, 1–11.
26 J.-F. Lutz, N. Jahed and K. Matyjaszewski, *J. Polym. Sci., Part A: Polym. Chem.*, 2004, **42**, 1939–1952.
27 C. Weber, C. R. Becer, R. Hoogenboom and U. S. Schubert, *Macromolecules*, 2009, **42**, 2965–2971.
28 J. Kronek, Z. Kroneková, J. Lustoň, E. Paulovičová, L. Paulovičová and B. Mendrek, *J. Mater. Sci.: Mater. Med.*, 2011, **22**, 1725–1734.
29 I. Yildirim, S. Crotty, C. H. Loh, G. Festag, C. Weber, P.-F. Caponi, M. Gottschaldt, M. Westerhausen and U. S. Schubert, *J. Polym. Sci., Part A: Polym. Chem.*, 2016, **54**, 437–448.
30 M. J. Stanford and A. P. Dove, *Macromolecules*, 2009, **42**, 141–147.
31 M. Westerhausen, *Inorg. Chem.*, 1991, **30**, 96–101.
32 A. M. Johns, S. C. Chmely and T. P. Hanusa, *Inorg. Chem.*, 2009, **48**, 1380–1384.
33 M. Westerhausen, J. Langer, S. Krieck and C. Glock, *Rev. Inorg. Chem.*, 2011, **31**, 143.
34 A. Torvisco, A. Y. O'Brien and K. Ruhlandt-Senge, *Coord. Chem. Rev.*, 2011, **255**, 1268–1292.
35 C. Weber, S. Rogers, A. Vollrath, S. Hoeppener, T. Rudolph, N. Fritz, R. Hoogenboom and U. S. Schubert, *J. Polym. Sci., Part A: Polym. Chem.*, 2013, **51**, 139–148.
36 U. Mansfeld, S. Hoeppener, K. Kempe, J.-M. Schumers, J.-F. Gohy and U. S. Schubert, *Soft Matter*, 2013, **9**, 5966–5974.
37 A. L. Parry, P. H. H. Bomans, S. J. Holder, N. A. J. M. Sommerdijk and S. C. G. Biagini, *Angew. Chem.*, 2008, **120**, 8991–8994.
38 H.-Y. Chang, Y.-L. Lin, Y.-J. Sheng and H.-K. Tsao, *Macromolecules*, 2012, **45**, 4778–4789.
39 H. Luo, J. L. Santos and M. Herrera-Alonso, *Chem. Commun.*, 2014, **50**, 536–538.
40 B. K. Banik and F. F. Becker, *Bioorg. Med. Chem.*, 2001, **9**, 593–605.
41 J. Sikkema, J. A. de Bont and B. Poolman, *Microbiol. Rev.*, 1995, **59**, 201–222.
42 M. Müllner, A. Schallon, A. Walther, R. Freitag and A. H. E. Müller, *Biomacromolecules*, 2010, **11**, 390–396.
43 M. Sasatsu, H. Onishi and Y. Machida, *Int. J. Pharm.*, 2008, **358**, 271–277.
44 Y. Zhang, Q. Zhang, L. Zha, W. Yang, C. Wang, X. Jiang and S. Fu, *Colloid Polym. Sci.*, 2004, **282**, 1323–1328.
45 J. Rejman, V. Oberle, I. S. Zuhorn and D. Hoekstra, *Biochem. J.*, 2004, **377**, 159–169.
46 L. Xiao, X. Xiong, X. Sun, Y. Zhu, H. Yang, H. Chen, L. Gan, H. Xu and X. Yang, *Biomaterials*, 2011, **32**, 5148–5157.
47 L. Treuel, X. Jiang and G. U. Nienhaus, *J. R. Soc., Interface*, 2013, **10**, 20120939.

Supporting Information

for

Fluorescent amphiphilic heterografted comb polymers comprising biocompatible PLA and PEtOx side chains

Ilknur Yildirim,[a,b] Tanja Bus,[a,b] Martin Sahn,[a,b] Turgay Yildirim,[a,b] Diana Kalden,[c] Stephanie Hoeppener,[a,b] Anja Traeger,[a,b] Matthias Westerhausen,[c] Christine Weber[a,b] and Ulrich S. Schubert*[a,b]

[a]Laboratory of Organic and Macromolecular Chemistry (IOMC), Friedrich Schiller University Jena, Humboldtstr. 10, 07743 Jena, Germany

[b]Jena Center for Soft Matter (JCSM), Friedrich Schiller University Jena, Philosophenweg 7, 07743 Jena, Germany

[c]Institute of Inorganic and Analytical Chemistry (IAAC), Friedrich Schiller University Jena, Humboldtstr. 8, 07743 Jena, Germany

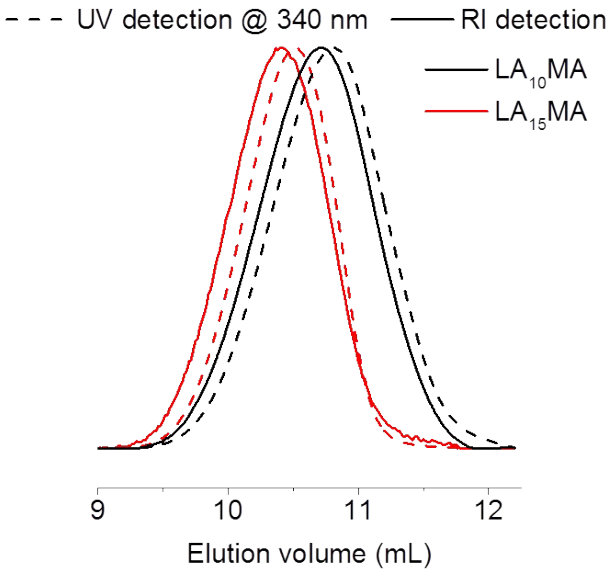

Figure S1. Normalized SEC traces (THF, PLA calibration) of the PLA macromonomers with RI and UV detection at 340 nm.

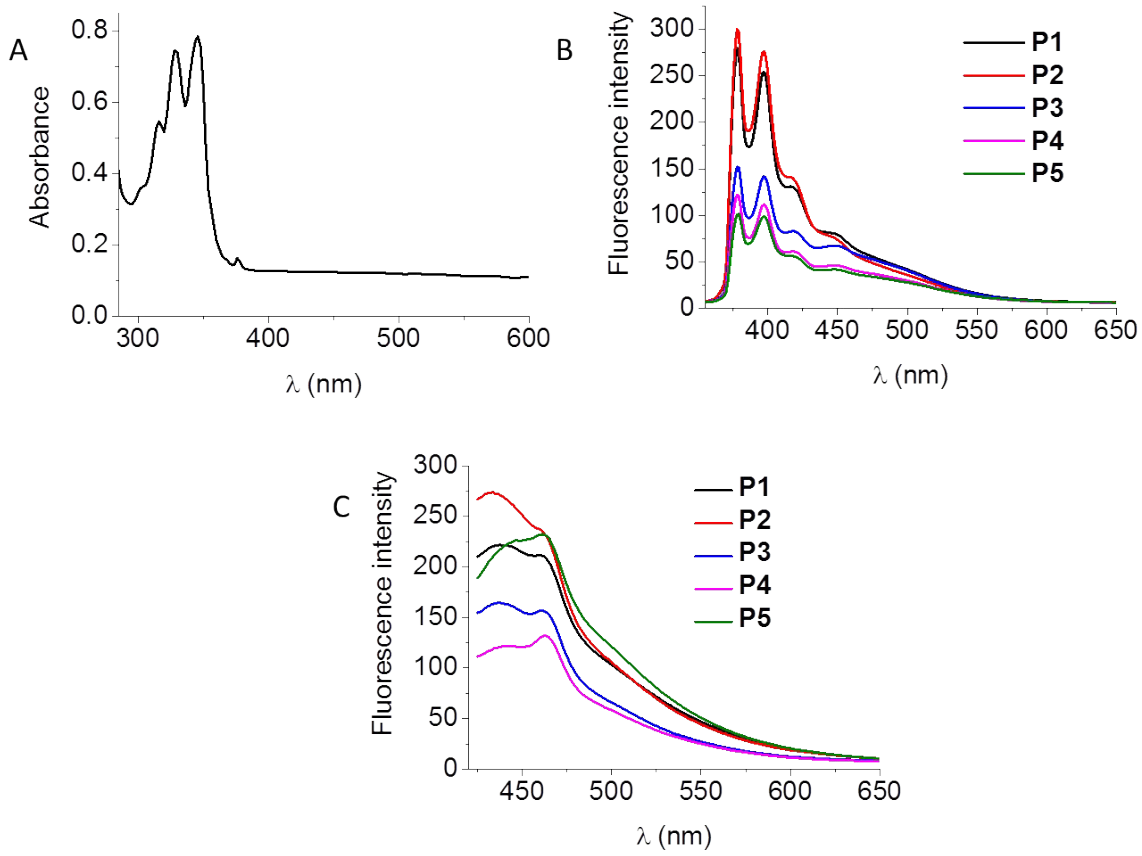

Figure S2. (A) UV-vis absorption spectrum recorded from the aqueous suspension of **P4** (c = 1 mg mL^{-1}). Overlay of fluorescence emission spectra (c = 50 µg mL^{-1}) (**B**) with the excitation wavelength set at 346 nm. (C) with the excitation wavelength set at 405 nm

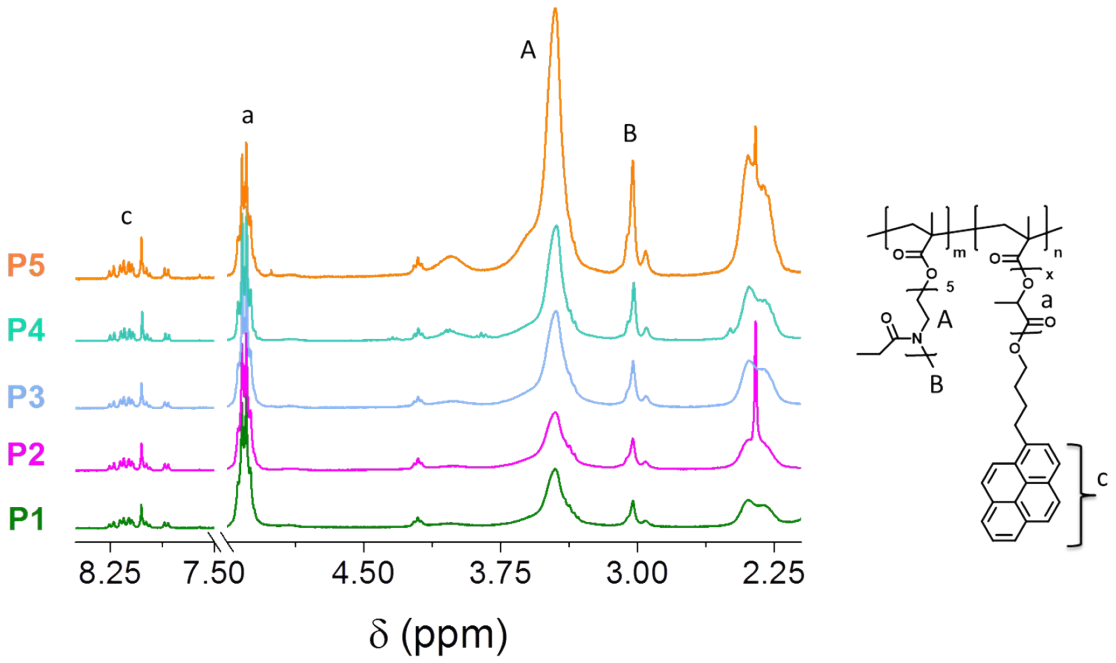

Figure S3. Overlay of the ^{1}H NMR spectra (300 MHz, $CDCl_3$) of all comb polymers **P1** to **P5**. For clarity, the spectra were normalized according to the signal of the methine protons of PLA. Only the signals used for calculation of the copolymer composition are labelled.

Table S1. Characterization results of the polymer suspension in water by means of DLS (the mean particle size was approximated as the effective (Z-average) diameter and the width of the distribution as the polydispersity index of the particles (PDI) obtained by the cumulants method).[a]

Polymer	Z-avg [d, nm]	PDI
P1	59 ± 0.7	0.349 ± 0.001
P2	103 ± 0.4	0.270 ± 0.01
P3	65 ± 0.6	0.178 ± 0.01
P4	19 ± 0.1	0.122 ± 0.002
P5	81 ± 0.3	0.309 ± 0.003

[a]c = 5 mg mL^{-1} in water.

Confocal live cell microscopy

Uptake studies I: Negative Control

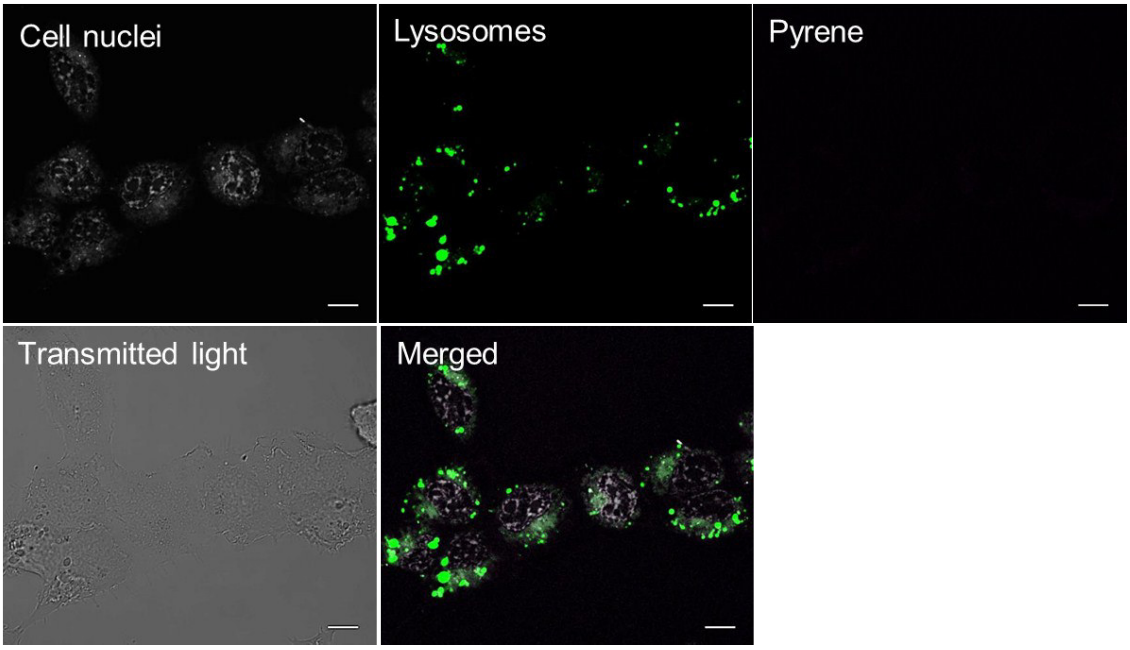

Figure S4. Confocal live cell imaging: HEK cells were cultivated for 4 h in serum-reduced media serving as negative control. The cell nucleus was stained with NucRed (grey) and the lysosomes with LysoTracker Green (green); pyrene is depicted in magenta (scale bars represent 10 μm).

Uptake studies II: **P2**

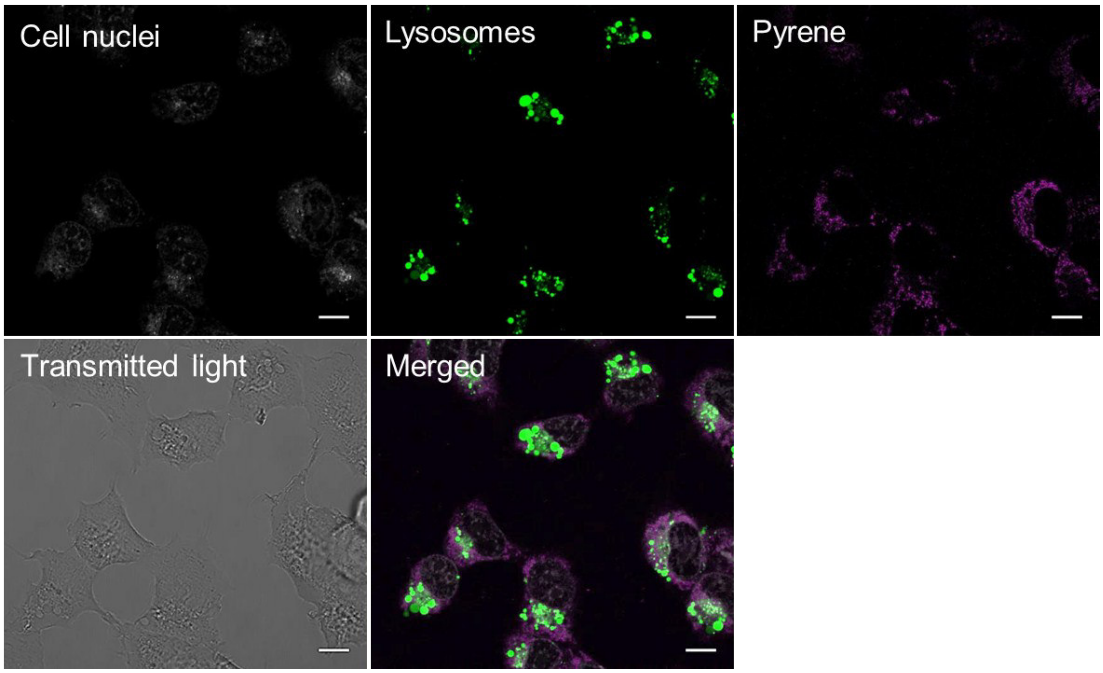

Figure S5: Confocal live cell imaging: For uptake studies, HEK cells were cultivated with **P2** for 4 h in serum-reduced media. The cell nucleus was stained with NucRed (grey) and the lysosomes with LysoTracker Green (green); pyrene is depicted in magenta (scale bars represent 10 μm).

Uptake studies III: **P3**

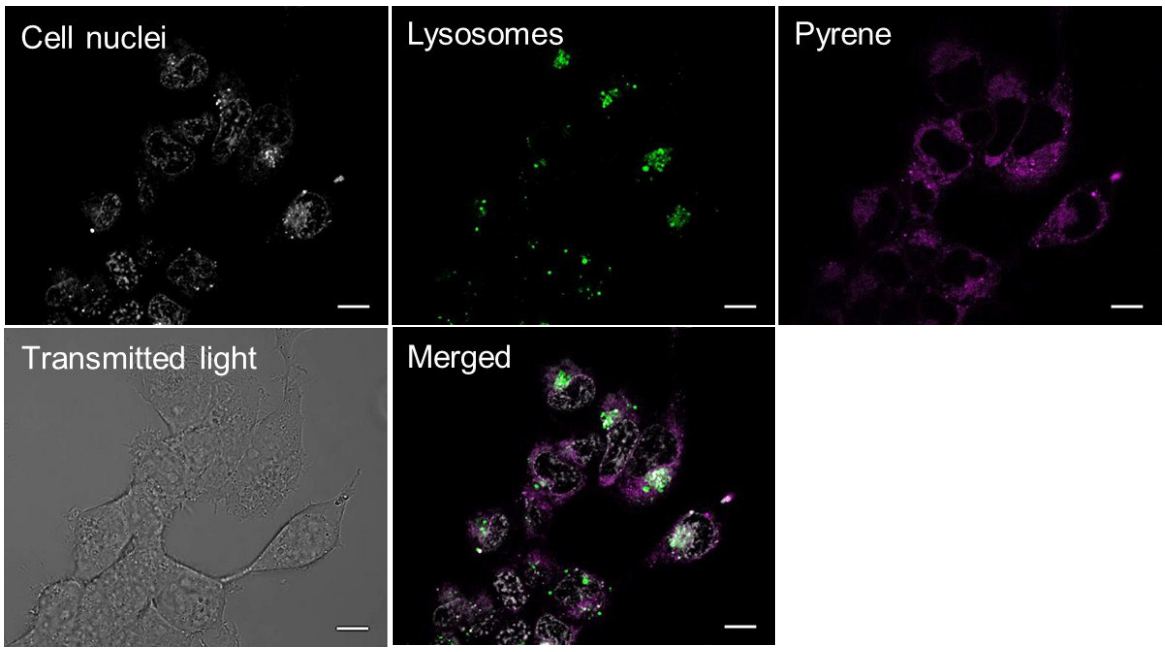

Figure S6: Confocal live cell imaging: For uptake studies, HEK cells were cultivated with **P3** for 4 h in serum-reduced media. The cell nucleus was stained with NucRed (grey) and the lysosomes with LysoTracker Green (green); pyrene is depicted in magenta (scale bars represent 10 μm).

Uptake studies IV: **P4**

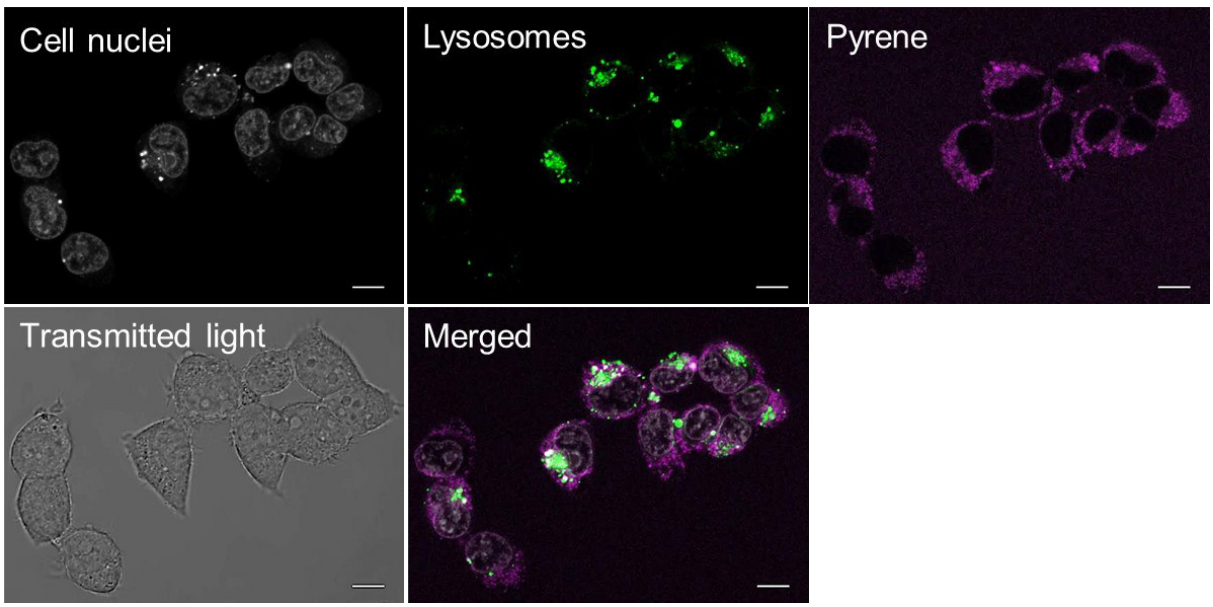

Figure S7: Confocal live cell imaging: For uptake studies, HEK cells were cultivated with **P4** for 4 h in serum-reduced media. The cell nucleus was stained with NucRed (grey) and the lysosomes with LysoTracker Green (green); pyrene is depicted in magenta (scale bars represent 10 μm).

Uptake studies V: **P5**

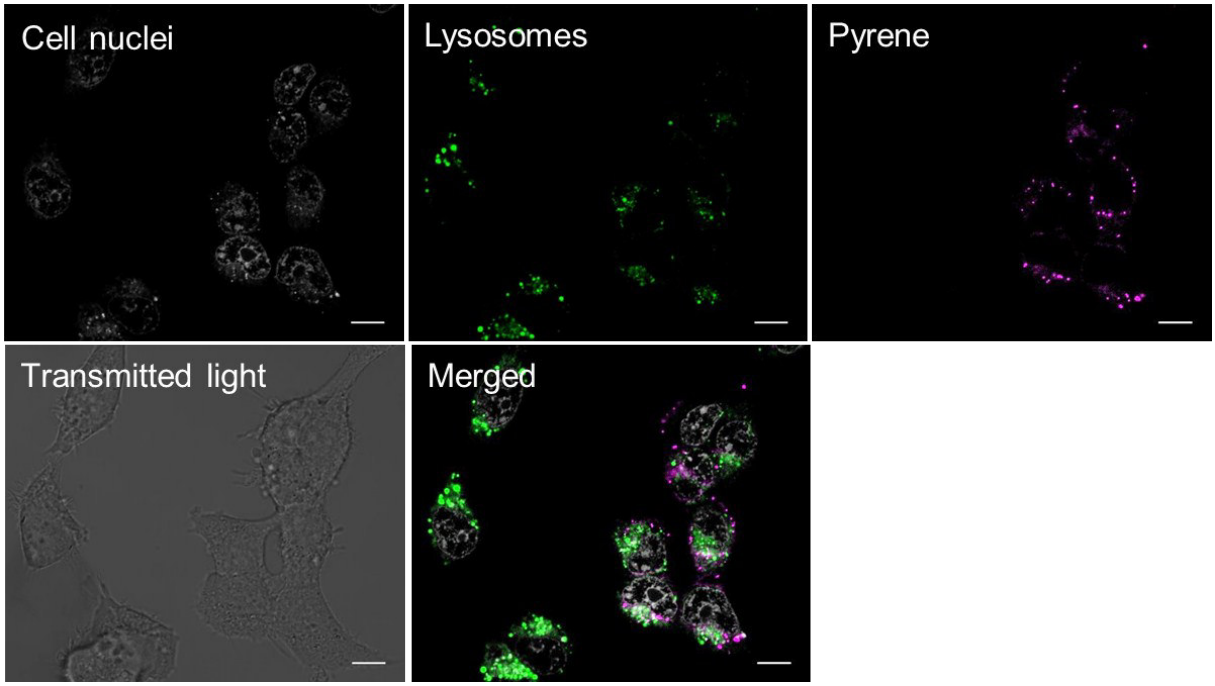

Figure S8: Confocal live cell imaging: For uptake studies, HEK cells were cultivated with **P5** for 4 h in serum-reduced media. The cell nucleus was stained with NucRed (grey) and the lysosomes with LysoTracker Green (green); pyrene is depicted in magenta (scale bars represent 10 µm).

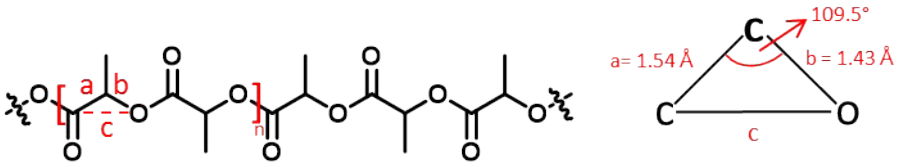

$c^2 = a^2 + b^2 - 2abcos(109.5)$

$c = 2.42\ Å = 0.242\ nm$

Length of one lactide unit = 3c

Figure S9: Estimation of the length of a fully stretched PLA side chain.

Publication Pub7

Tailoring cellular uptake and fluorescence of poly(2-oxazoline)-based nanogels

M. Hartlieb, T. Bus, J. Kübel, D. Pretzel, S. Hoeppener, M. N. Leiske, K. Kempe, B. Dietzek, U. S. Schubert

Bioconjugate Chem. **2017**, *28*, 1229-1235.

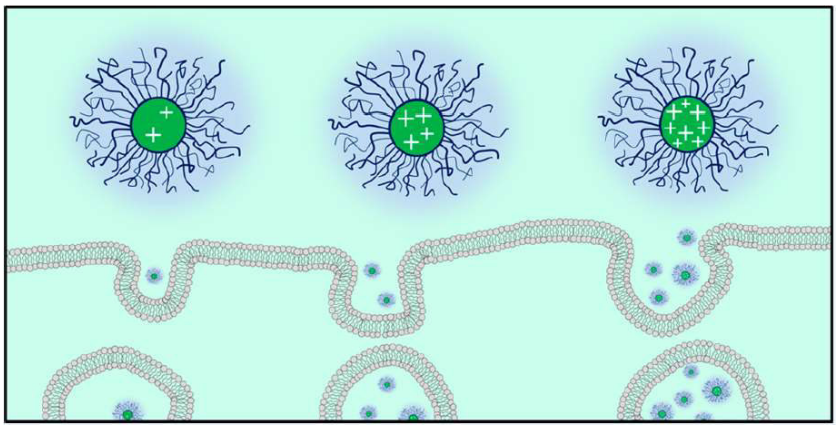

Bioconjugate Chemistry

Article

pubs.acs.org/bc

Tailoring Cellular Uptake and Fluorescence of Poly(2-oxazoline)-Based Nanogels

Matthias Hartlieb,[†,‡,#,¶] Tanja Bus,[†,‡,#] Joachim Kübel,[§,∥,⊥] David Pretzel,[†,‡] Stephanie Hoeppener,[†,‡] Meike N. Leiske,[†,‡] Kristian Kempe,[†,‡,¶] Benjamin Dietzek,[§,∥] and Ulrich S. Schubert*[,†,‡]

[†]Laboratory of Organic and Macromolecular Chemistry (IOMC), Friedrich Schiller University Jena, Humboldtstrasse 10, 07743, Jena, Germany

[‡]Jena Center for Soft Matter (JCSM), Friedrich Schiller University Jena, Philosophenweg 7, 07743, Jena, Germany

[§]Institute of Physical Chemistry (IPC) and Abbe Center of Photonics, Friedrich Schiller University Jena, Helmholtzweg 4, 07743 Jena, Germany

[∥]Leibniz Institute of Photonic Technology (IPHT), Albert-Einstein-Str. 9, 07745 Jena, Germany

Supporting Information

ABSTRACT: Controlling the size and charge of nanometer-sized objects is of upmost importance for their interactions with cells. We herein present the synthesis of poly(2-oxazoline) based nanogels comprising a hydrophilic shell and an amine containing core compartment. Amine groups were cross-linked using glutaraldehyde resulting in imine based nanogels. As a drug model, amino fluorescein was covalently immobilized within the core, quenching excessive aldehyde functions. By varying the amount of cross-linker, the zeta potential and, hence, the cellular uptake could be adjusted. The fluorescence of the nanogels was found to be dependent on the cross-linking density. Finally, the hemocompatibility of the described systems was studied by hemolysis and erythrocyte aggregation assays. While cellular uptake was shown to be dependent on the zeta potential of the nanogel, no harmful effects to red blood cells was observed, rendering the present system as an interesting toolbox for the production of nanomaterials with a defined biological interaction profile.

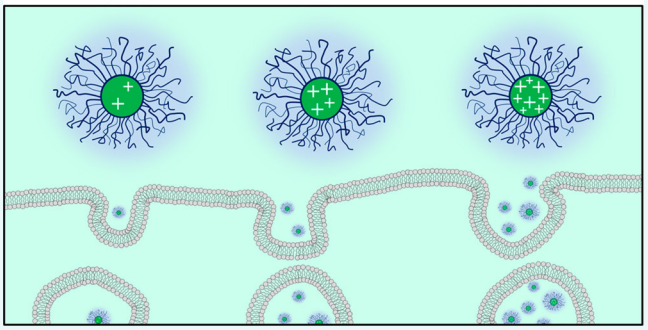

INTRODUCTION

Nanomedicine, the use of nanoscopic objects for biomedical applications such as diagnostics or treatment of diseases, has attracted increasing interest in recent years.[1,2] By using (polymeric) carriers, it is possible to solubilize, protect, and deliver drug molecules to the desired site of action in the body. Nanogels, such as (reversibly) cross-linked polymer micelles,[3] are particularly valuable in this context as, if the chemistry is chosen appropriately, premature drug release or disassembly can be reduced.[4] In the nanomedicine based treatment of cancer, the enhanced permeability and retention (EPR) effect is used to generate a tumor specific accumulation of the drug.[5] The concept exploits the leaky nature of tumor tissue and the passive accumulation of nanosized objects within those cavities. However, in order to take advantage of the EPR effect, a drug carrier has to exhibit long blood circulation times and a low level of unspecific cellular interactions. Many parameters such as size, shape, hydrophilicity or charge influence the cellular uptake,[6,7] and with regard to new nanomedicines, the ability to tailor the cellular interaction in an easy way is highly beneficial. It was shown that a positively charged surface significantly increases the uptake of nanoparticles.[6,8−12] This effect is also used in gene therapy approaches in terms of a complexation of negatively charged genetic material by positively charged polymers in order to penetrate cellular membranes.[13] However, a positively charged surface usually also increases the cytotoxicity induced by the system.[14,15] In addition, in the context of the EPR effect, a hydrophilic, low fouling surface is indispensable to maintain low protein adsorption levels. Poly(2-oxazoline)s (POx) display a promising material in a biomedical context, as certain derivatives bearing small side chains, like poly(2-methyl-2-oxazoline) (PMeOx) or poly(2-ethyl-2-oxazoline) (PEtOx), show excellent biocompatibility.[16−18] Indeed, their performance in biological applications is often compared to poly(ethylene glycol) (PEG), since they also show a stealth effect.[19,20] Recent studies show that in terms of circulation time in the bloodstream and unspecific accumulation in the body, PEtOx is even more advantageous than PEG.[21] Their versatile functionalization chemistry displays another advantage.[22] There are sparse examples of POx based nanogels using PEtOx or PMeOx as a polymer shell[23,24] and only a few were utilized for biomedical applications.[25,26]

Received: February 7, 2017
Revised: February 9, 2017
Published: February 16, 2017

DOI: 10.1021/acs.bioconjchem.7b00067
Bioconjugate Chem. 2017, 28, 1229−1235

Recently, we reported the synthesis of nanogels based on the self-assembly of POx block copolymers consisting of an amine-containing, cationic block (poly(4-amino-butyl-2-oxazoline (PAmOx))[27] and a hydrophilic PEtOx segment.[26] The nanogels maintained low toxicity levels while possessing a positive zeta potential. Within the present contribution, the influence of the cross-linking process on the properties of nanogels, in particular, on the cellular uptake, is investigated.

RESULTS AND DISCUSSION

A highly defined POx-based diblock copolymer P($EtOx_{98}$-*b*-$BocOx_{32}$), **1**, $Đ$ = 1.07, Table 1, was synthesized via cationic ring opening polymerization by sequential monomer addition. The Boc-group was abstracted using trifluoroacetic acid to yield P($EtOx_{98}$-*b*-$AmOx_{32}$), **2** with a dispersity of 1.07. To produce nanogels this polymer was dissolved in chloroform, which leads to the formation of micellar structures comprising an PAmOx core. The charged nature of the amine groups leads to a phase segregation of the PAmOx block while PEtOx is readily soluble in chloroform, stabilizing the micelle.

Table 1. Composition and Analytical Data of the POx Block Copolymers

		NMR	SEC	
sample	composition (NMR)	M_n (g mol^{-1})	M_n (g mol^{-1})	$Đ$
1[a]	P($EtOx_{98}$-*b*-$BocOx_{32}$)	17 500	8 200	1.07
2[b]	P($EtOx_{98}$-*b*-$AmOx_{32}$)	14 200	13 900	1.11

[a]SEC measurement in $CHCl_3$. [b]SEC Measurement in DMAc.

Cross-linking was applied using glutaraldehyde (GA) resulting in the formation of nanogels cross-linked by imine bonds, which are pH responsive.[28] To quench the gelation and to obtain systems that are stable within an aqueous environment, 6-amino fluorescein (6AF) was used. The free amino group of 6AF reacts with residual aldehyde groups of the cross-linker resulting in a reversible covalent attachment to the nanogel (Scheme 1). In order to use these systems in drug delivery applications, the interaction of the produced nanogels with cells is of utmost importance. Therefore, the content of cross-linker was varied to alter the charge of the resulting nanogels (**3** to **7**). A higher degree of cross-linking and, consequently, a lower amount of free amine groups should result in a reduced zeta potential and, henceforth, in a reduction of the cellular uptake. The content of GA was varied between 1 and 3 equiv. (per 2 amine groups) (Table 2).

As displayed in Figure 1, an increase of GA leads to a reduction of the zeta potential from ζ = 28 mV for equimolar cross-linking to ζ = 7 mV for a 3-fold excess of GA. Moreover, an increase in size, as detected by DLS, can be observed for compounds **3** to **7**. These findings seem best explained by increased amounts of water present during gelation. GA was applied in a 70 wt % aqueous solution and during the cross-linking reaction water is produced as a byproduct. The additional water will accumulate within the hydrophilic core compartment of the micelle and swell the nanostructure prior to or during cross-linking resulting in larger nanogel sizes. This assumption is supported by cryoTEM measurements showing an increase in size with an increasing cross-linking density (Figure 2).

Table 2. Characterization of POx Nanogels in an Aqueous Environment

sample	cross-linker (equiv per 2 NH_2)	size[a] (nm, r)	ζ (mV)	content of 6AF (wt %)	size[b] (r, nm)
3	1	13	28	17	12
4	1.5	17	13	27	13
5	2	20	10	20	14
6	2.5	22	8	24	15
7	3	24	7	17	15

[a]Determined by DLS. [b]determined by cryo-TEM.

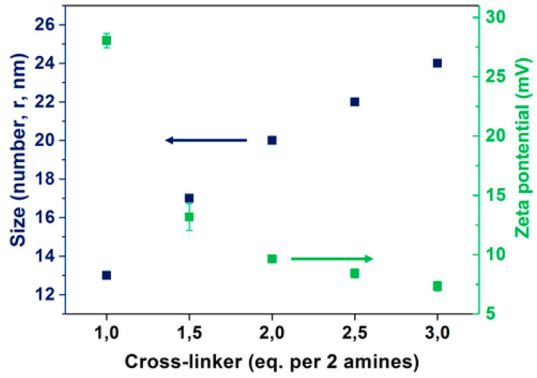

Figure 1. Dependency of zeta potential, as well as size by DLS on the cross-linking density of POx nanogels.

The obtained values are, however, smaller compared to DLS data indicating a falsification of the DLS derived values possibly caused by the presence of a small fraction of agglomerates. A third parameter investigated, depending on the cross-linking density, was the dye-loading of the resulting systems by evaluating their absorption and fluorescence. Based on its absorbance, the amount of 6AF conjugated to the nanogels can be estimated to values between 17 and 27 wt %, without an obvious dependence on the degree of cross-linking. However, determined by fluorescence intensity, a steady increase in the amount of dye could be monitored up to values which would correspond to a loading efficiency above 100 wt % when

Scheme 1. Schematic Representation of the Synthesis and Self-Assembly of P(EtOx-*b*-AmOx) in Chloroform to Form Micelles with a Cationic Core and a PEtOx Shell, as Well as the Subsequent Cross-Linking and 6AF Conjugation to Obtain Dye-Loaded Nanogels

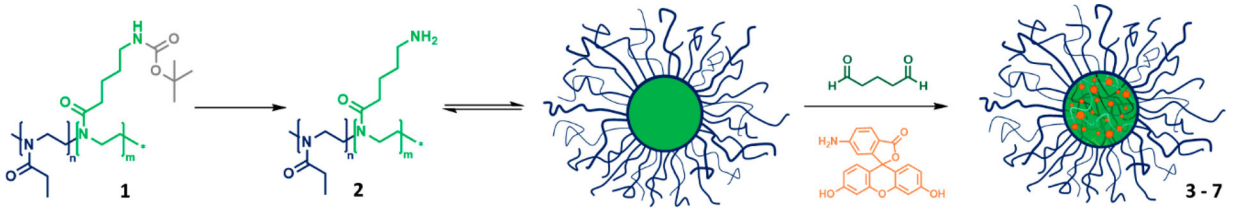

DOI: 10.1021/acs.bioconjchem.7b00067
Bioconjugate Chem. 2017, 28, 1229−1235

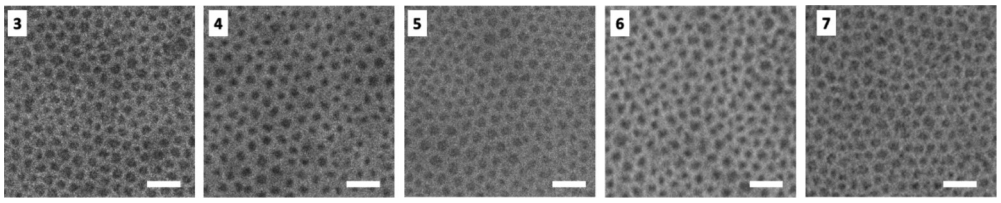

Figure 2. CryoTEM images of nanogels (**3** to **7**) in water. Scale bars represent 100 nm.

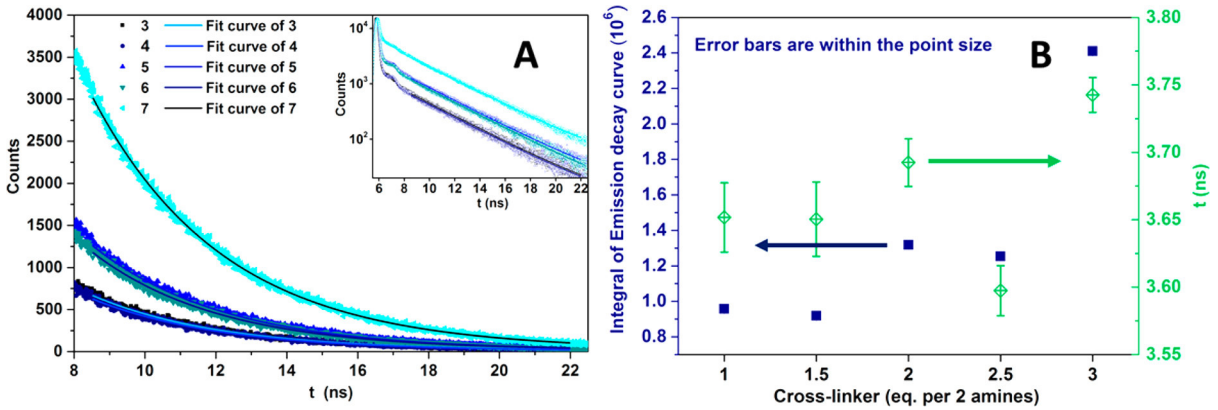

Figure 3. Fluorescence lifetime measurements of POx nanogels with varying degrees of cross-linking. (A) Fluorescence decay curves. (B) Fluorescence life times and decay integrals of nanogels **3** to **7**.

compared to a calibration of free 6AF, indicating a boost in fluorescence intensity by varying the core composition (Figure S1). To study this effect in detail, fluorescence lifetime measurements were conducted (Figure 3).

The investigations revealed an increase in fluorescence lifetime with increasing degree of cross-linking except for 2.5 equiv. of GA. Also, the integrals of the decay curves, which serve as a measure of the fluorescence quantum yield, increase within the series. As depicted in Figure S1, the absolute amount of dye within the nanogels is relatively constant between 17 and 27 wt %. It is described for fluorescein and its derivatives that electrostatic interactions between the dye and a cationic (surfactant) micelle are able to stabilize the anionic form of the molecule which leads to an increase in fluorescence lifetime and quantum yield.[29] However, the cationic character decreases with a higher degree of cross-linking and can, therefore, be held responsible for a general boost of fluorescence compared to pure 6AF, but not for the increasing lifetimes within the series.

Also, the dye−dye distance can be estimated as roughly constant. Therefore, dye−dye interactions such as excimer formation are unlikely to be responsible for the observed effects. Presumably, increasing the amount of cross-linker will increase the stiffness of the core. Thus, the increases in quantum yield and emission lifetime could be explained by frozen degrees of freedom, resulting in a reduced rate constant for nonradiative decay processes.[30,31] This is supported by proton NMR measurements of the nanogels (Figure S2). In contrast to the precursor polymer, only signals of the PEtOx constituting the shell are visible, while PAmOx signals are absent. This indicates a restriction of degrees of freedom of the block forming the core compartment of the micellar structure and supports the hypothetic cause for the increase in quantum yield.

In order to determine the influence of the varying cross-linking density on the cellular uptake, flow cytometry investigations were performed using L929 mouse fibroblasts (Figure 4). The decrease in mean fluorescence with an increasing cross-linking degree within the series of nanogels demonstrates the influence of the zeta potential on the internalization for all concentrations investigated. Moreover, time dependent uptake experiments visualize this behavior. The

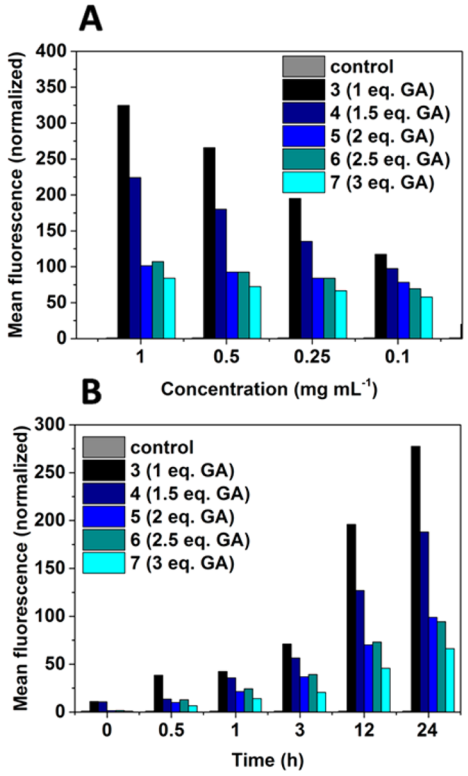

Figure 4. Cellular internalization of nanogels **3** to **7** dependent on the concentration (A) after 24 h incubation at 37 °C or at varying incubation times (B) at a concentration of 0.5 mg mL^{-1} at 37 °C.

DOI: 10.1021/acs.bioconjchem.7b00067
Bioconjugate Chem. 2017, 28, 1229−1235

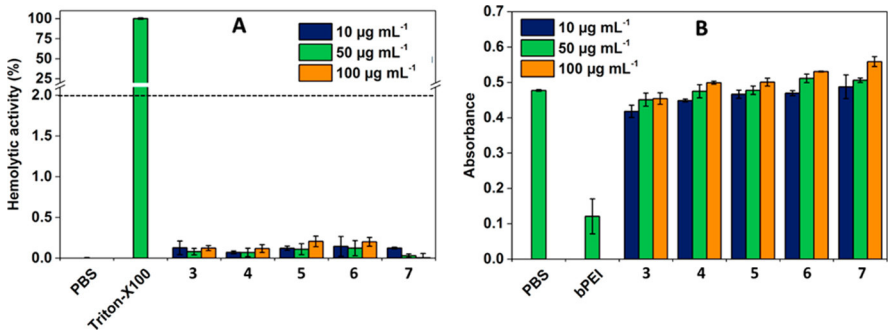

Figure 5. Induction of hemolysis (A) as well as erythrocyte aggregation (B) by 6AF loaded nanogels (**3** to **7**) in a concentration range between 10 and 100 μg mL^{-1} using sheep blood of three different donor batches.

difference in the fluorescence intensity between the nanogels was considered by referencing to the absolute fluorescence intensity of the measurement. This finding is in agreement with literature reports where objects having a positive net charge are described to be taken up more efficiently as compared to neutral or anionic structures.[32] The reported investigation shows that the cellular uptake, which displays a crucial factor for the utilization as a drug delivery agent, can be fine-tuned for the presented nanogel systems.

In order to investigate the nature of the cellular internalization, uptake studies at 4 °C were performed (Figure S3). The diminished uptake at low temperatures suggests an energy dependent internalization via endocytosis as expected for objects in such a size range.[7,33]

Besides cellular uptake, the biocompatibility of the drug carriers represents an essential parameter. It was reported that an increase in zeta potential of nanoparticles negatively affects the cell viability.[14,15] Nanogel **3**, investigated in a previous study, possesses the highest zeta potential (ζ = +28 mV) within the series and is, therefore, expected to induce the highest toxicity, although the system did not interfere with the metabolism of L929 mouse fibroblasts in a negative way up to a concentration of 5 mg mL^{-1}.[26] While this is a promising indication regarding the biocompatibility of the material, the most important environment a drug delivery system is facing is the bloodstream. Long circulation times, leading to a passive targeting, require a low level of interaction with the components of the blood. An interaction with erythrocytes resulting in clotting or disruption is highly undesired. The hemolytic activity of 6AF loaded nanogels was studied depending on the applied concentration (Figure 5A). All nanogels in a concentration range between 10 and 100 μg mL^{-1} resulted in hemolytic activity values well below 2%, which is defined as the threshold for a hemolysis (according to the ASTM F756−00 standard).

Furthermore, the erythrocyte aggregation was investigated and found to be negligible in the given concentration range with absorbance values comparable with the negative control (Figure 5B, Figure S4).

These findings are remarkable, since positively charged nanomaterials are expected to feature a decreased blood compatibility. In contrast to nanoparticle systems with an altered surface chemistry, the charge of the nanogels presented herein results from amine groups within the core of the micellar structure, whereas the periphery is covered with noncharged PEtOx chains. While this setup enables tailoring of the cellular interaction, as shown by the cellular uptake studies, the biocompatibility of the nanogels is maintained in all cases.

CONCLUSION

Within this contribution, we present a straightforward synthetic route to poly(2-oxazoline)-based polymeric nanogels with a tailored cellular uptake. The gels are produced by phase segregation of a diblock copolymer, containing a cationic and a neutral block forming micellar structures in chloroform. Cross-linking is conducted using glutaraldehyde and the fluorescent dye 6-amino fluorescein is loaded covalently. By changing the cross-linking density, it is possible to alter the properties of the nanogels in terms of fluorescence intensity and zeta potential. Hence, it is possible to adjust their cellular uptake as shown by flow cytometry measurements. Due to the unique nature of the nanogels, which carry the charged units within the core of the micellar structure, the biocompatibility is not affected by the variation in charge as demonstrated by hemocompatibility experiments. Therefore, the herein presented material displays a versatile toolbox for the production of drug delivery vehicles. Further studies will focus on the extension of the concept to in vivo investigations as well as on the loading of anticancer drugs such as doxorubicin, and the utilization of drug loaded nanogels in vitro and in vivo.

EXPERIMENTAL SECTION

Material and Instrumentation. Chemicals and solvents were purchased from Sigma-Aldrich, Merck, Fluka, and Acros. 2-Ethyl-2-oxazoline (EtOx) and methyl tosylate (MeOTos) were distilled to dryness prior to use. EtOx was dried using barium oxide before distillation. 2-(4-((*tert*-Butoxycarbonyl)-amino)butyl)-2-oxazoline (BocOx) was synthesized as described in a previous publication.[27] If not stated otherwise, cell culture media and supplements (L-Glutamin, antibiotics) were obtained from Biochrom (Merck Millipore, Germany).

The Initiator Sixty single-mode microwave synthesizer from Biotage, equipped with a noninvasive IR sensor (accuracy: 2%), was used for polymerizations under microwave irradiation. Microwave vials were heated overnight to 110 °C and allowed to cool to room temperature under an argon atmosphere before use. All polymerizations were carried out under temperature control. Size-exclusion chromatography (SEC) measurements of the protected polymers were performed on a Shimadzu system equipped with a SCL-10A system controller, a LC-10AD pump, a RID-10A refractive index detector, and a PSS SDV column with chloroform/triethylamine (NEt_3)/*iso*-propanol (94:4:2) as eluent. The column oven was set to 50 °C. SEC of the deprotected statistical copolymers was performed on a Shimadzu system with a LC-10AD pump, a RID-10A refractive index detector, a system controller SCL-10A, a degasser DGU-14A, and a CTO-10A column oven using *N,N*-

DOI: 10.1021/acs.bioconjchem.7b00067
Bioconjugate Chem. 2017, 28, 1229−1235

dimethylacetamide (DMAc) with 2.1 g L^{-1} LiCl as the eluent and the column oven set to 50 °C. Poly(styrene) (PS) samples were used as calibration standards for both solvent systems. Proton NMR spectroscopy (^{1}H NMR) measurements were performed at room temperature on a Bruker AC 300 and 400 MHz spectrometer, using $CDCl_3$ or *N,N*-dimethylformamide (DMF)-D_7 as solvents. The chemical shifts are given in ppm relative to the signal of the residual nondeuterated solvent.

Batch dynamic light scattering (DLS) was performed on a Zetasizer Nano ZS (Malvern Instruments, Herrenberg, Germany). All measurements were performed in folded capillary cells (DTS1071, Malvern Instruments, Herrenberg, Germany). After an equilibration time of 180 s, 3 × 30 s runs were carried out at 25 °C (λ = 633 nm). The counts were detected at an angle of 173°. Each measurement was performed in triplicate. Apparent hydrodynamic radii, R_h, were calculated according to the Stokes−Einstein equation.

Laser Doppler velocimetry was used to measure the electrokinetic potential, also known as zeta potential. The measurements were performed on a Zetasizer Nano ZS (Malvern Instruments, Herrenberg, Germany) in folded capillary cells (DTS1071). For each measurement, 15 runs were carried out using the fast-field and slow-field reversal mode at 150 V. Each experiment was performed in triplicate at 25 °C. The zeta potential (ζ) was calculated from the electrophoretic mobility (μ) according to the Henry equation.[34] The Henry coefficient, f(ka), was calculated according to Ohshima.[35]

CryoTEM investigations were conducted utilizing a FEI Tecnai G^2 20 at 200 kV acceleration voltage. Specisms were vitrified by a Vitrobot Mark V system on Quantifoil grids (R2/2). The blotting time was 1 s with blotting force offset of 0. The amount of solution was 7 μL. Samples were plunge frozen in liquid ethane and stored under liquid nitrogen until transferred to the Gatan cryo-holder and brought into the microscope. Images were acquired with a 4k × 4k CCD Eagle camera.

Absorbance and fluorescence spectra as well as hemolysis and erythrocyte aggregation assays were recorded using a Tecan M200 Pro fluorescence microplate reader (Crailsheim, Germany) by the use of black well plates with a flat and transparent bottom.

The cellular uptake studies of nanogels were performed with a Beckmann Coulter Cytomics FC-500 equipped with a Uniphase Argon ion laser (488 nm, 20 mW output) and analyzed with the Cytomics CXP software.

Block Copolymer of 2-Ethyl-2-oxazoline (EtOx) and 2-(4-((*tert*-Butoxycarbonyl)amino)butyl)-2-oxazoline (BocOx) (P(EtOx-*b*-BocOx)), (1). In a microwave vial, EtOx (757 μL, 7.5 mmol), MeOTos (16.2 μL, 0.107 mmol) and acetonitrile (3.4 mL) were mixed under inert conditions. After heating in the microwave synthesizer at 140 °C for 25 min the vial was introduced into a glovebox with nitrogen atmosphere and BocOx (803 μL, 3.2 mmol) was added. The closed vial was heated again in the microwave synthesizer (140 °C, 20 min). The solution was precipitated in cold (−80 °C, 300 mL) diethyl ether. The white precipitate was filtered and dried in high vacuum (1.4 g, 92%).

^{1}H NMR ($CDCl_3$, 300 MHz): δ = 7.66, (d, 8.1 Hz, 0.019 H, tosylate), 7.14 (d, 8.21 Hz, 0.019 H, tosylate), 3.45 (s, 4 H, backbone), 3.10 (s, 0.58 H, CH_2−CH_2−NH (BocOx)), 2.50−2.15 (m, 1.96 H, CH_2 (EtOx)/CH_2−CH_2−NHBoc), 1.62 (s, 0.52 H, CH_2−CH_2−CH_2 (BocOx)), 1.52 (s, 0.52 H, CH_2−CH_2 (BocOx)), 1.42 (s, 2.3 H, CH_3 (BocOx)), 1.21 (s, 2.1 H, CH_3 (EtOx)) ppm.

SEC (eluent: $CHCl_3$/*iso*-propanol/NEt_3, PS-standard): M_n = 8200 g mol^{-1}, $Đ$ = 1.07.

Deprotection of P(EtOx-*b*-BocOx) (1) to yield (P(EtOx-*b*-AmOx), (2). P(EtOx-*b*-BocOx) (**1**, 1.3 g) was dissolved in TFA (5 mL) and heated to 60 °C for 1 h. After stirring for 12 h at room temperature, the mixture was diluted with 10 mL methanol and precipitated in 400 mL of cold (−80 °C) diethyl ether. The precipitate was redissolved in methanol (100 mL) and stirred with Amberlyst A21 for 48 h. Subsequently, the solvent was removed, the polymer was dissolved in deionized water and freeze-dried (−80 °C, 0.003 mbar). The polymer was obtained as white powder (1.2 g, 92%).

^{1}H NMR (DMF-D_7, 300 MHz): δ = 4.9 (s, 2.3 H, NH_2), 3.51 (s, 4 H, backbone), 3.07 (s, 0.49 H, CH_2−CH_2−NH_2), 2.44 (m, 2.1 H, CH_2 (EtOx)/CH_2−CH_2−CO (AmOx)), 1.9−1.54 (m, 0.96 H, CH_2−CH_2−CH_2−CH_2 (AmOx)), 1.2 (s, 2,3 H, CH_3 (EtOx)) ppm.

SEC (eluent: DMAc/LiCl, PS-standard): M_n = 13 900 g mol^{-1}, $Đ$ = 1.11.

General Procedure for Self-Assembly and Cross-Linking (3−7). To create nanostructures, block copolymer (**2**, 90 mg, 0.006 mmol) was dissolved in $CHCl_3$, (5 mg mL^{-1}) and stirred for 3 h. Subsequently, glutaraldehyde (30 mg, 0.3 mmol, 1.5 equiv per amine (**4**)) was added and the solution was stirred another 3 h. With proceeding reaction time the color of the solution changed from colorless to yellow. To quench the excess of aldehyde functionalities, 6-amino fluorescein (50 mg) was added and the mixture was stirred for 12 h. Subsequently, the amount of solvent was reduced under an argon stream and the residual was precipitated in 100 mL cold diethyl ether (−80 °C). To purify the self-assembled structures from residual capping agent and cross-linker, dialysis in MeOH/water (1:4) was applied using a membrane with a molar mass cut off of 3500 g mol^{-1} (Roth Zellutrans). After the extraction was finished, the dialysis medium was changed to pure water and the aqueous solution was freeze-dried to yield an orange powder.

Determination of Dye Loading Content by Absorbance/Fluorescence. The absorbance/fluorescence of 6AF loaded nanostructures was investigated under alkaline conditions (1 mol L^{-1} NaOH in water) in diluted solution (0.1 mg mL^{-1}). The absorbance was determined at a wavelength of 490 nm and compared to a sequential dilution series of 6AF in the same aqueous NaOH solution. A 100-fold excess of glutaraldehyde was added to the control to ensure that only the imine species of 6AF is present. Emission was detected at an excitation wavelength of 450 nm. Nanogels as well as 6AF calibration exhibit an emission maximum at 510 nm. The readout was accomplished using a Tecan M200 Pro fluorescence microplate reader (Crailsheim, Germany).

Fluorescence Lifetime Measurements. The emission decay curves were obtained by time-correlated-single-photon-counting. After excitation with a frequency-doubled Ti-sapphire laser adjusted to 870 nm (Tsunami, Newport Spectra-Physics GmbH, pulse-to-pulse repetition rate 400 kHz after passing a pulse selector, model 3980, Newport Spectra-Physics GmbH), i.e., at λ_{ex} = 435 nm, the luminescence of the sample was collected in a 90°-geometry and detected with a Becker & Hickl PMC-100-4 photon-counting module. A long-pass filter (455 nm) is inserted in the detection beam path. The samples were adjusted to yield optical densities <0.03 at the excitation

DOI: 10.1021/acs.bioconjchem.7b00067
Bioconjugate Chem. 2017, 28, 1229−1235

wavelength in aqueous NaOH (0.1 mol L^{-1}). The measurements were accumulated at count rates <3% of the rep.-rate until 15 000 counts in the maximum were reached.

Blood Compatibility Measurements. To assess the hemolytic activity of the polymer solutions, blood from sheep collected in heparinized tubes (Institute of Laboratory Animal Science and Animal Welfare, Friedrich Schiller University Jena) was centrifuged at 4500 × *g* for 5 min, and the pellet was washed three times with cold 1.5 mmol L^{-1} phosphate buffered saline (PBS, pH 7.4). After dilution with PBS in a ratio of 1:7, aliquots of erythrocyte suspension were mixed 1:1 with the polymer solution and incubated in a water bath at 37 °C for 60 min. After centrifugation at 2400 × *g* for 5 min the hemoglobin release was determined by measuring the absorbance of the supernatant with a microplate reader at 544 nm wavelength. Complete hemolysis (100%) was achieved using 1% Triton X-100 serving as positive control. Thereby, PBS served as negative control (0%). A value less than 2% hemolysis rate was taken as nonhemolytic. Experiments were run in triplicate and were performed with three different batches of donor blood.

The hemolytic activity of the polycations was calculated as follows (eq 1):

$$\%\text{Hemolysis} = 100 \times \frac{(A_{\text{Sample}} - A_{\text{Negative control}})}{A_{\text{Positive control}}} \quad (1)$$

For the examination of the erythrocyte aggregation, the erythrocyte suspension was mixed with the same volume of polymer solution in a clear flat-bottomed 96-well plate. The cells were incubated at 37 °C for 2 h, and the absorbance was measured at 645 nm in a microplate reader. 25 kDa bPEI (50 μg mL^{-1}) was used as positive control, and as negative control, cells were treated with PBS. Absorbance values of the test solutions lower than negative control were regarded as aggregation. Experiments are the result of triplicates and were performed with three different donor blood batches.

Investigation of the Cellular Uptake. The evaluation of the nanogel uptake was performed with the cell line L929 (CCL-1, ATCC). In general, the cells were cultured in Dulbecco's modified Eagle's medium (DMEM) supplemented with 10% fetal calf serum (FCS), 100 U mL^{-1} penicillin and 100 μg mL^{-1} streptomycin at 37 °C in a humidified 5% CO_2 atmosphere. For the uptake studies, cells were seeded at 10^5 cells per mL in a 24-well plate and incubated for 24 h.

For the time-dependent uptake studies, cells were incubated with nanogels at a concentration of 0.5 mg mL^{-1} for 30 min to 24 h, whereas the concentration-dependent uptake was investigated over an incubation time of 24 h using nanogel concentrations in the range between 0.1 and 1 mg mL^{-1}. Cells incubated with culture medium only served as control. For uptake studies at low temperature, the cells were incubated with nanogels (0.5 mg mL^{-1}) for 4 h at 4 and 37 °C, respectively, and the internalization was monitored using FC analysis as described above.

■ ASSOCIATED CONTENT

Supporting Information

The Supporting Information is available free of charge on the ACS Publications website at DOI: 10.1021/acs.bioconjchem.7b00067.

Details on nanogel characterization regarding fluorescence, cellular uptake and biocompatibility (PDF)

■ AUTHOR INFORMATION

Corresponding Author

*E-mail: ulrich.schubert@uni-jena.de.

ORCID

Ulrich S. Schubert: 0000-0003-4978-4670

Present Addresses

[¶]Department of Chemistry, University of Warwick, Gibbet Hill Road, Coventry, CV4 7AL, United Kingdom.

[⊥]Department of Chemistry and Molecular Biology University of Gothenburg 40530 Gothenburg, Sweden.

Author Contributions

[#]Matthias Hartlieb and Tanja Bus contributed equally.

Notes

The authors declare no competing financial interest.

■ ACKNOWLEDGMENTS

T.B. acknowledges the German Federal Ministry of Education & Research (BMBF, #031A518B Vectura). CryoTEM investigations were performed at the cryoTEM facilities of the Jena Center for Soft Matter (JCSM). TEM facilities were funded by a grant of the DFG (German Research Foundation) and the EFRE (European Fund for Regional Development). MH gratefully acknowledges the German Research Foundation (DFG, GZ: HA 7725/1-1) for funding. U.S.S. and M.N.L. acknowledge German Federal Ministry of Education & Research (BMBF, #13NI3417, smart-dye-livery).

■ REFERENCES

(1) Duncan, R., and Vicent, M. J. (2013) Polymer therapeutics-prospects for 21st century: The end of the beginning. *Adv. Drug Delivery Rev. 65*, 60−70.

(2) Duncan, R., and Gaspar, R. (2011) Nanomedicine(s) under the Microscope. *Mol. Pharmaceutics 8*, 2101−2141.

(3) van Nostrum, C. F. (2011) Covalently cross-linked amphiphilic block copolymer micelles. *Soft Matter 7*, 3246−3259.

(4) Talelli, M., Rijcken, C. J. F., Hennink, W. E., and Lammers, T. (2012) Polymeric micelles for cancer therapy: 3 C's to enhance efficacy. *Curr. Opin. Solid State Mater. Sci. 16*, 302−309.

(5) Maeda, H., Greish, K., and Fang, J. (2006) The EPR effect and polymeric drugs: A paradigm shift for cancer chemotherapy in the 21st century, in *Polymer Therapeutics II* (Satchi-Fainaro, R., and Duncan, R., Eds.) pp 103−121, Springer, Berlin Heidelberg.

(6) Zhu, M., Nie, G., Meng, H., Xia, T., Nel, A., and Zhao, Y. (2013) Physicochemical Properties Determine Nanomaterial Cellular Uptake, Transport, and Fate. *Acc. Chem. Res. 46*, 622−631.

(7) Albanese, A., Tang, P. S., and Chan, W. C. W. (2012) The Effect of Nanoparticle Size, Shape, and Surface Chemistry on Biological Systems. *Annu. Rev. Biomed. Eng. 14*, 1−16.

(8) Adjei, I. M., Sharma, B., and Labhasetwar, V. (2014) Nanoparticles: Cellular Uptake and Cytotoxicity, in *Nanomaterial: Impacts on Cell Biology and Medicine* (Capco, G. D., and Chen, Y., Eds.) pp 73−91, Springer, Netherlands, Dordrecht.

(9) Cho, E. C., Xie, J., Wurm, P. A., and Xia, Y. (2009) Understanding the Role of Surface Charges in Cellular Adsorption versus Internalization by Selectively Removing Gold Nanoparticles on the Cell Surface with a I2/KI Etchant. *Nano Lett. 9*, 1080−1084.

(10) Hauck, T. S., Ghazani, A. A., and Chan, W. C. W. (2008) Assessing the Effect of Surface Chemistry on Gold Nanorod Uptake, Toxicity, and Gene Expression in Mammalian Cells. *Small 4*, 153−159.

(11) Yue, Z.-G., Wei, W., Lv, P.-P., Yue, H., Wang, L.-Y., Su, Z.-G., and Ma, G.-H. (2011) Surface Charge Affects Cellular Uptake and Intracellular Trafficking of Chitosan-Based Nanoparticles. *Biomacromolecules 12*, 2440−2446.

DOI: 10.1021/acs.bioconjchem.7b00067
Bioconjugate Chem. 2017, 28, 1229−1235

(12) He, C., Hu, Y., Yin, L., Tang, C., and Yin, C. (2010) Effects of particle size and surface charge on cellular uptake and biodistribution of polymeric nanoparticles. *Biomaterials 31*, 3657−3666.
(13) Rinkenauer, A. C., Schubert, S., Traeger, A., and Schubert, U. S. (2015) The influence of polymer architecture on in vitro pDNA transfection. *J. Mater. Chem. B 3*, 7477−7493.
(14) Fröhlich, E. (2012) The role of surface charge in cellular uptake and cytotoxicity of medical nanoparticles. *Int. J. Nanomed. 7*, 5577−5591.
(15) Xia, T., Kovochich, M., Liong, M., Meng, H., Kabehie, S., George, S., Zink, J. I., and Nel, A. E. (2009) Polyethyleneimine Coating Enhances the Cellular Uptake of Mesoporous Silica Nanoparticles and Allows Safe Delivery of siRNA and DNA Constructs. *ACS Nano 3*, 3273−3286.
(16) Kronek, J., Kroneková, Z., Lustoň, J., Paulovičová, E., Paulovičová, L., and Mendrek, B. (2011) In vitro bio-immunological and cytotoxicity studies of poly(2-oxazolines). *J. Mater. Sci.: Mater. Med. 22*, 1725−1734.
(17) Luxenhofer, R., Sahay, G., Schulz, A., Alakhova, D., Bronich, T. K., Jordan, R., and Kabanov, A. V. (2011) Structure-property relationship in cytotoxicity and cell uptake of poly(2-oxazoline) amphiphiles. *J. Controlled Release 153*, 73−82.
(18) Kronek, J., Paulovičová, E., Paulovičová, L., Kroneková, Z., and Lustoň, J. (2012) Immunomodulatory efficiency of poly(2-oxazolines). *J. Mater. Sci.: Mater. Med. 23*, 1457−1464.
(19) Woodle, M. C., Engbers, C. M., and Zalipsky, S. (1994) New Amphipatic Polymer-Lipid Conjugates Forming Long-Circulating Reticuloendothelial System-Evading Liposomes. *Bioconjugate Chem. 5*, 493−496.
(20) Zalipsky, S., Hansen, C. B., Oaks, J. M., and Allen, T. M. (1996) Evaluation of blood clearance rates and biodistribution of poly(2-oxazoline)-grafted liposomes. *J. Pharm. Sci. 85*, 133−137.
(21) Wyffels, L., Verbrugghen, T., Monnery, B. D., Glassner, M., Stroobants, S., Hoogenboom, R., and Staelens, S. (2016) μPET imaging of the pharmacokinetic behavior of medium and high molar mass 89Zr-labeled poly(2-ethyl-2-oxazoline) in comparison to poly(ethylene glycol). *J. Controlled Release 235*, 63−71.
(22) Guillerm, B., Monge, S., Lapinte, V., and Robin, J.-J. (2012) How to modulate the chemical structure of polyoxazolines by appropriate functionalization. *Macromol. Rapid Commun. 33*, 1600−1612.
(23) Wilson, P., Ke, P. C., Davis, T. P., and Kempe, K. (2016) Poly(2-oxazoline)-based micro- and nanoparticles: A review. *Eur. Polym. J.*, 1 DOI: 10.1016/j.eurpolymj.2016.09.011.
(24) Hartlieb, M., Kempe, K., and Schubert, U. S. (2015) Covalently cross-linked poly(2-oxazoline) materials for biomedical applications - from hydrogels to self-assembled and templated structures. *J. Mater. Chem. B 3*, 526−538.
(25) Legros, C., Wirotius, A.-L., De Pauw-Gillet, M.-C., Tam, K. C., Taton, D., and Lecommandoux, S. (2015) Poly(2-oxazoline)-Based Nanogels as Biocompatible Pseudopolypeptide Nanoparticles. *Biomacromolecules 16*, 183−191.
(26) Hartlieb, M., Pretzel, D., Wagner, M., Hoeppener, S., Bellstedt, P., Gorlach, M., Englert, C., Kempe, K., and Schubert, U. S. (2015) Core cross-linked nanogels based on the self-assembly of double hydrophilic poly(2-oxazoline) block copolymers. *J. Mater. Chem. B 3*, 1748−1759.
(27) Hartlieb, M., Pretzel, D., Kempe, K., Fritzsche, C., Paulus, R. M., Gottschaldt, M., and Schubert, U. S. (2013) Cationic poly(2-oxazoline) hydrogels for reversible DNA binding. *Soft Matter 9*, 4693−4704.
(28) Jackson, A. W., and Fulton, D. A. (2012) Triggering Polymeric Nanoparticle Disassembly through the Simultaneous Application of Two Different Stimuli. *Macromolecules 45*, 2699−2708.
(29) Song, A., Zhang, J., Zhang, M., Shen, T., and Tang, J. a. (2000) Spectral properties and structure of fluorescein and its alkyl derivatives in micelles. *Colloids Surf., A 167*, 253−262.
(30) Humphry-Baker, R., Graetzel, M., and Steiger, R. (1980) Drastic fluorescence enhancement and photochemical stabilization of cyanine dyes through micellar systems. *J. Am. Chem. Soc. 102*, 847−848.
(31) Wu, W.-C., Chen, C.-Y., Tian, Y., Jang, S.-H., Hong, Y., Liu, Y., Hu, R., Tang, B. Z., Lee, Y.-T., Chen, C.-T., et al. (2010) Enhancement of Aggregation-Induced Emission in Dye-Encapsulating Polymeric Micelles for Bioimaging. *Adv. Funct. Mater. 20*, 1413−1423.
(32) Verma, A., and Stellacci, F. (2010) Effect of Surface Properties on Nanoparticle−Cell Interactions. *Small 6*, 12−21.
(33) Rejman, J., Oberle, V., Zuhorn, I. S., and Hoekstra, D. (2004) Size-dependent internalization of particles via the pathways of clathrin- and caveolae-mediated endocytosis. *Biochem. J. 377*, 159−169.
(34) Delgado, A. V., Gonzalez-Caballero, F., Hunter, R. J., Koopal, L. K., and Lyklema, J. (2007) Measurement and interpretation of electrokinetic phenomena. *J. Colloid Interface Sci. 309*, 194−224.
(35) Ohshima, H. (1994) A Simple Expression for Henry's Function for the Retardation Effect in Electrophoresis of Spherical Colloidal Particles. *J. Colloid Interface Sci. 168*, 269−271.

DOI: 10.1021/acs.bioconjchem.7b00067
Bioconjugate Chem. 2017, 28, 1229−1235

Supporting Information

Tailoring Cellular Uptake and Fluorescence of Poly(2-oxazoline)-based Nanogels

Matthias Hartlieb,[a,b,‡,†] Tanja Bus,[a,b,‡] Joachim Kübel,[c,d] David Pretzel,[a,b] Stephanie Hoeppener,[a,b] Meike N. Leiske,[a,b] Kristian Kempe,[a,b,†] Benjamin Dietzek,[c,d] Ulrich S. Schubert[a,b,*]

[a] Laboratory of Organic and Macromolecular Chemistry (IOMC), Friedrich Schiller University Jena, Humboldtstrasse 10, 07743, Jena, Germany

[b] Jena Center for Soft Matter (JCSM), Friedrich Schiller University Jena, Philosophenweg 7, 07743, Jena, Germany

[c] Institute of Physical Chemistry (IPC) and Abbe Center of Photonics, Friedrich Schiller University Jena, Helmholtzweg 4, 07743 Jena, Germany

[d] Leibniz Institute of Photonic Technology (IPHT), Albert-Einstein-Str. 9, 07745 Jena, Germany

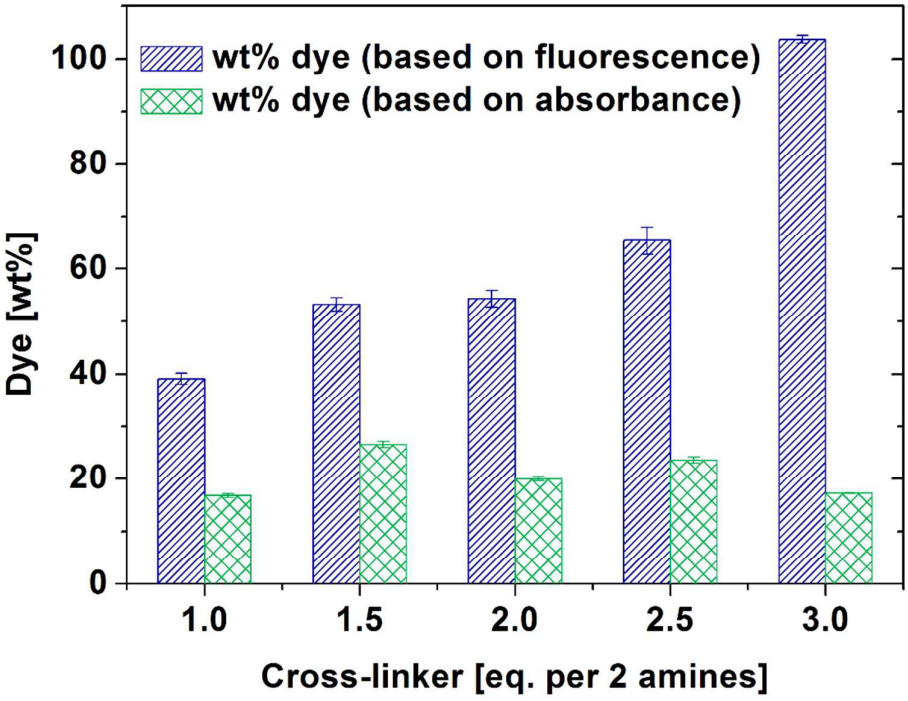

Figure S1: Dye loading of nanogels determined using the fluorescence and the absorbance of 6AF.

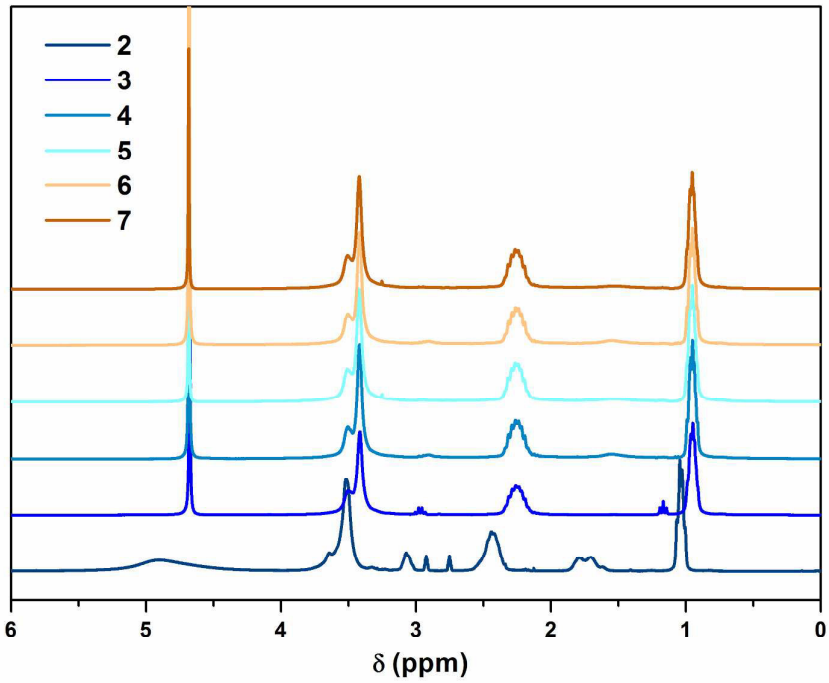

Figure S2: ^{1}H-NMR spectra of polymer **2** (measured in deuterated DMF) and nanogels **3** to **7** (measured in D_2O).

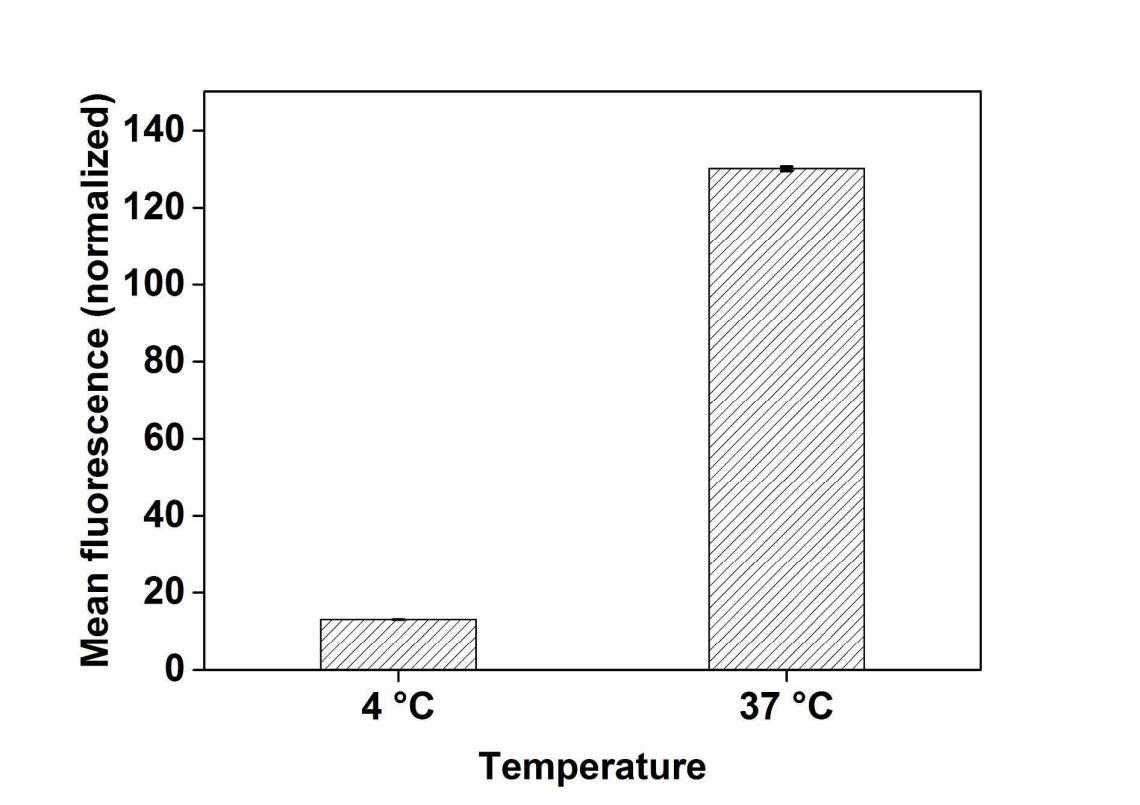

Figure S3: Temperature dependent cellular internalization of nanogel **3** (0.5 mg ml^{-1}) after an incubation period of 4 h.

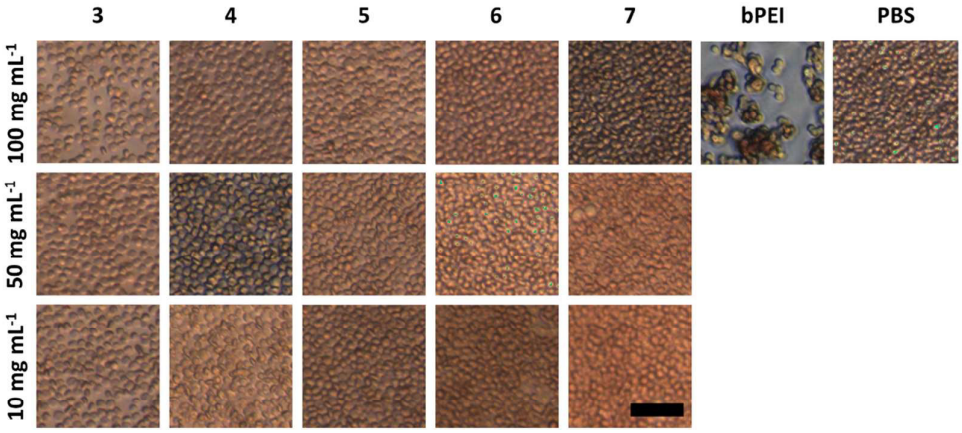

Figure S4: Microscope images of red blood cells treated with nanogels, bPEI (25 kDa, 50 µg mL^{-1},positive control) and PBS (negative control). Scale bar = 50 µm.

Publication Pub8

Tumor targeting with pH-responsive poly(2-oxazoline)-based nanogels for metronomic doxorubicin treatment

D. Hoelzer, M. N. Leiske, M. Hartlieb, T. Bus, D. Pretzel, S. Hoeppener, K. Kempe, R. Thierbach, U. S. Schubert

Oncotarget **2018**, *9*, 22316-22331.

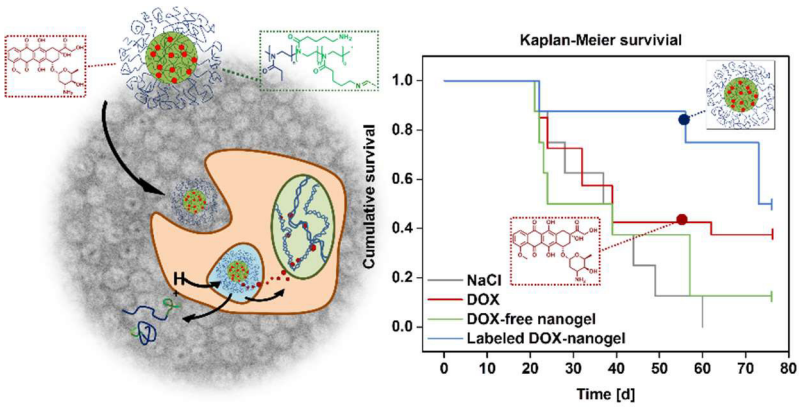

www.oncotarget.com Oncotarget, 2018, Vol. 9, (No. 32), pp: 22316-22331

Research Paper

Tumor targeting with pH-responsive poly(2-oxazoline)-based nanogels for metronomic doxorubicin treatment

Doerte Hoelzer[1,*], Meike N. Leiske[2,3,*], Matthias Hartlieb[2,3,4], Tanja Bus[2,3], David Pretzel[2,3], Stephanie Hoeppener[2,3], Kristian Kempe[2,3,5], René Thierbach[1] and Ulrich S. Schubert[2,3]

[1]Institute of Nutrition, Friedrich Schiller University Jena, 07743 Jena, Germany

[2]Laboratory of Organic and Macromolecular Chemistry (IOMC), Friedrich Schiller University Jena, 07743 Jena, Germany

[3]Jena Center for Soft Matter (JCSM), Friedrich Schiller University Jena, 07743 Jena, Germany

[4]Current address: Institute of Biomaterial Science, Helmholtz-Zentrum Geesthacht, 14513 Teltow, Germany

[5]Current address: Monash Institute of Pharmaceutical Sciences, Monash University, Parkville, VIC 3052, Australia

[*]These authors contributed equally to the work

Correspondence to: *Ulrich S. Schubert,* ***email:*** *ulrich.schubert@uni-jena.de*

Keywords: *poly(2-oxazoline); doxorubicin; drug delivery; nanogel; metronomic*

Received: *October 18, 2017* ***Accepted:*** *February 24, 2018* ***Published:*** *April 27, 2018*

ABSTRACT

The synthesis of a new nanogel drug carrier system loaded with the anti-cancer drug doxorubicin (DOX) is presented. Poly(2-oxazoline) (POx) based nanogels from block copolymer micelles were cross-linked and covalently loaded with DOX using pH-sensitive Schiff' base chemistry. DOX loaded POx based nanogels showed a toxicity profile comparable to the free drug, while unloaded drug carriers showed no toxicity. Hemolytic activity and erythrocyte aggregation of the drug delivery system was found to be low and cellular uptake was investigated by flow cytometry and fluorescence microscopy. While the amount of internalized drug was enhanced when incorporated into a nanogel, the release of the drug into the nucleus was delayed. For *in vivo* investigations the nanogel drug delivery system was combined with a metronomic treatment of DOX. Low doses of free DOX were compared to equivalent DOX loaded nanogels in a xenograft mouse model. Treatment with POx based nanogels revealed a significant tumor growth inhibition and increase in survival time, while pure DOX alone had no effect on tumor progression. The biodistribution was investigated by microscopy of organs of mice and revealed a predominant localization of DOX within tumorous tissue. Thus, the POx based nanogel system revealed a therapeutic efficiency despite the low DOX concentrations and could be a promising strategy to control tumor growth with fewer side effects.

INTRODUCTION

In modern oncology it is a major challenge to deliver therapeutic agents more safely and directly to the tumor. Doxorubicin (DOX) is an anthracycline antibiotic and is one of the most effective as well as commonly used chemotherapeutic drugs. It is used as a first-line treatment of various types of cancer, including hematologic malignancies, breast and ovarian carcinoma, neuroblastoma as well as soft tissue and bone sarcoma. The antitumor activity of DOX can be triggered by different mechanisms: (i) By intercalating into DNA strands and (ii) prevention of replication and transcription of DNA by inhibiting the enzyme topoisomerase II or, (iii) formation of free radicals leading to membrane and DNA damage as well as apoptosis [1, 2] However, the clinical benefit of DOX is limited by different side effects, *i.e.* cardiotoxicity [3, 4].

The use of nanosized drug carriers is rapidly emerging and can help to reduce these side effects as well as improve the drugs solubility [5], blood circulation time [6] and tissue distribution [7]. In particular nanogels, hydrogel nanoparticles with crosslinked hydrophilic polymers, offer several advantages for their use as a drug delivery system [8]. For this reason, the utilization of nanocarriers (*e.g.* nanoparticles) in terms of delivery of anti-cancer drugs has increased significantly during the last years [9–11]. Nanogels enable a high drug loading capacity, can protect and shield drugs until they reach their desired target and are highly biocompatible and biodegradable [12]. Due to the leaky structure of cancerous tissue together with the lack of effective lymphatic drainage, nanogels tend to accumulate in the tumor tissue known as enhanced permeability and retention (EPR) effect [13]. To achieve an effective delivery of the drug to the tumor it is also very important to prevent a premature disassembly or drug release from the carrier. A common strategy is the use of covalently cross-linked drug delivery systems (*i.e.* core cross-linked micelles or other nanogels) and a likewise covalently but reversibly attached drug [14–16].

The majority of drug delivery systems utilize a poly(ethylene glycol) (PEG) shell to shield themselves from unspecific interactions with healthy tissue or the components of the blood stream. However, reports about complement activation by PEG [17–19] and vacuolation [20–22] in the body have raised concerns about safety and reliability of the polymer. Poly(2-oxazoline)s (POx) represent a promising alternative as they are biocompatible, [13, 23, 24] and show a stealth behavior similar to PEG when the side chain substitution is chosen correctly [25, 26]. Recent studies elucidate the pharmacokinetic behavior of the polymer dependent on its molar mass, demonstrating superior behavior when compared to PEG [27, 28]. The first clinical study using a POx derivative is currently ongoing (SER-214, phase I) [14] and the polymer was approved by the federal food administration (FDA) as an indirect additive used in food contact substances (21CFR175.105) in 2016. In addition, POx based formulations of the cancer drug paclitaxel show great promise *in vivo* [5]. One major advantage of the polymer over PEG is its versatile functionalization chemistry [29] enabling easy access to a multitude of functional polymers and materials [15]. POx based nanogels have been reported, [30] but far have not been exploited for the use as a cancer drug delivery system.

Recently, we reported the synthesis of nanogels based on double hydrophilic POx block copolymers. They were based on micellar architecture with a cationic block forming the core and a poly(2-ethyl-2-oxazoline) (P(EtOx)) shell. The material was cross-linked and dye loaded by imine bonds [31]. The materials showed excellent biocompatibility and their charge and cellular uptake could be tailored by varying the cross-linking density [32]. Within this contribution, DOX is to be used as a payload in order to increase the efficiency and specificity of the drug towards cancer cells *in vitro* and *in vivo*. Drug attachment as well as cross-linking is accomplished using pH sensitive Schiff's base chemistry, to enable intracellular drug release [31, 33].

In addition to the drug delivery system itself, the regime of drug administration is of particular interest. Conventional chemotherapy relies on the administration of the maximum tolerated dose (MTD) to achieve the desired effect without unacceptable side effects. Because of the high toxicity and potential development of chemoresistance other concepts of drug administration are evolving. Metronomic chemotherapy is defined as a chronic administration of low doses of cytotoxic agents and can help to improve the efficiency of cancer treatment [34, 35]. Herein we report the straightforward synthesis of a POx based nanogel in a one pot approach, reversibly linked to (or loaded with) the anti-cancer drug DOX. The drug delivery system is biocompatible and able to release its payload as shown by *in vitro* investigations. In addition, *in vivo* experiments in mice show a promising increase in survival rate as compared to pure DOX at relatively low concentrations.

RESULTS AND DISCUSSION

Synthesis and loading of the poly(2-oxazoline)-based nanogels

Polymers were synthesized by sequential monomer addition using microwave technology employing 2-ethyl-2-oxazoline (EtOx) for the first and 2-(4-((*tert*-butoxycarbonyl)amino)butyl)-2-oxazoline (BocOx) for the second block. The second monomer was introduced within a glove box under nitrogen atmosphere to reduce termination prior to block extension. P($EtOx_{98}$-*b*-$BocOx_{32}$) (1) was synthesized with a narrow dispersity of Đ = 1.07, which did not increase drastically after deprotection of the amine groups to yield poly(2-ethyl-2-oxazoline)-*block*-(poly(2-(4-amino)butyl)-2-oxazoline)) (P(EtOx-*b*-AmOx)) (Supplementary Table 1, Supplementary Scheme 1, Supplementary Figures 1–2). While size exclusion chromatography (SEC) measurements of initial polymers could be performed in chloroform, deprotected P($EtOx_{98}$-*b*-$AmOx_{32}$) (2) had to be measured in *N*,*N*-dimethylacetamide (DMAc), explaining the difference in molar mass compared to the precursor polymer.

While DOX is fluorescent and can, therefore, be tracked directly within cells, its emission is highly dependent on the environment [36, 37]. To circumvent this issue and create nanogels, which can be tracked independent of their DOX release, polymer 2 was labeled with a fluorescent dye prior to the nanogel preparation. To this end, a dye with a near-infra red fluorescence (Alexafluor 660) was chosen to not interfere with the fluorescence of the drug. The dye possesses a *N*-hydroxy succinimide

(NHS) ester function, able to react with the amine groups of the P(AmOx) block of polymer 2. One equivalent of dye per polymer chain was applied to retain a sufficient amount of free amine groups for further self-assembly processes, and cross-linking reactions. To separate the labeled polymer 3 from unreacted dye molecules, precipitation in diethyl ether, as well as dialysis in deionized water was performed. The success of the attachment was confirmed by SEC measurements (Supplementary Figure 2) comparing the refractive index (RI). and UV traces of the polymer. The lack of an UV signal at high elution volumes indicates the absence of unbound dye. The fluorescence maximum of the dye coupled to the polymer was found to be similar to the free chromophore (Supplementary Figure 3). The coupling efficiency as determined by the emission of the polymer was determined *via* UV/Vis measurements and found to be 30%.

The self-assembly of these systems to form polymeric micelles was conducted as reported previously [31]. Briefly, the polymers were dissolved in chloroform, which leads to the formation of micellar structures comprising a P(AmOx) core and a P(EtOx) shell. Cross-linking was performed using glutaraldehyde (GA) resulting in the formation of nanogels. As previous investigations [32] showed a reduced cellular uptake of systems with a higher cross linking density, three equivalents of cross-linker (in respect to amine groups) were used. A reduced positive charge density is supposed to lead to prolonged circulation times *in vivo*. Drug loading was performed by reacting excessive aldehyde functionalities with DOX. The free amine groups of the molecule reacts with free aldehyde groups of the cross-linker resulting in a covalent attachment to the nanogel (Figure 1). As the imine function, which stabilizes the nanogel core and the drug, is labile at low pH values, created systems are expected to be disintegrating. Alexafluor-labeled (referred to as "labeled DOX-nanogel"), as well as unlabeled DOX-containing (referred to as "unlabeled DOX-nanogel") nanogels were produced. As a non-toxic equivalent DOX-free 6-aminofluorescein (6AF) loaded nanogels (referred to as "DOX-free nanogel") were synthesized using the same method.

Characterization of the nanogels

Due to the fact that the drug is not encapsulated into, but covalently bound to the nanogel, the term loading efficiency is used instead of the commonly utilized encapsulation efficiency. To determine the loading efficiency of produced nanogels the absorbance of the system was measured and compared to a calibration of the small molecule (Supplementary Figure 4). In the case of DOX-free nanogels, absorbance was measured at λ_{ex} = 490 nm whereas for labeled and unlabeled DOX-nanogels the absorbance was detected at λ_{ex} = 480 nm. A three-fold difference in mass loading was observed between fluorescein (17 wt%) and DOX (5 to 6 wt%) immobilization, (Table 1), while loading was relatively independent on the presence of Alexafluor 660 labels on the polymer chain. The difference can be explained by the nature of the cargo molecules. While both possess an amine functionality, which can be coupled covalently to aldehyde functionalities, 6AF also possesses a carboxylic acid function, which can interact in an electrostatic way with the positively charged core of the nanogel, leading to an increase in loading efficiency by electrostatic interaction.

As shown in Supplementary Figure 4, the fluorescence spectrum of DOX broadens significantly when incorporated into nanogels. The emission properties of the chromophore are known to be highly dependent on

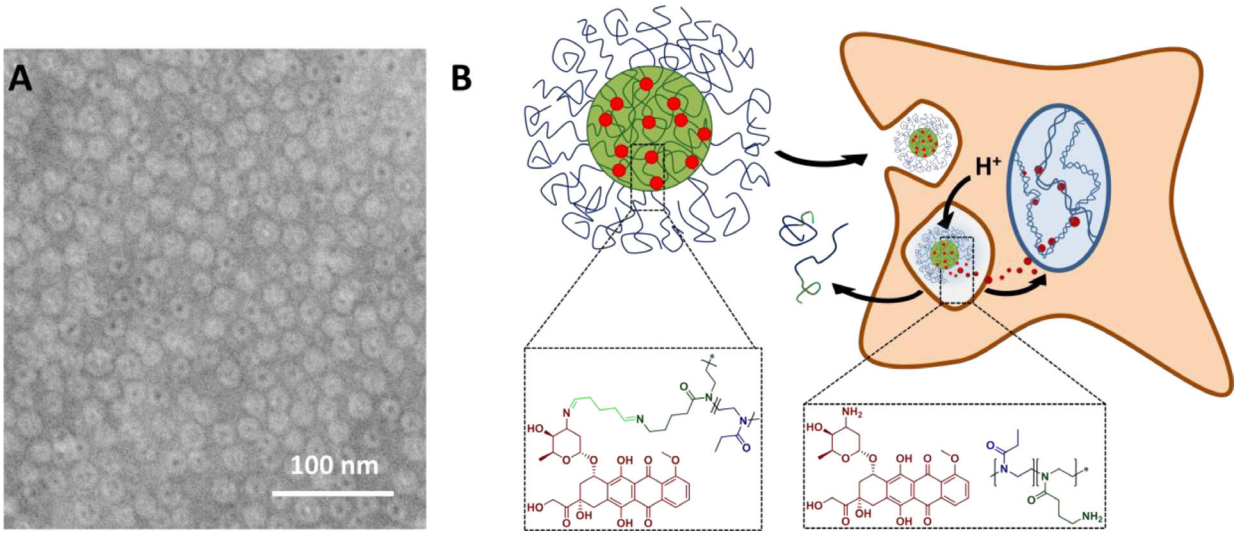

Figure 1: (**A**) Schematic representation of nanogels obtained from P($EtOx_{98}$-*b*-$BocOx_{32}$) with a P(AmOx) core loaded with DOX and a P(EtOx) shell, cryo-TEM image of unlabeled DOX-nanogel in water (scale bar represents 100 nm), and (**B**) a schematic depiction of the drug delivery route of DOX.

Table 1: Analytical data of nanogels formed by the self-assembly of polymers 2 and 3

Sample	Precursor polymer	Capping agent	Size (DLS) [d, nm]	ζ [mV]	Content of capping agent [wt%]	Size (cryoTEM) [d, nm]
DOX-free nanogel	2	6AF	24	7	17	15
Unlabeled DOX-nanogel	2	DOX	26	18	5	20
Labeled DOX-nanogel	3	DOX	15	25	6	15

DLS and zeta potential values are determined in water. Sizes determined by DLS are derived from the number distribution.

environmental factors [36, 37]. The presence of amine groups within the core of the nanogel and other factors are likely to influence the fluorescence of DOX. In the case of the Alexafluor 660 labeled systems a high wavelength shoulder is visible in the emission spectrum indicating the presence of the near-IR dye. Upon excitation at λ_{ex} = 600 nm a pronounced fluorescence with a maximum at λ_{em} = 675 nm can be observed (Supplementary Figure 5).

To visualize the synthesized nanostructures, cryoTEM measurements were performed (Figure 1, Supplementary Figure 6). The images showed monodisperse spherical structures for all samples. For DOX-free and labeled DOX-nanogels an average diameter of 15 nm was obtained while the diameter of unlabeled DOX-nanogels was found to be 20 nm (Table 1, Supplementary Figure 6B and 6C). In addition, in the case of unlabeled DOX-nanogels a core-shell structure could be visualized showing a dark center and a lighter corona. The core is likely to be compact in water due to the presence of the hydrophobic DOX, whereas the shell is water swollen resulting in a lower contrast. For DOX-free nanogels and labeled DOX-nanogels this structure could not be visualized, which is possibly a result of the dense packing of nanostructures on the TEM grid. If the P(EtOx) shell is partially not visible due to overlap and lacking contrast this could explain the size discrepancy between the nanogels. The size was confirmed by dynamic light scattering (DLS) measurements (Table 1). Zeta potential measurements show positive values for all nanogels, which was expected due to the cationic nature of the micellar core. Fluorescein loaded nanogels show a lower zeta potential as compared to DOX loaded samples, which can be explained by the compensation of cationic charges by the anionic nature of fluorescein. This finding is in line with the increased loading of fluorescein quenched nanogels as compared to structures with DOX as a cargo.

The most important requirement for a drug carrier is the site specific release of the drug. As cargo molecules within the produced nanogels are attached *via* imine bonds, which are known to be reversible at pH values below 7, [38] a release within endosomal or lysosomal cellular compartments is likely as previously shown by M. Hruby and co-workers [39]. In order to investigate the stability of the nanogels at 4° C (storage temperature) and 37° C (human body temperature) at a pH value of 7.4, the z-average and the polydispersity index (PDI) as well as the number mean size value of the nanogels was determined using DLS measurements (Supplementary Figure 7). Nanogels were determined to be stable during the entire measurement time of two weeks, revealing no significant changes in size or PDI. Furthermore, it was necessary to determine the possibility of a drug release at a lysosomal pH value of 5. J. S. Basuki *et al.* previously investigated iron oxide nanoparticles that were loaded with DOX *via* pH sensitive imine bond *via* DLS measurements, revealing an increase in the particle size at a pH value of 5, caused by drug release [40]. Since glycine was determined to be essential for cancer cell proliferation and, consequently, is present within tumorous compartments, [41] DLS investigations of the labeled DOX-nanogels were conducted in phosphate buffered saline (PBS) and glycine was added representing a competitive amine to the imine bond (Supplementary Figure 8). While labeled DOX-nanogels did not reveal significant changes in size or PDI at a pH value of 7.4, both increase at a pH value of 5.0. Herein, it is noteworthy that after a second addition of glycine, this trend further increases. This might be beneficial for triggering the endosomal burst, as recently shown in gene transfection applications within our group [42]. In order to obtain additional qualitative information about the release of DOX from the labeled DOX-nanogel, diffusion order spectroscopy (DOSY) NMR measurements were also conducted (Supplementary Figures 9 and 10). Hereby, the diffusion coefficients of labeled DOX-nanogels in NaCl were compared to labeled DOX-nanogels in 150 mM PBS (pH = 5.0), which contained glycine. Pure DOX and glycine were evaluated for comparison. A stacking of the spectra suggests the release of DOX at pH 5.0, while no DOX release could be determined in NaCl (Supplementary Figure 9). Unfortunately, a quantification of the DOX release from the labeled DOX-nanogels was not possible by the applied methods.

In vitro cytotoxicity of nanogels

One major mechanism of DOX is the intercalation into the minor groove of DNA [3]. Therefore, the molecule

must penetrate the barrier of the nucleus to take effect. In order to verify whether DOX loaded nanogels are able to release DOX within cells, the cytotoxicity of labeled DOX-nanogels in comparison to free DOX and DOX-free nanogels was investigated (Figure 2, Supplementary Figure 11). The influence of the materials on the cell viability was probed using two different cell lines. L292 mouse fibroblasts are known to be sensitive to cytotoxic substances [43] and are used in the general assessment of biocompatibility (ISO 10993-5). Cytotoxicity tests were also performed with the human colorectal cancer cells HT-29, due to their ability to form tumors in nude mice and their usage for the nanogel *in vivo* studies that are described in later sections.

Cells were treated with nanogels or pure drug at varying concentrations for 24 h (Supplementary Figure 11) and 72 h (Figure 2), respectively. The amount of DOX loaded nanogels was chosen, so that the concentration of cargo drug matches the concentration of the free drug used for the tests. The concentration of DOX-free nanogels used, was identical to its DOX carrying equivalent in order to investigate the influence of the bare drug delivery system. DOX-free nanogels showed no adverse effects on both cell lines independent of incubation time or concentration. This was expected as P(EtOx) is considered to be biocompatible [13, 23, 24] and proves that neither cationic charges, nor potentially released 6AF influence the metabolism of the cells in a negative way. In contrast free DOX, as well as labeled DOX-nanogels, both show a time- and concentration-dependent decrease in cell viability for both cell lines. The effect is more pronounced for L929 mouse fibroblasts as they are more sensitive to cytotoxic effects. A 72 h treatment of L929 cells (Figure 2A) with labeled DOX-nanogels showed an increased cytotoxicity revealing an IC_{50} value of 0.043 µg mL^{-1} compared to a 24 h treatment (Supplementary Figure 11). Cytotoxicity of pure DOX was found to be lower, with an IC_{50} value of 0.547 µg mL^{-1} (72 h). This might be attributed to an enhanced internalization of the nanogels compared to the free drug [44]. For HT-29 cells (Figure 2B) this difference is less pronounced, with IC_{50} values of labeled DOX-nanogels of 0.752 µg mL^{-1} and pure DOX of 1.998 µg mL^{-1}, respectively. From the reduced viability of cells a release of DOX from the nanogels can be assumed, which is essential for the known toxic effect of the drug.

Cellular uptake and biocompatibility *in vitro*

To investigate whether the improved performance of nanogels is a result of an enhanced cellular uptake, flow cytometry measurements were performed after incubation with labeled DOX-nanogels and free DOX (Figure 3A and Supplementary Figure 12). HT-29 cells were used for the experiments as an *in vitro* cancer model, which was later used for xenograft mouse experiments. The fluorescence of DOX was quantified to determine the amount of DOX internalized within the cells. To elucidate the nature of uptake (energy dependent *vs.* energy independent) the experiments were performed at 37° C and 4° C [45], respectively. For an energy dependent uptake, a significant decrease of the amount of internalized drug would be expected as the metabolism of cells at 4° C is considerably slowed down. Incubation of HT-29 cells with labeled DOX-nanogels or pure DOX at 4° C reduced the cellular uptake compared to an incubation at 37° C. Therefore, cellular uptake seems to be energy-dependent, which would suggest an uptake by endocytosis. Additionally, cells treated with labeled DOX-nanogels possessed a higher fluorescence signal after 24 h treatment at 37° C compared to DOX

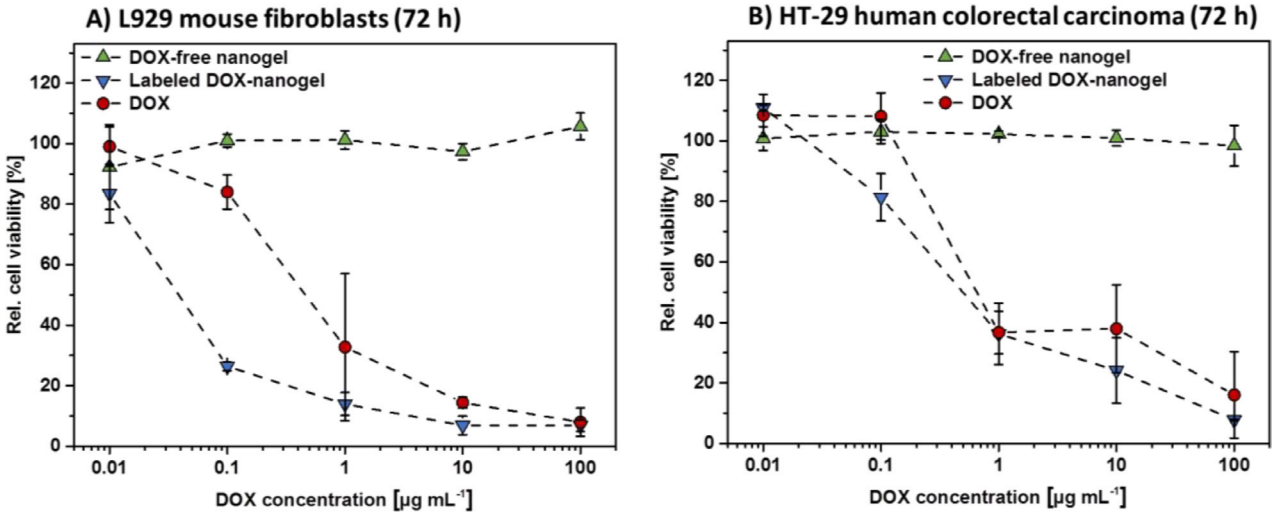

Figure 2: Cytotoxicity of DOX-free nanogels, labeled DOX-nanogels as well as free DOX were determined by XTT assay. L292 mouse fibroblasts (**A**) as well as HT-29 human colorectal carcinoma cells (**B**) were incubated for 72 h with testing substances. DOX-nanogels were used at a concentration where the amount of loaded drug resembles the amount of DOX used per data point (polymer concentration 17 times higher than DOX concentration). DOX-free nanogels were used at the same polymer concentration as DOX-nanogels. Data are expressed as mean ± SD of six determinations.

alone. These findings suggest a higher accumulation of the nanogels in the cells [44, 46] caused by a P-glycoprotein mediated efflux of the pure drug, mostly known from multi drug resistant breast cancer cells [47, 48].

Besides cellular uptake and intracellular drug release, a further requirement of a drug carrier that strives to target cancerous tissue by *i.e.* the EPR effect is a low level of unspecific interaction with *i.e.* healthy tissue or the components of the blood stream. For this reason P(EtOx) was chosen as a shell material as it is well-known that P(EtOx) exhibits stealth properties and shows a blood circulation behavior *in vivo* similar to PEG [27] One prerequisite for a prolonged circulation in the blood stream is the hemocompatibility of the compound comprising the absence of blood clotting as well as lysis of red blood cells. The biocompatibility of labeled DOX-nanogels was tested against sheep blood (Figure 3B and 3C). The compound induced no major aggregation of red blood cells as compared to the positive control branched poly(ethylene imine) (*b*PEI) (25 kDa) as demonstrated in Figure 3B. While the high cationic charge density of PEI results in blood clotting, the cationic charges of the nanogels are shielded within the core of the structure and cannot directly lead to a precipitation of erythrocytes. Also, hemolysis as measured by the absorbance intensity in the blood plasma caused by leakage of hemoglobin release from red blood cells supports the biocompatibility of the drug carrier. While nanogels show slight hemoglobin release of erythrocytes, the total amount as compared to the surfactant Triton-X100 which served as a positive control is well below 2%, which is generally considered as a threshold for hemolytic activity (according to the ASTM F756-00 standard).

To elucidate the uptake and intracellular activity of the nanogels further, their intracellular localization in L929 (Supplementary Figure 13) and HT-29 cells (Figure 4) was investigated using confocal laser scanning microscopy (CLSM). The nucleus was stained using Hoechst 33342 in order to examine its colocalization with DOX, which is indicative for release and activity of the drug. Lysosomal cellular compartments were stained using LysoTracker Green DND-26 and DOX was monitored *via* its fluorescence between λ_{em} = 600 to 650 nm. In addition, the polymer was tracked using the attached Alexafluor label measuring the emission between λ_{em} = 725 to 800 nm (Supplementary Figure 14). A first measurement was conducted after 6 h (Figure 4). Free DOX mainly shows a diffuse localization in the cytosol but is also to a certain extend present in the nucleus. Previous studies already reported a successful uptake and nucleus co-localization of DOX after 3 h incubation time, while the drug in polymersomes exhibited significantly longer times to enter the cell nucleus [46, 49]. In contrast, DOX-nanogels do not show a colocalization with the staining of the nucleus. For the labeled DOX- nanogels the overlap between red and green channel as well as the dotted structure of the signal suggests a lysosomal localization, which indicates an endocytic uptake mechanism [50] The presence of a polymer signal at the same position indicates that these signals represent intact nanogels that have not yet released the drug or been degraded.

Previous studies within our group already showed slower drug accumulation of the drug within the nucleus when using polymeric nanoparticles as drug delivery scaffolds [51]. For this reason, a second set of images was taken after 24 h incubation. After this time, the free drug is mostly localized in the nucleus of the cell. It can be assumed that DOX has either intercalated into the DNA in the nucleus or was excreted by the cells. However, also in the case of labeled DOX-nanogels a release of DOX into the nucleus was observed. The, in comparison to the DOX fluorescence, faint signal of the polymer suggests a partial degradation of the micelles. In addition, the signal is mostly associated with an extra nuclear localization. For longer incubation times it was increasingly difficult to locate intact cells for imaging due to the toxicity of the drug loaded system.

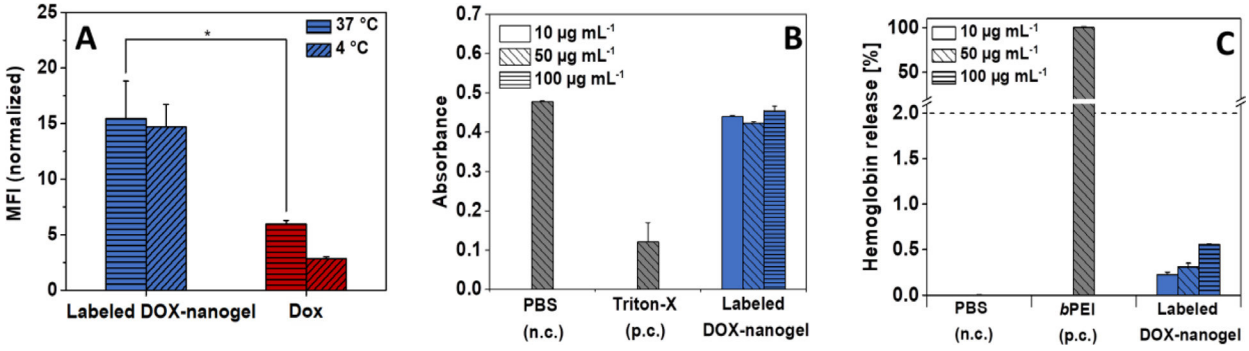

Figure 3: (**A**) Cellular uptake of DOX and labeled DOX-nanogels into HT-29 cells (0.01 mg mL^{-1}) in dependence on the incubation time and temperature. Statistical differences are displayed as $^{*}p < 0.05$ and according to a Student's *t*-test. For amount of fluorescent cells see Supplementary Figure 12. (**B**) Erythrocyte aggregation of DOX-nanogels compared to PBS (negative control) and branched poly(ethylene imine) (positive control) using sheep blood of three different donors. (**C**) Hemolytic activity of DOX-nanogels compared to PBS (negative control) and *b*PEI (positive control) using sheep blood of three different donors.

These results suggest that the uptake of nanogels is partially realized through endocytosis and that the material is degraded intracellularly, which leads to a release of the drug. Toxicity levels of the drug delivery system as well as co-localization studies indicate an accumulation of DOX in the nucleus after delivery to the cell. The kinetic as compared to the free drug is markedly slowed, which is probably associated to the release kinetic from the nanogel. An additional reason could be found in the dependence of the fluorescence of DOX on its environment. It is reported that the fluorescence signal of the drug strongly decreases upon intercalation with genetic material [36] and can be increased by incorporation in membranes or micelles [37]. Consequently, in the case of DOX associated nanogels, the fluorescence of the drug carrier in the cytosol is likely to outshine the intercalated drug. The similar toxicity of both, the free drug and the nanogel, however, suggests an efficient uptake and release of DOX within the cell.

In vivo biocompatibility and biodistribution

The conclusion that can be drawn from the *in vitro* results is that DOX loaded nanogels are relatively stable outside cells but will release the drug once taken up into the endosome, which can later on fuse with a lysosome due to pH sensitivity in acidic compartments. Furthermore, they represent ideal candidates to exploit the EPR effect, since they reveal optimal sizes of approximately 20 nm in diameter as well as the P(EtOx) shell, which will shield them to a certain extend from unspecific interactions. To test this hypothesis *in vivo* studies on male athymic nude mice (Crl:CD1-Foxn1^{nu}) with HT-29 originated tumors were conducted. In comparison to other studies with DOX loaded drug delivery systems [39] a relatively low DOX concentration was used in line with the concept of metronomic chemotherapy. In a first stage of the investigation the general biocompatibility was probed. Tumor-free nude mice were injected *via* tail vein with a single dose of labeled DOX-nanogels (corresponding to a DOX concentration of 0.3 or 1 mg kg^{-1}) or with the same volume of the 0.9 wt% NaCl solution as the negative control. Body weight was monitored for 2 weeks (Supplementary Figure 15). As expected, no negative influence on the development of body weight was detected and no obvious signs of toxicity (changes in physical activity or constitution) were observed for these low DOX

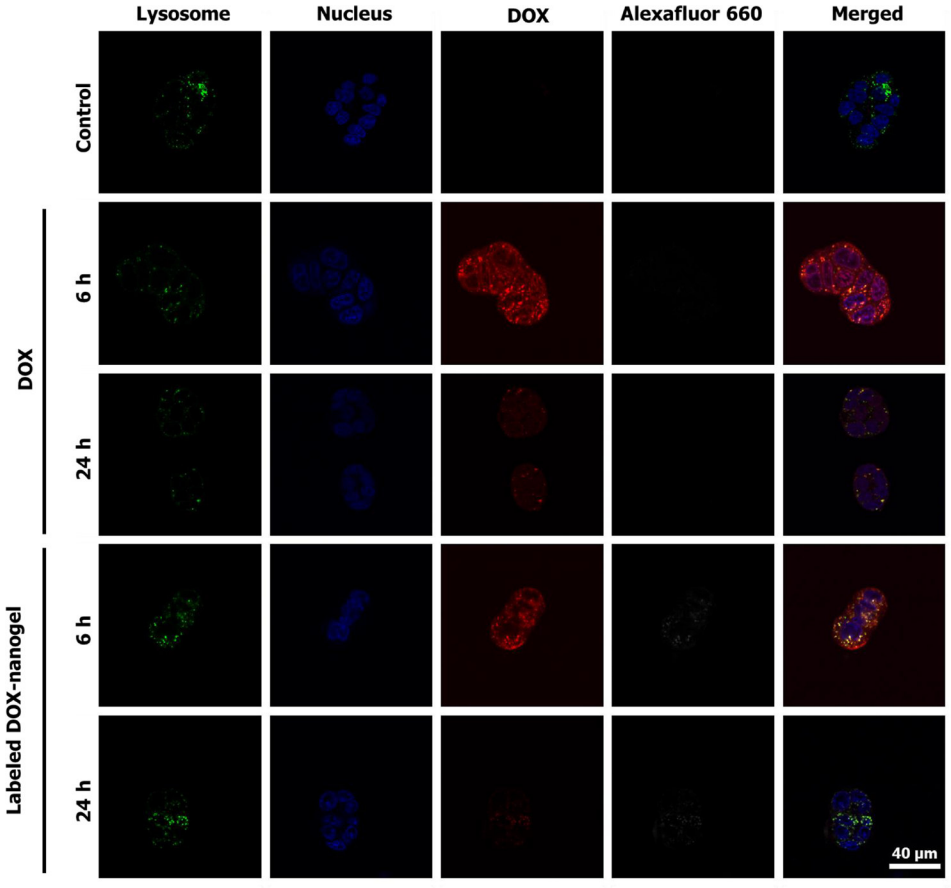

Figure 4: CLSM images of free DOX and labeled DOX-nanogels incubated with HT-29 colorectal carcinoma for 6 h or 24 h. Lysosomal cellular compartments were stained green using LysoTracker Green DND-26 and the nucleus was labeled with Hoechst 33342 (blue). The fluorescence of DOX is depicted in red and the Alexafluor label of the polymer is shown in white.

concentrations. For further analysis the 1 mg kg^{-1} DOX concentration was chosen.

It is already known that the biodistribution of drugs can be influenced by polymeric drug carriers, [52] *i.e.* when equipped with targeting units [53, 54]. Furthermore, the blood clearance and organ accumulation rates of POx-DOX conjugates were determined to be advantageous for cancer therapy, as the conjugates express high blood circulation times of more than 24 h ($t_{1/2}$ DOX = 4 min [55]) and tumor accumulation [39]. For this reason, the biodistribution of the drug carrier within the body was investigated using male nude mice, which received a subcutaneous injection of HT-29 cells (1×10^6 cells in 250 µL) into the flank. When the tumor reached 6 to 8 mm, mice were treated with a single dose of either labeled DOX-nanogels at 1 mg kg^{-1} (150 µl) or of a NaCl solution with the same volume. The mice were sacrificed after predetermined time points (6, 48, and 72 h) and several organs (heart, liver, and kidney) as well as the tumor were excised and prepared for cryo-sections. Sections of mentioned organs were cut to a thickness of 8 µm and embedded in a water-based mounting medium on glass slides. The obtained samples were investigated by CLSM in order to monitor the accumulation of DOX in different body compartments. Histological samples of the tumor clearly show an accumulation of DOX as evident by the inhomogeneous red fluorescence (Figure 5, Supplementary Figure 16). The fluorescence signal is most pronounced 6 h after the injection and is still detectable after 48 h, but to a lesser extent. This phenomenon is also known from other studies. M. Hruby and coworkers determined the radioactive intensity of a ^{125}I-labeled DOX carrier. Here, the mean radioactive intensity decreases significantly between 24 h and 72 h. Furthermore, the main amount of the carrier remains within the blood [39]. Since we used a comparable polymer system, a similar pharmacokinetic behavior might be favorable. Traces of DOX could also be observed in the liver in the form of small aggregates of about 1 µm size. The number of these aggregates increases over time, which points into the direction of either an accumulation in liver tissue or an excretion *via* the organ. Previously, a diminished accumulation of DOX loaded glycolchitosan nanoparticles within the heart could be determined [52]. Also in our study, only minor traces of DOX could be detected in the heart, which is promising, as cardiotoxicity is the most common side effect of DOX. No signal could be detected in the kidney indicating either a fast renal clearance of the nanogels or, more probably, no involvement of the kidney on the excretion of the nanogels. Small polymer-drug conjugates and nanoparticles with an average size below 5 nm are preferably renal excreted [56] and consequently accumulate within the kidney [39]. However, the utilized nanogels within this study possess an average diameter of around 20 nm and for this reason, an accumulation within the liver is more likely [56].

In vivo anti-tumor efficiency

To test the therapeutic efficiency of labeled DOX-nanogels, a xenograft mouse model was established by subcutaneous injection of HT-29 cells. When the tumor volume reached 100–200 mm^3 mice received 6 doses of

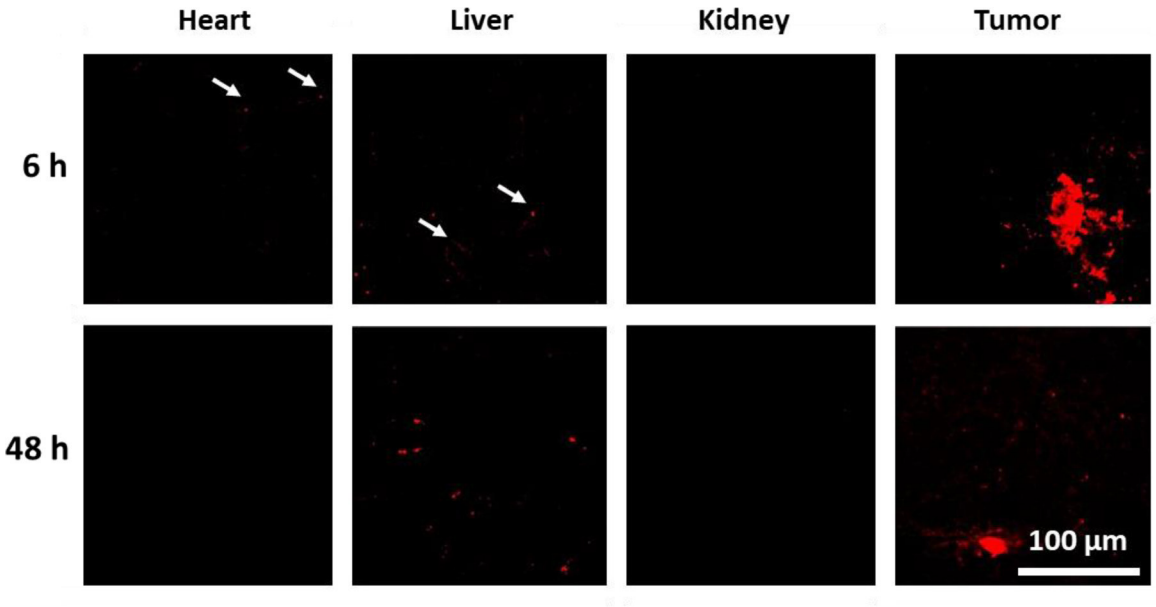

Figure 5: Confocal fluorescence images of histological samples derived from organs of mice that were treated with labeled DOX-nanogels at 1 mg kg^{-1}. Fluorescence of DOX is shown in red. See Supplementary Figure 16 for control sample and 72 h labeled DOX-nanogel sample. See Supplementary Figure 17 for transmitted light images.

drug or control every three days (day 0–15) according to a metronomic schedule. Mice were treated with saline (control), low dose of free DOX (1 mg kg^{-1}), DOX-free nanogels and labeled DOX-nanogels (corresponding to 1 mg kg^{-1} DOX.). The absolute tumor volume was monitored until it reached the termination condition of 1500 mm^3 (Supplementary Figure 18). No negative influence on the development of body weight was detected (Supplementary Figure 19). The individual time course of tumor development for each animal in the different treatment groups (n = 7–8) is shown in Figure 6A. The use of labeled DOX-nanogels reduced the tumor growth of mice compared to a treatment with NaCl, DOX-free nanogels or free DOX. These results are supported by the Kaplan–Meier survival of the HT-29 xenograft model (Figure 6B). Treatment with NaCl or DOX-free nanogels did not slow down the tumor growth, while the median survival time was 37 days for NaCl or 24 days for DOX-free nanogels, respectively. Administration of 1 mg kg^1 DOX also had no effect on tumor inhibition compared to control groups with a median survival time of 39 days (p = 0.202). This might be attributed to the low DOX concentration used in this study. However, even though pure DOX did not seem to be able to reduce tumor progression in the xenograft model, the labeled DOX-nanogels were highly effective. Mice treated with labeled DOX-nanogels had a significant prolonged median survival time of 73 days compared to the NaCl control (p = 0.002) or pure DOX (p = 0.031). This might be explained by the more direct impact of DOX-nanogels on tumor tissue due to the EPR effect. As DOX is shielded within the nanogel, protected by a P(EtOx) shell, a prolonged circulation time can be expected, as shown for linear P(EtOx) [27]. These findings are in agreement with a recently published study by O. Sedlacek *et al.*, prolonging the median survival time of DOX-POx conjugates from 19 to 36 days [39]. However, the utilized DOX dose within the mentioned study was 20 mg kg^1, while our nanogels already possess an effect at an administration of 1 mg kg^1. With an equal or higher toxicity after cellular uptake, as demonstrated by *in vitro* investigations the nanogels are able to interfere with tumor growth more efficiently than the free drug. Combined with their excellent biocompatibility the presented drug carriers proved to be a promising material for cancer therapy.

MATERIALS AND METHODS

Material and instrumentation

Chemicals and solvents were purchased from Sigma-Aldrich, Merck, Fluka, and Acros. Hoechst 33342 trihydrochloride as well as LysoTracker® Green DND-26 were obtained from Life Technologies (Thermo Fisher, Germany). 2-Ethyl-2-oxazoline (EtOx) and methyl tosylate (MeOTos) were distilled to dryness prior to use. EtOx was dried using barium oxide before distillation. 2-(4-((*tert*-Butoxycarbonyl)amino)butyl)-2-oxazoline (BocOx) was synthesized as described in a previous publication [57]. Consumables for cell culture, like pipettes and cell culture plates (96 well) were obtained from Greiner Bio-one (Austria/ Germany). If not stated otherwise, cell culture media and supplements (L-Glutamin, antibiotics) were obtained from Biochrom (Merck Millipore, Germany).

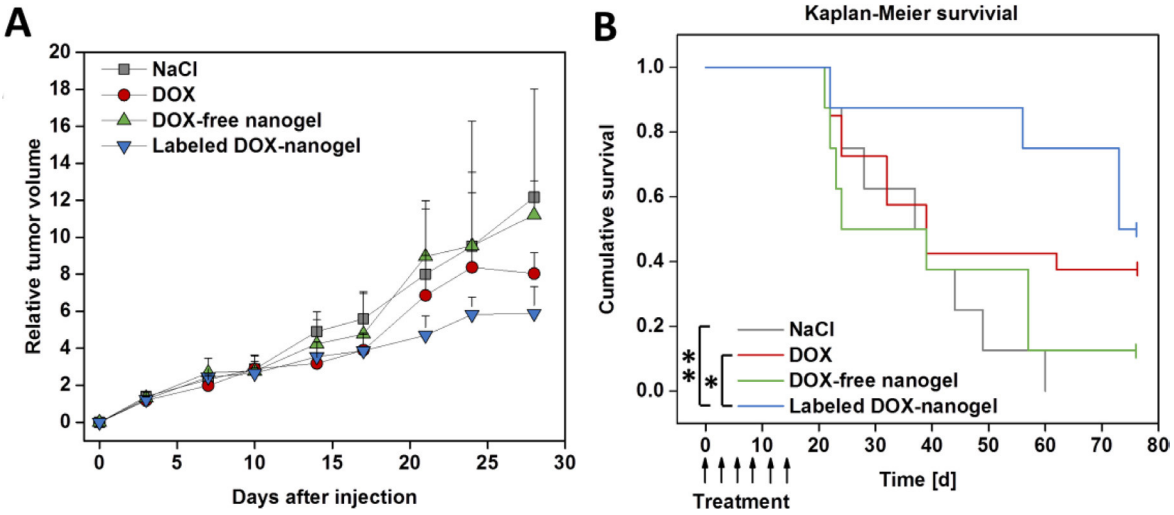

Figure 6: Anti-tumor activity of the DOX-nanogels was evaluated in a xenograft mouse model. Male nude mice received a subcutaneous injection of HT-29 cells into the flank. When tumors reached 100 to 200 mm^3 mice received 6 doses of 0.9 wt% NaCl, DOX (1 mg kg^{-1}), DOX-free nanogel and labeled DOX-nanogel (corresponding to 1 mg kg^{-1} DOX) *via* tail vein injection from day 0 to day 15. (**A**) Development of the relative tumor volume is illustrated over time. Results are indicated as median + semi interquartile range. (**B**) Survival of mice bearing HT-29 derived tumors presented as a Kaplan–Meier survival curve. The individual endpoint of each animal was achieved when the tumor volume reached 1500 mm^3. Statistical differences are displayed as $^*p < 0.05$ and $^{**}p < 0.01$ according to the log-rank test.

The Initiator Sixty single-mode microwave synthesizer from Biotage, equipped with a non-invasive IR sensor (accuracy: 2%), was used for polymerizations under microwave irradiation. Microwave vials were heated overnight to 110° C and allowed to cool to room temperature under an argon atmosphere before use. All polymerizations were carried out under temperature control. Size-exclusion chromatography (SEC) measurements of the protected polymers were performed on a Shimadzu system equipped with a SCL-10A system controller, a LC-10AD pump, a RID-10A refractive index detector and a PSS SDV column with chloroform/triethylamine (NEt_3)/*iso*-propanol (94:4:2) as eluent. The column oven was set to 50° C. SEC of the deprotected statistical copolymers was performed on a Shimadzu system with a LC-10AD pump, a RID-10A refractive index detector, a system controller SCL-10A, a degasser DGU-14A, and a CTO-10A column oven using *N,N*-dimethyl acetamide (DMAc) with 2.1 g L^{-1} LiCl as the eluent and the column oven set to 50° C. Poly(styrene) (PS) samples were used as calibration standards for both solvent systems. Proton NMR spectroscopy (^{1}H NMR) measurements were performed at room temperature on a Bruker AC 300 and 400 MHz spectrometer, using $CDCl_3$ or *N,N*-dimethyl formamide (DMF)-D_7 as solvents. Diffusion-ordered spectroscopy (DOSY) NMR measurements were performed at room temperature on a Bruker AC 400 MHz spectrometer using D_2O as the deuterated solvent. The chemical shifts are given in ppm relative to the signal of the residual non-deuterated solvent.

Batch dynamic light scattering (DLS) was performed on a Zetasizer Nano ZS (Malvern Instruments, Herrenberg, Germany). All measurements were performed in folded capillary cells (DTS1071, Malvern Instruments, Herrenberg, Germany). After an equilibration time of 180 s, 3 × 30 s runs were carried out at 4° C, 25° C or 37° C (λ = 633 nm). If not stated explicitly, 25° C was used for measurements. The counts were detected at an angle of 173°. Each measurement was performed in triplicate. Apparent hydrodynamic radii, R_h, were calculated according to the Stokes–Einstein equation.

Laser Doppler velocimetry was used to measure the electrokinetic potential, also known as zeta potential. The measurements were performed on a Zetasizer Nano ZS (Malvern Instruments, Herrenberg, Germany) in folded capillary cells (DTS1071). For each measurement, 15 runs were carried out using the fast-field and slow-field reversal mode at 150 V. Each experiment was performed in triplicate at 25° C. The zeta potential (ζ) was calculated from the electrophoretic mobility (μ) according to the Henry Equation [58]. The Henry coefficient, f(ka), was calculated according to Ohshima [59].

cryoTEM investigations were conducted with a FEI Tecnai G^2 20 at 200 kV acceleration voltage. Specisms were vitrified by a Vitrobot Mark V system on Quantifoil grids (R2/2). The blotting time was 1 s with blotting force offset of 0. The amount of solution was 7 µL. Samples were plunge frozen in liquid ethane and stored under liquid nitrogen until transferred to the Gatan cryo-holder and brought into the microscope. Images were acquired with a 4k × 4k CCD Eagle camera.

Absorbance and fluorescence spectra were recorded using a Tecan Infinite M200 Pro micro plate reader (Crailsheim, Germany) by the use of black well plates with a flat and transparent bottom.

Block copolymer of 2-ethyl-2-oxazoline (EtOx) and 2-(4-((tert-butoxycarbonyl)amino)butyl)-2-oxazoline (BocOx) (P(EtOx-b-BocOx)), (1)

In a microwave vial, EtOx (757 µL, 7.5 mmol), MeTos (16.2 µL, 0.107 mmol) and acetonitrile (3.4 mL) were mixed under inert conditions. After heating in the microwave synthesizer at 140° C for 25 min the vial was introduced into a glove box with nitrogen atmosphere, a sample was taken for NMR and SEC measurements and BocOx (803 µL, 3.2 mmol) was added. The closed vial was heated again in the microwave synthesizer (140° C, 20 min). The solution was precipitated in cold (−80° C, 300 mL) diethyl ether. The white precipitate was filtered and dried in high vacuum (1.4 g, 92%).

^{1}H NMR ($CDCl_3$, 300 MHz) (6): δ = 7.66, (d, 8.1 Hz, 0.019 H, tosylate), 7.14 (d, 8.21 Hz, 0.019 H, tosylate), 3.45 (s, 4 H, backbone), 3.10 (s, 0.58 H, CH_2-CH_2-NH (BocOx)), 2.50–2.15 (m, 1.96 H, CH_2 (EtOx)/CH_2-CH_2-NHBoc), 1.62 (s, 0.52 H, CH_2-CH_2-CH_2 (BocOx)), 1.52 (s, 0.52 H, CH_2-CH_2-CH_2 (BocOx)), 1.42 (s, 2.3 H, CH_3 (BocOx)), 1.21 (s, 2.1 H, CH_3 (EtOx)) ppm.

SEC (eluent: $CHCl_3$/*iso*-propanol/NEt_3, PS-standard): M_n = 8,200 g mol^{-1}, M_w = 9.900 g mol^{-1}, Đ = 1.07.

Deprotection of (P(EtOx-b-BocOx)) (1) to yield (P(EtOx-*b*-AmOx)), (2)

P(EtOx-*b*-BocOx) (1, 1.3 g) was dissolved in TFA (5 mL) and heated to 60° C for 1 h. After stirring for 12 h at room temperature, the mixture was diluted with 10 mL methanol and precipitated in 400 mL of cold (−80° C) diethyl ether. The precipitate was re-dissolved in methanol (100 mL) and stirred with Amberlyst A21 for 48 h. Subsequently, the solvent was removed, the polymer was dissolved in de-ionized water and freeze dried (−80° C, 0.003 mbar). The polymer was obtained as white powder (1.2 g, 92%).

^{1}H NMR (DMF-D_7, 300 MHz) (2): δ = 4.9 (s, 2.3 H, NH_2), 3.51 (s, 4 H, backbone), 3.07 (s, 0.49 H, CH_2-CH_2-NH_2), 2.44 (m, 2.1 H, CH_2 (EtOx)/CH_2-CH_2-CO (AmOx)), 1.9–1.54 (m, 0.96 H, CH_2-CH_2-CH_2-CH_2 (AmOx)), 1.2 (s, 2,3 H, CH_3 (EtOx)) ppm.

SEC (eluent: DMAc/LiCl, PS-standard): M_n = 13,900 g mol^{-1}, Đ = 1.11.

Labeling of (P(EtOx-b-AmOx)) (2) using Alexafluor 660, (3)

P(EtOx-*b*-AmOx) (2, 14 mg) was dissolved in DMF (5 mL) and Alexfluor 660® (1 mg, ~1 eq. per macromolecule) as well as triethyl amine (1 µL) were added under stirring. The solution was stirred at room temperature overnight and subsequently precipitated in cold diethyl ether, (300 mL, –80° C). The precipitated was filtered off, dissolved in water and transferred to a dialysis tube (6,000 to 8,000 g mol^{-1} cut off, Spectra/Por®). The polymer was dialysed against water until the solution outside the tube stayed colorless. After freeze drying, the product was obtained as deep blue powder (8 mg, 53%, degree of functionalization = 30%).

SEC (eluent: DMAc/LiCl, PS-standard): M_n = 14,600 g mol^{-1}, Đ = 1.11.

UV/Vis: λ_{Abs} = 660 nm, λ_{Em} (excitation at 600 nm) = 690 nm.

Self-assembly and cross-linking

To create nanostructures, the unlabeled block copolymer (2, 90 mg, 0.006 mmol) or a mixture of the polymers 2 and 3 (9:1, 90 mg, 0.006 mmol) were dissolved in $CHCl_3$, (5 mg mL^{-1}) and stirred for 3 h. Subsequently, glutaraldehyde (30 mg, 0.3 mmol, 1.5 eq. per amine) was added and the solution was stirred another 3 h. With proceeding reaction time the colour of the solution changed from colourless to yellow. To quench the excess of aldehyde functionalities, 6-amino fluorescein (50 mg) or DOX (50 mg) were added, respectively, and stirred for 12 h. Subsequently, the amount of solvent was reduced under an argon stream and the residual was precipitated in 100 mL cold diethyl ether (−80° C). To purify the self-assembled structures from residual capping agent and cross-linker, dialysis in MeOH/water (1:4) was applied using a membrane with a molar mass cut off of 3,500 g mol^{-1} (Roth Zellutrans). After the extraction was finished, the dialysis medium was changed to pure water and the aqueous solution was freeze dried to yield an orange or, in the case of DOX, a red powder.

Determination of dye loading content by absorbance/fluorescence

The absorbance/fluorescence of 6AF loaded nanostructures was investigated under alkaline conditions (1 mol L^{-1} NaOH in water) in diluted solution (0.1 mg mL^{-1}). The absorbance was determined at a wavelength of 490 nm and compared to a dilution series of 6AF in the same aqueous NaOH solution. To the 6AF stock solution a 100 fold excess of glutaraldehyde was added to ensure that only the imine species of 6AF is present. Emission was detected at an excitation wavelength of λ = 450 nm. Micellar samples as well as 6AF calibration exhibit an emission maximum at λ = 510 nm.

DOX conjugated samples were measured in water (0.1 mg mL^{-1}) and compared to a dilution series of DOX in water. All measurements were carried out in a 96 well-plate format with 200 µL per well and double determination for each measuring point. The read out was accomplished using a Tecan Infinite M200 Pro micro plate reader (Crailsheim, Germany).

Determination of the nanogel stability

Labeled DOX-nanogels were dissolved in 150 mM phosphate buffered saline (PBS) buffer (pH = 7.4) and measured by means of size (z-average and number mean) and uniformity (PDI) using DLS measurements as described above. Measurements were conducted at 4° C or 37° C, and nanogel solutions were stored at the respective temperature in between measurements.

Determination of the DOX release

Labeled DOX-nanogels were dissolved in 0.9 wt % NaCl or 150 mM phosphate buffered saline (PBS) buffer (pH = 5.0) containing 200 mM glycine. Qualitative DOX release was determined using DOSY NMR measurements as described above. A sample containing pure DOX dissolved in 0.9 wt % NaCl was used for comparison.

Determination of the cytotoxicity by XTT assay

Cytotoxicity studies were performed with the sensitive mouse fibroblast cell line L929, as recommended by ISO10993-5, and with the human colorectal adenocarcinoma cell line HT-29. The L929 cells were routinely cultured in Dulbecco's modified eagle's medium (DMEM) and HT-29 cells in RPMI 1640 supplemented with 10% fetal calf serum (FCS), 100 U mL^{-1} penicillin and 100 µg mL^{-1} streptomycin at 37° C in a humidified 5% (v/v) CO_2 atmosphere. Cells were seeded at 10^4 cells per well in a 96-well plate and incubated for 24 h, whereas no cells were seeded in the outer wells. Afterwards, the testing substances (nanogels or DOX) at indicated end concentrations were added to the cells and the plates were incubated for further 24 h. Subsequently, a XTT assay (Cell Proliferation Kit II, Roche Diagnostics) was performed according to supplier's information. After a further incubation of 4 h, the absorbance was measured at a wavelength of λ = 450 nm and a reference wavelength of λ = 630 nm with untreated cells on the same well plate serving as negative controls. The negative control was standardized as 0% of metabolism inhibition and referred as 100% viability. Cell viability below 70% was considered indicative of cytotoxicity. Data are expressed as mean ± SD of six determinations. The half maximal

inhibitory concentration (IC_{50}) was calculated with the GraphPad Prism Software.

Blood compatibility measurements

To assess the hemolytic activity of the polymer solutions, blood from sheep, collected in heparinized-tubes (Institut für Versuchstierkunde und Tierschutz/Laboratory of Animal Science and Animal Welfare, Friedrich Schiller University Jena), was centrifuged at 4500 × g for 5 min, and the pellet was washed three times with cold 1.5 mmol L^{-1} phosphate buffered saline (PBS, pH 7.4). After dilution with PBS in a ratio of 1:7, aliquots of erythrocyte suspension were mixed 1:1 with the polymer solution and incubated in a water bath at 37° C for 60 min. After centrifugation at 2400 × g for 5 min the hemoglobin release into the supernatant was determined spectrophotometrically using a microplate reader (TECAN Infinite M200 PRO) at λ = 544 nm wavelength. Complete hemolysis (100%) was achieved using 1% Triton X-100 serving as positive control. Thereby, PBS served as negative control (0%). A value less than 2% hemolysis rate was taken as non-hemolytic. Experiments were run in triplicates and were performed with three different blood donors.

For the examination of the erythrocyte aggregation, erythrocytes were isolated as described above. An erythrocytes suspension was mixed with the same volume of polymer solution in a clear flat bottomed 96-well plate. The cells were incubated at 37° C for 2 h, and the absorbance was measured at λ = 645 nm in a microplate reader (TECAN Infinite M200 Pro). 25 kDa *b*PEI (50 µg mL^{-1}) was used as positive control and PBS treated cells served as negative control. Absorbance values of the test solutions lower than negative control were regarded as aggregation. Experiments are the result of triplicates and were performed with three different donor blood batches.

Confocal microscopy

For live CLSM analysis of cell uptake, HT-29 cells (0.2×10^6 cells mL^{-1}) were seeded in glass-bottomed, 4-chamber dishes (CELLVIEW, Greiner Bio-One) and cultured for 24 h. One hour prior to nanogel/ drug treatment, a media change with fresh culture media occurred. Cells were incubated with nanogel or DOX (10 µg mL^{-1}) for 6 h or 24 h, respectively. For examination of nanogel/ drug co-localization with cell organelles, the lysosomes were stained with LysoTracker Green® DND-26 and the cell nuclei were counterstained with Hoechst 33342. Live cell CLSM images were acquired using a Zeiss LSM 880, Elyra PS.1 system (Carl Zeiss, Germany) with excitation wavelengths/emission filters of 405nm/BP 405–480 nm for Hoechst 33342, 488 nm/ BP 505 to 530 nm for LysoTracker® Green DND-26 and 488 nm/BP 585 to 615 nm for DOX and 633 nm/BP 724 to 777 nm for Alexafluor 660®. Images were captured with a 1.4 NA Plan-Apochromat 63 × oil objective and in multitrack mode, enabling single excitation and emission of fluorescence dyes. Co-localization was visualized in overlay images of the multiple channels.

The imaging of histological tissue sections (heart, liver, kidney, tumor) were performed with excitation wavelengths/ emission filters of 488 nm/BP 580 to 615 nm and a 1.4 NA Plan-Apochromat 40 × oil objective.

Cellular uptake studies

The evaluation of the nanogel and free DOX uptake was performed by flow cytometry (FC) measured on a Beckmann Coulter Cytomics FC-500 equipped with an Uniphase Argon ion laser (488 nm, 20 mW output) and analyzed with the Cytomics CXP software. In brief, HT-29 cells (0.2×10^6 cells mL^{-1} seeded in 24-well plates) were incubated for 6 h and 24 h with labeled labeled DOX-nanogel or free DOX (0.01 mg mL^{-1}) at 37° C or 4° C, respectively. In the case of the 4° C uptake study, cell culture media was supplemented with 15 mM HEPES (4-(2-hydroxyethyl)-1-piperazineethanesulfonic acid, Biochrom, Merck) as buffering agent. Afterwards, cells were harvested by trypsinization and trypan blue (1:10) was added to quench the outer fluorescence. 10^4 cells were measured by flow cytometry, whereby the number of all viable cells, showing signals at 575 nm, were gated. Cells incubated with culture medium only served as control. The experiments were performed at least three times independently.

Animals

Male athymic nude mice (Crl:CD1-Foxn1^{nu}), 6 to 8 weeks age, were purchased by Charles River and were kept in a standard pathogen-free barrier facility accredited by the Association for Assessment and Accreditation of Laboratory Animal Care. All experiments were approved by the local Institutional Animal Care and Use Committee (Jena, 02-011/15). Mice had free access to standard chow and tap water at all times. Body weight and tumor size (measured with a digital caliper) were monitored twice a week. Tumor volume was calculated with the formula $(L \times W^2)/2$, were L is the longest and W the shortest diameter (mm) of the tumor.

In vivo toxicity and biodistribution

Safety evaluation of the nanogels was carried out on healthy male nude mice without tumors, which were randomly assigned to 3 groups (4 mice per group). A single dose (150 µl) of saline (control) or nanogels corresponding to a DOX concentration of 0.3 and 1 mg kg^{-1} body weight were injected *via* tail vein. Body weight, animal constitution and physical activity were monitored for 2 weeks.

For biodistribution experiments HT-29 cells (1×10^6 in 250 µl) were injected subcutaneously into the flank of

nude mice. Mice bearing tumors approximately 6–8 mm received a single dose (150 µl) of saline or nanogels with a DOX concentration of 1 mg kg^{-1} *via* tail vein injection. At 6, 48 and 72 h after injection mice were sacrificed and tumor, heart, liver and kidney were excised for further analysis, immediately frozen with liquid nitrogen and stored at –70° C prior to tissue sectioning. Single tissue sections (8 µm thickness) of organs and tumors were cut with a CM 1860 Crystat (Leica Biosystems, Wetzlar, Germany), air-dried on glass slides and embedded in a water-based mounting media (Aquatex, Merck).

Anti-tumor activity *in vivo*

The xenograft model was established by subcutaneous injection of HT-29 cells (1×10^6 in 250 µl) into the flank of male nude mice. When tumors reached a volume of 100–200 mm^3 mice were assigned to 4 treatment groups (10 mice per group) with no significant differences in body weight or tumor volume between the groups. Mice were injected with treatment solutions (saline, 1 mg kg^{-1} DOX, labeled DOX loaded nanogel (6) (corresponding to 1 mg kg^{-1} DOX), and Dox-free nanogel at the same concentration as nanogel 6) *via* tail vein injection on day 0, 3, 6, 9, 11 and 15. Mice were sacrificed when the tumor volume reached 1500 mm^3, which was determined as the individual end point of the survival curve. After sacrifice tumors were excised and weighed. Mice reaching any termination condition (maximum tumor volume, weight loss over 15%, infected wound or limited mobility) before the end of the treatment period were excluded from the survival study.

Statistical analysis

The values represent the mean ± SD (standard deviation). For uptake studies direct comparison of two different groups was done with two-tailed, non-paired Student's *t*-test. A value of $p < 0.05$ was considered as statistically significant. The body weight or tumor volume of the nude mice were tested regarding normal distribution and homogeneity of variances with the IBM SPSS software. Statistical differences were calculated according to a one-way ANOVA. Survival analysis was performed with SPSS and calculated with the Kaplan–Meier method. Significant differences were assessed with the log-rank test. A value of $p < 0.05$ was considered as statistically significant.

CONCLUSIONS

Within this report, a straightforward approach to POx based nanogels, covalently loaded with the anti-cancer drug DOX is presented. Nanogels were synthesized *via* cross-linking of a block copolymer micelle with a cationic poly(2-(4-aminobutyl)-2-oxazoline) core and a poly(2-ethyl-2-oxazoline) shell. Cross-linking as well as drug loading was accomplished by pH responsive imine chemistry. Moreover, the amine groups of the drug delivery system allowed the irreversible labeling with a near infra-red fluorescent dye. In *in vitro* studies DOX loaded POx based nanogels showed a toxicity profile comparable to the free drug, while unloaded drug carriers showed no toxicity. The blood compatibility of the drug delivery system was found to be suitable for the envisioned application, therefore the cellular uptake was investigated by flow cytometry and fluorescence microscopy. While the amount of internalized drug was enhanced when incorporated into a nanogel, the release of the drug into the nucleus was delayed compared to free DOX. This is beneficial as a lower amount of drug is required to yield the same effect. Furthermore, the nanogels were shown to be more tumor specific than DOX, which reduces side-effects during therapy. *In vivo* investigation on xenograft mouse models were conducted to assess the ability of the designed system to reduce tumor growth. In combination to the new nanogel-based drug delivery system a metronomic schedule of DOX treatment was applied. Initial studies on healthy mice showed no adverse effects of the DOX-free nanogels or low dosed labeled DOX-nanogels on body weight and behavior. The biodistribution was investigated by microscopy of organs of mice treated with labeled DOX-nanogels and showed a localization of DOX within tumorous tissue, most likely associated to the enhanced permeability and retention (EPR) effect. Finally, the therapeutic efficiency of the POx based drug delivery system was investigated in a survival study of xenograft mice. While the low doses of pure DOX did not show a significant reduction in tumor progression, the metronomic schedule of the labeled DOX-nanogels proved a significant tumor growth inhibition and increase in survival time. Future studies will focus on detailed investigations of the pharmacokinetics of the presented system as well as on studying the biocompatibility of higher drug doses.

Author contributions

T. B. designed and performed the *in vitro* experiments. D. H., M. H., M. N. L. and R. T. designed the *in vivo* experiments. D. H., M. N. L. and R. T. performed the mouse experiments and analyzed the *in vivo* data. S. H. performed the TEM measurements. M. H., D. P., K. K. and U. S. S. designed the nanogels. M. H. synthesized and characterized the nanogels. D. H., M. N. L and M. H. wrote the manuscript, which was edited and approved by all authors.

ACKNOWLEDGMENTS

MNL and TB acknowledge the German Federal Ministry of Education and Research (BMBF, #13N13416 smart-dye-livery, #031A518B Vectura) for funding.

CryoTEM investigations were performed at the cryoTEM facilities of the Jena Center for Soft Matter (JCSM). TEM facilities were funded by a grant of the DFG (German Research Foundation) and the EFRE (European Fund for Regional Development). The LSM880 ELYRA PS.1 was further founded with a grant from the German Research Council (DFG). MH gratefully acknowledges the German Research Foundation (DFG, GZ: HA 7725/1-1) for funding.

CONFLICTS OF INTEREST

The authors declare no conflicts of interest.

REFERENCES

1. Gewirtz DA. A critical evaluation of the mechanisms of action proposed for the antitumor effects of the anthracycline antibiotics adriamycin and daunorubicin. Biochem Pharmacol. 1999; 57:727–41. https://doi.org/10.1016/S0006-2952(98)00307-4.
2. Thorn CF, Oshiro C, Marsh S, Hernandez-Boussard T, McLeod H, Klein TE, Altman RB. Doxorubicin pathways: pharmacodynamics and adverse effects. Pharmacogenet Genomics. 2011; 21:440–46. https://doi.org/10.1097/FPC.0b013e32833ffb56.
3. Yang F, Teves SS, Kemp CJ, Henikoff S. Doxorubicin, DNA torsion, and chromatin dynamics. Biochim Biophys Acta. 2014; 1845:84–9.
4. Lipshultz SE, Scully RE, Lipsitz SR, Sallan SE, Silverman LB, Miller TL, Barry EV, Asselin BL, Athale U, Clavell LA, Larsen E, Moghrabi A, Samson Y, et al. Assessment of dexrazoxane as a cardioprotectant in doxorubicin-treated children with high-risk acute lymphoblastic leukaemia: long-term follow-up of a prospective, randomised, multicentre trial. Lancet Oncol. 2010; 11:950–61. https://doi.org/10.1016/S1470-2045(10)70204-7.
5. He Z, Wan X, Schulz A, Bludau H, Dobrovolskaia MA, Stern ST, Montgomery SA, Yuan H, Li Z, Alakhova D, Sokolsky M, Darr DB, Perou CM, et al. A high capacity polymeric micelle of paclitaxel: implication of high dose drug therapy to safety and *in vivo* anti-cancer activity. Biomaterials. 2016; 101:296–309. https://doi.org/10.1016/j.biomaterials.2016.06.002.
6. Luxenhofer R, Han Y, Schulz A, Tong J, He Z, Kabanov AV, Jordan R. Poly(2-oxazoline)s as polymer therapeutics. Macromol Rapid Commun. 2012; 33:1613–31. https://doi.org/10.1002/marc.201200354.
7. Bertrand N, Wu J, Xu X, Kamaly N, Farokhzad OC. Cancer nanotechnology: the impact of passive and active targeting in the era of modern cancer biology. Adv Drug Deliv Rev. 2014; 66:2–25. https://doi.org/10.1016/j.addr.2013.11.009.
8. Eckmann DM, Composto RJ, Tsourkas A, Muzykantov VR. Nanogel carrier design for targeted drug delivery. J Mater Chem B Mater Biol Med. 2014; 2:8085–97. https://doi.org/10.1039/C4TB01141D.
9. Pathak RK, Wen R, Kolishetti N, Dhar S. A prodrug of two approved drugs, cisplatin and chlorambucil, for chemo war against cancer. Mol Cancer Ther. 2017; 16:625–36. https://doi.org/10.1158/1535-7163.MCT-16-0445.
10. Wen R, Banik B, Pathak RK, Kumar A, Kolishetti N, Dhar S. Nanotechnology inspired tools for mitochondrial dysfunction related diseases. Adv Drug Deliv Rev. 2016; 99:52–69. https://doi.org/10.1016/j.addr.2015.12.024.
11. Wen R, Dhar S. Turn up the cellular power generator with vitamin E analogue formulation. Chem Sci (Camb). 2016; 7:5559–67. https://doi.org/10.1039/C6SC00481D.
12. Sultana F, Imran-Ul-Haque M, Arafat M, Sharmin S. An Overview of Nanogel Drug Delivery System. J Appl Pharm Sci. 2013; 3:95–105.
13. Kronek J, Kroneková Z, Lustoň J, Paulovičová E, Paulovičová L, Mendrek B. *In vitro* bio-immunological and cytotoxicity studies of poly(2-oxazolines). J Mater Sci Mater Med. 2011; 22:1725–34. https://doi.org/10.1007/s10856-011-4346-z.
14. Eskow Jaunarajs KL, Standaert DG, Viegas TX, Bentley MD, Fang Z, Dizman B, Yoon K, Weimer R, Ravenscroft P, Johnston TH, Hill MP, Brotchie JM, Moreadith RW. Rotigotine polyoxazoline conjugate SER-214 provides robust and sustained antiparkinsonian benefit. Mov Disord. 2013; 28:1675–82. https://doi.org/10.1002/mds.25625.
15. Wilson P, Chun Ke P, Davis TP, Kempe K. Poly(2-oxazoline)-based micro- and nanoparticles: A review. Eur Polym J. 2017; 88:486–515. https://doi.org/10.1016/j.eurpolymj.2016.09.011.
16. Chen F, Zhang J, Wang L, Wang Y, Chen M. Tumor pH(e)-triggered charge-reversal and redox-responsive nanoparticles for docetaxel delivery in hepatocellular carcinoma treatment. Nanoscale. 2015; 7:15763–79. https://doi.org/10.1039/C5NR04612B.
17. Dams ET, Laverman P, Oyen WJ, Storm G, Scherphof GL, van Der Meer JW, Corstens FH, Boerman OC. Accelerated blood clearance and altered biodistribution of repeated injections of sterically stabilized liposomes. J Pharmacol Exp Ther. 2000; 292:1071–79.
18. Chanan-Khan A, Szebeni J, Savay S, Liebes L, Rafique NM, Alving CR, Muggia FM. Complement activation following first exposure to pegylated liposomal doxorubicin (Doxil): possible role in hypersensitivity reactions. Ann Oncol. 2003; 14:1430–37. https://doi.org/10.1093/annonc/mdg374.
19. Armstrong JK, Hempel G, Koling S, Chan LS, Fisher T, Meiselman HJ, Garratty G. Antibody against poly(ethylene glycol) adversely affects PEG-asparaginase therapy in acute lymphoblastic leukemia patients. Cancer. 2007; 110:103–11. https://doi.org/10.1002/cncr.22739.
20. Rudmann DG, Alston JT, Hanson JC, Heidel S. High molecular weight polyethylene glycol cellular distribution

and PEG-associated cytoplasmic vacuolation is molecular weight dependent and does not require conjugation to proteins. Toxicol Pathol. 2013; 41:970–83. https://doi.org/10.1177/0192623312474726.

21. Bendele A, Seely J, Richey C, Sennello G, Shopp G. Short communication: renal tubular vacuolation in animals treated with polyethylene-glycol-conjugated proteins. Toxicol Sci. 1998; 42:152–57. https://doi.org/10.1093/toxsci/42.2.152.

22. Baumann A, Tuerck D, Prabhu S, Dickmann L, Sims J. Pharmacokinetics, metabolism and distribution of PEGs and PEGylated proteins: quo vadis? Drug Discov Today. 2014; 19:1623–31. https://doi.org/10.1016/j.drudis.2014.06.002.

23. Luxenhofer R, Sahay G, Schulz A, Alakhova D, Bronich TK, Jordan R, Kabanov AV. Structure-property relationship in cytotoxicity and cell uptake of poly(2-oxazoline) amphiphiles. J Control Release. 2011; 153:73–82. https://doi.org/10.1016/j.jconrel.2011.04.010.

24. Kronek J, Paulovičová E, Paulovičová L, Kroneková Z, Lustoň J. Immunomodulatory efficiency of poly(2-oxazolines). J Mater Sci Mater Med. 2012; 23:1457–64. https://doi.org/10.1007/s10856-012-4621-7.

25. Zalipsky S, Hansen CB, Oaks JM, Allen TM. Evaluation of blood clearance rates and biodistribution of poly(2-oxazoline)-grafted liposomes. J Pharm Sci. 1996; 85:133–37. https://doi.org/10.1021/js9504043.

26. Woodle MC, Engbers CM, Zalipsky S. New amphipatic polymer-lipid conjugates forming long-circulating reticuloendothelial system-evading liposomes. Bioconjug Chem. 1994; 5:493–96. https://doi.org/10.1021/bc00030a001.

27. Wyffels L, Verbrugghen T, Monnery BD, Glassner M, Stroobants S, Hoogenboom R, Staelens S. μPET imaging of the pharmacokinetic behavior of medium and high molar mass (89)Zr-labeled poly(2-ethyl-2-oxazoline) in comparison to poly(ethylene glycol). J Control Release. 2016; 235:63–71. https://doi.org/10.1016/j.jconrel.2016.05.048.

28. Glassner M, Palmieri L, Monnery BD, Verbrugghen T, Deleye S, Stroobants S, Staelens S, Wyffels L, Hoogenboom R. The Label Matters: μPET Imaging of the Biodistribution of Low Molar Mass 89Zr and 18F-Labeled Poly(2-ethyl-2-oxazoline). Biomacromolecules. 2017; 18:96–102. https://doi.org/10.1021/acs.biomac.6b01392.

29. Guillerm B, Monge S, Lapinte V, Robin JJ. How to modulate the chemical structure of polyoxazolines by appropriate functionalization. Macromol Rapid Commun. 2012; 33:1600–12. https://doi.org/10.1002/marc.201200266.

30. Hartlieb M, Kempe K, Schubert US. Covalently cross-linked poly(2-oxazoline) materials for biomedical applications - from hydrogels to self-assembled and templated structures. J Mater Chem B Mater Biol Med. 2015; 3:526–38. https://doi.org/10.1039/C4TB01660B.

31. Hartlieb M, Pretzel D, Wagner M, Hoeppener S, Bellstedt P, Görlach M, Englert C, Kempe K, Schubert US. Core cross-linked nanogels based on the self-assembly of double hydrophilic poly(2-oxazoline) block copolymers. J Mater Chem B Mater Biol Med. 2015; 3:1748–59. https://doi.org/10.1039/C4TB02069C.

32. Hartlieb M, Bus T, Kübel J, Pretzel D, Hoeppener S, Leiske MN, Kempe K, Dietzek B, Schubert US. Tailoring Cellular Uptake and Fluorescence of Poly(2-oxazoline)-Based Nanogels. Bioconjug Chem. 2017; 28:1229–35. https://doi.org/10.1021/acs.bioconjchem.7b00067.

33. Xin Y, Yuan J. Schiff's base as a stimuli-responsive linker in polymer chemistry. Polym Chem. 2012; 3:3045–55. https://doi.org/10.1039/c2py20290e.

34. Kareva I, Waxman DJ, Lakka Klement G. Metronomic chemotherapy: an attractive alternative to maximum tolerated dose therapy that can activate anti-tumor immunity and minimize therapeutic resistance. Cancer Lett. 2015; 358:100–06. https://doi.org/10.1016/j.canlet.2014.12.039.

35. Romiti A, Cox MC, Sarcina I, Di Rocco R, D'Antonio C, Barucca V, Marchetti P. Metronomic chemotherapy for cancer treatment: a decade of clinical studies. Cancer Chemother Pharmacol. 2013; 72:13–33. https://doi.org/10.1007/s00280-013-2125-x.

36. Fiallo M, Laigle A, Borrel MN, Garnier-Suillerot A. Accumulation of degradation products of doxorubicin and pirarubicin formed in cell culture medium within sensitive and resistant cells. Biochem Pharmacol. 1993; 45:659–65. https://doi.org/10.1016/0006-2952(93)90140-R.

37. Mohan P, Rapoport N. Doxorubicin as a molecular nanotheranostic agent: effect of doxorubicin encapsulation in micelles or nanoemulsions on the ultrasound-mediated intracellular delivery and nuclear trafficking. Mol Pharm. 2010; 7:1959–73. https://doi.org/10.1021/mp100269f.

38. Meyer CD, Joiner CS, Stoddart JF. Template-directed synthesis employing reversible imine bond formation. Chem Soc Rev. 2007; 36:1705–23. https://doi.org/10.1039/b513441m.

39. Sedlacek O, Monnery BD, Mattova J, Kucka J, Panek J, Janouskova O, Hocherl A, Verbraeken B, Vergaelen M, Zadinova M, Hoogenboom R, Hruby M. Poly(2-ethyl-2-oxazoline) conjugates with doxorubicin for cancer therapy: *in vitro* and *in vivo* evaluation and direct comparison to poly[N-(2-hydroxypropyl)methacrylamide] analogues. Biomaterials. 2017; 146:1–12. https://doi.org/10.1016/j.biomaterials.2017.09.003.

40. Basuki JS, Duong HT, Macmillan A, Erlich RB, Esser L, Akerfeldt MC, Whan RM, Kavallaris M, Boyer C, Davis TP. Using fluorescence lifetime imaging microscopy to monitor theranostic nanoparticle uptake and intracellular doxorubicin release. ACS Nano. 2013; 7:10175–89. https://doi.org/10.1021/nn404407g.

41. Amelio I, Cutruzzolá F, Antonov A, Agostini M, Melino G. Serine and glycine metabolism in cancer. Trends Biochem Sci. 2014; 39:191–98. https://doi.org/10.1016/j.tibs.2014.02.004.

42. Leiske MN, Sobotta FH, Richter F, Hoeppener S, Brendel JC, Traeger A, Schubert US. How to tune the gene delivery and biocompatibility of poly(2-(4-aminobutyl)-2-oxazoline) by self and co assembly. Biomacromolecules. 2018; 19:748–60. https://doi.org/10.1021/acs.biomac.7b01535.

43. Thonemann B, Schmalz G, Hiller KA, Schweikl H. Responses of L929 mouse fibroblasts, primary and immortalized bovine dental papilla-derived cell lines to dental resin components. Dent Mater. 2002; 18:318–23. https://doi.org/10.1016/S0109-5641(01)00056-2.

44. Misra R, Sahoo SK. Intracellular trafficking of nuclear localization signal conjugated nanoparticles for cancer therapy. Eur J Pharm Sci. 2010; 39:152–63. https://doi.org/10.1016/j.ejps.2009.11.010.

45. Cai S, Alhowyan AA, Yang Q, Forrest WC, Shnayder Y, Forrest ML. Cellular uptake and internalization of hyaluronan-based doxorubicin and cisplatin conjugates. J Drug Target. 2014; 22:648–57. https://doi.org/10.3109/1061186X.2014.921924.

46. Yildirim T, Traeger A, Sungur P, Hoeppener S, Kellner C, Yildirim I, Pretzel D, Schubert S, Schubert US. Polymersomes with Endosomal pH-Induced Vesicle-to-Micelle Morphology Transition and a Potential Application for Controlled Doxorubicin Delivery. Biomacromolecules. 2017; 18:3280–90. https://doi.org/10.1021/acs.biomac.7b00931.

47. Kubota T, Furukawa T, Tanino H, Suto A, Otan Y, Watanabe M, Ikeda T, Kitajima M. Resistant mechanisms of anthracyclines—pirarubicin might partly break through the P-glycoprotein-mediated drug-resistance of human breast cancer tissues. Breast Cancer. 2001; 8:333–38. https://doi.org/10.1007/BF02967534.

48. Mi Y, Lou L. ZD6474 reverses multidrug resistance by directly inhibiting the function of P-glycoprotein. Br J Cancer. 2007; 97:934–40. https://doi.org/10.1038/sj.bjc.6603985.

49. Upadhyay KK, Bhatt AN, Mishra AK, Dwarakanath BS, Jain S, Schatz C, Le Meins JF, Farooque A, Chandraiah G, Jain AK, Misra A, Lecommandoux S. The intracellular drug delivery and anti tumor activity of doxorubicin loaded poly(γ-benzyl L-glutamate)-b-hyaluronan polymersomes. Biomaterials. 2010; 31:2882–92. https://doi.org/10.1016/j.biomaterials.2009.12.043.

50. Upadhyay KK, Le Meins JF, Misra A, Voisin P, Bouchaud V, Ibarboure E, Schatz C, Lecommandoux S. Biomimetic doxorubicin loaded polymersomes from hyaluronan-block-poly(γ-benzyl glutamate) copolymers. Biomacromolecules. 2009; 10:2802–08. https://doi.org/10.1021/bm9006419.

51. Yildirim T, Traeger A, Preussger E, Stumpf S, Fritzsche C, Hoeppener S, Schubert S, Schubert US. Dual Responsive Nanoparticles from a RAFT Copolymer Library for the Controlled Delivery of Doxorubicin. Macromolecules. 2016; 49:3856–68. https://doi.org/10.1021/acs.macromol.5b02603.

52. Hyung Park J, Kwon S, Lee M, Chung H, Kim JH, Kim YS, Park RW, Kim IS, Bong Seo S, Kwon IC, Young Jeong S. Self-assembled nanoparticles based on glycol chitosan bearing hydrophobic moieties as carriers for doxorubicin: *in vivo* biodistribution and anti-tumor activity. Biomaterials. 2006; 27:119–26. https://doi.org/10.1016/j.biomaterials.2005.05.028.

53. Gao Y, Li Y, Li Y, Yuan L, Zhou Y, Li J, Zhao L, Zhang C, Li X, Liu Y. PSMA-mediated endosome escape-accelerating polymeric micelles for targeted therapy of prostate cancer and the real time tracing of their intracellular trafficking. Nanoscale. 2015; 7:597–612. https://doi.org/10.1039/C4NR05738D.

54. Qiu LY, Yan L, Zhang L, Jin YM, Zhao QH. Folate-modified poly(2-ethyl-2-oxazoline) as hydrophilic corona in polymeric micelles for enhanced intracellular doxorubicin delivery. Int J Pharm. 2013; 456:315–24. https://doi.org/10.1016/j.ijpharm.2013.08.071.

55. Seymour LW, Ulbrich K, Strohalm J, Kopeček J, Duncan R. The pharmacokinetics of polymer-bound adriamycin. Biochem Pharmacol. 1990; 39:1125–31. https://doi.org/10.1016/0006-2952(90)90293-T.

56. Wang J, Masehi-Lano JJ, Chung EJ. Peptide and antibody ligands for renal targeting: nanomedicine strategies for kidney disease. Biomater Sci. 2017; 5:1450–59. https://doi.org/10.1039/C7BM00271H.

57. Hartlieb M, Pretzel D, Kempe K, Fritzsche C, Paulus RM, Gottschaldt M, Schubert US. Cationic poly(2-oxazoline) hydrogels for reversible DNA binding. Soft Matter. 2013; 9:4693–704. https://doi.org/10.1039/c3sm00114h.

58. Delgado AV, González-Caballero F, Hunter RJ, Koopal LK, Lyklema J, and International Union of Pure and Applied Chemistry, Physical and Biophysical Chemistry Division IUPAC Technical Report. Measurement and interpretation of electrokinetic phenomena. J Colloid Interface Sci. 2007; 309:194–224. https://doi.org/10.1016/j.jcis.2006.12.075.

59. Ohshima H. A Simple Expression for Henry's Function for the Retardation Effect in Electrophoresis of Spherical Colloidal Particles. J Colloid Interface Sci. 1994; 168:269–71. https://doi.org/10.1006/jcis.1994.1419.

Tumor targeting with pH-responsive poly(2-oxazoline)-based nanogels for metronomic doxorubicin treatment

SUPPLEMENTARY MATERIALS

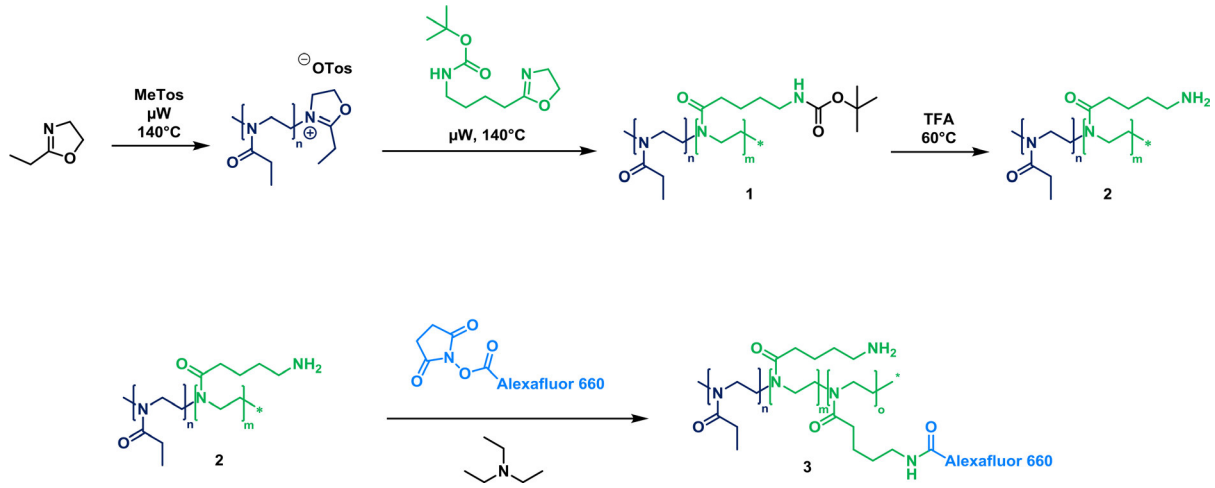

Supplementary Scheme 1: Schematic representation of the production of poly(2-oxazoline) block copolymers using cationic ring opening polymerization followed by deprotection of the Boc protected amine groups. Labelling was conducted by amidation of amine groups with Alexafluor 660 NHS ester.

Supplementary Table 1: Composition and analytical data of the POx block copolymers

Sample	NMR		SEC	
	Composition	M_n [g mol^{-1}]	M_n [g mol^{-1}]	Đ
1[a]	P($EtOx_{98}$-*b*-$BocOx_{32}$)	17,500	8,200	1.07
2[b]	P($EtOx_{98}$-*b*-$AmOx_{32}$)	14,200	13,900	1.11
3[b]	P($EtOx_{98}$-*b*-[AmOx31-*stat*-FOx_1])	15,300	14,100	1.12

[a]SEC measurement in $CHCl_3$; [b]SEC Measurement in DMAc. A poly(styrene) calibration was used in both cases.

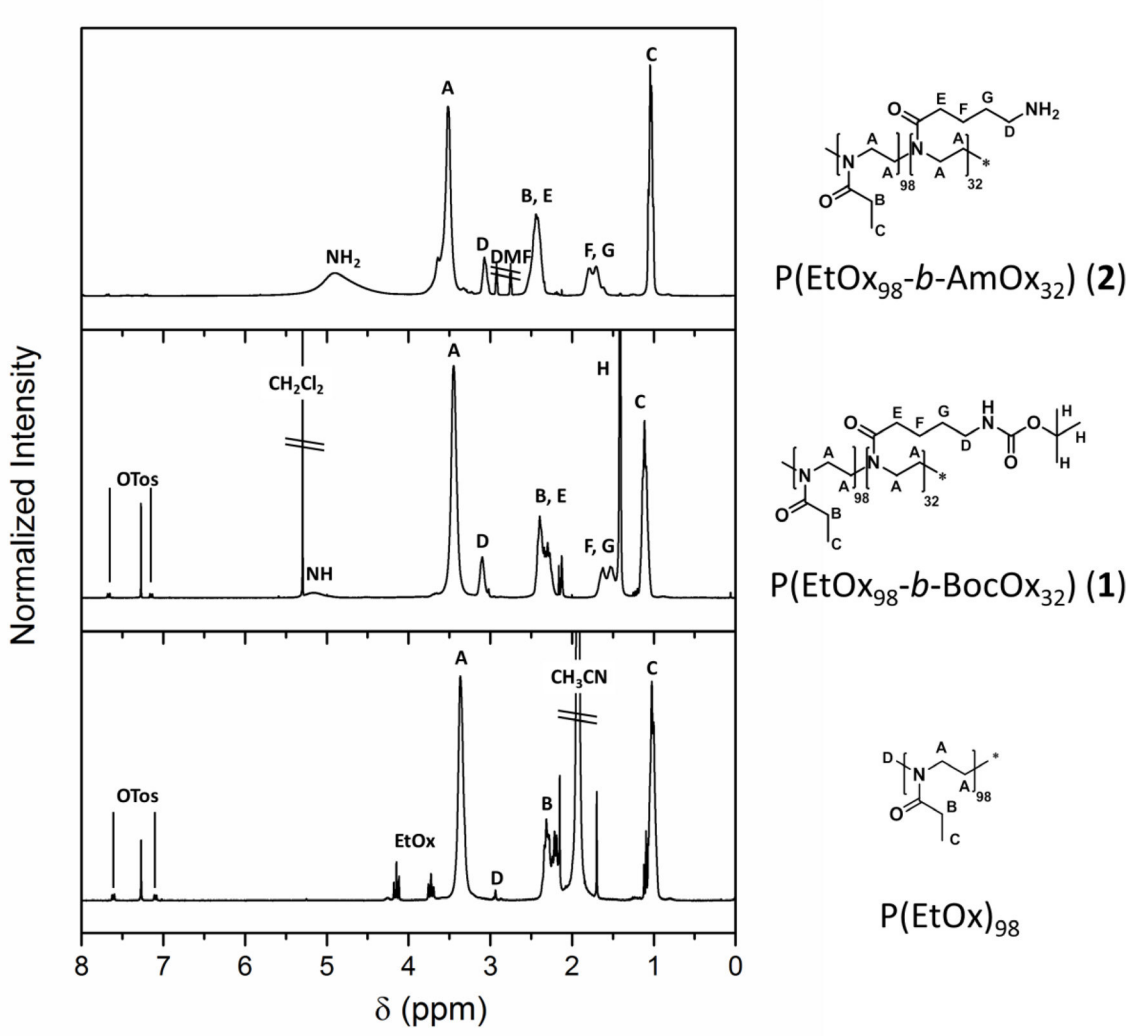

Supplementary Figure 1: ^{1}H-NMR spectra (300 MHz, top: MeOD, middle and bottom: $CDCl_3$) of poly(2-oxazoline) block copolymers.

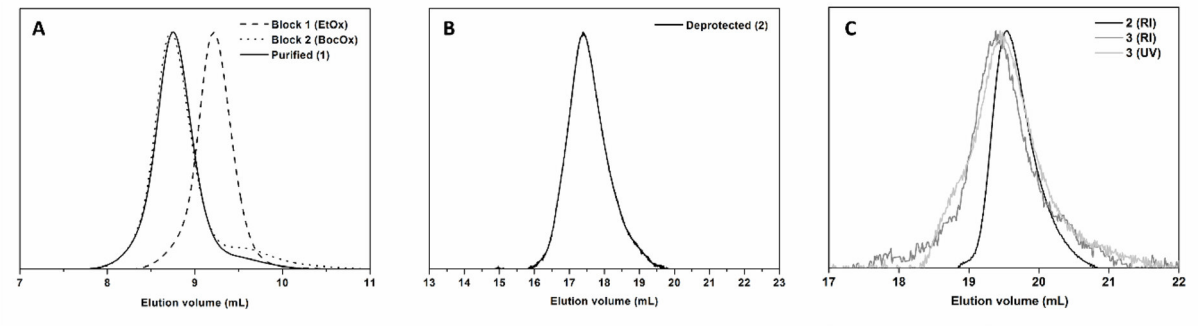

Supplementary Figure 2: SEC traces (DMAc, PS-cal.) of block copolymers before (**A**), and after (**B**) deprotection (in $CHCl_3$) as well as after labelling (**C**).

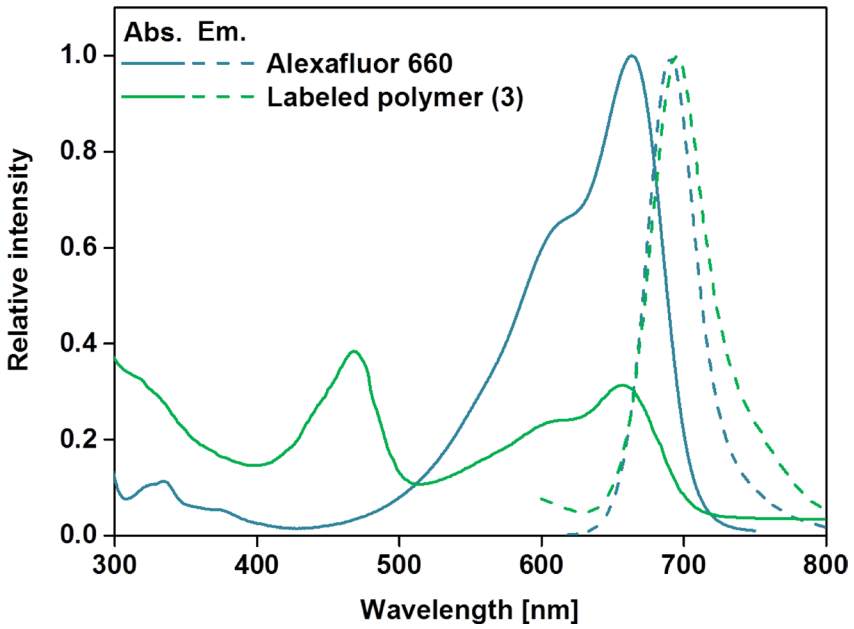

Supplementary Figure 3: Absorption and emission spectra (λ_{Ex} = 600 nm) of Alexafluor 660 and labeled poly(2-oxazoline) (3).

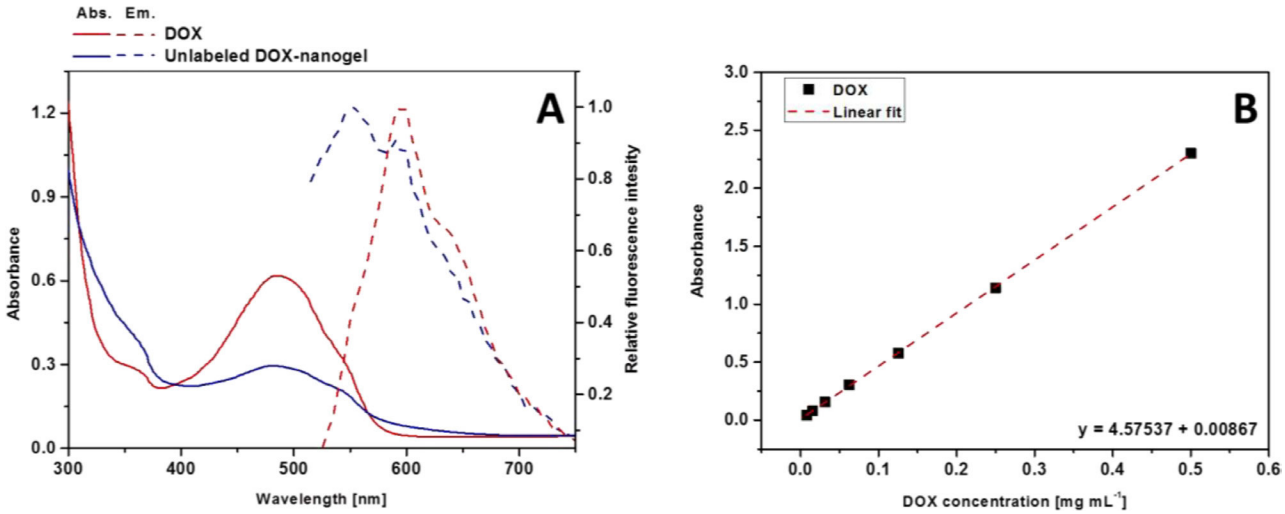

Supplementary Figure 4: (**A**) Absorption and emission spectra (excitation at λ = 450 nm) of DOX treated with a 10-fold excess of glutaraldehyde and the unlabeled DOX-nanogel. (**B**) Absorption calibration of DOX for the determination of nanogel loading efficiency.

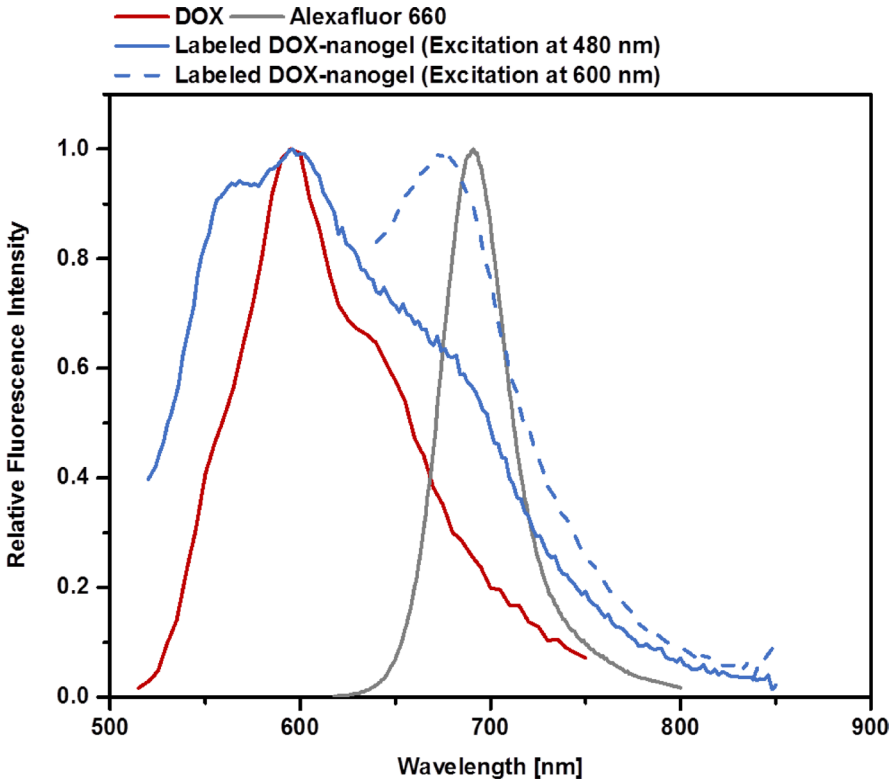

Supplementary Figure 5: Fluorescence spectra of DOX and the labeled DOX-nanogel excited at λ = 480 nm and Alexafluor 660 and the labeled DOX-nanogel excited at λ = 600 nm.

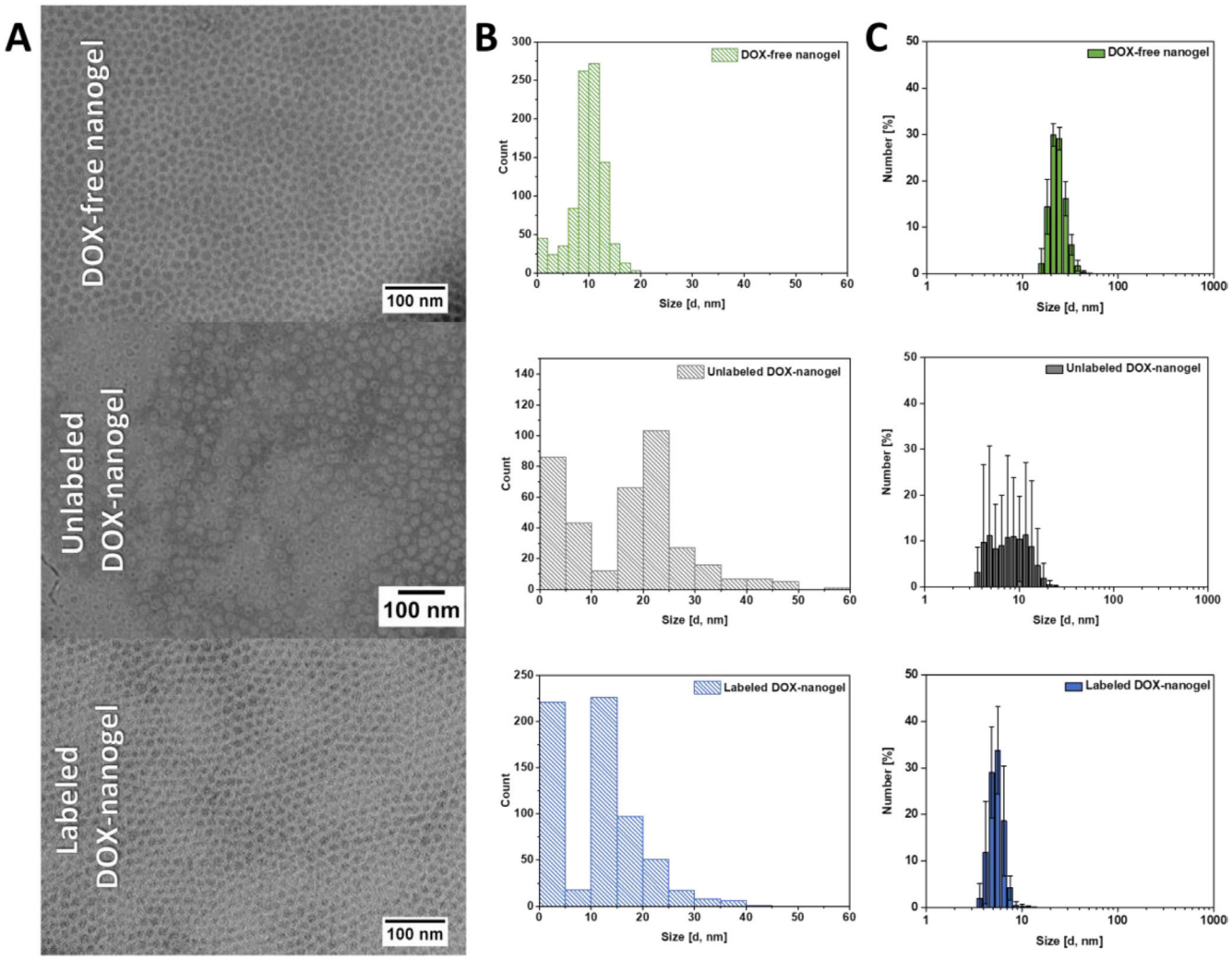

Supplementary Figure 6: (**A**) CryoTEM micrographs of DOX-free as well as labeled and unlabeled DOX-nanogels. (**B**) Size distribution histograms derived from cryoTEM image analysis using ImageJ. (**C**) Number weighted size distribution histograms as derived from Malvern Zetasizer software.

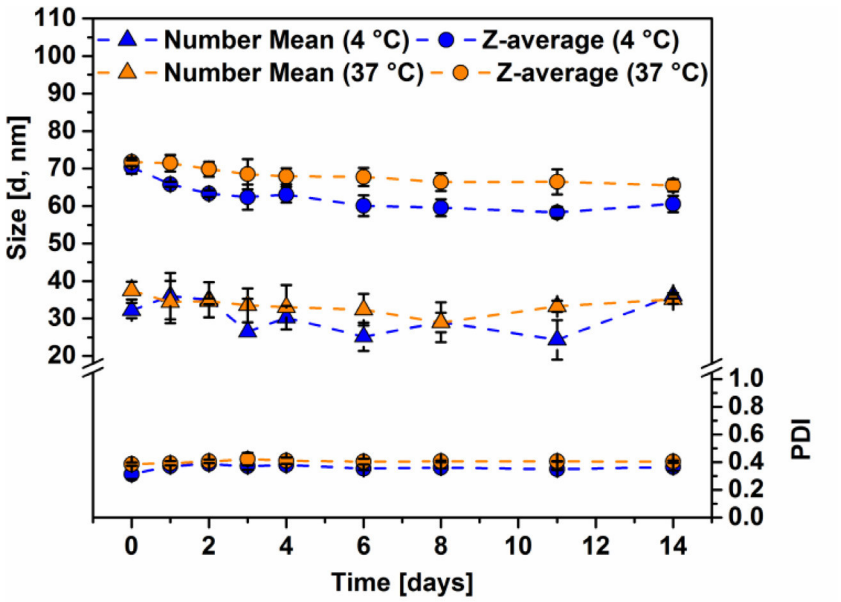

Supplementary Figure 7: Properties of labeled DOX-nanogels in 150 mM PBS (pH = 7.4) determined by DLS measurements. Nanogels were incubated at indicated temperatures for a certain time. Measurements were conducted at the indicated temperatures. PDI is derived from z-average.

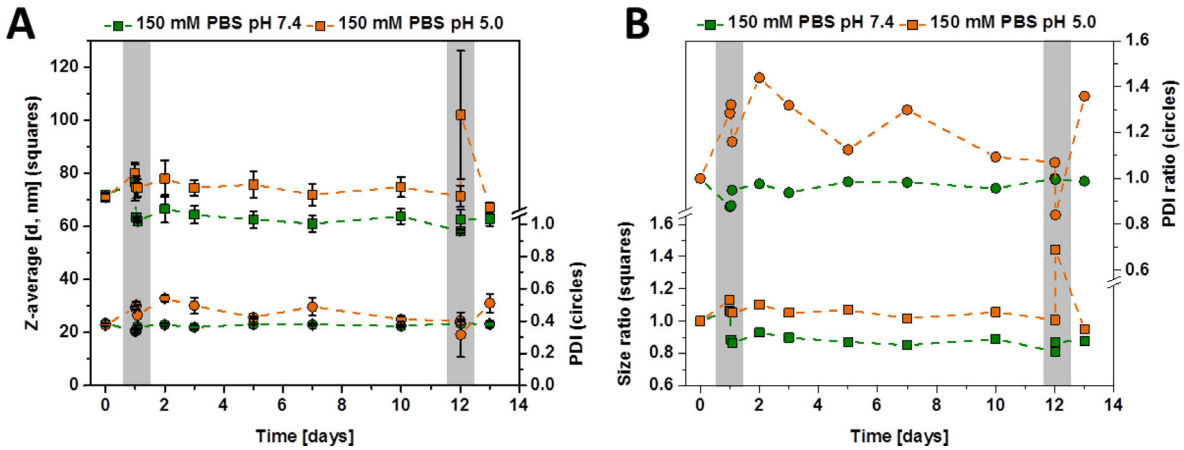

Supplementary Figure 8: Properties of labeled DOX-nanogels in 150 mM PBS (pH = 7.4 or 5.0) determined by DLS measurements. Nanogels were incubated at 37° C for a certain time. Measurements were conducted at 37° C. Grey boxes indicate time points of the addition of 100 mmol Glycine. (**A**) Actual values obtained by DLS measurements ($n = 3$, three measurements each). (**B**) Size and PDI ratios calculated by division of the value obtained on a certain day by the initial value (day 0).

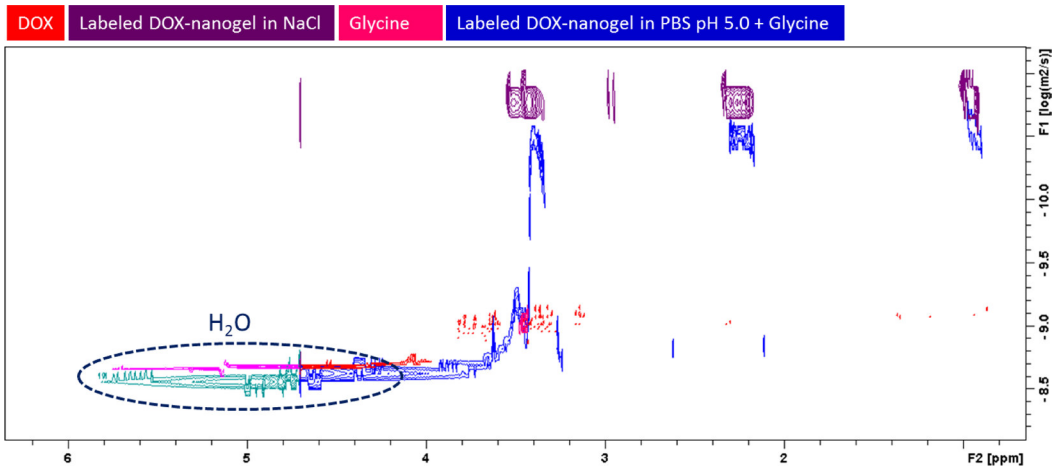

Supplementary Figure 9: Spectra of DOSY NMR (400 MHz, D2O) data of DOX in NaCl (red), the labeled DOX-nanogel in NaCl (purple), glycine (pink), and the labeled DOX-nanogel in PBS (pH = 5.0) + glycine. Peak superimpositions indicate similar diffusion coefficients of substances. Encircled area denotes water peak caused by the buffer. Peak overlays indicate similar diffusion coefficients of substances caused by the molar mass.

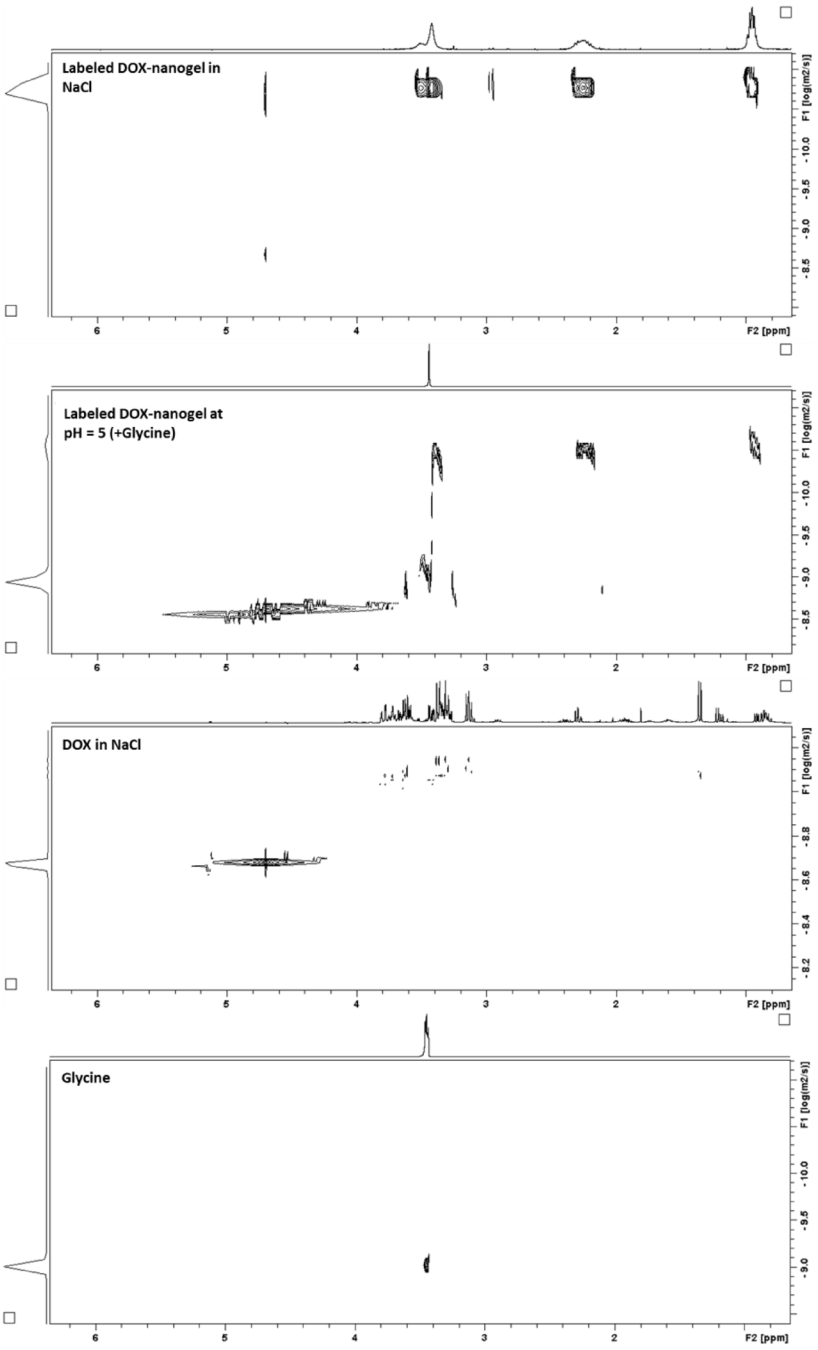

Supplementary Figure 10: Spectra of DOSY NMR (400 MHz, D_2O) data of the labeled DOX-loaded nanogel in PBS pH 5.0 + glycine, the labeled DOX-loaded nanogel in NaCl, DOX in NaCl and glycine (top to bottom).

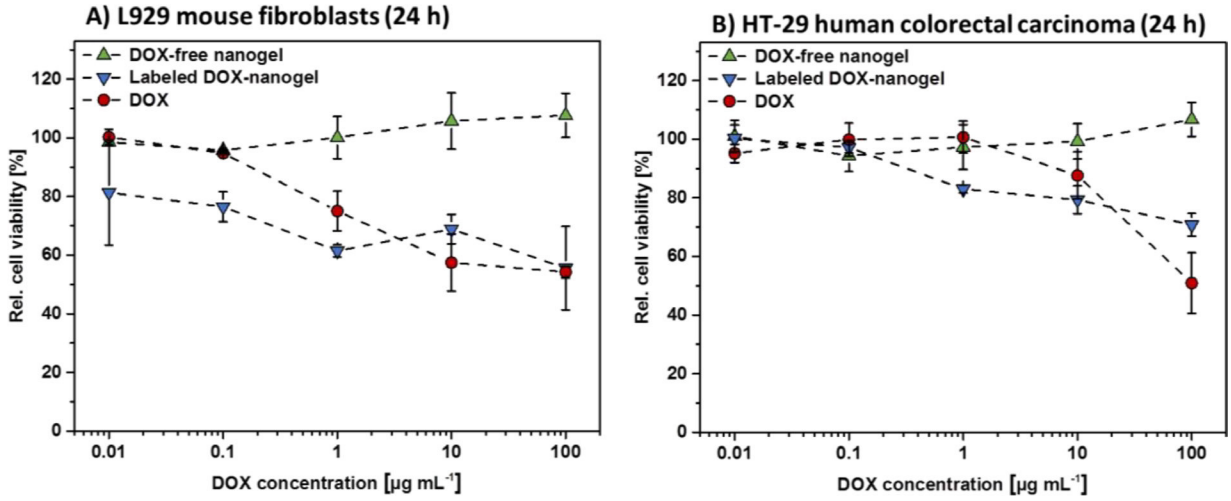

Supplementary Figure 11: Cytotoxicity of DOX-free nanogels, labeled DOX-nanogels as well as free DOX were determined by XTT assay. L292 mouse fibroblasts (**A**) as well as HT-29 human colorectal carcinoma cells (**B**) were incubated for 24 h. DOX loaded nanogels were used at a concentration where the amount of loaded drug resembles the amount of DOX used per data point (polymer concentration 17 times higher than DOX concentration). DOX-free nanogels were used at the same polymer concentration as labeled DOX-nanogels. Data are expressed as mean ± SD of six determinations.

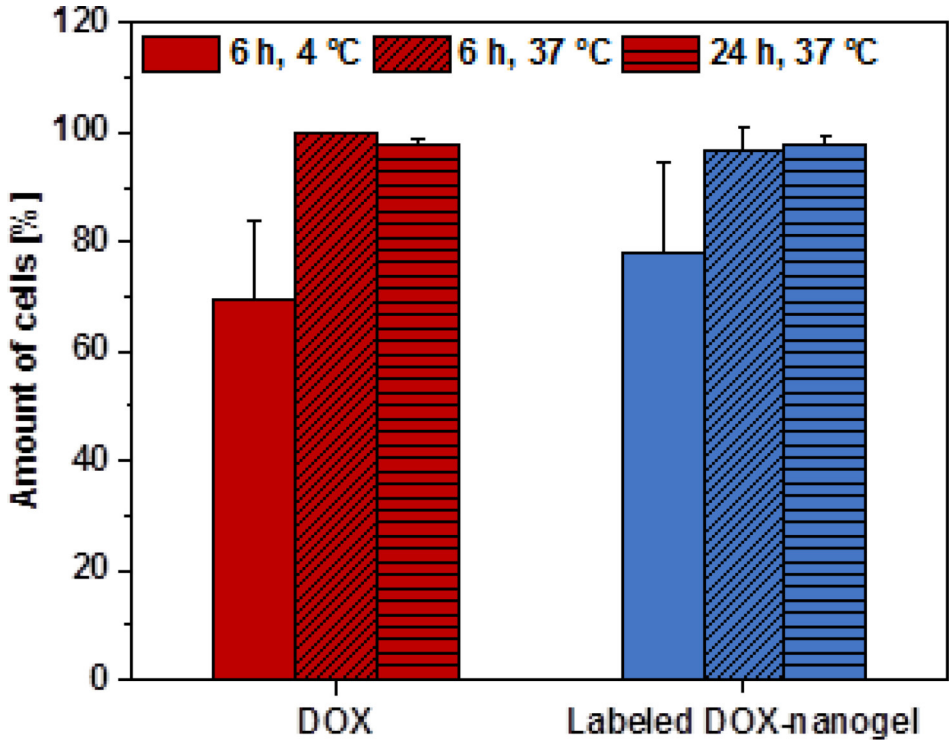

Supplementary Figure 12: Uptake of DOX and labeled DOX-nanogels into HT-29 cells (0.01 mg mL^{-1}) in dependence on the cultivation time and temperature. For MFI see Figure 3.

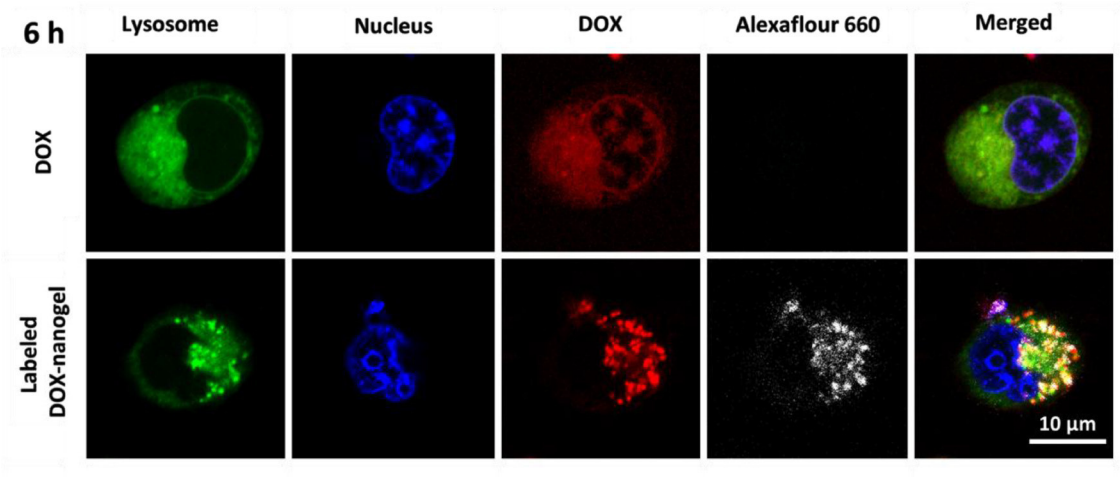

Supplementary Figure 13: CLSM images of free DOX as well as the labeled DOX-nanogels incubated with L929 mouse fibroblasts for 6 h. Lysosomal cellular compartments were stained green using LysoTracker Green DND-26 and the nucleus was labeled with Hoechst 33342 (blue). The fluorescence of DOX is depicted in red and the Alexafluor label of the polymer is shown in white.

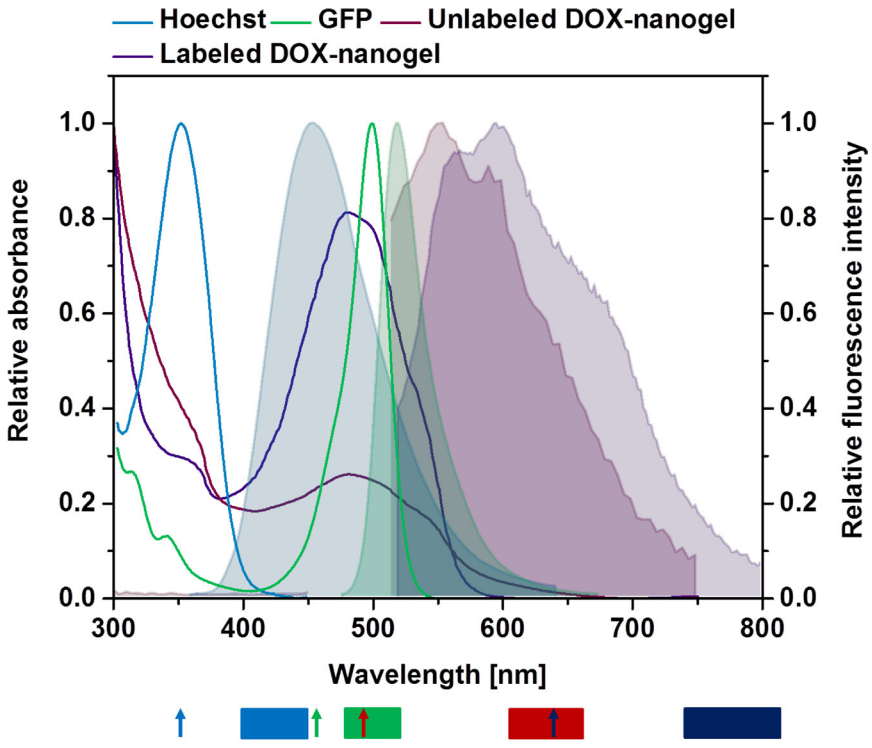

Channel	Name	Excitation [nm]	Emission [nm]
1	Hoechst	355	400 to 500
2	LysGFP	458	475 to 515
3	DOX	488	600 to 650
4	Polymer	633	725 to 800

Supplementary Figure 14: Absorption and emission spectra of dyes and compounds used in colocalization studies by CLSM.

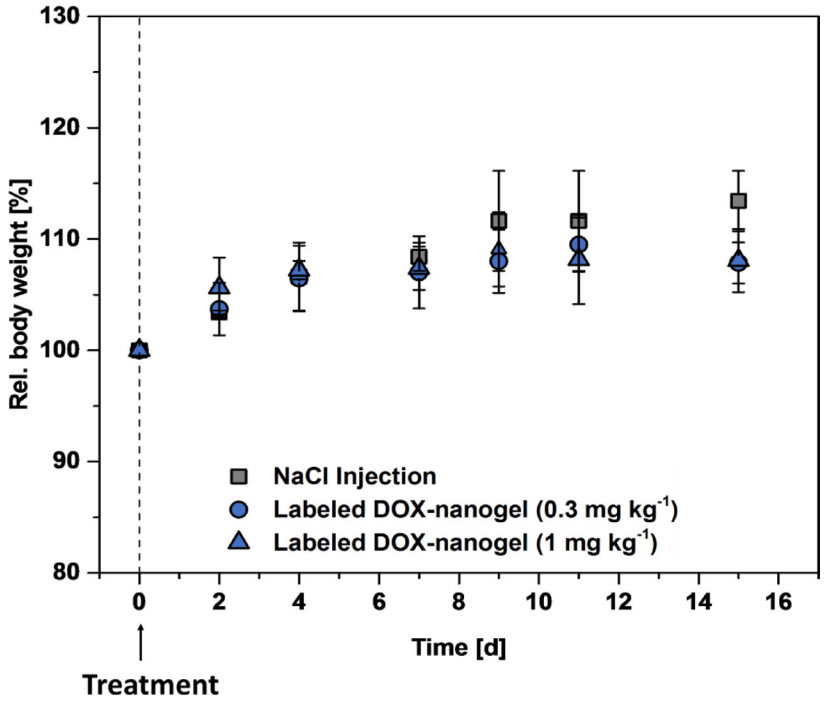

Supplementary Figure 15: Body weight development of male athymic nude mice after injection (dashed line) of a solution of labeled DOX-nanogel (corresponding to a DOX concentration of 0.3 or 1 mg kg^{-1}) dissolved in a 0.9 wt% NaCl solution or with the same volume of the 0.9 wt% NaCl solution as the negative control. Data are expressed as mean ± SD of 4 mice per group.

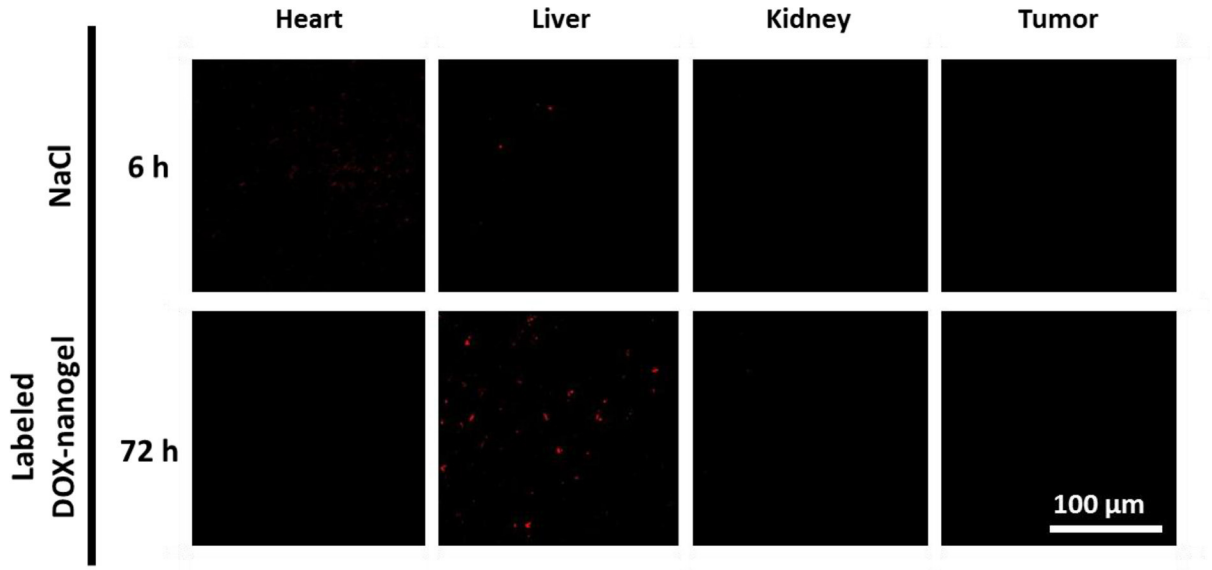

Supplementary Figure 16: Confocal fluorescence images of histological samples derived from organs of mice that were treated with either labeled DOX-nanogel (6) at 1 mg kg^{-1} or the same volume of a solution of 0.9 wt% NaCl in water. Fluorescence of DOX is shown in red. See Figure 7 for 6 h and 24 h samples of labeled DOX-nanogels (6).

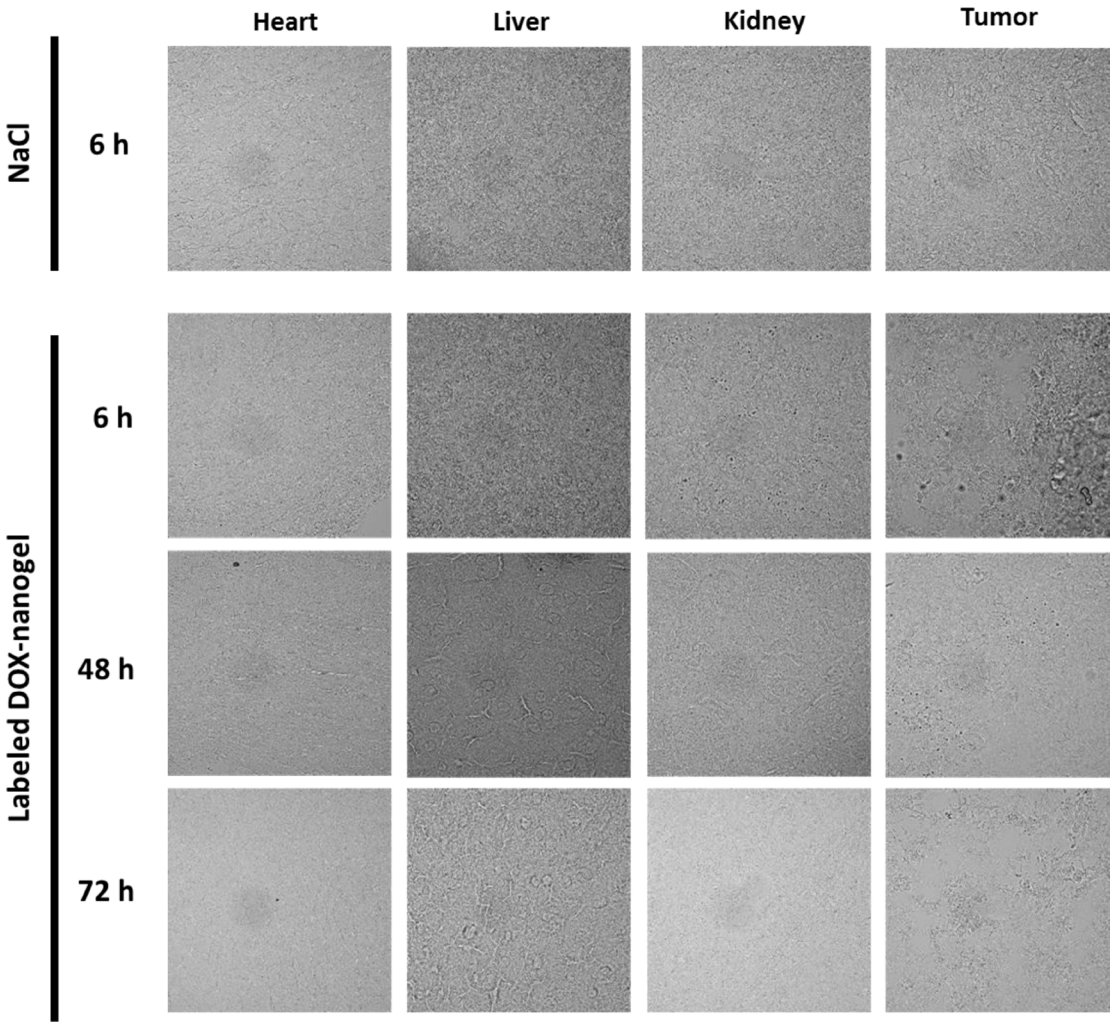

Supplementary Figure 17: Transmitted light CLSM measurements of histological samples derived from organs of mice that were treated with either labeled DOX-nanogel at 1 mg kg^{-1} or the same volume of a solution of 0.9 wt% NaCl in water. See Figure 7 for fluorescence pictures.

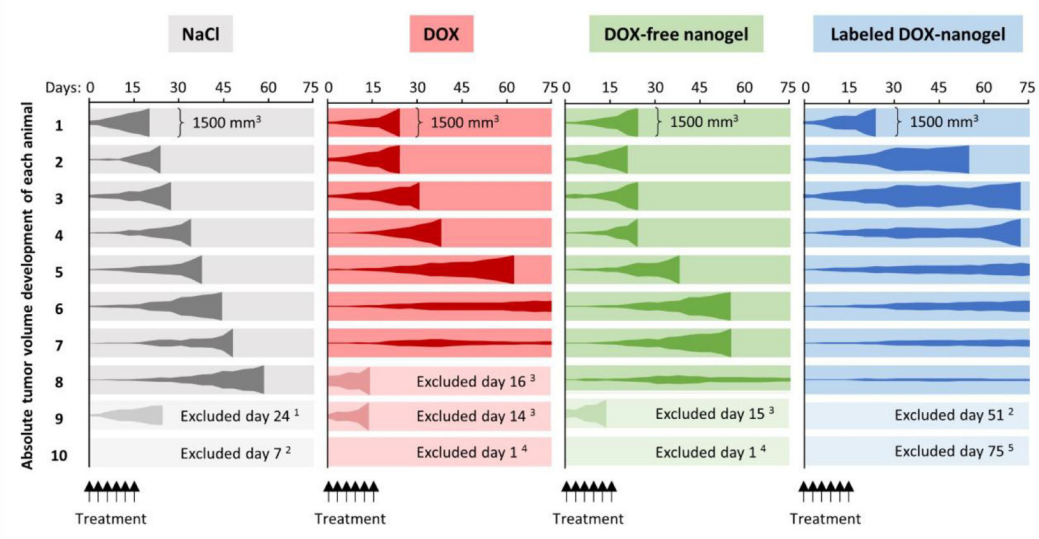

Supplementary Figure 18: Development of absolute tumor volume for each animal is illustrated over time from the beginning of treatment (day 0) until the maximum tumor volume of 1500 mm³ was reached. Male nude mice were subcutaneously injected with HT-29 cells. When tumors reached a volume of 100 to 200 mm³, mice received six doses of 0.9 wt% NaCl, DOX (1 mg kg-1), DOX-free nanogel and labeled DOX-nanogel (corresponding to 1 mg kg^{-1} DOX) via tail vein injection from day 0 to day 15. Individual animals were excluded from the study due to several reasons: [1]Termination because of infected wound, [2]Termination because of weight loss > 15%, [3]Termination because of maximum tumor volume before last injection, [4]Deceased during injection, 5 No palpable tumor.

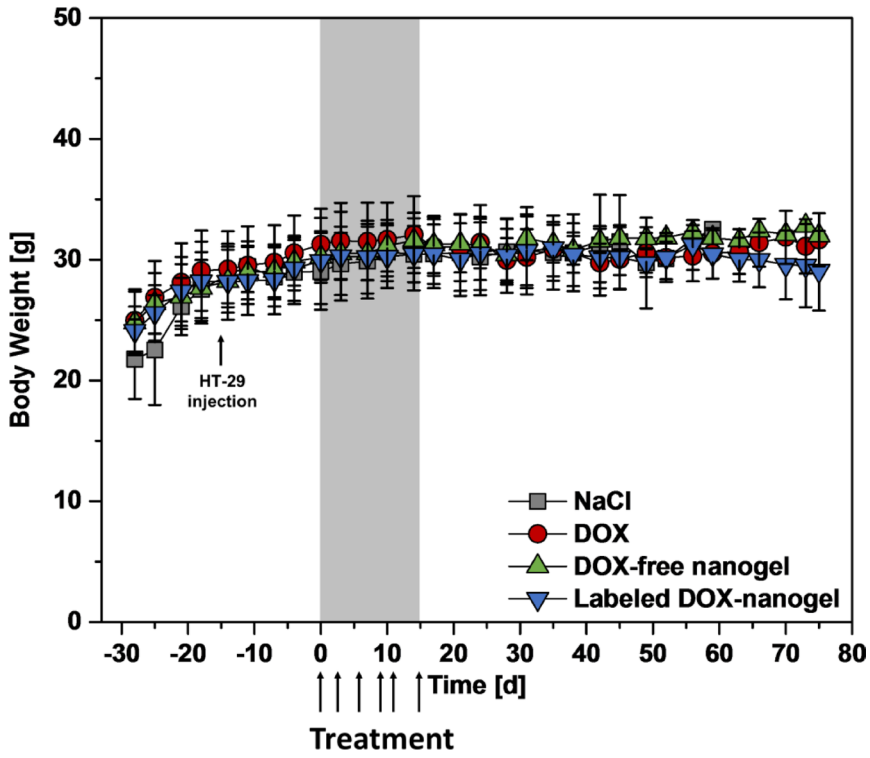

Supplementary Figure 19: Body weight development of male athymic nude mice over time from the beginning of the survival study until the maximum tumour volume of 1500 mm³ was reached. Mice bearing HT-29 derived tumors received 6 doses of 0.9 wt% NaCl, DOX (1 mg kg^{-1}), DOX-free nanogel and labeled DOX-nanogel (corresponding to 1 mg kg^{-1} DOX) via tail vein injection from day 0 to day 15 (shown as grey area). Data are expressed as mean ± SD of 7–8 mice per group.